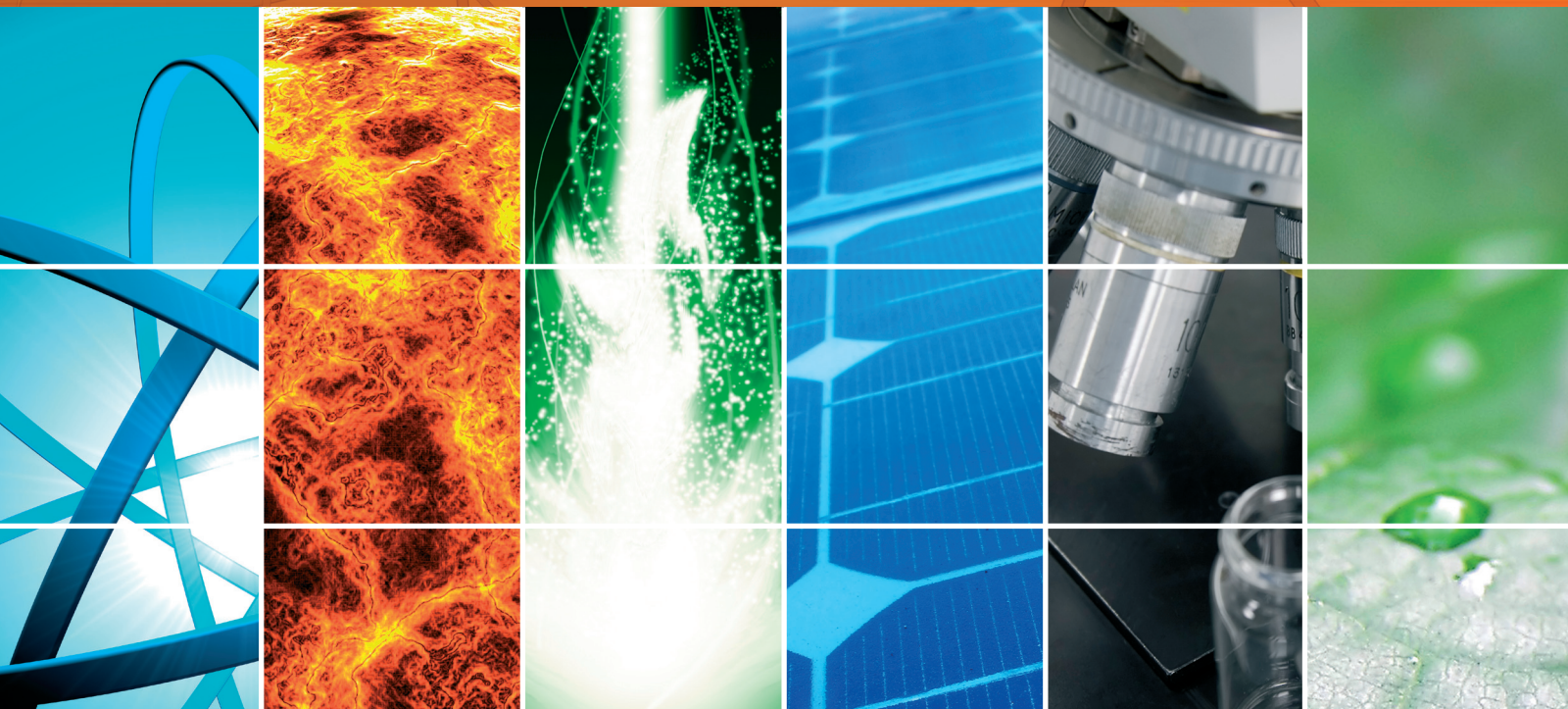


Thin-Film Photovoltaics 2013

Guest Editors: Gaetano Di Marco, Antonino Bartolotta,
Francesco Bonaccorso, Stefano Caramori, Giuseppe Calogero,
and Leonardo Palmisano





Thin-Film Photovoltaics 2013

International Journal of Photoenergy

Thin-Film Photovoltaics 2013

Guest Editors: Gaetano Di Marco, Antonino Bartolotta,
Francesco Bonaccorso, Stefano Caramori, Giuseppe Calogero,
and Leonardo Palmisano



Copyright © 2014 Hindawi Publishing Corporation. All rights reserved.

This is a special issue published in "International Journal of Photoenergy." All articles are open access articles distributed under the Creative Commons Attribution License, which permits unrestricted use, distribution, and reproduction in any medium, provided the original work is properly cited.

Editorial Board

M. Sabry Abdel-Mottaleb, Egypt
Nihal Ahmad, USA
Nicolas Alonso-Vante, France
Wayne A. Anderson, USA
Vincenzo Augugliaro, Italy
Detlef W. Bahnemann, Germany
Mohammad A. Behnajady, Iran
Ignazio Renato Bellobono, Italy
Raghu N. Bhattacharya, USA
Pramod H. Borse, India
Gion Calzaferri, Switzerland
Adriana G. Casas, Argentina
Wonyong Choi, Korea
Vra Cimrova, Czech Republic
Vikram Dalal, USA
Dionysios Dionysiou, USA
Mahmoud M. El-Nahass, Egypt
Ahmed Ennaoui, Germany
Chris Ferekides, USA
Beverley Glass, Australia
Mohammed A. Gondal, KSA
Shinya Higashimoto, Japan
Yadong Jiang, China

Chun-Sheng Jiang, USA
Shahed Khan, USA
Cooper Harold Langford, Canada
Yuexiang Li, China
Stefan Lis, Poland
Niyaz Mohammad Mahmoodi, Iran
Dionissios Mantzavinos, Greece
Ugo Mazzucato, Italy
Jacek Miller, Poland
Jarugu N. Moorthy, India
Franca Morazzoni, Italy
Fabrice Morlet-Savary, France
Ebinazar B. Namdas, Australia
Maria da Graa P. Neves, Portugal
Leonidas Palilis, Greece
Leonardo Palmisano, Italy
Ravindra K. Pandey, USA
David Lee Phillips, Hong Kong
Pierre Pichat, France
Gianluca Li Puma, UK
Xie Quan, China
Tijana Rajh, USA
Peter Robertson, UK

Avigdor Scherz, Israel
Lukas Schmidt-Mende, Germany
Panagiotis Smirniotis, USA
Zofia Stasicka, Poland
Juliusz Sworakowski, Poland
Nobuyuki Tamaoki, Japan
G. N. Tiwari, India
Nikolai V. Tkachenko, Finland
Veronica Vaida, USA
Roel van De Krol, Germany
Mark van Der Auweraer, Belgium
Ezequiel Wolcan, Argentina
Man Shing Wong, Hong Kong
David Worrall, UK
Fahrettin Yakuphanoglu, Turkey
Minjoong Yoon, Republic of Korea
Hongtao Yu, USA
Jimmy C. Yu, Hong Kong
Klaas Zachariasse, Germany
Lizhi Zhang, China
Jincai Zhao, China

Contents

Thin-Film Photovoltaics 2013, Gaetano Di Marco, Antonino Bartolotta, Francesco Bonaccorso, Stefano Caramori, Giuseppe Calogero, and Leonardo Palmisano
Volume 2013, Article ID 675321, 3 pages

Reliability Analysis of III-V Solar Cells Grown on Recycled GaAs Substrates and an Electroplated Nickel Substrate, Ray-Hua Horng, Ming-Chun Tseng, and Shui-Yang Lien
Volume 2013, Article ID 108696, 9 pages

Effect of TCO/ $\mu\text{c-Si:H}$ Interface Modification on Hydrogenated Microcrystalline Silicon Thin-Film Solar Cells, Shin-Wei Liang, Cheng-Hang Hsu, and Chuang-Chuang Tsai
Volume 2013, Article ID 756084, 6 pages

The Effect of Bandgap Graded Absorber on the Performance of $\text{a-Si}_{1-x}\text{Ge}_x\text{:H}$ Single-Junction Cells with $\mu\text{c-SiO}_x\text{:H}$ N-Type Layer, Hung-Jung Hsu, Cheng-Hang Hsu, and Chuang-Chuang Tsai
Volume 2013, Article ID 364638, 6 pages

Effects of Anodic Buffer Layer in Top-Illuminated Organic Solar Cell with Silver Electrodes, Tien-Lung Chiu, Himadri Mandal, Mi Zhang, Shun-Po Yang, and Ya-Ting Chuang
Volume 2013, Article ID 131984, 7 pages

Near Infrared Lateral Photovoltaic Effect in LaTiO_3 Films, Wujun Jin, Shasha Zhang, Hao Ni, Wenfeng Xiang, Jianfeng Xi, Xin Feng, and Kun Zhao
Volume 2013, Article ID 352738, 5 pages

Optical and Structural Investigation of CdSe Quantum Dots Dispersed in PVA Matrix and Photovoltaic Applications, Pallabi Phukan and Dulen Saikia
Volume 2013, Article ID 728280, 6 pages

Dye-Sensitized Solar Cells with Anatase TiO_2 Nanorods Prepared by Hydrothermal Method, Ming-Jer Jeng, Yi-Lun Wung, Liann-Be Chang, and Lee Chow
Volume 2013, Article ID 280253, 8 pages

Photovoltaic Performance of ZnO Nanorod and ZnO : CdO Nanocomposite Layers in Dye-Sensitized Solar Cells (DSSCs), Sule Erten-Ela
Volume 2013, Article ID 436831, 6 pages

Effects of Sulfurization Temperature on Properties of CZTS Films by Vacuum Evaporation and Sulfurization Method, Jie Zhang, Bo Long, Shuying Cheng, and Weibo Zhang
Volume 2013, Article ID 986076, 6 pages

Spectroscopic and Morphological Studies of Metal-Organic and Metal-Free Dyes onto Titania Films for Dye-Sensitized Solar Cells, Gabriella Di Carlo, Daniela Caschera, Roberta G. Toro, Cristina Riccucci, Gabriel M. Ingo, Giuseppina Padeletti, Luisa De Marco, Giuseppe Gigli, Giovanna Pennesi, Gloria Zanotti, Anna M. Paoletti, and Nicola Angelini
Volume 2013, Article ID 582786, 11 pages

Thin Film CIGS Solar Cells, Photovoltaic Modules, and the Problems of Modeling, Antonino Parisi, Luciano Curcio, Vincenzo Rocca, Salvatore Stivala, Alfonso C. Cino, Alessandro C. Busacca, Giovanni Cipriani, Diego La Cascia, Vincenzo Di Dio, Rosario Miceli, and Giuseppe Ricco Galluzzo
Volume 2013, Article ID 817424, 11 pages

Effectively Improved SiO₂-TiO₂ Composite Films Applied in Commercial Multicrystalline Silicon Solar Cells, Chih-Hsiang Yang, Shui-Yang Lien, Chia-Ho Chu, Chung-Yuan Kung, Tieh-Fei Cheng, and Pai-Tsun Chen
Volume 2013, Article ID 823254, 8 pages

Enhanced Photoelectrochemical Response from Copper Antimony Zinc Sulfide Thin Films on Transparent Conducting Electrode, Prashant K. Sarswat and Michael L. Free
Volume 2013, Article ID 154694, 7 pages

C-V Calculations in CdS/CdTe Thin Films Solar Cells with a CdS_xTe_{1-x} Interlayer, A. Gonzalez-Cisneros, F. L. Castillo-Alvarado, J. Ortiz-Lopez, and G. Contreras-Puente
Volume 2013, Article ID 513217, 4 pages

Effect of Hydrogen Content in Intrinsic a-Si:H on Performances of Heterojunction Solar Cells, Yun-Shao Cho, Chia-Hsun Hsu, Shui-Yang Lien, Dong-Sing Wu, and In-Cha Hsieh
Volume 2013, Article ID 121875, 6 pages

Numerical Simulation of Luminescent Downshifting in Top Cell of Monolithic Tandem Solar Cells, Mahfoud Abderrezek, Mohamed Fathi, Farid Djahli, and Mohammed Ayad
Volume 2013, Article ID 480634, 6 pages

Effects of Hole-Collecting Buffer Layers and Electrodes on the Performance of Flexible Plastic Organic Photovoltaics, Sungho Woo, Hong-Kun Lyu, Yoon Soo Han, and Youngkyoo Kim
Volume 2013, Article ID 398912, 8 pages

Enhanced Efficiency of GaAs Single-Junction Solar Cells with Inverted-Cone-Shaped Nanoholes Fabricated Using Anodic Aluminum Oxide Masks, Kangho Kim, Hoang Duy Nguyen, Sunil Mho, and Jaejin Lee
Volume 2013, Article ID 539765, 5 pages

Characterization and Modeling of CdS/CdTe Heterojunction Thin-Film Solar Cell for High Efficiency Performance, Hamid Fardi and Fatima Buny
Volume 2013, Article ID 576952, 6 pages

Nanostructured ZnO, TiO₂, and Composite ZnO/TiO₂ Films for Application in Dye-Sensitized Solar Cells, Myrsini Giannouli
Volume 2013, Article ID 612095, 8 pages

Material Properties of Laser-Welded Thin Silicon Foils, M. T. Hessmann, T. Kunz, M. Voigt, K. Cvecek, M. Schmidt, A. Bochmann, S. Christiansen, R. Auer, and C. J. Brabec
Volume 2013, Article ID 724502, 6 pages

The Effects of Malonic Acid Derivatives and Acetic Acid Derivatives as Coadsorbents on the Photovoltaic Performance of Dye-Sensitized Solar Cells, Hiroaki Matsuyoshi, Haruo Tomita, Hitoshi Nishino,
Hiroki Sakamoto, and Kyohei Manabe
Volume 2013, Article ID 439717, 6 pages

Advantages of N-Type Hydrogenated Microcrystalline Silicon Oxide Films for Micromorph Silicon Solar Cells, Amornrat Limmanee, Songkiate Kittisontirak, Sorapong Inthisang, Taweewat Krajangsang, Jaran Sritharathikhun, and Kobsak Sriprapha
Volume 2013, Article ID 513284, 5 pages

Editorial

Thin-Film Photovoltaics 2013

Gaetano Di Marco,¹ Antonino Bartolotta,¹ Francesco Bonaccorso,¹ Stefano Caramori,² Giuseppe Calogero,¹ and Leonardo Palmisano³

¹ CNR-IPCF, Istituto per i Processi Chimico-Fisici, Viale Ferdinando Stagno d'Alcontres 37, 98158 Messina, Italy

² Dipartimento di Chimica, Università degli Studi di Ferrara, Via L. Borsari 46, 44100 Ferrara, Italy

³ DEIM, Università degli Studi di Palermo, Viale delle Scienze, Edificio 6, 90128 Palermo, Italy

Correspondence should be addressed to Gaetano Di Marco; dimarco@its.me.cnr.it

Received 11 December 2013; Accepted 11 December 2013; Published 12 January 2014

Copyright © 2014 Gaetano Di Marco et al. This is an open access article distributed under the Creative Commons Attribution License, which permits unrestricted use, distribution, and reproduction in any medium, provided the original work is properly cited.

This special issue is the third edition in a series that has the purpose to collect original contributions by specialists in the field of thin-films photovoltaics (PVs). The fundamental mechanisms at the base of architectures and working principles of PV devices have been investigated both theoretically and experimentally. Particular attention has been paid to key aspects such as electronic transport in semiconducting materials, modelling, structural investigation, sensitizing agents, and so forth, with the aim to increase the efficiency of PV technologies. The contributions are very heterogeneous and although, for some articles, just proofs of principle devices are presented, for others a more viable commercial application can be foreseen. Here we give a brief overview, highlighting the main results, of the articles enclosed in this volume.

In *"The effects of malonic acid derivatives and acetic acid derivatives as coadsorbents on the photovoltaic performance of dye-sensitized solar cells"*, the coadsorption of malonic acid and acid derivatives are instrumental in improving both photocurrent and photovoltage of solar cells. This is probably due to suppression of self-quenching of the excited states and increased electron-injection yields, in parallel to suppression of electron recapture by I_3^- .

In *"Dye-sensitized solar cells with anatase TiO₂ nanorods prepared by hydrothermal method"*, the photoanode in the dye-sensitized solar cell (DSSC) can be optimized by improving the electron collection efficiency, as consequence of the exploitation of nanocrystalline materials with high purity, well-controlled crystallinity, and enhanced surface area such as hydrothermal anatase nanorods with a large surface roughness. These nanostructures can also be associated with TiO₂

nanoparticles to prepare highly efficient multiple layer photoanodes.

In *"Nanostructured ZnO, TiO₂, and composite ZnO/TiO₂ films for application in dye-sensitized solar cells"*, efficiency and stability of photoanodes obtained from composite semiconductor films (ZnO/TiO₂) and sensitized with the organic molecules Coumarin 343 and Rose Bengal are investigated. It is observed that DSSCs with ZnO/TiO₂ ratio equal to 90/10 have higher stability than the other cells. The performances of DSSCs using various multicomponent electrolytes are assessed.

In *"Spectroscopic and morphological studies of metal-organic and metal-free dyes onto titania films for dye-sensitized solar cells"*, the spectroscopic behavior of cis-di(thiocyanato)bis(2,2'-bipyridyl-4,4'-dicarboxylato)ruthenium(II) (N719), 3-(5-(4-(diphenylamino)styryl)thiophen-2-yl)-2-cyanoacrylic acid (D5), and a push-pull zinc phthalocyanine sensitizer (ZnPc) adsorbed onto three types of titania thin films with different morphology were investigated. The mesoporous titania films deposited by spin-coating and by doctor-blade were compared with P25 (Degussa) titania deposited by doctor-blade. The use of mesoporous structure allows increasing the dye loading and it is considered promising to realize thin titania photoanodes with high harvesting properties.

In *"Effects of hole-collecting buffer layers and electrodes on the performance of flexible plastic organic photovoltaics"*, the influences on the performance of flexible plastic organic photovoltaic (OPV) devices caused by the sheet resistance of hole-collecting electrodes (ITO) and by the conductivity of a hole-collecting buffer layers are investigated in detail. These

results indicated that the series resistance originating from the limited surface conductivity may quickly become a major issue to consider in the fabrication of large area cells.

In “*Photovoltaic performance of ZnO nanorod and ZnO:CdO nanocomposite layers in dye-sensitized solar cells (DSSCs)*”, a triphenylene diamine sensitizer was synthesized and its absorption spectra, electrochemical behavior, and photovoltaic performance for a potential application in DSSCs were investigated. In the study two different electrodes are employed: ZnO nanorod and ZnO:CdO nanocomposite. The best photovoltaic performance was demonstrated with the ZnO:CdO nanocomposite electrode based DSSCs with respect to the ZnO nanorod electrode one.

In “*Effects of anodic buffer layer in top-illuminated organic solar cell with silver electrodes*”, a relatively efficient molecular planar heterojunction is achieved by spinning a buffer layer of PEDOT:PSS on Ag-AgO_x anodes. The PEDOT:PSS thin film separates the active layer far from the Ag anode preventing metal quenching and redistributing the strong internal optical field toward dissociated interface. The thickness and morphology of this anodic buffer layer are the key factors in determining device performances.

In “*Effect of bandgap graded absorber on the performance of a-Si_{1-x}Ge_x:H single-junction cells with μ c-SiO_x:H N-type layer*”, the effect of bandgap grading of absorbers on the performance of a-Si_{1-x}Ge_x:H cells using μ c-SiO_x:H n-layer is reported. The influence of the p/i and the i/n grading widths on carrier collection and photon absorption in the cells were evaluated in terms of external quantum efficiency (EQE), total reflection spectra of cells, and the *J-V* measurement. Compared to those without grading, these cells show improved efficiency from 5.5 to 7.5%.

In “*Numerical simulation of luminescent downshifting in top cell of monolithic tandem solar cells*”, the performances in monolithic tandem solar cells is limited by the short-circuit current density matching between the top and the bottom cells. A theoretical survey of the luminescence downshifting approach for this device, in order to increase the short circuit current density in the top cell, is presented. The PV glass encapsulation material is replaced with Poly(methyl methacrylate) which is doped with diverse kinds of organic dyes.

In “*Effectively improved SiO₂-TiO₂ composite films applied in commercial multicrystalline silicon solar cells*”, a sol-gel spin-coating technique for fabricating composite films, alternative to plasma enhanced chemical vapor deposition (PECVD) for fabricating antireflective coatings (ARCs), useful to increase the efficiency of multicrystalline solar cells, is proposed. This result proves that sol-gel-deposited ARCs process has potential applications in manufacturing low-cost, large-area solar cells.

In “*Effect of hydrogen content in intrinsic a-Si:H on performances of heterojunction solar cells*”, the influences of hydrogen content in intrinsic hydrogenated amorphous silicon (i-a-Si:H) on performances of heterojunction (HJ) solar cells are investigated. Simulation and experimental results are performed to evaluate solar cells with higher i-layer hydrogen content and HJ solar cells with low hydrogen, respectively. The presence of voids and Si particles is explained from plasma point of view using optical emission spectroscopy.

In “*Characterization and modeling of CdS/CdTe heterojunction thin-film solar cell for high efficiency performance*”, device simulation is used to investigate the photoelectric efficiency in CdTe/CdSc solar cell. The roles of several limiting factors such as back contact Schottky barrier, doping density, thickness, recombination velocity, and extended CdTe layer are examined. Results obtained indicate that higher performance efficiency may be achieved by adding and optimizing an extended CdTe electron reflector layer at the back Schottky contact.

In “*Enhanced photoelectrochemical response from copper antimony zinc sulfide thin films on transparent conducting electrode*”, it is reported that the presence of zinc in copper antimony sulfide thin films influenced the photoelectrochemical performance and in particular gave rise to an enhancement of the photocurrent. A detailed investigation was carried out by changing the stoichiometry of films and the corresponding surface and optical characterization results have been evaluated.

In “*Material properties of laser-welded thin silicon foils*”, the properties of extended monocrystalline silicon base foils consisting of individual thin silicon wafers welded together are studied. The different approaches of (i) laser spot welding with low constant feed speed, (ii) laser line welding, and (iii) keyhole welding were compared. The cross-sections of the foils were analyzed by electron backscatter diffraction to reveal changes in the crystal structure after laser irradiation. The induced internal stress was investigated by micro-Raman analysis. The keyhole welding was found to be the most favorable process to produce thin silicon foils.

In “*Advantages of N-type hydrogenated microcrystalline silicon oxide films for micromorph silicon solar cells*”, a detailed investigation on the advantages to use N-type hydrogenated microcrystalline silicon oxide films in micromorph silicon solar cells is reported. The electrical and optical properties of the micromorph silicon solar cells were evaluated via the open circuit voltage, fill factor and the short circuit density.

In “*Enhanced efficiency of GaAs single-junction solar cells with inverted-cone-shaped nanoholes fabricated using anodic aluminum oxide masks*”, the growth and fabrication of GaAs solar cells with various methods are investigated. Anodized aluminum oxide masks were prepared from an aluminum foil by a two-step anodization method. Nanoholes were formed on the top surface of the solar cells after the anodized aluminum oxide mask removal. Photovoltaic and optical characteristics of the GaAs solar cells in the presence and in the absence of the nanohole arrays and the dependence of the efficiency enhancement on the etching depth of the nanoholes were investigated.

In “*Thin film CIGS solar cells, photovoltaic modules, and the problems of modeling*”, are focused on the methodological problems of modeling at cell structure and photovoltaic module levels for thin film CIGS solar cells. The structural cell simulation and the five-parameter analysis of a commercial CIGS module have been described. From their comparison, the authors have extracted the values of the local parasitic network resistance to be associated with the structural simulation of the cell, thus obtaining a good agreement between the two models.

In “Reliability analysis of III-V solar cells grown on recycled GaAs substrates and an electroplated nickel substrate”, the reliability of III-V solar cell grown on new/recycled GaAs substrate and thin-film solar cell transferred on electroplated Ni substrate has been explored. The work aims to achieve two basic goals. The first is to provide a thin-film solar cell characterized by high heat dissipation values and, in this context, the thermal conductivity κ of Ni ($=91 \text{ W/m}\cdot\text{K}$) is better than that of GaAs ($55 \text{ W/m}\cdot\text{K}$). The second target is to reuse the GaAs substrate after the epitaxial lift-off processing for cost reduction.

In “Optical and structural investigation of CdSe quantum dots dispersed in PVA matrix and its photovoltaic application”, the effect of the concentrations of the cadmium source on the optical properties of CdSe quantum dots (QDs) dispersed in polyvinyl alcohol (PVA) matrix thin films was investigated through UV-Vis absorption spectroscopy. The CdSe QDs were synthesized via simple heat induced thermolysis technique. The structural analysis, particle size determination, and morphological studies of the CdSe/PVA nanocomposite thin films were done with the help of X-ray diffraction (XRD) and transmission electron microscopy (TEM). Furthermore a CdSe/CdTe based solar cell was prepared and its photovoltaic parameters were measured and reported.

In “Near infrared lateral photovoltaic effect in LaTiO_3 films”, LaTiO_3 (LTO) films grown epitaxially by physical layer deposition (PLD) on SrTiO_3 (STO) substrate have shown great potential application in NIR position-sensitive detector. The irradiated as-grown LTO/STO structure presented a near infrared lateral photovoltaic effect, with the open-circuit photovoltage of the LTO film dependent on the laser beam position. It was demonstrated that photosensitivity can be modified with bias current.

In “Effect of TCO/ $\mu\text{c-Si:H}$ interface modification on hydrogenated microcrystalline silicon thin-film solar cells”, a very thin aluminum-doped zinc oxide (AZO) coating (3–5 nm) was capped onto the textured fluorine-doped tin oxide (FTO) glass to maintain high light trapping and preserve the quality of the TCO/ $\mu\text{c-Si:H}$ interface for c-Si:H single-junction solar cells. The AZO coating avoids the Sn reduction on the FTO surface during the Si-based thin-film deposition with hydrogen rich plasma exposure. The as-obtained $\mu\text{c-Si:H}$ cell exhibited a significantly higher J_{SC} from 15.97 to 19.40 mA/cm^2 and an increased conversion efficiency from 5.69% to 7.09%, with respect to standard FTO photoanode.

In “Effect of sulfurization temperature on properties of CZTS films by vacuum evaporation and sulfurization method”, copper zinc tin sulfur thin films (CZTS) thanks to their high absorption coefficient are suitable absorbers for thin-film solar cells. CZTS were prepared on glass substrates by vacuum evaporation and sulfurization method. The optimization of the thin-films deposition and sulfurization temperature permitted a control on their crystallite size, density, and consequently the electrical properties. The authors reported 1.49 eV, 9.37 $\Omega\cdot\text{cm}$, $1.714 \times 10^{17} \text{ cm}^{-3}$, and 3.89 $\text{cm}^2/(\text{Vs})$ for band gap energy, resistivity, carrier concentration, and mobility of the CZTS thin films, respectively.

In “C-V calculations in CdS/CdTe thin films solar cells with a $\text{CdS}_x\text{Te}_{1-x}$ interlayer”, theoretical effect of interlayer

ternary compound $\text{CdS}_x\text{CdTe}_{1-x}$ formation in CdS/CdTe solar cell, due to chemical interdiffusion interface, was evaluated. The authors predicted how the ternary layer acquires the properties of CdS behaving like an N-type semiconductor. The understanding of this “additive” interlayer will be useful for the optimization and efficiency improvement of CdS/CdTe thin-film solar cells.

Gaetano Di Marco
Antonino Bartolotta
Francesco Bonaccorso
Stefano Caramori
Giuseppe Calogero
Leonardo Palmisano

Research Article

Reliability Analysis of III-V Solar Cells Grown on Recycled GaAs Substrates and an Electroplated Nickel Substrate

Ray-Hua Horng,¹ Ming-Chun Tseng,¹ and Shui-Yang Lien²

¹ Graduate Institute of Precision Engineering, National Chung Hsing University, Taichung 402, Taiwan

² Department of Materials Science and Engineering, DaYeh University, Changhua 515, Taiwan

Correspondence should be addressed to Ming-Chun Tseng; tseng1026@dragon.nchu.edu.tw

Received 14 June 2013; Revised 30 October 2013; Accepted 4 November 2013

Academic Editor: Antonino Bartolotta

Copyright © 2013 Ray-Hua Horng et al. This is an open access article distributed under the Creative Commons Attribution License, which permits unrestricted use, distribution, and reproduction in any medium, provided the original work is properly cited.

This study involved analyzing the reliability of two types of III-V solar cells: (1) III-V solar cells grown on new and recycled gallium arsenide (GaAs) substrates and (2) the III-V solar cells transferred onto an electroplated nickel (Ni) substrate as III-V thin-film solar cells by using a cross-shaped pattern epitaxial lift-off (CPELO) process. The III-V solar cells were grown on new and recycled GaAs substrates to evaluate the reliability of the substrate. The recycled GaAs substrate was fabricated by using the CPELO process. The performance of the solar cells grown on the recycled GaAs substrate was affected by the uneven surface morphology of the recycled GaAs substrate, which caused the propagation of these dislocations into the subsequently grown active layer of the solar cell. The III-V solar cells were transferred onto an electroplated Ni substrate, which was also fabricated by using CPELO technology. The degradation of the III-V thin-film solar cell after conducting a thermal shock test could have been caused by microcracks or microvoids in the active layer or interface of the heterojunction, which resulted in the reduction of the external quantum efficiency response and the increase of recombination loss.

1. Introduction

High manufacturing cost is the major limitation for III-V electronic devices because the single crystal substrates (gallium arsenide, GaAs, or germanium, Ge, substrates) used to obtain the desired high crystalline quality are expensive. For example, multijunction III-V solar cells are always grown on single crystal GaAs substrates to prevent the degradation of the high bandgap junction caused by misfit dislocation from the low bandgap junction [1].

In general, single crystal substrates do not involve the photovoltaic effect. Therefore, the epitaxial structure of III-V solar cells can be transferred to any desired functional substrate [2]. Lightweight substrates [3] and materials with high thermal conductivities [4] can also be used as carrier substrates in space and terrestrial concentrator applications, respectively. Aluminum arsenide (AlAs) layers are usually used as the sacrificial layer between GaAs substrates and solar cell structures; therefore, epitaxial lift-off (ELO), a recycled

substrate method, could potentially lower manufacturing costs. The chemical etchant used for the ELO process is an aqueous HF solution. However, prolonged exposure to the HF etchant increases the surface roughness of a wafer because of the byproduct from the chemical reaction between AlAs and the HF etchant [5], preventing the direct reuse of wafer and deteriorating the performance of a solar cell. To solve this problem, using different concentrations of chemical etchant to modify surface morphology of wafer was proposed [6]. Chemical cleaning is difficult to conduct because the etching mechanisms are sensitive to wafer contamination. Furthermore, the IBM Corporation [5] proposed using a surface-tension-assisted epitaxial lift-off (STA-ELO) process to separate a device layer from a GaAs substrate by using aqueous hydrochloric acid (HCl), which selectively etches an AlInP sacrificial layer inserted between the device film and the substrate. The novel ELO process minimizes the amount of postetching residue and keeps the surface smooth, which leads to the direct reuse of the GaAs substrate.

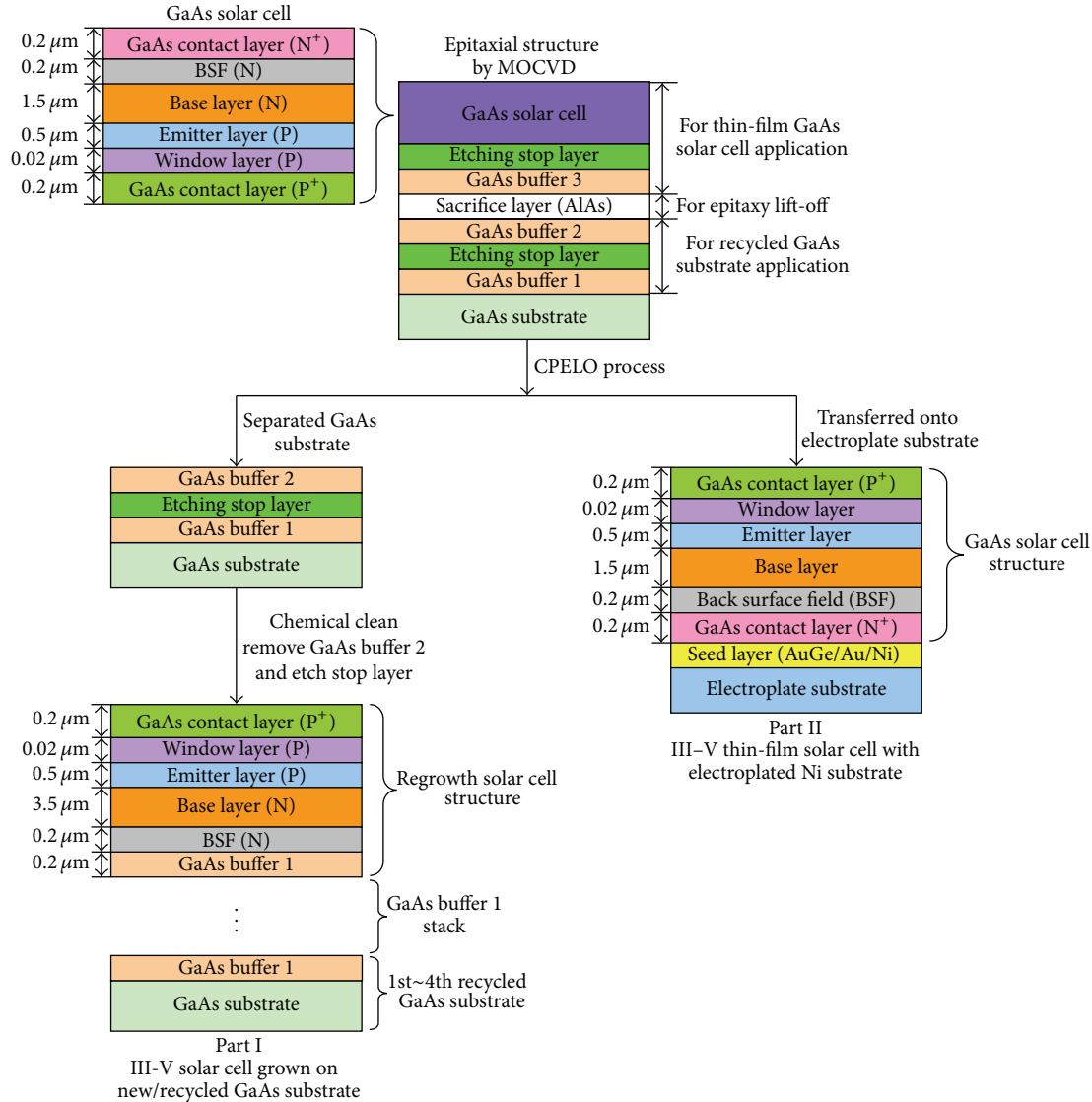


FIGURE 1: Device fabrication flowchart of experiment design.

In our previous study [7], an etching stop layer was added to the epitaxial structure of a III-V solar cell to prevent damage to the GaAs substrate caused by prolonged exposure to the HF solution. In addition, the etching stop layer protected the device structure of thin-film III-V solar cells during the lift-off process. Exposing the GaAs substrate to the HF solution roughens the surface of the GaAs substrate, which could be avoided by using a special epilayer design: GaAs substrate/GaAs buffer 1/etching stop layer/GaAs buffer 2/sacrificial layer/GaAs buffer 3/etch stop layer/device structure. Optimally, the GaAs substrate can be reused twice [7]. Applying the proposed technique substantially reduces the manufacturing cost. In this study, the performance reliability of an III-V solar cell grown on new and recycled GaAs substrates and III-V solar cells transferred onto an electroplated nickel (Ni) substrate as III-V thin-film solar cells were studied.

2. Experiments

Single junction GaAs solar cells were epitaxially grown by using low-pressure metalorganic chemical vapor deposition on 2-inch-diameter (100) GaAs wafers with a misorientation of 15° toward (111). The growth temperature and reactor pressure were 650°C and 60 mbar, respectively. The device fabrication flowchart is shown in Figure 1. The epitaxial structure of the GaAs solar cell consisted of GaAs buffer 1/etching stop layer/GaAs buffer 2/sacrifice layer (AlAs)/GaAs buffer 3/etching stop layer/heavily Mg-doped GaAs contact layer (0.2 μm)/Ga_{0.49}In_{0.51}P:Mg window layer (0.02 μm)/GaAs:Mg emitter layer (0.5 μm)/GaAs:Si base layer (1.5 μm)/Ga_{0.49}In_{0.51}P:Si back surface field (BSF; 0.2 μm)/heavily Si-doped GaAs contact layer (0.2 μm) (top of Figure 1). The GaAs solar cell structure was transferred onto

an electroplated Ni substrate with a mirror structure as III-V thin-film solar cell by using a cross-shaped pattern epitaxial lift-off (CPELO) process, which is denoted as the “TF cell” and shown in the bottom right of Figure 1.

After the CPELO process was complete, the GaAs buffer 3 and etching stop layer were removed using a chemical solution. AuGe/Au/Ni (50/150/300 nm) metal films were used to define the cross-shaped pattern array using photolithography. A cross-shaped hole was etched by using inductively coupled plasma-reactive ion etching (ICP-RIE) from the heavily Si-doped GaAs contact layer (N^+) to GaAs buffer 2. The metal layer (AuGe/Au/Ni) provided a hard mask for the ICP-RIE dry etching process as well as a seed layer for the subsequently used Ni substrates (50 μm thick), which were directly electroplated onto the bottom of the solar cell without using an adhesive layer. The bottom contact metal of the AuGe/Au/Ni layer was deposited onto the heavily Si-doped GaAs contact layer (N^+) by using a thermal evaporation system. AuGe/Au/Ni functioned as an ohmic contact with the solar cell and a metal reflector for incident light. Details on the CPELO process, recycled GaAs substrate process, and solar cell fabrication process are described in the authors’ previous study [7]. In this study, a conventional single junction solar cell was grown on the recycled GaAs substrate to evaluate the quality of this substrate, as shown in the bottom left of Figure 1. The regrowth and chemical cleaning process was repeated 1–4 times after performing the ELO process to form a recycled GaAs substrate. The solar cell fabricated on the new GaAs substrate was prepared and labeled “Initial” for comparison. The solar cell structures grown on the GaAs substrate were labeled “1st,” “2nd,” “3rd,” and “4th” according to the number of times they were recycled for comparison. The solar cell fabrication procedure is described as follows. First the front grid metal of AuBe/Au with coverage of approximately 10% was deposited and annealed. After that, the bottom contact metal of AuGe/Au was deposited on the heavily Si-doped GaAs layer by using thermal evaporation. Finally, SiO_2 ($n = 1.42$) and TiO_2 ($n = 2.32$) were deposited on the top surface as an antireflection coating to reduce the surface reflection of the solar cell. The external quantum efficiency (EQE) was measured by using the Newport-Oriel IQE-200 system with a quartz-tungsten halogen lamp and monochromator at 25°C. The spot size was 1 mm \times 1 mm. The AM1.5G solar irradiation was obtained from a 150 W solar simulator (SAN-EI XES-40S1) with a one-sun air mass 1.5 global filter, and a 100 mW/cm^2 light intensity was calibrated using a Si-based reference cell with a KG-5 filter at 25°C. The photovoltaic parameters underwent continuous strong light soaking in a home-built test facility, consisting of a xenon lamp light source and a heater system. The solar cells were heated to 60°C and exposed to the xenon lamp (200 mW/cm^2) to estimate the reliability of using the recycled GaAs substrate to grow solar cells. A thermal shock test of the III-V thin-film solar cells was performed 1500 times at temperature cycles of -40°C – 150°C at a ramp setting of 40°C/min and a dwell time of 5 min.

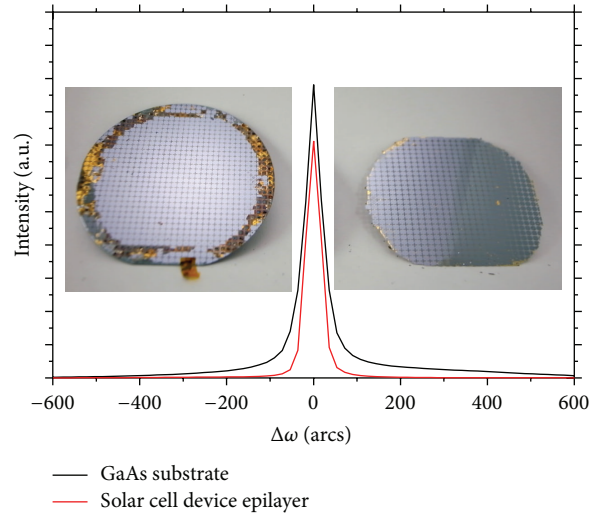


FIGURE 2: (004) XRD rocking curves of solar cell device epilayer and GaAs substrates (the y -axis is shown in linear scale). The left insert figure is GaAs substrate after epitaxial lift-off and without chemical cleaning; right insert figure is solar cell device epilayer transferred to the Ni substrate.

3. Results and Discussion

3.1. Analysis of the Recycled GaAs Substrates. Evaluating the quality of the thin epilayer transferred to the Ni substrate is crucial. The GaAs substrate and the solar cell device epilayer with the Ni substrate were examined by using X-ray diffraction (XRD) rocking curves of the (004) reflection to confirm crystalline quality, as shown in Figure 2. Based on the XRD results, the full widths at half maximum of the 350 μm -thick GaAs substrate and solar cell device epilayer on the Ni substrate were 53 and 54 arcsec, respectively. The inset of Figure 2 shows a photograph of the 2 inch GaAs epilayer transferred onto the Ni substrate and the separated GaAs substrate before they were chemical cleaning. On the left side of Figure 2, the gold ring on the edge of the separated GaAs substrate was the residual seed layer of the electroplating process and was removed during the chemical cleaning process. The practical area of the electroplating process was the center of the blackness zone of the separated GaAs substrate. Therefore, the area of the solar cell device epilayer transferred onto the electroplated Ni substrate was slightly smaller than a diameter of 2 inches. The diameter of the electroplated Ni substrate was reduced to 6 mm because of the electroplating process (compared with the 2-inch GaAs substrate); the electroplated Ni substrate with solar cell device epilayer is shown on the right side of Figure 2.

Figure 3 shows the electronic properties of the single junction solar cells grown on the new and recycled GaAs substrates. The detailed performance of the initial and the 1st–4th solar cell devices is summarized in Table 1. The reverse-bias dark I-V characteristics in a p-n junction can serve as sensitive tools for monitoring crystalline defect reduction [8]. The solar cells can be measured to confirm the presence of recombination centers; a comparison of the solar cells

TABLE 1: Performance of III-V solar cell grown on new/recycled GaAs substrate and GaAs thin film solar cell transferred onto Ni substrate before and after thermal shock test.

| | V_{oc} (V) | J_{sc} (mA/cm ²) | FF (%) | η (%) | I_{01} (A) | I_{02} (A) | R_s (Ω) | R_{sh} (Ω) |
|---|--------------|--------------------------------|--------|------------|------------------------|------------------------|--------------------|-----------------------|
| III-V solar cells grown on new and recycled GaAs substrate | | | | | | | | |
| Recycled times | | | | | | | | |
| Initial device | 0.99 | 22.59 | 81.54 | 18.23 | 1.34×10^{-20} | 1.69×10^{-13} | 15.6 | 3.23×10^6 |
| 1st device | 0.99 | 22.42 | 80.86 | 17.94 | 8.22×10^{-20} | 2.52×10^{-12} | 17.4 | 2.80×10^6 |
| 2nd device | 0.97 | 22.47 | 80.47 | 17.53 | 1.06×10^{-19} | 5.22×10^{-12} | 19.4 | 2.30×10^6 |
| 3rd device | 0.83 | 20.64 | 76.52 | 13.10 | 2.01×10^{-17} | 6.33×10^{-11} | 43.5 | 1.07×10^6 |
| 4th device | 0.82 | 19.40 | 74.01 | 11.77 | 3.72×10^{-17} | 4.05×10^{-11} | 56.5 | 1.47×10^5 |
| Performance of GaAs thin films solar cell with Ni substrate before and after thermal shock test | | | | | | | | |
| Thermal shock test times | | | | | | | | |
| 0 time | 0.99 | 22.37 | 80.01 | 17.71 | 3.32×10^{-20} | 2.47×10^{-12} | 15.8 | 3.10×10^6 |
| 800 times | 0.98 | 21.74 | 78.48 | 16.72 | 5.54×10^{-20} | 3.32×10^{-12} | 21.8 | 2.10×10^6 |
| 1200 times | 0.97 | 21.10 | 77.89 | 15.94 | 6.02×10^{-20} | 4.24×10^{-12} | 27.5 | 1.25×10^6 |
| 1500 times | 0.95 | 20.19 | 76.41 | 14.65 | 1.70×10^{-19} | 5.50×10^{-12} | 43.3 | 2.50×10^5 |

I_{01} and I_{02} : diode saturation current, R_s : series resistances, and R_{sh} : shunt resistances.

Initial device: the GaAs solar cell grown on new GaAs substrate; 1st, 2nd, 3rd, and 4th devices: the GaAs solar cell grown on recycled GaAs substrate.

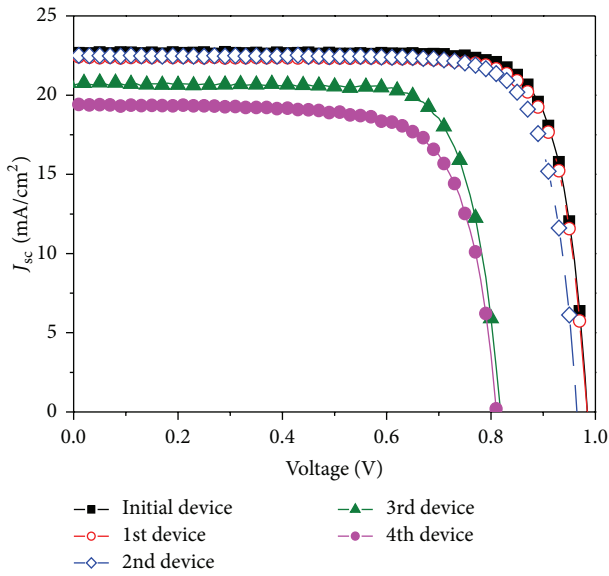


FIGURE 3: Photovoltaic performance comparison of single-junction solar cells grown on the new and recycled GaAs substrate.

grown on the new and recycled GaAs substrates is shown in Figure 4. The reverse-bias leakage current of the solar cell was increased at the reverse bias of 5 V when the GaAs substrate was recycled because of the high amount of recombination centers in the depletion region. The high reverse-bias leakage current was caused by defects in the solar cells; crystalline deformation and strain relaxation were expected to form recombination centers and deteriorate the performance of the solar cells by increasing the reverse-bias leakage current.

The EQE responses of the solar cells grown on the new and the recycled GaAs substrates (Figure 5) were measured to evaluate the effect of crystalline defects on photovoltaic performance. The overall profile of the EQE responses was

clearly influenced by the recycled number of GaAs substrate. As shown in Figure 5(a), the EQE response of the solar cells grown on the new GaAs substrate (the initial device) was considerably higher than that of the solar cells grown on recycled GaAs substrates (the 1st–4th devices), especially at the wavelength range of 600 to 870 nm (details are shown in the inset of Figure 5(a)). This could be attributed to the increase in density of defects [9], such as dislocation defects, strain-relaxation induced dislocation, or recombination loss. Generally, the EQE response of a solar cell can be attributed to the following three factors: the absorption coefficient of the active layer, surface recombination velocity, and minority carrier lifetime [10]. The absorption coefficient and the surface recombination velocity are dependent on the thicknesses of the active layers and the window layer. These factors mainly depend on epilayer quality, especially minority carrier lifetime. The defective creations resulted in a short minority carrier lifetime, which contributed to the high reverse saturation current of the solar cells and the poor EQE responses at all wavelengths. Solar cells with higher EQE response probably have longer minority-carrier lifetimes. As shown in Figure 5(b), the EQE responses of the solar cells grown on the new and the recycled GaAs substrates measured after a light soaking test were lower than those measured before the light soaking test.

3.2. Reliability Analysis of the III-V Thin-Film Solar Cell. The thermal shock test (TST) is crucial for III-V thin-film solar cells with Ni substrates because of the considerable mismatch in thermal expansion coefficients between the epilayers ($6.5 \times 10^{-6}/K$) and Ni ($13.4 \times 10^{-6}/K$). The performance of the thin-film GaAs solar cells after conducting 1500 thermal shock tests is shown in Figure 6. The performance of 20 cell samples was summarized, with an error bar to further evaluate the quality of the thin-film GaAs solar cells. The 20 different cell samples were selected from two-time experimental results. The corresponding open circuit voltage (V_{oc}), short circuit

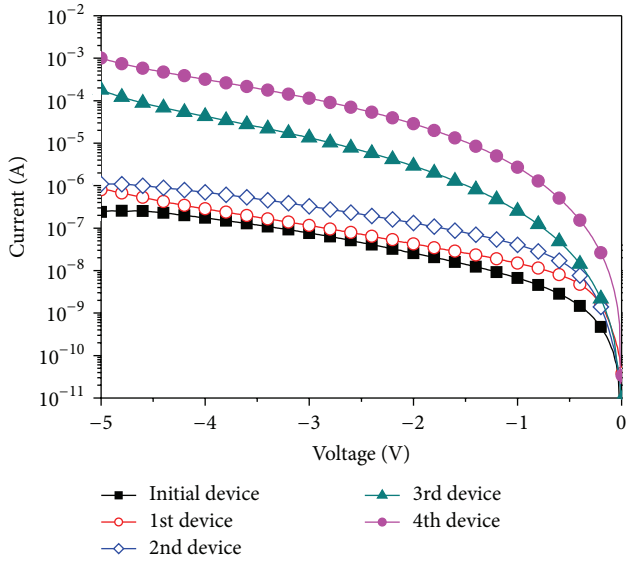


FIGURE 4: Reverse-bias dark I-V characteristics of the solar cells grown on new and recycled GaAs substrate.

current density (J_{sc}), fill factor (FF), and η for the TF cells were collected from the closed square point of the y -axis by using an error bar to further investigate the degradation of thin-film solar cells (summarized in Table 1).

The performance of the TF-cells did not substantially degrade before 800 thermal shock tests. After 1200 thermal shock tests, the performance of the TF-cells was 90% lower than the initial performance. The degradation of TF-cells could be attributed to two reasons: the presence of a microcrack in the epilayer or microvoids in the electroplated substrate/seed layer interface or seed layer/epilayer interface. Microcracks can cause a solar cell's current leakage rate to increase, which deteriorates V_{oc} and J_{sc} [11]. Moreover, the microvoids could cause the deformation of the GaAs epilayer, resulting in dislocation (misfit or threading dislocations) at the heteroepitaxial interface. The distortion of the heteroepitaxial interface causes the doping concentration of the epilayer to decrease, which further reduces the FF [12, 13].

A scanning acoustic microscope (SAM) equipped with a 140 MHz probe (SAM, Hitachi FS300II) was used to examine whether microcracks or microvoids existed in the the electroplated substrate/seed layer or seed layer/epilayer interfaces after the thermal shock tests. The SAM images (shown in Figure 7) show that no substantial microcracks existed in the epilayer with the Ni substrate.

Moreover, scanning electron microscopy (SEM) was performed to examine the surface morphology of the TF-cells after the thermal shock tests were conducted and to further observe the microcracks or microvoids. Figure 8(a) shows the electrode pattern for the TF cells. Figures 8(b)–8(d) show the surface morphologies of the TF cells at amplification factors of 3000 \times , 5000 \times , and 7000 \times . The SEM images did not show substantial microcracks in the epilayer, on which the thermal

shock test was performed 1500 times. Two reasons could explain this observation. First, SAM and, especially, SEM cannot provide overall observations of high amplification factors. The observational image area was small for high amplification factors; therefore, some details could have been missed when performing SEM. Second, the deformation of the GaAs epilayer may have caused dislocation (misfit or threading dislocations) in the epilayer structure. The dislocation could not propagate to the surface; therefore, it could not be observed on the surface by using SEM or SAM. The SEM and SAM images cannot exhibit distortion of the crystalline structure or dislocation (misfit or threading dislocations) at the epilayer structure, confirming the reason for the deterioration of the GaAs thin-film solar cells transferred onto the electroplated substrate after thermal shock tests. The reverse-bias dark I-V curves and double diode modes of the solar cells are provided in Section C to further understand the degradation of thin-film solar cells.

The EQE responses of the solar cells transferred onto the electroplated Ni substrate undergone various numbers of thermal shock test times, which were used to evaluate the effects of mismatched thermal expansion coefficients on the photovoltaic performance, are shown in Figure 9. The overall profiles of the EQE responses were clearly influenced by the number of thermal shock tests. This could be because of the substantial mismatch in thermal expansion coefficients that distorted the crystalline quality of the active layers by generating dislocations (e.g., the increased leakage current and recombination loss). The dislocations were associated with threading dislocations, which propagate upward through the epilayer to the surface or active layer of solar cells. The propagation of dislocations influences the interface defects of solar cells in the heterostructure (e.g., the window/emitter layer and base/BSF layer). The performance of solar cells is considerably influenced by the heterostructure design.

Two types of surface recombination occurred in the solar cells. The first type of surface recombination (labeled S_p) occurred in the interface of the windows/emitter layer, and the second type (labeled S_n) occurred in the interface of the base/BSF layer. A high S_p caused the blue response (the range of short wavelengths) [14, 15] to decrease dramatically. However, a high S_p also caused a reduction in the red response (the range of long wavelengths). By contrast, a high S_n caused a reduction only the in red response [16]. An increase in the surface recombination of solar cells also increases the dark current of the solar cells, reducing the V_{oc} . To confirm this observation, the double diode mode of the solar cells and the reverse-bias dark I-V characteristics are provided.

The reverse-bias leakage currents of the solar cells were measured to confirm the presence of recombination centers. The comparisons of solar cells that underwent various numbers of thermal shock tests are shown in Figure 10. When 800 thermal shock tests were performed, the reverse-bias leakage currents of solar cells were drastically increased at the reverse bias of 5 V because of the great amount of recombination centers in the depletion region. A dramatic decrease of 3

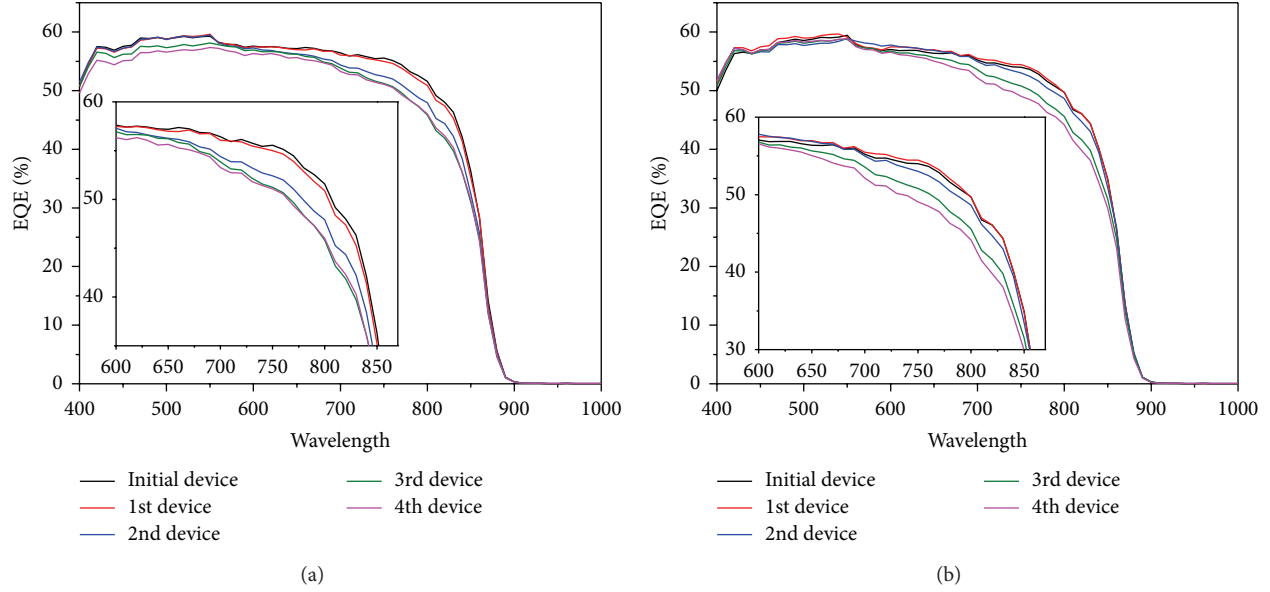


FIGURE 5: EQE responses of solar cell grown on new and recycled GaAs substrate; (a) before light soaking test (b) with light soaking test of 267 hours. (The inset figure is the magnification of EQE curve at wavelength from 600 to 870 nm.)

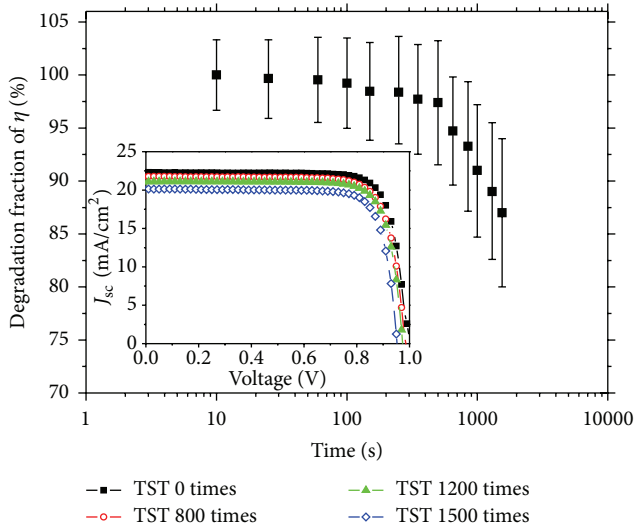


FIGURE 6: The degradation fraction of conversion efficiency for GaAs thin-film solar cell transferred to electroplated Ni substrate after thermal shock test (cycle time are 0, 800, 1200, and 1500 times). The inset is the I-V curve of thin-films GaAs solar cell with different thermal shock test times.

orders of magnitude in the reverse-bias leakage currents of solar cells from 0 to 1500 thermal shock tests was at the reverse bias of 5 V because of the dislocation generated from microcracks or microvoids.

3.3. Analysis of the Double-Diode Model of Solar Cells. The double-diode model of solar cells under illumination conditions was used to fit the I-V curve using (1) [17]. The solar cells

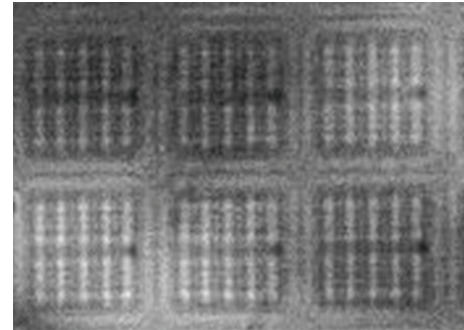


FIGURE 7: SAM images of TF-cells after the thermal shock test.

grown on the new and the recycled GaAs substrates and the GaAs solar cell transferred onto the electroplated Ni substrate as thin-film solar cell which underwent various numbers of thermal shock tests, are given as follows:

$$I = I_{ph} - I_{01} \left(\exp \frac{q(V + IR_s)}{kT} - 1 \right) - I_{02} \left(\exp \frac{V + IR_s}{2kT} - 1 \right) - \frac{V + IR_s}{R_{sh}}, \quad (1)$$

where k is the Boltzmann's constant, T is the cell's temperature, q is the elementary charge, I_{ph} is the photocurrent, I_{01} and I_{02} are the diode saturation currents (with diode ideality factors of 1 and 2, resp.), and R_s and R_{sh} are the series resistance and shunt resistance, respectively. The values of I_{01} can be associated with similar minority carrier diffusion lengths and interface recombination velocities. The I_{02} corresponds with the recombination in the depletion

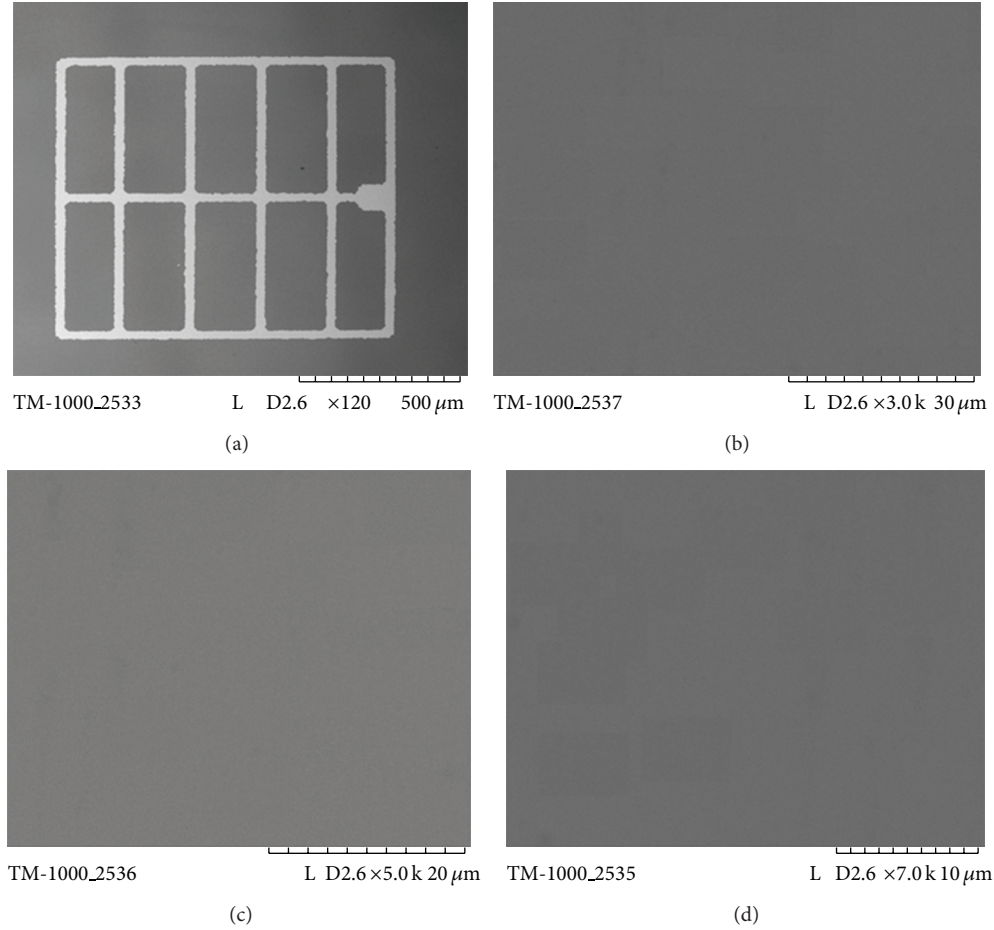


FIGURE 8: SEM images of the TF cell after the thermal shock test; (a) electrode pattern for the TF-cell; surface morphology images of the TF cell with amplification factors of (b) 3000 \times , (c) 5000 \times , and (d) 7000 \times .

region. If the number of crystalline defects increases substantially, the recombination of minority carriers occurs in the depletion region, which, in turn, contributes to items in the I_{02} [18].

The performance of solar cells grown on new and recycled GaAs substrates and GaAs thin-film solar cells grown on electroplated Ni substrates, which underwent various numbers of thermal shock tests, are summarized in Table 1. For the recycled GaAs substrates, the V_{oc} and FF of the solar cells grown on new or recycled GaAs substrates were considerably deteriorated. The V_{oc} of solar cells grown on recycled GaAs substrates decreased when recycled more than 2 times. A low V_{oc} could be caused by solar cell interface defects in the heterostructure because the surface roughness of the recycled GaAs substrate rapidly increased from 0.255 nm to 4.420 nm. It was reported that a low V_{oc} results from high diode saturation currents (I_0) in solar cells. A high diode saturation current was attributable to the recombination loss caused by defects in both the quasineutral and space-charge regions of the solar cell [19, 20].

The I_{01} and I_{02} values of the solar cells grown on the new and the recycled GaAs substrates were considerably altered

by the number of recycled times. A dramatic decrease of 3 and 2 orders of magnitude in the I_{01} and I_{02} terms from the initial device to the 4th ELO TF cell was observed because of the uneven surface morphology, especially for the I_{01} term.

The I_{02} increased because of two factors. The first factor was the size of the high concentrator solar cells. They are inherently small devices that have huge perimeter-to-area ratios; therefore, they are strongly affected by changes in the recombination properties of the perimeter (a main contribution to the I_{02} factor is the recombination at the PN junction [18]). Another possible factor was the generation of a great number of dislocations in the space charge region [20]. If the amount of dislocations considerably increases, then the recombination in the space charge regions contributes to I_{02} .

The reduction in the FF is principally attributable to two factors. The first factor is the high series resistance (R_s) and shunt resistance (R_{sh}); the second factor is the low doping level of the emitter layer to increase R_s . The principal factor in most studies has been R_s . The FF considerably decayed in the 3rd and 4th ELO TF-cells compared with that of the initial cell. In this study, the low FF of the 3rd and 4th ELO TF-cells is attributable to poor crystalline quality and the deteriorated doping-level of the contact layer caused by

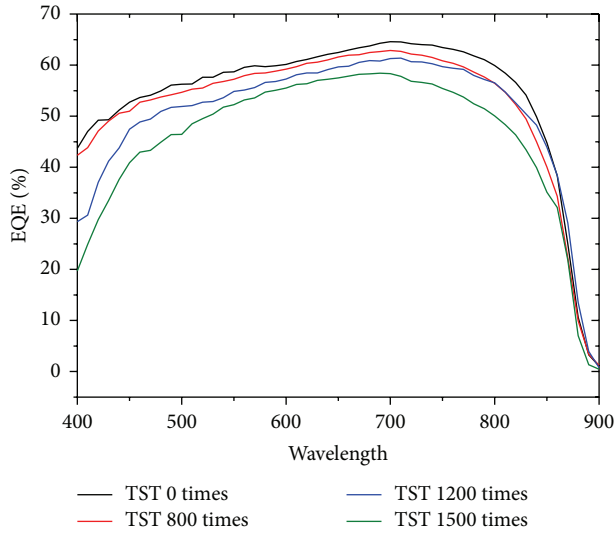


FIGURE 9: EQE responses of thin-film solar cell grown on electroplated Ni substrate with different thermal shock times.

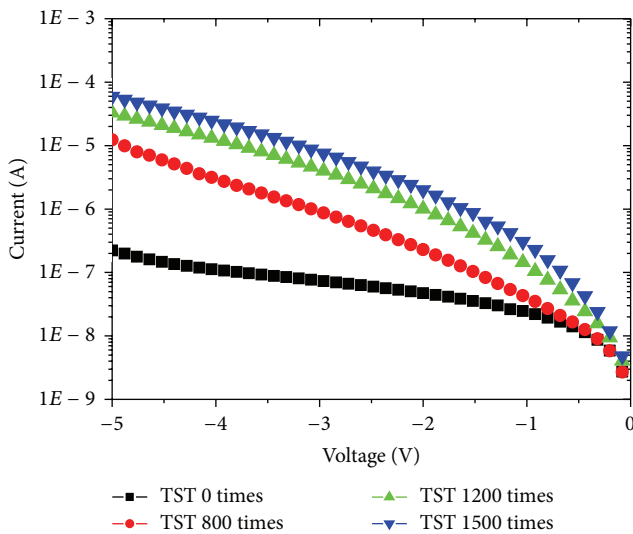


FIGURE 10: Reverse-bias dark I-V characteristics of the thin-film solar cells grown on electroplate nickel substrate.

the high surface roughness of the recycled GaAs substrate or wafer contamination.

For the GaAs thin-film solar cells grown on the electroplated Ni substrate, a dramatic decrease in 1 order of magnitude in the I_{01} term from 0 to 1500 thermal shock tests was observed because of microcracks or microvoids in the active layer or interface of the heterojunction. The microcracks or microvoids were generated during thermal shock tests because of a great mismatch in thermal expansion coefficients. The variation range of the I_{02} term did not considerably exceed 1 order of magnitude. Because of the high crystalline quality of the active layer, the different thermal shock tests did not considerably deteriorate the TF-cell.

4. Conclusion

A reliability analysis of III-V solar cells grown on new and recycled GaAs substrates and a III-V solar cell transferred onto an electroplated Ni substrate as III-V thin-film solar cell are reported. For the solar cells grown on the new and the recycled GaAs substrates, the main factor for the degradation of solar cell performance was the surface morphology of the recycled GaAs substrate. The uneven surface morphology caused the quality of the subsequently active layer of the solar cell to deteriorate and affected the V_{oc} and FF. The performance of the TF cell that underwent numerous shock tests was not considerably influenced after 800 thermal shock tests. After 1500 thermal shock tests, a substantial amount of microcracks or microvoids were generated in the active layer of the solar cell, which deteriorated the performance, especially the EQE response of the solar cell.

Acknowledgment

This work was financially supported by the National Science Council of the Republic of China, under the contract numbers NSC 101-2218-E-451-002 and NSC 99-2221-E-006-097-MY3.

References

- [1] J. F. Geisz, D. J. Friedman, J. S. Ward et al., "40.8% efficient inverted triple-junction solar cell with two independently metamorphic junctions," *Applied Physics Letters*, vol. 93, no. 12, Article ID 123505, 2008.
- [2] J. F. Geisz, S. Kurtz, M. W. Wanlass et al., "High-efficiency GaInP/GaAs/InGaAs triple-junction solar cells grown inverted with a metamorphic bottom junction," *Applied Physics Letters*, vol. 91, no. 2, Article ID 023502, 2007.
- [3] D. C. Law, K. M. Edmondson, N. Siddiqi et al., "Lightweight, flexible, high-efficiency III-V multijunction cells," in *Proceedings of the Conference Record of the IEEE 4th World Conference on Photovoltaic Energy Conversion (WCPEC-4 '06)*, pp. 1879–1882, Waikoloa, Hawaii, USA, May 2006.
- [4] M.-C. Tseng, R.-H. Horng, F.-L. Wu, C.-H. Wu, and M.-D. Yang, "Performance of GaAs/mirror/Cu-substrate thin-film solar cells," *IEEE Transactions on Electron Devices*, vol. 58, no. 11, pp. 3898–3904, 2011.
- [5] C. W. Cheng, K. T. Shiu, N. Li, S. J. Han, L. Shi, and D. K. Sadana, "Epitaxial lift-off process for gallium arsenide substrate reuse and flexible electronics," *Nature Communications*, vol. 4, pp. 1–4, 2013.
- [6] G. J. Bauhuis, P. Mulder, E. J. Haverkamp et al., "Wafer reuse for repeated growth of III-V solar cells," *Progress in Photovoltaics*, vol. 18, no. 3, pp. 155–159, 2010.
- [7] R.-H. Horng, M.-C. Tseng, F.-L. Wu, C.-H. Li, C.-H. Wu, and M.-D. Yang, "Thin film solar cells fabricated using cross-shaped pattern epilayer lift-off technology for substrate recycling applications," *IEEE Transactions on Electron Devices*, vol. 59, no. 3, pp. 666–672, 2012.
- [8] P. Kozdoy, J. P. Ibbetson, H. Marchand et al., "Electrical characterization of GaN p-n junctions with and without threading dislocations," *Applied Physics Letters*, vol. 73, no. 7, pp. 975–977, 1998.

- [9] T. Sasaki, K. Arafune, H. S. Lee et al., "Effects of thermal cycle annealing on reduction of defect density in lattice-mismatched InGaAs solar cells," *Physica B*, vol. 376-377, no. 1, pp. 626–629, 2006.
- [10] J. Nelson, *The Physics of Solar Cells*, Imperial College Press, London, UK, 2003.
- [11] I. Rey-Stolle and C. Algora, "Analysis of wirebonding techniques for contacting high concentrator solar cells," *IEEE Transactions on Advanced Packaging*, vol. 26, no. 1, pp. 47–53, 2003.
- [12] T. Takamoto, M. Kaneiwa, M. Imaizumi, and M. Yamaguchi, "InGaP/GaAs-based multijunction solar cells," *Progress in Photovoltaics*, vol. 13, no. 6, pp. 495–511, 2005.
- [13] T. Takamoto, T. Kodama, H. Yamaguchi et al., "Paper-thin InGaP/GaAs solar cells," in *Proceedings of the Conference Record of the IEEE 4th World Conference on Photovoltaic Energy Conversion (WCPEC-4 '06)*, pp. 1769–1772, Waikoloa, Hawaii, USA, May 2006.
- [14] R. Jaakkola, J. Lammasniemi, A. B. Kazantsev, and K. Tappura, "Comparison of $\text{Al}_{0.51}\text{In}_{0.49}\text{P}$ and $\text{Ga}_{0.51}\text{In}_{0.49}\text{P}$ window layers for GaAs and GaInAsP solar cells," in *Proceedings of the IEEE 26th Photovoltaic Specialists Conference*, pp. 891–894, October 1997.
- [15] G. Létay, M. Hermle, and A. W. Bett, "Simulating single-junction GaAs solar cells including photon recycling," *Progress in Photovoltaics*, vol. 14, no. 8, pp. 683–696, 2006.
- [16] B. Galiana, I. Rey-Stolle, M. Baudrit, I. García, and C. Algora, "A comparative study of BSF layers for GaAs-based single-junction or multijunction concentrator solar cells," *Semiconductor Science and Technology*, vol. 21, no. 10, article no. 003, pp. 1387–1392, 2006.
- [17] D. S. H. Chan and J. C. H. Phang, "Analytical methods for the extraction of solar-cell single- and double-diode model parameters from I–V characteristics," *IEEE Transactions on Electron Devices*, vol. 34, no. 2, pp. 286–293, 1987.
- [18] V. diaz and C. Algora, "The influence of perimeter recombination in the design of very high concentrator GaAs solar cells," in *Proceedings of the 16th European PVSEC*, pp. 1034–1037, Glasgow, Scotland, 2000.
- [19] A. Luque and S. Hegedus, *Handbook of Photovoltaic Science and Engineering*, Wiley, Hoboken, NJ, USA, 2003.
- [20] J. C. Zolper and A. M. Barnett, "The Effect of dislocations on the open-circuit voltage of gallium arsenide solar cells," *IEEE Transactions on Electron Devices*, vol. 37, no. 2, pp. 478–484, 1990.

Research Article

Effect of TCO/ $\mu\text{c-Si:H}$ Interface Modification on Hydrogenated Microcrystalline Silicon Thin-Film Solar Cells

Shin-Wei Liang, Cheng-Hang Hsu, and Chuang-Chuang Tsai

Department of Photonics and Institute of Electro-Optical Engineering, National Chiao Tung University,
1001 University Road, Hsinchu 300, Taiwan

Correspondence should be addressed to Shin-Wei Liang; singwayshepherd@gmail.com

Received 19 July 2013; Accepted 21 November 2013

Academic Editor: Francesco Bonaccorso

Copyright © 2013 Shin-Wei Liang et al. This is an open access article distributed under the Creative Commons Attribution License, which permits unrestricted use, distribution, and reproduction in any medium, provided the original work is properly cited.

The effects of H_2 plasma exposure on optical, electrical, and structural properties of fluorine-doped tin oxide (FTO) and AZO/FTO substrates have been investigated. With increasing the time of H_2 -plasma exposure, the hydrogen radical and ions penetrated through the FTO surface to form more suboxides such as SnO and metallic Sn , which was confirmed by the XPS analysis. The Sn reduction on the FTO surface can be effectively eliminated by capping the FTO with a very thin layer of sputtered aluminum-doped zinc oxide (AZO), as confirmed by the XPS analysis. By using the AZO/FTO as front TCO with the subsequent annealing, the p-i-n $\mu\text{c-Si:H}$ cell exhibited a significantly enhanced J_{SC} from 15.97 to 19.40 mA/cm^2 and an increased conversion efficiency from 5.69% to 7.09%. This significant enhancement was ascribed to the effective elimination of the Sn reduction on the FTO surface by the thin AZO layer during the Si-based thin-film deposition with hydrogen-rich plasma exposure. Moreover, the subsequent annealing of the sputtered AZO could lead to less defects as well as a better interface of AZO/FTO.

1. Introduction

Hydrogenated microcrystalline silicon ($\mu\text{c-Si:H}$) is a promising material for high efficiency thin-film solar cells due to its advantages of reduced light-induced degradation and a lower bandgap, which lead to a higher photocurrent compared to hydrogenated amorphous silicon [1–6]. However, the superstrate p-i-n $\mu\text{c-Si:H}$ solar cells are usually prepared by exposing the textured transparent conductive oxide (TCO) substrate to strongly hydrogen-diluted silane plasma. This can lead to the interactions of TCO with hydrogen plasma which results in chemical reduction of TCO surface. Schade et al. reported that the optical transmission of tin oxide was reduced by the formation of an oxygen-depleted surface layer due to the chemical reduction of the oxide by the hydrogen plasma [7]. This surface of chemical reduction containing Sn and SnO not only affected the optical properties of the film but also may act as the source for Sn diffusion into the subsequent deposited film upon the tin oxide. Several groups have also studied the chemical reduction of a tin oxide surface due to hydrogen or argon plasma exposure [8–12]. To eliminate or alleviate the chemical reduction of

the TCO surface, other group has replaced indium tin oxide (ITO) or fluorine-doped tin oxide (FTO) with a layer of textured aluminum-doped zinc oxide (AZO), which is more resistant to plasma damage [13, 14]. However, thicker layers of sputtered AZO are not so desirable, with their flattened surface, which tend to show reduced haze and poor light trapping. In this study, we introduced a very thin AZO coating (3–5 nm) onto the textured FTO glass to maintain the light trapping and preserve the quality of the TCO/ $\mu\text{c-Si:H}$ interface for $\mu\text{c-Si:H}$ single-junction solar cells.

2. Experimental Details

A commercial textured FTO ($\text{SnO}_2\text{:F}$) glass was used as a substrate for a superstrate (glass/FTO/p-i-n) $\mu\text{c-Si:H}$ single-junction solar cells. A very thin layer of AZO (3–5 nm) was capped on the top of the textured FTO film by a radio frequency magnetron sputtering system, using a commercial AZO target with 4 inches in diameter at the power of 100 W. The target-substrate distance was 15 cm, and the substrate temperature was room temperature. Subsequent annealing of the FTO or AZO/FTO (FTO capped with a very thin

AZO) films was done in O_2 or N_2 environment at $200^\circ C$ for up to 4 hours. The $1.2\ \mu m$ -thick μc -Si:H single-junction solar cells were prepared by a 27.12 MHz PECVD system with NF_3 *in situ* plasma cleaning and a load-lock system. The doped and undoped μc -Si:H thin films were deposited by introducing SiH_4 , B_2H_6 , PH_3 , and CO_2 with high H_2 dilution.

To investigate the property change of FTO and AZO/FTO films after H_2 plasma exposure, the H_2 plasma was generated by the 27.12 MHz PECVD system with H_2 flow rate of 800 sccm, a pressure of 500 Pa, and a power density of $0.33\ W/cm^2$. These were the same deposition parameters of μc -Si:H p-layer except the introduction of SiH_4 and B_2H_6 . The optical and electrical properties of the FTO or AZO/FTO films were measured by a UV-Vis-IR spectroscopy and a Hall measurement, respectively. To further identify the plasma-induced changes on the FTO surface, an X-ray photoelectron spectroscopy (XPS) was performed on both treated and untreated samples, and the morphology was studied by a scanning electron microscopy (SEM). All XPS spectra were obtained in a fixed analyzer transmission mode, with 280 and 55 eV pass energies for survey spectra and high resolution spectra, respectively. AM 1.5 G solar simulator and external quantum efficiency (EQE) were employed for the device characterization. The cell area was defined by the metal electrode which was $0.25\ cm^2$.

3. Results and Discussion

To simulate the condition of the μc -Si:H p-layer deposition on the FTO films, we exposed the FTO substrate in the H_2 -plasma for 72 seconds, which was the same conditions as the μc -Si:H p-layer except the SiH_4 and B_2H_6 . To examine the durability of FTO substrate after H_2 -plasma exposure, a very thin layer of AZO (3–5 nm) was capped on the top of the textured FTO film for comparison with the only FTO substrate, due to the better chemical resistance of AZO against H_2 -plasma exposure.

Figure 1 shows the effect of H_2 -plasma treatment duration on optical transmission for FTO and AZO capped FTO (AZO/FTO) films. As the time of H_2 -plasma exposure increased from 0 to 900 seconds, the total transmission of FTO samples decreased from 81.41% to 46.71% at the wavelength of 550 nm, and the diffuse transmission exhibited the same trend. The decrease in transmission should be ascribed to the increased reflection and absorption of the increasing metallic Sn and the suboxide, SnO, with the increasing penetration depth of hydrogen ions. Chantarat et al. also mentioned that the optical bandgap became narrower due to the upward valence band and the downward conduction band since the both excess Sn and SnO may create crystal disorder and trap electron carriers [15]. Moreover, the AZO/FTO after 72-second H_2 -plasma exposure showed comparable transmission compared to the FTO without H_2 -plasma exposure, which should be due to the suppression of tin reduction by the thin AZO. This indicated that a very thin layer of AZO can significantly mitigate the deterioration of optical transmission after H_2 -plasma exposure.

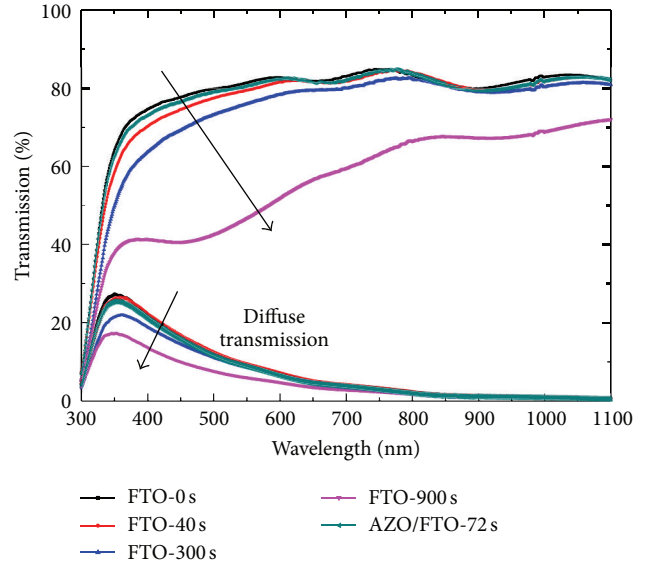


FIGURE 1: Effect of H_2 -plasma treatment time on optical transmission of FTO and AZO/FTO films.

We further investigated the effect of chemical reduction on electrical properties of FTO and AZO/FTO films after H_2 -plasma exposure. Although the combination of the surface layer after H_2 -plasma exposure and the underlying FTO was inhomogeneous, the dependence of the sheet resistance on the time of H_2 -plasma exposure can still be obtained by the Hall measurement. As the time of H_2 -plasma exposure increased from 0 to 900 seconds, the sheet resistance increased from 6.76 to 10.00 Ω/sq . With the increasing exposure time, the hydrogen radical and ions penetrated through the FTO surface to form more suboxides such as SnO and Sn, which was revealed by the XPS. The decrease in the sheet resistance was ascribed to the formation of less conductive suboxides as SnO [9]. Moreover, after the same time of 72-second H_2 -plasma exposure, the FTO substrate showed a sheet resistance of 8.52 Ω/sq and the AZO/FTO substrate showed a sheet resistance of 7.75 Ω/sq , which should be ascribed to the restraint on tin reduction by the thin AZO. Based on the mention above, the thin layer of AZO can alleviate the deterioration of sheet resistance and optical transmission after H_2 -plasma exposure.

Figure 2 displays the plane-view SEM images of the textured FTO films with or without H_2 plasma exposure. The sharp microstructures on the FTO films before H_2 plasma exposure were approximately 100–500 nm in grain size. After the H_2 -plasma exposure for 72 seconds, the surface morphology exhibited many small particles (20–30 nm in grain size) on the original FTO. As the time of H_2 -plasma exposure increased to 900 seconds, the original FTO microstructures were damaged heavily and the size of small particles increased to 50 nm. These small particles may be ascribed to the reduction of the $SnO_2:F$ (FTO) surface which became SnO and metallic Sn with increasing the duration of plasma exposure [9]. The study also reported that the thickness of the surface layer of chemical reduction was found

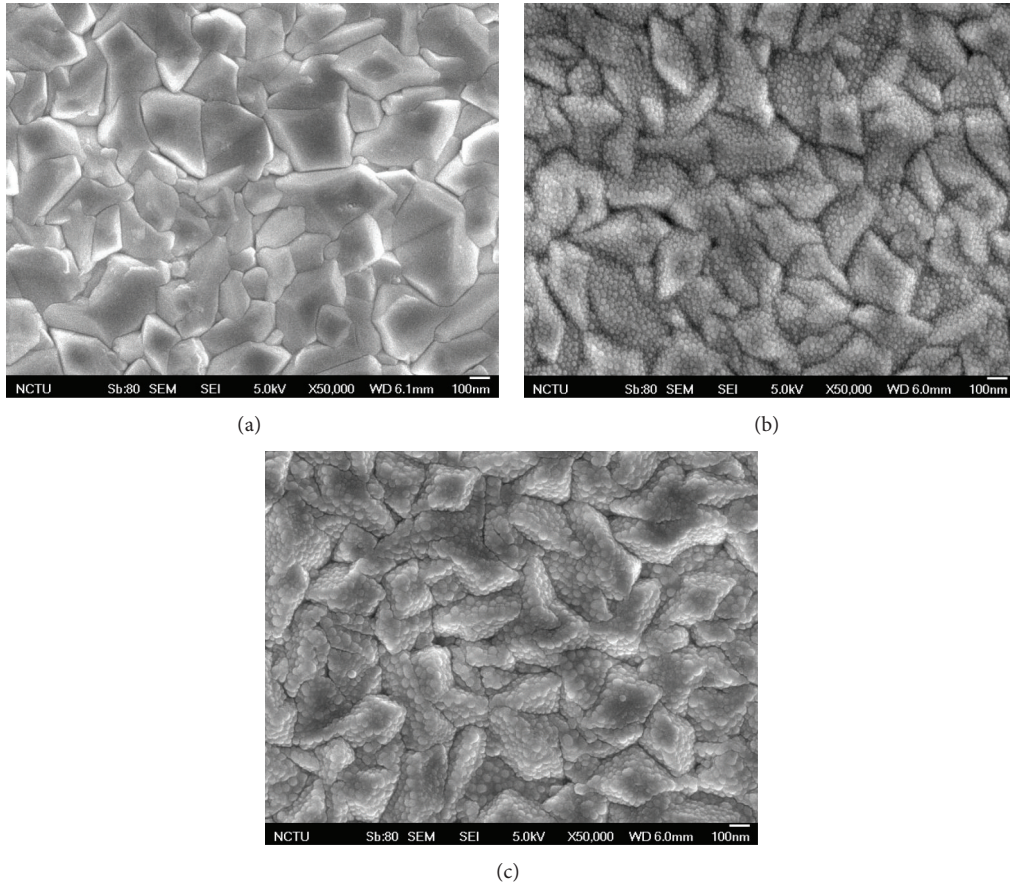


FIGURE 2: Plane-view SEM images of the textured FTO films (a) without H₂ plasma exposure, or with the H₂ plasma exposure for (b) 72 seconds and (c) 900 seconds.

to be 100 and 150 nm after H₂-plasma (0.25 W/cm², 13 Pa) exposure for 900 and 1800 seconds, respectively. In contrast, the surface damage and chemical reduction in our study would be more severe due to the higher power density and higher pressure (0.33 W/cm², 500 Pa).

The combination of the optical, electrical, and structural results showed the FTO films were deteriorated after H₂-plasma exposure, which may be originated from the chemical reduction to form the metallic Sn or suboxides of SnO. To further identify the plasma-induced changes on the SnO₂ surface, the survey spectra and high resolution spectra of XPS were obtained. The measured signals including oxygen and carbon (a surface contaminant) were not shown for brevity. The Sn 3d_{5/2} peaks of high resolution spectra as a function of H₂ plasma exposure for FTO and AZO/FTO films were shown in Figure 3. A single Sn peak of the FTO without H₂-plasma exposure was observed at 487.0 eV. As the time of H₂-plasma exposure increased from 0 to 900 seconds, the main peak shifted to lower binding energy. Schade et al. reported that the core level peak of SnO₂ is 487.0 eV, the main SnO peak is 486.7 eV, and the peak at 484.6 eV is due to elemental Sn [7]. These results confirmed that FTO film was reduced to the suboxide as SnO and metallic Sn with the increasing H₂-plasma exposure duration. However, the AZO/FTO after 72-second H₂-plasma exposure showed similar main peak at

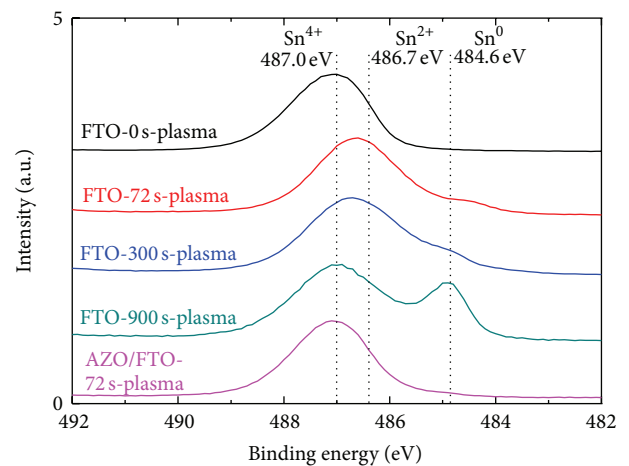


FIGURE 3: Sn 3d_{5/2} signal of XPS spectrum as a function of H₂ plasma exposure time for FTO and AZO/FTO films.

487.0 eV compared to the FTO without H₂-plasma exposure. This demonstrated that a layer of AZO can effectively protect the FTO films from chemical reduction during H₂-plasma exposure.

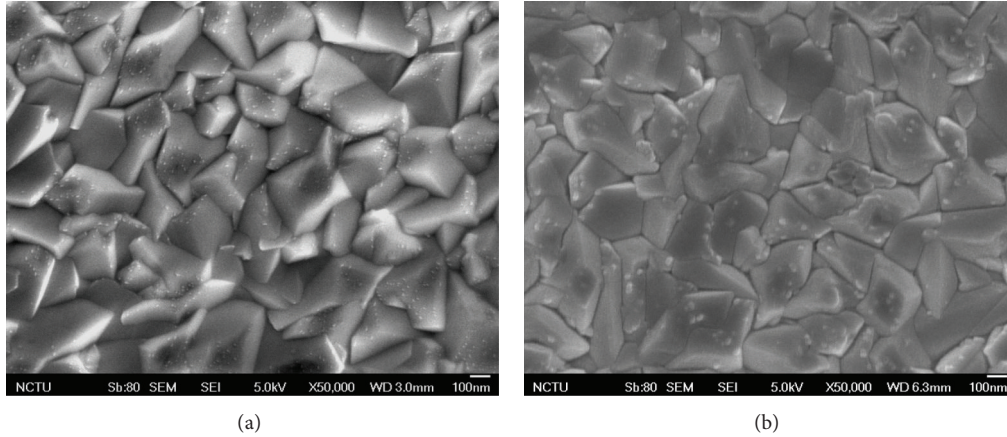


FIGURE 4: Plane-view SEM images of the 5 nm AZO capped FTO films (a) without and (b) with 72-second H_2 -plasma exposure.

The plane-view SEM images of the surface morphology of 5 nm AZO layer capped FTO films with and without 72-second H_2 -plasma exposure are shown in Figure 4. Before 72-second H_2 -plasma exposure, the thin AZO layer covered well on the original FTO texture, as shown in Figure 4(a). Compared to the FTO films undergoing 72-second H_2 -plasma exposure (shown in Figure 2(b)), the amount of the small particles on the original FTO microstructure arising from chemical reduction was significantly lowered by capping the 5 nm-thick AZO, which is shown in Figure 4(b). Combined with the XPS results, this confirmed that 5 nm-thick AZO layer can prevent the FTO surface from the reduction of tin oxide and ion bombardment during H_2 -plasma exposure. However, due to the less conductive nature of AZO material, the AZO film should be kept as thin as possible to retain the optoelectrical properties, while maintaining chemical reduction resistance. In this study, we have found that an optimized thickness of 5 nm-thick AZO film was obtained for the resistance to the hydrogen plasma as well as the cell performance. Based on the above results, the AZO/FTO structure with subsequent annealing in O_2 or N_2 environment at $200^\circ C$ was employed for the fabrication of μc -Si:H solar cells.

Figure 5 provides the J-V characteristics of $1.2 \mu m$ -thick μc -Si:H single-junction cells using the FTO or AZO/FTO as front TCO with subsequent annealing in N_2 or O_2 environment. The p-i-n μc -Si:H cell using only FTO exhibited a lower short circuit current density (J_{SC}) of 15.97 mA/cm^2 and a poor conversion efficiency of 5.69%. By using the unannealed AZO/FTO as front TCO, the J_{SC} increased to 17.42 mA/cm^2 . This was attributed to more optical transmission through the AZO/FTO substrate into the absorber due to the elimination of Sn reduction, which was confirmed by the results of optical transmission, as shown in Figure 1. However, the low efficiency and FF implied that the interface of TCO or TCO itself may need subsequent annealing for sputtered AZO. By using the AZO/FTO as front TCO with the subsequent annealing at $200^\circ C$ in O_2 environment for 0.5 hour, the p-i-n μc -Si:H cell exhibited a surprisingly enhanced J_{SC} from 15.97 to 19.40 mA/cm^2 , and the increased conversion efficiency

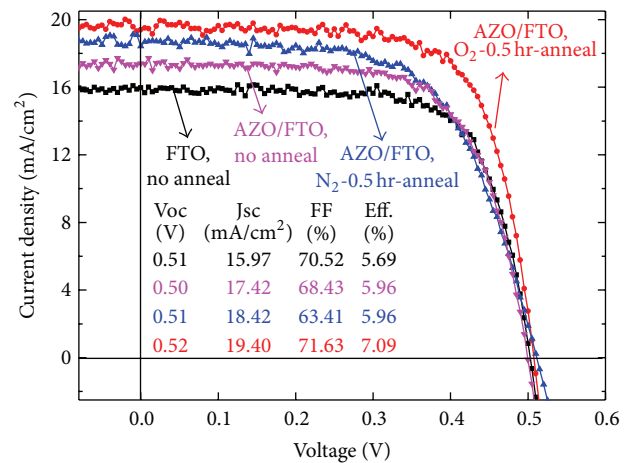


FIGURE 5: J-V characteristics of $1.2 \mu m$ -thick μc -Si:H single-junction cells using the FTO or AZO/FTO with subsequent annealing in N_2 or O_2 environment as front TCO.

from 5.69% to 7.09%. This significant enhancement was ascribed to the effective elimination of the Sn reduction on the FTO surface by the thin AZO layer during the Si-based thin-film deposition with hydrogen-rich plasma exposure. Moreover, the subsequent annealing of sputtered AZO could diminish the sputtering damage, leading to less defects and better interface of AZO/FTO. These results also corresponded to the quantum efficiency measurement, as demonstrated in Figure 6.

Figure 6 reveals the quantum efficiency (QE) of $1.2 \mu m$ -thick p-i-n μc -Si:H cells using the FTO or AZO/FTO as front TCO with subsequent annealing in N_2 or O_2 environment. Compared to the μc -Si:H cell using only FTO, the quantum efficiency of the μc -Si:H cell using AZO/FTO without annealing increased over wide wavelength range due to the suppression of the Sn reduction. The 0.5 hour annealing treatment of AZO/FTO in N_2 environment exhibited higher quantum efficiency than that of the AZO/FTO without annealing. The major QE enhancement at the wavelength

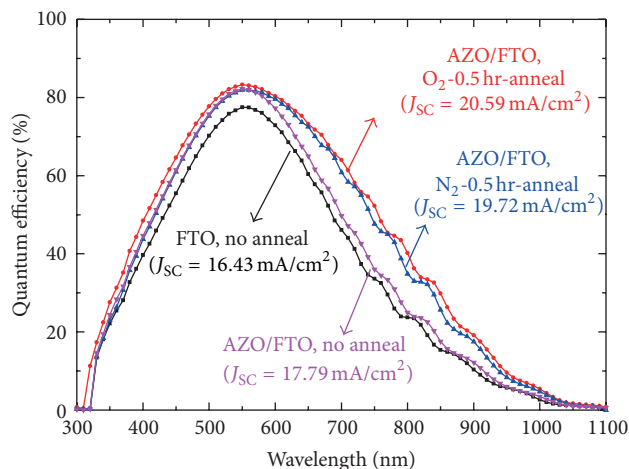


FIGURE 6: Quantum efficiency of 1.2 μm -thick p-i-n $\mu\text{c-Si:H}$ single-junction cells using the FTO or AZO/FTO as front TCO with subsequent annealing in N_2 or O_2 environment.

from 550 to 1100 nm may originate from the increased transmission after annealing in N_2 environment due to the reduction in the density of grain boundaries [16]. Besides, it is observed that the AZO/FTO after annealing in O_2 environment showed even higher quantum efficiency across whole measured wavelength than that in N_2 environment, which might be ascribed to the higher transmission after annealing in O_2 environment due to the decreased bulk defects and a small increase in bandgap [17]. By employing the AZO/FTO with O_2 annealing treatment for 0.5 hour, the $\mu\text{c-Si:H}$ solar cell exhibited a relative enhancement of the QE of more than 25% compared to the FTO configuration without annealing.

4. Conclusion

The effects of H_2 plasma exposure on optical, electrical, and structural properties of FTO and AZO/FTO substrates have been investigated. With increasing the time of H_2 -plasma exposure, the hydrogen radical and ions penetrated through the FTO surface of chemical reduction to form more suboxides such as SnO and metallic Sn , which was confirmed by the XPS analysis. The Sn reduction on the FTO surface can be effectively eliminated by capping the FTO with a very thin layer of sputtered AZO (3–5 nm), as confirmed by the XPS analysis. By using the AZO/FTO as front TCO with the subsequent annealing, the p-i-n $\mu\text{c-Si:H}$ cell exhibited a significantly enhanced J_{SC} from 15.97 to 19.40 mA/cm^2 and an increased conversion efficiency from 5.69% to 7.09%. This significant enhancement was ascribed to the effective elimination of the Sn reduction on the FTO surface by the thin AZO layer during the Si-based thin-film deposition with hydrogen-rich plasma exposure. Moreover, the subsequent annealing of the sputtered AZO could lead to less defects as well as a better interface of AZO/FTO. The quantum efficiency of the AZO/FTO configuration cell

exhibited a relative enhancement of more than 25% compared to the FTO configuration without annealing.

Conflict of Interests

The authors do not have any conflict of interests with the content of the paper.

Acknowledgment

This work was supported by the National Science Council of Taiwan under Grant number 102-3113-P-008-001.

References

- [1] J. Meier, R. Flückiger, H. Keppner, and A. Shah, "Complete microcrystalline p-i-n solar cell—crystalline or amorphous cell behavior," *Applied Physics Letters*, vol. 65, no. 7, pp. 860–862, 1994.
- [2] A. Shah, E. Vallat-Sauvain, P. Torres et al., "Intrinsic microcrystalline silicon ($\mu\text{c-Si:H}$) deposited by VHF-GD (very high frequency-glow discharge): a new material for photovoltaics and optoelectronics," *Materials Science and Engineering B*, vol. 69-70, pp. 219–226, 2000.
- [3] M. Kondo, "Microcrystalline materials and cells deposited by RF glow discharge," *Solar Energy Materials and Solar Cells*, vol. 78, no. 1–4, pp. 543–566, 2003.
- [4] A. V. Shah, J. Meier, E. Vallat-Sauvain et al., "Material and solar cell research in microcrystalline silicon," *Solar Energy Materials and Solar Cells*, vol. 78, no. 1–4, pp. 469–491, 2003.
- [5] J. Kočka, "Relation of defects and grain boundaries to transport and photo-transport: solved and unsolved problems in microcrystalline silicon," *Journal of Non-Crystalline Solids*, vol. 358, pp. 1946–1953, 2012.
- [6] R. B. Bergmann, T. J. Rinke, R. M. Hausner, M. Grauvogl, M. Vetter, and J. H. Werner, "Thin film solar cells on glass by transfer of monocrystalline Si films," *International Journal of Photoenergy*, vol. 1, no. 2, pp. 89–93, 1999.
- [7] H. Schade, Z. E. Smith, J. H. Thomas III, and A. Catalano, "Hydrogen plasma interactions with tin oxide surfaces," *Thin Solid Films*, vol. 117, no. 2, pp. 149–155, 1984.
- [8] J. H. Thomas III, "X-ray photoelectron spectroscopy study of hydrogen plasma interactions with a tin oxide surface," *Applied Physics Letters*, vol. 42, no. 9, pp. 794–796, 1983.
- [9] S. Major, M. C. Bhatnagar, S. Kumar, and K. L. Chopra, "The degradation of fluorine doped tin oxide films in a hydrogen plasma," *Journal of Vacuum Science and Technology A*, vol. 6, pp. 2415–2420, 1988.
- [10] T. Minami, H. Sato, H. Nanto, and S. Takata, "Heat treatment in hydrogen gas and plasma for transparent conducting oxide films such as ZnO , SnO_2 , and indium tin oxide," *Thin Solid Films*, vol. 176, no. 2, pp. 277–282, 1989.
- [11] J.-M. Themlin, M. Chtaib, L. Henrard, P. Lambin, J. Darville, and J.-M. Gilles, "Characterization of tin oxides by x-ray-photoemission spectroscopy," *Physical Review B*, vol. 46, no. 4, pp. 2460–2466, 1992.
- [12] L. Raniero, I. Ferreira, A. Pimentel et al., "Role of hydrogen plasma on electrical and optical properties of ZGO, ITO and IZO transparent and conductive coatings," *Thin Solid Films*, vol. 511-512, pp. 295–298, 2006.

- [13] H. C. Weller, R. H. Mauch, and G. H. Bauer, "Studies on the interface between novel type ZnO and p-a-SiC:H in 1.5 eV a-SiGe:H pin diodes in comparison to SnO_x and ITO," *Solar Energy Materials and Solar Cells*, vol. 27, no. 3, pp. 217–231, 1992.
- [14] H. N. Wanka, G. Bilger, and M. B. Schubert, "CO₂ plasma treatment of tin oxides," *Applied Surface Science*, vol. 93, no. 4, pp. 339–348, 1996.
- [15] N. Chantarat, S.-H. Hsu, C.-C. Lin, M.-C. Chiang, and S.-Y. Chen, "Mechanism of an AZO-coated FTO film in improving the hydrogen plasma durability of transparent conducting oxide thin films for amorphous-silicon based tandem solar cells," *Journal of Materials Chemistry*, vol. 22, no. 16, pp. 8005–8012, 2012.
- [16] A. Mahmood, N. Ahmed, Q. Raza et al., "Effect of thermal annealing on the structural and optical properties of ZnO thin films deposited by the reactive e-beam evaporation technique," *Physica Scripta*, vol. 82, no. 6, Article ID 065801, 2010.
- [17] O. Hamad, G. Braunstein, H. Patil, and N. Dhere, "Effect of thermal treatment in oxygen, nitrogen, and air atmospheres on the electrical transport properties of zinc oxide thin films," *Thin Solid Films*, vol. 489, no. 1-2, pp. 303–309, 2005.

Research Article

The Effect of Bandgap Graded Absorber on the Performance of a-Si_{1-x}Ge_x:H Single-Junction Cells with $\mu\text{c-SiO}_x\text{:H}$ N-Type Layer

Hung-Jung Hsu, Cheng-Hang Hsu, and Chuang-Chuang Tsai

Department of Photonics, National Chiao Tung University, 1001 University Road, Hsinchu 300, Taiwan

Correspondence should be addressed to Hung-Jung Hsu; bear0300022@gmail.com

Received 27 July 2013; Revised 24 October 2013; Accepted 28 October 2013

Academic Editor: Gaetano Di Marco

Copyright © 2013 Hung-Jung Hsu et al. This is an open access article distributed under the Creative Commons Attribution License, which permits unrestricted use, distribution, and reproduction in any medium, provided the original work is properly cited.

We reported the effect of bandgap grading of absorbers on the performance of a-Si_{1-x}Ge_x:H cells employing $\mu\text{c-SiO}_x\text{:H}$ *n*-layer. The influence of bandgap grading widths extended from the *p*-layer (the *p/i* grading) and the *n*-layer (the *i/n* grading) to the absorber on the cell performance which were systematically studied. The *p/i* grading reduced the interface defects and thus improved the V_{OC} . The reduced J_{SC} and FF were presumably due to the degraded hole transport by the potential gradient of *p/i* grading. Increasing the *i/n* grading width improved the carrier collection significantly. The EQE, the J_{SC} , and the FF were improved substantially. Bias-dependent EQE revealed that the carrier collection is efficient in the cell employing optimal *i/n* grading. On the other hand, increasing the *i/n* grading width was accompanied by the decrease in long-wavelength response which potentially constrained the *i/n* grading width. Compared to the cell without grading, the a-Si_{1-x}Ge_x:H cells with optimal *p/i* and *i/n* grading width improved the efficiency from 5.5 to 7.5%.

1. Introduction

Hydrogenated amorphous silicon germanium (a-Si_{1-x}Ge_x:H) has been shown to be a promising material for low-bandgap absorber in the multijunction structure [1]. Yan et al. reported that an initial efficiency over 16% was achieved by using a-Si:H/a-Si_{1-x}Ge_x:H/nc-Si:H triple-stacked structure and by employing *n*-type microcrystalline silicon oxide ($\mu\text{c-SiO}_x\text{:H}(n)$) as the *n*-layer for each subcell [2]. The $\mu\text{c-SiO}_x\text{:H}(n)$ has larger bandgap and lower refractive index compared to conventional amorphous or microcrystalline silicon *n*-layer, which reduced the parasitic absorption loss and increased the current density of component cell due to internal reflection, respectively [3, 4]. Moreover, the $\mu\text{c-SiO}_x\text{:H}(n)$ has been intensively studied for the application as the intermediate reflecting layer between component cells [5, 6], as the window layer in the *n*-side illuminated $\mu\text{c-Si:H}$ single-junction cells [7], and as the back reflector in a-Si:H single-junction cells [8]. We also found that the $\mu\text{c-SiO}_x\text{:H}(n)$ functioned well as back reflector in a-Si_{1-x}Ge_x:H single-junction cells in our previous work [9]. This functional $\mu\text{c-SiO}_x\text{:H}$ *n*-layer can significantly improve the performance of single- and multijunction cells.

On the other hand, one of the major challenges in developing a-Si_{1-x}Ge_x:H solar cells is the defective interfaces between the low-bandgap a-Si_{1-x}Ge_x:H absorber and the doped layers, which deteriorated, cell performance significantly. The *p/i* and the *i/n* interfaces contained considerable defects due to sharp changes in material composition [4]. The situation is even worse at the interface between the undoped a-Si_{1-x}Ge_x:H and *n*-type $\mu\text{c-SiO}_x\text{:H}$. High defect density at the interfaces increases the carrier recombination loss and weakened the built-in electric field in the absorber, which leads to the decrease in V_{OC} , J_{SC} , and FF. Guha et al. have reported that the employment of bandgap graded layers in the absorber can facilitate carrier collection, strengthen the built-in electric field, and thus improve the cell efficiency [10]. Several groups have reported the optimized bandgap grading structure in a-Si_{1-x}Ge_x:H absorber with a-Si:H *n*-layer through numerical simulation approaches [11–16]. However, there are still possibilities in designing the graded bandgap structure.

In this work, we systematically investigated the effect of bandgap grading widths on the performance and spectral responses of a-Si_{1-x}Ge_x:H cells with $\mu\text{c-SiO}_x\text{:H}(n)$ as *n*-layer.

The biased quantum efficiency serves as an important tool in the investigation of carrier collection losses in a-Si_{1-x}Ge_x:H single-junction cells [15]. This approach would give us physical insight into the correlation among carrier collection, carrier generation, and bandgap grading width in the absorber.

2. Materials and Methods

Silicon-based thin films were prepared in a 27.12 MHz single-chamber PECVD system with a load-lock and a transfer chamber. Gas mixture of SiH₄, GeH₄, CO₂, B₂H₆, PH₃, and H₂ was used as source gases. *N*-type μc-SiO_x:H layer was prepared under power of 30 W and CO₂-to-SiH₄ flow ratio of 0.54. The resulting refractive index (at wavelength of 650 nm) and the optical bandgap, E_{04} (photon energy where the absorption coefficient is 10⁴ cm⁻¹), were 3.2 and 2.2 eV, respectively. The a-Si_{1-x}Ge_x:H single-junction solar cells were deposited on the SnO₂:F coated glass substrates in a *p-i-n* superstrate configuration. The bandgap graded absorber was prepared by continuously varying the germane-to-silane flow rate ratio during the deposition process while maintaining the total thickness of the absorber at 230 nm. The bandgap graded layers were extended from the *p/i* and *i/n* interfaces toward the middle of the absorber with the bandgap changed from 1.75 to 1.53 eV. Photoconductivities of the bandgap graded layers decreased from 1.2 × 10⁻⁵ to 3.1 × 10⁻⁶ S/cm while the dark conductivities are quite similar (~4 × 10⁻¹⁰ S/cm) with decreasing the bandgap from 1.75 to 1.53 eV. After the deposition, the cells were transferred to a sputter chamber to deposit the ITO/Ag back contacts.

The bandgaps were obtained by analyzing the transmittance and reflection spectra of a-Si_{1-x}Ge_x:H films using Tauc's method [17]. The optical reflection of cells was measured by UV/VIS spectroscopy. The external quantum efficiency (EQE) was characterized under both short-circuit and voltage-biased conditions. The *J-V* characteristics of a-Si_{1-x}Ge_x:H single-junction solar cells were obtained from the *J-V* measurement under illumination of AM1.5G light source with the electrode area of 0.25 cm².

3. Results and Discussion

3.1. Inefficient Carrier Collection in a-Si_{1-x}Ge_x:H Single-Junction Cells with Single-Bandgap Absorber. Figure 1 shows the external quantum efficiency (EQE) of a-Si_{1-x}Ge_x:H single-junction cells measured under different reverse biases. Bandgap graded layers were not employed in this cell. As the bias voltage increased from 0 to -0.5 V, the EQE increased significantly in longer wavelength region (>450 nm). Further increase in bias voltage from -1.0 to -1.5 V had only marginal enhancement in EQE which indicated that most carriers were extracted from the device. The difference in EQE between 0 and -1.5 V revealed that the carrier collection is inefficient in a-Si_{1-x}Ge_x:H cells using single-bandgap absorber. We believed that the asymmetric EQE enhancement is due to the inefficient hole collection coming from the low drift mobility of holes in amorphous material. Both the bulk defects and interface defects can trap carriers and hinder photogenerated carriers from being collected. Moreover, trapped carriers can

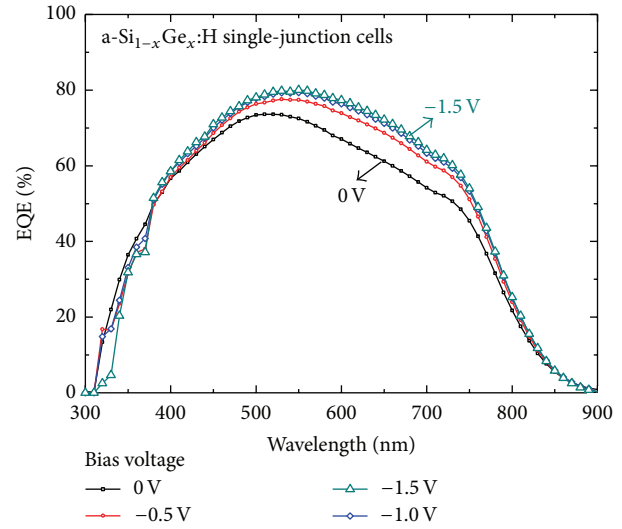


FIGURE 1: External quantum efficiency (EQE) of a-Si_{1-x}Ge_x:H single-junction cells with different reverse biases. The bias voltage was changed from 0 to -1.5 V.

weaken the built-in electric field in the middle of the absorber which worsened the carrier collection efficiency. To mitigate the detrimental effect of the inefficient carrier collection in the single-bandgap absorber, we employ the bandgap graded layers extended from the *p/i* and the *i/n* interfaces toward the middle of the absorber. The effect of *p/i* and *i/n* grading widths on cell performance was systematically studied.

The schematic band structures of a-Si_{1-x}Ge_x:H single-junction solar cells without and with bandgap grading at the *p/i* and the *i/n* interfaces were illustrated in Figures 2(a) and 2(b). The valence and the conduction band were assumed to shift equally as the film Ge content varied in the bandgap graded layer. The lowest bandgap of a-Si_{1-x}Ge_x:H undoped-layer was 1.53 eV, while the a-Si:H *p*-layer and μc-SiO_x:H *n*-layer had bandgaps of 1.75 eV and 1.1 eV, respectively. The bandgap of μc-SiO_x:H *n*-layer was approximately 1.1 eV because of its microcrystalline nature and the low oxygen (~4 at.%) we used. The bandgaps of the bandgap graded layers were changed from 1.75 to 1.53 eV. To investigate the appropriate bandgap grading structure, the *p/i* grading width was varied from 0 to 70 nm and the *i/n* grading width was varied from 0 to 180 nm. The total thickness of a-Si_{1-x}Ge_x:H was fixed at 230 nm for every cell presented.

3.2. The Effect of *p/i* Grading Width on the Performance of a-Si_{1-x}Ge_x:H Single-Junction Cells. Figure 3 illustrates the absorbance (*A*) and EQE of a-Si_{1-x}Ge_x:H single-junction cells as a function of the *p/i* grading width. The EQEs were measured under 0 and -0.5 V bias voltages. For EQEs measured under short-circuit condition (0 V), increasing the *p/i* grading width from 0 to 20 nm reduced the EQE at wavelength from 700 to 800 nm. Since the absorbance of cells had no noticeable change in this region, the decrease in EQE can be attributed to the degradation of carrier collection. Presumably, the degraded hole collection was responsible for the reduced EQE [10–12]. Holes generated by long-wavelength

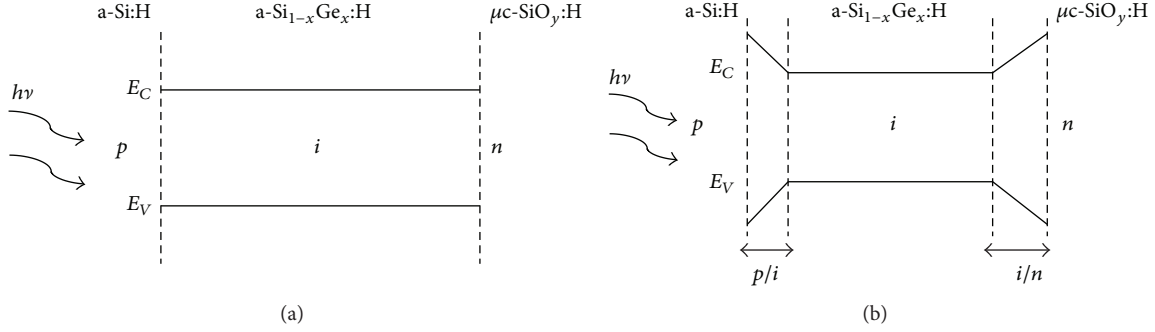


FIGURE 2: The schematic band structure of a-Si_{1-x}Ge_x:H single-junction cell (a) without bandgap grading and (b) with bandgap grading at both the p/i and the i/n interfaces.

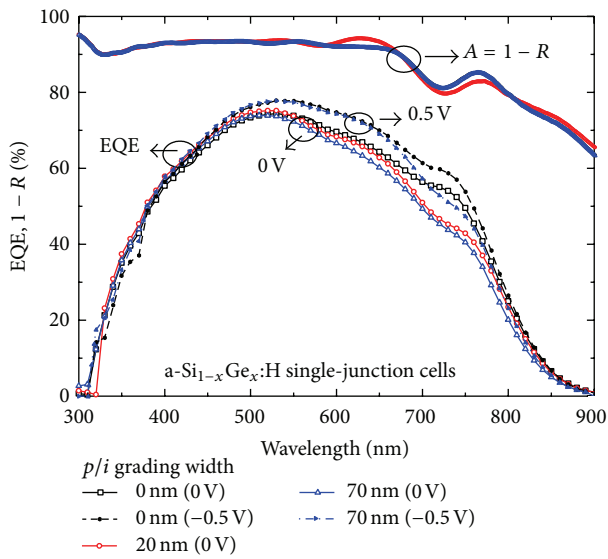


FIGURE 3: Absorbance (A) and EQE of a-Si_{1-x}Ge_x:H single-junction cells measured with 0 V and -0.5 V biases as a function of the p/i grading width. The p/i grading width was changed from 0 to 70 nm meanwhile keeping the total thickness of the absorber as 230 nm for all the cells.

photons near back contact would travel longer distance before being collected than the generated electrons. The potential gradient created by the p/i grading would hinder the hole transport which made the hole collection more difficult. Further increase in the p/i grading width to 70 nm reduced the EQE from 550 to 900 nm, which revealed that the hole collection was further degraded.

Table 1 summarizes the difference of current densities (ΔJ) measured with bias voltages of 0 and -0.5 V in EQE as a function of the p/i grading width. The ΔJ increased from 1.07 to 1.40 mA/cm² as the p/i grading width increased from 0 to 70 nm. The increased ΔJ manifested that the p/i grading degraded the carrier collection.

The performance of a-Si_{1-x}Ge_x:H single-junction cells with different p/i grading width was demonstrated in Figure 4. The short-circuit current (J_{SC}) and FF were slightly decreased as the p/i grading width increased from 0 to 20 nm.

TABLE 1: The reverse saturation current (J_0) and the difference of current densities (ΔJ) measured with bias voltages of 0 and -0.5 V in EQE as a function of the p/i grading width.

| p/i grading width (nm) | 0 | 20 | 70 |
|--|----------------------|----------------------|----------------------|
| $\Delta J (J_{EQE(-0.5V)} - J_{EQE(0V)})$ (mA/cm ²) | 1.07 | 1.44 | 1.40 |
| J_0 (A) | 2.8×10^{-8} | 1.3×10^{-9} | 2.9×10^{-9} |

Further increase in the grading width to 70 nm reduced the J_{SC} and the FF to 14.6 mA/cm² and 0.50, respectively. The reduction in the J_{SC} and the FF as the grading width increased from 0 to 70 nm was due to the degraded hole transport arising from the reduced potential gradient created by the p/i grading.

On the other hand, as the p/i grading width increased from 0 to 20 nm, the open-circuit voltage (V_{OC}) increased from 0.63 to 0.67 V. Further increase in the grading width to 70 nm increased the V_{OC} to 0.69 V. The improvement in V_{OC} may be due to the reduced defects at interfaces by bandgap graded layers [11, 12, 14]. Table 1 summarizes the reverse saturation current (J_0) of cells with different p/i grading width. As the grading width increased from 0 to 20 nm, the J_0 decreased approximately one order in magnitude from 2.8×10^{-8} to 1.3×10^{-9} A. The reduction in J_0 revealed that the defect density at the p/i interface was reduced by the bandgap graded layers, which improved the V_{OC} . In consequence, the thickness of the p/i grading width should be 10 to 20 nm to reduce the interface defects meanwhile minimizing the loss in J_{SC} and FF.

3.3. Effect of i/n Grading Width on the Performance of a-Si_{1-x}Ge_x:H Single-Junction Cells. Figure 5 illustrates the absorbance (A) and EQE of a-Si_{1-x}Ge_x:H cells with different i/n grading width. The p/i grading width and the total thickness of absorber were 15 and 230 nm, respectively, for all the cells. As the i/n grading width increased from 0 to 100 nm, the EQE at wavelength from 400 to 720 nm improved significantly. Since the absorbance had no obvious change from 400 to 720 nm, the increased EQE in this region can be attributed to the improved hole collection. Presumably, the potential gradient established by i/n grading facilitated

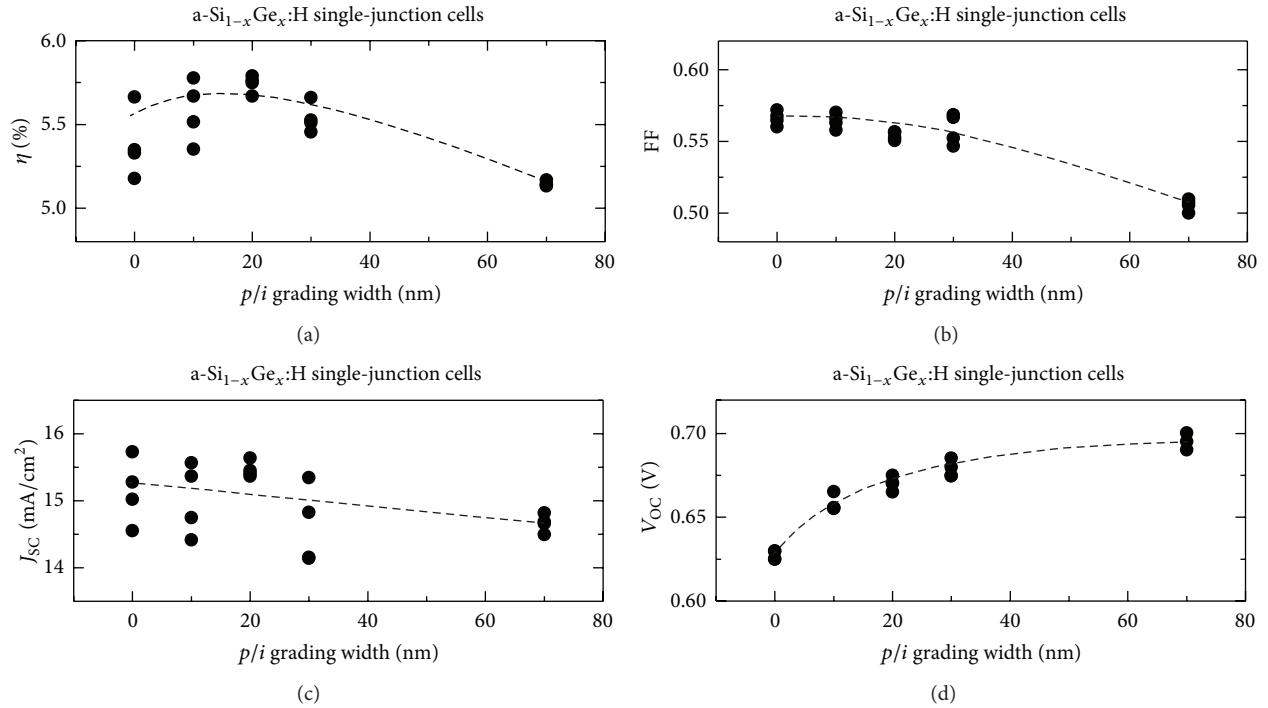


FIGURE 4: The performance of $a\text{-Si}_{1-x}\text{Ge}_x\text{:H}$ single-junction cells as a function of the p/i grading width under illumination of AM1.5G light source. The p/i grading width was changed from 0 to 70 nm meanwhile keeping the total thickness of the absorber at 230 nm for all the cells. The lines were drawn to guide the eye.

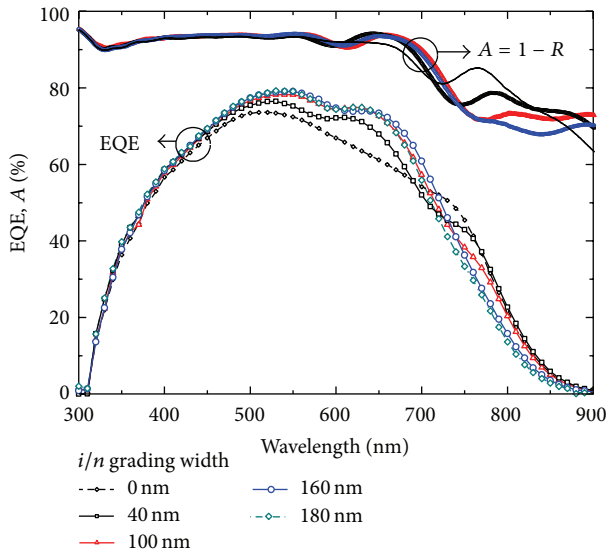


FIGURE 5: Absorbance (A) and EQE of $a\text{-Si}_{1-x}\text{Ge}_x\text{:H}$ single-junction cells as a function of the i/n grading width. The i/n grading width was changed from 0 to 180 nm meanwhile keeping the p/i grading width and the total thickness of the absorber at 15 and 230 nm, respectively.

the hole transport. Also, the i/n grading modified the distribution of defects in the absorber which strengthened the built-in electric field that improved the carrier collection [11, 12, 14]. The reduction at the wavelength approximately 750 nm as the i/n grading width increased from 0 to 100 nm

coincided with the decrease in absorbance in the same region, which was due to the reduction in carrier generation by the wider-bandgap graded layers.

As the i/n grading width increased from 100 to 160 nm, the EQE was further improved at wavelength from 650 to 750 nm while the EQE from 750 to 900 nm decreased noticeably. The former was due to the improved carrier collection while the latter, which coincided with the reduction in absorbance, revealed that the carrier generation was further reduced by wider bandgap graded absorbers. Further increase of i/n grading width to 180 nm reduced the EQE at the wavelength from 680 to 900 nm, which implied that the carrier generation was further suppressed.

The effect of the i/n grading width on the performance of $a\text{-Si}_{1-x}\text{Ge}_x\text{:H}$ cells was demonstrated in Figure 6. As the i/n grading width increased from 0 to 180 nm, the V_{oc} increased monotonically from 0.66 to 0.69 V. The improvement in V_{oc} was due to the reduced defect density at the interfaces and the redistribution of defects in the absorber which strengthened the built-in electric field [11, 12, 14]. Since the p/i interface is the dominant junction for high V_{oc} , the modification of the i/n grading width had relatively smaller improvement on V_{oc} than the p/i grading presented in Figure 4.

In addition, when the i/n grading width increased from 0 to 100 nm, the J_{sc} increased significantly from approximately 15 to 16 mA/cm^2 and the FF increased from 0.56 to 0.61 accordingly. The increase in J_{sc} and FF suggested that the i/n grading enhanced the carrier collection in the absorber. Presumably, the potential gradient created by the i/n grading

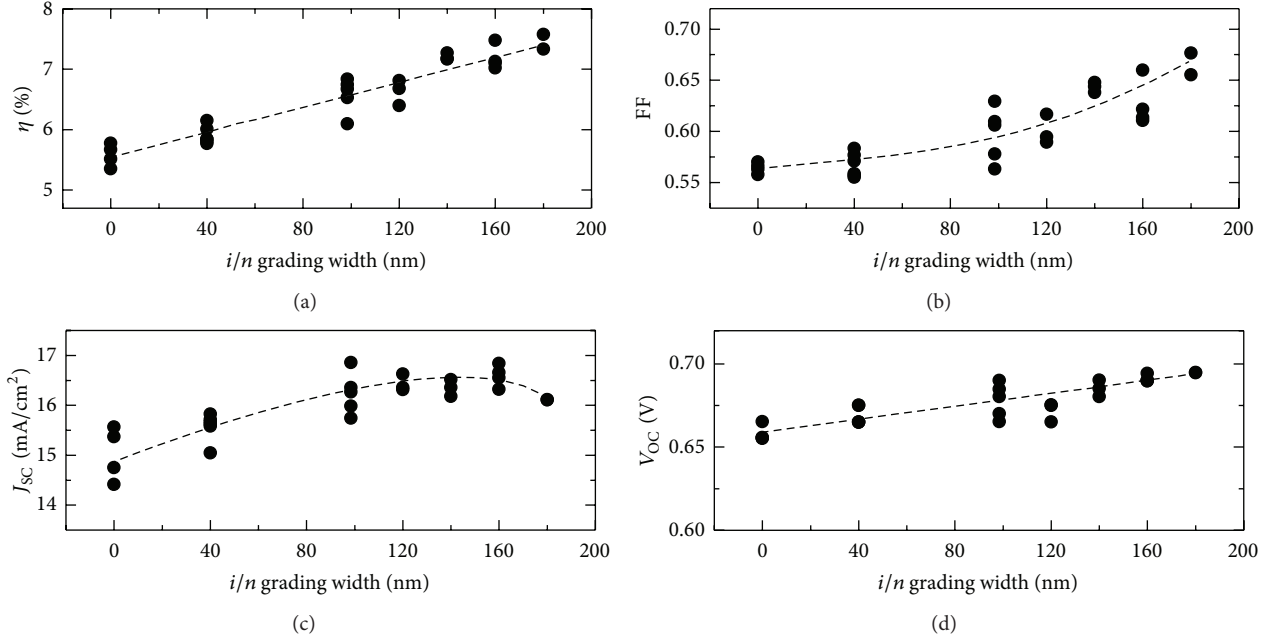


FIGURE 6: The performance of a-Si_{1-x}Ge_x:H single-junction cells as a function of the *i/n* grading width under illumination of AM1.5G light source. The *p/i* grading width and the total thickness of absorber were 15 and 230 nm, respectively, for all the cells. The lines were drawn to guide the eye.

facilitated the hole transport and also strengthened the built-in electric field in the absorber [12, 14]. As the *i/n* grading width increased from 100 to 160 nm, the J_{SC} seemed saturated at approximately 16.5 mA/cm² while the FF increased from 0.61 to 0.65 monotonically. The increased FF suggested that the carrier collection was further improved by the *i/n* grading. The saturated J_{SC} was due to the cancellation of improved EQE at wavelength from 650 to 750 nm and the reduced EQE from 750 to 900 nm as shown in Figure 5. Further increase in the *i/n* grading width to 180 nm improved the FF to 0.66 while reducing J_{SC} to 16.1 mA/cm² due to the reduced longer-wavelength response. The cell efficiency improved significantly from 5.5% to 7.5% as the *i/n* grading width increased from 0 to 180 nm. However, since a-Si_{1-x}Ge_x:H cells were generally used as bottom cells, thicker *i/n* grading width would lead to substantial reduction in long-wavelength response which may be potentially unfavorable in the tandem cell design. As a result, the *i/n* grading should be as thick as 100 to 160 nm to take advantage of the improved carrier collection meanwhile minimizing the reduction in longer-wavelength response.

Figure 7 compares the EQEs of a-Si_{1-x}Ge_x:H cells with and without bandgap graded layers measured under different bias voltages. The cell without bandgap grading exhibited substantially larger increase at wavelength from 400 to 900 nm under -0.5 V bias. In contrast, the cell employing bandgap graded layers showed only marginal increase in EQE under -0.5 V at wavelength from 450 to 700 nm, which suggested that most carriers were extracted under short-circuit condition. This result suggested that the bandgap graded layers improved the carrier collection significantly and thus can make a more efficient light management in a-Si_{1-x}Ge_x:H

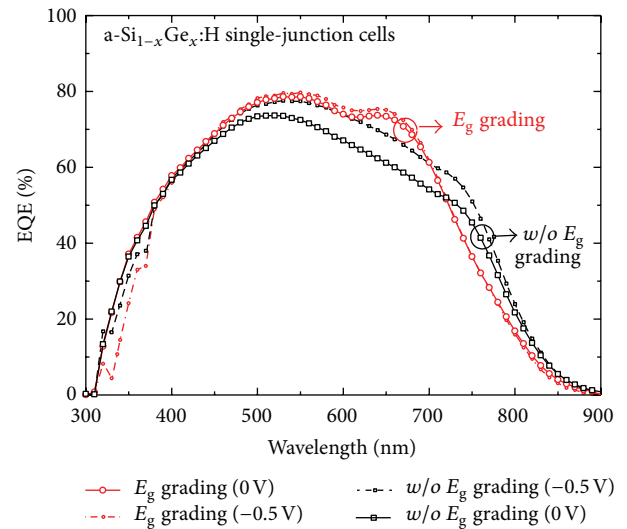


FIGURE 7: Comparison between EQEs of a-Si_{1-x}Ge_x:H single-junction cells with and without bandgap graded layers at the *p/i* and the *i/n* regions. The circle and square symbols denote the cell with and without bandgap grading, respectively. The *p/i* and *i/n* grading widths and the total thickness of absorber were 15, 160, and 230 nm, respectively. The EQEs measured under reverse bias of -0.5 V were represented by the dash lines.

cells. On the other hand, the reduction in the EQE at wavelength below 400 nm with reverse bias was probably due to the electron collection issues or the signal instability of the EQE system under biased condition. Further exploration on the nonlinear bandgap grading profiles shall lead to enhanced longer-wavelength response.

4. Conclusions

In this work, the effect of bandgap grading of absorbers on the performance of a-Si_{1-x}Ge_x:H cells employing $\mu\text{c-SiO}_x\text{:H}$ *n*-layer was investigated. The influence of the *p/i* and the *i/n* grading widths on carrier collection and photon absorption in the cells was evaluated by the bias-dependent EQE measurement, the total reflection spectra of cells, and the *J-V* characteristics. The cell employing 20 nm thick *p/i* grading improved the V_{OC} by 0.4 V, which was 6.3% relative increment compared to the cell without grading. The *p/i* grading seemed to reduce the interface defects as evidenced by the decreased dark leakage current. On the other hand, the cell with 160 nm thick *i/n* grading relatively enhanced the V_{OC} , J_{SC} , FF, and efficiency by 5.0%, 10.4%, 11.0%, and 28.7%, respectively, compared to the cell without *i/n* grading. The bias-dependent EQE manifested that the carrier collection was significantly improved which was likely due to the facilitation of hole transport. One trade-off was the long-wavelength response reduced with the increasing of *i/n* grading width. Compared to the cell without grading, the a-Si_{1-x}Ge_x:H cells with optimal *p/i* and *i/n* grading widths improved the efficiency from 5.5 to 7.5%.

Conflict of Interests

The authors do not have any conflict of interests concerning the content of the paper.

Acknowledgment

This work was financially sponsored by the National Science Council under Grant no. 102-3113-P-008-001.

References

- [1] S. Guha, J. S. Payson, S. C. Agarwal, and S. R. Ovshinsky, "Fluorinated amorphous silicon-germanium alloys deposited from disilane-germane mixture," *Journal of Non-Crystalline Solids*, vol. 97-98, no. 2, pp. 1455-1458, 1987.
- [2] B. Yan, G. Yue, L. Sivec, J. Yang, S. Guha, and C. S. Jiang, "Innovative dual function nc-SiO_x:H layer leading to a >16% efficient multi-junction thin-film silicon solar cell," *Applied Physics Letters*, vol. 99, no. 11, Article ID 113512, 2011.
- [3] A. Lambertz, T. Grundler, and F. Finger, "Hydrogenated amorphous silicon oxide containing a microcrystalline silicon phase and usage as an intermediate reflector in thin-film silicon solar cells," *Journal of Applied Physics*, vol. 109, no. 11, Article ID 113109, 2011.
- [4] A. Lambertz, V. Smirnov, T. Merdzhanova et al., "Microcrystalline silicon-oxygen alloys for application in silicon solar cells and modules," *Solar Energy Materials and Solar Cells*, vol. 119, pp. 134-143, 2013.
- [5] P. Buehlmann, J. Bailat, D. Dominé et al., "In situ silicon oxide based intermediate reflector for thin-film silicon micromorph solar cells," *Applied Physics Letters*, vol. 91, no. 14, Article ID 143505, 2007.
- [6] C. Das, A. Lambertz, J. Huepkes, W. Reetz, and F. Finger, "A constructive combination of antireflection and intermediate-reflector layers for thin film solar cells," *Applied Physics Letters*, vol. 92, no. 5, Article ID 053509, 2008.
- [7] V. Smirnov, W. Bottler, A. Lambertz, H. Wang, R. Carius, and F. Finger, "Microcrystalline silicon n-i-p solar cells prepared with microcrystalline silicon oxide ($\mu\text{c-SiO}_x\text{:H}$) n-layer," *Physica Status Solidi C*, vol. 7, no. 3-4, pp. 1053-1056, 2010.
- [8] P. Delli Veneri, L. V. Mercaldo, and I. Usatii, "Silicon oxide based n-doped layer for improved performance of thin film silicon solar cells," *Applied Physics Letters*, vol. 97, no. 2, Article ID 023512, 2010.
- [9] H.-J. Hsu, S.-W. Liang, C.-H. Hsu, and C. C. Tsai, "Optical enhancement in a-Si:H/a-SiGe:H tandem and a-SiGe:H single-junction solar cells," in *Proceedings of the 25th International Conference on Amorphous and Nano-Crystalline Semiconductors (ICANS-25 '13)*, Toronto, Canada, August 2013.
- [10] S. Guha, J. Yang, A. Pawlikiewicz, T. Glatfelter, R. Ross, and S. R. Ovshinsky, "Band-gap profiling for improving the efficiency of amorphous silicon alloy solar cells," *Applied Physics Letters*, vol. 54, no. 23, pp. 2330-2332, 1989.
- [11] B. E. Pieters, M. Zeman, R. A. C. M. M. van Swaaij, and W. J. Metselaar, "Optimization of a-SiGe:H solar cells with graded intrinsic layers using integrated optical and electrical modeling," *Thin Solid Films*, vol. 451-452, pp. 294-297, 2004.
- [12] F. Rubinelli, R. Jiménez, J. Rath, and R. Schropp, "Using computer modeling analysis in single junction a-SiGe:H solar cells," *Journal of Applied Physics*, vol. 91, no. 4, article 2409, 2002.
- [13] R. J. Zambrano, F. A. Rubinelli, W. M. Arnoldbik, J. K. Rath, and R. E. I. Schropp, "Computer-aided band gap engineering and experimental verification of amorphous silicon-germanium solar cells," *Solar Energy Materials and Solar Cells*, vol. 81, no. 1, pp. 73-86, 2004.
- [14] J. Zimmer, H. Stiebig, and H. Wagner, "a-SiGe:H based solar cells with graded absorption layer," *Journal of Applied Physics*, vol. 84, no. 1, pp. 611-617, 1998.
- [15] E. Maruyama, Y. Yoshimine, A. Terakawa et al., "Improvement in performance of a-SiGe:H solar cells for multi-junction cells," in *Proceedings of the MRS Spring Meeting*, pp. 821-826, April 1993.
- [16] X. Deng, X. Liao, S. Han, H. Povolny, and P. Agarwal, "Amorphous silicon and silicon germanium materials for high-efficiency triple-junction solar cells," *Solar Energy Materials and Solar Cells*, vol. 62, no. 1, pp. 89-95, 2000.
- [17] J. Tauc, "Optical properties and electronic structure of amorphous Ge and Si," *Materials Research Bulletin*, vol. 3, no. 1, pp. 37-46, 1968.

Research Article

Effects of Anodic Buffer Layer in Top-Illuminated Organic Solar Cell with Silver Electrodes

Tien-Lung Chiu, Himadri Mandal, Mi Zhang, Shun-Po Yang, and Ya-Ting Chuang

Department of Photonics Engineering, Yuan Ze University, Taoyuan 32003, Taiwan

Correspondence should be addressed to Tien-Lung Chiu; tlchiu@saturn.yzu.edu.tw

Received 19 July 2013; Accepted 16 September 2013

Academic Editor: Stefano Caramori

Copyright © 2013 Tien-Lung Chiu et al. This is an open access article distributed under the Creative Commons Attribution License, which permits unrestricted use, distribution, and reproduction in any medium, provided the original work is properly cited.

An efficient ITO-free top-illuminated organic photovoltaic (TOPV) based on small molecular planar heterojunction was achieved by spinning a buffer layer of poly(3,4-ethylenedioxythiophene):poly(styrenesulfonate) (PEDOT:PSS), on the Ag-AgO_x anode. The PEDOT:PSS thin film separates the active layer far from the Ag anode to prevent metal quenching and redistributes the strong internal optical field toward dissociated interface. The thickness and morphology of this anodic buffer layer are the key factors in determining device performances. The uniform buffer layer contributes a large short-circuit current and open-circuit voltage, benefiting the final power conversion efficiency (PCE). The TOPV device with an optimal PEDOT:PSS thickness of about 30 nm on Ag-AgO_x anode exhibits the maximum PCE of 1.49%. It appreciates a 1.37-fold enhancement in PCE over that of TOPV device without buffer layer.

1. Introduction

Organic photovoltaic (OPV) cells based on a small molecular planar heterojunction have attracted much attention since Tang reported the first efficient device in 1986 [1]. At present, the power conversion efficiency (PCE) of OPV cells is less than that of inorganic solar cells [2, 3]. However, OPV is a promising candidate for the next generation renewable power source because of its easily tunable optical and electrical properties, simple process, flexible application, and low cost [4–7]. The continuous improvement of PCE has focused on material development, interface modification, structural engineering, and absorption enhancement [8–11]. In addition, there is an increasing trend towards the indium-tin-oxide- (ITO-) free devices because of the potential indium shortages and flexible applications [12–15]. OPV plays a capital role in the concept of flexibility applied to mass production by roll-to-roll process [16–18]. Hence, the interface modification between organic layer and substitute anode is an important factor affecting device performance [19]. Various materials are suitable for use as the anode, including aurum (Au) [20], aluminum (Al) [21], silver (Ag) [19, 22], and

poly(3,4-ethylenedioxythiophene):poly(styrenesulfonate) (PEDOT:PSS) [4, 23].

In our previous reports [24, 25], we used Ag film as the anode and cathode to obtain an efficient top-illuminated organic photovoltaic (TOPV) device. However, many studies indicated that metal-induced exciton quenching degrades the number of excitons by nonradiative energy transfer to the metal [26–28]. For OPV device without anodic or cathodic buffer layer, the exciton quenching occurs in active layer close to metallic anode or cathode, leading to the demoted PCE [29–31]. The strength of exciton quenching depends on the exciton drift-length from formation to the donor/acceptor dissociated interface and the distance between exciton and quencher. It can be foreseen that the metal-induced exciton quenching effects in planar heterojunction OPV is stronger than that in bulk heterojunction one, because of the longer drift-length. Currently, bathocuproine (BCP) or 4,7-diphenyl-1,10-phenanthroline (BPhen), and so forth become an essential cathodic buffer layer to prevent the cathodic quenching to achieve the efficient planar heterojunction OPV device. Hence, to further upgrade the PCE of our TOPV device with Ag anode, the anodic buffer layer to separate

the active layer far from anode and so prevent the anodic metal quenching is out of necessity.

Several metal oxides used to be buffer layer were reported to induce exciton quenching, for example, molybdenum trioxide (MoO_3) [32], calcium oxide (CaO) [33], tin oxide (SnO) [34], and so forth. Hence, the high conductive polymeric thin film, PEDOT:PSS, is considered to be the anodic buffer layer that alleviates the exciton quenching in our TOPV devices. Thus, a great enhancement in short-circuit current (J_{sc}) of the TOPV device could be anticipated by using the anodic and cathodic buffer layers at the same time to prevent exciton quenching.

In this paper, we investigate the optimization of the optical-electrical performance of a TOPV device to obtain the maximal PCE by utilizing a series of anodic buffer layers fabricated at various spin speeds. By characterizing these buffer layers, their thicknesses and surface morphologies were found to be important parameters that affect the optical field distribution and carrier dynamics inside device and then determine the final device performance.

2. Experiment

The basic layer configuration of TOPV follows that in our previous report, comprising a glass substrate/ Ag-AgO_x (100 nm)/PEDOT:PSS (0 to 7000 rpm)/copper phthalocyanine (CuPc 20 nm)/fullerene (C_{60} 40 nm)/BCP (7 nm)/Ag (12.5 nm)/naphthylphenylbiphenyldiamine (NPB 40 nm) [25], where CuPc is electron donor layer, C_{60} is electron acceptor layer, BCP is exciton block layer to prevent the cathodic quenching, and NPB is capping layer to have more incident photons. Natively, Ag with low work function 4.2 eV is suitable for electron collection as cathode and its film thickness determines the optical behaviors, highly reflection or semitransparency. AgO_x was formed on the surface of thick Ag film using UV-Ozone (Jelight mode: 42) for 45 sec to raise the work function for anode application. In our previous work, we disclosed that 45 sec UV-Ozone treatment was the optimal parameter for the Ag anode of TOPV. In fabricating the buffer layer, PEDOT:PSS was spun onto the Ag- AgO_x anode at 500 rpm for 10 sec, and then at 1000 to 8000 rpm for 20 sec. The physical properties of these buffer layers were sequentially characterized by dynamic force microscope (DFM: SEIKO SPA400), water contact angle analysis, photoelectron spectrometer (Riken Keiki AC-2), and spectrometer (Hitachi U4100). Apart from PEDOT:PSS layer, the organic thin films and Ag films were deposited by a multisource thermal evaporator under high vacuum 5×10^{-6} and 2×10^{-5} Torr, respectively. The active area of each cell was 4 mm^2 defined by the anode and cathode mask cross-section. These devices were carefully encapsulated in a glovebox. Their dark/illuminated current densities (J) versus voltage (V) curves were measured using a source meter (Keithley 2400) without/with an AM 1.5 G 1-sun solar simulator (Newport 91195A). We also employed a system comprising a solar simulator (Newport 66983), a monochromator (Newport 74045), a lock-in amplifier (Stanford Research SR830), a chopper (Stanford Research SR540) and some optical components, to

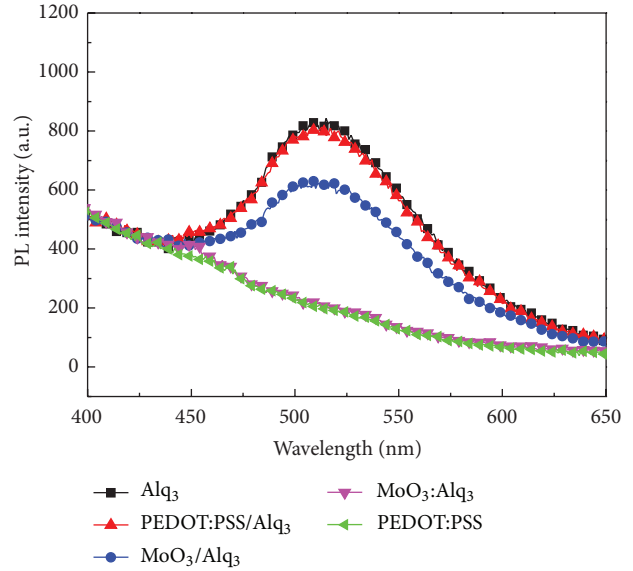


FIGURE 1: Photoluminescence spectra of five thin films: Alq_3 , PEDOT:PSS, PEDOT:PSS/ Alq_3 , molybdenum trioxide $\text{MoO}_3/\text{Alq}_3$, and $\text{MoO}_3:\text{Alq}_3$ (1:10).

measure their external quantum efficiency (EQE) spectra. In addition, the refractive index and absorption coefficient of the each single thin film were measured with the use of an ellipsometer (Raditech SE-950).

3. Results and Discussions

To prove that the exciton quenching effect induced by metal oxide and it can be neglected by using PEDOT:PSS, we fabricated five thin films on glass substrates such as Alq_3 (10 nm), PEDOT:PSS (20 nm), PEDOT:PSS (20 nm)/ Alq_3 (10 nm), and MoO_3 (1 nm)/ Alq_3 (10 nm), MoO_3 doped Alq_3 (doping ratio in volume 1:10, 11 nm) to measure their photoluminescence (PL) spectra as shown in Figure 1, using spectrometer (Hitachi F4500) with the fixed excitation wavelength of 350 nm. One can see that Alq_3 and PEDOT:PSS/ Alq_3 show the almost identical PL intensity. It means that the energy transfer between PEDOT:PSS and excitons in Alq_3 layer is negligible. Less exciton quenching effect resulting from PEDOT:PSS can be detected. However, the $\text{MoO}_3/\text{Alq}_3$ shows the decayed PL intensity due to exciton quenching effect [32]. A number of excitons in Alq_3 layer are quenched by MoO_3 , especially their position closed to MoO_3 . The considerable exciton quenching can be observed when MoO_3 doped into Alq_3 layer because the distances between MoO_3 atoms and excitons are very short, corresponding to the strongest nonradiative energy transfer between them. Reasonably, its PL intensity is almost naught comparing to that of the pure PEDOT:PSS film. It means that MoO_3 does actuate the exciton quenching effects, whereas PEDOT:PSS does not.

Good surface wettability of anode substrate is a basic requirement for the following uniform film deposition [35]. The wetted substrate corresponding to the small static water contact angle benefits the qualified film deposition in atomic

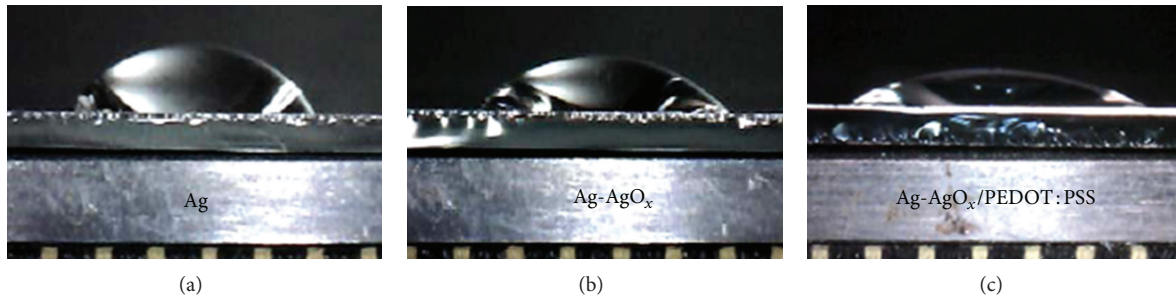


FIGURE 2: Static water contact angle on the surface of Ag, Ag-AgO_x, Ag-AgO_x/PEDOT:PSS thin films is 56°, 48°, and 31°, respectively.

layer by layer without aggregated islands. There is an agreement on that the organic film deposition on the wetter substrate exhibits the higher carrier mobility, less defect formation, and smoother surface roughness and is good for device performance [35–37]. Figure 2 shows photos for the static water contact angle on the surface of Ag, Ag-AgO_x, and Ag-AgO_x/PEDOT:PSS thin films, used to assess surface wettability. The original Ag film surface is hydrophobic and exhibits a large water contact angle of 56°. After 45 sec UV-Ozone treatment, the water contact angle a little reduces to 48° due to the generation of AgO_x on the Ag surface. There is $\pm 1^\circ$ and $\pm 2^\circ$ uncertainty in the contact angle on the different Ag and Ag-AgO_x film surfaces, respectively. To improve further the anodic surface wettability, we coated the anode surface with PEDOT:PSS. UV-Ozone treatment of Ag surface is helpful for the sequential PEDOT:PSS coating to avoid film breakage, because the contact angle of PEDOT:PSS on bare Ag surface is very large [38]. For example, forming a PEDOT:PSS at 5000 rpm provides the conspicuous decrease in water contact angle to 31° as shown in Figure 2. The average water contact angle on various PEDOT:PSS surfaces fabricated at the spin speed of 1000 to 8000 rpm is $30.1^\circ \pm 3^\circ$. This implies that PEDOT:PSS lamination easily transforms the hydrophobic AgO_x surface to be hydrophilic. In addition, the work function of Ag, Ag-AgO_x, and Ag-AgO_x/PEDOT:PSS thin films were 4.16, 4.9, and 5.1 eV, respectively. Hence, the fabrication of Ag-AgO_x/PEDOT:PSS anode provides good wettability and high work function, suitable for organic layer deposition.

We characterized layer thickness and surface roughness for the various PEDOT:PSS films as shown in Figure 3. As coating speed increased, the thickness of PEDOT:PSS films thinned due to the greater centrifugal force. The figure shows that film thickness fabricated at 1000, 3000, 5000, and 7000 rpm were 59.7, 39.8, 29, 11.9 nm, respectively. Under our coating process, the uniformity of film thickness was greater than 90% while the spin speed is greater than 3000 rpm. Distinctively, the uniformity of film thickness less than 70% was observed as spin speed less than 2000 rpm. The average roughness (R_a) of $5 \times 5 \mu\text{m}^2$ scanning area dwindles as spin speed grows from 1000 rpm to 5000 rpm, and then R_a gets large as the spin speed over 5000 rpm. The R_a curve shows two distinct tendencies with a demarcation at 5000 rpm, beyond which speed, defects appear on the PEDOT:PSS surface. Two inserted DFM photos in Figure 3 exhibit the

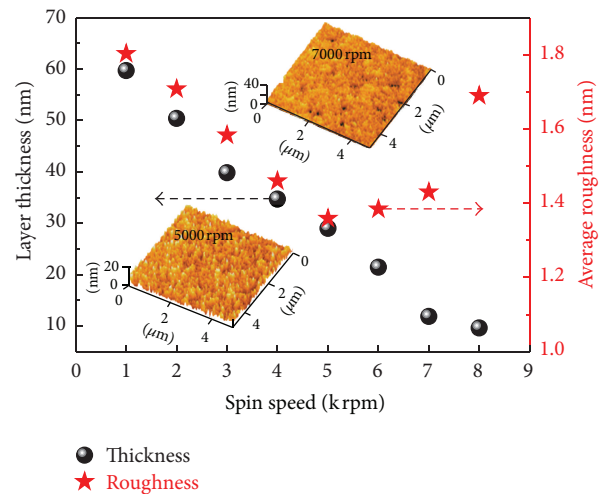


FIGURE 3: Layer thickness and average roughness for various PEDOT:PSS films fabricated at 1000 to 8000 rpm on Ag-AgO_x anode. The inset DFM photos show the surface of 5000 and 7000 rpm films.

smooth surface at 5000 rpm, and the appearance of holes on the surface at 7000 rpm. This defect formation results from an interaction between the weak surface tension of PEDOT:PSS solution and the strongly hydrophobic AgO_x surface. Hence, a PEDOT:PSS film thickness of less than 20 nm is hard to obtain with perfect surface using AgO_x substrate because the surface tension of PEDOT:PSS solution is not strong enough to allow spreading on the hydrophobic AgO_x surface. This problem can be anticipated to be much greater for the bare Ag substrate.

Figure 4 presents the wavelength dependent refractive index (n) and absorption coefficient (k), as well as simulated optical field distribution inside the TOPV devices with/without 30 nm PEDOT:PSS layer. The involved refractive indexes and absorption coefficients of the organic layers such as PEDOT:PSS, CuPc, C₆₀, and BCP were individually measured from a fixed layer thickness of 50 nm utilizing an ellipsometer (Raditech SE-950) as shown in Figure 4(a). Furthermore, the simulation program was using the optical model of transfer matrix to illustrate the optical field distribution inside TOPV as shown in Figures 4(b) and 4(c) [39–41]. Both simulate diagrams show two divisions in the optical

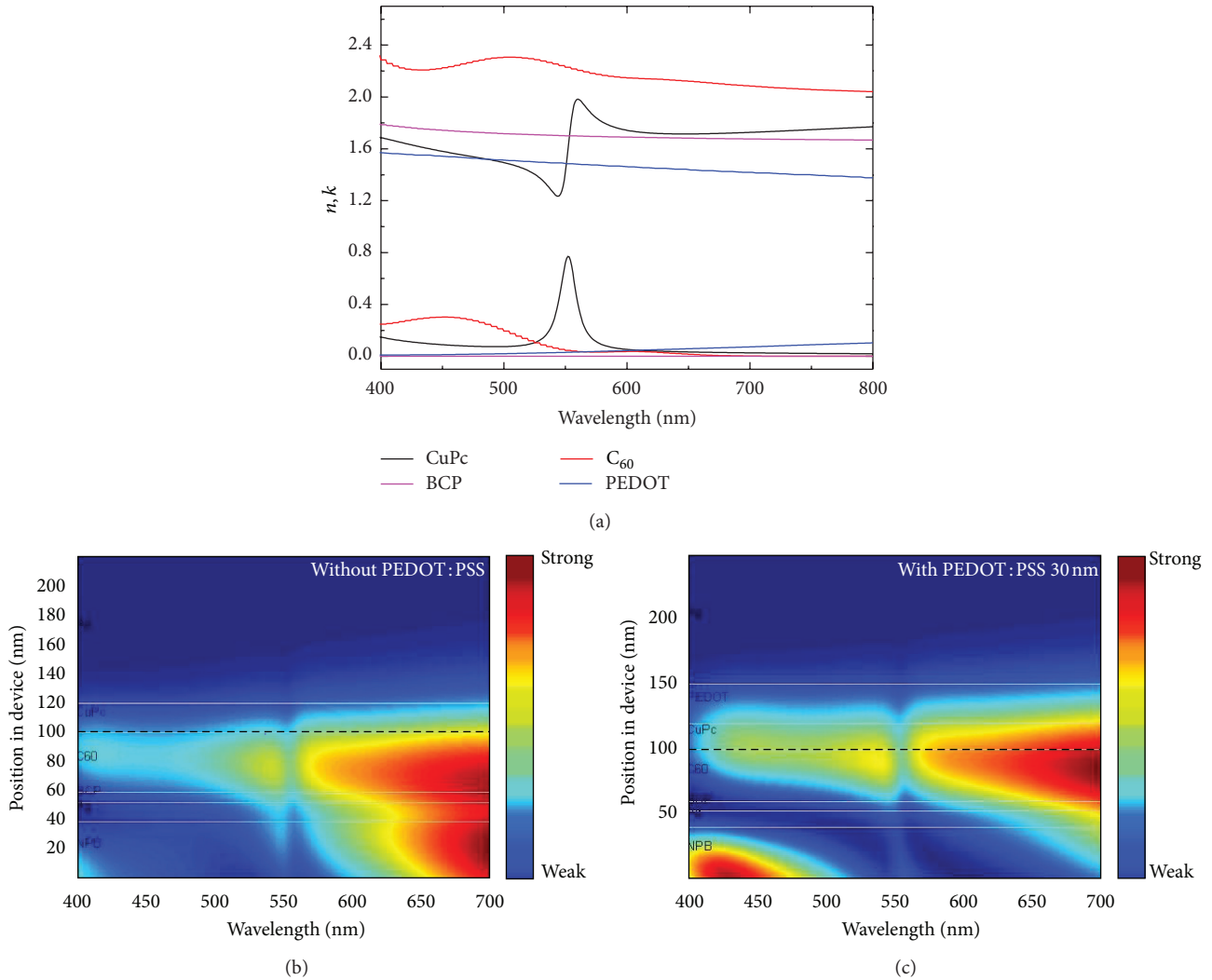


FIGURE 4: (a) Wavelength dependent refractive index (n) and absorption coefficient (k). Simulated optical field distribution inside TOPVs (b) with and (c) without 30 nm PEDOT:PSS layer.

field spectrum with a boundary near 550 nm, dominated by the refractive index of the CuPc thin film. Comparing these two diagrams, the inserted PEDOT:PSS layer causes a rearrangement of the optical field. Also it is obvious to detect that the thickness of PEDOT:PSS is efficiently used to adjust the region of stronger optical field close to or far from the anode. In particular, the optical field intensity near the interface between donor (CuPc) and acceptor (C₆₀) is the critical region to dissociate the excitons and determine the converted current. Here, the 30 nm PEDOT:PSS shifts the stronger optical field region (red part) towards the CuPc and C₆₀ junction, reducing the exciton-loss in drift and increasing the probability of exciton dissociation. This implies that the device with 30 nm PEDOT:PSS has a higher converted current.

We used our series anodes to fabricate the TOPV devices. Figure 5 shows J - V performances of the devices were measured in the dark. The control TOPV device without PEDOT:PSS indicates the best J - V performance, caused by the short distance between anode and cathode.

For a fixed driving voltage, the small electrode separation distance produces the strong electrical field inside device and accelerates the carrier mobility of organic layers [42]. Although the PEDOT:PSS generally used to be the conducting polymer layer, its thickness is still a key factor in determining anisotropic layer conductivity [43, 44]. Sandwiching it in between two electrodes, bulk conduction of PEDOT:PSS layer diminishes as increasing film thickness. Hence, 1000 rpm OPV device with the thickest PEDOT:PSS film presents a poor J - V behavior. Decreasing PEDOT:PSS film thickness by rising spin speed improves bulk conduction and reduces the electrode separation distance, leading to the improvement in J - V performance. However, the 7000 rpm corresponding to a very thin film exhibits degrade J - V performance. This is resulted from some defects on the film surface to hinder the carrier transport at the interface between anode and CuPc. Among these cases, the optimal spin speed is 5000 rpm to form a PEDOT:PSS thin film with good conduction and smooth surface without defects. However, it is hard to avoid that an electrical lag exists

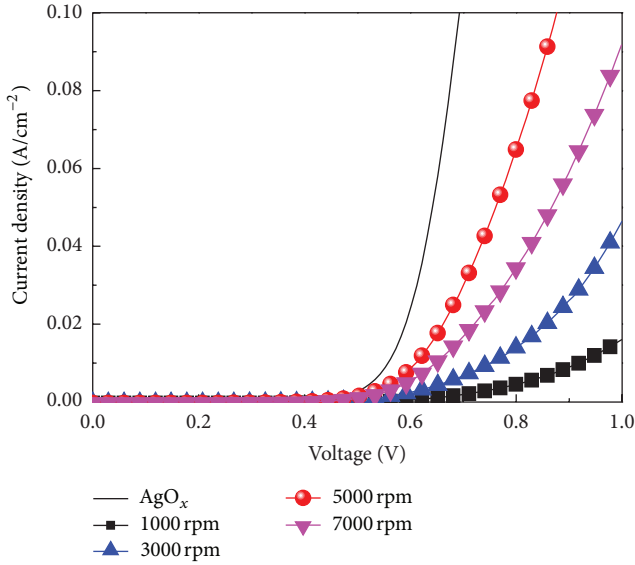


FIGURE 5: J - V characteristics of TOPVs under darkness.

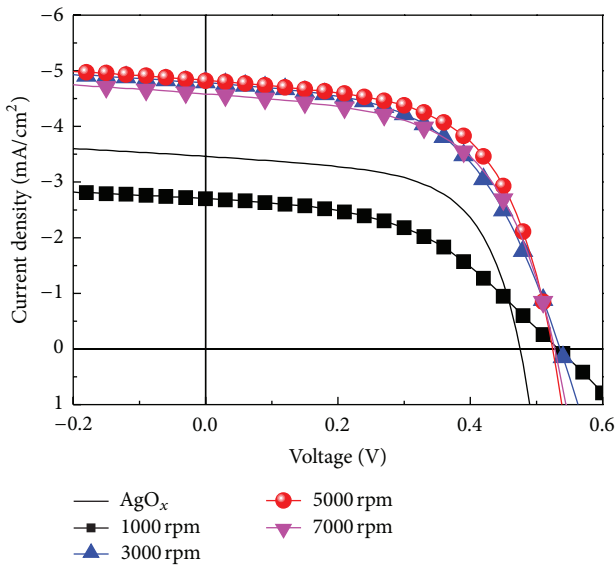


FIGURE 6: J - V characteristics of TOPVs under AM1.5 solar simulator illumination.

between the optimal device and control device, due to the additional PEDOT:PSS layer.

Figure 6 illustrates J - V curves of OPV devices under AM1.5 solar simulator illumination. Table 1 lists the photovoltaic characterizations: open-circuit voltage (V_{oc}), short-circuit current (J_{sc}), fill factor (FF), PCE, shunt resistor (R_{sh}), and series resistor (R_s). The OPV devices incorporated with various PEDOT:PSS films have an almost identical V_{oc} to each other (0.53–0.54 V). The V_{oc} values are greater than 0.49 V as indicated for the control OPV device containing Ag-AgO_x anode. The reason for this is that PEDOT:PSS has a greater work function than that of AgO_x. Their J_{sc} values are 2.74, 4.77, 4.8, and 4.56 mA/cm² for 1000, 3000, 5000, and 7000 rpm fabrication spin speeds, respectively. As spin

speed raises from 1000 to 5000 rpm, the diminishing film thickness results in enhanced J_{sc} , because of the better bulk conduction of PEDOT:PSS film, the greater carrier mobility of organic layer, and the stronger optical field intensity nears the exciton dissociation region. Distinctively, a degraded J_{sc} obtained at 7000 rpm device is resulted from the deteriorated hole collection induced by a few defects at the interface between CuPc and anode. Beyond 3000 rpm, OPV devices have greater J_{sc} values than 3.54 mA/cm² seen for control device because the presence of PEDOT:PSS reduced the energy barrier between organic layer and anode, benefits the hole transport at this interface, and moves the strong optical field close to exciton dissociation region. Furthermore, the reported effect of exciton quench close to the Ag anode is eliminated by incorporating a PEDOT:PSS layer. Taking into account FF, the control device has an excellent FF of 61.66% coming from the smallest R_s and the largest R_{sh} . Here, the FF is slightly affected by R_{sh} , as the R_{sh} values are all greater than 1 k Ω ·cm²; the difference in R_{sh} among these devices is negligible. Notably, R_s is affected by the conduction of anode substrate to determine FF. Hence, the control device with the excellent conductor Ag-AgO_x anode shows the smallest R_s of 0.56 Ω ·cm². The thinner PEDOT:PSS film performs the better bulk conduction to reduce the R_s from 21.15 to 2.13 Ω ·cm², except 7000 rpm device with few defects on the PEDOT:PSS film surface. These defects hindered the carrier transport and lowered bulk conduction of the anode. Reasonably, 7000 rpm device shows the increased R_s behavior. Hence, the spin speed of 5000 rpm is an optimal fabrication parameter for formation of buffer layer on the anode of TOPV device and provides the average PCE of 1.44% (maximum is 1.49%). It is significant that 1.38-fold PCE enhancement was obtained by inserting a PEDOT:PSS buffer layer between AgO_x and organic layer.

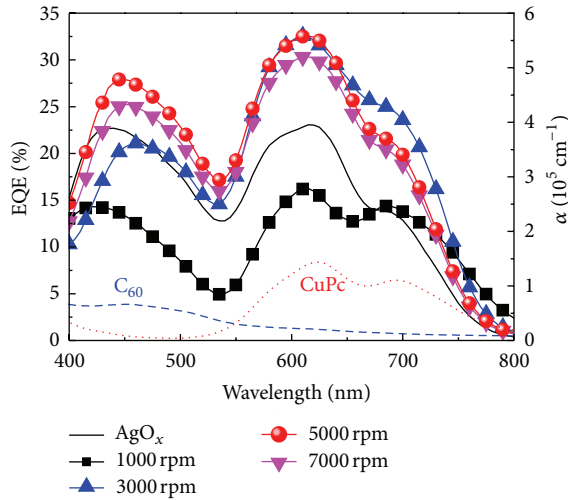
Figure 7 depicts the EQE spectra of devices and the absorption spectrum of CuPc and C₆₀. It is clear that there are two divisions of each EQE spectrum individually mirroring the CuPc and C₆₀ absorption band. Accordingly, it can be easily understood that the thickest case, 1000 rpm device, shows the lowest EQE for the whole band. Excluding this worse case, the uniform PEDOT:PSS thin film obviously improves EQE at the CuPc band. The interface modification between CuPc and anode is responsible for observable improvement at CuPc band. Defects on the 7000 rpm PEDOT:PSS surface indicate a small degradation at CuPc band. In this study, we did not have any modifications near the cathode. The EQE peak wavelength at C₆₀ band blueshifts with decreasing PEDOT:PSS thickness, dominated by the cavity effect inside device in a manner similar to the description in Figure 4. The EQE amplitude at the C₆₀ band is affected by the optical field distribution. 5000 rpm device shows a better overall EQE spectrum, particularly for the C₆₀ band. This device exhibits the greatest PCE of all devices.

4. Conclusion

In summary, we have successfully introduced PEDOT:PSS as an anode buffer layer to enhance the work function of

TABLE I: Photovoltaic characteristics of TOPVs with various PEDOT:PSS thin films on Ag-AgO_x anode.

| PEDOT:PSS | V _{oc} (V) | J _{sc} (mA/cm ²) | FF (%) | Eff (%) | R _{sh} (kΩ*cm ²) | R _s (Ω*cm ²) |
|-----------|---------------------|---------------------------------------|--------------|-------------|---------------------------------------|-------------------------------------|
| UVO 45 s | 0.48 ± 0.01 | 3.54 ± 0.02 | 61.66 ± 0.18 | 1.08 ± 0.02 | 1.36 ± 0.02 | 0.56 ± 0.2 |
| 1000 rpm | 0.54 ± 0.01 | 2.74 ± 0.04 | 45.71 ± 0.15 | 0.69 ± 0.02 | 1.48 ± 0.02 | 21.15 ± 2.51 |
| 3000 rpm | 0.54 | 4.77 ± 0.05 | 52.26 ± 0.82 | 1.36 ± 0.02 | 1.12 ± 0.05 | 7.47 ± 1.1 |
| 5000 rpm | 0.53 ± 0.01 | 4.8 ± 0.05 | 58.4 ± 0.38 | 1.44 ± 0.05 | 1.08 ± 0.01 | 2.13 ± 0.8 |
| 7000 rpm | 0.53 | 4.56 ± 0.02 | 57.41 ± 0.24 | 1.39 ± 0.01 | 1.14 ± 0.06 | 3.69 ± 0.13 |

FIGURE 7: EQE spectra of TOPVs and absorption spectra of CuPc and C₆₀.

Ag anode and then eliminated the energy barrier between organic layer and anode, thereby preventing the anode quenching and enhancing the J_{sc} for TOPV device. After characterizing PEDOT:PSS layers fabricated at various spin speeds, the optimal film thickness ~ 30 nm with good morphological quality could be obtained at 5000 rpm. In particular, a great enhancement in J_{sc} was observed by assembling the TOPV device with a PEDOT:PSS buffer layer fabricated at this optimal spin parameter. The optimized device offered a 1.37-fold enhancement in PCE compared to that of OPV without a buffer layer.

Acknowledgments

The authors acknowledge with great appreciation the financial support provided by the National Science Council (NSC), R.O.C. under Grant nos. 102-2221-E-155-047, 102-2622-E-155-008-CC3, and Bureau of Energy, Ministry of Economic Affairs, R.O.C. under Grant no. 102-E0616.

References

- [1] C. W. Tang, "Two-layer organic photovoltaic cell," *Applied Physics Letters*, vol. 48, no. 2, article 183, 3 pages, 1986.
- [2] B. A. Gregg and M. C. Hanna, "Comparing organic to inorganic photovoltaic cells: theory, experiment, and simulation," *Applied Physics Letters*, vol. 93, no. 6, article 3605, 10 pages, 2003.
- [3] B. P. Jelle, C. Breivik, and H. D. Rkenes, "Building integrated photovoltaic products: a state-of-the-art review and future research opportunities," *Solar Energy Materials and Solar Cells*, vol. 100, pp. 69–96, 2012.
- [4] R. Po, C. Carbonera, A. Bernardi, F. Tinti, and N. Camaioni, "Polymer- and carbon-based electrodes for polymer solar cells: toward low-cost, continuous fabrication over large area," *Solar Energy Materials and Solar Cells*, vol. 100, pp. 97–114, 2012.
- [5] P. Peunmans, A. Yakimov, and S. R. Forrest, "Small molecular weight organic thin-film photodetectors and solar cells," *Journal of Applied Physics*, vol. 93, no. 7, article 3693, p. 31, 2003.
- [6] R. Schueppel, R. Timmreck, N. Allinger et al., "Controlled current matching in small molecule organic tandem solar cells using doped spacer layers," *Journal of Applied Physics*, vol. 107, no. 4, Article ID 044503, 2010.
- [7] N. Espinosa, M. Hösel, D. Angmo, and F. C. Krebs, "Solar cells with one-day energy payback for the factories of the future," *Energy and Environmental Science*, vol. 5, no. 1, pp. 5117–5132, 2012.
- [8] C. F. Lin, M. Zhang, S. W. Liu, T. L. Chiu, and J. H. Lee, "High photoelectric conversion efficiency of metal phthalocyanine/fullerene heterojunction photovoltaic device," *International Journal of Molecular Sciences*, vol. 12, no. 1, pp. 476–505, 2011.
- [9] C. F. Lin, S. W. Liu, C. C. Lee et al., "Open-circuit voltage and efficiency improvement of subphthalocyanine-based organic photovoltaic device through deposition rate control," *Solar Energy Materials and Solar Cells*, vol. 103, pp. 69–75, 2012.
- [10] B. Kippelen and J. L. Brédas, *Energy & Environmental Science*, vol. 2, no. 3, pp. 251–261, 2009.
- [11] B. B. Yang, D. D. Zhang, S. T. Lee, Y. Q. Li, and J. X. Tang, "Efficiency enhancement of organic photovoltaic devices using a Sm:Al compound electrode," *Applied Physics Letters*, vol. 102, no. 7, Article ID 073301, 4 pages, 2013.
- [12] F. C. Krebs, "Roll-to-roll fabrication of monolithic large-area polymer solar cells free from indium-tin-oxide," *Solar Energy Materials and Solar Cells*, vol. 93, no. 9, pp. 1636–1641, 2009.
- [13] F. C. Krebs, "All solution roll-to-roll processed polymer solar cells free from indium-tin-oxide and vacuum coating steps," *Organic Electronics*, vol. 10, no. 5, pp. 761–768, 2009.
- [14] J. Meiss, M. K. Riede, and K. Leo, "Towards efficient tin-doped indium oxide (ITO)-free inverted organic solar cells using metal cathodes," *Applied Physics Letters*, vol. 94, no. 1, Article ID 013303, 3 pages, 2009.
- [15] M. Manceau, D. Angmo, M. Jørgensen, and F. C. Krebs, "ITO-free flexible polymer solar cells: from small model devices to roll-to-roll processed large modules," *Organic Electronics*, vol. 12, no. 4, pp. 566–574, 2011.
- [16] R. Søndergaard, M. Hösel, D. Angmo, T. T. Larsen-Olsen, and F. C. Krebs, "Roll-to-roll fabrication of polymer solar cells," *Materialtoday*, vol. 15, p. 36, 2012.

- [17] F. C. Krebs, J. Fyenbo, and M. Jørgensen, "Product integration of compact roll-to-roll processed polymer solar cell modules: methods and manufacture using flexographic printing, slot-die coating and rotary screen printing," *Journal of Materials Chemistry*, vol. 20, pp. 8994–9001, 2010.
- [18] F. C. Krebs, "Fabrication and processing of polymer solar cells: a review of printing and coating techniques," *Solar Energy Materials and Solar Cells*, vol. 93, no. 4, pp. 394–412, 2009.
- [19] H. W. Lin, S. W. Chiu, L. Y. Lin et al., "Device engineering for highly efficient top-illuminated organic solar cells with microcavity structures," *Advanced Materials*, vol. 24, no. 17, pp. 2269–2272, 2012.
- [20] B. Kouskoussa, M. Morsli, K. Benchouk et al., "On the improvement of the anode/organic material interface in organic solar cells by the presence of an ultra-thin gold layer," *Physica Status Solidi A*, vol. 206, no. 2, pp. 311–315, 2009.
- [21] H. Jin, C. Tao, M. Velusamy et al., "Efficient, large area ITO-and-PEDOT-free organic solar cell sub-modules," *Advanced Materials*, vol. 24, no. 19, pp. 2572–2577, 2012.
- [22] S. D. Yambem, K.-S. Liao, N. J. Alley, and S. A. Curran, "Stable organic photovoltaics using Ag thin film anodes," *Journal of Materials Chemistry*, vol. 22, no. 14, pp. 6894–6898, 2012.
- [23] S. I. Na, S. S. Kim, J. Jo, and D. Y. Kim, "Efficient and flexible ITO-free organic solar cells using highly conductive polymer anodes," *Advanced Materials*, vol. 20, no. 21, pp. 4061–4067, 2008.
- [24] C. F. Lin, S. W. Liu, W. F. Hsu et al., "Modification of silver anode and cathode for a top-illuminated organic photovoltaic device," *Journal of Physics D*, vol. 43, no. 39, Article ID 395101, 2010.
- [25] M. Zhang, T. L. Chiu, C. F. Lin, J. H. Lee, J. K. Wang, and Y. Wu, "Roughness characterization of silver oxide anodes for use in efficient top-illuminated organic solar cells," *Solar Energy Materials and Solar Cells*, vol. 95, no. 9, pp. 2606–2609, 2011.
- [26] V.-E. Choong, Y. Park, N. Shivaparan, C. W. Tang, and Y. Gao, "Deposition-induced photoluminescence quenching of tris-(8-hydroxyquinoline) aluminum," *Applied Physics Letters*, vol. 71, no. 8, pp. 1005–1007, 1997.
- [27] T. L. Chiu, W. F. Xu, C. F. Lin, J. H. Lee, C. C. Chao, and M. K. Leung, "Optical and electrical characteristics of Ag-doped perylene diimide derivative," *Applied Physics Letters*, vol. 94, no. 1, Article ID 013307, 3 pages, 2009.
- [28] Y. Wu, H. R. Wu, M. L. Wang et al., "Metal-induced photoluminescence quenching in thin organic films originating from noncontact energy transfer between single molecule and atom," *Applied Physics Letters*, vol. 90, Article ID 154105, 3 pages, 2007.
- [29] M. Y. Chan, C. S. Lee, S. L. Lai et al., "Efficient organic photovoltaic devices using a combination of exciton blocking layer and anodic buffer layer," *Journal of Applied Physics*, vol. 100, no. 9, Article ID 094506, 2006.
- [30] D. W. Zhao, P. Liu, X. W. Sun et al., "An inverted organic solar cell with an ultrathin Ca electron-transporting layer and MoO₃ hole-transporting layer," *Applied Physics Letters*, vol. 95, no. 15, Article ID 153304, 3 pages, 2009.
- [31] M. Vogel, S. Doka, C. Breyer, M. C. Lux-Steiner, and K. Fostiropoulos, "On the function of a bathocuproine buffer layer in organic photovoltaic cells," *Applied Physics Letters*, vol. 89, no. 16, Article ID 163501, 2006.
- [32] D. Kabra, M. H. Song, B. Wenger, R. H. Friend, and H. J. Snaith, "High efficiency composite metal oxide-polymer electroluminescent devices: a morphological and material based investigation," *Advanced Materials*, vol. 20, no. 18, pp. 3447–3452, 2008.
- [33] Y. Park, V.-E. Choong, B. R. Hsieh, C. W. Tang, and Y. Gao, "Gap-state induced photoluminescence quenching of phenylene vinylene oligomer and its recovery by oxidation," *Physical Review Letters*, vol. 78, no. 20, pp. 3955–3958, 1997.
- [34] J. Mei, M. S. Bradley, and V. Bulović, "Photoluminescence quenching of tris-(8-hydroxyquinoline) aluminum thin films at interfaces with metal oxide films of different conductivities," *Physical Review B*, vol. 79, no. 23, Article ID 235205, 8 pages, 2009.
- [35] D. L. Smith, *Thin-Film Disposition Principles and Practice*, McGraw-Hill, New York, NY, USA, 1995.
- [36] S. Khodabakhsh, B. M. Sanderson, J. Nelson, and T. S. Jones, "Using self-assembling dipole molecules to improve charge collection in molecular solar cells," *Advanced Functional Materials*, vol. 16, no. 1, pp. 95–100, 2006.
- [37] M. Massi, M. Cavallini, and F. Biscarini, "Influence of the substrate hydrophilicity on the grid assisted deposition of tris-(8-hydroxyquinolinato) aluminum(III) thin films," *Surface Science*, vol. 603, no. 3, pp. 503–506, 2009.
- [38] C. Cioarec, P. Melpignano, N. Gherardi, R. Clergereaux, and C. Villeneuve, "Ultrasmooth silver thin film electrodes with high polar liquid wettability for OLED microcavity application," *Langmuir*, vol. 27, no. 7, pp. 3611–3617, 2011.
- [39] G. F. Burkhard, E. T. Hoke, and M. D. McGehee, "Accounting for interference, scattering, and electrode absorption to make accurate internal quantum efficiency measurements in organic and other thin solar cells," *Advanced Materials*, vol. 22, no. 30, pp. 3293–3297, 2010.
- [40] R. Häusermann, E. Knapp, M. Moos, N. A. Reinke, T. Flatz, and B. Ruhstaller, "Coupled optoelectronic simulation of organic bulk-heterojunction solar cells: parameter extraction and sensitivity analysis," *Journal of Applied Physics*, vol. 106, no. 10, Article ID 104507, 9 pages, 2009.
- [41] F. Deschler, D. Riedel, B. Ecker, E. Hauff, E. D. Como, and R. C. I. MacKenzi, "Increasing organic solar cell efficiency with polymer interlayers," *Physical Chemistry Chemical Physics*, vol. 15, no. 3, pp. 764–769, 2013.
- [42] S. C. Tse, S. W. Tsang, and S. K. So, "Polymeric conducting anode for small organic transporting molecules in dark injection experiments," *Journal of Applied Physics*, vol. 100, no. 6, Article ID 063708, 5 pages, 2006.
- [43] A. M. Nardes, M. Kemerink, and R. A. J. Janssen, "Anisotropic hopping conduction in spin-coated PEDOT:PSS thin films," *Physical Review B*, vol. 76, no. 8, Article ID 085208, 7 pages, 2007.
- [44] Y. H. Kim, C. Sachse, M. L. Machala, C. May, L. Müller-Meskamp, and K. Leo, "Highly conductive PEDOT:PSS electrode with optimized solvent and thermal post-treatment for ITO-free organic solar cells," *Advanced Functional Materials*, vol. 21, no. 6, pp. 1076–1081, 2011.

Research Article

Near Infrared Lateral Photovoltaic Effect in LaTiO₃ Films

Wujun Jin, Shasha Zhang, Hao Ni, Wenfeng Xiang, Jianfeng Xi, Xin Feng, and Kun Zhao

College of Science, China University of Petroleum, Beijing 102249, China

Correspondence should be addressed to Hao Ni; nihona@163.com

Received 11 June 2013; Revised 5 September 2013; Accepted 23 September 2013

Academic Editor: Francesco Bonaccorso

Copyright © 2013 Wujun Jin et al. This is an open access article distributed under the Creative Commons Attribution License, which permits unrestricted use, distribution, and reproduction in any medium, provided the original work is properly cited.

We have reported on the lateral photovoltaic effect of LaTiO₃ films epitaxially grown on (100) SrTiO₃ substrates. Under illumination of continuous 1064 nm laser beam on the LaTiO₃ film through SrTiO₃ substrate, the open-circuit photovoltage depended linearly on the illuminated position. The photosensitivity can be modified by bias current. These results indicated that the LaTiO₃ films give rise to a potentially photoelectronic device for near infrared position-sensitive detection.

1. Introduction

Lateral photovoltaic effect (LPE) discovered by Schottky in 1930 has been widely used as position sensitive detectors (PSDs) in many fields requiring precision measurements, such as robotic vision, remote optical alignment, machine tool alignment, and medical instrumentation, [1, 2]. In order to improve the sensitivity and linearity of PSDs, many researchers have made efforts to study LPE in various kinds of materials systems, such as conventional p-n junctions, hydrogenated amorphous silicon based structures, porous silicon, Ti/Si amorphous superlattices, semiconducting polymer, metal-semiconductor and metal-insulator-semiconductor structures, modulation-doped AlGaAs/GaAs heterostructure, and Cu₂O nanoscale film, [3–11]. Almost all of the reported LPEs were applied in visible or ultraviolet region, while works concerning large LPE in near infrared (NIR) region have been rarely reported [10, 11].

Recently, the strongly correlated electron systems composed of transition-metal oxides have attracted many interests [12, 13]. By the advanced preparation technology of thin film, such as terminate oxide substrates at well-defined ionic planes, pulsed-laser deposition (PLD) and molecular-beam epitaxy (MBE), and high-pressure reflection high-energy electron diffraction, many new physical phenomena have been discovered in oxide interfaces [14, 15]. Ohtomo et al. have studied the Mott insulator LaTiO₃ (LTO) embedded in the band insulator LaTiO₃ (STO) and found interface-specific conducting states between the two different insulators [16–18]. And then the investigations of LaTiO₃/SrTiO₃

have been focused on their electro-optic properties [19–23]. These results have shown that the different structures among bulk materials, films, and interfaces have generated a large difference in physical properties, even when the same component materials are used.

In this paper, we have grown epitaxial LTO films on STO substrates using PLD technique and presented a near infrared lateral photovoltaic effect by irradiating the structure of LTO/STO. The open-circuit photovoltage of the LTO film depended linearly on illuminated 1064 nm laser beam position. The photosensitivity can be modified with bias current. The results demonstrated that the present film has a great potential application in NIR position-sensitive detector.

2. Experimental

The LTO film with a thickness of about 100 nm was deposited on a 0.5 mm thick single crystalline (100) STO substrate with an area of 5.0 mm × 5.0 mm using a polycrystalline La₂Ti₂O₇ target by pulsed laser deposition. The substrate temperature was kept at 850°C and the oxygen background pressure was 2.38 × 10⁻⁶ Torr. After the deposition, the LTO film was then cooled to room temperature with the substrate heater power cutoff. The structure of the sample was characterized by X-ray diffraction (XRD).

The schematic setup for LPE measurement is shown in the inset of Figure 2(b). For photovoltaic measurement, two silver electrodes of 4.0 mm × 1.0 mm in area, separated by about 3.0 mm, were fabricated on the as-prepared LTO film

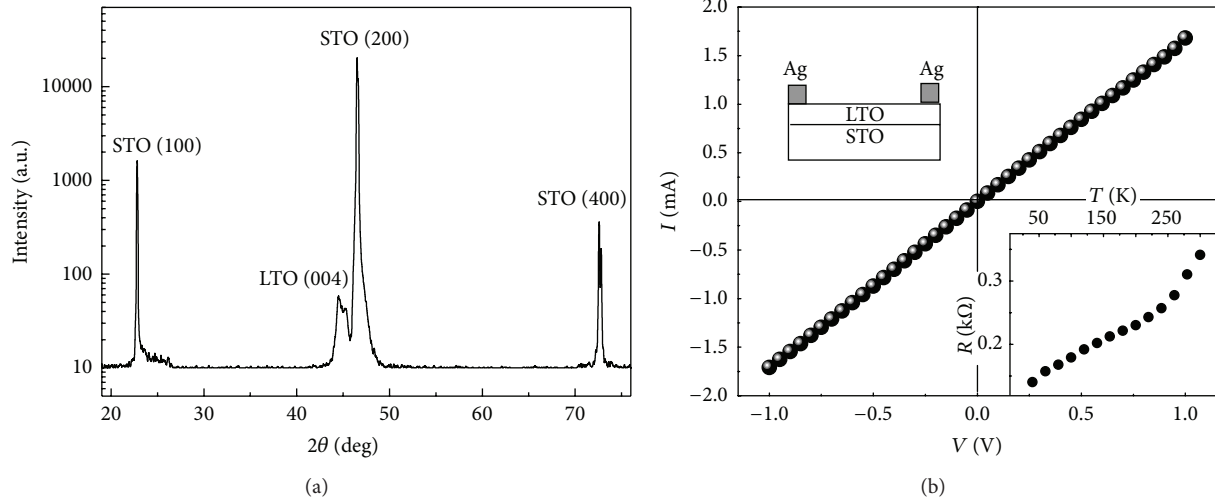


FIGURE 1: (a) XRD pattern of LTO/STO sample. (b) The typical I - V characteristics of the LTO/STO at room temperature. The top inset shows the schematic measurement setup. The bottom inset shows the temperature dependence of resistance of LTO/STO film.

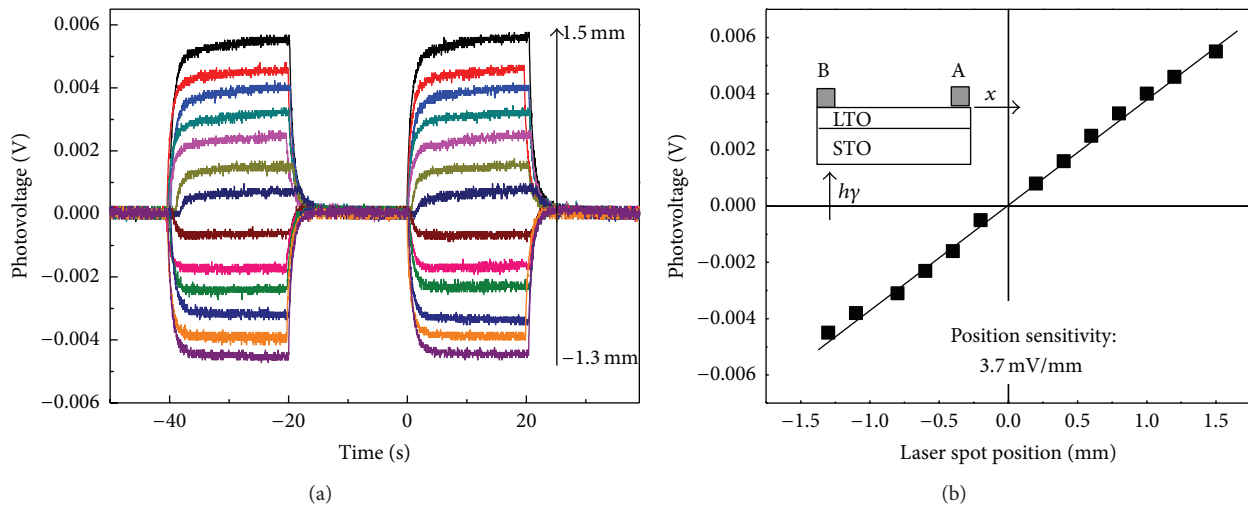


FIGURE 2: (a) The typical waveforms recorded by oscilloscope with $1\text{ M}\Omega$ input impedance without any bias when laser spot irradiated region from A to B. (b) The steady waveforms' peak voltages depended linearly on the spot positions through the zero point.

surface. A small area of 1 mm diameter was irradiated on the LTO/STO interface by a 1064 nm continuum solid state laser. The lateral photovoltage (LPV) between the Ag electrodes A ($x = 1.5\text{ mm}$) and B ($x = -1.5\text{ mm}$) on the LTO film surface was measured and recorded by a sampling oscilloscope of 350 MHz terminated into $1\text{ M}\Omega$ at ambient temperature.

3. Results and Discussion

The XRD scan curve of the LTO/STO is presented in Figure 1(a). Except for the diffraction peaks of STO (100) and LTO ($00l$), there are no diffraction peaks from impurity phases or randomly oriented grains, indicating that the LTO

film is a single phase and (001) oriented. Figure 1(b) shows the typical current-voltage (I - V) curve of the LTO film measured by tuning the applied voltage with a pulse-modulated voltage source at room temperature, and the resistance of the sample increases with the temperature range from 20 to 300 K as shown in the inset. These results were consistent with the metallic behavior and also confirmed the ohmic contacts between electrodes and LTO surface.

Figure 2(a) shows the typical waveforms recorded by oscilloscope when the 1064 nm laser irradiated the LTO film through the STO substrate at different positions x (from A to B shown in the inset of Figure 2(b)). The on-sample laser power is 98 mW. When the laser irradiated the sample, the LPV rises fast at the beginning of about 3 s and then

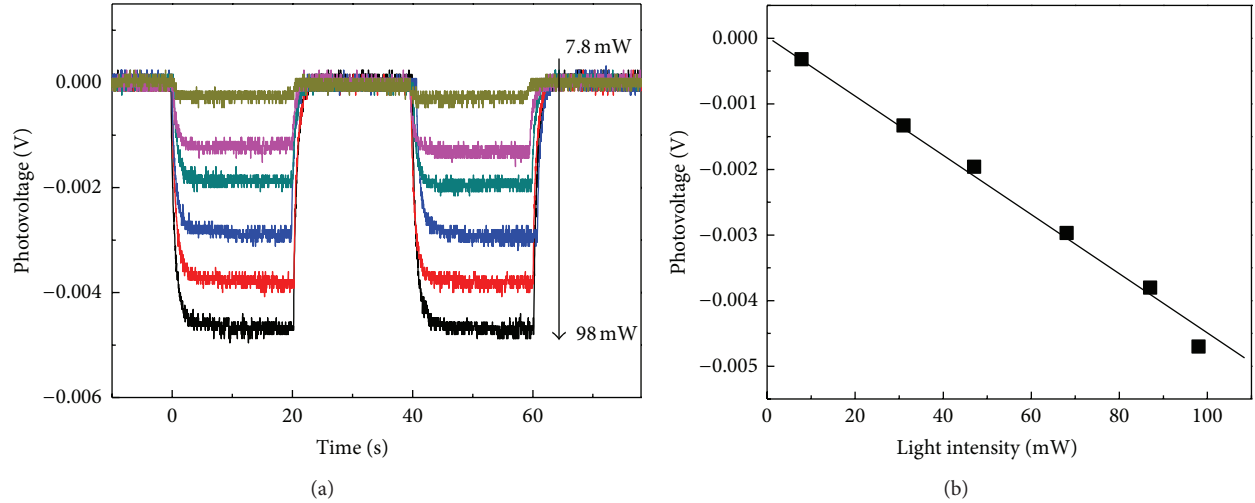


FIGURE 3: (a) The typical waveforms with different on-sample laser power from 7.8 to 98 mW at $x = -1.4$ mm. (b) The LPV dependence on the on-sample laser power.

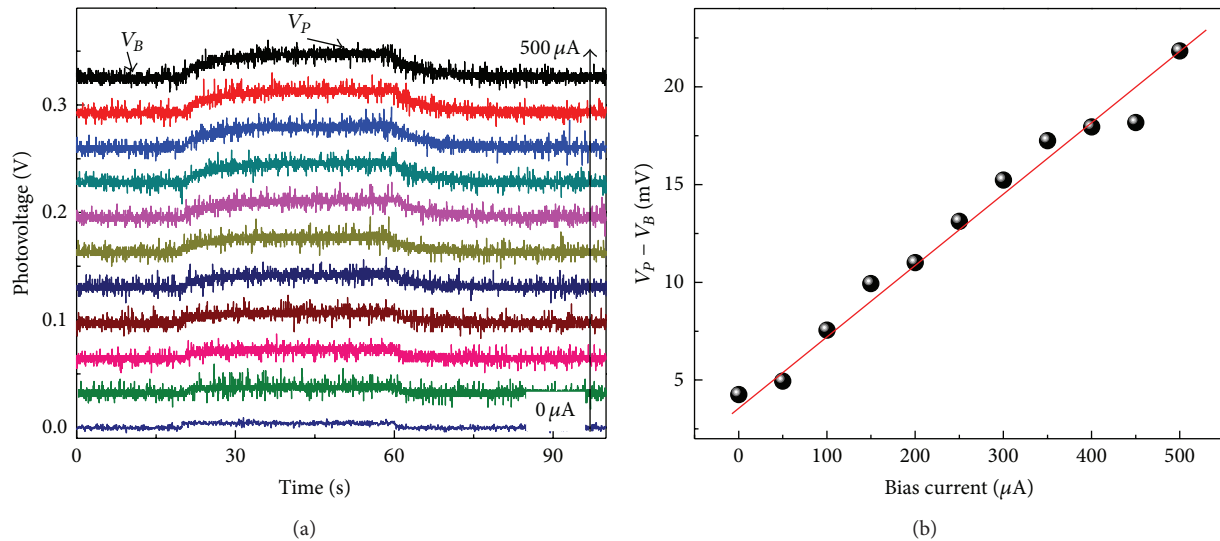


FIGURE 4: (a) The typical waveforms with bias currents applied from 0 to 500 μA at $x = 1.5$ mm. (b) The photoinduced LPV defined by $(V_P - V_R)$ dependence on the bias current.

gets stable. The LPVs at $x = 1.5$ mm and $x = -1.3$ mm were 5.52 mV and -4.52 mV, respectively. The LPV was dramatically changed when the laser irradiated at different positions, and Figure 2(b) shows the LPV as a function of laser spot position. It is clear that the photovoltage shows good linear relationship with the illuminated position. The position sensitivity of LPV in the sample is about 3.7 mV/mm.

In addition we also measured the photovoltaic responses at -1.4 mm with the laser power increasing from 7.8 to 98 mW (see Figure 3(a)). Figure 3(b) shows the photovoltaic response dependence on laser power. It is clear that the LPV is linear to the light power as the power is increased, which means that the position sensitivities of LPV are stable.

To improve the laser position photovoltaic sensitivity, a bias current was applied to the sample. LPVs were measured

by gradually increasing the bias current from 0 to 500 μA under 1064 nm laser illumination at $x = 1.5$ mm. The on-sample power was kept at 98 mW. The V_B in Figure 4(a) denotes the baseline recorded by the oscilloscope for laser-off state, which was caused by the external bias and the input impedance, and shifts from 0.3 to 325 mV for bias current from 0 to 500 μA . The photoinduced LPV defined by $(V_P - V_R)$ is plotted in Figure 4(b) as a function of the applied bias and increases from ~ 5 to 22 mV with bias increasing from 0 to 500 μA .

In our case the band gap of LTO and STO is ~ 0.2 eV and ~ 3.2 eV, respectively. When we used 1064 nm laser to scan the back STO side of sample, the photon can pass through the STO substrate without being absorbed. Under the illumination in LTO, electrons were excited from valance

band to conduction band by absorbing the photon energy and generated nonequilibrium carriers. The light-induced nonequilibrium electrons in LTO will thus generate a gradient laterally between the illuminated and nonilluminated zones, resulting in excess electrons diffusing laterally along the film away from the illuminated spot toward two sides (at anode and cathode). When the lateral distance of the laser spot from each contact is different, the electron density impacting in built-in electric field is different. Thus a lateral photovoltage is generated to be proportional to the difference of electron density between two lateral electrodes and strongly dependent on laser spot position.

Previously the PSDs based on LPE were mainly concentrated in the visible or ultraviolet region. The large IR LPE has been a challenge for a long time because the light in this region is hard to be absorbed. Recently a lateral photovoltage position sensitivity of 16.4 mV/mm/mW was observed at 832 nm light wavelength in nanoscale Co/Si structures [10]. Under pulsed IR laser irradiation the position sensitivity of Cu₂O/Si thin film PSD reached 15.3 mV/mm [11]. Different from the reported IR PSD [10, 11], the present NIR PSD is composed of LTO film and STO substrate, named as all-perovskite-oxide (APO) PSD. The waveform of the present detector shows that the rising time of LPV is about 3 seconds. To meet the challenges of applying APO in NIR PSD, we will improve the position sensitivity and resolve the slow response time in the future.

4. Conclusions

In summary, lateral photovoltaic effect was investigated in LTO film. The LPVs were observed by chopping mechanically 1064 nm continuous laser beam, which showed a linear relationship with irradiated position, suggesting a potential application for position sensitive detectors at room temperature. The strong dependence on the laser intensity and bias current implied that LTO film may be of great use in light power measurement.

Acknowledgments

This work was supported by the National Key Basic Research Program of China (Grant no. 2013CB328706), the Specially Funded Program on National Key Scientific Instruments and Equipment Development (Grant no. 2012YQ14005), the Beijing National Science Foundation (Grant no. 4122064), and the Science Foundation of the China University of Petroleum (Beijing) (Grant nos. QZDX-2010-01 and KYJJ2012-06-27). Shasha Zhang and Wujun Jin contributed equally to this work.

References

- [1] W. Schottky, "Über den enstellungsort der photoelektronen in kuper-kuperoxydul-photozellen," *Physikalische Zeitschrift*, vol. 31, pp. 913–925, 1930.
- [2] J. T. Wallmark, "A new semiconductor photocell using lateral photoeffect," *Proceedings of the IRE*, vol. 45, no. 4, pp. 474–483, 1957.
- [3] J. Henry and J. Livingstone, "Thin-film amorphous silicon position-sensitive detectors," *Advanced Materials*, vol. 13, no. 12-13, pp. 1023–1026, 2001.
- [4] D. W. Boeringer and R. Tsu, "Lateral photovoltaic effect in porous silicon," *Applied Physics Letters*, vol. 65, no. 18, pp. 2332–2334, 1994.
- [5] B. F. Levine, R. H. Willens, C. G. Bethea, and D. Brasen, "Lateral photoeffect in thin amorphous superlattice films of Si and Ti grown on a Si substrate," *Applied Physics Letters*, vol. 49, no. 22, pp. 1537–1539, 1986.
- [6] D. Kabra, T. B. Singh, and K. S. Narayan, "Semiconducting-polymer-based position-sensitive detectors," *Applied Physics Letters*, vol. 85, no. 21, pp. 5073–5075, 2004.
- [7] C. Q. Yu, H. Wang, S. Q. Xiao, and Y. X. Xia, "Direct observation of lateral photovoltaic effect in nano-metal-films," *Optics Express*, vol. 17, no. 24, pp. 21712–21722, 2009.
- [8] H. Águas, L. Pereira, D. Costa, E. Fortunato, and R. Martins, "Super linear position sensitive detectors using MIS structures," *Optical Materials*, vol. 27, no. 5, pp. 1088–1092, 2005.
- [9] N. Tabatabaie, M.-H. Meynadier, R. E. Nahory, J. P. Harbison, and L. T. Florez, "Large lateral photovoltaic effect in modulation-doped AlGaAs/GaAs heterostructures," *Applied Physics Letters*, vol. 55, no. 8, pp. 792–794, 1989.
- [10] C. Q. Yu and H. Wang, "Large near-infrared lateral photovoltaic effect observed in Co/Si metal-semiconductor structures," *Applied Physics Letters*, vol. 96, no. 17, Article ID 171102, 2010.
- [11] L. Du and H. Wang, "Infrared laser induced lateral photovoltaic effect observed in Cu₂O nanoscale film," *Optics Express*, vol. 18, no. 9, pp. 9113–9118, 2010.
- [12] M. Imada, A. Fujimori, and Y. Tokura, "Metal-insulator transitions," *Reviews of Modern Physics*, vol. 70, no. 4, pp. 1039–1263, 1998.
- [13] Y. Tokura and N. Nagaosa, "Orbital physics in transition-metal oxides," *Science*, vol. 288, no. 5465, pp. 462–468, 2000.
- [14] A. Ohtomo, D. A. Muller, J. L. Grazul, and H. Y. Hwang, "Epitaxial growth and electronic structure of LaTiOx films," *Applied Physics Letters*, vol. 80, no. 21, pp. 3922–3924, 2002.
- [15] K. H. Kim, D. P. Norton, J. D. Budai et al., "Epitaxial structure and transport in LaTiO_{3+x} films on (001) SrTiO₃," *Physica Status Solidi A*, vol. 200, no. 2, pp. 346–351, 2003.
- [16] A. Ohtomo, D. A. Muller, J. L. Grazul, and H. Y. Hwang, "Artificial charge-modulation in atomic-scale perovskite titanate superlattices," *Nature*, vol. 419, no. 6905, pp. 378–380, 2002.
- [17] S. Okamoto and A. J. Millis, "Electronic reconstruction at an interface between a Mott insulator and a band insulator," *Nature*, vol. 428, no. 6983, pp. 630–633, 2004.
- [18] S. Okamoto, A. J. Millis, and N. A. Spaldin, "Lattice relaxation in oxide heterostructures: LaTiO₃/SrTiO₃ superlattices," *Physical Review Letters*, vol. 97, no. 5, Article ID 056802, 4 pages, 2006.
- [19] M. Takizawa, H. Wadati, K. Tanaka et al., "Photoemission from buried interfaces in SrTiO₃/LaTiO₃ superlattices," *Physical Review Letters*, vol. 97, no. 5, Article ID 057601, 4 pages, 2006.
- [20] S. S. A. Seo, W. S. Choi, H. N. Lee et al., "Optical study of the free-carrier response of LaTiO₃/SrTiO₃ superlattices," *Physical Review Letters*, vol. 99, no. 26, Article ID 266801, 4 pages, 2007.
- [21] A. Rastogi, A. K. Kushwaha, T. Shiyani, A. Gangawar, and R. C. Budhani, "Electrically tunable optical switching of a Mott insulator-band insulator interface," *Advanced Materials*, vol. 22, no. 40, pp. 4448–4451, 2010.

- [22] H. W. Jang, D. A. Felker, C. W. Bark et al., "Metallic and insulating oxide interfaces controlled by electronic correlations," *Science*, vol. 331, no. 6019, pp. 886–889, 2011.
- [23] A. Rastogi and J. J. Pulikkotil, "Photoconducting state and its perturbation by electrostatic fields in oxide-based two-dimensional electron gas," *Physical Review B*, vol. 86, no. 7, Article ID 075127, 9 pages, 2012.

Research Article

Optical and Structural Investigation of CdSe Quantum Dots Dispersed in PVA Matrix and Photovoltaic Applications

Pallabi Phukan and Dulen Saikia

Material Science Laboratory, Department of Physics, Sibsagar College, Joysagar, Assam 785665, India

Correspondence should be addressed to Dulen Saikia; dulen.s@rediffmail.com

Received 30 May 2013; Revised 21 August 2013; Accepted 4 September 2013

Academic Editor: Giuseppe Calogero

Copyright © 2013 P. Phukan and D. Saikia. This is an open access article distributed under the Creative Commons Attribution License, which permits unrestricted use, distribution, and reproduction in any medium, provided the original work is properly cited.

CdSe quantum dots (QDs) dispersed in polyvinyl alcohol (PVA) matrix with their sizes within the quantum dot regime have been synthesized via a simple heat induced thermolysis technique. The effect of the concentrations of the cadmium source on the optical properties of CdSe/PVA thin films was investigated through UV-Vis absorption spectroscopy. The structural analysis and particle size determination as well as morphological studies of the CdSe/PVA nanocomposite thin films were done with the help of X-ray diffraction (XRD) and transmission electron microscopy (TEM). The XRD analysis reveals that CdSe/PVA nanocomposite thin film has a hexagonal (wurtzite) structure. A prototype thin film solar cell of CdSe/CdTe has been synthesized and its photovoltaic parameters were measured.

1. Introduction

Polymer nanocomposites are diverse and versatile functional materials in which nanoscale (1–100 nm) inorganic particles are dispersed in an organic polymer matrix to display enhanced optical, mechanical, magnetic, and optoelectronic properties [1–3]. The incorporation of semiconductor nanoparticles into polymer matrices is of great importance because of the potential applications of the resulting materials in wide variety of fields such as in fabrication of electronic devices [4–6], catalysis [7], gas sensors [8, 9], and nonlinear optics [10]. Bulk CdSe is a direct bandgap (1.74 eV) II-VI semiconductor with an exciton Bohr radius of 6 nm [11, 12]. It exhibits either sphalerite cubic (zinc-blende type) or hexagonal (wurtzite type) structure. The hexagonal state is the stable phase while the sphalerite cubic is the metastable state [13]. From technological perspective, CdSe nanoparticles (NPs) are of significant interest because of their unique quantum confinement properties, bright photoluminescence, narrow emission band, and photostability [14]. CdSe-polymer nanocomposites find potential applications in the fabrication of devices like photovoltaic cells, laser, thin film transistors, light emitting diodes, and other nanoscale devices [15, 16]. Many methods have been developed to synthesize CdSe

in thin film form which includes chemical bath deposition (CBD) [17], vacuum evaporation [18], electrodeposition [19], spray pyrolysis [20], and successive ionic layer adsorption and reaction (SILAR) [21]. However, among these, CBD technique is preferable for the synthesis of polymer-capped CdSe nanocomposite thin film as it is easy to handle, cost effective, and suitable for large area deposition [22, 23].

In recent years, various works have focused on the synthesis and characterization of cadmium selenide (CdSe) QDs in polymeric matrices by wet chemical synthetic method [24–29]. Pecherska et al. successfully prepared CdSe QDs embedded in polymer matrix, and the effects of annealing temperature on the luminescent properties of the nanostructures were investigated [24]. PVA-capped CdSe NPs were synthesized by Shah et al. via a simple chemical route and studied the influence of precursor concentration, aging time, and reaction temperature on the size of the as-synthesized CdSe NPs as well as on their optical properties [25]. Photoluminescence properties of CdSe-PVA nanocomposites with small and narrow size distribution obtained by varying the polymer concentrations were reported by Kushwaha et al. [26]. Ma et al. reported the room temperature synthesis of CdSe nanoparticles dispersed in PVA matrix via one-step solution growth technique and studied their optical and

structural properties [27]. Suo et al. fabricated the poly (vinyl alcohol) nanocomposite thin film reinforced with CdSe-ZnS quantum dots by drop casting method and investigated their optical properties [28]. Mansur et al. reported the synthesis and characterization of CdSe nanoparticles using acid-functionalized PVA as capping ligands via aqueous route at room temperature by methods of colloidal chemistry [29].

The aim of the present study is to synthesize CdSe/PVA nanocomposite thin films tuned with hexagonal phase by heat induced thermolysis technique and also to study the effect of concentrations of cadmium ion on its optical properties. The optimised CdSe/PVA nanocomposite thin film will be utilised for fabrication and evaluation of a prototype CdSe/CdTe solar cell.

2. Experimental

2.1. Materials and Characterizing Techniques. All reagents such as sodium sulphite (Na_2SO_3), metallic selenium powder, cadmium chloride ($\text{CdCl}_2 \cdot \text{H}_2\text{O}$), and polyvinyl alcohol were purchased from Merk (India) Ltd. and used directly as received without any further purification. Deionised water was used throughout the experimental work.

The structural properties of the CdSe/PVA thin films were analysed with a Rigaku Ultima-IV X-ray diffractometer using $\text{CuK}\alpha$ radiations operated at 40 kV and 40 mA. For optical studies, absorption spectra were recorded with a Scinco (S 3100) PD UV-Vis spectrophotometer. The high resolution transmission electron microscopy (HRTEM) images were taken by a TECNAI-T 30 model instrument operated at an accelerating voltage of 300 kV. The photovoltaic parameters of the cell were measured by Keithley-2400 source meter under illumination with a 100 mW cm^{-2} (1 SUN) xenon lamp.

2.2. Synthesis of CdSe/PVA Nanocomposite. The CdSe/PVA nanocomposite thin films were deposited on chemically clean glass substrate by reacting Cd^{2+} dispersed PVA with sodium selenosulphite via heat induced thermolysis technique. The synthesis technique is derived from Saikia et al. [30] for CdS/PVA nanocomposite thin film. At first, 1M sodium selenosulphite (Na_2SeSO_3) solution was prepared by adding 0.05 mol of powdered selenium into 100 mL of 1M sodium sulphite (Na_2SO_3) solution. The resultant mixture was refluxed at 70°C for 3 hr with constant stirring. After refluxing, the final solution was filtered with a Whatman filter paper and was stored in the dark at $(60 \pm 5)^\circ\text{C}$ to prevent decomposition against its instability at room temperature.

In a typical reaction, a matrix solution was prepared by adding 1 mL of 0.01 M cadmium chloride into 20 mL of 5% (W/V) aqueous solution of PVA and stirred continuously for 15–20 minutes. 1 mL of diluted sodium selenosulphite (0.1 M) was added drop by drop into this matrix solution, and the reactants were stirred continuously for another 15 minutes. On stirring, the resulting precursor solution becomes transparent, and gradually the colour changes to orange. The final solution containing Cd^{2+} and Se^{2-} ions in the polymeric matrix was coated onto chemically clean glass substrate by dip coating technique and then subjected

to thermolysis at 300°C . The colour of the film changes from transparent to brown within 15–20 minutes indicating the formation of CdSe nanocrystals in the PVA matrix. A set of five samples were prepared for various concentrations of CdCl_2 (0.01 M, 0.05 M, 0.1 M, 0.6 M, and 1.1 M) and a fixed concentration of Na_2SeSO_3 (0.1 M). Further, the films were annealed at 100°C for 6 hours. The samples were labelled as S1, S2, S3, S4, and S5 for CdCl_2 concentrations of 0.01 M, 0.05 M, 0.1 M, 0.6 M, and 1.1 M, respectively.

2.3. Fabrication of the Cell. A thin film solar cell with the structure Glass/ITO/CdSe/CdTe/Al has been fabricated in which CdSe layer was deposited on top of the ITO coated glass substrate by heat induced thermolysis technique at 300°C as described above. Prior to the deposition of CdTe thin film, the CdSe thin film was annealed at 100°C for 6 hours. Then, a layer of CdTe was deposited on the top of the CdSe layer by the thermal evaporation method at a pressure of 10^{-6} mbar. Finally, a layer of Al was deposited on the top as a back contact by the thermal evaporation method. The final cell structure is shown in Figure 4(a), and the device had an area of $1 \times 1 \text{ cm}^2$.

3. Results and Discussions

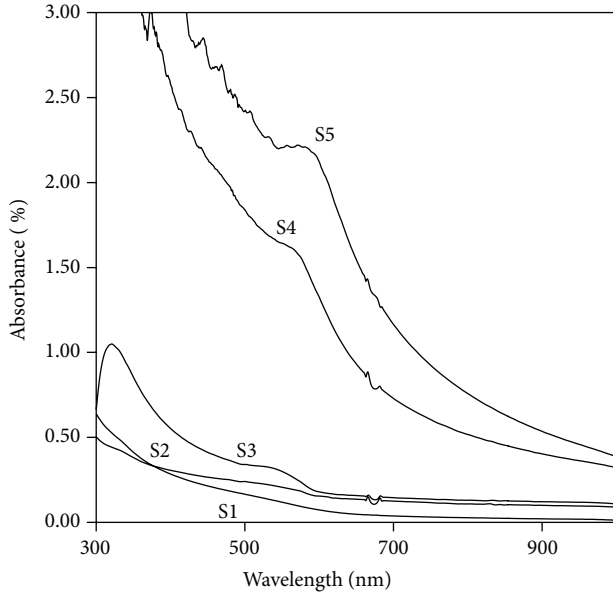
3.1. Optical Studies. The UV-Vis absorption spectra of the CdSe/PVA nanocomposite thin films (S1, S2, S3, S4, and S5) are shown in Figure 1(a). The absorbance in the spectra is found to increase gradually as the concentration of CdCl_2 is increased from 0.01 M to 1.1 M. It is observed that at a lower concentration of CdCl_2 (S1, S2), the CdSe/PVA thin films exhibited low absorbance, and no absorption peak was found, while those deposited at higher concentration of CdCl_2 (S3, S4, S5) exhibited high absorbance and prominent peaks were observed (in the range of 560 nm–660 nm). The absorption edges in the CdSe thin films (S1 to S4) are found to be blue-shifted relative to the bulk CdSe band edge of 713 nm [25, 29], whereas the absorption edge in case of sample S5 is red-shifted. The blue shift in the absorption edges may be attributed due to the quantum confinement effect in CdSe nanoparticles [25, 31]. From the spectra, it is observed that the sharp increase in absorbance near the fundamental absorption edge for the CdSe/PVA thin films (S4 and S5) is an indication of good crystalline nature of the films [32]. The red shift in the spectra (S5) indicates the formation of nanoparticles greater than the exciton Bohr radius (EBR) of CdSe [25, 31].

The optical bandgaps of the films were obtained using the following equation [33] for a semiconductor:

$$A = \frac{k(h\nu - E_g)^{m/2}}{h\nu}, \quad (1)$$

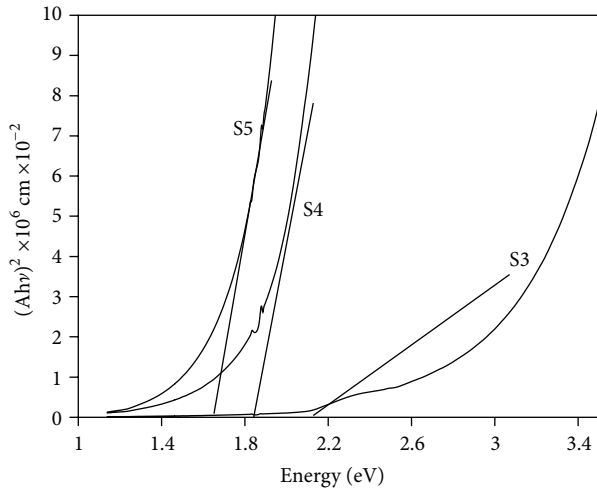
where A is the absorbance, K a constant, and m equal to 1 for direct transition and 2 for indirect transition. Linearity of the plots of $(Ah\nu)^2$ versus photon energy $h\nu$ for the CdSe/PVA films indicates that the material is of direct bandgap nature.

The extrapolation of the straight line to the $(Ah\nu)^2 = 0$ axis (Figure 1(b)) gives the energy bandgap of the film



S1: 0.01M
S2: 0.05M
S3: 0.1M
S4: 0.6M
S5: 1.1M

(a)



S3: 0.1M
S4: 0.1M
S5: 0.1M

(b)

FIGURE 1: (a) UV-Vis absorption spectra of CdSe/PVA nanocomposite thin films (S1, S2, S3, S4, and S5) prepared by thermolysis at 300°C. (b) Bandgap calculation of CdSe/PVA nanocomposite thin films (S3, S4, and S5) prepared by thermolysis at 300°C.

material (S3, S4, and S5). The bandgaps of the films S3 and S4 were found to be 2.1 eV and 1.8 eV, respectively, which is higher than that of the bulk CdSe bandgap of 1.74 eV. But the bandgap of the film S5 is found to be 1.6 eV which is smaller than the bulk bandgap of CdSe and as such is not preferable for application in solar cell. The increase in the

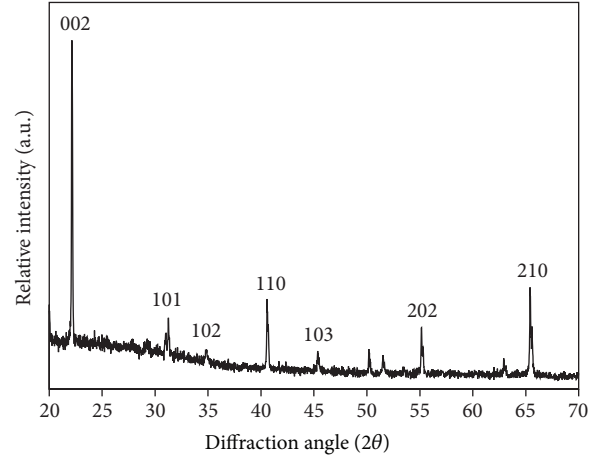


FIGURE 2: XRD of CdSe thin film (S4) prepared by thermolysis at 300°C.

TABLE 1: Bandgap, shift in bandgap, and particle size calculated from absorption spectra.

| Sample | Bandgap from UV-Vis (eV) | Shift in bandgap (eV) | Particle size from EMA (nm) |
|--------|--------------------------|-----------------------|-----------------------------|
| S3 | 2.1 | 0.36 | 4.5 |
| S4 | 1.8 | 0.06 | 11.1 |

bandgap is due to the formation of small size CdSe NPs. From the bandgap information, the size of the CdSe nanoparticles for the samples S3 and S4 was calculated using effective mass approximation (EMA) method [31] and the following equation for a semiconductor:

$$E_{gn} - E_{gb} = \frac{(\hbar^2 \pi^2 / 2R^2)}{\mu}, \quad (2)$$

where μ is the effective mass of the specimen [$1/\mu = 1/m_e^* + 1/m_h^*$], m_e^* is the effective mass of electron ($0.13 m_e$), m_h^* is the effective mass of hole ($0.45 m_e$), R is the radius of the particle, E_{gb} is the bulk bandgap, and E_{gn} is the bandgap of the sample. The observations are shown in Table 1.

From the above discussion, it is found that the film S4 is preferable for application as window layer in solar cell due to its suitable bandgap and high absorbance in the visible range.

3.2. XRD Analysis. A typical X-ray diffraction pattern of CdSe/PVA nanocomposite thin film (sample S4) is shown in Figure 2. The XRD pattern shows several peaks at 2θ values of 22.1°, 31.1°, 35°, 40.5°, 45.36°, 55.1°, and 65.4° which may be assigned to the diffraction lines produced by the (002), (101), (102), (110), (103), (202), and (210) planes of hexagonal (wurtzite) structure of CdSe, respectively [14, 34]. The appearance of the (102) and (103) reflection planes at diffraction angles $2\theta = 35.1^\circ$ and 45.36° is an indication of the hexagonal (wurtzite) structure of CdSe thin film [35]. The appearance of many peaks in the XRD pattern is an indication of polycrystalline nature of the CdSe thin film. The crystallite

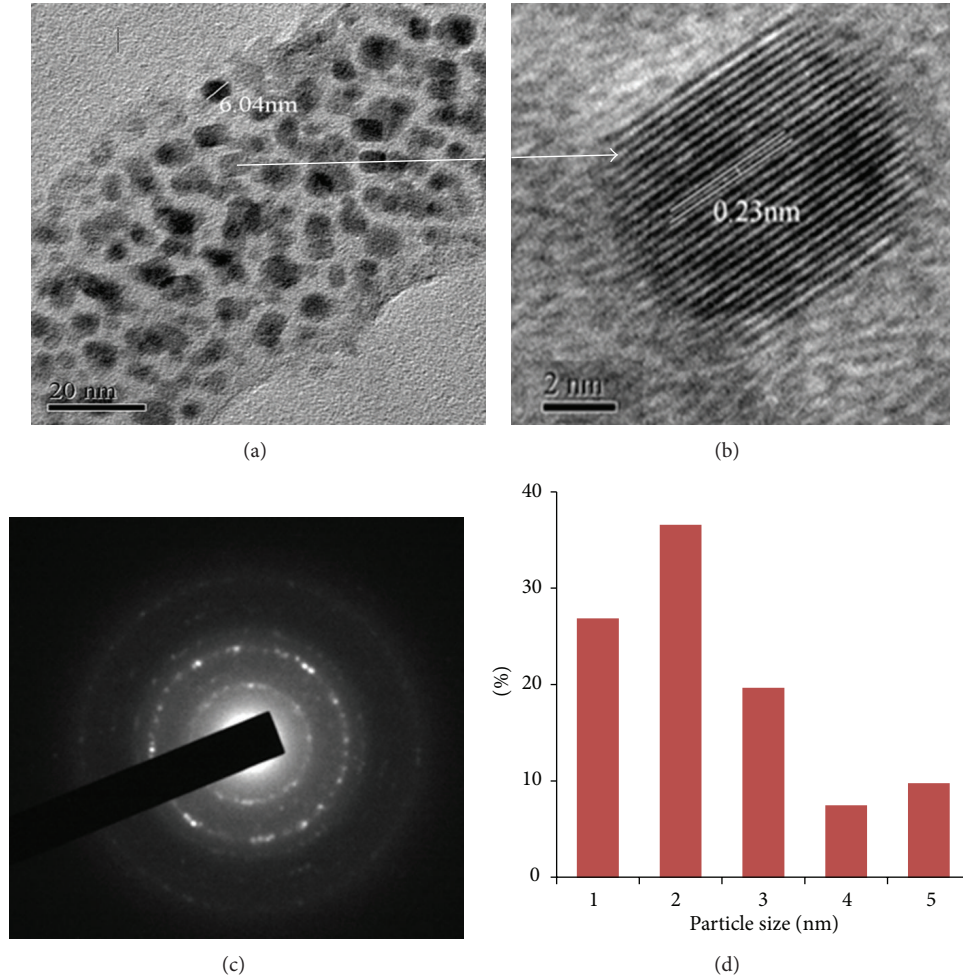


FIGURE 3: (a) TEM image of CdSe thin film (S4) prepared by thermolysis at 300°C. (b) HRTEM image of CdSe thin film (S4) prepared by thermolysis at 300°C. (c) SAED image of CdSe thin film (S4) prepared by thermolysis at 300°C. (d) Size distribution of CdSe nanoparticles.

size in CdSe thin film is evaluated from the intensity peaks of XRD by a Gaussian fit, using Debye-Scherrer formula:

$$D = \frac{0.9\lambda}{\beta \cos \theta}, \quad (3)$$

where β is the full width at half maximum, λ is the wavelength for X-ray used, and θ is Bragg's angle.

3.3. TEM Analysis. The TEM micrograph of CdSe/PVA nanocomposite thin film (S4) prepared at 300°C is presented in Figure 3(a). From the micrograph, it is observed that CdSe NPs has uniform size distribution with an average size of 4-5 nm in diameter, almost spherical in shape and are well dispersed within the pores of PVA matrix. The HRTEM image of CdSe NPs (S4) is depicted in Figure 3(b). The image shows the lattice fringes in the as-synthesized CdSe/PVA thin film and the spacing between the lattice fringes was found to be 0.23 nm which is very close to the d value of 0.22 nm (Table 2) for (110) reflection plane in the XRD spectrum. The selected area electron diffraction (SAED) pattern of the CdSe/PVA thin film prepared at 300°C is shown in Figure 3(c). The SAED

pattern indicates the hexagonal phase of the as-synthesized CdSe NPs. The analysis of particle size distribution is done with the help of histogram and is presented in Figure 3(d). The size histogram of CdSe nanoparticles is constructed by counting the total numbers of particles spread on the region of TEM grid as shown in Figure 3(a). Out of 41 numbers of total calculated particles, highest population is obtained in the 4–6 nm size range. From the analysis, it is found that as-synthesized CdSe nanoparticles exhibit an average size of about 4–6 nm in diameter. A comparative study of the average grain size of CdSe NPs obtained by TEM, EMA, and XRD measurements is presented in Table 3.

4. Characterization of the Cell

The current-voltage (I - V) characteristic of the CdSe/CdTe solar cell was measured with a Keithley (M: 2400) source meter under one sun illumination intensity and is shown in Figure 4(b). The photovoltaic parameters are tabulated in Table 4. A conversion efficiency of 2.43% has been obtained for the cell.

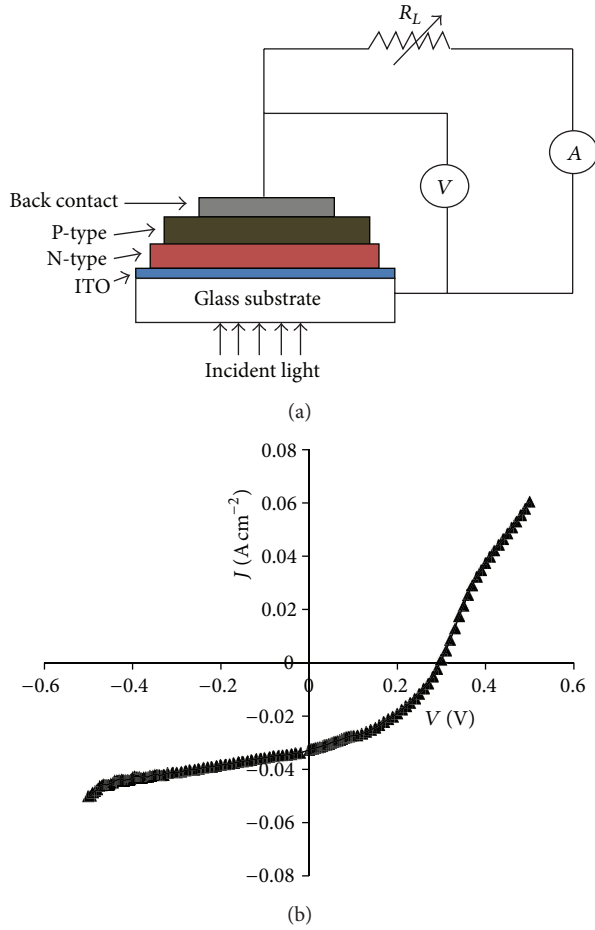


FIGURE 4: (a) Experimental setup for measuring the current-voltage characteristics of CdSe/CdTe thin film solar cell and (b) I - V characteristics of CdSe/CdTe thin film solar cell.

TABLE 2: Grain size and structural parameters of CdSe thin film from XRD.

| Sample | 2θ (degree) | Reflection planes (hkl) | d value (Å) | Grain size (nm) | Average grain size (nm) |
|--------|--------------------|-------------------------|---------------|-----------------|-------------------------|
| S4 | 22.1 | 002 | 4.0117 | 13.3 | 10.69 |
| | 31.1 | 101 | 3.0299 | 7 | |
| | 35 | 102 | 2.8077 | 10.93 | |
| | 40.5 | 110 | 2.2213 | 13.6 | |
| | 45.36 | 103 | 1.9977 | 8.45 | |
| | 55.1 | 202 | 1.6643 | 9.3 | |
| | 65.4 | 210 | 1.4254 | 12.2 | |

5. Conclusion

CdSe quantum dots of average size of 4–6 nm in diameter dispersed in PVA matrix have been synthesized in thin film form by heat induced thermolysis technique. The XRD analysis indicated the hexagonal (wurtzite) structure of CdSe/PVA nanocomposite thin film. The optical studies reveal that CdSe/PVA nanocomposite thin film prepared from 0.6 M

TABLE 3: Average grain size obtained from XRD, EMA, and TEM analysis.

| Sample | Growth temperature | Particle size from XRD (nm) | Particle size from EMA (nm) | Particle size from TEM (nm) |
|--------|--------------------|-----------------------------|-----------------------------|-----------------------------|
| S4 | 300°C | 10.69 | 11.1 | 5 |

TABLE 4: Photovoltaic parameters for the CdSe/CdTe thin film solar cell under 100 mW cm⁻² illumination intensity.

| Solar cell | I (mW cm ⁻²) | V_{oc} (mV) | J_{sc} (mA/cm ²) | FF (%) | η (%) |
|------------|----------------------------|---------------|--------------------------------|--------|------------|
| CdSe/CdTe | 100 | 290 | 33 | 25.3 | 2.43 |

I , V_{oc} , J_{sc} , FF, and η represent illumination intensity, open circuit voltage, short circuit current density, fill factor, and efficiency, respectively.

concentration of CdCl₂ (S4) is found to be suitable for application as a window layer in fabrication of solar cell. The efficiency of the as-fabricated CdSe/CdTe solar cell was found to be 2.43%.

Acknowledgments

One of the authors D. Saikia acknowledges the financial support from the Department of Electronics and Information Technology (DeitY), R&D Electronics Group, Government of India, New Delhi, India, under a major research project to Sibsagar College, Joysagar, Assam, India.

References

- [1] R. Shenhar, T. B. Norsten, and V. M. Rotello, "Polymer-mediated nanoparticle assembly: structural control and applications," *Advanced Materials*, vol. 17, no. 6, pp. 657–669, 2005.
- [2] D. R. Paul and L. M. Robeson, "Polymer nanotechnology: nanocomposites," *Polymer*, vol. 49, no. 15, pp. 3187–3204, 2008.
- [3] A. Lagashetty and A. Venkataraman, "Polymer nanocomposites," *Resonance*, vol. 10, no. 7, pp. 49–60, 2005.
- [4] O. M. Folarin, E. R. Sadiku, and A. Maity, "Polymer-noble metal nanocomposites: review," *International Journal of Physical Sciences*, vol. 6, no. 21, pp. 4869–4882, 2011.
- [5] I. S. Liu, H. H. Lo, C. T. Chien et al., "Enhancing photoluminescence quenching and photoelectric properties of CdSe quantum dots with hole accepting ligands," *Journal of Materials Chemistry*, vol. 18, pp. 675–682, 2008.
- [6] Y. J. Lai, Y. C. Lin, C. P. Fu et al., "Growth mode transfer of self-assembled CdSe quantum dots grown by molecular beam epitaxy," *Journal of Crystal Growth*, vol. 286, no. 2, pp. 338–344, 2006.
- [7] S. H. Liu, X. F. Qian, J. Yin, H. A. Xi, Z. H. Huang, and Z. K. Zhu, "Fabrication of CdS nanocrystals embedded in copolymer matrix by an in situ simultaneous copolymerization-sulfidation technique," *Materials Science and Engineering B*, vol. 98, no. 2, pp. 99–103, 2003.
- [8] H. Zan, C. Li, C. Yeh, M. Dai, H. Meng, and C. Tsai, "Room-temperature-operated sensitive hybrid gas sensor based on amorphous indium gallium zinc oxide thin-film transistors," *Applied Physics Letters*, vol. 98, no. 25, Article ID 253503, 3 pages, 2011.

- [9] R. A. Potyrailo and A. M. Leach, "Selective gas nanosensors with multisize CdSe nanocrystal/polymer composite films and dynamic pattern recognition," *Applied Physics Letters*, vol. 88, no. 13, Article ID 134110, 2006.
- [10] X. Liu, Y. Adachi, Y. Tomita, J. Oshima, T. Nakashima, and T. Kawai, "High-order nonlinear optical response of a polymer nanocomposite film incorporating semiconductor CdSe quantum dots," *Optics Express*, vol. 20, no. 12, pp. 13457–13469, 2012.
- [11] C. Baban, G. I. Rusu, and P. Prepelita, "On the optical properties of polycrystalline CdSe thin films," *Journal of Optoelectronics and Advanced Materials*, vol. 7, no. 2, pp. 817–821, 2005.
- [12] R. Blargava, *Properties of Wide Band Gap II-VI Semiconductors*, INSPEC, London, UK, 1997.
- [13] P. U. Asogwa, "Optical and structural properties of chemical bath deposited CdSe nanoparticle thin films for photovoltaic applications," *Journal of Non-Oxide Glasses*, vol. 2, no. 4, pp. 183–189, 2010.
- [14] P. Srivastava and K. Singh, "Synthesis of CdSe nanoparticles by solvothermal route: structural, optical and spectroscopic properties," *Advanced Materials Letters*, vol. 3, no. 4, pp. 340–344, 2012.
- [15] D. Yu, B. L. Wehrenberg, P. Jha, J. Ma, and P. Guyot-Sionnest, "Electronic transport of n-type CdSe quantum dot films: effect of film treatment," *Journal of Applied Physics*, vol. 99, no. 10, Article ID 104315, 2006.
- [16] D. C. Oertel and M. G. Bawendi, "Photodetectors based on treated CdSe quantum-dot films," *Applied Physics Letters*, vol. 87, Article ID 213505, 2005.
- [17] S. Erat, H. Metin, and M. Ari, "Influence of the annealing in nitrogen atmosphere on the XRD, EDX, SEM and electrical properties of chemical bath deposited CdSe thin films," *Materials Chemistry and Physics*, vol. 111, no. 1, pp. 114–120, 2008.
- [18] C. Baban and G. I. Rusu, "On the structural and optical characteristics of CdSe thin films," *Applied Surface Science*, vol. 211, no. 1–4, pp. 6–12, 2003.
- [19] A. Acharya, R. Mishra, and G. S. Roy, "Characterization of CdSe/Polythiophene nanocomposite by TGA/DTA, XRD, UV-VIS Spectroscopy, SEM-EDXA and FTIR," *Armenian Journal of Physics*, vol. 3, no. 3, pp. 195–202, 2010.
- [20] M. M. Betkar and G. D. Bagde, "Structural and optical properties of spray deposited CdSe Thin films," *Materials Physics and Mechanics*, vol. 14, pp. 74–77, 2012.
- [21] B. Guzeldir, M. Saglam, and A. Ates, "Preparation and characterization of CdSe, ZnSe and CuSe thin films deposited by the successive ionic layer adsorption and reaction method," *Journal of Optoelectronics and Advanced Materials*, vol. 14, no. 3–4, pp. 224–229, 2012.
- [22] A. M. Salem, "Structure, refractive-index dispersion and the optical absorption edge of chemically deposited $Zn_xCd_{(1-x)}S$ thin films structure, refractive-index dispersion and the optical absorption edge of chemically deposited $Zn_xCd_{(1-x)}S$ thin films," *Applied Physics A*, vol. 74, no. 2, pp. 205–211, 2002.
- [23] J. McAleese and P. O'Brien, "Developing an understanding of the processes controlling the chemical bath deposition of ZnS and CdS," *Journal of Materials Chemistry*, vol. 8, pp. 2309–2314, 1998.
- [24] K. Y. Pechers'ka, L. P. Germash, N. O. Korsunskaya et al., "Effect of annealing on the luminescent characteristics of CdSe quantum dots in a polymer," *Ukrainian Journal of Physics*, vol. 55, no. 4, pp. 403–409, 2010.
- [25] C. P. Shah, M. Rath, M. Kumar, and P. N. Bajaj, "Precursor concentration and temperature controlled formation of polyvinyl alcohol-capped CdSe-quantum dots," *Beilstein Journal of Nanotechnology*, vol. 1, pp. 119–127, 2010.
- [26] K. Kushwaha, N. Gautam, P. Singh, and M. Ramrakhaini, "Synthesis and photoluminescence of CdSe/PVA nanocomposites," *Journal of Physics*, vol. 365, Article ID 012014, 2012.
- [27] X.-D. Ma, X.-F. Qian, J. Yin, H.-A. Xi, and Z.-K. Zhu, "Preparation and characterization of polyvinyl alcohol-capped CdSe nanoparticles at room temperature," *Journal of Colloid and Interface Science*, vol. 252, no. 1, pp. 77–81, 2002.
- [28] B. Suo, X. Su, J. Wu, D. Chen, A. Wang, and Z. Guo, "Poly(vinyl alcohol) thin film filled with CdSe-ZnS quantum dots: fabrication, characterization and optical properties," *Materials Chemistry and Physics*, vol. 119, no. 1–2, pp. 237–242, 2010.
- [29] H. S. Mansur and A. A. P. Mansur, "CdSe quantum dots stabilized by carboxylic-functionalized PVA: synthesis and UV-vis spectroscopy characterization," *Materials Chemistry and Physics*, vol. 125, no. 3, pp. 709–717, 2011.
- [30] D. Saikia, P. K. Saikia, P. K. Gogoi, M. R. Das, P. Sengupta, and M. V. Shelke, "Synthesis and characterization of CdS/PVA nanocomposite thin films from a complexing agent free system," *Materials Chemistry and Physics*, vol. 131, no. 1–2, pp. 223–229, 2011.
- [31] L. E. Brus, "Electron-electron and electron hole interactions in small semiconductor crystallites: the size dependence of the lowest excited electronic state," *Journal of Chemical Physics*, vol. 80, no. 9, article 4403, 7 pages, 1984.
- [32] D. Saikia, P. K. Gogoi, P. K. Saikia, and S. Sarma, "Synthesis of polymer-PbS nanocomposite by solar irradiation-induced thermolysis process and its photovoltaic applications," *Journal of Experimental Nanoscience*, vol. 8, no. 3, pp. 403–411, 2013.
- [33] B. Subramanian, C. Sanjeevviraja, and M. Jayachandran, "Brush plating of tin(II) selenide thin films," *Journal of Crystal Growth*, vol. 234, no. 2–3, pp. 421–426, 2002.
- [34] G. Ramalingam and J. Madhavan, "Investigation on the structural and morphological behaviour of CdSe nanoparticles by hydrothermal method," *Archives of Applied Science Research*, vol. 3, no. 3, pp. 217–224, 2011.
- [35] Z. Deng, L. Cao, F. Tang, and B. Zou, "A new route to zinc-blende CdSe nanocrystals: mechanism and synthesis," *Journal of Physical Chemistry B*, vol. 109, no. 35, pp. 16671–16675, 2005.

Research Article

Dye-Sensitized Solar Cells with Anatase TiO₂ Nanorods Prepared by Hydrothermal Method

Ming-Jer Jeng,¹ Yi-Lun Wung,¹ Liann-Be Chang,¹ and Lee Chow²

¹ Department of Electronic Engineering and Green Technology Research Center, Chang-Gung University, Taoyuan 333, Taiwan

² Department of Physics, University of Central Florida, Orlando, FL 32816, USA

Correspondence should be addressed to Ming-Jer Jeng; mjjeng@mail.cgu.edu.tw

Received 29 June 2013; Revised 20 August 2013; Accepted 6 September 2013

Academic Editor: Stefano Caramori

Copyright © 2013 Ming-Jer Jeng et al. This is an open access article distributed under the Creative Commons Attribution License, which permits unrestricted use, distribution, and reproduction in any medium, provided the original work is properly cited.

The hydrothermal method provides an effective reaction environment for the synthesis of nanocrystalline materials with high purity and well-controlled crystallinity. In this work, we started with various sizes of commercial TiO₂ powders and used the hydrothermal method to prepare TiO₂ thin films. We found that the synthesized TiO₂ nanorods were thin and long when smaller TiO₂ particles were used, while larger TiO₂ particles produced thicker and shorter nanorods. We also found that TiO₂ films prepared by TiO₂ nanorods exhibited larger surface roughness than those prepared by the commercial TiO₂ particles. It was found that a pure anatase phase of TiO₂ nanorods can be obtained from the hydrothermal method. The dye-sensitized solar cells fabricated with TiO₂ nanorods exhibited a higher solar efficiency than those fabricated with commercial TiO₂ nanoparticles directly. Further, triple-layer structures of TiO₂ thin films with different particle sizes were investigated to improve the solar efficiency.

1. Introduction

Dye-sensitized solar cells (DSSCs) have attracted much attention as possible candidates for low cost, high stability, and high efficient solar cells [1, 2]. There are many innovations in this emerging technology such as new dyes which are absorbed at a wider range of wavelengths and the introduction of nanostructure titanium oxides (TiO₂) to increase the surface area [3–5]. The DSSCs with the nanostructure titanium oxide/Porphyrins dye thin films on transparent conducting oxide- (TCO-) coated glass can achieve a solar efficiency as high as 13% [6]. The major improvements of the research are made not only by introducing highly absorbing dyes as light harvesters, but also by using the nanostructure layer to improve the absorption and collection efficiency. In principle, fast electron transport and slow recombination will be needed to obtain a high solar conversion efficiency. For conventional DSSC, the mesoporous film consisted of nanocrystalline TiO₂ particles, enjoying the advantages of a large surface for greater dye adsorption and facilitating electrolyte diffusion within their pores [7–12]. The hydrothermal method provides an effective reaction environment for the synthesis of nanocrystalline TiO₂ with high purity and

well-controlled crystallinity [13–15]. Therefore, we use the hydrothermal method to prepare TiO₂ thin films in this work. The Taguchi method [16–20] is used to find the optimal parameters for the formation of high-quality TiO₂ films. The Taguchi method [16] is a process optimization technique that investigates how multiparameters affect the performance of a process. It can minimize the variation in a process through robust design of experiments. The Taguchi method uses orthogonal arrays [17] to organize the parameters affecting the process and the levels at which they should be varied. It allows for the determination of factors mostly affecting a process performance characteristic with a minimum amount of experimentation. Generally, it employs a generic signal-to-noise (*S/N*) ratio to quantify the variation. These *S/N* ratios are used as measures of the effect of noise factors on performance characteristics. There are several *S/N* ratio types of characteristics: larger is better, nominal is best, smaller is better, and so forth [16, 18].

In addition, it is known that the strong back-scattering light due to the large particles near the conducting glass results in a light loss. To reduce light loss due to this strong back-scattering light, multiple-layer structure of TiO₂ with

TABLE 1: Level of process parameters.

| Symbol | Factor level | 1 | 2 | 3 |
|--------|-------------------------------------|-----|-----|-----|
| A | NaOH concentration (M) | 10 | 8 | 12 |
| B | TiO ₂ particle size (nm) | 14 | 21 | 100 |
| C | Autoclave temperature (°C) | 180 | 200 | 230 |
| D | Annealing temperature (°C) | 450 | 500 | 550 |

different particle sizes has been proposed in the past [21–27]. Here triple TiO₂ layer structure with small particle sizes is at the bottom, medium sizes in the middle, and large particle sizes on top which are also investigated to improve the solar performance of DSSCs.

2. Experiments

The 2 cm × 1.5 cm fluorine-doped SnO₂- (FTO-) coated glass electrodes (sheet resistance 8 Ω/□) were cleaned by acetone, isopropanol, and deionized water sequentially. In the hydrothermal procedure, 3 g TiO₂ powders were placed into a Teflon lined autoclave of 100 mL capacity. The autoclave was filled with 8 M, 10 M, or 12 M NaOH aqueous solution and sealed into a stainless steel tank and maintained at 180°C for 24 hrs. It was cooled down naturally to room temperature. The obtained sodium titanate was put into 200 mL of 1N HCl aqueous solution at pH = 2 and stirred for 24 h. This HCl treatment was repeated many times in order to exchange Na⁺ ions completely by H⁺ ions leading to the formation of hydrogen titanate nanorods. Then these hydrogen titanate nanorods were washed with distilled water until the pH reached 7 and filtered to obtain the precipitated hydrogen titanate nanorods. These nanorods were dehydrated and recrystallized into the anatase TiO₂ nanorods. Table 1 shows the four factors and three levels used in our experiment according to the Taguchi method [16–20]. If three levels were assigned to each of these factors, then conventional method would require 3⁴ or 81 experiments to find the optimal condition. Using the Taguchi method, we can reduce the number of experiments to nine. The orthogonal array of L9 type [17] is used and shown in Table 2. This design requires nine experiments with four parameters at three levels of each. The interactions of these four parameters were neglected. TiO₂ solutions are prepared by mixing 3 g of TiO₂ powders, 1 mL of titanium tetraisopropoxide (TTIP), 0.5 g of Polyethylene glycol (PEG), and 0.5 mL of triton X-100 in 50 mL of isopropanol (IPA). The mixture was then grinded and stirred by zirconia ball for 8 hours. It is known that the addition of TTIP in the solution can reduce the surface crack and the PEG can make a porous thin film after annealing. The TiO₂ thin films were formed by spin-coating TiO₂ solutions on FTO-coated glass and annealed at 500°C for one hour. The coated TiO₂ photo-electrodes were then immersed for 24 hrs in a hydrous ethanol solution containing 3 × 10⁻⁴ M N719 dye. The liquid electrolyte consisted of 1M lithium Iodide (LiI), 0.1 M Iodine (I₂), 0.5 M 4-tert-butyl pyridine (TBP), and 0.6 M 1,2-Dimethyl-3-propylimidazolium iodide (DMPII) in acetonitrile. The cathode electrode was made of

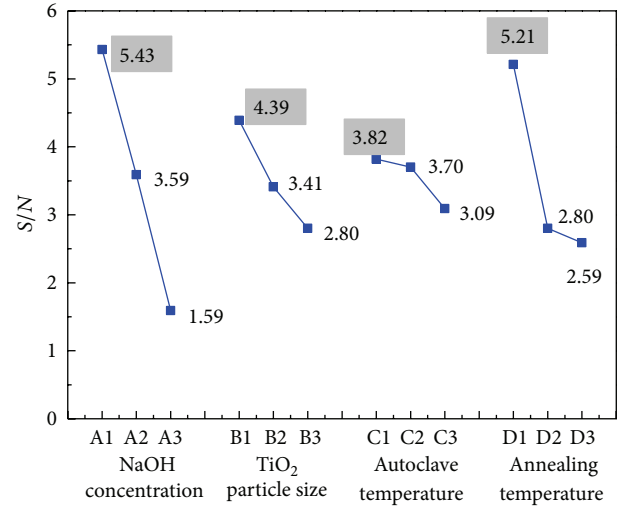


FIGURE 1: The factor effects on the S/N ratio.

FTO-coated glass, which was further coated with H₂PtCl₆ precursor and annealed at 450°C for 30 min. The cell was fabricated by applying a surlyn spacer, which is a hot-melting film with a thickness of 60 μm, between two electrodes. Two FTO-coated glasses were made with the surlyn heated at 100°C. The electrolyte was injected into the space between the electrodes by capillary action. Finally, these two FTO-coated glasses were sealed completely. The active area of cells is 1 cm². The photocurrent-voltage (*I*-*V*) characteristic curves were measured using Keithley 2420 under AM1.5G illumination.

3. Results and Discussions

Nine different hydrothermal experiments were performed using the design parameter combinations shown in Table 2. Three specimens were fabricated for each of the parameter combinations. The factor effects on the solar efficiency and S/N ratio for each experiment are listed in Table 3. The higher solar efficiency is the indication of better performance. Therefore, the larger-is-better criterion was selected for the solar efficiency to obtain the optimal solar performance. The following S/N ratios for the larger-is-better case can be calculated [16, 18]:

$$\left(\frac{S}{N}\right)_{LB} = -10 \log \frac{\sum_{i=1}^n 1/(y_i)^2}{n}, \quad (1)$$

where (S/N)_{LB} stands for the larger-is-better signal-to-noise ratio, *y_i* is the individually measured solar efficiency, and *n* is the number of solar cell samples measured. Figure 1 shows the factor effects on the S/N ratio. The larger slope means that the factor has a stronger effect on solar efficiency. It indicates that NaOH concentration (factor A) has a stronger effect on solar efficiency. The annealing temperature (factor D) is the next most significant factor. The objective is to maximize the S/N ratio. This implies that one can obtain high solar efficiency by using the factor with higher S/N ratio. It is clear from Figure 1 that the highest S/N ratio values in each factor are

TABLE 2: Taguchi L9 orthogonal array.

| Order | Factor | | | |
|-------|--------------------------|---------------------------------------|------------------------------|------------------------------|
| | A NaOH concentration (M) | B TiO ₂ particle size (nm) | C Autoclave temperature (°C) | D Annealing temperature (°C) |
| 1 | 10 M | 14 nm | 180°C | 450°C |
| 2 | 10 M | 21 nm | 200°C | 500°C |
| 3 | 10 M | 100 nm | 230°C | 550°C |
| 4 | 8 M | 14 nm | 200°C | 550°C |
| 5 | 8 M | 21 nm | 230°C | 450°C |
| 6 | 8 M | 100 nm | 180°C | 500°C |
| 7 | 12 M | 14 nm | 230°C | 500°C |
| 8 | 12 M | 21 nm | 180°C | 550°C |
| 9 | 12 M | 100 nm | 200°C | 450°C |

TABLE 3: The factor effects on the solar efficiency and S/N ratio.

| A NaOH concentration (M) | Factor | | | | Efficiency (%) | S/N ratio |
|--------------------------|---------------------------------------|------------------------------|------------------------------|------|----------------|-----------|
| | B TiO ₂ particle size (nm) | C Autoclave temperature (°C) | D Annealing temperature (°C) | | | |
| 1 | 1 | 1 | 1 | 2.31 | 7.27 | |
| 1 | 2 | 2 | 2 | 1.80 | 5.11 | |
| 1 | 3 | 3 | 3 | 1.57 | 3.92 | |
| 2 | 1 | 2 | 3 | 1.27 | 2.08 | |
| 2 | 2 | 3 | 1 | 2.06 | 6.28 | |
| 2 | 3 | 1 | 2 | 1.32 | 2.41 | |
| 3 | 1 | 3 | 2 | 1.11 | 0.91 | |
| 3 | 2 | 1 | 3 | 1.23 | 1.80 | |
| 3 | 3 | 2 | 1 | 1.27 | 2.08 | |

5.43, 4.39, 3.82, and 5.21, which correspond to the factor A1, B2, C1, and D1, respectively. Therefore, the best parameters of hydrothermal methods are (A1) NaOH concentration of 10 M, (B2) commercial TiO₂ particle size of 21 nm, (C1) the temperature of 180°C, and (D1) the annealing temperature of 450°C. Thus, these best parameters were used to prepare our TiO₂ nanorods.

Figures 2(a) and 2(b) show the surface morphology of TiO₂ films prepared by commercial TiO₂ particles and TiO₂ nanorods which we prepared using hydrothermal methods, respectively. Clearly, a particle-like surface in the film is prepared using commercial particles versus a nanorod-shape surface in the film prepared by our TiO₂ nanorods. From atomic force microscopy (AFM) measurement, it is observed that the mean roughness (~63 nm) of the TiO₂ thin films prepared by the TiO₂ nanorods is larger than that (~41.5 nm) prepared by the commercial TiO₂ particles. The large surface roughness in TiO₂ nanorods is beneficial for dye adsorption. In addition, a very pure anatase structure of TiO₂ nanorods is obtained by the hydrothermal method, as shown in Figure 3. There are no characteristic peaks of other impurity phases such as sodium titanium oxide or rutile TiO₂, except pure anatase TiO₂ nanorods. This pure anatase structure of TiO₂ is extremely important to achieve high performance for electrons transport and dye adsorption

in TiO₂-based dye-sensitized solar cells [28, 29]. Figure 4 compares the *I-V* characteristics of dye-sensitized solar cell prepared with hydrothermally grown TiO₂ nanorods and the DSSC prepared with commercial TiO₂ particles. The dye-sensitized solar cells prepared with the hydrothermally grown TiO₂ nanorods clearly exhibit higher solar efficiency than that prepared with the commercial TiO₂ particles. This is due to the fact that TiO₂ nanorods have large surface area and pure anatase structure, which can absorb more dye and therefore better photoresponse.

It is also noted that the size of TiO₂ nanorods synthesized by hydrothermal method depends on the initial TiO₂ particle size. The nanorods are thin and long when small-size TiO₂ particles (size ~14 nm) are used; however the nanorods become thick and short when large-size TiO₂ particles, are used (size, ~100 nm), as shown in Figures 5(a) and 5(b). One can control the shape of TiO₂ nanorods by suitably choosing the initial TiO₂ particle sizes used in the hydrothermal process. Next we will examine the effect of TiO₂ thin film thickness on the solar efficiency of the fabricated DSSCs. In Figure 6, the cross-section scanning electron microscopy (SEM) images of different thickness of TiO₂ thin films are shown. We can see that a nanorod-like morphology is observed when 21 nm TiO₂ powder is used in the hydrothermal reaction. The optical absorption and

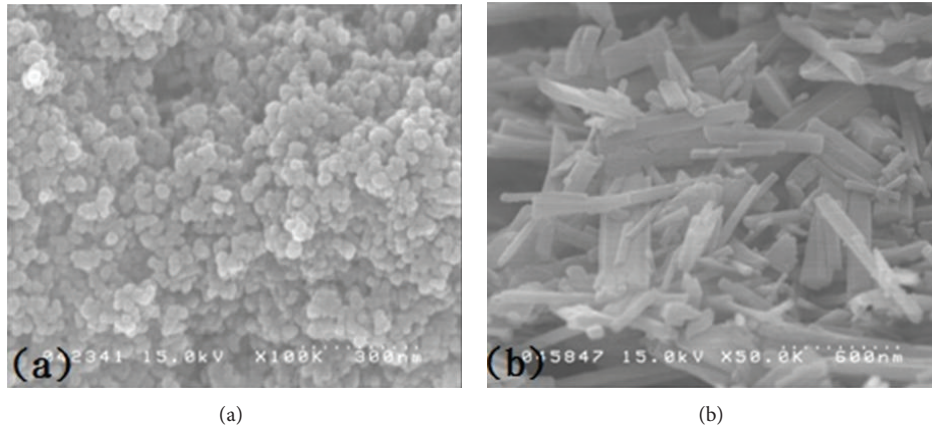


FIGURE 2: Surface morphology of TiO₂ thin films prepared by (a) commercial particles and (b) hydrothermal method.

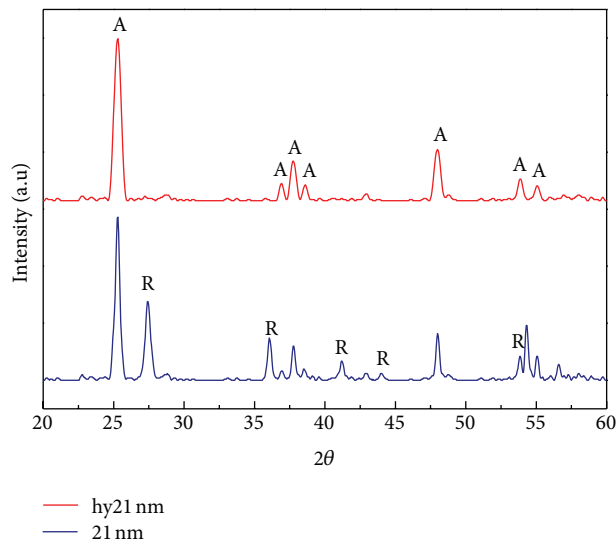


FIGURE 3: XRD spectra of TiO₂ thin films prepared by hydrothermal method (red color) and commercial particle (blue color).

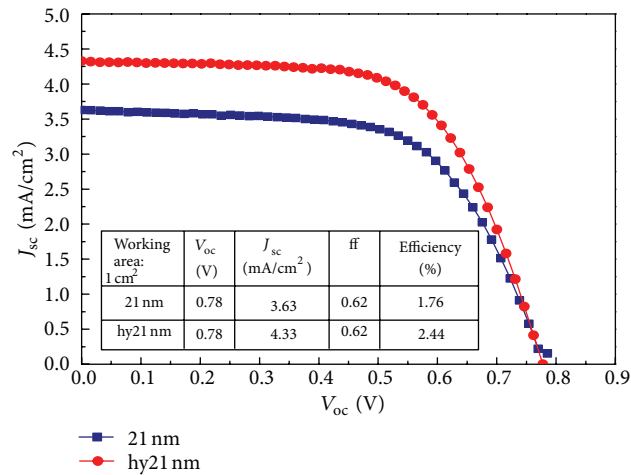


FIGURE 4: The *I-V* curve of dye-sensitized solar cells with the TiO₂ prepared by hydrothermal method and commercial particle.

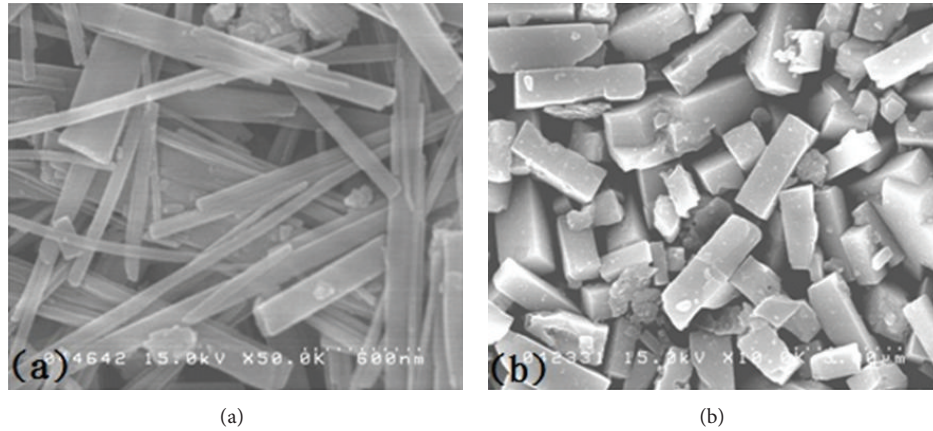


FIGURE 5: Nanorod size dependence on the using of the particle size of (a) 14 nm and (b) 100 nm.

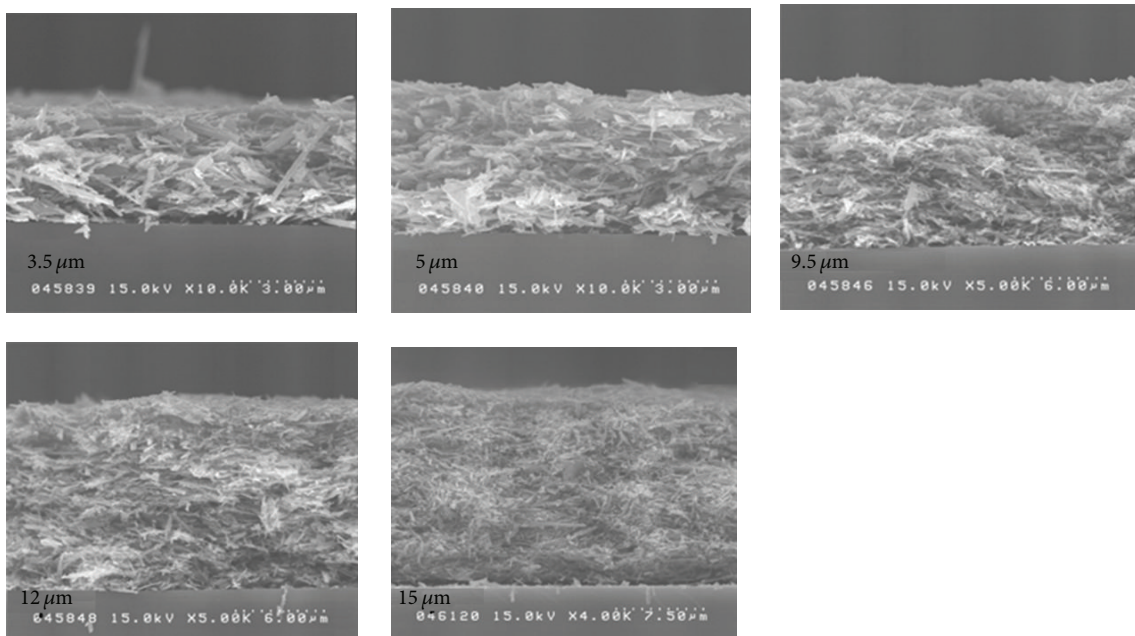


FIGURE 6: The cross-section scanning electron microscopy (SEM) images of TiO_2 thin films with different thicknesses.

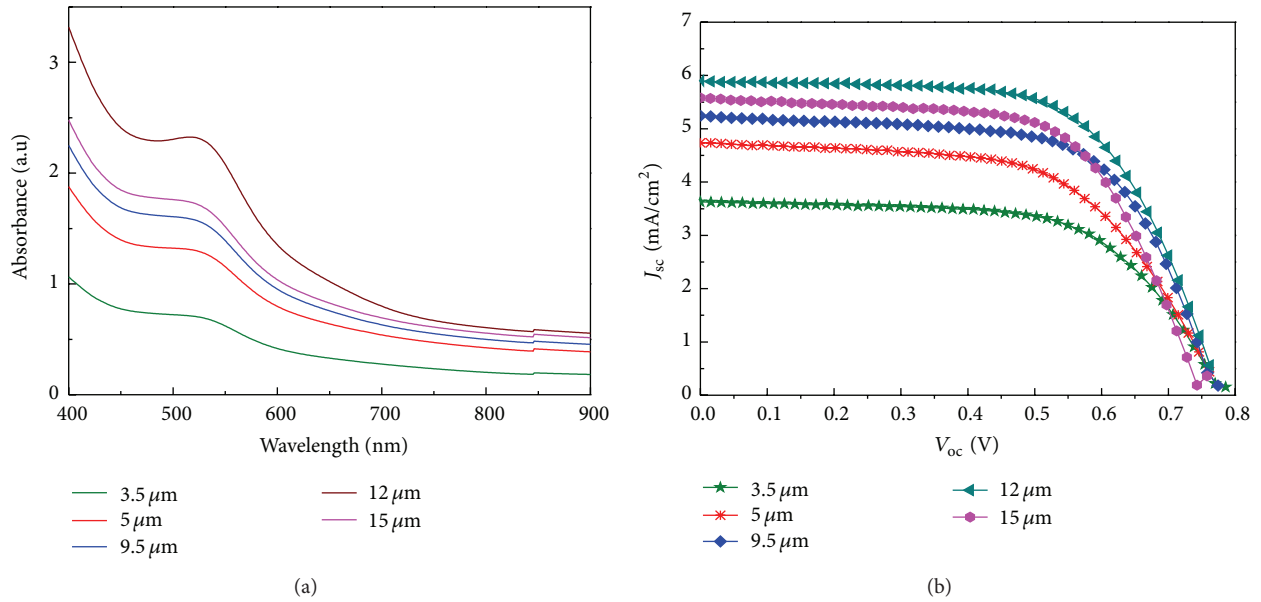
I - V characteristic curve of dye-sensitized solar cells with different TiO_2 thicknesses are shown in Figures 7(a) and 7(b), respectively. The optical absorption initially increases with increasing TiO_2 thickness and reaches a maximum at $12 \mu\text{m}$. For further increase in the TiO_2 film thickness, the light absorption begins to drop. The same behavior is observed in the photocurrent, as shown in Figure 7(b). The solar performance parameters of DSSCs with different TiO_2 thicknesses are listed in Table 4. The efficiencies of DSSCs with the TiO_2 thicknesses of 3.5, 5, 9.5, 12, and $15 \mu\text{m}$ are 2.12, 2.44, 2.63, 2.85, and 2.67%, respectively. The DSSC with the TiO_2 thicknesses of $12 \mu\text{m}$ exhibits the highest efficiency. It is known that dye in the film will build up with increasing TiO_2 thickness and hence increase the photocurrent. However, thicker TiO_2 layers will result in a decrease in the transmittance of light

through these TiO_2 layers and thus reduce the incident light absorbed by the dyes. In addition, the charge recombination between electrons from the excited dye to the conduction band of TiO_2 and the I^{3-} ions in the electrolyte will become more difficult in thicker TiO_2 layers. Thus, there exists an optimal TiO_2 thickness to achieve higher solar efficiency for each particle size. In this work, the optimal TiO_2 thickness is $12 \mu\text{m}$ for particle size of 21 nm used in the hydrothermal reaction.

It is known that large-size TiO_2 particles have the advantage of strong light scattering ability, while small size TiO_2 particles have the advantages of large contact area and low contact resistance [18–24]. In order to take the advantages of both the strong light scattering and the large contact area/low contact resistance, we constructed a triple-layer TiO_2 DSSC

TABLE 4: Solar performance parameters of DSSCs with different TiO₂ thicknesses.

| Working area: 1 cm ² | V _{oc} (V) | J _{sc} (mA/cm ²) | Fill factor | Efficiency (%) |
|---------------------------------|---------------------|---------------------------------------|-------------|----------------|
| 3.5 μm | 0.79 | 3.63 | 0.62 | 2.12 |
| 5 μm | 0.76 | 4.73 | 0.62 | 2.44 |
| 9.5 μm | 0.77 | 5.25 | 0.64 | 2.63 |
| 12 μm | 0.76 | 5.89 | 0.63 | 2.85 |
| 15 μm | 0.76 | 5.58 | 0.62 | 2.67 |

FIGURE 7: (a) Light absorption and (b) I - V curve of dye-sensitized solar cells with different TiO₂ thicknesses.TABLE 5: Solar performance parameters of DSSCs with different particle sizes on the top in triple TiO₂ layers.

| Particle size (nm) | V _{oc} (V) | J _{sc} (mA/cm ²) | Fill factor | Efficiency (%) |
|--------------------|---------------------|---------------------------------------|-------------|----------------|
| 50/hy21/9/FTO | 0.67 | 8.85 | 0.61 | 3.62 |
| 100/hy21/9/FTO | 0.75 | 12.02 | 0.62 | 5.68 |
| 200/hy21/9/FTO | 0.76 | 14.32 | 0.61 | 6.54 |

with varying TiO₂ particle size. The structure of the triple-layer TiO₂ DSSC is as follows: (1) a TiO₂ thin film prepared with 9 nm TiO₂ particles is on the bottom layer; (2) a TiO₂ film prepared with hydrothermally grown TiO₂ nanorods is placed on the middle layer; (3) on the top, TiO₂ films are prepared with three different sizes of 50 nm, 100 nm, and 200 nm TiO₂ nanorods used for comparison. Figure 8(a) shows the cross-sectional scanning electron microscopy (SEM) images of TiO₂ thin films with triple-layer structures. The I - V curves of dye-sensitized solar cells with triple-layer structures are shown in Figure 8(b). The solar performance parameters of DSSCs with triple-layer structures are listed in Table 5. The efficiencies of DSSCs with the scattering layer prepared by 50, 100, and 200 nm particles are 3.62, 5.68,

and 6.54%, respectively. The TiO₂ layers with larger particle sizes on the top layer exhibit higher solar efficiency than that with smaller particle sizes due to the strong back-scattering effect. It is known that smaller particles of TiO₂ layers have large surface area and adsorb more dyes. Hence, it has low contact resistance and high photocurrent. The strong back-scattering light due to large particle size will also increase the reabsorption in the small particle size of TiO₂ layer. This smaller particle size on the bottom is beneficial to recapture the scattering light from the top scattering layer. The larger particle sizes of TiO₂ layers on the top can enhance the back-scattering light effectively and result in higher photocurrent. Thus, the combination of larger particle sizes of TiO₂ on the top and smaller particle sizes of TiO₂ at the bottom will be better for achieving higher solar efficiency.

4. Conclusions

The dye-sensitized solar cells with the TiO₂ prepared by the hydrothermal method have demonstrated good solar performance. A high surface roughness and pure anatase structure are achieved by this method. The dye-sensitized solar cells with the TiO₂ nanorods exhibit higher solar efficiency than that with the commercial TiO₂ particles. The optimal TiO₂ thickness depends on the nanorod sizes of

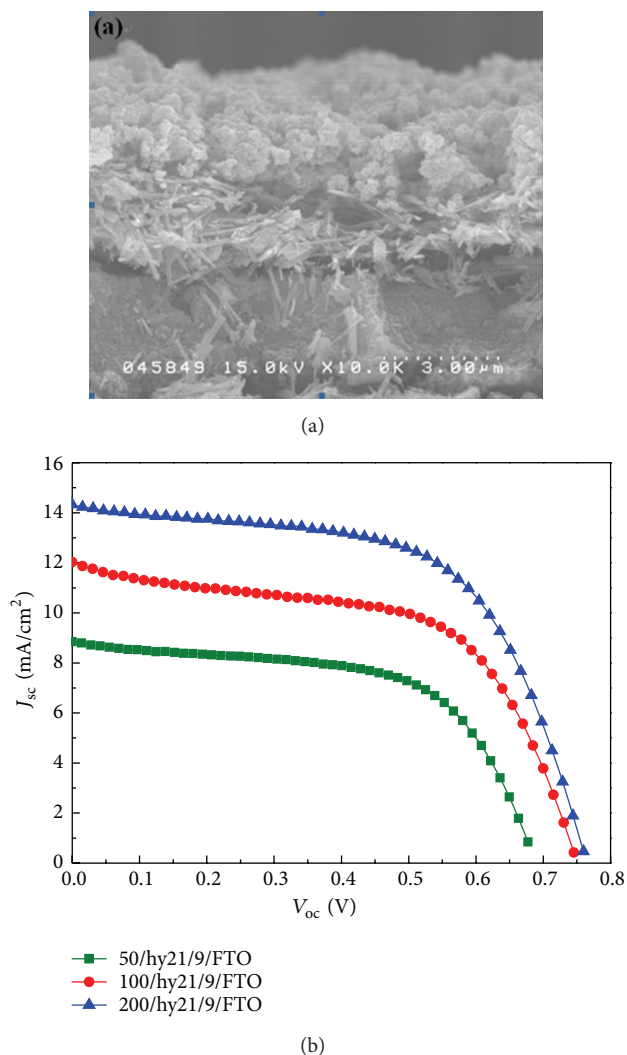


FIGURE 8: (a) The cross-section scanning electron microscopy (SEM) images of TiO₂ thin films with triple layer structures. (b) I - V curve of dye-sensitized solar cells with triple layer structures of TiO₂ thin films.

TiO₂ layer for achieving the maximum efficiency. The TiO₂ nanorod size formed through the hydrothermal method will depend on the initial TiO₂ particle size.

Acknowledgment

The authors want to thank the National Science Council of Taiwan, Taiwan, for supporting this research under the Contract no. NSC 100-2221-E-182-037.

References

- [1] B. O'Regan and M. Grätzel, "A low-cost, high-efficiency solar cell based on dye-sensitized colloidal TiO₂ films," *Nature*, vol. 353, no. 6346, pp. 737–740, 1991.
- [2] M. Grätzel, "Conversion of sunlight to electric power by nanocrystalline dye-sensitized solar cells," *Journal of Photochemistry and Photobiology A*, vol. 164, no. 1-3, pp. 3–14, 2004.
- [3] Q. Zhang, C. S. Dandeneau, X. Zhou, and C. Cao, "ZnO nanostructures for dye-sensitized solar cells," *Advanced Materials*, vol. 21, no. 41, pp. 4087–4108, 2009.
- [4] S. Ito, T. N. Murakami, P. Comte et al., "Fabrication of thin film dye sensitized solar cells with solar to electric power conversion efficiency over 10%," *Thin Solid Films*, vol. 516, no. 14, pp. 4613–4619, 2008.
- [5] D. Kuang, S. Ito, B. Wenger et al., "High molar extinction coefficient heteroleptic ruthenium complexes for thin film dye-sensitized solar cells," *Journal of the American Chemical Society*, vol. 128, no. 12, pp. 4146–4154, 2006.
- [6] A. Yella, H.-W. Lee, H. N. Tsao et al., "Porphyrin-sensitized solar cells with cobalt (II/III)-based redox electrolyte exceed 12 percent efficiency," *Science*, vol. 334, no. 6056, pp. 629–634, 2011.
- [7] Q. Zhang and G. Cao, "Nanostructured photoelectrodes for dye-sensitized solar cells," *Nano Today*, vol. 6, no. 1, pp. 91–109, 2011.
- [8] M. Wei, Y. Konishi, H. Zhou, M. Yanagida, H. Sugihara, and H. Arakawa, "Highly efficient dye-sensitized solar cells composed of mesoporous titanium dioxide," *Journal of Materials Chemistry*, vol. 16, no. 13, pp. 1287–1293, 2006.
- [9] W.-G. Yang, F.-R. Wan, Q.-W. Chen, J.-J. Li, and D.-S. Xu, "Controlling synthesis of well-crystallized mesoporous TiO₂ microspheres with ultrahigh surface area for high-performance dye-sensitized solar cells," *Journal of Materials Chemistry*, vol. 20, no. 14, pp. 2870–2876, 2010.
- [10] D. Chen, F. Huang, Y.-B. Cheng, and R. A. Caruso, "Mesoporous anatase TiO₂ beads with high surface areas and controllable pore sizes: a superior candidate for high-performance dye-sensitized solar cells," *Advanced Materials*, vol. 21, no. 21, pp. 2206–2210, 2009.
- [11] Y. J. Kim, M. H. Lee, H. J. Kim et al., "Formation of highly efficient dye-sensitized solar cells by hierarchical pore generation with nanoporous TiO₂ spheres," *Advanced Materials*, vol. 21, no. 36, pp. 3618–3673, 2009.
- [12] F. Sauvage, D. Chen, P. Comte et al., "Dye-sensitized solar cells employing a single film of mesoporous TiO₂ beads achieve power conversion efficiencies over 10%," *ACS Nano*, vol. 4, no. 8, pp. 4420–4425, 2010.
- [13] A. C. Zaman, C. B. Üstündağ, F. Kaya, and C. Kaya, "Synthesis and electrophoretic deposition of hydrothermally synthesized multilayer TiO₂ nanotubes on conductive filters," *Materials Letters*, vol. 66, no. 1, pp. 179–181, 2012.
- [14] S. K. S. Patel, N. S. Gajbhiye, and S. K. Date, "Ferromagnetism of Mn-doped TiO₂ nanorods synthesized by hydrothermal method," *Journal of Alloys and Compounds*, vol. 509, no. 1, pp. S427–S430, 2011.
- [15] J. S. Chen and X. W. Lou, "Anatase TiO₂ nanosheet: an ideal host structure for fast and efficient lithium insertion/extraction," *Electrochemistry Communications*, vol. 11, no. 12, pp. 2332–2335, 2009.
- [16] R. H. Lochner and J. E. Matar, *Design for Quality: An Introduction to the Best of Taguchi and Western Methods of Statistical Experimental Design*, Chapman and Hall, New York, NY, USA, 1990.
- [17] P. Sharma, A. Verma, R. K. Sidhu, and O. P. Pandey, "Process parameter selection for strontium ferrite sintered magnets using Taguchi L9 orthogonal design," *Journal of Materials Processing Technology*, vol. 168, no. 1, pp. 147–151, 2005.
- [18] G. P. Sycos, "Die casting process optimization using Taguchi methods," *Journal of Materials Processing Technology*, vol. 135, no. 1, pp. 68–74, 2003.

- [19] S. S. Mehdi, M. T. Khorasani, and A. Jamshidi, "Hydrothermal processing of hydroxyapatite nanoparticles—a Taguchi experimental design approach," *Journal of Crystal Growth*, vol. 361, pp. 73–84, 2012.
- [20] M. Dargahi, H. Kazemian, M. Soltanieh, M. Hosseinpour, and S. Rohani, "High temperature synthesis of SAPO-34: applying an L9 Taguchi orthogonal design to investigate the effects of experimental parameters," *Powder Technology*, vol. 217, pp. 223–230, 2012.
- [21] H. P. Wu, C. M. Lan, J. Y. Hu et al., "Hybrid titania photoanodes with a nanostructured multi-layer configuration for highly efficient dye-sensitized solar cells," *The Journal of Physical Chemistry Letters*, vol. 4, no. 9, pp. 1570–1577, 2013.
- [22] J.-Y. Liao, B.-X. Lei, D.-B. Kuang, and C.-Y. Su, "Tri-functional hierarchical TiO₂ spheres consisting of anatase nanorods and nanoparticles for high efficiency dye-sensitized solar cells," *Energy and Environmental Science*, vol. 4, no. 10, pp. 4079–4085, 2011.
- [23] Z.-S. Wang, H. Kawauchi, T. Kashima, and H. Arakawa, "Significant influence of TiO₂ photoelectrode morphology on the energy conversion efficiency of N719 dye-sensitized solar cell," *Coordination Chemistry Reviews*, vol. 248, no. 13-14, pp. 1381–1389, 2004.
- [24] K. Yan, Y. Qiu, W. Chen, M. Zhang, and S. Yang, "A double layered photoanode made of highly crystalline TiO₂ nanooctahedra and agglutinated mesoporous TiO₂ microspheres for high efficiency dye sensitized solar cells," *Energy and Environmental Science*, vol. 4, no. 6, pp. 2168–2176, 2011.
- [25] I. G. Yu, Y. J. Kim, H. J. Kim, C. Lee, and W. I. Lee, "Size-dependent light-scattering effects of nanoporous TiO₂ spheres in dye-sensitized solar cells," *Journal of Materials Chemistry*, vol. 21, no. 2, pp. 532–538, 2011.
- [26] Y.-C. Park, Y.-J. Chang, B.-G. Kum et al., "Size-tunable mesoporous spherical TiO₂ as a scattering overlayer in high-performance dye-sensitized solar cells," *Journal of Materials Chemistry*, vol. 21, no. 26, pp. 9582–9586, 2011.
- [27] M.-J. Jeng, Y.-L. Wung, L.-B. Chang, and L. Chow, "Particle size effects of TiO₂ layers on the solar efficiency of dye-sensitized solar cells," *International Journal of Photoenergy*, vol. 2013, Article ID 563897, 9 pages, 2013.
- [28] N.-G. Park, J. Van De Lagemaat, and A. J. Frank, "Comparison of dye-sensitized rutile- and anatase-based TiO₂ solar cells," *Journal of Physical Chemistry B*, vol. 104, no. 38, pp. 8989–8994, 2000.
- [29] C. S. Karthikeyan, M. Thelakkat, and M. Willert-Porada, "Different mesoporous titania films for solid-state dye sensitised solar cells," *Thin Solid Films*, vol. 511-512, pp. 187–194, 2006.

Research Article

Photovoltaic Performance of ZnO Nanorod and ZnO : CdO Nanocomposite Layers in Dye-Sensitized Solar Cells (DSSCs)

Sule Erten-Ela

Ege University, Solar Energy Institute, Bornova, 35100 Izmir, Turkey

Correspondence should be addressed to Sule Erten-Ela; suleerten@yahoo.com

Received 20 May 2013; Revised 8 August 2013; Accepted 4 September 2013

Academic Editor: Giuseppe Calogero

Copyright © 2013 Sule Erten-Ela. This is an open access article distributed under the Creative Commons Attribution License, which permits unrestricted use, distribution, and reproduction in any medium, provided the original work is properly cited.

Triphenylene diamine sensitizer comprising donor, electron conducting, and anchoring group is synthesized for a potential application in dye-sensitized solar cells. Absorption spectrum, electrochemical and photovoltaic properties of triphenylene diamine have been investigated. Two different electrodes are used for dye-sensitized solar cells. The performances of ZnO nanorod electrodes are compared to ZnO : CdO nanocomposite electrode. Also, the theoretical calculations for HOMO and LUMO orbitals are used to estimate the photovoltaic properties of organic sensitizer in the design stage. ZnO : CdO nanocomposite electrode-based dye-sensitized solar cell sensitized with organic sensitizer exhibits higher efficiencies than ZnO nanorod electrode. For a typical device, a solar energy conversion efficiency (η) of 0.80 based on ZnO : CdO nanocomposite is achieved under simulated AM 1.5 solar irradiation (100 mW cm^{-2}) with a short circuit photocurrent density (J_{sc}) of 3.10 mA/cm^2 , an open-circuit voltage (V_{oc}) of 480 mV, and a fill factor (FF) of 0.57. These results suggest that the ZnO : CdO nanocomposite system is a good selection and a promising candidate for electrode system in dye-sensitized solar cells.

1. Introduction

The modern society has intensively consumed energy resources, a large portion of which is accounted for by fossil fuel, such as petroleum, coal and natural gas. Development of alternative, renewable sources of energy is essential to reduce emission of carbon dioxide and other harmful substances when fossil fuel is burnt, as well as attain stable energy provision. Solar energy is one of several promising clean energy sources that could contribute to a stable energy supply and mitigate global environmental issues. In particular, the direct creation of electric energy is made possible through a solar cell. Much attention is now being focused on solar cells as potential energy-conversion systems. Dye sensitized nanocrystalline solar cells (DSSC) are of great interest as a cost-effective alternative to conventional silicon photovoltaics. The photoanode in DSSC is a mesoporous metal oxide film, sensitized by a monolayer of dye molecules. Upon visible light absorption, excited sensitizer molecules inject an electron into the conduction band of metal oxide. These carriers are transported and collected by a contact electrode [1, 2]. Among the other metal oxides such as SnO_2 , In_2O_3 ,

and WO_3 , ZnO nanostructures are promising materials for photovoltaic materials in solar cell. ZnO has large exciton binding energy (60 MeV) with the 3.4 eV energy band gap. Physical properties are similar to TiO_2 but its electron mobility is higher by 2-3 orders of magnitude [3–5].

A sensitizer, as the light-harvesting component in a dye-sensitized solar cell (DSSC), is of paramount importance to photovoltaic performance. The sensitizer is attached to the surface of a mesoporous wide band-gap semiconductor serving as electron transporter [6–8]. The interest in metal-free, organic dyes with high extinction coefficients has grown in recent years for organic solar cell research. In order to investigate organic dyes and, in the longer run, prepare an efficient solar cell dye, a number of different organic dyes are designed and synthesized [9–13]. Dye-sensitized solar cells (DSSCs) appear to be highly promising alternatives to more expensive solar cell technologies. Considering the current maximal level of overall conversion efficiency (η) under simulated sunlight for DSSCs (12%), improvements in efficiency and durability would certainly facilitate widespread utilization of this technology. It is clear that there are a number of factors determining the efficiency of solar cells,

but the structural and physical properties of the sensitizer are clearly important ones [14, 15].

In this study, triphenylene diamine-based organic sensitizer is synthesized for dye sensitized solar cell application. Theoretical calculations for HOMO and LUMO orbitals of triphenylene diamine sensitizer are used to estimate the photovoltaic properties of organic sensitizer. Electrochemical properties are also investigated. Dye sensitized solar cell is operated with 4 μm thicknesses of ZnO nanorod electrode. To obtain the better efficiency in dye sensitized solar cell, ZnO : CdO nanocomposite structure is prepared. Efficiencies of ZnO : CdO nanocomposite-based dye sensitized solar cell are compared to ZnO nanorod-based dye sensitized solar cell. Results show that ZnO : CdO nanocomposite electrodes have higher efficiencies than ZnO nanorods. And ZnO : CdO nanocomposite electrodes are promising materials for dye sensitized solar cells.

2. Experimental

2.1. Materials. Tetraphenylbenzidine, triphenyl phosphine, POCl_3 , cyanoacetic acid, and piperidine are purchased from Aldrich. Solvents are of spectroscopic grade and are used without any further purification.

2.2. Synthesis and Characterization of Triphenylene Diamines. The synthesis of TPD dye is conducted in two steps with moderate yields. Tetraphenylbenzidine is supplied from Aldrich company. First reaction is the Vilsmeier reaction, to form aldehyde product.

In the second reaction, the aldehyde is condensed with cyanoacetic acid by means of the Knoevenagel reaction in the presence of piperidine to form the target compound of TPD.

2.3. Synthesis and Characterization of TPD Dye

2.3.1. Synthesis Method of TPD. Aldehyde product and acrylic acid product are synthesized in the following procedure.

(1) *Step (synthesis of 4-[[4'-(diphenylamino)biphenyl-4-yl](phenyl)amino]benzaldehyde).* POCl_3 (1.36 mmol, 0.2 g) is stirred in a two-necked flask at 0°C for 1 hour in dried DMF under argon atmosphere. After additional stirring for 1 h at room temperature, this solution is added to a stirred solution of 5 g (0.0097 mol) of N,N'-Bis(diphenyl)benzidine in 20 mL of 1,2-dichloroethane. This reaction mixture is stirred for another hour at 60°C and allowed to cool to room temperature. Hereafter, the mixture is poured into a solution of 10 g sodium acetate in 100 mL water, and this mixture is extracted three times with dichloromethane. The combined organic layers are washed twice with water and dried over magnesium sulfate. After filtration and evaporation of the solvent, a yellow solid is obtained. The desired monoformylated product is isolated from this crude product by column chromatography using silica gel and solvent as the eluent, 4-[[4'-(diphenylamino)biphenyl-4-yl](phenyl)amino]benzaldehyde, yellow crystals; molecular structure is analysed with ^1H NMR spectrum. ^1H NMR

(CDCl_3): (ppm), 9.83 (1H, s, -CHO), 7.71 (2H, d, Ar-H), 7.55 (2H, t, Ar-H), 7.48 (2H, t, Ar-H), 7.21 (2H, m, Ar-H).

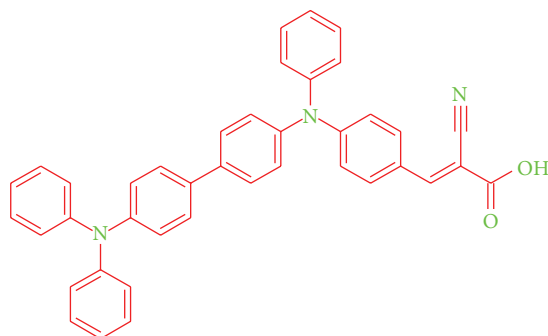
(2) *Step (Synthesis of (2Z)-2-(cyanomethyl)-3-{4-[[4'-(diphenylamino)biphenyl-4-yl](phenyl)amino]phenyl}acrylic acid, TPD).* To a solution of 4-[[4'-(diphenylamino)biphenyl-4-yl](phenyl)amino]benzaldehyde (0.16 mmol, 72.3 mg) and cyanoacetic acid (0.32 mmol, 27.95 mg) in a mixture of tetrahydrofuran : methanol (1 : 1) is added catalytic amount of piperidine, after which the solution is stirred for 2 h at 40°C . The solvent mixture is evaporated under reduced pressure and the resulting material is extracted with chloroform and 0.1 M HCl solution, washed with water, and dried over magnesium sulfate. The product is purified by column chromatography using silicagel and chloroform:methanol as the eluent. Molecular structure is characterized with IR and ^1H NMR spectrum, mass and elemental analysis. IR (KBr): cm^{-1} , 3551, 3412, 3031, 2214, 1583, 1487, 1392, 1323, 1270, 1178, 1074, 1028, 1003, 959, 818, 788, 749, 723, 693, 667. ^1H NMR (DMSO-d_6): (ppm), 7.88 (1H, s, -CH=), 7.79 (2H, d, Ar-H), 7.60 (4H, q, Ar-H), 7.36 (6H, m, Ar-H), 7.15 (5H, m, Ar-H), 7.10 (10H, m, Ar-H). MS/(ESI/100 eV): m/z : 583. $\text{C}_{40}\text{H}_{29}\text{N}_3\text{O}_2$ (583): Calcd: C 82.31%, H 5.01%, N 7.20%, O 5.48%; found: C 82.33%, H 5.00%, N 7.23%, O 5.48%.

Figure 1 shows the molecular structure of organic sensitizer. Absorption spectrum of TPD is taken in chlorobenzene solvent (Figure 2). It shows that organic sensitizer absorbs in the visible region between 380–550 nm.

2.4. Synthesis of ZnO Nanorods and CdO Nanostructures. ZnO nanorods and CdO nanostructures are synthesized from zinc salt and Cadmium salt in water solution using hydrothermal reaction. Microwave method is used for the synthesis of ZnO and CdO nanostructures. In a typical experiment, zinc acetate is dissolved in 25 mL deionized water in a beaker. The concentration of zinc acetate dehydrate is 0.55 M. The solution is stirred with magnetic bar at 100°C for 1 hour until a transparent mixture is obtained. Subsequently, solution is loaded into a 100 mL Teflon-lined container. Then solution is irradiated by microwave energy in the microwave oven at 200°C for 60 minutes (CEM MARS-5, frequency 2.45 GHz, maximum power 700 W, multimode oven). Then the solution is poured into a beaker and heated at 200°C until water is evaporated. After wet precipitate is dried in an oven at 90°C for 12 h. Finally, white powder is calcined in a furnace at 200°C for 36 hours. For CdO synthesis, we followed the same experimental method using cadmium acetate dehydrate. White powder is calcined at 450°C for 36 hours. Brown CdO nanoparticles are obtained. To obtain ZnO : CdO nanocomposite, ZnO is mixed with 5% CdO nanostructures.

3. Results and Discussion

3.1. AFM Image of Thin Film of Organic Sensitizer. Morphology of organic material is another important factor for DSSCs. The surface morphology of thin film of triphenylene diamine is prepared in chlorobenzene solvent on FTO glass by using spin coater in 1500 rpm. Atomic force microscopy (AFM)



(Z)-2-Cyano-3-4-[4-(4-diphenylaminophenyl)(phenyl)anilino]phenyl-2-propenoic Acid, TPD

FIGURE 1: Molecular Structure of TPD Dye.

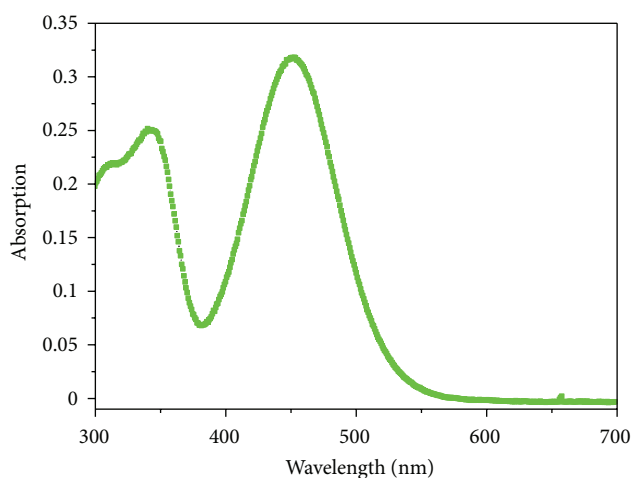


FIGURE 2: Absorption Spectrum of Organic Sensitizer in Chlorobenzene Solvent.

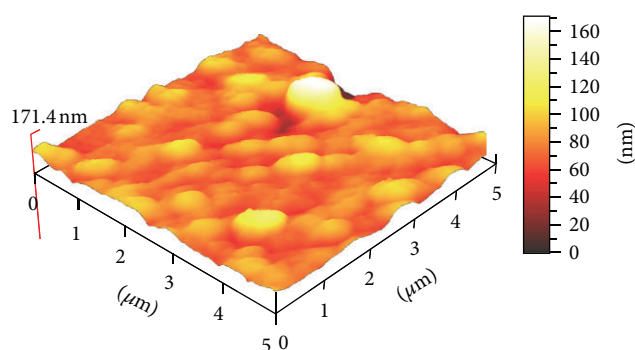


FIGURE 3: Atomic Force Microscopy of Organic Sensitizer on FTO Glass.

image is taken in noncontact mode (Figure 3). These measurements are performed under ambient conditions using a commercial scanning probe microscope. The AFM topographic image obtained is processed using the XEI program. Atomic force microscopy image of TPD which has 16.84 nm rms value is shown in Figure 3 on FTO glass.

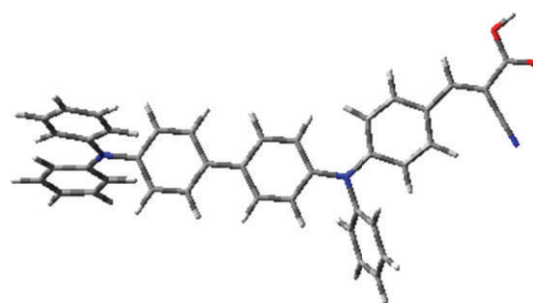


FIGURE 4: Ground State Optimization of Dye.

3.2. Theoretical Calculations of HOMO and LUMO Frontier Orbital of Organic Sensitizer. All ground-state geometry optimization and HOMO-LUMO orbital calculations are performed with the Gaussian 03 program package. Figure 4 shows the ground state optimization of organic dye. The HOMO is primarily comprised of π framework of the triphenylene diamine, with significant contributions from π electrons of the diphenylamino substituents (Figure 5(a)) whereas LUMO is very clearly confined to the π system of anchoring group (Figure 5(b)).

3.3. SEM and XRD Analysis of ZnO and ZnO: CdO Nanoelectrodes. The crystal structures of the ZnO nanorods are investigated using XRD. The XRD pattern reveals that with the use of calcination method, ZnO nanorods are formed. The diffraction peaks positioned at 2θ values of 31.8, 34.5, 36.3, 47.6, 56.6, 62.9, 66.3, 68.0, 69.2, 72.5, and 76.9° can be indexed to the hexagonal wurtzite phase of zinc oxide. The Nano-CdO materials are characterized using X-ray diffraction analysis (XRD). The XRD pattern shows the formation of nano-CdO materials. The diffraction peaks positioned at 2θ values of 32.9, 38.2, 55.2, 65.8, 69.2, 81.9° can be indexed to the phase of Cadmium oxide. Figure 6 shows the SEM images of ZnO nanorod (a) and ZnO: CdO nanocomposite (b).

3.4. Electrochemistry of Triphenylene Diamine Consisting of Anchoring Groups. E_{HOMO} and E_{LUMO} values of triphenylenediamine comprising anchoring groups are calculated by

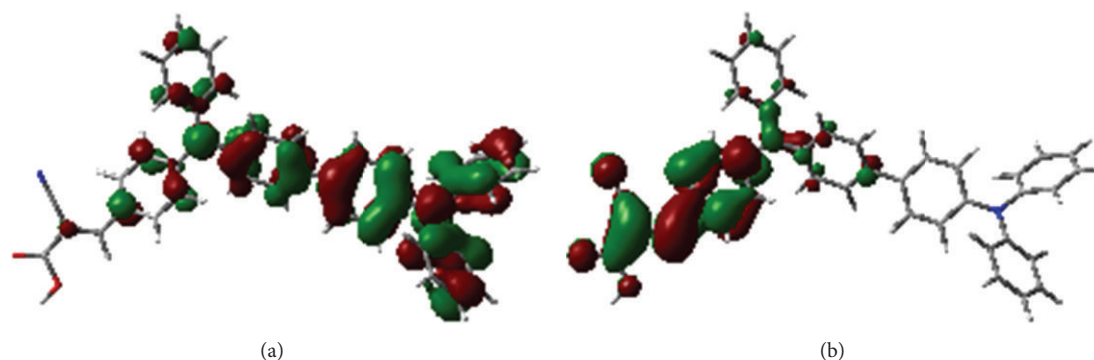


FIGURE 5: HOMO and LUMO Frontier Orbitals of Organic Sensitizer, HOMO Level (a), LUMO Level (b).

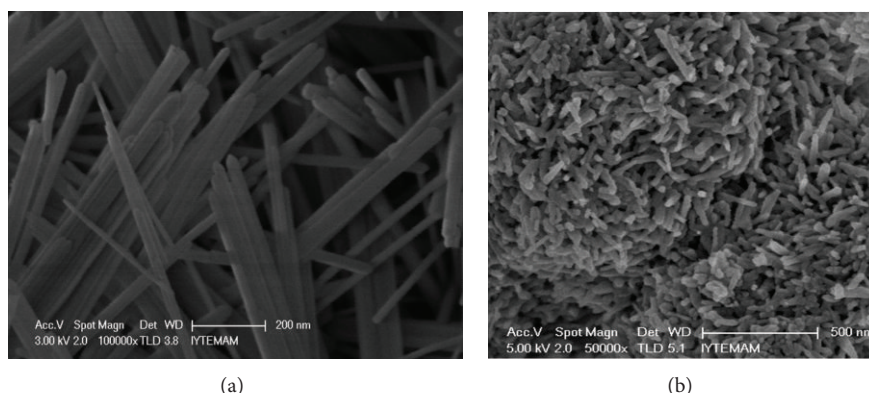


FIGURE 6: SEM image of ZnO nanorod (a) and ZnO:CdO nanocomposite (b).

using cyclic voltammograms. Solutions of TPD dye are prepared in dichloromethane (10^{-3} M). A three electrode cell set-up employed for the measurements consisted of glassy carbon working electrode, Pt wire counter electrode and Ag/AgCl reference electrode, all placed in a glass vessel. Tetrabutylammonium hexafluorophosphate (TBAPF₆), 0.1 M, is used as supporting electrolyte. Ferrocene is used as internal reference electrode. Table 1 summarizes the voltammetric behavior of 10^{-3} M solution of TPD. E_{HOMO} and E_{LUMO} levels are calculated from the onset potentials of oxidation and reduction and by assuming the energy level of ferrocene/ferrocenium (Fc/Fc⁺) to be 4.8 eV below the vacuum level. Results shows that TPD sensitizer can inject electrons to conduction band of metaloxide semiconductor.

3.5. Photovoltaic Device Fabrication and Characterization of DSSCs. The construction of the dye sensitized solar cell device requires first cleaning of the fluorine doped tin oxide (FTO) coated glass substrates in a detergent solution using an ultrasonic bath for 15 min, rinsed with water and ethanol. TPD has been used to manufacture solar cell devices to explore current-voltage characteristics using 4 μm thickness of ZnO nanorod electrode and 4 μm ZnO:CdO nanocomposite electrode (ZnO: 5% CdO) for comparison to electrode efficiencies. Electrodes are immersed into the TPD solution (0.5 mM in a mixture of acetonitrile: tert-butanol; chlorobenzene (volume ratio: 1:1:3) containing and kept

TABLE 1: Redox potentials of TPD derivatives.

| | $E_{\text{oxidation}}$ ^a (Volt) | $E_{\text{reduction}}$ ^b (Volt) | $E_{\text{ferrocene}}$ ^c | E_{HOMO} ^d | E_{LUMO} ^e | $E_{\text{Band Gap}}$ ^f |
|-------|---|---|-------------------------------------|--------------------------------|--------------------------------|------------------------------------|
| [TPD] | 0.85 | -1.08 | 0.39 | 5.26 | 3.33 | 1.93 |

^aFirst oxidation potentials of TPD.

^bReduction potentials of TPD.

^cPotentials of ferrocene, internal reference electrode.

^dHOMO energy level of TPD.

^eLUMO energy level of TPD.

^fEnergy Band Gap of TPD.

at room temperature overnight. TPD adsorbed ZnO and ZnO:CdO coated glasses are washed with pure chlorobenzene. The stained electrode and Pt-counter electrode are assembled into a sealed sandwich-type cell by heating with a hot-melt ionomer film (Surlyn 1702, Du-Pont) as a spacer between the electrodes. Platinized FTO glasses are used as counter electrode. Platinization of counter electrodes is done by coating of FTO glasses with 1% solution of hydrogen hexachloroplatinate (Aldrich) in 2-propanol and annealing at 400°C for 30 min. Cells are prepared in sandwich geometry. Surlyn 1702 (DuPont) frame is used as a spacer and a thermoplastic sealant between the two electrodes. Cells prepared in this way are then sealed by heating at 100°C. A drop of electrolyte solution (electrolyte of 0.6 M N-methyl-N-butyl-imidazolium iodide (BMII) + 0.1 M LiI + 0.05 M I₂ + 0.5 M

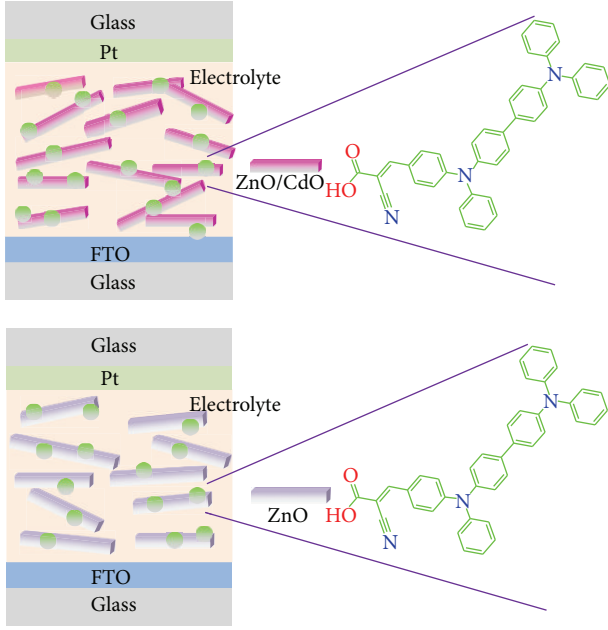


FIGURE 7: Schematic drawing of dye sensitized solar cells.

4-*tert*-butylpyridine (TBP) in acetonitrile) is placed on the drilled hole in the counter electrode of the assembled cell and is driven into the cell via vacuum backfilling. Finally, the hole is sealed using additional Bynel and a cover glass (0.1 mm thickness). Active areas of the cells are adjusted to 1 cm². *I-V* data collection is made by using Keithley 2400 Sourcemeter and LabView data acquisition software. *I-V* characteristics of dye sensitized solar cell in dark and under illumination are shown in Figure 6.

The entire energy conversion efficiency, η , is calculated by means of the following equations:

$$\eta = \frac{V_{oc} I_{sc} FF}{P_{light}}, \quad (1)$$

here, V_{oc} is open circuit voltage (V), I_{sc} is short circuit current (mA/cm²), and FF is fill factor:

$$FF = \frac{V_{max} I_{max}}{V_{oc} I_{sc}}, \quad (2)$$

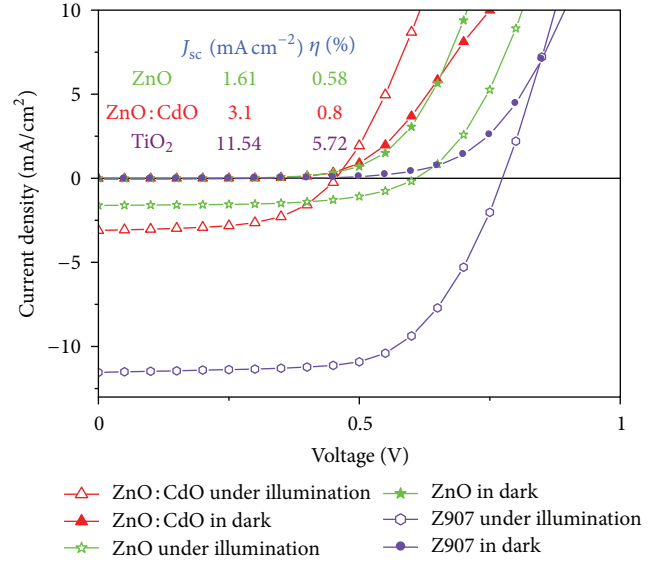
where, V_{max} and I_{max} are voltage and current at the point of maximum power output of cell.

Figure 7 shows the schematic illustration of dye sensitized solar cell.

3.6. Performance of Dye Sensitized Solar Cells. The TPD sensitizer has been used to manufacture solar cell devices to explore current-voltage characteristics by using 4 μ m ZnO electrode and 4 μ m ZnO : CdO layers. Under standard global AM 1.5 solar conditions, the organic sensitizer is tested for other electrode using 4 μ m ZnO nanorod and 4 μ m ZnO : CdO nanocomposite electrode for better comparison to electrode efficiency. Dye sensitized solar cell using 4 μ m ZnO nanorod electrode exhibits a short-circuit photocurrent

TABLE 2: Photovoltaic performance of ZnO and ZnO : CdO-based dye sensitized solar cells.

| | J_{sc} (mAcm ⁻²) | V_{oc} (mV) | FF | η (%) |
|-----------|--------------------------------|---------------|------|------------|
| ZnO | 1.61 | 600 | 0.60 | 0.58 |
| ZnO : CdO | 3.10 | 480 | 0.57 | 0.80 |
| Z907 | 11.54 | 772 | 0.66 | 5.72 |

FIGURE 8: *J-V* curve of ZnO and ZnO : CdO-based DSSCs.

density (J_{sc}) of 1.61 mA/cm², an open-circuit voltage (V_{oc}) of 600 mV, and a fill factor (FF) of 0.60, corresponding to an overall conversion efficiency, η of 0.58%. Normally, ZnO has lower efficiency than TiO₂ electrode because of ZnO crystal defects. Ruthenium Z907 gives higher efficiency in TiO₂ with overall conversion efficiency of 5.72 and short circuit photocurrent density of 11.54 mA/cm² in our laboratory condition. For this reason, *n*-type ZnO is doped with *n*-type CdO nanomaterial to improve the crystal quality of ZnO nanorods. 5% CdO nanostructures are mixed with ZnO nanorods to improve the crystal quality of ZnO nanorods. 4 μ m ZnO : CdO nanocomposite electrode is used for improving the dye sensitized solar cell efficiency. We have tested several ratios of ZnO : CdO composite, %5 CdO ratio is the optimum ratio for our experiments. ZnO : CdO-based dye sensitized solar cell using TPD sensitizer gives a short-circuit photocurrent density (J_{sc}) of 3.10 mA/cm², an open-circuit voltage (V_{oc}) of 480 mV, and a fill factor (FF) of 0.57, corresponding to an overall conversion efficiency η of 0.80%. ZnO nanorod electrode shows lower efficiency than ZnO : CdO electrode. Figure 8 shows the *J-V* curve of all dye sensitized solar cells. And all photovoltaic characterization results are shown in Table 2. Results show that ZnO : CdO nanocomposite is a good selection and improves the solar cell efficiency. According to SEM images in Figure 6, ZnO morphology is completely changed after doping with 5% CdO. Crystal morphology effects the dye sensitized solar cell efficiency.

In line with these statements, the higher efficiency is reported under standard conditions obtained for TPD sensitizer using $4\ \mu\text{m}$ ZnO: CdO layers. ZnO: CdO nanocomposite-based solar cells shows remarkably good efficiencies according to ZnO nanorod for the application of DSSCs.

4. Conclusion

In this paper, we have successfully fabricated dye sensitized solar cells using ZnO nanorod electrode and ZnO: CdO nanocomposite electrode. We report the good efficiency obtained with $4\ \mu\text{m}$ ZnO: CdO layers under standard conditions for TPD dye that performs a short-circuit photocurrent density (J_{sc}) of $3.10\ \text{mA}/\text{cm}^2$, an open-circuit voltage (V_{oc}) of $480\ \text{mV}$, and a fill factor (FF) of 0.57 , corresponding to an overall conversion efficiency η of 0.80% . ZnO nanorod-based DSSC gives a short-circuit photocurrent density (J_{sc}) of $1.61\ \text{mA}/\text{cm}^2$, an open-circuit voltage (V_{oc}) of 600 , and a fill factor (FF) of 0.60 , corresponding to an overall conversion efficiency η of 0.58% . As a conclusion, ZnO: CdO electrode exhibits higher efficiencies than ZnO nanorod electrode.

Acknowledgment

The author acknowledges the Alexander Von Humboldt Foundation and Scientific Research Council of Turkey (TUBITAK). The author thanks mechanical engineer Cagatay ELA for his unending support and valuable contribution to this paper.

References

- [1] B. O'Regan and M. Grätzel, "A low-cost, high-efficiency solar cell based on dye-sensitized colloidal TiO_2 films," *Nature*, vol. 353, no. 6346, pp. 737–740, 1991.
- [2] M. Grätzel, "Photoelectrochemical cells," *Nature*, vol. 414, no. 6861, pp. 338–344, 2001.
- [3] M. Grätzel, "Conversion of sunlight to electric power by nanocrystalline dye-sensitized solar cells," *Journal of Photochemistry and Photobiology A*, vol. 164, no. 1–3, pp. 3–14, 2004.
- [4] M. K. Nazeeruddin, F. de Angelis, S. Fantacci et al., "Combined experimental and DFT-TDDFT computational study of photoelectrochemical cell ruthenium sensitizers," *Journal of the American Chemical Society*, vol. 127, no. 48, pp. 16835–16847, 2005.
- [5] H. Imahori, T. Umeyama, and S. Ito, "Large π -aromatic molecules as potential sensitizers for highly efficient dye-sensitized solar cells," *Accounts of Chemical Research*, vol. 42, no. 11, pp. 1809–1818, 2009.
- [6] Q. Zhang, C. S. Dandeneau, X. Zhou, and C. Cao, "ZnO nanostructures for dye-sensitized solar cells," *Advanced Materials*, vol. 21, no. 41, pp. 4087–4108, 2009.
- [7] S. Kolemen, O. A. Bozdemir, Y. Cakmak et al., "Optimization of distyryl-Bodipy chromophores for efficient panchromatic sensitization in dye sensitized solar cells," *Chemical Science*, vol. 2, no. 5, pp. 949–954, 2011.
- [8] S. Erten-Ela, S. Cogal, G. Turkmen, and S. Icli, "Hybrid solar cells using nanorod zinc oxide electrodes and perylene monoimide-monoanhydride dyes," *Current Applied Physics*, vol. 10, no. 1, pp. 187–192, 2010.
- [9] S. Erten-Ela, S. Cogal, and S. Icli, "Conventional and microwave-assisted synthesis of ZnO nanorods and effects of PEG400 as a surfactant on the morphology," *Inorganica Chimica Acta*, vol. 362, no. 6, pp. 1855–1858, 2009.
- [10] S. Erten-Ela and A. C. Cakir, "Comparison between synthesis techniques to obtain ZnO nanorods and its effect on dye sensitized solar cells," *Advanced Powder Technology*, vol. 23, pp. 655–660, 2012.
- [11] H. Sarica and S. Erten-Ela, "Photovoltaic characterizations of Nano-CdO based dye sensitized solar cells," *Journal of Optoelectronics and Advanced Material*, vol. 14, no. 9-10, pp. 753–757, 2012.
- [12] S. Erten-Ela, J. Brendel, and M. Thelakkat, "Solid-state dye-sensitized solar cells fabricated with nanoporous TiO_2 and TPD dyes: analysis of penetration behavior and I-V characteristics," *Chemical Physics Letters*, vol. 510, no. 1–3, pp. 93–98, 2011.
- [13] S. Erten-Ela, M. D. Yilmaz, B. Icli, Y. Dede, S. Icli, and E. U. Akkaya, "A panchromatic boradiazaindacene (BODIPY) sensitizer for dye-sensitized solar cells," *Organic Letters*, vol. 10, no. 15, pp. 3299–3302, 2008.
- [14] P. A. Bouit, M. Marszalek, R. Humphry-Baker et al., "Donor-p-Acceptors containing the 10-(1,3-Dithiol-2-ylidene)anthracene unit for dye-sensitized solar cells," *European Journal of Chemistry*, vol. 18, pp. 11621–11629, 2012.
- [15] S. Feihl, R. D. Costa, S. Pflock et al., "Nickel oxide nanostructured electrodes towards perylenediimide-based dye-sensitized solar cells," *RSC Advances*, vol. 2, pp. 11495–11503, 2012.

Research Article

Effects of Sulfurization Temperature on Properties of CZTS Films by Vacuum Evaporation and Sulfurization Method

Jie Zhang, Bo Long, Shuying Cheng, and Weibo Zhang

College of Physics and Information Engineering and Institute of Micro-Nano Devices & Solar Cells, Fuzhou University, Fuzhou, Fujian 350108, China

Correspondence should be addressed to Shuying Cheng; sycheng@fzu.edu.cn

Received 19 May 2013; Revised 28 July 2013; Accepted 3 September 2013

Academic Editor: Francesco Bonaccorso

Copyright © 2013 Jie Zhang et al. This is an open access article distributed under the Creative Commons Attribution License, which permits unrestricted use, distribution, and reproduction in any medium, provided the original work is properly cited.

Copper zinc tin sulfur (CZTS) thin films have been extensively studied in recent years for their advantages of low cost, high absorption coefficient ($\geq 10^4 \text{ cm}^{-1}$), appropriate band gap ($\sim 1.5 \text{ eV}$), and nontoxicity. CZTS thin films are promising materials of solar cells like copper indium gallium selenide (CIGS). In this work, CZTS thin films were prepared on glass substrates by vacuum evaporation and sulfurization method. Sn/Cu/ZnS (CZT) precursors were deposited by thermal evaporation and then sulfurized in $\text{N}_2 + \text{H}_2\text{S}$ atmosphere at temperatures of 360–560°C to produce polycrystalline CZTS thin films. It is found that there are some impurity phases in the thin films with the sulfurization temperature less than 500°C, and the crystallite size of CZTS is quite small. With the further increase of the sulfurization temperature, the obtained thin films exhibit preferred (112) orientation with larger crystallite size and higher density. When the sulfurization temperature is 500°C, the band gap energy, resistivity, carrier concentration, and mobility of the CZTS thin films are 1.49 eV, $9.37 \Omega \cdot \text{cm}$, $1.714 \times 10^{17} \text{ cm}^{-3}$, and $3.89 \text{ cm}^2/(\text{V} \cdot \text{s})$, respectively. Therefore, the prepared CZTS thin films are suitable for absorbers of solar cells.

1. Introduction

$\text{Cu}_2\text{ZnSnS}_4$ (CZTS) is one of the promising materials for absorbers in thin film solar cells because of its excellent properties for obtaining high efficiency; that is, it has a direct band gap of 1.51 eV, very close to optimum band gap of semiconductor used for photovoltaic conversion, and high absorption coefficient ($\geq 10^4 \text{ cm}^{-1}$) [1]. At the same time, it has versatile electrical properties which can suitably be tailored and tuned to the specific need in a given device structure [2–5]. Various methods have been reported to fabricate the CZTS thin films including thermal evaporation [6], sputtering [7], pulsed laser deposition [8], electroplating [9], and hydrazine process [10]. The best efficiencies reported for the pure CZTS solar cells so far have been 8.4% using thermal evaporation and sulfurization [11]. In the study, the CZTS thin films were deposited using a 150°C vacuum thermal evaporation process and subsequent short (5 min) high-temperature (570°C) atmospheric pressure annealing. Though the efficiency of the solar cells is high, the annealing temperature is a little high and it does not correspond to the designing rule of solar

cells. Therefore, choosing a lower sulfurization temperature to produce CZTS thin films is important.

In our study, we also use thermal evaporation and sulfurization method to produce CZTS thin films. And the effects of the sulfurization temperature on the structural, optical, and electrical properties of the CZTS films are investigated.

2. Experiment Details

We fabricated CZTS thin films on floating glasses substrates by vapor-phase sulfurization of thermal and electron-beam (E-B) evaporated precursors. This process consisted of two stages with the sequential evaporation of precursors followed by the vapor-phase sulfurization. We formed the stacked precursors on the substrates by depositing ZnS layers with E-B evaporation, Cu and Sn layers with thermal evaporation orderly. The thickness of each layer was controlled by a film thickness monitor (FTM) on the evaporation equipment. And the thicknesses of the three layers are shown in Table 1 according to the ratio of the constituents. We sulfurized the precursors in an annealing furnace in the atmosphere

TABLE 1: The parameters of the CZT precursors.

| Precursors | d_{Sn} (nm) | d_{Cu} (nm) | d_{ZnS} (nm) | $n_{\text{Zn}}/n_{\text{Sn}}$ | $n_{\text{Cu}}/(n_{\text{Sn}} + n_{\text{Zn}})$ |
|------------|-------------------------|-------------------------|--------------------------|-------------------------------|---|
| CZT | 145 | 120 | 360 | 1.70 | 0.704 |

TABLE 2: Samples at different sulfurization temperatures (T_s).

| Sample | S11 | S12 | S13 | S14 | S15 |
|------------|-----|-----|-----|-----|-----|
| T_s (°C) | 360 | 400 | 450 | 500 | 560 |

of $\text{N}_2 + \text{H}_2\text{S}$ (5%) at temperatures of 360°C–560°C for 2 hours. After sulfurization of the precursors, CZTS thin films were formed. The samples obtained at different sulfurization temperatures are listed in Table 2.

The film thickness was measured by a stylus profiler (TENCOR D100). The crystallinity of the CZTS thin films was ascertained by an X-ray diffractometer with $\text{Cu K}\alpha$ radiation ($\lambda = 1.5406 \text{ \AA}$). The optical characteristics of the CZTS films were performed by a PerkinElmer Lambda 900 UV/VIS/NIR spectrometer in the wavelength range from 300 nm to 1400 nm at room temperature. The surface morphology was observed by a scanning electron microscope (SEM) (HITACHI S-4800) and an atom force microscope (AFM) (Bruker). A HMS-3000 hall measurement system was used to carry out the carrier concentration, mobility, and resistivity.

3. Results and Discussions

3.1. Structure and Morphology. Figure 1 shows the XRD patterns of the CZTS films obtained at different sulfurization temperatures. For the films sulfurized at 360°C and 400°C, in the XRD patterns, there exist peaks from CZTS (JCPDS-ICDD no. 00-026-0575). However, there are also several peaks from SnS (JCPDS-ICDD no. 01-073-1859) and CuS (JCPDS-ICDD no. 01-075-2233). When the sulfurization temperature is 450°C, the phases of CuS and SnS disappear but there are some XRD peaks from SnS_2 (JCPDS-ICDD no. 00-022-0951) besides those from CZTS. When the sulfurization temperature is about 500°C and 560°C, the peaks from secondary phases disappear, and there are only the XRD peaks of CZTS. The result indicates that the CZTS thin films sulfurized below 500°C are a mixture of CZTS polycrystals with SnS, CuS, and SnS_2 as intermediates, and there is only the CZTS phase with the sulfurization temperature above 500°C. The films have the preferred (112) orientation, and the intensity of peak (112) is increased with the increase of the sulfurization temperature.

The size D_{hkl} of the crystallites is determined from XRD data by the Scherrer formula:

$$D_{hkl} = \frac{K\lambda}{\beta \cos \theta}, \quad (1)$$

where K is a constant, β is full width at half maximum (FWHM) in radians, λ is the wavelength of X-ray, and θ is the Bragg angle [12]. The K , λ values are taken as 0.89, 1.5406 Å for the calculations, respectively.

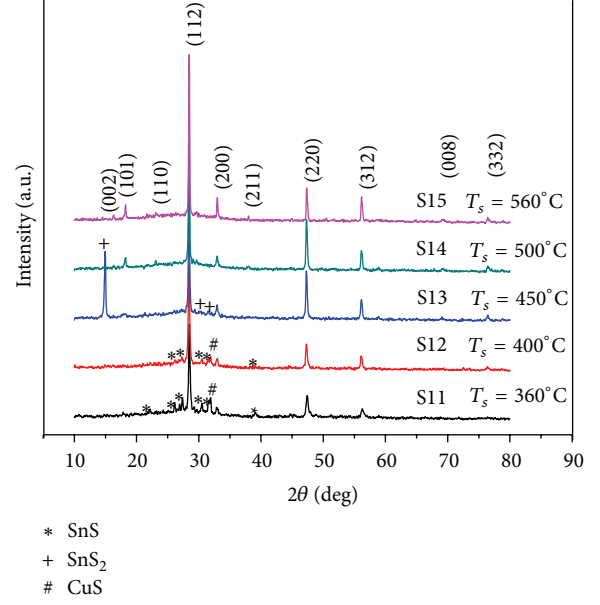


FIGURE 1: The XRD patterns of the CZTS films obtained at different sulfurization temperatures.

TABLE 3: The FWHM values and grain sizes of (112) orientation of the CZTS thin films obtained at different sulfurization temperatures.

| Sample | S11 | S12 | S13 | S14 | S15 |
|-----------------|--------|--------|--------|--------|--------|
| T_s (°C) | 360 | 400 | 450 | 500 | 560 |
| FWHM (°) | 0.1968 | 0.1574 | 0.1378 | 0.1200 | 0.1181 |
| Grain size (nm) | 39.92 | 49.91 | 57.01 | 65.47 | 66.52 |

TABLE 4: The R_{ms} values of the CZTS thin films obtained at different sulfurization temperatures.

| Sample | S11 | S12 | S13 | S14 | S15 |
|----------------------|-------|-------|-------|------|------|
| R_{ms} (nm) | 167.2 | 157.7 | 116.4 | 81.0 | 75.2 |

Table 3 shows the variation of the grain size from (112) orientation with the sulfurization temperature. With the increase of the sulfurization temperature from 360°C to 560°C, the grain size becomes larger and larger (from 39.92 nm to 66.52 nm).

Figures 2(a)–2(e) show the SEM graphs of the CZTS thin films obtained at different sulfurization temperatures. Figure 2(f) only shows the AFM image of sample S15 for simplification, and Table 4 shows the mean root roughness (R_{ms}) of the CZTS films. We can see that, with the increase of the sulfurization temperature, the grain sizes of the CZTS samples become larger, and the surfaces of the thin films become smoother and denser, which is in agreement with Tables 3 and 4. When the sulfurization temperature is less than 500°C, the CZTS may not be completely synthesized, and thus there are some secondary phases like SnS, SnS_2 , and CuS as shown in the XRD patterns. When the temperature is 500°C, the film is the most compact. When the temperature is higher than 500°C, the secondary phases disappear and the grain size of the film becomes larger, as seen in Figure 2(e).

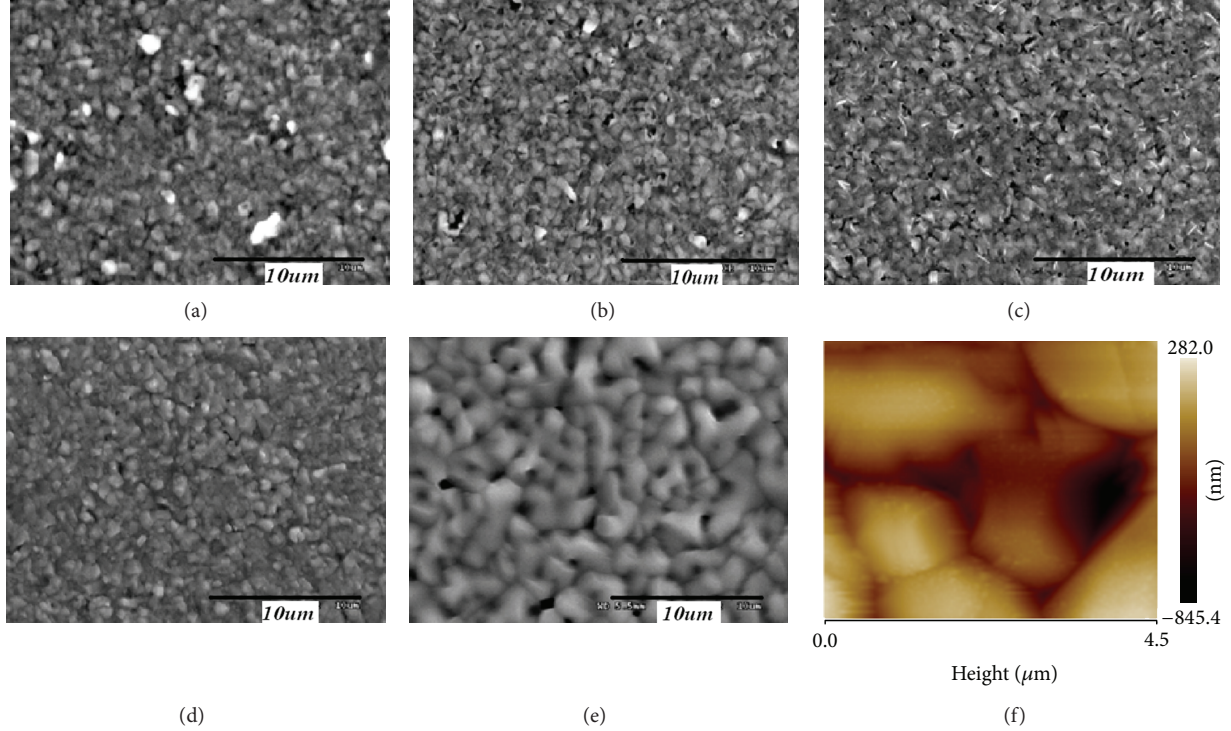


FIGURE 2: The SEM images of the CZTS thin films samples obtained at different sulfurization temperatures: (a) S11 (360°C), (b) S12 (400°C), (c) S13 (450°C), (d) S14 (500°C), (e) S15 (560°C), and (f) AFM image of sample S15.

TABLE 5: The values of E_g and α of the CZTS thin films obtained at different sulfurization temperatures.

| Sample | T_s (°C) | E_g (eV) | λ_0 (nm) | $\alpha(\lambda_0)$ (cm ⁻¹) |
|--------|------------|------------|------------------|---|
| S11 | 360 | 1.38 | 898.6 | 3.25×10^4 |
| S12 | 400 | 1.40 | 885.7 | 4.43×10^4 |
| S13 | 450 | 1.45 | 855.2 | 2.66×10^4 |
| S14 | 500 | 1.49 | 832.2 | 2.19×10^4 |
| S15 | 560 | 1.57 | 789.8 | 1.18×10^4 |

But there are some voids on the surface of the CZTS thin films. It may be due to the loss of Sn at higher sulfurization temperature ($\geq 500^\circ\text{C}$) [13]. It is obvious that the sulfurization temperature has some effects on the phase and crystallinity of the CZTS thin films. Therefore, the suitable sulfurization temperature of CZTS films should be no less than 500°C .

3.2. Optical Properties. Figure 3 shows the optical properties of the CZTS thin films obtained at different sulfurization temperatures. And Table 5 shows the values of E_g and α of the CZTS thin films. From Figures 3(a) and 3(b), we can see that, with the decrease of the sulfurization temperature, the transmittance and reflectance of the CZTS films decrease. The reasons may be as follows. One could be due to the surface roughness and the crystallinity. From the SEM graphs and Table 4, it can be seen that, with the decrease of the sulfurization temperature, the surfaces become rougher, resulting in more light scattering. The other one may be due to the secondary phases because the secondary phases are increased

with the decrease of the sulfurization temperature. However, most of these compounds have lower energy gap; thus they can absorb light with longer wavelength. Therefore, in the near-infrared waveband, the lower the sulfurization temperature is, the smaller transmittance and reflectance of the CZTS thin films are.

Figure 3(c) shows the absorbance versus the photon energy ($h\nu$) of the CZTS thin films with different sulfurization temperatures. With the decrease of the sulfurization temperature, the absorbance of the samples in the near-infrared waveband increases. The main reason may be due to the existence of the secondary phases. Figure 3(d) shows that the absorption coefficient (α) versus $h\nu$ of the CZTS thin films. From Figure 3(d), we can see that the absorption edge and the stable α are increased with the increase of the sulfurization temperature. Figure 3(e) gives that the energy bandgap (E_g) of the CZTS thin films becomes larger with the increase of the sulfurization temperature; the detailed data are listed in Table 5. Therefore, the temperature has some effects on the crystallinity, phase, and optical properties of the CZTS thin films. When the sulfurization temperature is below 500°C , there are some secondary phases, resulting in the worse crystallinity, rougher surface, and smaller E_g . When the sulfurization temperature is above 500°C , not only the grain size becomes larger, but also the E_g is very close to the optimum bandgap of semiconductor used for photovoltaic conversion.

3.3. Electrical Properties. Figure 4 shows the electrical properties of the CZTS thin films obtained at different sulfurization temperatures. All the films are of p-type conductivity.

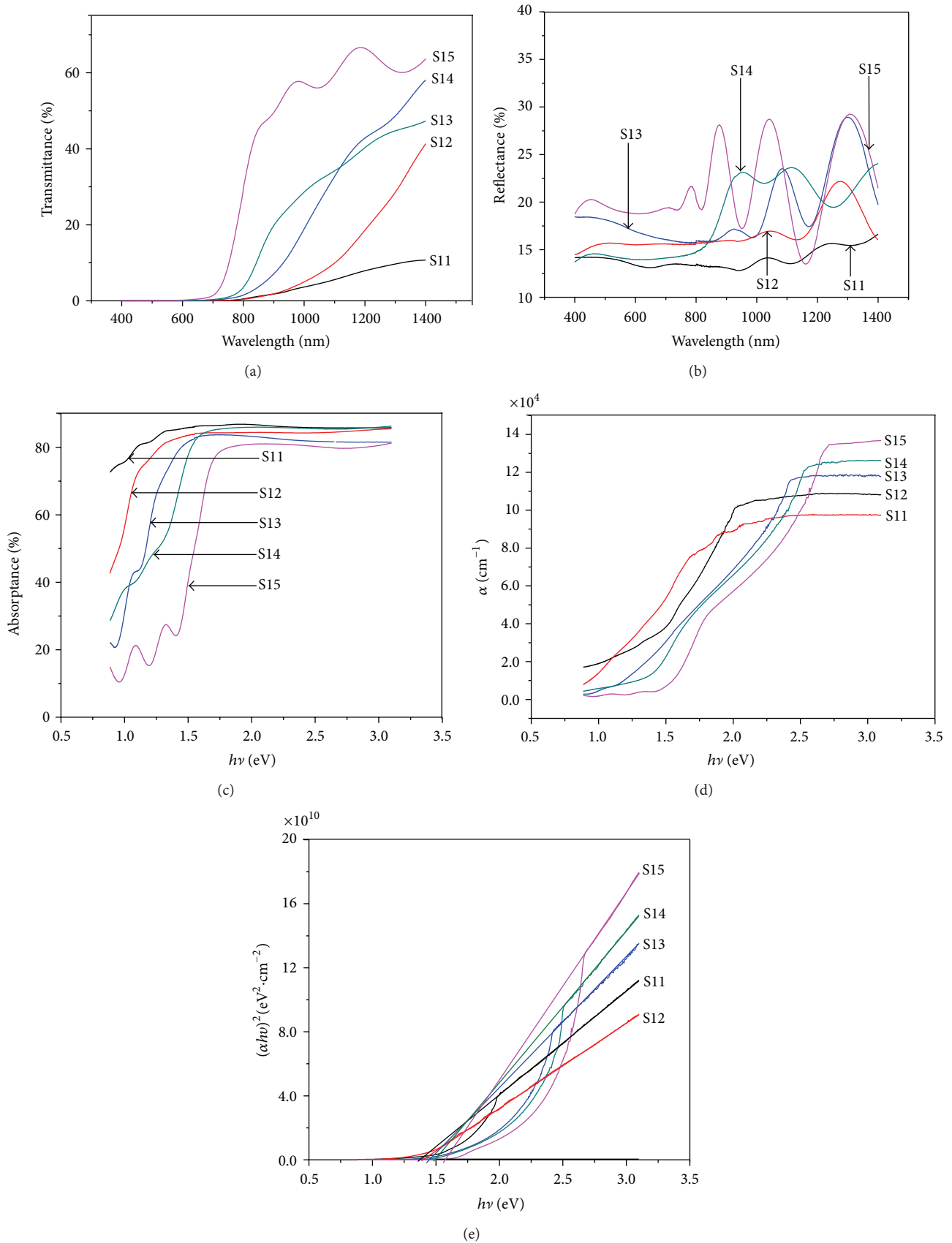


FIGURE 3: The optical properties of the CZTS thin films obtained at different sulfurization temperatures: (a) T, (b) R, (c) absorbance, (d) α , and (e) E_g .

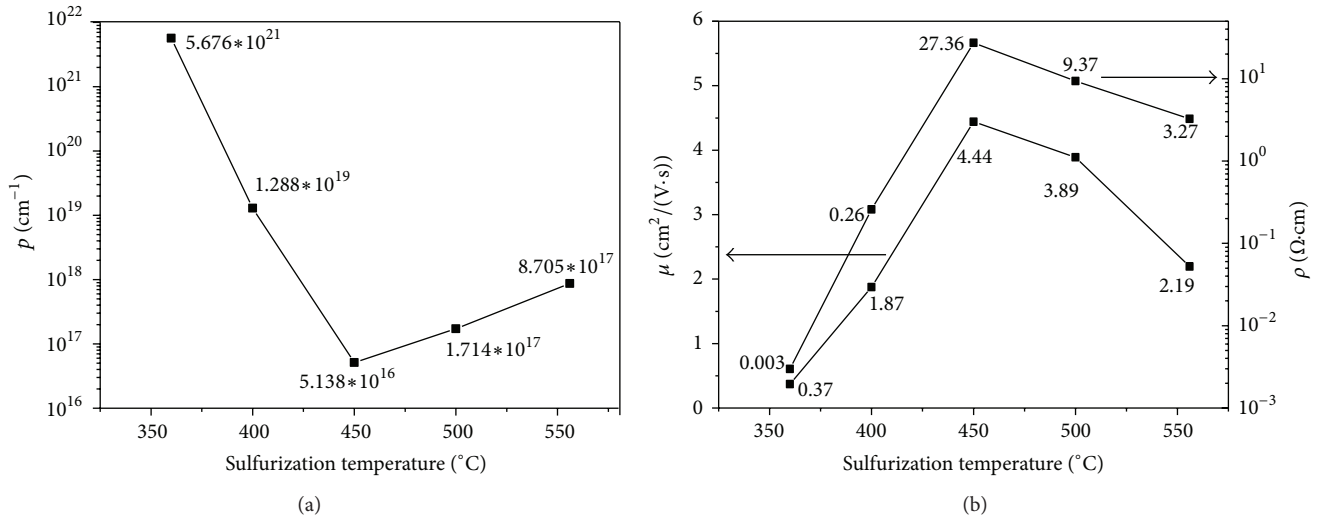


FIGURE 4: The electrical properties of the CZTS thin films obtained at different sulfurization temperatures: (a) carrier concentration (p), (b) mobility (μ) and resistivity (ρ).

With the increase of the sulfurization temperatures, the carrier concentration is decreased firstly and then increased slowly. But the variation tendency of the mobility and the resistivity are opposite to those of the carrier concentration. Because there are still some binary and ternary compounds in the samples under the low sulfurization temperature, these compounds make the carrier concentration increase. At the same time, they would result in the appearance of some defects and grain boundaries, so the mobility is decreased gradually. With the increase of the sulfurization temperature, the mixed phases are declined. When the temperature is 450°C , we can judge the existence of SnS_2 phase according to the XRD patterns. Whereas SnS_2 is a kind of compound with high resistivity, it may result in the highest resistivity ($27.36 \Omega\cdot\text{cm}$) and the lowest carrier concentration ($5.138 \times 10^{16} \text{ cm}^{-1}$) of the films. With the increase of the sulfurization temperature, Sn and Zn are lost seriously, resulting in the enlargement of $n_{\text{Cu}}/(n_{\text{Sn}} + n_{\text{Zn}})$. Thus, the carrier concentration is increased, and the resistivity is decreased gradually. From the above discussion, we can conclude that the CZTS thin films sulfurized at 500°C have the best electrical properties.

4. Conclusions

The CZTS films were deposited on the glass substrates by thermal and E-B evaporation following sulfurization. With the increase of the sulfurization temperature, the crystalline grain size becomes larger, and thereby the crystallinity of the CZTS thin films becomes better. With the increase of the sulfurization temperature, the E_g of the samples is close to the optimum band gap of the semiconductor used for photovoltaic conversion. At the sulfurization temperature of 500°C , the CZTS thin films have the best electrical properties for PV application.

Acknowledgments

This work was supported by the National Nature Sciences Funding of China (61076063) and Fujian Provincial Department of Science & Technology, China (2012J01266).

References

- [1] K. Ito and T. Nakazawa, "Electrical and optical properties of stannite-type quaternary semiconductor thin films," *Japanese Journal of Applied Physics*, vol. 27, pp. 2094–2097, 1988.
- [2] D. Park, D. Nam, S. Jung et al., "Optical characterization of $\text{Cu}_2\text{ZnSnSe}_4$ grown by thermal co-evaporation," *Thin Solid Films*, vol. 519, no. 21, pp. 7386–7389, 2011.
- [3] C. Shi, G. Shi, Z. Chen, P. Yang, and M. Yao, "Deposition of $\text{Cu}_2\text{ZnSnS}_4$ thin films by vacuum thermal evaporation from single quaternary compound source," *Materials Letters*, vol. 73, pp. 89–91, 2012.
- [4] L. Grenet, S. Bernardi, D. Kohen et al., " $\text{Cu}_2\text{ZnSn}(\text{S}_{1-x}\text{Se}_x)_4$ based solar cell produced by selenization of vacuum deposited precursors," *Solar Energy Materials and Solar Cells*, vol. 101, pp. 11–14, 2012.
- [5] P. M. P. Salomé, J. Malaquias, P. A. Fernandes et al., "The influence of hydrogen in the incorporation of Zn during the growth of $\text{Cu}_2\text{ZnSnS}_4$ thin films," *Solar Energy Materials and Solar Cells*, vol. 95, no. 12, pp. 3482–3489, 2011.
- [6] F. Biccari, R. Chierchia, M. Valentini, P. Mangiappane et al., "Fabrication of $\text{Cu}_2\text{ZnSnS}_4$ solar cells by sulfurization of evaporated precursors," *Energy Procedia*, vol. 10, pp. 187–191, 2011.
- [7] C. Platzer-Björkman, J. Scragg, H. Flammersberger, T. Kubart, and M. Edoff, "Influence of precursor sulfur content on film formation and compositional changes in $\text{Cu}_2\text{ZnSnS}_4$ films and solar cells," *Solar Energy Materials and Solar Cells*, vol. 98, pp. 110–117, 2012.
- [8] A. V. Moholkar, S. S. Shinde, A. R. Babar et al., "Synthesis and characterization of $\text{Cu}_2\text{ZnSnS}_4$ thin films grown by PLD: solar

- cells," *Journal of Alloys and Compounds*, vol. 509, no. 27, pp. 7439–7446, 2011.
- [9] S. Ahmed, K. B. Reuter, O. Gunawan, L. Guo, L. T. Romankiw, and H. Deligianni, "A high efficiency electrodeposited $\text{Cu}_2\text{ZnSnS}_4$ solar cell," *Advanced Energy Materials*, vol. 2, no. 2, pp. 253–259, 2012.
- [10] D. A. R. Barkhouse, O. Gunawan, T. Gokmen, T. K. Todorov, and D. B. Mitzi, "Device characteristics of a 10.1% hydrazine-processed $\text{Cu}_2\text{ZnSn}(\text{Se},\text{S})_4$ solar cell," *Progress in Photovoltaics*, vol. 20, no. 1, pp. 6–11, 2012.
- [11] B. Shin, O. Gunawan, Y. Zhu, N. A. Bojarczuk, S. J. Chey, and S. Guha, "Thin film solar cell with 8.4% power conversion efficiency using an earth-abundant $\text{Cu}_2\text{ZnSnS}_4$ absorber," *Progress in Photovoltaics*, vol. 21, no. 1, pp. 72–76, 2013.
- [12] P. K. Nair, J. Cardoso, O. Gomez Daza, and M. T. S. Nair, "Polyethersulfone foils as stable transparent substrates for conductive copper sulfide thin film coatings," *Thin Solid Films*, vol. 401, no. 1-2, pp. 243–250, 2001.
- [13] A. Weber, R. Mainz, and H. W. Schock, "On the Sn loss from thin films of the material system Cu-Zn-Sn-S in high vacuum," *Journal of Applied Physics*, vol. 107, no. 1, Article ID 013516, 6 pages, 2010.

Research Article

Spectroscopic and Morphological Studies of Metal-Organic and Metal-Free Dyes onto Titania Films for Dye-Sensitized Solar Cells

Gabriella Di Carlo,¹ Daniela Caschera,¹ Roberta G. Toro,¹ Cristina Riccucci,¹ Gabriel M. Ingo,¹ Giuseppina Padeletti,¹ Luisa De Marco,² Giuseppe Gigli,^{2,3,4} Giovanna Pennesi,⁵ Gloria Zanotti,⁵ Anna M. Paoletti,⁵ and Nicola Angelini⁵

¹ Institute for the Study of Nanostructured Materials (ISMN), CNR, Via Salaria km 29300, Monterotondo, 00015 Rome, Italy

² Center for Biomolecular Nanotechnologies (CBN), Fondazione Istituto Italiano di Tecnologia, Energy Platform Via Barsanti, Arnesano, 73010 Lecce, Italy

³ National Nanotechnology Laboratory (NNL), CNR Istituto Nanoscienze, c/o Distretto Tecnologico, Via Arnesano km 5, 73100 Lecce, Italy

⁴ Department of Mathematics and Physics "E. De Giorgi", University of Salento, Via per Arnesano, 73100 Lecce, Italy

⁵ Institute of Structure of Matter (ISM), CNR, Via Salaria km 29300, Monterotondo, 00015 Rome, Italy

Correspondence should be addressed to Gabriella Di Carlo; gabriella.dicarlo@ismn.cnr.it and Nicola Angelini; nicola.angelini@ism.cnr.it

Received 13 July 2013; Accepted 27 August 2013

Academic Editor: Giuseppe Calogero

Copyright © 2013 Gabriella Di Carlo et al. This is an open access article distributed under the Creative Commons Attribution License, which permits unrestricted use, distribution, and reproduction in any medium, provided the original work is properly cited.

We have investigated the spectroscopic behavior of three different sensitizers adsorbed onto titania thin films in order to gain information both on the electron transfer process from dye to titania and on the anchorage of the chromophore onto the semiconductor. We have examined by UV-Vis and fluorescence spectroscopy the widely used ruthenium complex *cis*-di(thiocyanato)bis(2,2'-bipyridyl-4,4'-dicarboxylato)ruthenium(II) (N719), the more recently developed organic molecular 3-(5-(4-(diphenylamino)styryl)thiophen-2-yl)-2-cyanoacrylic acid (D5), and a *push-pull* zinc phthalocyanine sensitizer (ZnPc). Three type of titania films with different morphology, characterized by SEM and FT-IR measurement, were considered: a mesoporous transparent film deposited by spin-coating (TiMS), a semiopaque film deposited by doctor-blade from mesoporous titania (TiMS-DB) and a semiopaque film deposited by doctor-blade from commercial P25 titania (P25-DB). The use of TiMS is responsible for the adsorption of a higher amount of dye since the mesoporous structure allows increasing the interfacial area between dye and titania. Moreover, the fluorescence emission peak is weaker when the sensitizers are adsorbed onto TiMS. These findings suggest that mesostructured films could be considered the most promising substrates to realize photoanodes with a fast electron transfer process.

1. Introduction

Dye-sensitized solar cells (DSSCs) are receiving increasing attention during the last decades since they are considered a viable and cost-effective technology for the conversion of sunlight into electricity [1–3]. In these devices, metal-organic or metal-free dyes are chemically adsorbed onto a wide band gap semiconductor oxide [1–8]. The working

principle of a DSSCs system is based on the photochemical and photophysical processes: upon photoexcitation of the dyes by visible light, electrons are excited from the ground state of the dye to its excited state, and then their injection can occur from the excited dye into the conduction band of the semiconductor.

To achieve a high power conversion efficiency, the electron injection process must be certain and faster than

the competing fluorescence and nonradiative processes. This photoinduced electron transfer leads to the production of photocurrent and consequently it is crucial to the device efficiency [1–3].

In DSSCs, the sensitizer is one of the critical components as it absorbs sunlight and induces the charge separation process. In order to enhance power conversion efficiencies of DSSCs, it is imperative to improve the light-harvesting ability of the dyes. It is also fundamental to investigate and to optimize the dye-substrate interaction that is involved in the electron transfer process [9].

Ruthenium sensitizers, such as *cis*-di(thiocyanato)-*bis*[2,2'-bipyridyl-4,4'-dicarboxylic acid] ruthenium (II) (N3) or its bistetrabutylammonium (TBA) salt counterpart (N719), in combination with thick titania films (>12–15 nm) have shown solar-to-electric power conversion efficiencies up to 11% [2, 10]. Several groups have also developed metal-free organic sensitizers, that are less expensive, and obtained efficiencies in the range of 4–8% [11–15]. Interest has been recently devoted to the design of sensitizers that are able to absorb at the near infrared region, by extending the spectral range for the photocurrent generation with respect to Ru-complexes. Porphyrins and phthalocyanines are being currently considered to this specific aim, and meaningful results have been achieved [16–18].

The critical factors that influence sensitization are the excited-state redox potential, which should match the energy of the conduction band edge of the semiconductor substrate, the light-harvesting ability, and the electron transfer process that is influenced by the electronic coupling between the lowest unoccupied molecular orbital (LUMO) of the dye and the TiO₂ conduction band. One of the major factors for low conversion efficiency of many organic dyes in the DSSC is the formation of dye aggregates on the semiconductor surface. Therefore, to obtain optimal performance, aggregation of dyes needs to be avoided by promoting the chemisorption onto the substrate and by increasing the surface area of the semiconductor oxide. High surface area substrates can also promote the adsorption of a larger amount of dye molecules enhancing the light-harvesting efficiency. However, in order to improve the power conversion efficiency of photoanodes for DSSCs, it is necessary to achieve both optimal morphological properties and fast electron transport [19–22].

To gain information about the photoinduced electron transfer process from the sensitizers to the semiconductors and indications about the linkage between dye and substrate, the study of the spectroscopic features of chromophores onto the semiconductor is of crucial importance. Absorption and steady-state emission spectral features can give information on the dye interaction with the substrate, since they are influenced by the chemical environment of the sensitizers and hence, it is expected that the structural and chemical nature of the sensitizers and the structural properties of titania substrates have a key role in determining the final spectral features of the chromophore. Moreover, time-resolved fluorescence decay can provide insights into the electron injection process, since it is competitive with fluorescence relaxation. Electron injection is found to generally occur with a time much shorter than the excited-state lifetime of typical dyes,

therefore time-resolved fluorescence decay studies are very useful to understand these dynamic photoinduced processes.

Herein, for the purpose of comparison, three different dyes were examined: the widely used inorganic ruthenium complex *cis*-di(thiocyanato) *bis*(2,2'-bipyridyl-4,4'-dicarboxylato)ruthenium(II) (N719), the more recently developed organic molecular 3-(5-(4-(diphenylamino) styryl)thiophen-2-yl)-2-cyanoacrylic acid (D5) [15], and the *push-pull* zinc phthalocyanine sensitizer (ZnPc) [23]. The dyes were adsorbed onto three types of thin film titania substrates: mesoporous transparent titania deposited by spin-coating (TiMS), mesoporous titania deposited by doctor-blade (TiMS.DB) and commercial P25 titania deposited by doctor-blade (P25.DB). Titania films were characterized by scanning electron microscopy (SEM) and by Fourier transform infrared (FT-IR) spectroscopy, whereas the dye-sensitized films were studied by UV-Vis and fluorescence spectroscopy.

2. Experimental Section

2.1. Preparation of Titania Thin Films

2.1.1. Transparent and Mesoporous Films. Mesoporous titania films were synthesized using the P123 block copolymer as template in order to obtain an ordered porous structure with a controlled geometry. The titania precursor solutions were prepared according to the procedures described in the literature using pluronic surfactant [24].

In a typical synthesis, 1.4 mL of concentrated HCl were slowly added to 2.1 g of titanium(IV) ethoxide at room temperature. In another flask, 0.65 g of P123 were dissolved in 6 g of 1-butanol and subsequently added to the titanium solution. The system was kept under stirring at room temperature for 3 hours. The as-prepared solution of titania precursor was deposited on FTO conducting glass substrates (Dyesol, 15 Ω sq⁻¹) by spin-coating at 2400 rpm. After aging at 25°C for 2 days, optically uniform and transparent films were obtained. These films were calcined at 350 for 30 minutes using a ramp rate of 1°C/min to remove the template and the residual organic precursors. TiO₂ electrodes were obtained by deposition of three layers with a final calcination at 350°C for 2 hours and were labeled as TiMS (Table 1). The resulting mesoscopic oxide film was around 1 μm thick and transparent.

2.1.2. Semiopaque Films from Mesoporous Titania. Mesoporous titania powder was prepared from the solution of titanium (IV) ethoxide and P123 described above after aging at 25°C for 5 days and subsequent calcination at 350°C for 4 hours using a ramp rate of 1°C/min, according to a recently published procedure [25].

Titania films were prepared from mesoporous titania powder by using the doctor-blade technique, according to a procedure described elsewhere [26]. Dried powder was dispersed in ethanol (EtOH), treated with ultrasonic bath for 30 min, then stirred at 50°C for 1 h. This procedure was repeated three times in order to obtain a homogeneous and

TABLE 1: Details about the preparation of titania films.

| Sample | TiO ₂ source | Deposition technique |
|---------|--|----------------------|
| TiMS | Alcoholic solution of titanium(IV) ethoxide and P123 | Spin-coating |
| TiMS_DB | Mesoporous titania powder prepared from alcoholic solution of titanium(IV) ethoxide and P123 | Doctor-blade |
| P25_DB | Commercial P25 titania powder | Doctor-blade |

opalescent colloidal suspension. The latter was mixed with ethylcellulose (5–15 mPa*s) previously dissolved in ethanol (10% w/w) and stirred again at 50°C overnight. Terpeneol was added, and the resulting mixture was further stirred for 6 h. Finally ethanol was removed by a rotary evaporator to obtain pastes suitable for doctor-blade deposition. The paste had the following weight percentage composition: TiO₂: 4%; ethylcellulose: 2%; terpeneol: 94%. The so-obtained titania paste was deposited on the FTO conducting glass (Dyesol, 15 Ω sq⁻¹). Two edges of the FTO glass plate were covered with a layer of adhesive tape (3M Magic) to control the thickness of the film; successively the titania paste was spread uniformly on the substrate by sliding a glass rod along the tape spacer. After drying the coated plates were sintered in air for 1 h at 450°C and labelled as TiMS_DB (Table 1). The resulting mesoscopic oxide film was around 1 μm thick and semiopaque.

2.1.3. Semiopaque Films from Commercial Titania. Reference titania films were prepared from commercial P25 titania powder by using the doctor-blade technique, according to a procedure described elsewhere [26]. Briefly, acetic acid, water and ethanol were added drop by drop into a mortar containing P25 titanium dioxide nanoparticles (provided by Evonik Degussa). The TiO₂ dispersion was transferred with excess of ethanol into a beaker for stirring a sonication steps; then anhydrous terpeneol and ethyl cellulose (previously dissolved in ethanol) were added. After further stirring and sonication steps the dispersion was concentrated by rotary evaporator. The final colloidal paste was characterized by the following composition (wt/wt): 5% TiO₂, 0.5% acetic acid, 2.5% ethylcellulose, 87% terpeneol, and 5% ethanol. The so-obtained titania paste was deposited on the FTO conducting glass (Dyesol, 15 Ω sq⁻¹). Two edges of the FTO glass plate were covered with a layer of adhesive tape (3M Magic) to control the thickness of the film; successively the titania paste was spread uniformly on the substrate by sliding a glass rod along the tape spacer. After drying, the coated plates were sintered in air for 1 h at 450°C and labelled as P25_DB (Table 1). The resulting mesoscopic oxide film was around 1 μm thick and semiopaque.

2.2. Adsorption of Dyes onto Titania Films. The dye-sensitized films were prepared using a 0.2 mM N719 solution (ditetra-butylammonium cis-bis(isothiocyanato) bis(2,2'-bipyridyl-4,4'-dicarboxylato)ruthenium(II)), which was obtained by

dissolving the dye in a mixture of acetonitrile and *tert*-butyl alcohol (1:1 volume ratio). The titania films were immersed into the N719 solution overnight at room temperature. After that all the dyed films were washed with acetonitrile and stored in the dark.

A similar procedure was used for the adsorption of D5 and ZnPc. The D5 dye was dissolved in acetonitrile to obtain a dye concentration of 0.2 mM, whereas the solution of ZnPc was obtained by dissolution in ethanol (0.89 mg of dye in 10 mL of ethanol).

2.3. Characterization. UV-vis spectra of the films were collected in the wavelength range 300–870 nm using a double beam spectrophotometer V-660 (Jasco) equipped with an integrated sphere. The absorbance of the dye solution was measured using a quartz cell of thickness 1 cm. The absorbance of dye-TiO₂ systems was recorded using 60 mm integrated sphere.

Steady-state fluorescence spectra for dyes solution and dyes-TiO₂ films were recorded in a Jobin Yvon Fluorolog3 spectrofluorometer, using grids of 5 nm for the excitation and 5 nm for emission.

Time-resolved fluorescence measurements were carried out by a time-correlated single-photon-counting (TCSPC) system (Horiba-Jobin Yvon). Time-resolved measurements are carried on exciting the samples using a 405 nm pulsed laser diode and collecting the emission decay at the corresponding maximum emission wavelength for the specific analysed dye. The fluorescence decay profiles were analysed through decay analysis software (DAS6a HORIBA Scientific) to a multiexponential decay equation. The quality of the fits was checked by examining the residual distribution and the χ^2 value.

Both steady-state and time-resolved fluorescence measurements of thin films TiO₂ systems were collected in right-angle (RA) configuration with a tilt angle of 30° to minimize substrate scattering effects.

Fourier transform infrared (FT-IR) spectra were collected using a Jasco 4100 FT/IR spectrophotometer equipped with an attenuated total reflectance (ATR) unit. The samples for the analysis were prepared through preliminary drying at 120°C.

FE-SEM characterizations were carried out with a high-brilliance LEO 1530 field emission scanning electron microscope apparatus equipped with an INCA 450 energy-dispersive X-ray spectrometer (EDS) and a four-sector backscattered electron detector (BSD). Before the analysis, the surfaces were coated with a thin layer of carbon in order to avoid charging effects. The carbon coating was deposited by using an Emitech sputter coater K550 unit, a K 250 carbon-coating attachment, and a carbon cord at a pressure of 1×10^{-2} mbar in order to produce a carbon film with a thickness of a few nanometers.

3. Results and Discussion

The spectral properties of different dyes have been compared in order to investigate the electron transfer process from the

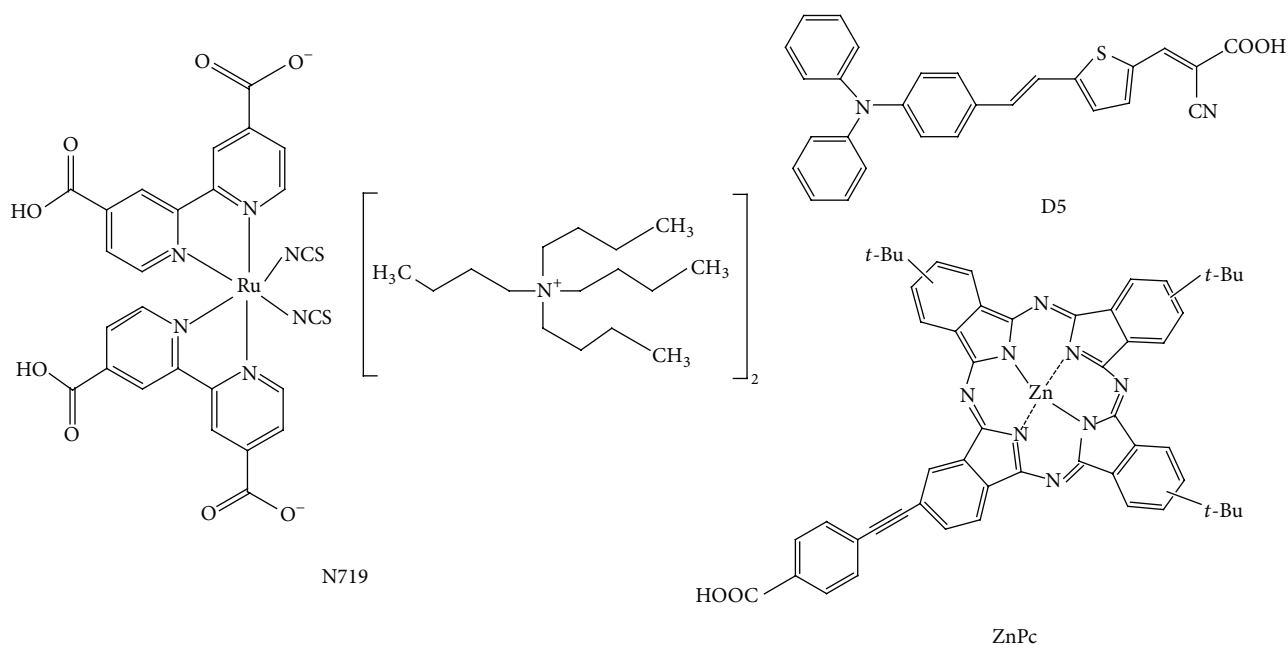


FIGURE 1: Chemical structure of the dyes: N719, D5, and ZnPc.

dye to the conduction band of titania films that is responsible for the production of photocurrent in DSSCs. Metal-organic and metal-free dyes were adsorbed onto transparent and semiopaque mesoporous titania thin films and onto a semiopaque film from commercial P25 titania. In particular, we have investigated the behaviour of a ruthenium complex (N719), an organic dye (D5), and a zinc phthalocyanine system (ZnPc). The chemical structure of these dyes is shown in Figure 1.

All the dyes have been adsorbed onto titania films with different morphology: a mesoporous transparent film deposited by spin-coating (TiMS), a semiopaque film deposited by doctor-blade from mesoporous titania (TiMS_DB), and a semiopaque film deposited by doctor-blade from commercial P25 titania (P25_DB). The preparation of the films was properly tailored in order to get thin substrates with a comparable thickness of about $1\ \mu\text{m}$.

3.1. FTIR Characterization. The surface functional groups of titania substrates play an important role in the chemisorption of the dyes. Indeed, the sensitizers that we are considering in this work are usually bonded to titania through their carboxylic groups, which interact with hydroxyl groups at titania surface.

ATR-FTIR measurements were used to investigate the amount of hydroxyl groups in the different titania films, and the spectra are displayed in Figure 2. Furthermore, by these analyses it is also possible to get more information on the presence of carbon species in the samples.

The ATR-FTIR spectra show similar trends, but with some significant differences. The bending vibration band of the surface hydroxyl groups is observed at about $1630\ \text{cm}^{-1}$,

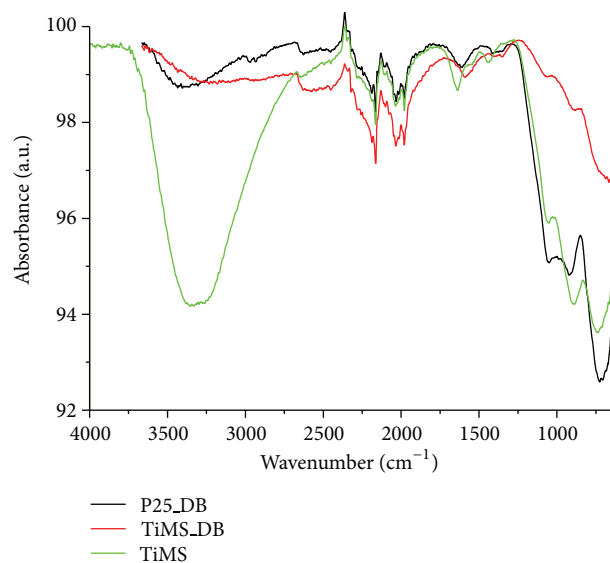


FIGURE 2: ATR-FTIR spectra of titania thin films: (a) P25_DB, (b) TiMS_DB, and (c) TiMS.

and the corresponding stretching vibration peak is located at $3200\text{--}3600\ \text{cm}^{-1}$ [27, 28]. From these spectra, a significantly higher amount of hydroxyl groups was noticed in transparent titania thin films (TiMS). This could be attributed to the lower sinterization temperature (350°C instead of 450°C used for DB films) that allows preserving a high amount of hydroxyl surface groups, and it seems also reasonable to assume that it could be also related to a higher surface area. On the contrary, the film from Degussa P25 has the lowest amount of surface hydroxyl groups.

Analyzing the FTIR spectra, it can also be observed that titania films contain carbon groups. Indeed, the peaks at

TABLE 2: Peak position of UV-Vis absorbance and fluorescence emission.

| Sample | λ_{Abs} (nm) | λ_{Em} (nm) |
|--------------|-----------------------------|----------------------------|
| N719 | 310, 386, 537 | 728 |
| N719@P25_DB | 478 | 726 |
| N719@TiMS_DB | 474 | 719 |
| N719@TiMS | 492 | 720 |
| D5 | 300, 479 | 630 |
| D5@P25_DB | 468 | 605 |
| D5@TiMS_DB | 469 | 623 |
| D5@TiMS | 472 | 618 |
| ZnPc | 352, 613, 687 | 694 |
| ZnPc@P25_DB | 689 | 695 |
| ZnPc@TiMS_DB | 692 | 698 |
| ZnPc@TiMS | 689 | 702 |

about $1000\text{--}1100\text{ cm}^{-1}$ suggest the presence of Ti–O–C bonds [27]. Furthermore, the peak at about 1400 cm^{-1} has been attributed to asymmetric bending vibrations of C–H bonds [27, 28]. The observation from FTIR that the films contain Ti–O–C and C–H bonds indicates the presence of residual organic groups. The intensity of these signals for P25_DB and TiMS is comparable, whereas the residual carbon content is apparently lower for TiMS_DB film (Figure 2).

3.2. Morphological Investigation. Further insights into the structural properties of titania films were obtained through FE-SEM analysis. The micrographs of titania surface films prepared by doctor-blade (Figure 3) reveal that when commercial P25 was used for the formulation of the paste the photoanode surface consists of small nanoparticles with voids into the structure. By using mesoporous titania, the photoanode surface is composed of small nanoparticles and a porous structure can be observed. It is worth to notice that in TiMS_DB the surface morphology is more uniform with the presence of small pores that could increase the interface between dye and titania, whereas larger voids are not detected.

In TiMS prepared by spin-coating, the surface morphology is completely different. The films are furthermore compact, and can be observed the presence of domains with an ordered structure. The latter are mesoporous channels, which are responsible for a nanoporous structure and high surface area.

3.3. UV-Vis and Fluorescence Measurements. In order to gain information on the anchorage of the chromophore onto the semiconductor and on the electron transfer process from the dyes to titania, the spectroscopic features of the dye solutions and of the dye-sensitized titania films have been investigated.

The absorption and the steady-state fluorescence spectra of the free dye solutions and the corresponding dye-sensitized TiO₂ films were recorded, and the data are summarized in Table 2.

The absorption spectra of N719 sensitized TiO₂ films along with the reference spectrum of the free dye in an

acetonitrile and *tert*-butyl alcohol solution (1:1 volume ratio) are shown in Figure 4. In particular, the UV-vis absorption spectrum of N719 solution is dominated by two broad bands at around 386 and 537 nm, generally assigned to a Metal-to-Ligand Charge-Transfer (MLCT) transition in which an electron is transferred from Ru to one of the bipyridine ligands, and an intense UV absorption at around 310 nm attributed to an electronic transition between the $\pi\text{-}\pi^*$ orbitals of the dcbpyH ligands [29–31]. When the N719 molecules are adsorbed onto the surface of mesoporous TiO₂ films, the MLCT band at 537 nm becomes predominant and shifts at lower wavelengths depending on the considered TiO₂ system. The measured blue shifts for all the dye-sensitized TiO₂ systems are reported in Table 2; as it can be seen it is higher for the N719 adsorbed onto TiO₂ films obtained by doctor-blade (P25 and TiMS_DB), whereas it is lower for the N719 adsorbed onto transparent TiO₂ obtained by spin-coating technique (TiMS). The observed shifts in the absorption spectra are probably due to chemical interactions between the dye and the semiconductor TiO₂ surface, which modify HOMO and LUMO levels of the adsorbed complexes with respect to those of the free dye. At the same time, we would like to underline the higher absorption intensity shown by the transparent N719@TiMS systems with respect to the other TiO₂ systems, which may indicate that this transparent layer can adsorb more N719 molecules compared with the other TiO₂ layers having the same thickness. This is also confirmed by the intense red coloration of the TiMS sample after the dye adsorption. These findings are in agreement with ATR-FTIR results previously discussed, since the most intense peaks in UV-vis spectra of dye-sensitized TiMS films is promoted by the presence of a high number of surface hydroxyl groups.

A similar trend has been also found in the case of the metal-free organic dye D5 adsorbed on TiO₂ mesoporous systems (Table 2). Two absorption bands at 479 nm and 300 nm are visible in the UV-Vis spectrum of dye solution; the band in the UV region corresponds to a $\pi\text{-}\pi^*$ transition of the conjugated molecules, whereas the band in the Vis can be assigned to an intramolecular charge-transfer state between the diphenylaniline electron donating moiety and the cyanoacetic acceptor [15]. When the dye is attached to TiO₂ surface, a blue shift of the absorption maximum at 479 nm is found (Table 2). Also in the case of D5, the transparent TiMS thin films have the highest intense absorption band and the lowest blue shift with respect to those observed for D5@TiMS_DB and D5@P25_DB, thus indicating a higher dye uptake.

The fluorescence measurements of N719 and D5 sensitized mesoporous TiO₂ systems, reported in Figures 5 and 6, show the characteristic fluorescence emission of the free dyes but shifted to lower wavelengths. In the case of N719 (Figure 5), for example, upon excitation at $\lambda_{\text{ex}} = 510\text{ nm}$, the solution has an emission maximum at 728 nm, which shifts at 725, 719, and 720 nm for N719@P25_DB, N719@TiMS_DB, and N719@TiMS, respectively. In analogy, the D5 sensitized TiO₂ systems have a blue shift in the emission spectra (Figure 6) that depend on the TiO₂ system. More interesting, if we consider the intensity of the emission band for both of the two sets of sample we observe that they decrease following

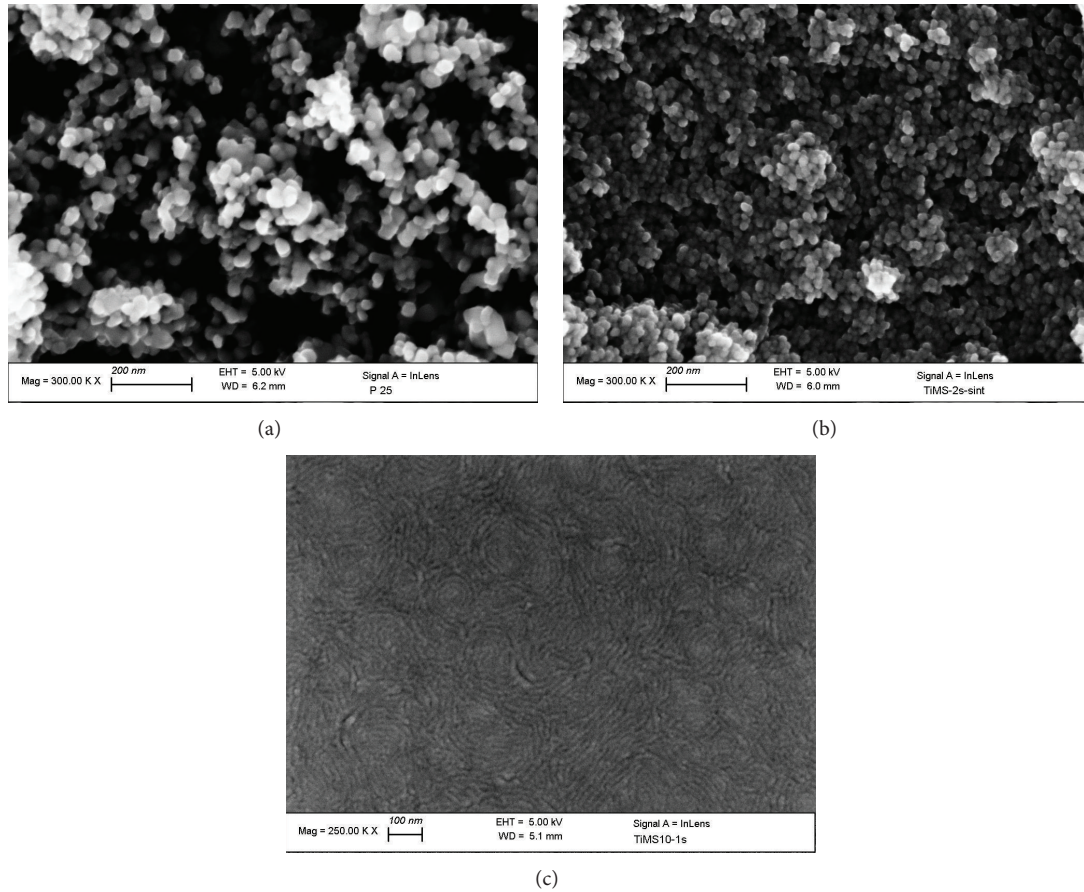


FIGURE 3: FE-SEM images of surface titania films: (a) P25_DB, (b) TiMS_DB, and (c) TiMS.

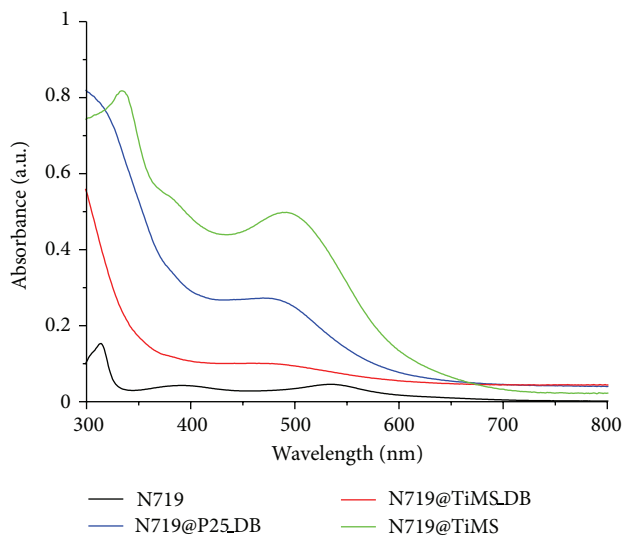


FIGURE 4: UV-Vis absorbance for N719 solution and N719 sensitised TiO_2 systems.

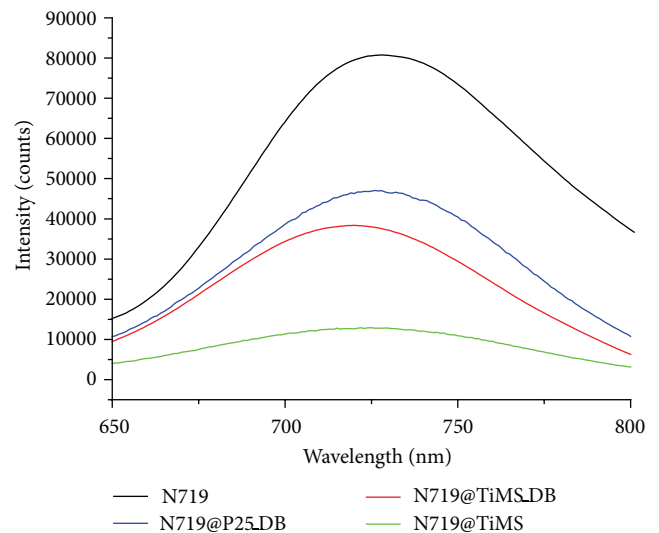


FIGURE 5: Steady-state fluorescence emission for N719 solution and N719 sensitised TiO_2 systems.

the order $\text{P25_DB} > \text{TiMS_DB} > \text{TiMS}$. The reduction in the emission intensity is thus more evident in the case of transparent mesoporous TiO_2 layer, and we hypothesized that it can be associated in first approximation to a better and more

efficient electron injection process from the excited state of the dye to the conduction band of the semiconductor.

The UV-Vis absorption spectra of the compound ZnPc in EtOH and on mesoporous TiO_2 films are displayed in

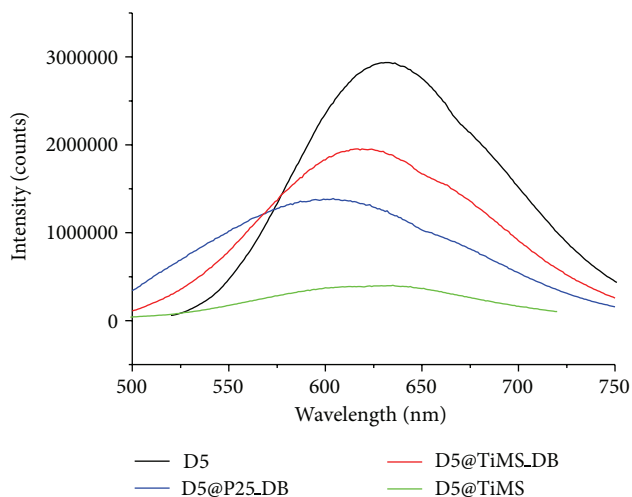


FIGURE 6: Steady-state fluorescence emission for D5 solution and D5 sensitised TiO_2 systems. The emission intensity values for D5 sensitised TiO_2 systems are multiplied by a factor 5.

Figure 7. The UV-Vis absorption spectrum of ZnPc exhibits an intense Soret band (300–400 nm) due to the π - π^* transition with charge-transfer character and a strong Q band centered at 687 nm [32]. In addition, compared with the solution, the zinc phthalocyanine derivative on mesoporous TiO_2 films show broader absorption spectra extended to 800 nm, suggesting the formation of aggregate on the surface of the semiconductor [33]. The absorption spectra of the phthalocyanine adsorbed onto TiO_2 systems exhibit a small red shift (Table 2) that may be due to the presence of carboxylic protons of phthalocyanine, which, upon adsorption on TiO_2 , release the proton and bind to Ti^{4+} centres. The Ti^{4+} sites act as electron withdrawing and produce the observed red shift in the absorption bands [34].

Figure 8 shows the steady-state fluorescence emission spectra ($\lambda_{\text{ex}} = 400 \text{ nm}$) of ZnPc solution: the typical phthalocyanine emission band centred around 700 nm is easily visible [35]. The ZnPc@P25_DB, ZnPc@TiMS_DB, and ZnPc@TiMS exhibit a strong Q band emission peak at 695 nm, 698 nm, and 702 nm, respectively. In analogy to the other two dyes, when ZnPc is adsorbed onto the TiO_2 layers, a net decrease in the emission intensity can be observed, thus suggesting the possibility of an electron injection process.

Time-correlated single-photon counting (TCSPC) measurements are performed to obtain information about the decay times of the relaxed excited state at S_1 of the dye interacting with the semiconductor materials. As reported by several studies [18, 23, 36, 37], TCSPC measurements can be useful to evaluate the photoelectron injection dynamics in dye-sensitized semiconductor films. In Figure 9 the time-resolved emission kinetics for the three dyes in solution and the correspondent dye sensitised TiO_2 systems are shown. In particular, the emission decay measurements are collected at $\lambda_{\text{em}} = 730 \text{ nm}$ (Figure 9(a)) for N719, at $\lambda_{\text{em}} = 640 \text{ nm}$ (Figure 9(b)) for D5, and at $\lambda_{\text{ex}} = 700 \text{ nm}$ for ZnPc (Figure 9(c)).

Fluorescence emission decay curves of the N719 solution have been deconvoluted by a biexponential function, while

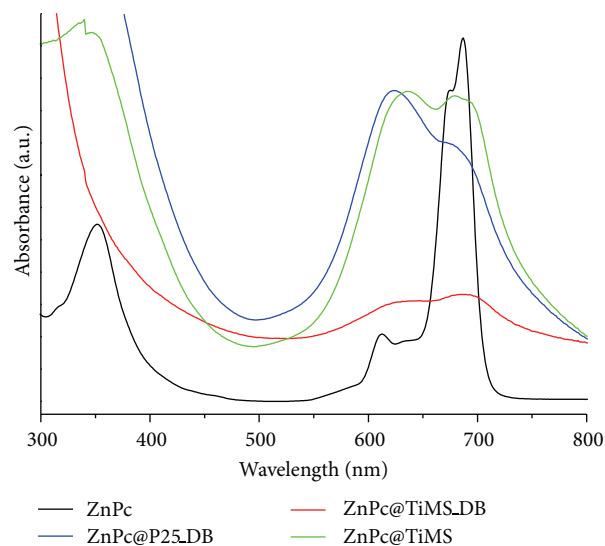


FIGURE 7: UV-Vis absorbance for ZnPc solution and ZnPc sensitised TiO_2 systems.

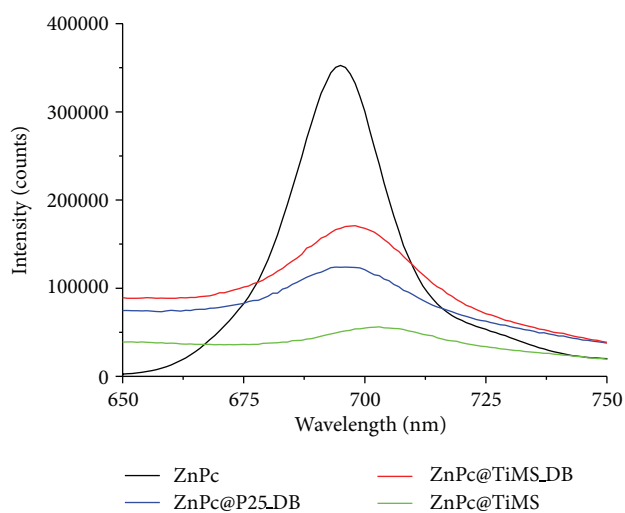


FIGURE 8: Steady-state fluorescence emission for ZnPc solution and ZnPc sensitised TiO_2 systems. The emission intensity values for ZnPc5 sensitised TiO_2 systems are multiplied by a factor 5.

for N719 interacting with different TiO_2 based films, the decays have a more complex behaviour and need a three component exponential function. The results shown in Table 3 reveal that for dye solution the most significant time value (τ_1) is about 3 ns ($A_1 = 93\%$) and a little percent of molecules decay with a time of $\tau_2 = 27.7 \text{ ns}$ ($A_2 = 7\%$). The longer decay is comparable with time decay reported in the literature for N719 systems [38], while the shorter excited-state lifetime indicates an enhancing of the nonradiative deactivation channels, probably due to the presence of protons on carboxyl groups [39]. The $\tau_1 = 3 \text{ ns}$ value appears to be retained in N719- TiO_2 systems, but the corresponding amplitude (A_1) decreases from 93% in solution to 30% in solid state. Also the longest time decay in solution ($\tau_2 = 27.7 \text{ ns}$) is preserved when the dye is adsorbed on TiO_2 surface, but this value is lower

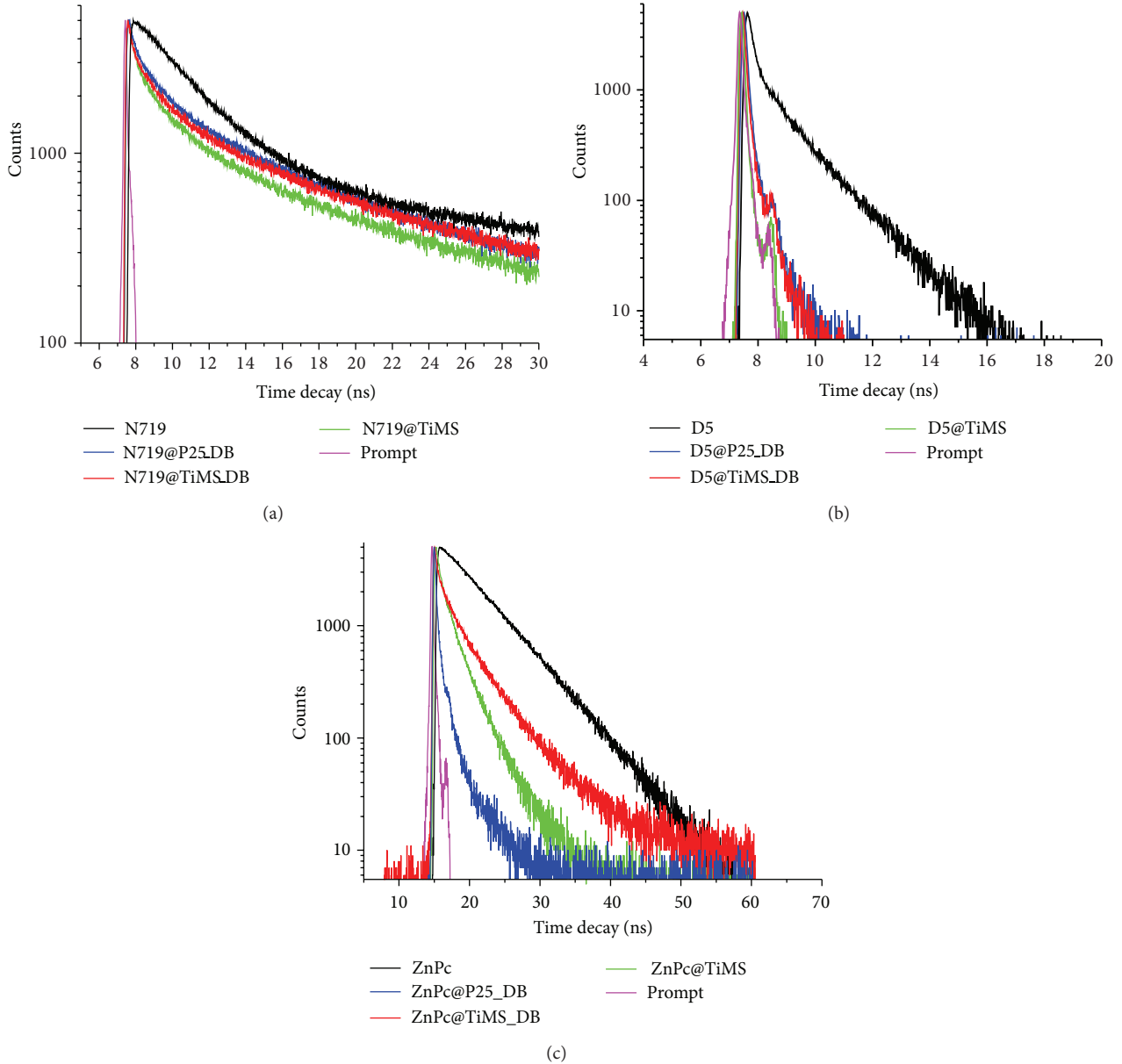


FIGURE 9: Fluorescence kinetics of (a) N719 solution and N719 sensitised TiO_2 systems, (b) D5 solution and D5 sensitised TiO_2 systems, and (c) ZnPc solution and ZnPc sensitised TiO_2 systems.

($\tau_2 = 15$ ns in solid state) because dye molecules are now closer to each other than in solution, and this results in the quenching phenomena. In addition, a third shorter time appears (0.56 ns for N719@P25.DB, 0.41 ns for N719@TiMS.DB and 0.36 ns for N719@TiMS) that can be related to the electron transfer process from the excited state of the dye to the conduction band of the semiconductor.

Lifetime of D5 dye in solution is analysed by a three exponential component function, and the result of 0.14 ns, associated with the most significant amplitude ($A_1 = 80\%$), presents a good agreement with analogous systems [40]. However, for D5 sensitised TiO_2 systems the resolution of the TCSPC setup does not allow for resolving numerically the changes in lifetime. They are all sub 0.01 ns, a time

close to the time response of the detector. Nevertheless, just from a qualitatively point of view, it is interesting to observe that D5@TiMS system seems to have the sharpest decay profile with respect to D5@TiMS.DB and D5@P25.DB. The better quenching effect could be related to a different dye- TiO_2 interaction that could promote electron injection in semiconductor bands.

In the case of ZnPc solution, the fluorescence emission decay exhibits a monoexponential behaviour with a lifetime of 3 ns, comparable for values reported in the literature for unsubstituted phthalocyanine systems [18, 41].

ZnPc sensitised TiO_2 systems fluorescence emission decays, instead, are analysed using a three component exponential function and the results are summarized in Table 3.

TABLE 3: Lifetime decay of dye-TiO₂ systems.

| Sample | τ_1 (ns) | τ_2 (ns) | τ_3 (ns) | A_1 (%) | A_2 (%) | A_3 (%) | χ^2 |
|--------------|---------------|---------------|---------------|-----------|-----------|-----------|----------|
| N719 | 2.89 | 27.7 | — | 93 | 7 | — | 1.2 |
| N719@P25_DB | 3.44 | 15.8 | 0.56 | 32 | 20 | 48 | 1.2 |
| N719@TiMS_DB | 2.74 | 14.5 | 0.41 | 33 | 20 | 47 | 1.2 |
| N719@TiMS | 2.60 | 15.6 | 0.36 | 32 | 15 | 53 | 1.2 |
| D5 | 0.14 | 0.63 | 1.61 | 80 | 9 | 11 | 1.0 |
| D5@P25_DB | <0.01 | — | — | — | — | — | — |
| D5@TiMS_DB | <0.01 | — | — | — | — | — | — |
| D5@TiMS | <0.01 | — | — | — | — | — | — |
| ZnPc | 3 | — | — | — | — | — | 1.2 |
| ZnPc@P25_DB | 2.05 | 0.48 | 0.05 | 24 | 29 | 47 | 1.3 |
| ZnPc@TiMS_DB | 2.46 | 0.87 | 0.13 | 21 | 23 | 56 | 1.1 |
| ZnPc@TiMS | 1.87 | 0.78 | 0.11 | 10 | 33 | 57 | 1.2 |

From the fitting results, the τ_1 component is preserved in solid state systems, even if the molecule population associated to this decay mechanism decreases to 10–20%. The component τ_2 , observable only in solid state systems, can be associated to a quenching effect with a mechanism similar to the behavior of J aggregates in solution [42]. The faster time decay component in dye-TiO₂ system (τ_3) could be, in principle, indicative of an efficient injection occurring at the interface between dye molecules and semiconductor surface. Mesoporous TiO₂ systems present τ_3 decay very similar in value (0.13 ns for ZnPc@TiMS_DB and 0.11 ns for ZnPc@TiMS), while ZnPc@P25_DB shows a quite lower τ_3 component, about 0.05 ns.

The two observed fast time decays τ_2 and τ_3 in dye-TiO₂ systems could be also attributable to a contemporary presence of different injection processes; due to different possible configurations of ZnPc molecules when they are interacting with TiO₂ surface, one is more favourable than the other.

4. Conclusions

The steady-state measurements and fluorescence emission decay of the dye-sensitized titania films suggest that the transparent mesoporous titania film (TiMS) could be responsible for a more efficient electronic injection when N719 and D5 are used as sensitizers. Indeed, the emission peak of these dyes has a lower intensity onto TiMS, and a faster time decay was observed. In the case of ZnPc, the fluorescence emission decay is faster if the dye is adsorbed onto P25_DB. Probably the formation of dye aggregates hinders the diffusion into the mesoporous structure, and only the external surface area can interact with the sensitizer. The mesoporous structure of TiMS could not be accessible to ZnPc aggregates with a consequent lower performance.

These findings suggest that mesoporous titania films could be considered the most efficient substrates for the adsorption of N719 and D5 to realize a photoanode with high efficient electronic injection.

In fact, as spectroscopic measurements showed, the N719@TiMS presents the highest UV-vis absorbance value,

compared to the other TiO₂ substrates, but the highest decrease in fluorescence emission intensity. These results suggest a strong interaction between the dye and the TiO₂ substrate, and this condition is particularly favourable to enhance the electron injection.

Acknowledgment

This work has been supported by the Italian project EFOR—Energia da Fonti Rinnovabili (Iniziativa CNR per il Mezzogiorno L. 191/2009 art. 2 comma 44).

References

- [1] B. O'Regan and M. Grätzel, "A low-cost, high-efficiency solar cell based on dye-sensitized colloidal TiO₂ films," *Nature*, vol. 353, no. 6346, pp. 737–740, 1991.
- [2] M. Grätzel, "Solar energy conversion by dye-sensitized photo-voltaic cells," *Inorganic Chemistry*, vol. 44, no. 20, pp. 6841–6851, 2005.
- [3] L. M. Goncalves, V. De Zea Bermudez, H. A. Ribeiro, and A. M. Mendes, "Dye-sensitized solar cells: a safe bet for the future," *Energy and Environmental Science*, vol. 1, no. 6, pp. 655–667, 2008.
- [4] M. K. Nazeeruddin, A. Kay, I. Rodicio et al., "Conversion of light to electricity by cis-X2bis(2,2'-bipyridyl-4,4'-dicarboxylate)ruthenium(II) charge-transfer sensitizers (X = Cl⁻, Br⁻, I⁻, CN⁻, and SCN⁻) on nanocrystalline TiO₂ electrodes," *Journal of the American Chemical Society*, vol. 115, no. 14, pp. 6382–6390, 1993.
- [5] L. Giribabu, K. Sudhakar, and V. Velkannan, "Phthalocyanines: potential alternative sensitizers to Ru(II) polypyridyl complexes for dye-sensitized solar cells," *Current Science*, vol. 102, no. 7, pp. 991–1000, 2012.
- [6] A. Mishra, M. K. R. Fischer, and P. Büuerle, "Metal-free organic dyes for dye-sensitized solar cells: from structure: property relationships to design rules," *Angewandte Chemie*, vol. 48, no. 14, pp. 2474–2499, 2009.
- [7] G. Calogero and G. D. Marco, "Red Sicilian orange and purple eggplant fruits as natural sensitizers for dye-sensitized solar cells," *Solar Energy Materials and Solar Cells*, vol. 92, no. 11, pp. 1341–1346, 2008.
- [8] G. Calogero, J.-H. Yum, A. Sinopoli, G. Di Marco, M. Grätzel, and M. K. Nazeeruddin, "Anthocyanins and betalains as light-harvesting pigments for dye-sensitized solar cells," *Solar Energy*, vol. 86, no. 5, pp. 1563–1575, 2012.
- [9] E. Ronca, M. Pastore, L. Belpassi, F. Tarantelli, and F. De Angelis, "Influence of the dye molecular structure on the TiO₂ conduction band in dye-sensitized solar cells: disentangling charge transfer and electrostatic effects," *Energy & Environmental Science*, vol. 6, no. 1, pp. 183–193, 2013.
- [10] M. K. Nazeeruddin, F. De Angelis, S. Fantacci et al., "Combined experimental and DFT-TDDFT computational study of photo-electrochemical cell ruthenium sensitizers," *Journal of the American Chemical Society*, vol. 127, no. 48, pp. 16835–16847, 2005.
- [11] D. P. Hagberg, J.-H. Yum, H. Lee et al., "Molecular engineering of organic sensitizers for dye-sensitized solar cell applications," *Journal of the American Chemical Society*, vol. 130, no. 19, pp. 6259–6266, 2008.

- [12] K. Hara, T. Sato, R. Katoh et al., "Molecular design of coumarin dyes for efficient dye-sensitized solar cells," *Journal of Physical Chemistry B*, vol. 107, no. 2, pp. 597–606, 2003.
- [13] T. Horiuchi, H. Miura, K. Sumioka, and S. Uchida, "High efficiency of dye-sensitized solar cells based on metal-free indoline dyes," *Journal of the American Chemical Society*, vol. 126, no. 39, pp. 12218–12219, 2004.
- [14] S. Kim, J. K. Lee, S. O. Kang et al., "Molecular engineering of organic sensitizers for solar cell applications," *Journal of the American Chemical Society*, vol. 128, no. 51, pp. 16701–16707, 2006.
- [15] D. P. Hagberg, T. Edvinsson, T. Marinado, G. Boschloo, A. Hagfeldt, and L. Sun, "A novel organic chromophore for dye-sensitized nanostructured solar cells," *Chemical Communications*, no. 21, pp. 2245–2247, 2006.
- [16] X.-F. Wang and H. Tamiaki, "Cyclic tetrapyrrole based molecules for dye-sensitized solar cells," *Energy and Environmental Science*, vol. 3, no. 1, pp. 94–106, 2010.
- [17] F. Silvestri, M. García-Iglesias, J.-H. Yum et al., "Carboxy-1,4-phenylenevinylene- and carboxy-2,6-naphthylene-vinylene unsymmetrical substituted zinc phthalocyanines for dye-sensitized solar cells," *Journal of Porphyrins and Phthalocyanines*, vol. 13, no. 3, pp. 369–375, 2009.
- [18] G. Rossi, G. Zanotti, N. Angelini et al., "Bridged phthalocyanine systems for sensitization of nanocrystalline TiO₂ films," *International Journal of Photoenergy*, vol. 2010, Article ID 136807, 11 pages, 2010.
- [19] P. Wen, Y. Han, and W. Zhao, "Influence of TiO₂ nanocrystals fabricating dye-sensitized solar cell on the absorption spectra of N719 sensitizer," *International Journal of Photoenergy*, vol. 2012, Article ID 906198, 7 pages, 2012.
- [20] S. K. Deb, "Dye-sensitized TiO₂ thin-film solar cell research at the national renewable energy laboratory (NREL)," *Solar Energy Materials and Solar Cells*, vol. 88, no. 1, pp. 1–10, 2005.
- [21] L. De Marco, M. Manca, R. Giannuzzi, M. R. Belviso, P. D. Cozzoli, and G. Gigli, "Shape-tailored TiO₂ nanocrystals with synergic peculiarities as building blocks for highly efficient multi-stack dye solar cells," *Energy & Environmental Science*, no. 6, pp. 1791–1795, 2013.
- [22] L. De Marco, M. Manca, R. Giannuzzi et al., "Novel preparation method of TiO₂-nanorod-based photoelectrodes for dye-sensitized solar cells with improved light-harvesting efficiency," *Journal of Physical Chemistry C*, vol. 114, no. 9, pp. 4228–4236, 2010.
- [23] G. Zanotti, N. Angelini, A. M. Paoletti et al., "Synthesis of a novel unsymmetrical Zn(ii) phthalocyanine bearing a phenyl ethynyl moiety as sensitizer for dye-sensitized solar cells," *Dalton Transactions*, vol. 40, no. 1, pp. 38–40, 2011.
- [24] S. Y. Choi, M. Mamak, N. Coombs, N. Chopra, and G. A. Ozin, "Thermally stable two-dimensional hexagonal mesoporous nanocrystalline anatase, meso-nc-TiO₂: bulk and crack-free thin film morphologies," *Advanced Functional Materials*, vol. 14, no. 4, pp. 335–344, 2004.
- [25] L. De Marco, G. Di Carlo, R. Giannuzzi et al., "Highly efficient photoanodes for dye solar cells with a hierarchical meso-ordered structure," *Physical Chemistry Chemical Physics*, vol. 15, pp. 16949–16955, 2013.
- [26] S. Ito, P. Chen, P. Comte et al., "Fabrication of screen-printing pastes from TiO₂ powders for dye-sensitized solar cells," *Progress in Photovoltaics*, vol. 15, no. 7, pp. 603–612, 2007.
- [27] H. Jensen, A. Soloviev, Z. Li, and E. G. Søgaard, "XPS and FTIR investigation of the surface properties of different prepared titania nano-powders," *Applied Surface Science*, vol. 246, no. 1–3, pp. 239–249, 2005.
- [28] T. López, J. A. Moreno, R. Gómez et al., "Characterization of iron-doped titania sol-gel materials," *Journal of Materials Chemistry*, vol. 12, no. 3, pp. 714–718, 2002.
- [29] M. K. Nazeeruddin, R. Humphry-Baker, P. Liska, and M. Grätzel, "Investigation of sensitizer adsorption and the influence of protons on current and voltage of a dye-sensitized nanocrystalline TiO₂ solar cell," *Journal of Physical Chemistry B*, vol. 107, no. 34, pp. 8981–8987, 2003.
- [30] C. Pérez León, L. Kador, B. Peng, and M. Thelakkat, "Influence of the solvent on the surface-enhanced Raman spectra of Ruthenium(II) Bipyridyl complexes," *Journal of Physical Chemistry B*, vol. 109, no. 12, pp. 5783–5789, 2005.
- [31] M. J. Root, B. P. Sullivan, T. J. Meyer, and E. Deutsch, "Thioether, thiolato, and 1,1-dithioato complexes of bis(2,2'-bipyridine)ruthenium(II) and bis(2,2'-bipyridine)osmium(II)," *Inorganic Chemistry*, vol. 24, no. 18, pp. 2731–2739, 1985.
- [32] C. C. Leznoff and A. B. P. Lever, Eds., *Phthalocyanines: Properties and Applications*, vol. 1, VCH Publishers, New York, NY, USA, 1990.
- [33] S. Mori, M. Nagata, Y. Nakahata et al., "Enhancement of incident photon-to-current conversion efficiency for phthalocyanine-sensitized solar cells by 3D molecular structuralization," *Journal of the American Chemical Society*, vol. 132, no. 12, pp. 4054–4055, 2010.
- [34] L. Giribabu, C. Vijay Kumar, V. Gopal Reddy et al., "Unsymmetrical alkoxy zinc phthalocyanine for sensitization of nanocrystalline TiO₂ films," *Solar Energy Materials and Solar Cells*, vol. 91, no. 17, pp. 1611–1617, 2007.
- [35] L. Giribabu, C. V. Kumar, P. Y. Reddy, J.-H. Yum, M. Grätzel, and M. K. Nazeeruddin, "Unsymmetrical extended π -conjugated zinc phthalocyanine for sensitization of nanocrystalline TiO₂ films," *Journal of Chemical Sciences*, vol. 121, no. 1, pp. 75–82, 2009.
- [36] S. E. Koops and J. R. Durrant, "Transient emission studies of electron injection in dye sensitised solar cells," *Inorganica Chimica Acta*, vol. 361, no. 3, pp. 663–670, 2008.
- [37] V. Biju, M. Micic, D. Hu, and H. P. Lu, "Intermittent single-molecule interfacial electron transfer dynamics," *Journal of the American Chemical Society*, vol. 126, no. 30, pp. 9374–9381, 2004.
- [38] M. K. Nazeeruddin, S. M. Zakeeruddin, R. Humphry-Baker et al., "Acid-base equilibria of (2,2'-bipyridyl-4,4'-dicarboxylic acid)ruthenium(II) complexes and the effect of protonation on charge-transfer sensitization of nanocrystalline titania," *Inorganic Chemistry*, vol. 38, no. 26, pp. 6298–6305, 1999.
- [39] M. K. Nazeeruddin and K. Kalyanasundaram, "Acid-base behavior in the ground and excited states of ruthenium (II) complexes containing tetraamines or dicarboxybipyridines as protonatable ligands," *Inorganic Chemistry*, vol. 28, no. 23, pp. 4251–4259, 1989.
- [40] M. Ziółek, X. Yang, L. Sun, and A. Douhal, "Interrogating the ultrafast dynamics of an efficient dye for sunlight conversion," *Physical Chemistry Chemical Physics*, vol. 12, no. 28, pp. 8098–8107, 2010.
- [41] G. Gümrükçü, G. K. Karaoglan, A. Erdogmus, A. Gül, and U. Avcıata, "A novel phthalocyanine conjugated with four salicylideneimino complexes: photophysics and fluorescence

quenching studies," *Dyes and Pigments*, vol. 95, no. 2, pp. 280–289, 2012.

- [42] X.-F. Zhang, Q. Xi, and J. Zhao, "Fluorescent and triplet state photoactive J-type phthalocyanine nano assemblies: controlled formation and photosensitizing properties," *Journal of Materials Chemistry*, vol. 20, no. 32, pp. 6726–6733, 2010.

Research Article

Thin Film CIGS Solar Cells, Photovoltaic Modules, and the Problems of Modeling

Antonino Parisi, Luciano Curcio, Vincenzo Rocca, Salvatore Stivala, Alfonso C. Cino, Alessandro C. Busacca, Giovanni Cipriani, Diego La Cascia, Vincenzo Di Dio, Rosario Miceli, and Giuseppe Ricco Galluzzo

DEIM, University of Palermo, Viale delle Scienze, Building 9, 90128 Palermo, Italy

Correspondence should be addressed to Rosario Miceli; rosario.miceli@unipa.it

Received 13 July 2013; Accepted 13 August 2013

Academic Editor: Leonardo Palmisano

Copyright © 2013 Antonino Parisi et al. This is an open access article distributed under the Creative Commons Attribution License, which permits unrestricted use, distribution, and reproduction in any medium, provided the original work is properly cited.

Starting from the results regarding a nonvacuum technique to fabricate CIGS thin films for solar cells by means of single-step electrodeposition, we focus on the methodological problems of modeling at cell structure and photovoltaic module levels. As a matter of fact, electrodeposition is known as a practical alternative to costly vacuum-based technologies for semiconductor processing in the photovoltaic device sector, but it can lead to quite different structural and electrical properties. For this reason, a greater effort is required to ensure that the perspectives of the electrical engineer and the material scientist are given an opportunity for a closer comparison and a common language. Derived parameters from ongoing experiments have been used for simulation with the different approaches, in order to develop a set of tools which can be used to put together modeling both at single cell structure and complete module levels.

1. Introduction

Thin film solar cells based on a compound of the elements Copper, Indium, Gallium, and Selenium, that is, CIGS semiconductors, are considered as highly promising light-to-electricity converters thanks to their direct bandgaps which can be efficiently matched to the solar spectrum [1]. Among different fabrication methods suitable for the absorber layer, electrodeposition represents an important alternative to the expensive vacuum-based technologies. Using a single-step electrodeposition, several groups have fabricated CIGS films [2], and in some case an efficiency exceeding 15% has been reported [3], not too far from top performances made possible by the most studied vacuum-based three-stage process [1].

One of the most important requirements for successful application of the one-step electrodeposition here considered, for CIGS film production, is to control composition of deposited films in a reliable and reproducible way (it is noteworthy that we found several technological requirements in common with optical applications we had previously

developed in different research contexts, to which we address the reader [4–19]).

Furthermore, film formation must be manufacturing friendly, possibly eliminating the selenization step, which is environmentally undesired due to the toxicity of Se.

In some recent works [20, 21], we described our first results on the option to fabricate CIGS-based solar cells directly using electrodeposited films by adjusting the concentration of the solution and eliminating the unwanted selenization step. Within the limits of the present discussion, it will be enough to mention that (1) electrodeposition of CIGS, with a controlled and reproducible Cu/(In+Ga) and Ga/(In+Ga) molar ratios, has been presented and (2) Cu-In-Se-Ga content and formation of secondary phases before and after the annealing process have been investigated [4, 6].

Also, in the context of our research project, it is required to derive parameters from ongoing experiments on the layered junction structures and use them for simulation with different approaches, in order to develop a set of tools which can be used to put together modeling both at single cell and module levels, what we will describe here. To complete the

overall picture of the ongoing activity, we will mention that we are adapting a previous sensor measurement setup to map solar cell performance with a light-beam-induced current (LBIC) configuration [22–24].

In particular, from real data, we have derived the five-parameter model and the complete characteristic of a CIGS module. Afterwards, from a structural model, setting real CIGS cells parameters, we have derived the cell characteristic. A circuitual model—able to describe the cells interconnections and packaging—took into account the simulated cells data, has been finally compared with the previously mentioned module simulation. This comparison could be very useful to determine the internal parameters that extend the structural cells model to the module characteristics, so that the different perspectives of the electrical engineer and the material scientist are given an opportunity for a closer collaboration and a common language we are actively looking for [25].

Hence, this paper is organized as follows. In Section 2 we describe a general introduction to model simulation methods and the five-parameter analysis of a real CIGS module. Then, structural cell simulation is described in Section 3 together with a parasitic network resistance modeling and a comparison with the module data. Finally, conclusions are drawn in Section 4.

2. Five Lumped Parameters Simulation

A photovoltaic (PV) module mathematical model is a very useful tool to evaluate electrical energy production during the operative working of PV plants [26]. Moreover, such models are important to perform economic evaluations and compare different PV plants implementations [27–30].

In the literature, seldom parametric mathematical models have been proposed to simulate the solar cell functioning on the basis of distributed parameters equivalent circuits, while lumped parameters equivalent circuits are largely more common [31–35]. Among the lumped parameters models, there are different implementations that consider four, five, or six parameters with various threshold accuracies. Model parameters can be evaluated on the basis of the numerical data from the manufacturers [31–34, 36, 37]. Finally, fitting methods are used to match I - V characteristic curves with different temperature and irradiance values.

Among lumped parameters equivalent circuit models, the five-parameter one has been here taken into account. The lumped parameters single diode model (Figure 1), thanks to the shunt resistor (R_{sh}), is able to simulate, with good accuracy, the solar cell working condition. It is also able to work correctly even at low irradiance conditions and it shows a lower computational burden in comparison, for example, to the double diode model.

The five lumped cell parameters are described herein:

- (i) the photoelectric current that depends on temperature, radiation, and structural characteristics (I_L);
- (ii) the diode saturation current that depends on temperature and structural characteristics (I_0);
- (iii) the diode quality factor that depends on the cell junction characteristics (γ);

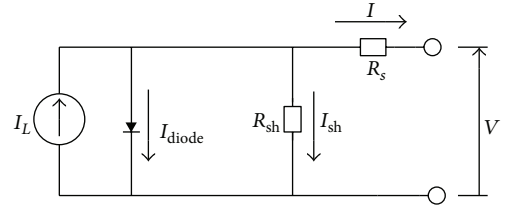


FIGURE 1: Five lumped parameters cell model.

- (iv) the series resistance that depends on the structural characteristics of the cell (R_s);
- (v) the shunt resistance that depends on the structural characteristics of the cell (R_{sh}).

The photocurrent depends on cell irradiance, temperature, and structural characteristics. Moreover, it is directly proportional to the irradiance. The diode, in the equivalent circuit, represents the recombination current in the quasi-neutral region of the p-n junction [32, 38]. The standard Shockley equation for the circuit in Figure 1 is as follows:

$$I_{\text{diode}} = I_0 \left[e^{q((V+IR_s)/(k\gamma T_c))} - 1 \right], \quad (1)$$

where

- (i) q is the electron charge [C],
- (ii) T_c is the cell temperature [K],
- (iii) k is the Boltzmann constant [J/K],
- (iv) V is the cell output voltage [V],
- (v) I is the cell output current [A].

The diode thermal voltage $\gamma(kT_c/q)$ is also indicated with V_t .

The series resistance R_s represent internal losses of different kind; more relevant are [39, 40]

- (i) front and back electrode resistances;
- (ii) lead resistance;
- (iii) metal semiconductor ohmic contact.

The shunt resistance takes into account the overall photovoltaic cell dispersion currents.

Eventually, the analytic relation of the cell characteristic is

$$I = I_L - I_0 \left[e^{q((V+IR_s)/(k\gamma T_c))} - 1 \right] - \frac{V + IR_s}{R_{sh}}. \quad (2)$$

It is fortunate that the same model can be extended to represent even the photovoltaic module when identical cells—also at the same temperature and irradiation—are connected either in series or in parallel.

For example, for the series of two cells, using the five-parameter model, the equivalent circuit is that depicted in Figure 2 [41, 42].

Having the two cells identical, at the same temperature and irradiated at the same intensity, we obtain

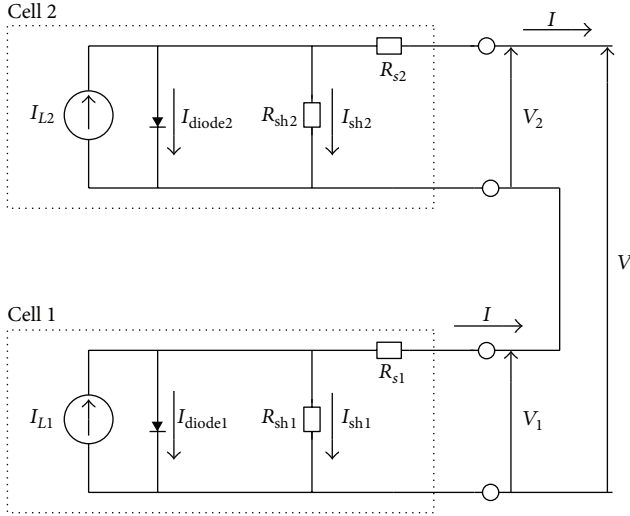


FIGURE 2: Equivalent circuit of the two cell series.

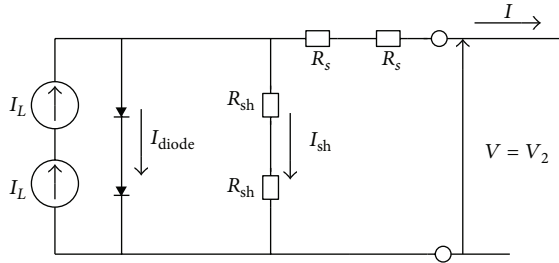


FIGURE 3: Equivalent circuit of a two identical cell series.

- (i) $I_{L1} = I_{L2}$;
- (ii) $V_1 = V_2$;
- (iii) $I_{diode1} = I_{diode2}$ having the two identical diodes the same working conditions;
- (iv) $R_{s1} = R_{s2}$;
- (v) $R_{sh1} = R_{sh2}$;
- (vi) $I_{sh1} = I_{sh2}$.

The aforementioned two cells scheme, in the previous hypothesis, is equivalent in the final analysis to the following simpler circuit of Figure 3 [41, 43, 44].

The extension to N_{CS} cells, connected in series, is obvious and the analytic relation for the module is then

$$I = I_L - I_0 \left[e^{q((V+IR_s)/k\gamma N_{CS} T_c)} - 1 \right] - \frac{V + IR_s}{R_{sh}}. \quad (3)$$

In order to evaluate the five-parameter values, the method hereafter reported has been adopted [33, 45, 46]. Equation (3) is written by the three characteristic points: maximum power, short-circuit, and open-circuit points, obtaining (4), (5), and (6), respectively. Moreover, the $dP/dV = 0$ condition by the maximum power point is derived, giving (7). Finally, the fifth equation is obtained by calculating the dI/dV value calculated in the short-circuit point, which results in (8).

Equations (4) and (6) allow to evaluate I_0^{ref} (9). Equations (9) and (5) are developed to build (10), where the three unknowns R_s , R_{sh} , and V_t have to be evaluated. Equation (10) together with (7) and (8) allow to get (12) and (13). R_s , R_{sh} and V_t values are determined from (10), (12), and (13) through the iterative method hereafter reported:

$$I_{SC}^{\text{ref}} = I_L^{\text{ref}} - I_0^{\text{ref}} \cdot e^{(I_{SC}^{\text{ref}} R_s)/(N_{CS} V_t)} - \frac{I_{SC}^{\text{ref}} R_s}{R_{sh}}, \quad (4)$$

$$I_{MP}^{\text{ref}} = I_L^{\text{ref}} - I_0^{\text{ref}} \cdot e^{(V_{MP}^{\text{ref}} + I_{MP}^{\text{ref}} R_s)/(N_{CS} V_t)} - \frac{V_{MP}^{\text{ref}} + I_{MP}^{\text{ref}} R_s}{R_{sh}}, \quad (5)$$

$$I_L^{\text{ref}} - I_0^{\text{ref}} \cdot e^{(V_{OC}^{\text{ref}})/(N_{CS} V_t)} - \frac{V_{OC}^{\text{ref}}}{R_{sh}} = 0, \quad (6)$$

$$\frac{dP}{dV} \Big|_{V=V_{MP}^{\text{ref}}, I=I_{MP}^{\text{ref}}} = I_{MP}^{\text{ref}} + \frac{dI}{dV} \Big|_{V=V_{MP}^{\text{ref}}, I=I_{MP}^{\text{ref}}} V_{MP}^{\text{ref}} = 0, \quad (7)$$

$$\frac{dI}{dV} \Big|_{I=I_{SC}^{\text{ref}}} = -\frac{1}{R_{sh}}, \quad (8)$$

$$I_0^{\text{ref}} = \left(I_{SC}^{\text{ref}} - \frac{V_{OC}^{\text{ref}} - I_{SC}^{\text{ref}} R_s}{R_{sh}} \right) \cdot e^{-(V_{OC}^{\text{ref}})/(N_{CS} V_t)}, \quad (9)$$

$$I_{MP}^{\text{ref}} = I_{SC}^{\text{ref}} - \frac{V_{MP}^{\text{ref}} + I_{MP}^{\text{ref}} R_s - I_{SC}^{\text{ref}} R_s}{R_{sh}} - \left(I_{SC}^{\text{ref}} - \frac{V_{OC}^{\text{ref}} - I_{SC}^{\text{ref}} R_s}{R_{sh}} \right) K_T, \quad (10)$$

where

$$K_T = e^{(V_{MP}^{\text{ref}} + I_{MP}^{\text{ref}} R_s - V_{OC}^{\text{ref}})/(N_{CS} V_t)} \quad (11)$$

$$\begin{aligned} \frac{dP}{dV} \Big|_{V=V_{MP}^{\text{ref}}, I=I_{MP}^{\text{ref}}} &= I_{MP}^{\text{ref}} \\ &+ V_{MP}^{\text{ref}} \\ &\cdot \frac{\left(I_{SC}^{\text{ref}} R_{sh} - V_{OC}^{\text{ref}} + I_{SC}^{\text{ref}} R_s \right) \cdot e^{(V_{MP}^{\text{ref}} + I_{MP}^{\text{ref}} R_s - V_{OC}^{\text{ref}})/(N_{CS} V_t)} - \frac{1}{R_{sh}}}{N_{CS} V_t R_{sh}} \\ &+ \frac{\left(I_{SC}^{\text{ref}} R_{sh} - V_{OC}^{\text{ref}} + I_{SC}^{\text{ref}} R_s \right) \cdot e^{(V_{MP}^{\text{ref}} + I_{MP}^{\text{ref}} R_s - V_{OC}^{\text{ref}})/(N_{CS} V_t)} - \frac{R_s}{R_{sh}}}{1 + \frac{R_s}{R_{sh}}} \end{aligned} \quad (12)$$

$$\begin{aligned}
& -\frac{1}{R_{sh}} \Big|_{I=I_{SC}^{ref}} \\
& - \frac{\left(I_{SC}^{ref} R_{sh} - V_{OC}^{ref} + I_{SC}^{ref} R_s \right) \cdot e^{(I_{SC}^{ref} R_s - V_{OC}^{ref}) / (N_{CS} V_t)}}{N_{CS} V_t R_{sh}} - \frac{1}{R_{sh}} \\
& = \frac{\left(I_{SC}^{ref} R_{sh} - V_{OC}^{ref} + I_{SC}^{ref} R_s \right) \cdot e^{(I_{SC}^{ref} R_s - V_{OC}^{ref}) / (N_{CS} V_t)}}{N_{CS} V_t R_{sh}} + \frac{R_s}{R_{sh}}. \quad (13)
\end{aligned}$$

In the equations detailed previously, standard test conditions, that is, STC, are indicated with “ref” as apex. To summarize the adopted iterative method, a block diagram is traced in Figure 4 [46].

At the first stage, the R_s and R_{sh} starting values are arbitrarily chosen and put into (10), in order to evaluate V_t . Subsequently, (13) is used to evaluate R_{sh} . The new R_{sh} value is put into (12) in order to check the $dP/dV = 0$ condition. If $dP/dV = 0$, the latter R_{sh} value is the right one and (2) can be used to evaluate the γ form factor; otherwise, the R_{sh} initial value has to be changed and the iteration goes on. The previously mentioned equations can be adopted in that form only under standard conditions. For this reason, it is necessary to take into account the changes of the I_0 , I_L , I_{SC} , and V_{OC} parameters with respect to temperature and irradiation. According to [46, 47],

- (i) I_0 does not depend on irradiation but only on temperature;
- (ii) I_L depends only on temperature;
- (iii) I_{SC} depends both on temperature and irradiation;
- (iv) V_{OC} depends only on irradiation.

The following equations describe what was stated previously:

$$I_0(T) = \left(I_{SC}(T) - \frac{V_{OC}(T) - I_{SC}(T) R_s}{R_{sh}} \right) \cdot e^{-V_{OC}(T)/(N_{CS} V_t)}, \quad (14)$$

$$V_{OC}(T) = V_{OC}^{ref} + \mu_{V_{OC}} (T_C - T_C^{ref}), \quad (15)$$

$$I_{SC}(T) = I_{SC}^{ref} \left[1 + \frac{\mu_{I_{SC}}}{100} (T_C - T_C^{ref}) \right], \quad (16)$$

$$I_{SC}(G) = I_{SC}^{ref} \cdot \frac{G}{G^{ref}}, \quad (17)$$

$$I_L(G) = I_L^{ref} \cdot \frac{G}{G^{ref}}, \quad (18)$$

$$I_L(G, T) = \frac{G}{G^{ref}} \cdot \left[I_0(T) \cdot e^{V_{OC}(T)/(N_{CS} V_t)} + \frac{V_{OC}(T)}{R_{sh}} \right], \quad (19)$$

$$\begin{aligned}
I_{SC}(G, T) &= \frac{G}{G^{ref}} \cdot I_{SC}(T) \\
&= \frac{G}{G^{ref}} \cdot I_{SC}^{ref} \left[1 + \frac{\mu_{I_{SC}}}{100} (T_C - T_C^{ref}) \right], \quad (20)
\end{aligned}$$

where

- (i) $\mu_{I_{SC}}$ is the short-circuit current temperature coefficient;
- (ii) $\mu_{V_{OC}}$ is the open-circuit voltage temperature coefficient.

Therefore, (14), (15), (19), and (20) represent the five-parameter mathematical model under changing temperature and radiation conditions. Finally, the PV module output voltage can be expressed to good purpose by (21), derived from (1):

$$V = \left[\ln \left(\frac{I_L - I}{I_0} + 1 - \frac{V + I R_s}{I_0 R_{sh}} \right) \right] N_{CS} V_t - I R_s. \quad (21)$$

For example, considering a commercial module with the following nominal data:

- (i) $I_{SC} = 6.50$ A,
- (ii) $V_{OC} = 46.8$ V,
- (iii) $I_{MP} = 5.70$ A,
- (iv) $V_{MP} = 34.4$ V,
- (v) $\mu_{I_{SC}} = -0.03\%/K$,
- (vi) $\mu_{V_{OC}} = -0.33\%/K$,

the resulting five lumped parameter values are:

- (i) $\gamma = 1.5$,
- (ii) $R_s = 0.94 \Omega$,
- (iii) $R_{sh} = 120 \Omega$,
- (iv) $I_L = 6.6$ A,
- (v) $I_0 = 3.7 \cdot 10^{-7}$ A.

In the following picture (Figure 5), the behavior of the commercial module characteristic obtained from the five-parameter model is depicted, which will be used later on for a paired comparison.

3. The Structural Model from the Cell to the Module

In parallel to the previously described approach, usually the first choice for the electrical engineer, it is worthwhile to follow as well the microscopic point of view, more familiar to the material scientist. In order to generate a current, energy derived from the sun must impact on a photovoltaic device having a preexisting electrical field such that free electrons can succeed in separating from holes. Nowadays, numerical simulation offers advantages to the design, performance prediction, and comprehension of the fundamental phenomena ruling the operation of complex devices, such as solar cells, also allowing to investigate the physics of their inner processes.

Our tool of choice was wxAMPS, a software capable of representing the electrical transport phenomena and the optical response of a wide variety of layered structures like

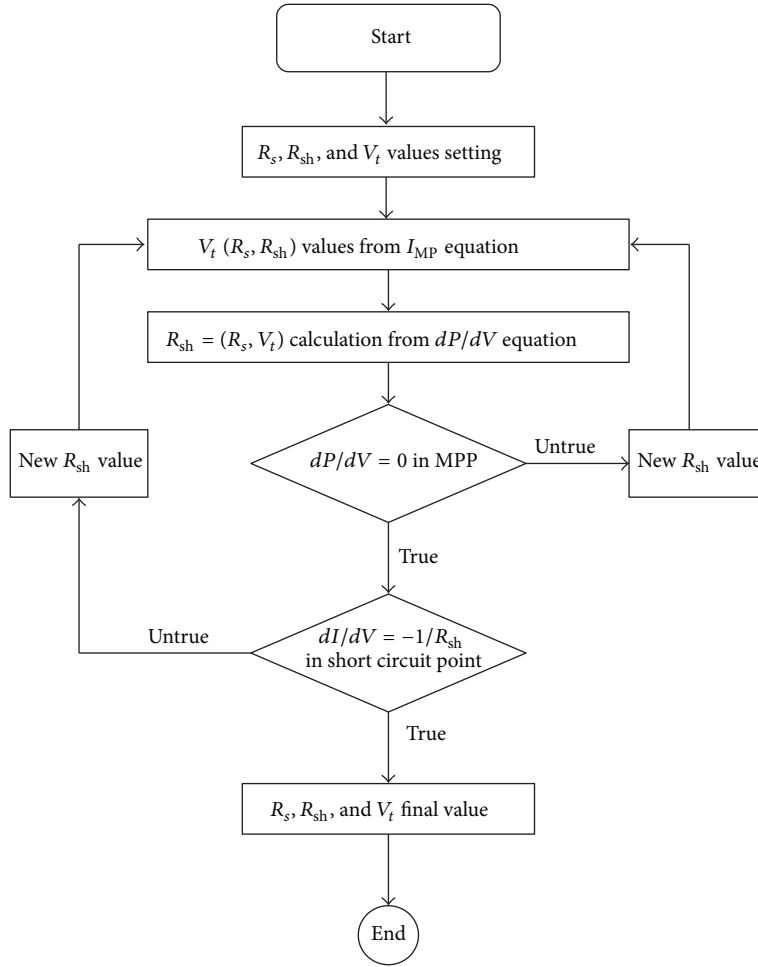


FIGURE 4: Determination of R_s , R_{sh} , and V_f : block diagram.

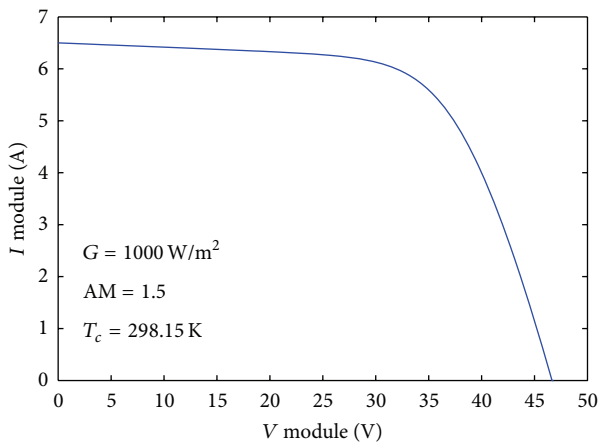


FIGURE 5: I - V curve from the five-parameter model of a commercial PV module.

those typical of solar cells. For this reason, it was also applied to simulate the behavior of the solar cell discussed

in this work. This software is an updated version, rewritten in C++, of the one-dimensional simulation program Analysis of Microelectronic and Photonic Structures (AMPS-1D) that was initially developed by Fonash et al. at Pennsylvania State University [48, 49]. Various layers of stacked materials, producing homojunctions, heterojunctions, and multijunctions, can be studied by appropriately selecting characteristic parameters.

Thus, wxAMPS is a modern, often updated, solar cell simulator for modeling one-dimensional devices composed of several materials. It accepts the same input parameters as AMPS and is based on similar physical principles and numerical descriptions of defects and recombinations [49], while adding tunnelling effects based on trap-assisted and intraband tunnelling models [50, 51]. This program incorporates a new algorithm combining the Gummel and Newton methods. In fact, Gummel's method alone is of limited usefulness when simulating devices with very high defect densities, while Newton's method alone works poorly when determining intraband tunnelling current. The advantages of the combination are in terms of better stability and more consistent convergence in problems in which intraband

tunnelling is critical in the determination of precise solutions [52].

With wxAMPS, a hypothetically unlimited number of layers can be modeled; this added flexibility is suited to tailoring designs of devices with parameters, at any given depth profile, so as to establish optimal degrees of efficiency conversions for solar cells. The program allows data input through three main windows that represent the ambient conditions, the properties of different materials for the individual layers, and the resolving model (trap-assisted tunnelling or intraband). You can use the simulation parameters provided by the University of Illinois, Engineering Wiki [53], or you can set custom data as needed. Operating temperature, solar spectrum, quantum efficiency, front and back contact data, surface recombination velocity, and bias voltages are the environmental parameters which set device working conditions. Once stored, ambient conditions are defined for environment simulation, but new settings can be edited by users loading a properly tailored file. In detail, it is possible to take into account the values of Φ_B (the barrier height defined as $E_c - E_f$) for the front and back contacts and reflection coefficients [54].

The material properties of each layer are divided into four groups accessed by separate tabs: electrical, defect, optical, and advanced. A grid allows users to control and edit the overall structure of the device. Tables organize material properties and these are provided by a Wiki [53] website or are editable using common worksheets. Likewise, absorption coefficients can be edited directly by users or be loaded from external data files.

Once all required input is entered, it is possible to start data analysis. The results are displayed by an efficient graphical layout that presents them. Output data can be provided in two main forms: directly through the graphical user interface or indirectly through files readable by common spreadsheet programs.

A CIGS thin film solar cell structure, with parameters derived from our experiments, was simulated after specifying, as the input data, the material parameters for each individual layer of the stacked device structures. Specifically, several layers including the top contact, bottom contact, intrinsic ZnO layer, CdS buffer layer, high-recombination interface, surface defect layer on top of the CIGS film, and CIGS absorber defined the CIGS solar-cell structure. The employed thicknesses of structural layers and the material parameters, which by the way fall into the acceptable ranges reported in the literature [55], are shown in Table 1.

As usual, room temperature and standard sunlight (AM 1.5 G) were the assumed working conditions. Furthermore, the material parameters used in the simulations were kept unchanged. Tables 2 and 3 summarize material Gaussian defect states and contact parameters, respectively; Table 4 provides an explanation of the symbols used in the previous tables. The front and back contacts are solely defined by their work functions Φ_B .

Considering that an accurate optical assessment of a photovoltaic cell is hardly trivial, in order to facilitate the discussion and describe the considered simplifications, we will try to follow and illustrate reflections and absorptions to

TABLE 1: Simulation material parameters of the CIGS thin-film solar cell.

| Parameter | ZnO:Al | ZnO | CdS | CIGS |
|---|---------------------|---------------------|---------------------|---------------------|
| d (μm) | 0.5 | 0.2 | 0.05 | 3 |
| ϵ_R | 9 | 9 | 10 | 13.6 |
| E_g (eV) | 3.3 | 3.3 | 2.4 | 1.18 |
| χ (eV) | 4.4 | 4.4 | 4.2 | 4.5 |
| N_C [cm^{-3}] | $2.2 \cdot 10^{18}$ | $2.2 \cdot 10^{18}$ | $2.2 \cdot 10^{18}$ | $2.2 \cdot 10^{18}$ |
| N_V [cm^{-3}] | $1.8 \cdot 10^{19}$ | $1.8 \cdot 10^{19}$ | $1.8 \cdot 10^{19}$ | $1.8 \cdot 10^{19}$ |
| μ_n [$\text{cm}^2/(\text{V}\cdot\text{s})$] | 100 | 100 | 100 | 100 |
| μ_p [$\text{cm}^2/(\text{V}\cdot\text{s})$] | 25 | 25 | 25 | 25 |
| N_D [cm^{-3}] | $1 \cdot 10^{18}$ | $1 \cdot 10^7$ | $1.1 \cdot 10^{18}$ | 0 |
| N_A [cm^{-3}] | 0 | 0 | 0 | $2 \cdot 10^{16}$ |

TABLE 2: Simulation material Gaussian defect for the CIGS solar layers.

| Parameter | ZnO:Al | ZnO | CdS | CIGS |
|------------------------------|---------------------|---------------------|---------------------|---------------------|
| Defect type | Donor | Donor | Acceptor | Donor |
| Energy level [eV] | 1.65 | 1.65 | 1.2 | 0.6 |
| Deviation [eV] | 0.1 | 0.1 | 0.1 | 0.1 |
| σ_n [cm^2] | 1×10^{-12} | 1×10^{-12} | 1×10^{-17} | 5×10^{-13} |
| σ_p [cm^2] | 1×10^{-15} | 1×10^{-15} | 1×10^{-12} | 1×10^{-15} |
| N_t [cm^{-3}] | 1×10^{17} | 1×10^{17} | 1×10^{18} | 1×10^{14} |

TABLE 3: Contact parameters applied to the simulations.

| Parameter | Back contact | Front contact |
|---------------|-----------------|-----------------|
| ϕ_B [eV] | 0.66 | 0 |
| S_n [cm/s] | 2×10^7 | 1×10^7 |
| S_p [cm/s] | 2×10^7 | 1×10^7 |

TABLE 4: Explanation of the symbols used to describe the simulation parameters.

| Parameter | Explanation |
|---------------------|---|
| D | Layer thickness |
| ϵ_R | Permittivity constant |
| χ | Electron affinity |
| N_C/N_V | Effective density of states in the conduction /valence band |
| μ_n/μ_p | Mobility of electrons/holes |
| σ_n/σ_p | Capture cross-section of electrons/holes |
| N_D/N_A | Doping concentration |
| N_t | Defect concentration |
| ϕ_B | Potential barrier height |
| S_n/S_p | Surface recombination velocity of electrons/holes |

which photons from incident sunlight impacting on cells are exposed in their path.

As illustrated in Figure 6, incident rays reflect at the air-glass (1), glass-encapsulant (3), and encapsulant-cell (5) interfaces. In the latter case, reflection is often diffuse, leading

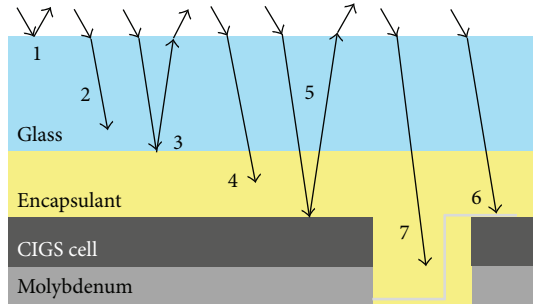


FIGURE 6: Cross-sectional diagram of a conventional photovoltaic module (not in scale), and the optical loss as described in the text.

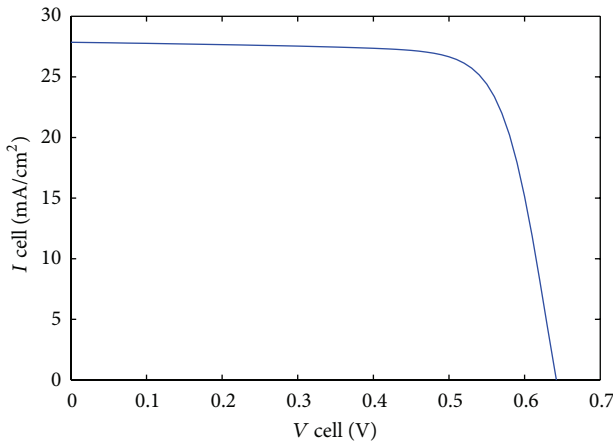


FIGURE 7: I - V curve (per cm^2) a simulated CIGS solar cell.

to some of the reflected light being totally internally reflected at the glass-air interface, remaining within the cell.

Furthermore, incident rays are absorbed by the glass (2), the encapsulant (4), and the cell’s antireflection coating or metal fingers (6). In addition, further losses arise from incident rays within interspace between adjacent cells (7).

These seven interactions depend on the light’s incident wavelength and angle [56].

In order to take into account overall losses due to reflection and absorption, we have set to 0.2 the reflection coefficient for light impinging on the uppermost surface. Instead, for the back surface, the reflection coefficient was set to 0.9.

As well known, a CIGS solar cell presents a composite structure and the study is difficult due to this stratified window, consisting of a thin Al doped ZnO layer, an un-doped ZnO, a CdS buffer layer (or using Cd-free buffer layers). In order to predict the behavior of solar cells with a complex structure, as in the case in analysis, it is important to use specific and detailed physical models which are implemented to the computer, so that the effect of considered input material parameters can be defined and assessed quantitatively.

Figure 7 shows the I - V characteristic (per cm^2), calculated using wxAMPS again, of the CIGS solar cell structure having material parameters listed in Tables 1–4, at room temperature and standard sunlight (AM 1.5 G).

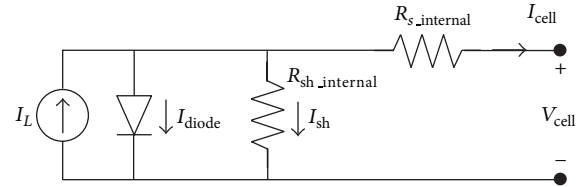


FIGURE 8: The one diode model for a p-n-junction solar cell.

Now, we will recall a brief qualitative description of the I - V characteristic curve of a common solar cell. In fact, a normal I - V curve presents a smooth shape in which it is possible to distinguish three distinct voltage regions: first, above 0 V, a slightly sloped region; second, below V_{OC} , a steeply sloped and, in the region of the maximum power point, a “knee.” As shown in Figure 7, normally the three regions are smooth and continuous, but the position of the knee depends on cell technology and manufacturer. In detail, crystalline silicon cells show sharper knees whereas thin film solar cells have gradual knees. The slopes of the curve in the first two regions are caused by parasitic effects.

Truth be told, several causes lead to the power dissipation in solar cells, but among these the most important is power dissipation due to parasitic resistances. Figure 8 represents the one diode equivalent circuit for a p-n-junction solar cell and, in this model, solar cells are described as a current generator in parallel with a diode and a shunt resistance, internal R_{sh} of cell which all are connected in series with another resistance, internal R_s of cell. I_L is the photo-generated current and I_{diode} is the current within a p-n-junction solar cell diode whereas I_{sh} and I_{cell} are the currents into parasitic resistances (i.e., internal R_{sh} and R_s). In order to design a performing solar cell, internal R_s should be as low as possible and R_{sh} as high as possible.

For a typical CIGS cell, formation of internal series resistance (R_s) of the cell, is mainly due to a ZnO:Al layer film resistance (typically $15 \Omega/\square$), resistances of various cell layers, and resistance of top and back contacts. In particular, the contact resistance between CIGS absorber layer and Molybdenum (back contact) can be ohmic or junction-like depending on type and CIGS doping level.

It is assumable that in a common solar cell, R_{sh} arises from current leaking within the cell in high-conducting paths cross the p-n-junction or around the edges. Shunt paths, that is, high-conducting paths, within the material can be a result of presence of the impurities or crystal damage during the production phases [57].

The simulation program wxAmps takes into account overall volume resistances and the two resistances of back and top contact that arise in different device layers. In particular, Figure 7 shows I - V curve obtained from simulations with wxAmps. This curve shows that the simulated cell has an internal series resistance equal to $1.8 [\Omega \times \text{cm}^2]$ and an internal shunt resistance equal to $890 [\Omega \times \text{cm}^2]$, respectively.

In order to determine the electrical behaviour of the module, starting from individual cells, other resistive contributions to those simply derivable from I - V characteristic of

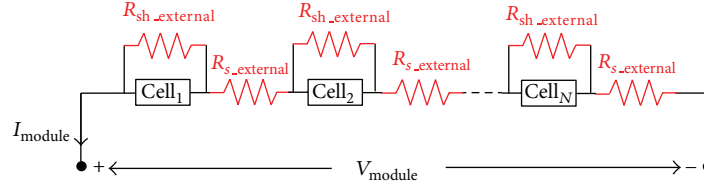
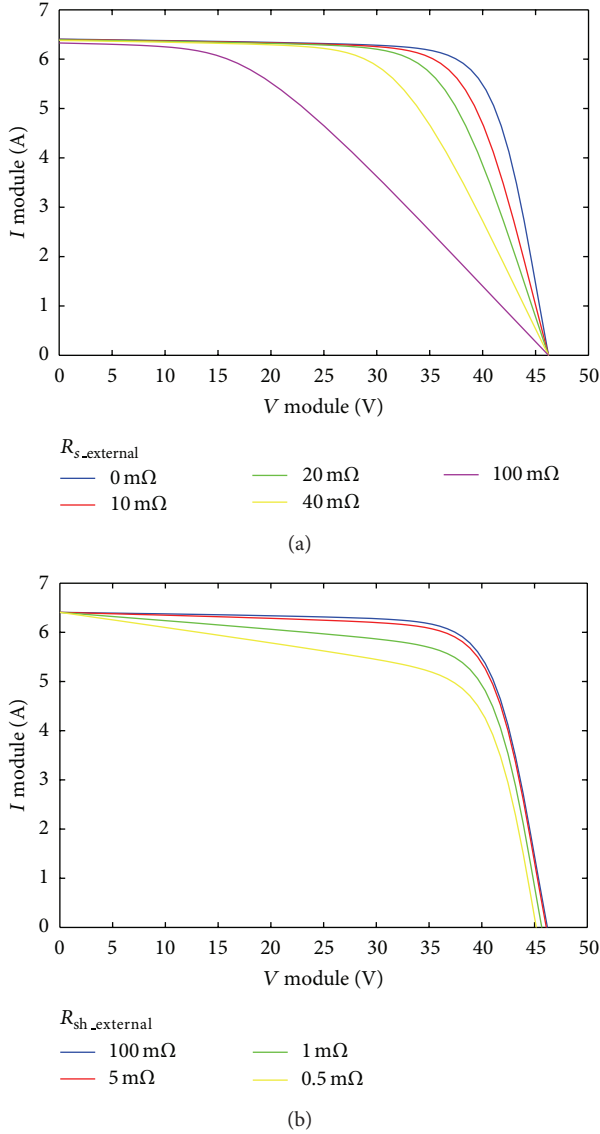


FIGURE 9: Equivalent electrical scheme of module.

FIGURE 10: Effects of parasitic resistance on the simulated I - V characteristics of 230 cm^2 CIGS solar cell. (a) Increasing external series resistance. (b) Increasing external shunt resistance.

elementary cell must be added: sheet resistance of ZnO:Al, grid contributions, and interconnection resistance between module cells (i.e., metallic interconnections and contacts) [58].

Such contributions shall be considered separately because wxAmps is a one-dimensional simulator and device's cross-sectional dimensions and interconnections between cells are neglected. Similarly, we must also consider additional shunt resistance of overall module mainly due to the fact that shunt paths exist in photovoltaic solar cell interconnects and module I_{sc} mismatch.

In detail, this additional shunt resistance is due to defects in materials or degradation of interconnections between cells monolithically integrated in a module. Dielectric material inhomogeneities and defects in thin-film solar cells or crystal damage that can produce a variation of the shunt resistance, extending to cells (shunt currents through the p-n junction), have been observed experimentally [59]. Unintentional partial shorting of cell near edges can cause a highly ohmic shunt path, for example, connection between front-front and the back-back contacts of all cells. Shunt currents between the front and back contacts of cells are other possible causes.

The set of all these additional resistances are simplified considering electrical model of Figure 9 obtained adding the resistors $R_{sh,external}$ and $R_{s,external}$. The electric model was properly evaluated to switch from single cell to complete module. The module considered in our study consists of 72 cells in series and each having an area of around 230 cm^2 .

This step complicates the discussion by introducing (as we have seen) a network of parasitic resistances.

If $R_{sh,external}$ and $R_{s,external}$ are taken into account, according to scheme in Figure 9, I - V , equation of module can be written as a function of single cell:

$$I_{mod} = \frac{R_{sh,external} * I_{cell}}{R_{sh,external} + (R_{sh,external}/2)} - \frac{V_{mod}/N}{R_{sh,external} + (R_{sh,external}/2)}. \quad (22)$$

$R_{s,external}$ and $R_{sh,external}$ are detrimental to solar cell and module performance, in fact, both reduce fill factor as is illustrated in Figures 10(a) and 10(b).

The current I_{sh} leaking through the R_{sh} of module decreases current output, I_{module} , to intended load. The smaller R_{sh} , the greater I_{sh} , and lower I_{module} for a given voltage, V . A very low R_{sh} reduces V_{OC} but does not affect I_{sh} . R_s gives rise to a potential drop, which reduces the voltage output, V , but leaves V_{OC} unaffected, whereas a very high R_s reduces I_{SC} .

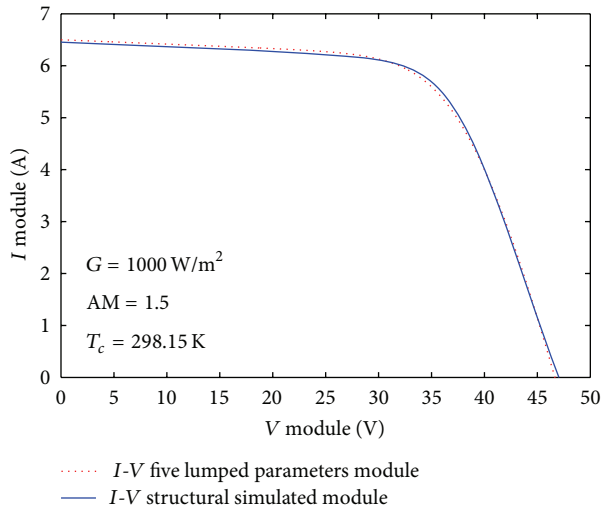


FIGURE 11: I - V curve from the five parameter model and structural model with parasitic resistances.

4. Comparison of Models and Conclusions

From the comparison of the five lumped parameters and the structural model of a PV commercial module, we have extracted the values of the local parasitic network resistances to be associated with the structural simulation. Figure 11 shows the good agreement which can be obtained between the two models.

Further refinements are required, but we think that the approach and methods here described can lead to the development of an important tool to evaluate intermediate results during CIGS cell technology development and assessment of its impact on global electrical module performance.

This is particularly useful in the course of a research activity which encompasses a variety of contributions from technical subjects such as electrochemistry, semiconductor science, electrical and electronic engineering, and optical measurements. We are trying to keep as linked as possible, during the task of modeling, both the level of single cell structure and that of the complete photovoltaic module. In other words, it is our way to look actively for a common language, so that the different perspectives of the electrical engineer and the material scientist are given an opportunity for a closer collaboration.

We are currently applying this approach to the fabrication of thin film CIGS solar cells by means of single-step electrodeposition, a technique which appears fairly easy and low cost but, at the same time, can lead to quite different structural and electrical properties, so that a reasonable estimation of its impact on module characteristics is required in all the intermediate steps of our project.

Conflict of Interests

Professor Rosario Miceli, declares the following: “MATLAB” and “SIMULINK” are registered trademarks of The MathWorks, Inc. “wxAMPS” is a freeware software made available

by the University of Illinois at Urbana-Champaign (UIUC), in collaboration with Nankai University of China. In both cases all the authors do not have any conflict of interests with the content of the paper.

Acknowledgments

The activity described previously has been supported by the PON 01_1725 “Nuove tecnologie fotovoltaiche per sistemi intelligenti integrati in Edifici” and the PON 02_00355 “Tecnologie per l’ENERGIA e l’Efficienza energetica—ENERGETIC” Research Programs. Contributions came also from SDESLab University of Palermo. Finally, the authors express their gratitude to Professor Rockett, Yiming Liu, and Professor Fonash for making freely available their simulation software wxAMPS.

References

- [1] T. Unold and C. A. Kaufmann, “1.18-chalcopyrite thin-film materials and solar cells,” in *Comprehensive Renewable Energy*, E. C. A. Sayigh, Ed., pp. 399–422, Elsevier, Oxford, UK, 2012.
- [2] V. S. Saji, I.-H. Choi, and C.-W. Lee, “Progress in electrodeposited absorber layer for $\text{CuIn}_{1-x}\text{Ga}_x\text{Se}_2$ (CIGS) solar cells,” *Solar Energy*, vol. 85, no. 11, pp. 2666–2678, 2011.
- [3] R. N. Bhattacharya, W. Batchelor, J. F. Hiltner, and J. R. Sites, “Thin-film $\text{CuIn}_{1-x}\text{Ga}_x\text{Se}_2$ photovoltaic cells from solution-based precursor layers,” *Applied Physics Letters*, vol. 75, no. 10, pp. 1431–1433, 1999.
- [4] A. C. Busacca, A. C. Cino, S. Riva-Sanseverino, M. Ravaro, and G. Assanto, “Silica masks for improved surface poling of lithium niobate,” *Electronics Letters*, vol. 41, no. 2, pp. 92–94, 2005.
- [5] A. C. Busacca, E. D’Asaro, A. Pasquazi, S. Stivala, and G. Assanto, “Ultraviolet generation in periodically poled lithium tantalate waveguides,” *Applied Physics Letters*, vol. 93, no. 12, Article ID 121117, 2008.
- [6] A. C. Busacca, C. A. Santini, S. R. Sanseverino et al., “Surface periodic poling in congruent lithium tantalate,” *Electronics Letters*, vol. 42, no. 9, pp. 546–547, 2006.
- [7] A. C. Busacca, C. L. Sones, R. W. Eason, and S. Mailis, “First-order quasi-phase-matched blue light generation in surface-poled Ti:indiffused lithium niobate waveguides,” *Applied Physics Letters*, vol. 84, no. 22, pp. 4430–4432, 2004.
- [8] A. C. Busacca, S. Stivala, L. Curcio, and G. Assanto, “Parametric conversion in micrometer and submicrometer structured ferroelectric crystals by surface poling,” *International Journal of Optics*, vol. 2012, Article ID 606892, 11 pages, 2012.
- [9] A. C. Busacca, S. Stivala, L. Curcio, and P. Livreri, “Random quasi-phase matching in congruent lithium tantalate waveguides by proton exchange,” *Electronics Letters*, vol. 48, pp. 783–784, 2012.
- [10] E. Cantelar, M. Domenech, G. Lifante et al., “Multi-line NIR-UV emission in $\text{Nd}:\text{LiNbO}_3$ RPE optical waveguides,” *Electronics Letters*, vol. 43, no. 11, pp. 632–633, 2007.
- [11] E. Cantelar, G. Lifante, F. Cussó et al., “Dual-polarization-pump CW laser operation in $\text{Nd}^{3+}:\text{LiNbO}_3$ channel waveguides fabricated by reverse proton exchange,” *Optical Materials*, vol. 30, no. 7, pp. 1039–1043, 2008.
- [12] M. Cherchi, S. Bivona, A. C. Cino, A. C. Busacca, and R. L. Oliveri, “Universal charts for optical difference frequency

- generation in the terahertz domain,” *IEEE Journal of Quantum Electronics*, vol. 46, no. 6, pp. 1009–1013, 2010.
- [13] M. Cherchi, S. Stivala, A. Pasquazi et al., “Second-harmonic generation in surface periodically poled lithium niobate waveguides: on the role of multiphoton absorption,” *Applied Physics B*, vol. 93, no. 2-3, pp. 559–565, 2008.
- [14] M. Cherchi, A. Taormina, A. C. Busacca et al., “Exploiting the optical quadratic nonlinearity of zinc-blende semiconductors for guided-wave terahertz generation: a material comparison,” *IEEE Journal of Quantum Electronics*, vol. 46, no. 3, pp. 368–376, 2010.
- [15] M. Clerici, L. Caspani, E. Rubino et al., “Counterpropagating frequency mixing with terahertz waves in diamond,” *Optics Letters*, vol. 38, pp. 178–180, 2013.
- [16] G. Nava, P. Minzioni, I. Cristiani et al., “Integrated frequency shifter in periodically poled lithium tantalate waveguide,” *Electronics Letters*, vol. 46, no. 25, pp. 1686–1688, 2010.
- [17] A. Pasquazi, A. Busacca, S. Stivala, R. Morandotti, and G. Assanto, “Nonlinear disorder mapping through three-wave mixing,” *IEEE Photonics Journal*, vol. 2, no. 1, 2010.
- [18] E. M. Rodríguez, D. Jaque, E. Cantelar et al., “Time resolved confocal luminescence investigations on Reverse Proton Exchange Nd:LiNbO₃ channel waveguides,” *Optics Express*, vol. 15, no. 14, pp. 8805–8811, 2007.
- [19] S. Stivala, A. Pasquazi, L. Colace et al., “Guided-wave frequency doubling in surface periodically poled lithium niobate: competing effects,” *Journal of the Optical Society of America B*, vol. 24, no. 7, pp. 1564–1570, 2007.
- [20] R. Inguanta, S. Piazza, C. Sunseri et al., “An electrochemical route towards the fabrication of nanostructured semiconductor solar cells,” in *Proceedings of the International Symposium on Power Electronics, Electrical Drives, Automation and Motion (SPEEDAM '10)*, pp. 1166–1171, June 2010.
- [21] R. L. Oliveri, R. Inguanta, T. Spanò et al., “CIGS thin film by one-step electrodeposition for solar cells,” in *Proceedings of 15th Italian National Conference of Photonic Technologies (Fotonica '13)*, Milan, Italy, 2013.
- [22] A. Parisi, A. C. Cino, A. C. Busacca, M. Cherchi, and S. Riva-Sanseverino, “Integrated optic surface plasmon resonance measurements in a borosilicate glass substrate,” *Sensors*, vol. 8, no. 11, pp. 7113–7124, 2008.
- [23] A. Parisi, F. P. D’Aleo, S. Guarino et al., “Integrated optic surface plasmon resonance measurements in glass substrates,” in *Proceedings of the 3rd European Workshop on Optical Fibre Sensors*, vol. 6619 of *Proceedings of SPIE*, Napoli, Italy, July 2007.
- [24] S. Stivala, A. Pasquazi, A. C. Busacca et al., “Frequency doubling in surface periodically poled lithium niobate waveguides: competing effects,” in *Proceedings of the European Conference on Lasers and Electro-Optics and the International Quantum Electronics Conference (CLEOE-IQEC '07)*, Munich, Germany, 2007.
- [25] A. Parisi, L. Curcio, V. Rocca et al., “Photovoltaic module characteristics from CIGS solar cell modelling,” in *Proceedings of the International Conference Renewable Energy Research and Applications (ICRERA '13)*, 2013.
- [26] R. Miceli, “Energy management and smart grids,” *Energies*, vol. 6, pp. 2262–2290, 2013.
- [27] G. Cipriani, V. Di Dio, D. La Manna, F. Massaro, R. Miceli, and G. Zizzo, “Economic analysis on dynamic photovoltaic systems in new italian “feed in tariffs” context,” in *Proceedings of the International Conference on Clean Electrical Power: Renewable Energy Resources Impact (ICCEP'13)*, 2013.
- [28] G. Cipriani, V. Di Dio, L. P. Di Noia et al., “A PV plant simulator for testing MPPT techniques,” in *Proceedings of the International Conference on Clean Electrical Power: Renewable Energy Resources Impact (ICCEP '13)*, 2013.
- [29] V. Di Dio, S. Favuzza, D. La Caseia, and R. Miceli, “Economical incentives and systems of certification for the production of electrical energy from renewable energy resources,” in *Proceedings of the International Conference on Clean Electrical Power (ICCEP '07)*, pp. 277–282, May 2007.
- [30] V. Di Dio, R. Miceli, C. Rando, and G. Zizzo, “Dynamics photovoltaic generators: technical aspects and economical valuation,” in *Proceedings of the International Symposium on Power Electronics, Electrical Drives, Automation and Motion (SPEEDAM '10)*, pp. 635–640, June 2010.
- [31] M. Bouzguenda, T. Salmi, A. Gastli, and A. Masmoudi, “Evaluating solar photovoltaic system performance using MATLAB,” in *Proceedings of the 1st International Conference on Renewable Energies and Vehicular Technology (REVET '12)*, pp. 55–559.
- [32] A. N. Celik and N. Acikgoz, “Modelling and experimental verification of the operating current of mono-crystalline photovoltaic modules using four- and five-parameter models,” *Applied Energy*, vol. 84, no. 1, pp. 1–15, 2007.
- [33] G. Cipriani, V. Di Dio, D. La Cascia, R. Miceli, and R. Rizzo, “A novel approach for parameters determination in four lumped PV parametric model with operative range evaluations,” *International Review of Electrical Engineering*, vol. 8, 2013.
- [34] G. Farivar and B. Asaei, “Photovoltaic module single diode model parameters extraction based on manufacturer datasheet parameters,” in *Proceedings of the IEEE International Conference on Power and Energy (PECon '10)*, pp. 929–934, December 2010.
- [35] M. G. Villalva, J. R. Gazoli, and E. R. Filho, “Comprehensive approach to modeling and simulation of photovoltaic arrays,” *IEEE Transactions on Power Electronics*, vol. 24, no. 5, pp. 1198–1208, 2009.
- [36] G. Cipriani, G. Ciulla, V. Di Dio, D. La Cascia, and R. Miceli, “A device for PV modules I-V characteristic detection,” in *Proceedings of the International Conference on Clean Electrical Power: Renewable Energy Resources Impact (ICCEP '13)*, 2013.
- [37] V. Lo Brano, A. Orioli, G. Ciulla, and A. Di Gangi, “An improved five-parameter model for photovoltaic modules,” *Solar Energy Materials and Solar Cells*, vol. 94, no. 8, pp. 1358–1370, 2010.
- [38] A. Luque and S. Egedus, *Handbook of Photovoltaic Science and Engineering*, Wiley, Chichester, UK, 2003.
- [39] F. Ghani, M. Duke, and J. Carson, “Numerical calculation of series and shunt resistance of a photovoltaic cell using the Lambert W-function: experimental evaluation,” *Solar Energy*, vol. 87, pp. 246–253, 2013.
- [40] M. A. Green, *Solar Cells: Operating Principles, Technology, and System Applications*, vol. 1, Prentice Hall, Upper Saddle River, NJ, USA, 1982.
- [41] A. Chatterjee, A. Keyhani, and D. Kapoor, “Identification of photovoltaic source models,” *IEEE Transactions on Energy Conversion*, vol. 26, no. 3, pp. 883–889, 2011.
- [42] S. Li and H. Zheng, “Energy extraction characteristic study of solar photovoltaic cells and modules,” in *Proceedings of the IEEE Power and Energy Society General Meeting: The Electrification of Transportation and the Grid of the Future*, San Diego, Calif, USA, July 2011.
- [43] H. -L. Tsai, C. S. Tu, and Y. J. Su, “Development of generalized photovoltaic model using MATLAB/SIMULINK,” in *Proceedings of the World Congress on Engineering and Computer Science WCECS ('08)*, San Francisco, Calif, USA, 2008.

- [44] M. G. Villalva, J. R. Gazoli, and E. Ruppert Filho, "Modeling and circuit-based simulation of photovoltaic arrays," in *Proceedings of the Brazilian Power Electronics Conference (COBEP '09)*, pp. 1244–1254, Bonito-Mato Grosso do Sul, Brazil, October 2009.
- [45] W. De Soto, S. A. Klein, and W. A. Beckman, "Improvement and validation of a model for photovoltaic array performance," *Solar Energy*, vol. 80, no. 1, pp. 78–88, 2006.
- [46] D. Sera, R. Teodorescu, and P. Rodriguez, "PV panel model based on datasheet values," in *Proceedings of the IEEE International Symposium on Industrial Electronics (ISIE '07)*, pp. 2392–2396, Vigo, Spain, June 2007.
- [47] V. Di Dio, D. La Cascia, R. Miceli, and C. Rando, "A mathematical model to determine the electrical energy production in photovoltaic fields under mismatch effect," in *Proceedings of the International Conference on Clean Electrical Power (ICCEP '09)*, pp. 46–51, Capri, Italy, June 2009.
- [48] H. Zhu, A. K. Kalkan, J. Hou, and S. J. Fonash, "Applications of AMPS-1D for solar cell simulation," *AIP Conference Proceedings*, vol. 462, pp. 309–314, 1999.
- [49] S. Fonash, J. Arch, J. Cuiffi et al. et al., "A manual for AMPS-1D for Windows 95/NT," The Pennsylvania State University, pp. 10–31, 1997.
- [50] G. A. M. Hurkx, D. B. M. Klaassen, and M. P. G. Knuvers, "A new recombination model for device simulation including tunneling," *IEEE Transactions on Electron Devices*, vol. 39, no. 2, pp. 331–338, 1992.
- [51] K. Yang, J. R. East, and G. I. Haddad, "Numerical modeling of abrupt heterojunctions using a thermionic-field emission boundary condition," *Solid-State Electronics*, vol. 36, no. 3, pp. 321–330, 1993.
- [52] Y. Liu, Y. Sun, and A. Rockett, "An improved algorithm for solving equations for intra-band tunneling current in heterojunction solar cells," *Thin Solid Films*, vol. 520, no. 15, pp. 4947–4950, 2012.
- [53] <https://wiki.engr.illinois.edu/display/solarcellsim>.
- [54] Y. Liu, Y. Sun, and A. Rockett, "A new simulation software of solar cells—wxAMPS," *Solar Energy Materials and Solar Cells*, vol. 98, pp. 124–128, 2012.
- [55] M. Gloeckler, A. L. Fahrenbruch, and J. R. Sites, "Numerical modeling of CIGS and CdTe solar cells: setting the baseline," in *Proceedings of the 3rd World Conference on Photovoltaic Energy Conversion*, vol. 1, pp. 491–494, Osaka, Japan, May 2003.
- [56] K. R. McIntosh, J. N. Cotsell, J. S. Cumpston, A. W. Norris, N. E. Powell, and B. M. Ketola, "An optical comparison of silicone and eva encapsulants for conventional silicon PV modules: a ray-tracing study," in *Proceedings of the 34th IEEE Photovoltaic Specialists Conference (PVSC '09)*, pp. 544–549, Philadelphia, Pa, USA, June 2009.
- [57] E. E. van Dyk and E. L. Meyer, "Analysis of the effect of parasitic resistances on the performance of photovoltaic modules," *Renewable Energy*, vol. 29, no. 3, pp. 333–344, 2004.
- [58] M. A. Green, *Solar Cells: Operating Principles, Technology, and System Applications*, vol. 1 of *Prentice-Hall Series in Solid state Physical Electronics*, Prentice Hall, New York, NY, USA, 1982.
- [59] U. Malm and M. Edoff, "Simulating material inhomogeneities and defects in CIGS thin-film solar cells," *Progress in Photo-voltaics*, vol. 17, no. 5, pp. 306–314, 2009.

Research Article

Effectively Improved SiO₂-TiO₂ Composite Films Applied in Commercial Multicrystalline Silicon Solar Cells

Chih-Hsiang Yang,¹ Shui-Yang Lien,² Chia-Ho Chu,³ Chung-Yuan Kung,¹
Tieh-Fei Cheng,⁴ and Pai-Tsun Chen⁴

¹ Department of Electrical Engineering, National Chung Hsing University, Taichung, Taiwan

² Department of Materials Science and Engineering, DaYeh University, ChungHua, Taiwan

³ Department of Materials Science and Engineering, MingDao University, 369 Wen-Hua Road, Peetow, ChungHua 52345, Taiwan

⁴ Gallant Precision Machining Co., Ltd., Taichung, Taiwan

Correspondence should be addressed to Shui-Yang Lien; syl@mail.dyu.edu.tw

Received 14 June 2013; Accepted 13 August 2013

Academic Editor: Gaetano Di Marco

Copyright © 2013 Chih-Hsiang Yang et al. This is an open access article distributed under the Creative Commons Attribution License, which permits unrestricted use, distribution, and reproduction in any medium, provided the original work is properly cited.

Composite silicon dioxide-titanium dioxide (SiO₂-TiO₂) films are deposited on a large area of 15.6 × 15.6 cm² textured multicrystalline silicon solar cells to increase the incident light trapped within the device. For further improvement of the antireflective coatings (ARCs) quality, dimethylformamide (DMF) solution is added to the original SiO₂-TiO₂ solutions. DMF solution solves the cracking problem, thus effectively decreasing reflectance as well as surface recombination. The ARCs prepared by sol-gel process and plasma-enhanced chemical vapor deposition (PECVD) on multicrystalline silicon substrate are compared. The average efficiency of the devices with improved sol-gel ARCs is 16.3%, only 0.5% lower than that of devices with PECVD ARCs (16.8%). However, from equipment depreciation point of view (the expiration date of equipment is generally considered as 5 years), the running cost (USD/watt) of sol-gel technique is 80% lower than that of PECVD method for the first five years and 66% lower than that of PECVD method from the start of the sixth year. This result proves that sol-gel-deposited ARCs process has potential applications in manufacturing low-cost, large-area solar cells.

1. Introduction

Antireflective coatings (ARCs) are now widely used in mass produced silicon photovoltaics [1–3]. High quality ARCs must be designed accurately on mono- and multicrystalline silicon solar cell surfaces, not only to passivate the surface dangling bonds acting as recombination centers [4–8], but also to minimize the loss of optical absorption. The conventional plasma-enhanced chemical vapor deposition (PECVD) technique is employed generally to deposit antireflection layers such as Si₃N₄ and SiO₂ [9–13]. However, this technique is always associated with vacuum processes and dangerous process gases. Therefore, replacing PECVD by other cost-effective methods can considerably reduce production costs of manufacturers and raise the security of the clean-room environment. Sol-gel spin-coating method applied extensively in preparing lots of different kinds of

coated films has become a popular technique for the past thirty years due to its high process speed, low-cost, continuous production, and suitability for the large-area process [14–17]. Nevertheless, ARCs deposited on textured silicon wafers by sol-gel method present worse uniformity than those deposited by PECVD technique. The severest nonuniformity areas resulting from centrifugal force appear on four corners of the substrate. For overcoming it, we control the spin rate of the spin coater, spin duration, and adjust the concentration of sol-gel solutions. Further, adding dimethylformamide (DMF) solution to the composite films is a critical step to solve the problem of film cracking. Mostly, cracks are caused owing to different coefficients of thermal expansion between the air and ARCs films [18–20]. Although the basic properties of most kinds of sol-gel-deposited films have been discussed, the application of composite films in solar cell research is not well investigated.

This study proposes a simple low-cost sol-gel method of preparing high-quality ARCs on large area multicrystalline wafers. DMF solution can help ARCs to be effectively coated on irregular and rough wafer surfaces treated by acid texturing. The average efficiency of solar cells with sol-gel-deposited antireflective films approaches that of ready-made crystalline solar cells. Thus, using sol-gel method instead of PECVD technique to deposit ARCs has potential applications in mass production of solar cells.

2. Experiment

2.1. Preparation of Sol-Gel Solution and Process of Spin Coating. The experimental SiO₂-TiO₂ colloid solutions in this study contained varying volume ratios of SiO₂ and TiO₂ solutions. The SiO₂ solution was prepared by reacting metal alkoxide with a mixture of a critical amount of water and hydrochloric acid (HCl) catalyst in a medium diluted with ethyl alcohol solvent. Tetraethyl orthosilicate (Si(OC₂H₅)₄) was then added into the resultant solutions and stirred with a magnetic stirrer. The TiO₂ solution was prepared similarly except that titanium isopropoxide (Ti(OC₃H₉)₄) was added instead of (Si(OC₂H₅)₄). The SiO₂ and TiO₂ were then mixed separately in different volume ratios. Tables 1, 2, and 3 show the detailed information for all solutions. Finally, a small amount of DMF was added into the SiO₂-TiO₂ synthetic colloid solution.

After adding several drops of synthetic solution to the 15.6 × 15.6 cm² multicrystalline wafers, the wafers were spin-coated for two rounds. The first coating was applied at a speed of 150 rpm to ensure uniform composite films, and the second round was performed at 330 rpm to obtain the desired film thickness. Each film was then prebaked at 80°C for 20 min and postbaked at 200°C for 40 min in atmosphere. Then, samples were further annealed in a quartz furnace from 100°C to 850°C for around 30 seconds firstly. Then furnace temperature cooled down from 850°C to around 100°C and lasted for 30 seconds.

Optical characteristics such as refractive index, thickness, and reflectance of films were subsequently measured by ellipsometer and fiber coupled CCD array spectrometer, respectively.

2.2. Design of Antireflection Coatings. More incident light is essential for mono- and multicrystalline solar cells to enhance their short-circuit current (J_{sc}). In some applications, zero reflectance is needed throughout a narrow spectrum band or at a single wavelength. For a substrate with a single ARC, the light from the ARC-substrate interface is reflected back to the ambient (air)-ARC interface with a phase change of 180° and interfere with the light reflected from the interface between ambient (air) and ARC in the opposite direction. In this state, the reflectance R can be described as

$$R = \left[\frac{n_{ARC}^2 - n_0 n_{sub}}{n_{ARC}^2 + n_0 n_{sub}} \right]^2, \quad (1)$$

TABLE 1: Preparation of SiO₂ solution.

| Contents | Ratio | Adding order |
|--|------------|--------------|
| H ₂ O/HCl | 0.2/0.0005 | 1 |
| C ₂ H ₅ OH | 0.5 | 2 |
| Si(OC ₂ H ₅) ₄ | 0.05 | 3 |

TABLE 2: Preparation of TiO₂ solution.

| Contents | Ratio | Adding order |
|--|-------|--------------|
| H ₂ O/HCl | 1 | 1 |
| C ₂ H ₅ OH | 80 | 2 |
| Ti(OC ₃ H ₉) ₄ | 1 | 3 |

TABLE 3: Preparation of mixed SiO₂-TiO₂ solution.

| Contents | Notation |
|--|----------|
| Ratio of SiO ₂ to TiO ₂ | 0.05~10 |
| Coating rate (r.p.m) | 100~400 |
| DMF ((CH ₃) ₂ NCHO) (%) | 0~20 |

where n_{ARC} , n_0 , and n_{sub} are the refractive indices of the ARC material, air, and substrate, respectively. To obtain zero reflectance, the term of $n_{ARC}^2 - n_0 n_{sub}$ must be zero. The resulting boundary condition can then be described as

$$n_{ARC} = \sqrt{n_0 n_{sub}}. \quad (2)$$

Moreover, the optimum thickness and refractive index with a minimum reflectance for a single-layer ARC can be deduced from

$$\lambda_0 = 4n_{ARC}d_{ARC}, \quad (3)$$

where λ_0 is the midrange wavelength of 630 nm, and where n_{ARC} and d_{ARC} are the refractive index and layer thickness, respectively [21].

2.3. Solar Cell Performance. Solar cells were fabricated from boron-doped multicrystalline Si wafers with resistivity of approximately 15 Ω-cm. Wafers were textured using hydrofluoric acid. After forming the emitter region by thermal diffusion of phosphorous atoms in a quartz tube furnace at 850°C, the back surface field was formed by annealing the aluminum contact deposited using screen printing method. The composite SiO₂-TiO₂ films and Si₃N₄ films were then deposited on the front of solar cells by spin-coating and PECVD techniques, respectively. Quasi-Steady-State Photo-conductance lifetime measurement technique (QSSPC) was carried out to evaluate the surface passivation effect of the ARCs on silicon substrate. Front silver contact prepared through screen printing method was then annealed at 700°C for 30 min. Finally, effective illuminated light (AM 1.5 G) from the solar simulator was slightly decreased by the grid-type collecting electrode, which occupied about 8% of the front surface area.

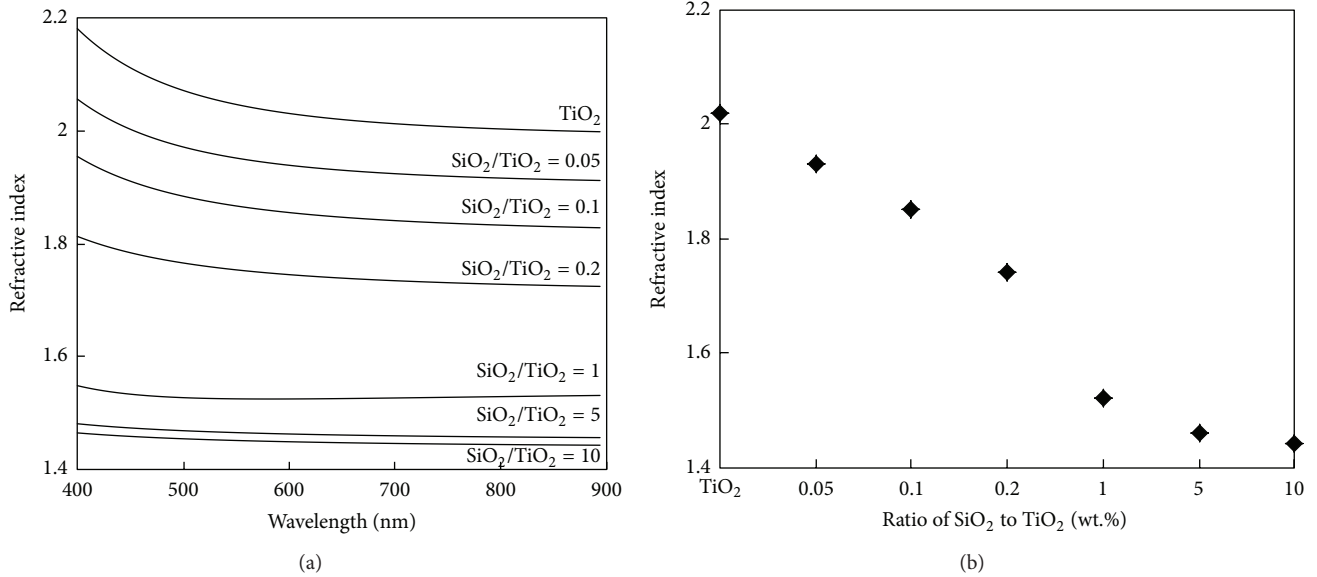


FIGURE 1: (a) Refractive index spectra and (b) refractive index at 630 nm for pure TiO_2 and SiO_2 - TiO_2 composite films deposited on monocrySTALLINE substrates.

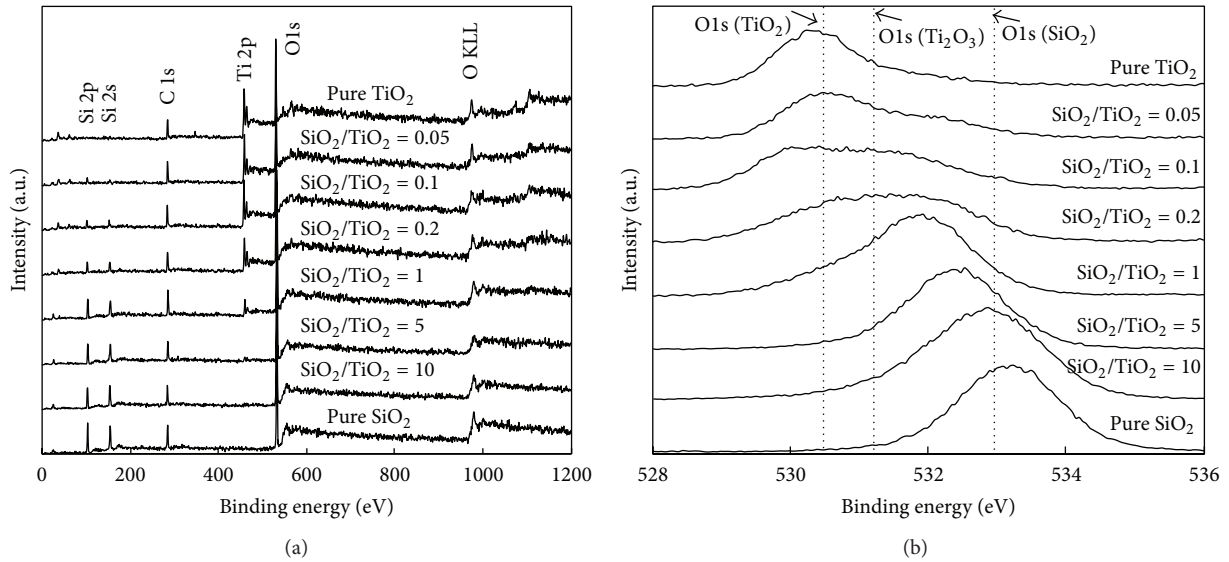


FIGURE 2: (a) XPS spectra and (b) O1s spectra for different ratios of SiO_2 - TiO_2 composite films.

3. Results and Discussion

When designing an ARC, the goal is to determine the refractive index and thickness of SiO_2 - TiO_2 films that provide optimal performance along the desired spectrum. Figure 1(a) shows refractive index spectra for pure TiO_2 and SiO_2 - TiO_2 composite films deposited on monocrySTALLINE substrates. The average refractive index is defined as the average value of all points on each curve. It can be found that as the pure TiO_2 solution adds more volumes of SiO_2 solution, the average refractive index decreases obviously from 2.1 to 1.45. Figure 1(b) further shows the different refractive indices corresponding to each ratio of SiO_2 to TiO_2 ($\text{SiO}_2/\text{TiO}_2$) at a wavelength of 630 nm. At this wavelength, spectral photon

intensity is the highest, and the strongest destructive interference happens, causing light to be trapped in devices [21]. Based on the boundary condition equation (2) mentioned previously, the appropriate refractive index 1.85 is obtained while the $\text{SiO}_2/\text{TiO}_2$ ratio is 0.1.

For analyzing the properties of composite films, X-ray photoelectron spectroscopy (XPS) spectra for pure SiO_2 film, pure TiO_2 film, and their mixture films in different $\text{SiO}_2/\text{TiO}_2$ ratios is carried out within the binding energy of 0–1200 eV as shown in Figure 2(a). The Si 2p, Si 2s, Ti 2p, and O 1s binding energy locate at 103.1, 155, 456.6, and 532.4 eV, respectively. The C 1s peak is 284.7 eV, which is attributable to carbon contamination at the outer surface of the composite films. The Ti 2p peaks gradually disappear with increasing of

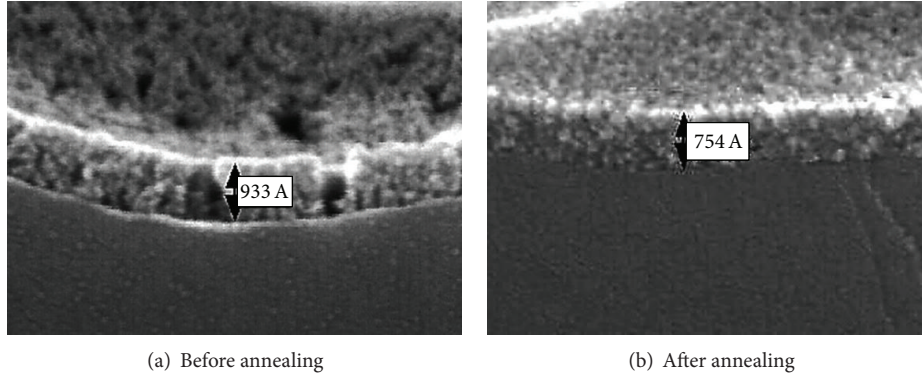


FIGURE 3: Cross-sectional SEM images (a) before firing and (b) after firing of SiO_2 - TiO_2 composite films.

$\text{SiO}_2/\text{TiO}_2$ ratio, whereas the Si 2s and Si 2p peaks strengthen, which validates that the components of all composite films changed momentarily. Figure 2(b) shows the results of further analysis of the behaviors of O 1s peaks in composite films with various $\text{SiO}_2/\text{TiO}_2$ ratios. The peak shifts from low binding energy (Ti-O bonds) to high binding energy (Si-O bond). Characteristics of composite film get close to that of pure SiO_2 film. From the materials analysis perspective, these changes explain why the refractive index of SiO_2 - TiO_2 composite films changes as different $\text{SiO}_2/\text{TiO}_2$ ratios.

Since the ratio of $\text{SiO}_2/\text{TiO}_2$ has been optimized to 0.1, we start to investigate the properties of composite films based on this ratio in later experiment. Figure 3 is a scanning electron microscope (SEM) cross-sectional image of the SiO_2 - TiO_2 composite films before and after annealing process. It can be seen in Figure 3(a) that, by adjusting spinning speed, the SiO_2 - TiO_2 composite film can be coated to the surface of textured multicrystalline wafer smoothly, but is still loose before annealing. After annealing at 850°C for 30 seconds, thickness of ARC decreases from 93.3 nm to 75.4 nm as shown in Figure 3(b). The film becomes denser, probably attributed to firing of the organic solvent and removal of resin [22]. However, in this case, a desirable thickness approximating 85 nm is calculated using (3) shown previously. A 10 nm deviation exists between theoretical value and experimental result, leading to a very slight influence on cell's performance. It's really difficult to control the film thickness accurately of using sol-gel technique; therefore, how to improve this disadvantage is a critical issue in the future.

The SEM images of surface morphology of composite SiO_2 - TiO_2 films with DMF ranging from 0% to 15% are schematically presented in Figure 4. Figure 4(a) exhibits lots of cracks in the composite SiO_2 - TiO_2 film without DMF. From the zoomed insert, visible cracks spread on the bottom of notches formed by acid texturing. The cracks, which probably formed during the annealing process, decrease the absorption of incident photons. Worse light absorption may lead to lower light-generated carriers, thus decreasing the J_{sc} of solar devices. Figures 4(b) to 4(d) show that adding 5% to 15% DMF to SiO_2 - TiO_2 solutions gradually improves the crack problems. When the DMF ratio reaches 15%, the cracks are almost entirely eliminated. This phenomenon may be

probably explained that DMF solution can not only diminish the reaction rate of sol hydrolyzing-polycondensation and prevent the little sol particle from growing up, but also promotes the lateral connection of particles by combining the hydrogen bonds with intermediates of sol during gelling process. Moreover, the pore tension of mixture solution could be diminished by DMF solution in thermal process, leading to lower vapor pressure. Hence, the composite films are coated uniformly. According to QSSPC measurement (not shown here), the lifetime of excess minor carrier of each composite film with 0% to 15% DMF solution are 2, 8, 17, and 23 μs , respectively, revealing that as the cracks in the films reduce, the lifetimes becomes higher. Compared to the lifetime of monocrystalline silicon substrate, these relative low lifetime values can be attributed to lots of grain boundaries in multicrystalline silicon substrate, which act as recombination centers.

Figure 5 displays the optical reflectance spectra of pure TiO_2 films, SiO_2 - TiO_2 composite films with different volume of DMF, and Si_3N_4 films fabricated by PECVD. The results show that the PECVD ARC has a higher reflectance compared to other films prepared by sol-gel technique at wavelengths lower than 500 nm. This relatively high value is attributed to its relatively higher refractive index of Si_3N_4 at short wavelength [16]. The PECVD ARC has an average reflectance of approximately 9.5%, and its minimum reflectance is approximately 1.5% at wavelengths approximating 770 nm. Further comparison of the curves of the other composite films with and without DMF shows that lowest average reflectance is obtained while the mixed SiO_2 - TiO_2 solution plus 15% DMF, presenting an average reflectance of 9% and minimum reflectance of approximately 4% at the wavelength around 670 nm. Obviously, composite films without cracks provide suitable path for incident light, reducing the reflection loss considerably. In summary, the entire measured tendency corresponds well with the SEM images shown in Figure 4, revealing the feasibility of adding DMF solution.

Figure 6 compares performances of solar cells between PECVD-ARC cells (ready-made multicrystalline cells for mass production) and improved sol-gel-ARC cells. All performance parameters for the fifty devices with optimal sol-gel

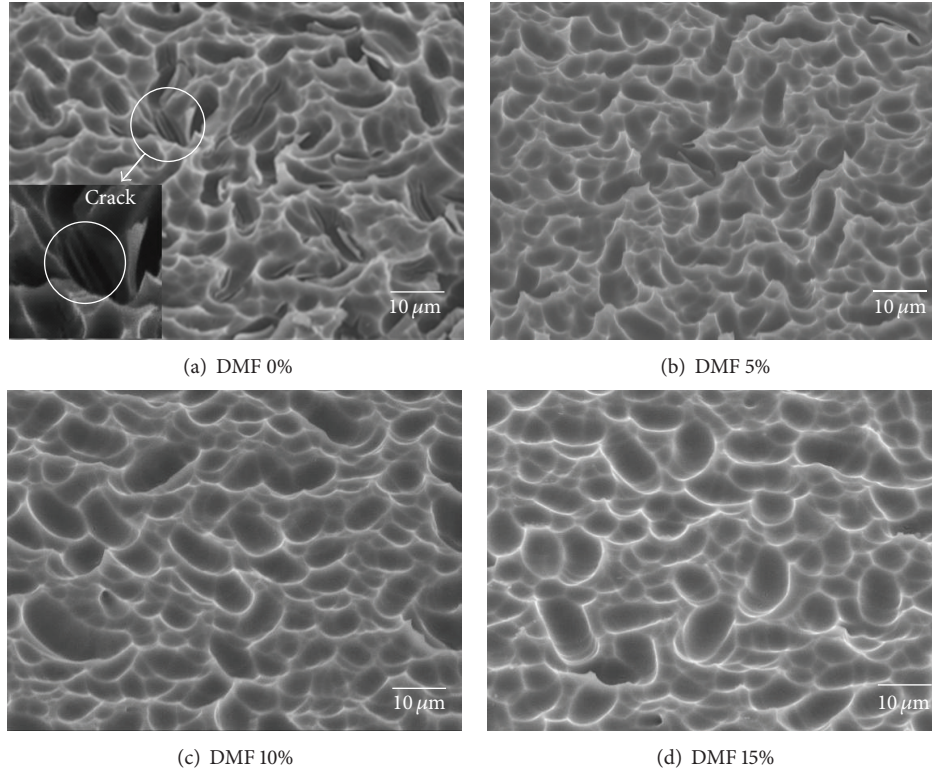


FIGURE 4: SEM images of surface morphology of composite $\text{SiO}_2\text{-TiO}_2$ films without DMF and with DMF ratios from 5% to 15%.

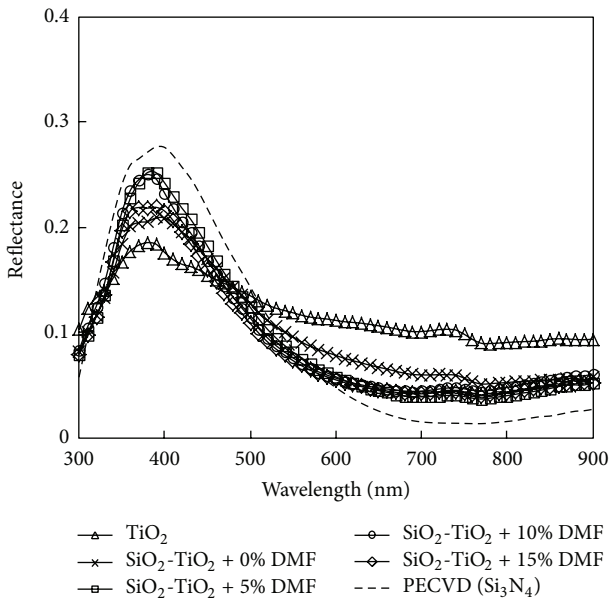


FIGURE 5: Optical reflectance spectra of pure TiO_2 film, $\text{SiO}_2\text{-TiO}_2$ mixture films with different volumes of DMF, and Si_3N_4 films fabricated by PECVD.

ARC are highly consistent, which confirms the reliability of the process. The optimum average efficiency is approximately 16.3%, about 0.5% lower than the average efficiency (around 16.8%) of PECVD-ARC cells. This 0.5% discrepancy is caused

mainly by short-circuit current and open-circuit voltage (V_{oc}). The chief reason of the lower J_{sc} of those sol-gel-ARCs devices can be discussed in two factors: reflectance and lifetime. As noted in Figure 5, the average reflectance of sol-gel-ARCs devices plus 15% DMF solution is 9%, which is lower than 9.5% of the PECVD-ARCs devices. It is expected that sol-gel-ARC device should absorb more incident light resulting in higher J_{sc} . However, average J_{sc} of the sol-gel-ARCs devices is 34.9 lower than 35.2 mA/cm^2 of the PECVD-ARC devices, which implies that the carrier lifetime substantially affects J_{sc} . Noted that the mean lifetime of PECVD-ARCs devices is around 27 μs and of the sol-gel-ARCs devices is around 23 μs . Moreover, lower mean lifetime of the sol-gel-ARCs devices also affects their V_{oc} performance. Michl et al. indicated that the excess minor carrier lifetime substantially affects the V_{oc} in multicrystalline devices [23]. This result is consistent with the experimental trend in this study. Hence, further studies are needed to improve the interface quality between a sol-gel-ARC and a silicon substrate.

Figure 7 compares the appearance of a PECVD-ARC device (Figure 7(a)) with a sol-gel-ARC device (Figure 7(b)). Before fabrication of the ARCs, both devices initially have the same multicrystalline silicon substrates. It can be seen that the colors of both devices are nearly the same after fabricating ARCs. Very little color variation is caused by the different reflectance of both devices at visible wavelength spectrum. The deep blue sol-gel-ARC is quite uniform without any uncoated areas formed on the four corners of the substrate, indicating that the proposed sol-gel process can potentially

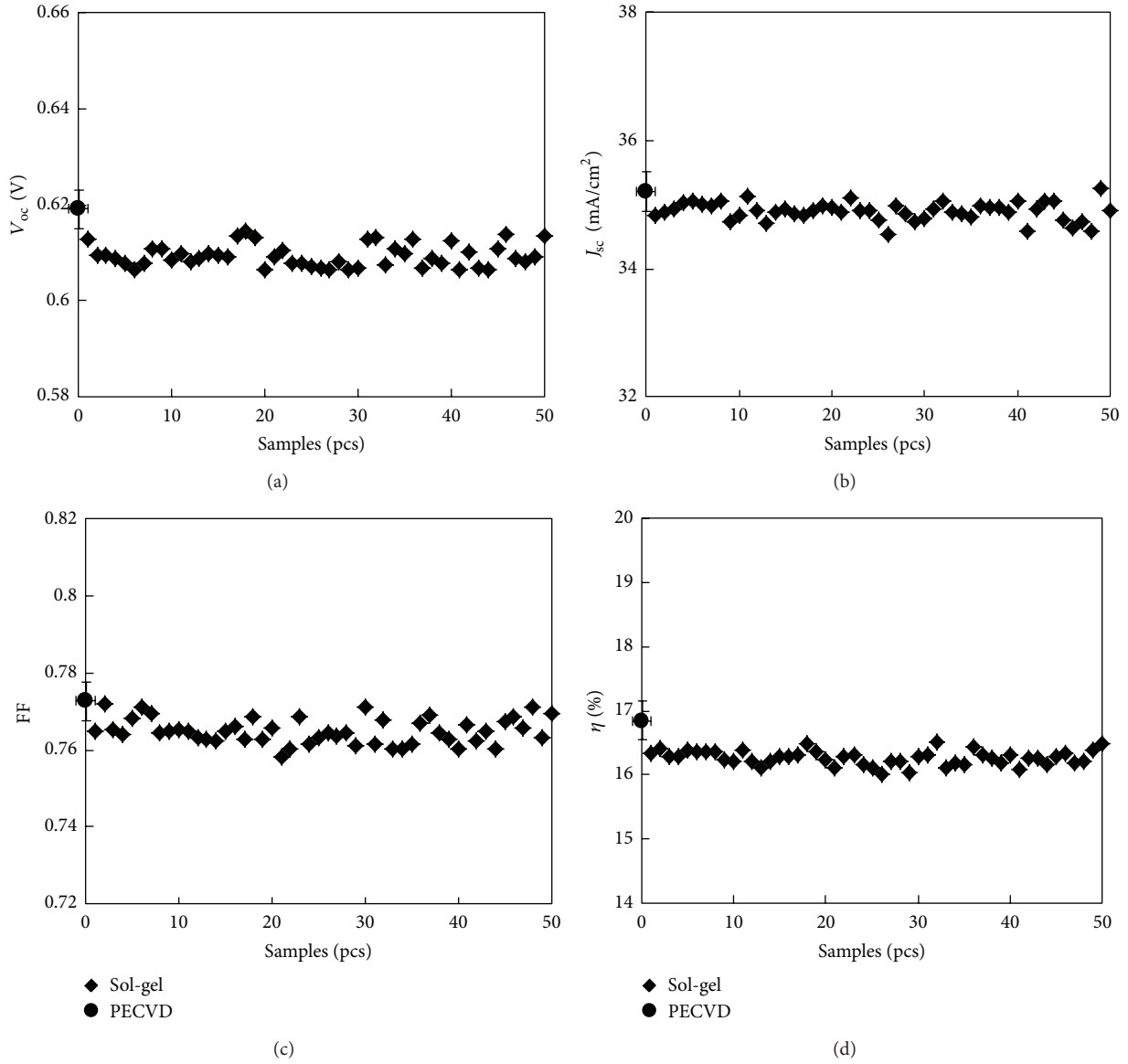


FIGURE 6: Performances of the PECVD-ARC solar cells and the sol-gel-ARC solar cells.

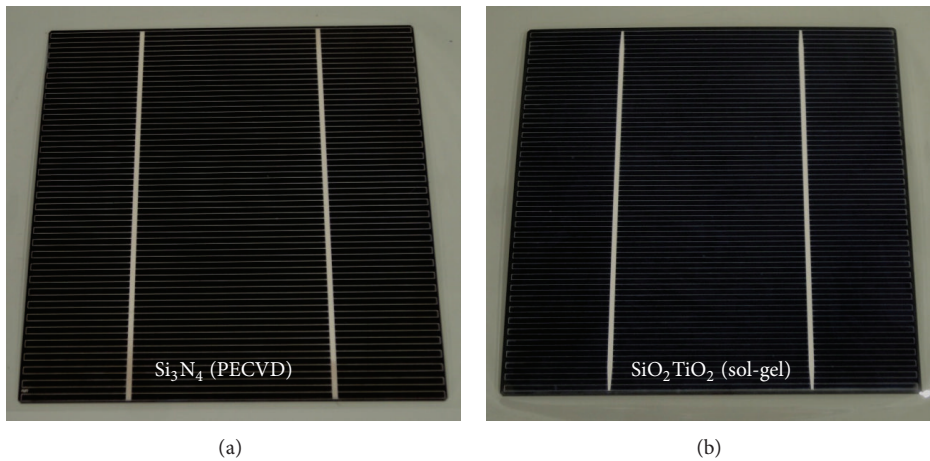


FIGURE 7: Photographs of (a) PECVD-ARC device and (b) sol-gel-ARC devices.

TABLE 4: Cost in fabricating ARCs.

| Cost in ARC process (USD) | PECVD (Si_3N_4) | Spin-coating (SiO_2 - TiO_2) |
|--|-----------------------------------|--|
| Equipments | 1,040,000 | 33,333 |
| Materials (1 year) | 407,000 | 121,300 |
| Running cost/Per Watt (first five years) | 0.0154 | 0.003 |
| Running cost/Per Watt (five years later) | 0.01 | 0.003 |

replace the PECVD process for the mass production of single- and multicrystalline silicon solar cells.

Table 4 provided by Gallant Precision Machining Co., Ltd., Taiwan compares equipment cost, materials cost, and running cost between various ARCs fabrication methods. The expiration date of equipment is generally considered as five years. From equipment depreciation point of view, the running cost (USD/watt) of sol-gel technique is around 80% lower than that of PECVD method for first five years and around 66% lower than that of PECVD method from the start of the sixth year. Although the efficiency of sol-gel-ARC device is lower than that of PECVD-ARC device, a huge difference in manufacturing cost still makes sol-gel-ARC device have enough competitiveness.

For further increasing efficiency of the proposed sol-gel-ARCs cells, it is necessary to fabricate double or even triple layers ARCs. A single layer ARC is able to be nonreflective only at one wavelength, often at the middle of the visible region, but multiple layers are more effective over the whole visible spectrum. Moreover, high conversion efficiency of monocrystalline silicon solar cells can probably be realized with the same sol-gel process.

4. Conclusion

A study aiming to improve the quality of sol-gel ARCs that could help increase the efficiency of multicrystalline solar cells is presented in this work. The effective refractive index and thickness of the films are adjusted by controlling the spin rate and annealing temperature. Average reflectance is eventually reduced to 9% by adding DMF solution to reduce cracks in the film while the average efficiency of devices is improved to 16.3%. Although the efficiency 16.3% still trails that of the ready-made multicrystalline solar cells by approximately 0.5%, the reliability and uniformity as well as lower running cost are highly attractive to manufacturers. In the future, use of the sol-gel technique, which combines spin-coating with furnace annealing to prepare ARCs, could enable a more efficient and a continuous mass production of Si solar cells compared to the use of PECVD method, which requires an expensive vacuum process and dangerous process gases.

Acknowledgments

This work is sponsored by Gallant Precision Machining Co., Ltd., Taiwan and the National Science Council of Taiwan

under the Grants nos. NSC 100-2628-E-451-002-MY2(2/2) and NSC 101-3113-E-451-001-CC2.

References

- [1] S.-M. Jung, Y.-H. Kim, S.-I. Kim, and S.-I. Yoo, "Design and fabrication of multi-layer antireflection coating for III-V solar cell," *Current Applied Physics*, vol. 11, no. 3, pp. 538–541, 2011.
- [2] S. Dutttagupta, F. Ma, B. Hoex, T. Mueller, and A. G. Aberle, "Optimised antireflection coatings using silicon nitride on textured silicon surfaces based on measurements and multidimensional modelling," *Energy Procedia*, vol. 15, pp. 78–83, 2012.
- [3] J. H. Selj, T. T. Mongstad, R. Søndena, and E. S. Marstein, "Reduction of optical losses in colored solar cells with multi-layer antireflection coatings," *Solar Energy Materials and Solar Cells*, vol. 95, no. 9, pp. 2576–2582, 2011.
- [4] H. J. Yang, K.-S. Ji, J. Choi, and H. M. Lee, "Annealing effect on surface passivation of a-Si:H/c-Si interface in terms of crystalline volume fraction," *Current Applied Physics*, vol. 10, no. 3, pp. S375–S378, 2010.
- [5] J. W. A. Schüttauf, C. H. M. V. der Werf, W. G. J. H. M. van Sark, J. K. Rath, and R. E. I. Schropp, "Comparison of surface passivation of crystalline silicon by a-Si:H with and without atomic hydrogen treatment using hot-wire chemical vapor deposition," *Thin Solid Films*, vol. 519, no. 14, pp. 4476–4478, 2011.
- [6] T. C. Thi, K. Koyama, K. Ohdaira, and H. Matsumura, "Passivation characteristics of SiN_x /a-Si and SiN_x /Si-rich- SiN_x stacked layers on crystalline silicon," *Solar Energy Materials and Solar Cells*, vol. 100, pp. 169–173, 2012.
- [7] T. F. Schulze, L. Korte, and B. Rech, "Impact of a-Si:H hydrogen depth profiles on passivation properties in a-Si:H/c-Si heterojunctions," *Thin Solid Films*, vol. 520, no. 13, pp. 4439–4444, 2012.
- [8] J. Ge, Z. P. Ling, J. Wong, T. Mueller, and A. G. Aberle, "Optimisation of intrinsic a-Si:H passivation layers in crystalline-amorphous silicon heterojunction solar cells," *Energy Procedia*, vol. 15, pp. 107–117, 2012.
- [9] J. Ko, D. Gong, K. Pillai et al., "Double layer SiN_x :H films for passivation and anti-reflection coating of c-Si solar cells," *Thin Solid Films*, vol. 519, no. 20, pp. 6887–6891, 2011.
- [10] W. R. Taube, A. Kumar, R. Saravanan et al., "Efficiency enhancement of silicon solar cells with silicon nanocrystals embedded in PECVD silicon nitride matrix," *Solar Energy Materials and Solar Cells*, vol. 101, pp. 32–35, 2012.
- [11] S. Wang, A. Lennon, B. Tjahjono, L. Mai, B. Vogl, and S. Wenham, "Overcoming over-plating problems for PECVD SiN_x passivated laser doped p-type multi-crystalline silicon solar cells," *Solar Energy Materials and Solar Cells*, vol. 99, pp. 226–234, 2012.
- [12] R. Bousbih, W. Dimassi, I. Haddadi, S. Ben Slema, P. Rava, and H. Ezzaouia, "Silicon lifetime enhancement by SiN_x :H anti-reflective coating deposited by PECVD using SiH_4 and N_2 reactive gas," *Solar Energy*, vol. 86, no. 5, pp. 1300–1305, 2012.
- [13] L. Remache, E. Fourmond, A. Mahdjoub, J. Dupuis, and M. Lemiti, "Design of porous silicon/PECVD SiO_x antireflection coatings for silicon solar cells," *Materials Science and Engineering B*, vol. 176, no. 1, pp. 45–48, 2011.
- [14] G. Guzman, B. Dahmani, J. Puetz, and M. A. Aegerter, "Transparent conducting sol-gel ATO coatings for display applications by an improved dip coating technique," *Thin Solid Films*, vol. 502, no. 1-2, pp. 281–285, 2006.

- [15] J. Puetz and M. A. Aegerter, "Dip coating technique," in *Handbook on Sol-Gel Technologies for Glass Producers and Users*, M. A. Aegerter and M. Mennig, Eds., p. 37, Kluwer Academic Publishers, 2004.
- [16] M. Vishwas, K. N. Rao, K. V. A. Gowda, and R. P. S. Chakradhar, "Optical, electrical and dielectric properties of TiO₂-SiO₂ films prepared by a cost effective sol-gel process," *Spectrochimica Acta A*, vol. 83, no. 1, pp. 614–617, 2011.
- [17] N. H. Aljufairi, "Electric properties and surface structure of TiO₂ for solar cells," *Energy*, vol. 39, no. 1, pp. 6–10, 2012.
- [18] Z. Zhang, P. Zhang, L. Guo, T. Guo, and J. Yang, "Effect of TiO₂-SiO₂ sol-gel coating on the cpTi-porcelain bond strength," *Materials Letters*, vol. 65, no. 7, pp. 1082–1085, 2011.
- [19] Ö. Kesmez, E. Burunkaya, N. Kiraz, H. E. Çamurlu, M. Asiltürk, and E. Arpaç, "Effect of acid, water and alcohol ratios on sol-gel preparation of antireflective amorphous SiO₂ coatings," *Journal of Non-Crystalline Solids*, vol. 357, no. 16-17, pp. 3130–3135, 2011.
- [20] A. Elfanaoui, E. Elhamri, L. Boulkaddat et al., "Optical and structural properties of TiO₂ thin films prepared by sol-gel spin coating," *International Journal of Hydrogen Energy*, vol. 36, no. 6, pp. 4130–4133, 2011.
- [21] T. Mizuta, T. Ikuta, T. Minemoto, H. Takakura, Y. Hamakawa, and T. Numai, "An optimum design of antireflection coating for spherical silicon solar cells," *Solar Energy Materials and Solar Cells*, vol. 90, no. 1, pp. 46–56, 2006.
- [22] N. Batra, P. Kumar, S. K. Srivastava et al., "Controlled synthesis and characteristics of antireflection coatings of TiO₂ produced from an organometallic colloid," *Materials Chemistry and Physics*, vol. 130, no. 3, pp. 1061–1065, 2011.
- [23] B. Michl, M. Rüdiger, J. A. Giesecke, M. Hermle, W. Warta, and M. C. Schubert, "Efficiency limiting bulk recombination in multicrystalline silicon solar cells," *Solar Energy Materials and Solar Cells*, vol. 98, pp. 441–447, 2012.

Research Article

Enhanced Photoelectrochemical Response from Copper Antimony Zinc Sulfide Thin Films on Transparent Conducting Electrode

Prashant K. Sarswat and Michael L. Free

Department of Metallurgical Engineering, University of Utah, Salt Lake City, UT 84112, USA

Correspondence should be addressed to Prashant K. Sarswat; saraswatp@gmail.com

Received 31 May 2013; Revised 10 August 2013; Accepted 11 August 2013

Academic Editor: Leonardo Palmisano

Copyright © 2013 P. K. Sarswat and M. L. Free. This is an open access article distributed under the Creative Commons Attribution License, which permits unrestricted use, distribution, and reproduction in any medium, provided the original work is properly cited.

Copper antimony sulfide (CAS) is a relatively new class of sustainable absorber material, utilizing cost effective and abundant elements. Band gap engineered, modified CAS thin films were synthesized using electrodeposition and elevated temperature sulfurization approach. A testing analog of copper zinc antimony sulfide (CZAS) film-electrolyte interface was created in order to evaluate photoelectrochemical performance of the thin film of absorber materials. $\text{Eu}^{3+}/\text{Eu}^{2+}$ redox couple was selected for this purpose, based on its relative band offset with copper antimony sulfide. It was observed that zinc has a significant effect on CAS film properties. An enhanced photocurrent was observed for CAS film, modified with zinc addition. A detailed investigation has been carried out by changing stoichiometry, and corresponding surface and optical characterization results have been evaluated. A summary of favorable processing parameters of the films showing enhanced photoelectrochemical response is presented.

1. Introduction

Sulphosalt group compounds such as chalcocite (CuSbS_2), famatinitite (Cu_3SbS_4), and tetrahedrite ($\text{Cu}_{12}\text{Sb}_4\text{S}_{13}$) are part of a relatively new class of material containing antimony. This class can be utilized for thin film solar cell, photoelectrochemical hydrogen production, and thermoelectricity production as well as its application as a topological insulator [1–4]. The sulphosalts containing Cu, Sb, and S are commonly known as “CAS” which is generally a p-type semiconducting material [1–3]. It is worth noting that most of these elements are cost effective and abundant. This class of compounds (or minerals) was widely explored during 1960s and 1980s and it was found that their electronic properties are highly dependent on valence electrons in unit cells [5, 6]. It was reported that some CAS sulphosalts act as large band gap semiconductors while some are metallic compounds, depending on the number of valence electrons and the stoichiometry. Interestingly, ab initio calculations suggest the presence of a “nontrivial 3D topological insulating” phase [4]. It was also anticipated that the electronic properties of such a

class of materials can be tuned by changing various cations and anions. Recently, optical properties of these materials have been explored and it was observed that CAS compounds with different stoichiometry exhibit different band gaps. The band gap of $\text{Cu}_{12}\text{Sb}_4\text{S}_{13}$ is ~ 1.72 eV, CuSbS_2 shows a band gap of 1.38 eV, and Cu_3SbS_3 has a band gap of 1.84 eV [1–4]. It was concluded that the band gap of this class of compounds is tunable and can be varied between 0.9 and 1.9 eV [1, 4]. This range of band gap is perfectly suitable for thin film photovoltaic cells and solar hydrogen splitting [1–4]. Recently, various solution-processed and vacuum based techniques have been utilized to grow thin films of CAS such as solvothermal (nanocrystal ink printing), electrodeposition-sulfur annealing, and heat treatment of Sb_2S_3 -CuS layer [1–3, 7]. In most cases, assessments of the photovoltaic properties of these thin films were conducted using a photoelectrochemical cell. Earlier published reports suggest that photoelectrochemical response for chalcocite thin film coated on ITO electrode was ~ 0.09 mA/cm² at saturation, whereas film synthesized using electrodeposition annealing shows the change in offset current of ~ 0.08 mA/cm² [2, 7]. It is important to note that

this change in photocurrent is relatively low compared to other types of chalcogenide films [8]. Such inefficiency can hinder the sufficient utilization of CAS for solar cell applications. It is highly essential, therefore, to make additional efforts for the enhancement of photovoltaic properties of CAS material. One of the approaches can be the modification of film stoichiometry and experimental parameters. It was reported that zinc is one of the common substitutes for copper antimony sulfide sulphosalt [5, 6]. For tetrahedrite (also a class of copper antimony zinc (or iron) sulfide), it was reported that up to ~30% of copper substitution is possible with zinc or iron [5, 6]. Phase relations of quaternary Cu-Zn-Sb-S or Cu-Fe-Sb-S were discussed by Tatsuka and Morimoto [5]. It was reported that tetrahedrite is more stable when it contains a relatively high amount of copper. It was concluded that tetrahedrite decomposes into iron (or zinc) rich tetrahedrite, antimony, famatinite, and digenite. It was also reported that the Cu-Sb-S alloy system is less stable compared to the iron (or zinc) bearing CAS alloy system at room temperature [5]. Hence, in view of this information, we have systematically synthesized and investigated Cu-Zn-Sb-S (CZAS) type of thin films, which is a modification of CAS films, on an FTO substrate.

2. Experiments

Electrodeposition of Cu-Zn-Sb Thin Films and Subsequent Sulfurization. Thin CZAS films were electrochemically grown on a fluorinated tin oxide (FTO) substrate using a bath containing ions of interest (Cu^{2+} , Zn^{2+} , and Sb^{3+}). Coelectrodeposition was done using a 3-electrode cell connected to Gamry Instruments Reference 600 potentiostat operated by Virtual Front Panel software. For synthesis of zinc-copper-antimony alloy thin as-deposited film, we utilized 50 mL of electrolyte containing copper sulfate pentahydrate, zinc sulfate, and antimony trichloride. It was reported that an excess of antimony is required in order to produce famatinite with low CuS [1, 5]. In light of this information, three different experiments were conducted for synthesis of as-deposited film (sample 1: 0.016 M $\text{CuSO}_4 \cdot 5\text{H}_2\text{O}$, 0.043 M SbCl_3 , 0.062 M ZnSO_4 ; sample 2: 0.016 M $\text{CuSO}_4 \cdot 5\text{H}_2\text{O}$, 0.0172 M SbCl_3 , 0.094 M ZnSO_4 ; sample 3: 0.016 M $\text{CuSO}_4 \cdot 5\text{H}_2\text{O}$, 0.062 M SbCl_3 , 0.038 M ZnSO_4). The pHs of these baths were 1.57, 2.3, and 1.9, respectively. To mitigate preferential electroplating, potassium sodium tartrate was used as a complexing or chelating agent. It is a very common method to modify the electrode potential of different metal ions closure in the electrolyte (or plating solution) by conversion of simple ions into complex ions [9]. The electrodepositions were carried out at ~-1.6 V. Time of electrodeposition was limited to ~160–180 s, in order to obtain 1–1.5 μm thick as-deposited film. The precursor's films were annealed (duration ~2 h) in an evaporated sulfur environment to get CZAS thin film. Sulfurization was carried out in a tube furnace (temperature ~450°C), in an argon environment. Photoelectrochemical study was conducted using a Gamry PCI4/750 Potentiostat and a three-electrode system containing CZAS electrode, saturated calomel reference electrode (SCE), and a platinum

counter electrode, which were immersed in an aqueous solution of 0.07 M $\text{Eu}(\text{NO}_3)_3 \cdot 6\text{H}_2\text{O}$. The advantages of europium nitrate have been discussed elsewhere [10]. To examine the photoelectrochemical responses of the CZAS films, the change in transient photocurrents was monitored, which were generated during alternating illumination from a high-intensity white light optical illuminator.

2.1. Film Characterization. Thin films were investigated by X-ray diffraction (XRD), scanning electron microscopy (SEM), X-ray photoelectron spectroscopy (XPS), Raman spectroscopy, and UV-Vis spectroscopy, in order to evaluate phase and structure, oxidation state, and morphological features. XRD patterns were obtained using a Philips X'Pert XRD diffractometer with Cu $K\alpha$ radiation over the 2θ range 20–80°. For high resolution, small step sizes and a receiving slit size of 1/8° were used. SEM was performed using an FEI Quanta 600 scanning electron microscope. Raman spectra were obtained by using an R 3000 QE portable Raman spectrometer (made by Raman Systems). A 785 nm laser with a power of ~140 mW was used for excitation. Optical transmittance measurements were performed using an Ocean Optics spectrophotometer equipped with OOI Base 32 software. X-ray photoelectron spectroscopy (XPS) measurements were carried out using the monochromatic $\text{AlK}\alpha$ source equipped Kratos Axis Ultra DLD instrument. The spot size was ~400 μm , dwell time was ~200 ms, and step size was kept ~1 eV.

3. Results and Discussion

Figures 1(a) and 1(b) show the X-ray diffractograms of CZAS thin films deposited on FTO substrate. It can be seen that apart from main characteristics peaks, SnO_2 peaks are also prominent in this diffractogram for sample from experiment 1 (see Figure 1(a)). This diffraction analysis suggests the presence of famatinite CAS (strong peaks at ~28.67° and 33.7°) as well as peak at ~56° [1]. Sample 2 shows one distinct peak at ~29.7° and two low-intensity peaks at ~34° and 50°, respectively. These peaks closely match with diffraction pattern of tetrahedrite [3, 11]. Sample 3 shows almost amorphous behavior; hence, most of the analysis was focused on sample 1 and sample 2. Further investigation was also conducted to confirm phase and purity of these samples. We have synthesized some films with a relatively high amount of antimony; hence, the possibility of binary sulfide will be investigated in XPS analysis.

Raman spectra of thin films are shown in Figure 2. It can be seen that for sample 1, two distinct peaks at ~335 and 365 cm^{-1} are present. For sample 2 an intense peak was found at ~362 cm^{-1} . Sample 3 shows a low-intensity peak at ~305 cm^{-1} . For reference and comparison, we have investigated Raman spectra of copper antimony chalcogenide minerals [12]. It was found from the literature that chalcostibite shows a strong Raman peak at ~337 cm^{-1} , tetrahedrite at ~351 cm^{-1} , and famatinite at ~333 cm^{-1} (strong peak), 283 and 369 cm^{-1} (low-intensity peak) [12]. Based on these values and our observation it can be said that experiment 1 results in

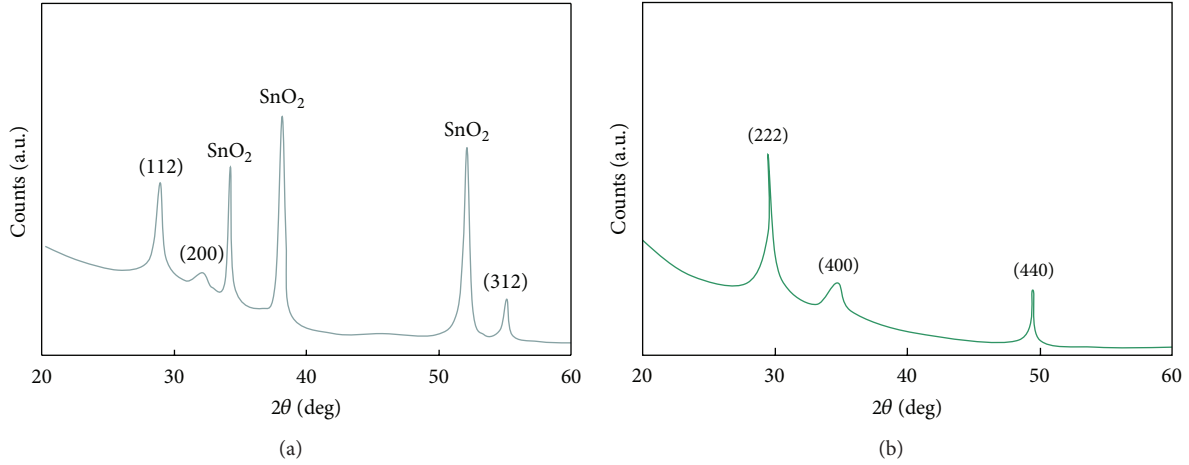


FIGURE 1: X-ray diffraction pattern of modified copper antimony sulfide thin film: (a) sample 1; and (b) sample 2.

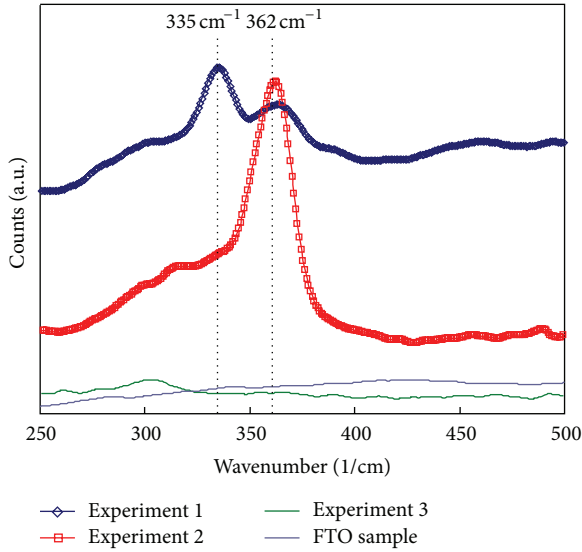


FIGURE 2: Raman spectra of copper antimony sulfide thin films of different stoichiometry and FTO coated glass sample.

the formation of famatinite phase. It was observed that our Raman peaks show a shift (from the standard peak position of undoped Cu_3SbS_4) towards higher frequency for CZAS film. Such an observation can be explained. Analysis of Bilbao Crystallographic Server suggests that for famatinite, A_1 mode is Raman active and strong, very similar to that for a kesterite crystal structure [13, 14]. For a structurally similar compound, CZTS, it was reported that A_1 symmetry mode, which is a vibrational mode, shift in the frequencies of these peaks is only due to different force constants $f_{\text{M-S}}$ and free from change in reduced mass effects [15]. The larger force constant generally results in higher Raman frequencies. Famatinite is a class I-V-VI type of semiconductor and it crystallizes in an ordered sphalerite superstructure with a $\bar{1}42m$ space group with lattice parameters $a = b = 5.391 \text{ \AA}$ and $c = 10.764 \text{ \AA}$ [1]. In randomly substituted CAS: Zn solid solution, zinc

occupies a copper position in the lattice [5, 6]. Hence, there is a possibility of new Zn-S bonds in a lattice. As the mass of zinc is greater than copper, which indicates $f_{\text{Zn-S}} > f_{\text{Cu-S}}$, hence, it results in the shifting of a strong Raman peak. It is very likely that the strong Raman peak from sample 2 is characteristic of a tetrahedrite peak, which is possibly shifted due to stoichiometry modifications. Such modification often causes a change in bonding interaction. Both samples 1 and 2 were prepared from the electrochemical bath containing similar concentrations of copper but bath 1 contained a relatively low amount of zinc. Sample 2 contains high zinc, hence, more shift in Raman peak position is expected. Raman spectra of samples were also compared with standard samples of Sb_2S_3 from the database. It was concluded that the presence of Sb_2S_3 results in strong peaks at ~ 270 and 305 cm^{-1} [12], however, we did not observe strong peaks at these wavenumbers for samples 1 and 2. Such observation also eliminates the possibility of enhanced presence of Sb_2S_3 for samples 1 and 2. On the other hand, sample 3 shows a low-intensity peak at $\sim 306 \text{ cm}^{-1}$, which indicates the presence of antimony sulfide. This investigation also suggests that there is less possibility of $\beta\text{-Cu}_3\text{SbS}_3$ as there is an absence of a strong peak at $\sim 321 \text{ cm}^{-1}$ [16]. It is essential to note that sample 1 (famatinite rich film doped with zinc) and sample 2 (tetrahedrite rich film doped with zinc) are more photoactive. The formation of Cu_3SbS_3 (famatinite) at 400°C is more spontaneous compared to CuSbS_2 , Cu_2S , and Sb_2S_3 [17]. It was concluded that the formation of Cu_3SbS_3 and CuSbS_2 from the parent elements is more favorable rather than from secondary sulfide phase [5, 6, 17]. The formation of famatinite from tetrahedrite is also spontaneous and remains up to temperature $\sim 770^\circ\text{C}$. It is important to mention that no strong Raman peaks of FTO were obtained in Raman spectra of CZAS film. In contrast, very strong peaks, which correspond to FTO, were observed in XRD. An investigation of FTO coated glass sample suggests that its Raman intensity is very low compared to CZAS coated sample (see Figure 2). In this situation there are various Raman peaks of FTO between 250 and 500 cm^{-1} , although they are not visible in CZAS spectra.

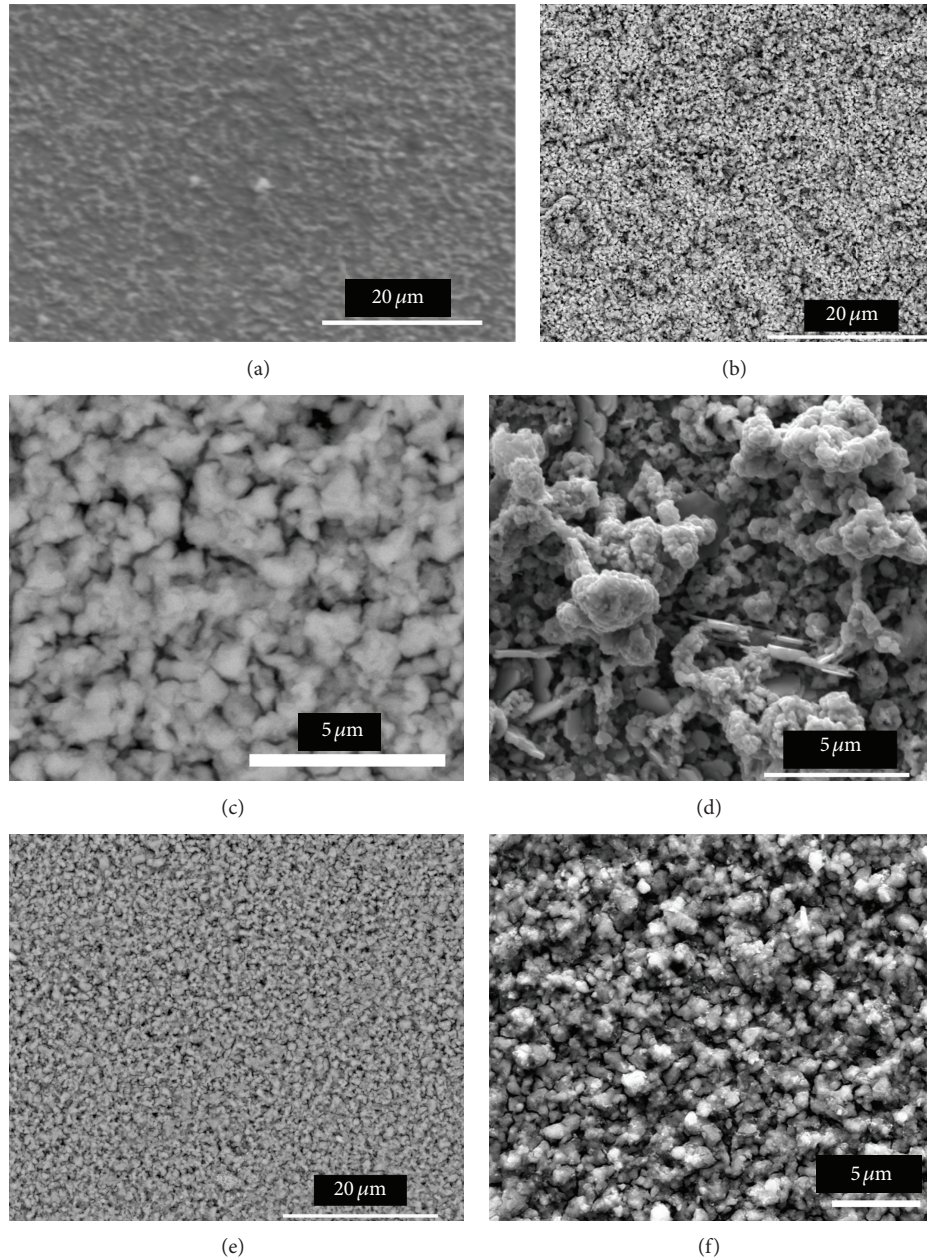


FIGURE 3: Scanning electron micrograph of modified copper antimony sulfide coated substrate: (a) low-magnification image of sample 1, (b) low-magnification image of sample 1 (different area), (c) high-magnification image of sample 1, (d) high-magnification image of sample 1 showing flower-like structures, (e) low-magnification image of sample 2, and (f) high-magnification image of sample 2.

The SEM images of CZAS samples are shown in Figures 3(a)–3(f). KCN etching was not performed in any of our samples presented and evaluated in this report. A low-magnification SEM image (sample 1) suggests that CZAS film forms over the entire FTO substrate (see Figure 3(a)). No peel or cracking is observed. Figure 3(b) shows an image from another area, which suggests that film is rough. It also can be seen that film contains a spherical-globular type of grains in most places. Grain size of film extends from 500 nm to 1 μm . High-resolution imaging (Figure 3(c)) suggests that most of the grains are adjacent to each other

and in many cases they form clusters of grains. Another high-resolution image (Figure 3(d)) suggests that thin film from sample 1 contains flake- and flower-like crystals. The average diameters for these crystals are ~ 100 nm. A low-magnification image (Figure 3(e)) of sample 2 suggests that grains are more uniform compared to sample 1. Although most of the grains and film composition are uniform, at some places a few grains with different texture (Figure 3(f)) can be seen. Such texture indicates the possibility of secondary phase traces. It can be observed that most portions of the film are crack free; however, some pinholes are present. Such an

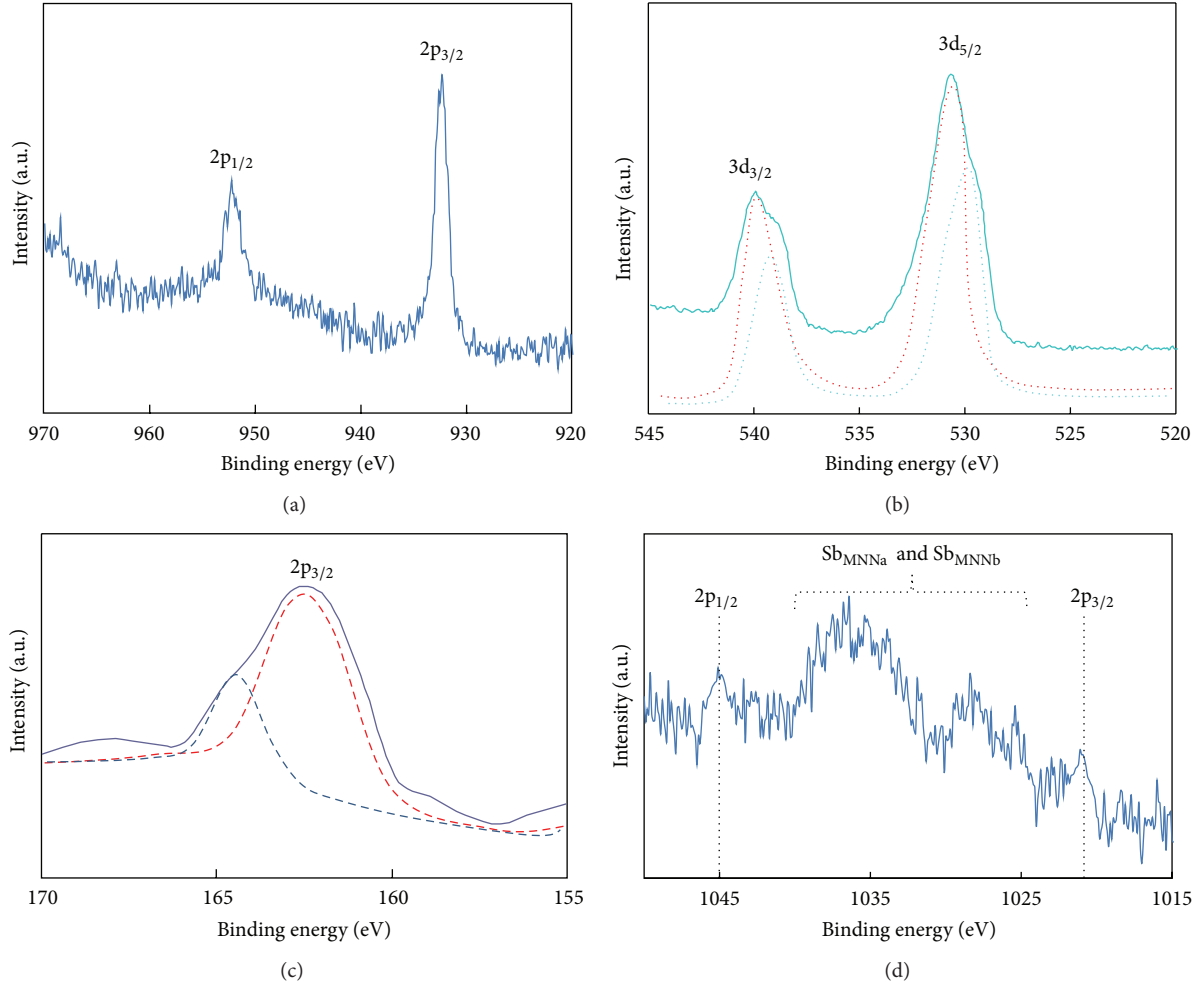


FIGURE 4: X-ray photoelectron spectroscopy of sample 1: (a) Cu 2p peaks, (b) Sb 3d doublet, (c) S 2p peaks, and (d) Zn 2p doublet.

observation suggests that zinc has a significant effect on film morphology, which subsequently affects device performance. Recent investigation by Warren et al. [18] indicates that high photon to current efficiency can be due to many factors, but spatial distribution of current carrying domains in the crystals plays an important role. It is very likely that high-structural complexity results in high photocurrent.

Sample showing highest photocurrent response (from experiment 1) was chosen for XPS analysis. A 2p doublet for copper at 932.3 and 952.1 eV ($2p_{3/2}$ and $2p_{1/2}$) was separated by a gap of 19.8 eV (see Figure 4(a)). These positions and gap are indications of the Cu(I) oxidation state [19, 20]. We did not observe any satellite peaks, which correspond to the Cu(II) oxidation state. The antimony lines are found at 530.8 and 540 eV (see Figure 4(b)) and are separated with a gap of 9.2 eV, which perfectly matches with 3d doublet ($3d_{5/2}$ and $3d_{3/2}$) [19]. Careful observation indicates that each of these peaks is overlapped with peaks at 529.6 and 539 eV. This observation suggests the presence of Sb(III) oxidation state. It was reported that a controlled sample of amorphous Sb_2S_3 also shows peaks at very similar positions ~ 529.60 and 538.97 eV [21]. A shift towards higher binding energy was

found which indicates that Sb is present in the form of Sb^{5+} . It suggests the presence of $A_3B^IVX_4$ type crystal structure. One of the doublets (Figure 4(c)) of S 2p perfectly matches with the reported value of $2p_{1/2}$ at ~ 162.9 eV [19]. The S 2p line also shows asymmetry, which is due to spin orbit coupling. In XPS spectra Zn 2p doublet (see Figure 4(d)) was observed at ~ 1022 eV ($2p_{3/2}$) and 1045 eV ($2p_{1/2}$), which was consistent with the standard splitting ~ 22.9 eV. It suggests Zn(II) oxidation state [19]. Elemental analysis suggests that the atomic ratio of Cu : Zn : Sb : S is 1.18 : 0.40 : 1.90 : 7.2.

The optical properties of CZAS thin films (samples 1 and 2) were analyzed using Ultra Violet-Visible optical transmission spectroscopy. The transmittance of a CZAS film was examined as a function of wavelength. Using the transmittance data from the absorption spectra, the energy gap of thin film can be determined as follows:

$$\alpha = A(h\nu - E_g)^{1/2}, \quad (1)$$

where α is the absorption coefficient, A is a constant, $h\nu$ is the incident photon energy, and E_g is the energy gap. Figure 5 shows squared absorption coefficient and incident

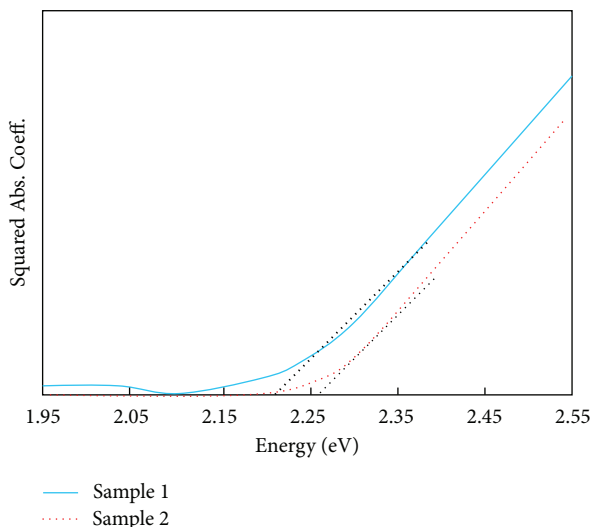


FIGURE 5: (α^2) versus photon energy $h\nu$ for CZAS films.

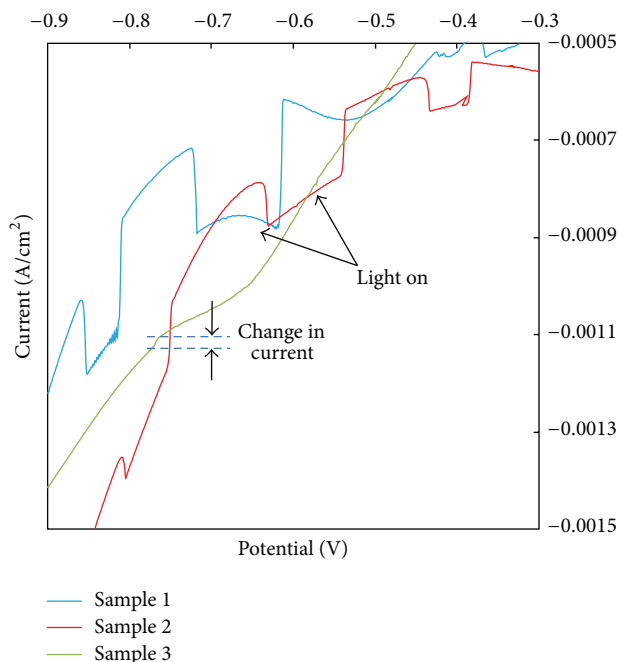


FIGURE 6: Photoelectrochemical response of CZAS thin films (grown on FTO substrate), immersed in europium nitrate electrolyte solution.

photon energy relationship for CZAS films, deposited on FTO coated glass. By extrapolating the squared absorption coefficient versus photon energy curve to zero, the band gap was evaluated to be ~ 2.20 eV (sample 1) and ~ 2.25 eV (sample 2).

The current density potential plots obtained after photoelectrochemical examination for three different samples are shown in Figure 6. J - V curves were recorded during white LED illumination (incident illuminance on substrate $\sim 3.2 \times 10^4$ lux at wavelength of ~ 550 nm) and in the dark.

The photocurrent was recorded during chopping illumination and change in photocurrent was evaluated for relative photovoltaic performance. The highest photoelectrochemical response of the film (experiment 1) is ~ 0.15 mA. The dark current was very insignificant up to the biased potential of ~ -0.6 V (SCE) but started increasing beyond a potential ~ -0.7 V. It should be noted that this photocurrent response is relatively high (~ 1.7 times greater), compared to earlier reported values [2, 7]. Sample 2, which was prepared from the bath of depleted antimony and high zinc, showed a relatively low current response. Highest current response for this sample was ~ 0.08 mA, which is approximately half of the first sample. The lowest current response (overall) was obtained for sample 3, which contains the highest level of antimony. Dark current for this sample was also higher. The high photocurrent response from sample 1 can be explained based on the presence of a more stable crystalline phase, structural complexity, relatively low-band gap of film, and more uniform and interconnected grains. On the other hand, sample 2 shows some secondary phase traces on SEM, which can create a trap or recombination centers throughout the film volume. Such a phenomenon may diminish the photovoltaic performance. Another possibility of reduced photoelectrochemical performance of sample 2 is a relatively high band gap, compared to sample 1. More analysis such as simulations using density functional theory tools and finite-difference time-domain methods are required to explain such behavior in detail. This work is in progress.

4. Conclusions

In summary, modified copper antimony sulfide thin films were synthesized using electrochemical growth of “Cu-Sb-Zn” alloy and subsequent elevated temperature sulfurization. These films were investigated for phase and structural analyses as well as for photoelectrochemical performance. Raman and XRD characterizations suggest that film grown on sample 1 is a famatinite rich, while sample 2 contains a tetrahedrite rich film. High-zinc content results in the strengthening of the force constant which subsequently causes shifting of the Raman peak towards higher frequency. The band gap of the film deposited on sample 1 (moderate antimony) was ~ 2.20 eV, whereas band gap of the sample 2 (zinc rich film) was ~ 2.25 eV. Thin film synthesized from an electrochemical bath containing a moderate level of antimony chloride, shows the highest photocurrent response. However, film from bath with excess antimony exhibits very poor photoelectrochemical response. Enhanced photoelectrochemical response of the modified CAS film was explained on the basis of a more stable crystalline phase, a low-band gap of film, and more uniform-interconnected grains.

References

- [1] J. V. Embden and Y. Tachibana, “Synthesis and characterisation of famatinite copper antimony sulfide nanocrystals,” *Journal of Materials Chemistry*, vol. 22, no. 23, pp. 11466–11469, 2012.

- [2] C. Yan, Z. Su, E. Gu et al., "Solution-based synthesis of chalcocite (CuSbS_2) nanobricks for solar energy conversion," *RSC Advances*, vol. 2, no. 28, pp. 10481–10484, 2012.
- [3] C. An, Y. Jin, K. Tang, and Y. Qian, "Selective synthesis and characterization of famatinite nanofibers and tetrahedrite nanoflakes," *Journal of Materials Chemistry*, vol. 13, no. 2, pp. 301–303, 2003.
- [4] Y. J. Wang, H. Lin, T. Das, M. Z. Hasan, and A. Bansil, "Topological insulators in the quaternary chalcogenide compounds and ternary famatinite compounds," *New Journal of Physics*, vol. 13, no. 8, Article ID 085017, 2010.
- [5] K. Tatsuka and N. Morimoto, "Tetrahedrites stability relations in the Cu-Fe-Sb-S system," *American Mineralogist*, vol. 62, pp. 1101–1109, 1977.
- [6] R. O. Sack and R. R. Loucks, "Thermodynamic properties of tetrahedrite-tennantites: constraints on the interdependence of the $\text{Ag} \rightleftharpoons \text{Cu}$, $\text{Fe} \rightleftharpoons \text{Zn}$, $\text{Cu} \rightleftharpoons \text{Fe}$, and $\text{As} \rightleftharpoons \text{Sb}$ exchange reactions," *American Mineralogist*, vol. 70, no. 11–12, pp. 1270–1289, 1985.
- [7] D. Colombara, L. M. Peter, K. D. Rogers, J. D. Painter, and S. Roncallo, "Formation of CuSbS_2 and CuSbSe_2 thin films via chalcogenisation of Sb-Cu metal precursors," *Thin Solid Films*, vol. 519, no. 21, pp. 7438–7443, 2011.
- [8] S. C. Riha, S. J. Fredrick, J. B. Sambur, Y. Liu, A. L. Prieto, and B. A. Parkinson, "Photoelectrochemical characterization of nanocrystalline thin-film $\text{Cu}_2\text{ZnSnS}_4$ photocathodes," *ACS Applied Materials and Interfaces*, vol. 3, no. 1, pp. 58–66, 2011.
- [9] L. J. Durney, *Graham's Electroplating Handbook*, Springer, New York, NY, USA, 1984.
- [10] P. K. Sarswat and M. L. Free, "An evaluation of depletion layer photoactivity in $\text{Cu}_2\text{ZnSnS}_4$ thin film," *Thin Solid Films*, vol. 520, no. 13, pp. 4422–4426, 2012.
- [11] X. Lu and D. T. Morelli, "Natural mineral tetrahedrite as a direct source of thermoelectric materials," *Physical Chemistry Chemical Physics*, vol. 15, no. 16, pp. 5762–5766, 2013.
- [12] <http://rruff.info> (data base).
- [13] M. I. Aroyo, A. Kirov, C. Capillas, J. M. Perez-Mato, and H. Wondratschek, "Bilbao crystallographic server. II. Representations of crystallographic point groups and space groups," *Acta Crystallographica A*, vol. 62, no. 2, pp. 115–128, 2006.
- [14] P. K. Sarswat, M. L. Free, and A. Tiwari, "Temperature-dependent study of the Raman A mode of $\text{Cu}_2\text{ZnSnS}_4$ thin films," *Physica Status Solidi B*, vol. 248, no. 9, pp. 2170–2174, 2011.
- [15] C. Huang, Y. Chan, F. Liu et al., "Synthesis and characterization of multicomponent $\text{Cu}_2(\text{Fe}_x\text{Zn}_{1-x})\text{SnS}_4$ nanocrystals with tunable band gap and structure," *Journal of Material Chemistry A*, vol. 1, no. 17, pp. 5402–5407, 2013.
- [16] A. Pfitzner, " $(\text{CuI})_2\text{Cu}_3\text{SbS}_3$: copper iodide as solid solvent for thiometalate ions," *Chemistry*, vol. 3, no. 12, pp. 2032–2038, 1997.
- [17] J. R. Craig and W. R. Lees, "Thermochemical data for sulfosalt ore minerals: formation from simple sulfides," *Economic Geology*, vol. 67, no. 3, pp. 373–377, 1972.
- [18] S. C. Warren, K. Voitchovsky, H. Dotan et al., "Identifying champion nanostructures for solar water-splitting," *Nature Materials*, vol. 12, pp. 842–849, 2013.
- [19] "NIST X-ray Photoelectron Spectroscopy Database, Version 4.1," National Institute of Standards and Technology, Gaithersburg, <http://srdata.nist.gov/xps/>, 2012.
- [20] P. K. Sarswat and M. L. Free, "Utility of by-product quantum dots obtained during synthesis of $\text{Cu}_2\text{ZnSnS}_4$ colloidal ink," *Ceramics International*, 2013.
- [21] H. Yang, M. Li, L. Fu, A. Tang, and S. Mann, "Controlled assembly of Sb_2S_3 nanoparticles on silica/polymer nanotubes: insights into the nature of hybrid interfaces," *Scientific Reports*, vol. 3, no. 1336, 2013.

Research Article

C-V Calculations in CdS/CdTe Thin Films Solar Cells with a $\text{CdS}_x\text{Te}_{1-x}$ Interlayer

A. Gonzalez-Cisneros, F. L. Castillo-Alvarado, J. Ortiz-Lopez, and G. Contreras-Puente

Escuela Superior de Física y Matemáticas-IPN, Edificio 9 U.P.A.L.M., 07738 México, DF, Mexico

Correspondence should be addressed to A. Gonzalez-Cisneros; omeyotl@gmail.com

Received 3 June 2013; Accepted 9 August 2013

Academic Editor: Francesco Bonaccorso

Copyright © 2013 A. Gonzalez-Cisneros et al. This is an open access article distributed under the Creative Commons Attribution License, which permits unrestricted use, distribution, and reproduction in any medium, provided the original work is properly cited.

In CdS/CdTe solar cells, chemical interdiffusion at the interface gives rise to the formation of an interlayer of the ternary compound $\text{CdS}_x\text{CdTe}_{1-x}$. In this work, we evaluate the effects of this interlayer in CdS/CdTe photovoltaic cells in order to improve theoretical results describing experimental C-V (capacitance versus voltage) characteristics. We extended our previous theoretical methodology developed on the basis of three cardinal equations (Castillo-Alvarado et al., 2010). The present results provide a better fit to experimental data obtained from CdS/CdTe solar cells grown in our laboratory by the chemical bath deposition (for CdS film) and the close-spaced vapor transport (for CdTe film) techniques.

1. Introduction

Polycrystalline solar cells based on the thin films technology are outstanding candidates for an aggressive expansion of the photovoltaic industry. During the past few years, despite the world economic recession, the photovoltaic market has continued to grow. In Europe and Asia, the market has expanded from the Mega Watt (MW) to the Giga Watt (GW) scale. PV installations grew to 7.3 GW in 2009, which represents 20% from the previous year. The various forecast scenarios predict an increase in the demand from 15.4 to 37 GW in 2014, more than five times the size of the 2009 market [1, 2]. Today, there is much interest and research activity concerning second generation solar cells based on polycrystalline cadmium telluride CdTe thin films and cadmium sulfide CdS as “window” layer. Capacitance versus voltage is one of the most important techniques for the device characterization. In this work, we extend the theoretical model used in a previous paper [3] in order to take into account the formation of a layer of the ternary compound $\text{CdS}_x\text{Te}_{1-x}$ (x , the concentration) at the CdS/CdTe interface generated by interdiffusion processes [4]. During manufacturing of these solar cells, the CdTe/CdS interface is subjected to relatively high

temperatures giving rise to atomic interdiffusion and the formation of an interfacial region of composition $\text{Cd}_x\text{Te}_{1-x}$. The understanding of this ternary $\text{CdS}_x\text{Te}_{1-x}$ interlayer will help to conceive improvements in the efficiency of the photovoltaic cell. In this work, we use a C-V theoretical method for the determination of the interface charge density σ in the CdS/ternary/CdTe heterojunction and the band discontinuity ΔE_v , simultaneously. The methodology is based on three cardinal equations as discussed in the theory below. For comparison with our calculations, we used solar cells of maximum efficiency (12.4%) fabricated in our group [5].

2. Theoretical Method

We present the methodology for the simultaneous calculations of the valence band offset ΔE_v and the interface charge density σ . It is assumed that these two quantities are independent of the bias voltage. This assumption is justified because we are interested in heterojunctions with fixed defect densities.

The clue for obtaining the energy bands at both sides of the interfaces are (a) the two interfacial potentials (φ_{s1} , φ_{s2}

which give the band bending at each side of the interface), (b) the energy increment of the valence band, and (c) the interface charge density. In addition to these, three cardinal equations originating from the displacement of the band line-up equation, charge neutrality, and the total capacitance of the interface are necessary. This method makes no use of any approximations and provides simultaneous determination of the discontinuities of the valence band and the interfacial charge density.

Assuming that the heterojunction is like a parallel plate capacitor, the capacitance-voltage characteristics for low bias voltages V_a are given by

$$C = \left[\frac{q\epsilon_{S1}\epsilon_{S2}N_dN_a}{2(\epsilon_{S1}N_a + \epsilon_{S2}N_d)} \right]^{1/2} * (V_d - V_a)^{-1/2}, \quad (1)$$

where V_d is the potential well in the heterojunction, V_a is the bias voltage, q is the electron charge, N_a is the acceptor concentration, N_d is the donor concentration, and ϵ_{S1} and ϵ_{S2} are the dielectric constants of n-type and p-type semiconductor [6]. Therefore, in our case, we have a linear dependence of $1/C^2$ versus V_a close to $V_a = 0$. We solve numerically the band energy in any site of the heterojunction using the interface according to the experimental data [7]; the spectral response of champion CdS/CdTe solar cells has an increase in a photon energy close to the band gap CdS. Thus, we have assumed in our equations that the physical properties of the ternary compound are closer to those of CdS for each part of the ternary compound, which are the total bending on each side of the two heterojunction ($\text{CdTe}/\text{CdS}_x\text{Te}_{1-x}$).

We note that the total band curvature at each side of the interface depends on the bias voltage V_a , that is, $\varphi_{S1}(V_a)$ and $\varphi_{S2}(V_a)$. We assume that the discontinuities of the valence band and the charge density at the interface are independent of the applied voltage, which is a usual assumption for low voltages. Validity of this assumption is validated by a good agreement with experiment.

Because there are a fixed equal number of separated positive and negative charges at the interface between different materials, we consider that the region of spatial charge behaves like a parallel plate capacitor.

2.1. Cardinal Equations for the $\text{CdTe}/\text{CdS}_x\text{Te}_{1-x}$ Interface (C-V Matching Method). The band line-up equation in this case is (Figure 1)

$$E_{FV1} - E_{FV2} - \Delta E_{V(\text{ternary})} - qV_a = q[\varphi_{S2}(V_a) - \varphi_{S1}(V_a)], \quad (2)$$

where “ x ” is the ternary concentration and E_{FV1} and E_{FV2} are the differences between the quasi-Fermi energy levels with subscripts 1 and 2 corresponding to CdTe and $\text{CdS}_x\text{Te}_{1-x}$,

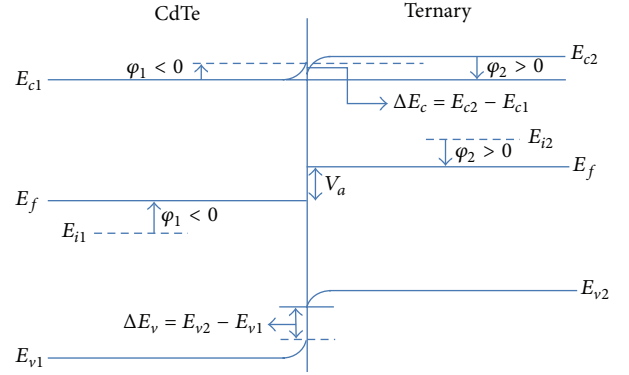


FIGURE 1: Energy band (band lineup) diagram of two n-p heterojunctions under reversible bias. The reference level for the potential of each semiconductor is at the intrinsic energy level. We assume that the ternary behaves like an n-type semiconductor for union with CdTe.

respectively. The valence band offset $\Delta E_{V(\text{ternary})}$ and the respective bulk valence band levels are given by

$$E_{FV1} = E_{Fn1} - E_{V1} = \frac{E_{g1}}{2} + \frac{3}{4}kT \ln \left(\frac{m_{h1}^*}{m_e^*} \right) - q\varphi_{F1}, \quad (3)$$

$$E_{FV2} = E_{Fp2} - E_{V2} = \frac{E_{g2}}{2} + \frac{3}{4}kT \ln \left(\frac{m_{h2}^*}{m_e^*} \right) - q\varphi_{F2}.$$

The separation between the quasi-Fermi energy levels is determined for the bias voltage:

$$E_{Fn1} = E_{Fp2} + qV_a, \quad (4)$$

where V_a is the bias voltage in the p-n junction.

The charge neutrality equation under nonequilibrium is given by

$$Q_1 [\varphi_{S1}(V_a)] + Q_2 [\varphi_{S2}(V_a)] + q\sigma = 0, \quad (5)$$

where the expressions for the semiconductor charge under nonequilibrium, Q_1 and Q_2 , are the half semiconductor charges (per unit area) which are given by [8]

$$Q_1 = \text{sign} [\varphi_{S1}(V_a)] \cdot \frac{\sqrt{2}\epsilon_0\epsilon_{S1}}{\beta L_{D1}} \cdot e^{\Delta u_1/2} \times \{ \varphi_{S1}(V_a) \cdot \sinh(u_1^*) + \cosh[u_1^* - u_{S1}(V_a)] - \cosh(u_1^*) \}^{1/2}, \quad (6)$$

$$Q_2 = \text{sign} [\varphi_{S2}(V_a)] \cdot \frac{\sqrt{2}\epsilon_0\epsilon_{S2}}{\beta L_{D2}} \cdot e^{\Delta u_2/2} \times \{ \varphi_{S2}(V_a) \cdot \sinh(u_2^*) + \cosh[u_2^* - u_{S2}(V_a)] - \cosh(u_2^*) \}^{1/2},$$

where

$$\text{sign} = \begin{cases} +1, & u < 0 \\ -1, & u > 0. \end{cases} \quad (7)$$

Here, $u^* = \beta((\varphi_{F1} + \varphi_{F2})/2)$ and $\beta = q/kT$.

The third cardinal equation is obtained from the expression of the half capacitance per unit area of the device:

$$\frac{1}{C_{\text{CdTe-ter}}} = \frac{1}{C_1 [\varphi_{S1}(V_a)]} + \frac{1}{C_2 [\varphi_{S2}(V_a)]}, \quad (8)$$

where

$$\begin{aligned} C_1 &= \frac{(\epsilon_0 \epsilon_{S1})^2}{\beta L_{D1}^2 \cdot Q_1} \\ &\cdot e^{\Delta u_1/2} \cdot \{\sinh(u_1^*) - \sinh[u_1^* - u_{S1}(V_a)]\} \\ &= \frac{q \epsilon_0 \epsilon_{S1}}{Q_1} \{N_1 + 2n_{i1} \cdot e^{\Delta u_1/2} \cdot \sinh[u_1^* - u_{S1}(V_a)]\}, \\ C_2 &= \frac{(\epsilon_0 \epsilon_{S2})^2}{\beta L_{D2}^2 \cdot Q_2} \\ &\cdot e^{\Delta u_2/2} \cdot \{\sinh(u_2^*) - \sinh[u_2^* - u_{S2}(V_a)]\} \\ &= \frac{q \epsilon_0 \epsilon_{S2}}{Q_2} \{N_2 + 2n_{i2} \cdot e^{\Delta u_2/2} \cdot \sinh[u_2^* - u_{S2}(V_a)]\} \end{aligned} \quad (9)$$

$$\frac{1}{C_{\text{Total}}} \approx \frac{1}{C_{\text{CdTe-ter}}}. \quad (10)$$

It is important to note that the energy gap of the ternary is not a simple linear combination but a more complex function of x [9]:

$$E_g(x) = (1-x)E_g(\text{CdS}) + xE_g(\text{CdTe}) - bx(1-x), \quad (11)$$

where b is the “optical bowing coefficient” given by 1.69 eV and the valence band offset ΔE_V .

3. Results

We find the ternary concentration value of 0.75 with the best fitting of the curve, which is in good agreement with the results described by Cediel et al. [10]. The various quantities or constants in the cardinal equations were taken from the previous paper [3]. We show the result of the C - V fitting method in Figure 2 for a voltage range from 0 to 0.5 V. A much better fit is obtained by assuming the formation of a ternary compound at the CdTe/CdS interface.

In addition, we have also obtained the values of the valence band offset and the interface charge density simultaneously, namely,

$$\begin{aligned} \Delta E_V &= 0.99 \text{ eV}, \\ \sigma &= 1 \times 10^{13} \text{ cm}^{-2}, \end{aligned} \quad (12)$$

which are in good agreement with the reported values [9, 11, 12].

4. Conclusions

In summary, we have calculated the capacitance versus applied voltage of CdS/CdTe thin film solar cells considering

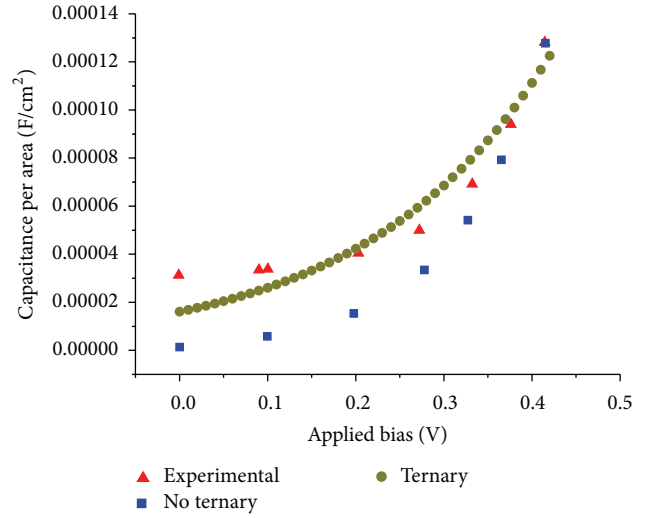


FIGURE 2: Calculated C - V characteristics of a CdTe/CdS PV cell assuming the formation of a ternary compound at the CdTe/CdS interface. Comparison is made with C - V measurements of a 12.4% efficient PV cell [5] and with calculated results within a model without the assumption of the ternary compound at the interface [3].

the formation of a $\text{CdS}_x\text{Te}_{1-x}$ interlayer using the C - V matching method. Our results are in better agreement with experimental data than our previous theoretical results that did not assume the presence of the $\text{CdS}_x\text{Te}_{1-x}$ interlayer. We may also say that the ternary layer acquires the properties of CdS and behaves like the type n semiconductor instead of the CdS itself. This could be taken as evidence of the existence of a ternary compound that plays an important role in solar cell devices. This can be taken as evidence of the existence of the ternary interlayer which plays an important role in the solar cell.

Acknowledgments

F. L. Castillo-Alvarado, J. Ortiz-Lopez, and G. Contreras-Puente gratefully acknowledge fellowships granted by COFAA-IPN, EDI-IPN, and EDD-IPN. This work was partially supported by CONACyT (Mexico).

References

- [1] Manufacturing cost per watt at First Solar falls to US\$0.76cents: Module Faults Hit Earnings, 2011, <http://www.pv-tech.org/news/>.
- [2] M. Osborne, First Solar First to 1GW Annual Production, Photovoltaics, 2009, <http://www.pv-tech.org/>.
- [3] F. L. Castillo-Alvarado, J. A. Inoue-Chávez, O. Vigil-Galán, E. Sánchez-Meza, E. López-Chávez, and G. Contreras-Puente, “ C - V calculations in CdS/CdTe thin films solar cells,” *Thin Solid Films*, vol. 518, no. 7, pp. 1796–1798, 2010.
- [4] M. M. Aliyu, S. Hossain, M. A. Islam et al., “Evaluation of the effects and impacts of the CdS_xTe interlayer in CdS/CdTe solar cells through modeling and simulations,” in *Proceedings of the*

- 2nd International Conference on the Developments in Renewable Energy Technology (ICDRET '12)*, pp. 248–251, January 2012.
- [5] O. Vigil-Galán, A. Arias-Carbajal, and R. Mendoza-Pérez, “Improving the efficiency of CdS/CdTe solar cells by varying the thiourea/CdCl₂ ratio in the CdS chemical bath,” *Semiconductor Science and Technology*, vol. 20, no. 8, p. 819, 2005.
- [6] B. L. Sharma and R. K. Purohit, *Semiconductor Heterojunctions*, Pergamon Press.
- [7] First Solar New Releases, 2011, <http://www.firstsolar.com>.
- [8] R. S. C. Cobbolt, *Theory and Applications of Field Effect Transistors*, Willey, London, UK, 1970.
- [9] S.-H. Wei, S. B. Zhang, and A. Zunger, “First-principles calculation of band offsets, optical bowings, and defects in CdS, CdSe, CdTe, and their alloys,” *Journal of Applied Physics*, vol. 87, no. 3, pp. 1304–1311, 2000.
- [10] G. Cediél, F. Rojas, H. L. Infante, and G. Gordillo, “Determinación de constantes ópticas y simulación teórica del espectro de transmitancia de películas delgadas de CdS, CdTe y Cd(S,Te) depositadas por evaporación,” *Revista Colombiana de Física*, vol. 34, no. 1, 2002.
- [11] A. Balcioglu, F. Hasoon, D. Levi, and R. K. Ahceukiel, “Investigation of deep impurity levels in CdTe/CdS solar cells (2000) (NCPV) program review meeting,” in *N Spu Program Review Meeting Proceeding*, p. 279, 2006.
- [12] S. Vatana, I. Caraman, G. Rasu, V. Fedorov, and P. Gasin, “The study of the nonequilibrium charge carrier transport mechanism through the interface of CdS/CdTe heterojunctions,” *Chalcogenide Letters*, vol. 13, p. 9, 2006.

Research Article

Effect of Hydrogen Content in Intrinsic a-Si:H on Performances of Heterojunction Solar Cells

Yun-Shao Cho,¹ Chia-Hsun Hsu,² Shui-Yang Lien,³ Dong-Sing Wu,¹ and In-Cha Hsieh²

¹ Department of Materials Science and Engineering, National Chung Hsing University, Taichung 402, Taiwan

² Graduate Institute of Precision Engineering, National Chung Hsing University, Taichung 402, Taiwan

³ Department of Materials Science and Engineering, DaYeh University, ChungHua 51591, Taiwan

Correspondence should be addressed to Shui-Yang Lien; syl@mail.dyu.edu.tw

Received 14 June 2013; Accepted 9 August 2013

Academic Editor: Gaetano Di Marco

Copyright © 2013 Yun-Shao Cho et al. This is an open access article distributed under the Creative Commons Attribution License, which permits unrestricted use, distribution, and reproduction in any medium, provided the original work is properly cited.

Influences of hydrogen content in intrinsic hydrogenated amorphous silicon (i-a-Si:H) on performances of heterojunction (HJ) solar cells are investigated. The simulation result shows that in the range of 0–18% of the i-layer hydrogen content, solar cells with higher i-layer hydrogen content can have higher degree of dangling bond passivation on single crystalline silicon (c-Si) surface. In addition, the experimental result shows that HJ solar cells with a low hydrogen content have a poor a-Si:H/c-Si interface. The deteriorate interface is assumed to be attributed to (i) voids created by insufficiently passivated c-Si surface dangling bonds, (ii) voids formed by SiH₂ clusters, and (iii) Si particles caused by gas phase particle formation in silane plasma. The proposed assumption is well supported and explained from the plasma point of view using optical emission spectroscopy.

1. Introduction

The hydrogenated amorphous silicon/crystalline silicon (a-Si:H/c-Si) heterojunction (HJ) solar cell is one of the most interesting technological solutions for the photovoltaic market owing to its excellent performance and also its low processing costs. Some groups have already reported encouraging results for silicon HJ cells with a-Si:H emitters deposited by plasma-enhanced chemical vapor deposition (PECVD) [1]. Recently, efficiencies of up to 23% using PECVD have been demonstrated [2, 3]. In HJ solar cells, the control of the interface between different materials is an important factor for high-cell performances. Particularly, the reduction of carrier recombination at the p/n interface is critical. Extensive studies have also demonstrated that the use of a very thin intrinsic (i-) a-Si:H buffer layer inserted at the interface can minimize the interface recombination and thus increase the efficiency of HJ solar cells [4–6].

In i-a-Si:H deposition, process parameters should be carefully controlled since they determine the film properties. It is found that lowering the deposition temperature tended to raise Si-H₂ bond concentration and thus lowering the dangling bond passivation quality [7]. High temperature can

somewhat lead to partial epitaxial Si growth which contains more defects than amorphous films [8, 9]. Moreover, hydrogen dilution is usually adopted for lowering electron temperature and suppressing poly silane radicals [10, 11]. A moderate dilution ratio is reported to result in a longer effective lifetime of Si wafer [12]. However, the effects of i-layer hydrogen content and plasma status on performances of HJ solar cells are rarely reported.

In this study, the i-layer hydrogen content effect is investigated by computational simulation. Then, we practically fabricate 156 × 156 mm² large-size HJ solar cells with high- and low-hydrogen content to validate the simulation result. Furthermore, the interface quality between i-layer and c-Si in high- and low-hydrogen content cases is discussed from the plasma emission spectra point of view.

2. Experimental

The two-dimensional, commercially available software Silvaco technology computer aided design (TCAD), from Silvaco Inc., was used to solve the Poisson equation coupled with the continuity equations of electrons and holes for virtual devices by dividing the whole structure into finite elements.

TABLE 1: TCAD input parameters for n-Si/i-Si/c-Si HJ solar cells with various hydrogen content of i-layer.

| Device parameters | Value | | | |
|---|---|----------------------|----------------------|----------------------|
| Device area (cm ²) | 1 | | | |
| Front surface | Texture | | | |
| Solar cell structure | n-Si/i-Si/c-Si/BSF | | | |
| Exterior rear reflectance (%) | 90 | | | |
| Light source | One sun (AM 1.5, 100 mW/cm ²) | | | |
| Layer parameter | a-Si:H(n) | a-Si:H(i) | c-Si(p) | Al-BSF |
| Thickness (μm) | 0.01 | 0.005 | 250 | 5 |
| Band gap (eV) | 1.92 | 1.7 | 1.12 | 1.12 |
| Dielectric constant | 11.7 | 11.7 | 11.7 | 11.7 |
| Electron affinity (eV) | 3.9 | 3.9 | 4.05 | 4.05 |
| Electron mobility (cm ² /V ⁻¹ s ⁻¹) | 20 | 20 | 1417 | 200 |
| Hole mobility (cm ² /V ⁻¹ s ⁻¹) | 10 | 10 | 470 | 80 |
| Doping concentration (cm ⁻³) | 1 × 10 ¹⁹ | 1 × 10 ¹⁹ | 1 × 10 ¹⁶ | 1 × 10 ¹⁹ |
| Hydrogen content (%) | — | 0–18 | — | — |

The physical models that we used were Shockley-Read-Hall recombination model and concentration-dependent lifetimes. The photogeneration model including a ray tracing algorithm was used for calculating the transmission and absorption of incident light in the semiconductor layers. The solar cells considered here operate under the global standard solar spectrum (AM1.5G) illumination with 100 mW/cm² total incident power density. The model structure was (n) a-Si:H/(i) a-Si:H/(p) c-Si/aluminum back surface field (Al-BSF). For the individual layer and the a-Si:H/c-Si interfaces, the distributions of defect states are specified. Note that for a-Si:H-related materials, the correct material parameters could be varied subject to their preparation conditions. Table 1 summarizes the main parameters used for calculation including measured and assumed values which can be found elsewhere [13–16]. The correlation between the i-layer hydrogen content and performance indicators of solar cells is calculated.

For HJ solar cell fabrication, the cell structure was Al/indium tin oxide (ITO)/(n) a-Si/(i) a-Si/(p) c-Si/Al-BSF. The boron-doped c-Si wafers with thickness of 250 nm, resistivity of 1–10 Ωcm, and surface texturization were used as a substrate. The sample size was 156 × 156 mm². To form the Al-BSF, a 5 μm Al film was sputtered on the wafer backside followed by annealing at 800°C for 30 s. The deposition of the n-type a-Si:H was done in a PECVD system with the following process parameters: plasma frequency of 27.12 MHz, power density of 37.5 mW/cm², substrate temperature of 200°C, deposition pressure of 90 Pa, SiH₄ flow rate of 40 sccm, and total gases flow rate (PH₃ + SiH₄ + H₂) of 125 sccm. The i-layers with low- and high-hydrogen content were prepared using hydrogen dilution ratios, H₂/SiH₄, of 0 and 8, respectively. Detailed parameters for the i-a-Si:H layers are summarised in Table 2. The thicknesses of n-layer and i-layer were 10 nm and 5 nm, respectively. The ITO with

TABLE 2: Deposition conditions of low-H and high-H.

| Parameter | Value | |
|--------------------------------------|-------|--------|
| | Low-H | High-H |
| Power density (mW/cm ²) | 25 | 25 |
| Pressure (Pa) | 90 | 90 |
| Electrode-to-substrate distance (mm) | 30 | 30 |
| Substrate temperature (°C) | 180 | 180 |
| SiH ₄ flow rate (sccm) | 40 | 40 |
| H ₂ flow rate (sccm) | 0 | 320 |
| Hydrogen content (%) | 6 | 18 |

thickness of 90 nm was formed using sputtering to enhance the lateral conductivity and minimize reflection losses. For i-a-Si:H film properties, Fourier transform infrared (FTIR) spectroscopy was used to determine hydrogen content in the films. The hydrogen content (C_H) was calculated from the integrated intensity of the Si-H rocking/wagging mode at 640 cm⁻¹ in the FTIR spectra using the following formula [17]:

$$C_H = \frac{A_\omega}{N_{Si}} \int_{\omega_r/\omega} \frac{\alpha(\omega)}{\omega} d\omega, \quad (1)$$

where $\alpha(\omega)$ is the absorption coefficient of the film at the wavenumber ω , ω_r/ω stands for the rocking/wagging bands around 640 cm⁻¹. $A_\omega = 1.6 \times 10^{19}$ cm⁻² is the proportionality constant and $N_{Si} = 5 \times 10^{22}$ cm⁻³ is the atomic density of pure silicon. The film thickness was evaluated by an alpha-step profiler (Tencor, alpha-step 500). For HJ solar cells, J-V characteristics were measured under AM1.5G (1 sun, 100 mW/cm²) solar simulator irradiation. External quantum efficiencies (EQE) were measured using a lock-in amplifier with a current preamplifier under short-circuit conditions. The devices were illuminated by monochromatic light from a 150 W xenon lamp passing through a monochromator. A calibrated single crystalline silicon photodiode with known spectral response was used as a reference. The cross-sectional microstructure image was observed by high-resolution transmission electron microscopy (HRTEM). For plasma characterization, optical emission spectroscopy (OES) [18, 19] equipped with a spectra colorimeter was used to collect optical emission spectra of the plasma glowed. The measuring point was near the substrate surface.

3. Results and Discussion

Figure 1 schematically shows the mechanism of passivation of dangling bonds at c-Si surface. Without surface passivation, the dangling bonds act as recombination centers to trap electrons, resulting in a large recombination rate at the a-Si:H/c-Si interface of final HJ solar cells. These dangling bonds can be passivated by H atoms to obtain a relatively high-quality heterojunction. This in turn implies that H content in the i-a-Si:H layer plays a crucial role on the c-Si surface passivation for HJ solar cells. In this study the H content in the i-layer is controlled by adjusting the input hydrogen gas flow rate, and their relationship is shown in Figure 1(b). It can be seen that

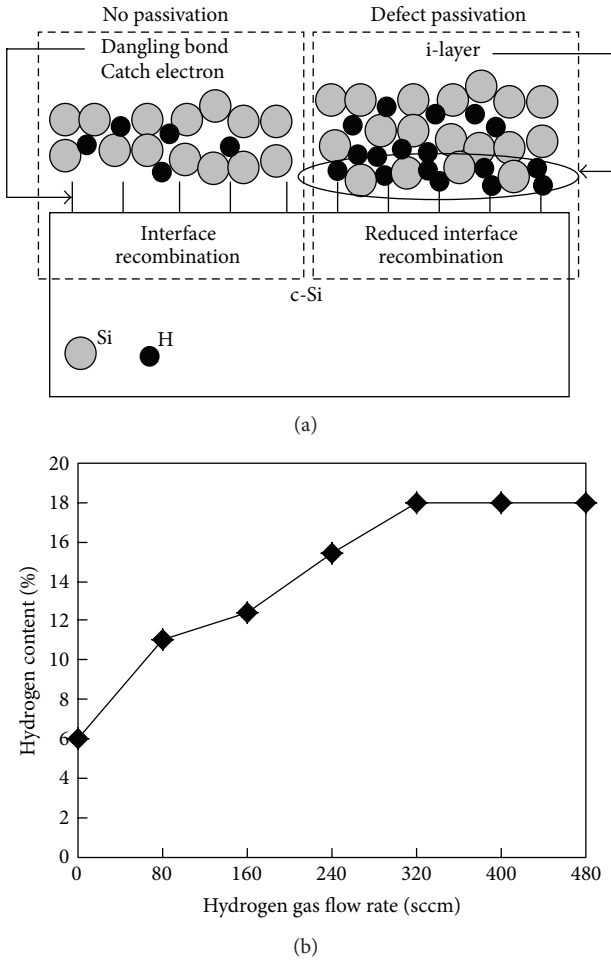


FIGURE 1: (a) Scheme of the mechanism of surface passivation on c-Si. (b) The relationship between hydrogen flow rate and i-layer hydrogen content.

the hydrogen content increases with increasing the hydrogen gas flow rate due to more H atoms incorporated in the i-layer during the deposition process. However, the H content finally saturates to a value of about 18% at the hydrogen flow rate of 320 sccm. According to this result, in TCAD simulation the H content is set to be in the range of 0–18% to investigate its effect on the device performances.

Figure 2 shows the TCAD simulation result of the device external parameters such as open-circuit voltage (V_{oc}), short-circuit current density (J_{sc}), fill factor (FF), and conversion efficiency (η) as a function of the H content in the i-layer. It can be seen that V_{oc} show a strong dependence on the i-layer H content. The pure i-a-Si (H content = 0%) leads to V_{oc} of 0.55 V, while the i-a-Si:H with H content of 6%–12% results in V_{oc} around 0.6 V. Increasing the H content up to 18% further improves the V_{oc} to 0.72 V. The better a-Si:H/c-Si interface passivation with an increase in i-layer H content could decrease the interface defect (dangling bond) density and recombination for carriers that overcome the a-Si:H/c-Si barrier, and thus could be the reason for the increase in V_{oc} with an increase in i-layer H content [20]. J_{sc} and FF also

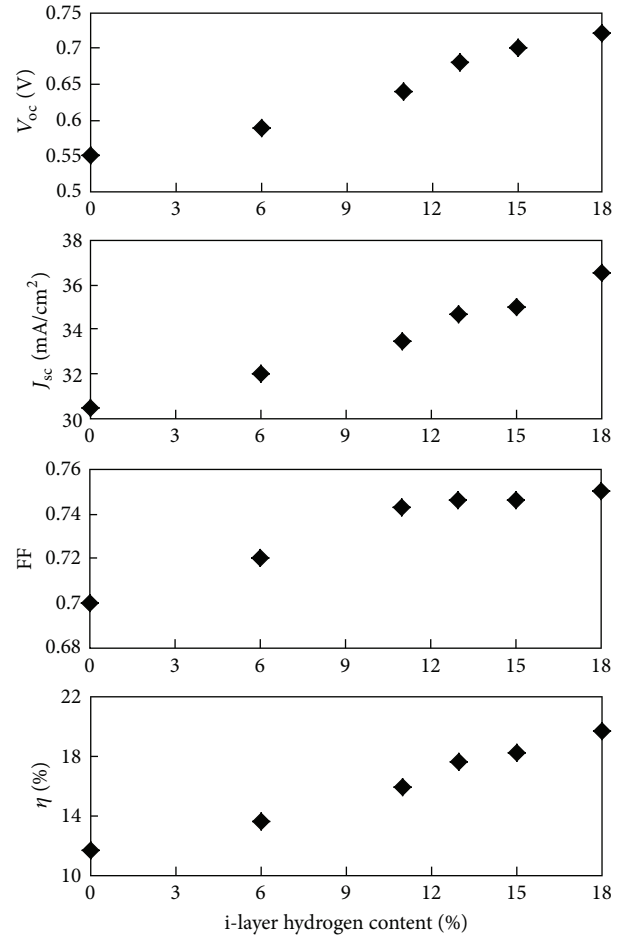


FIGURE 2: Simulation results of the performances of HJ solar cells as a function of the i-layer hydrogen content.

show a similar tendency to that of V_{oc} . Consequently, η can be significantly improved from about 11.7% to 19.7% when the H content increases from 0% to 18%. It is worth pointing out that high-H content i-layer leads to high-cell performances, which agrees well with the proposed mechanism of passivation mentioned above.

To validate the simulation result, experimental tests were carried out. The i-layers with low-H content of 6% and high-H content of 18% were selected for device fabrication. For each type of i-layer, 10 HJ solar cells were fabricated and their performances are quite close to each other with an error of less than 3%. Figure 3(a) illustrates the J-V characteristics of the two types of HJ solar cells. It is observed that the tendency of the experimental result is in good agreement with the simulation data. The high-H cell has better conversion efficiency indicating an improved surface passivation. As compared to the low-H cell, V_{oc} , J_{sc} , and FF are improved by 12.1%, 9.3%, and 9.4%, respectively. This consequently leads to an increase in η by about 34.2%. Note that FF values are slightly lower than the corresponding simulation values since the resistances of Al, ITO, and their interface are not taken into account in the simulation work.

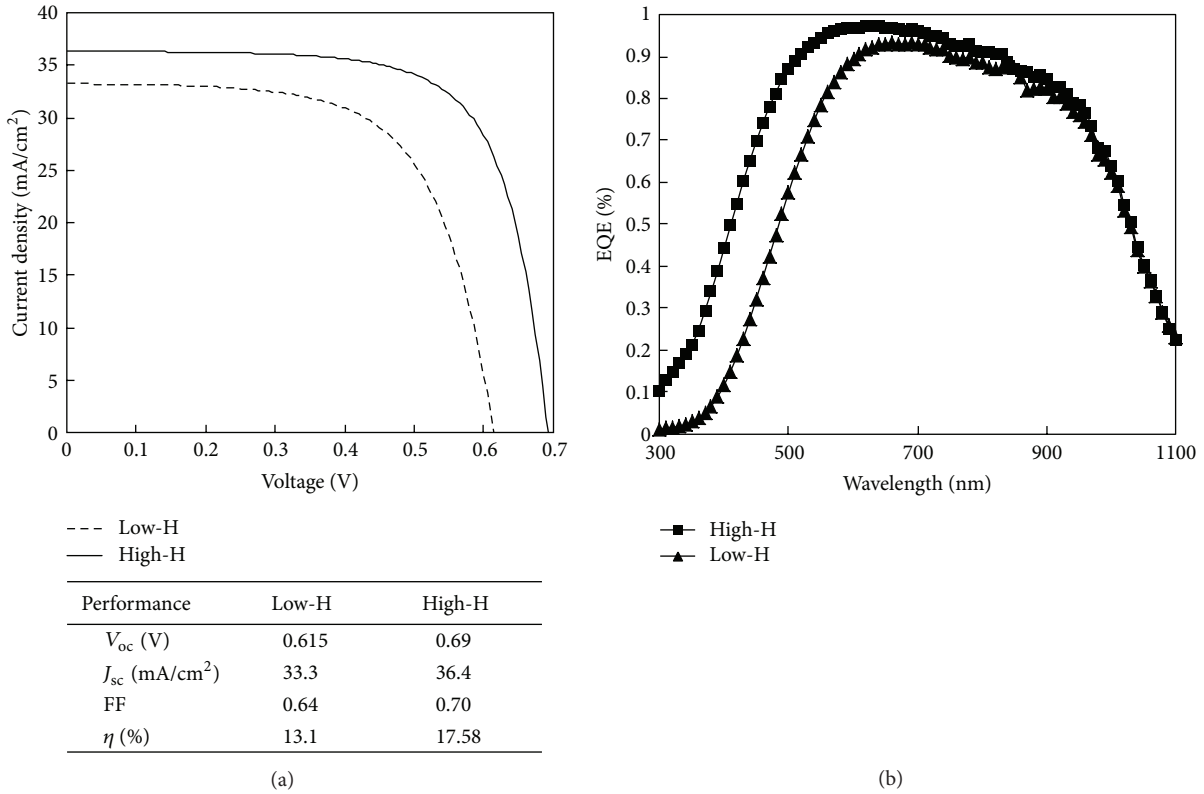


FIGURE 3: Experimental results of (a) J-V characteristics and (b) EQE spectra response for HJ solar cells with different i-layer hydrogen content.

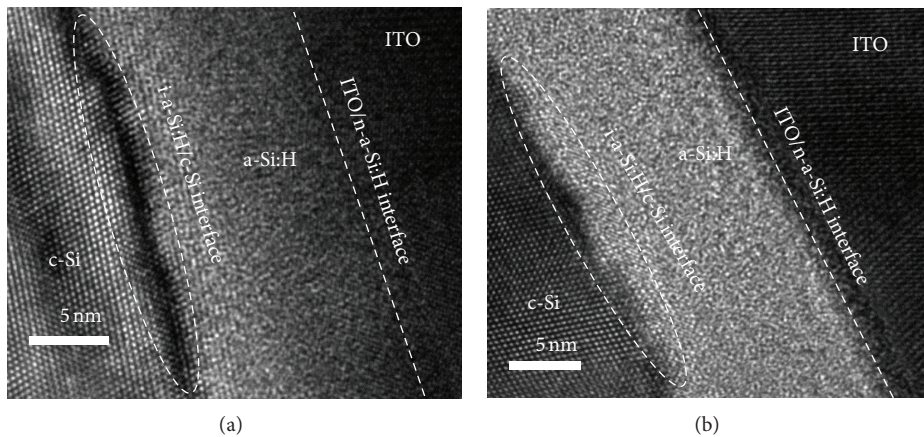


FIGURE 4: HRTEM images of the i-a-Si:H/p c-Si interface for (a) low-H and (b) high-H HJ solar cells.

The J_{sc} of the fabricated low- and high-H solar cells can be investigated by EQE measurement as shown in Figure 3(b). Clearly, the EQE response can be divided into two wavelength regions. First, in the wavelength range of 300 to 700 nm, EQE values of the high-H cell are always higher than these of the low-H cell. Since blue light is absorbed close to the surface, the higher blue portion of EQE reflects a lower surface recombination and thus reflect better collection efficiency of minority carriers. Note that although the absorption of the two a-Si:H layers possibly may not be the same, the

absorption loss due to very thin a-Si:H is trivial and is not one of the factors causing the observed EQE difference. Second, in the wavelength range of 700 to 1100 nm, the EQE values of the two cells become similar, since the light absorption depth in this wavelength range corresponds to deeper region in c-Si and thus irrelevant to the junction properties. The EQE at the wavelength of 1100 nm [21], close to the cut-off wavelength, is still over 20% owing to contributions of surface texturing and back surface field [22]. In summary the EQE result indicates that the higher J_{sc} of the high-H

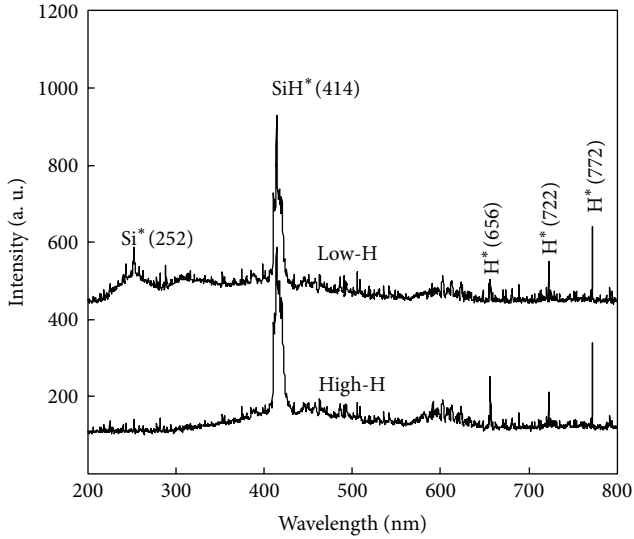
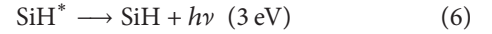
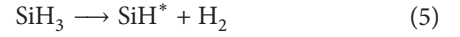
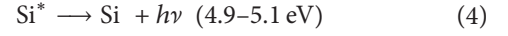
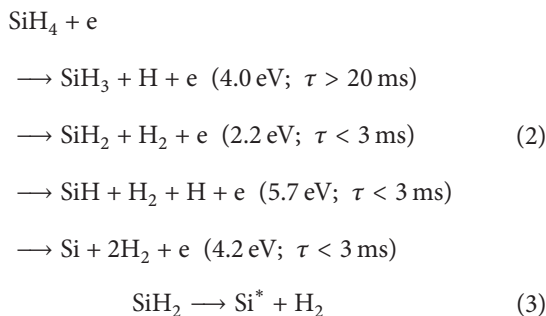


FIGURE 5: Optical emission spectra for the plasmas during low- and high-H i-layer deposition.

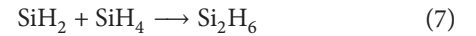
cells, as observed in Figure 3(a), is a consequence of the much higher spectral response in the short wavelengths due to better surface passivation.

The cross-sectional HRTEM images of a-Si:H/c-Si interface in low- and high-H cells are shown in Figures 4(a) and 4(b), respectively. The a-Si:H layer (including i- and n-layer) thickness of about 15 nm can also be evidenced by the TEM images. Interestingly, the low-H interface is deteriorated, whereas the interface region in the high-H case is quite smooth. The poor interface region can be assumed to mainly result from two factors. First, it is likely that the interface region contains voids or vacancies related to unpassivated dangling bonds on c-Si surface, illustrated in Figure 1(a), or from SiH₂ bonds clustered in the i-layer [23]. Second, it seems that particles occur around the interface, and this phenomenon can be linked to plasma gas particle formation to c-Si substrate interaction. The assumptions are further discussed and explained below using the OES spectra from the plasma point of view.

Figure 5 compares the OES spectra between plasmas during i-layer deposition of low- and high-H solar cells. The peaks shown in the spectra result from several collision of energetic electrons with gas molecules involving the formation of neutral (SiH₃, SiH₂, SiH, Si), emissive (Si*, SiH*), and ionic (SiH_x⁺) species, as given by [24, 25]



where e is the electron, $h\nu$ is the released photon energy, and τ is the life time of the Si-based radicals. Among the various radicals, SiH₂-related reactions described in (3), and (4) finally release a photon energy from Si* radiative decay corresponding to a wavelength of 252 nm. Interestingly, this released photon is detected by OES only in the plasma for the low-H cell, while this peak vanishes for the high-H cell. Thus, the plasma in low-H i-layer deposition contains a much larger amount of SiH₂, finally leading to void-rich and low-quality i-layer [26, 27]. In addition, another effect accompanied with high SiH₂ amount is the increased generation rate of poly silane (gas particle formation), Si₂H₆, according to [28]



The resultant Si₂H₆ species will interfere with film deposition and thus lead to a poor interface. Therefore, the OES spectra confirm the assumptions as mentioned in Figure 4. On the contrary, the Si-related peak found in the spectra of the high-H cell is only SiH* at 414 nm (see (5) and (6)), and thus the increased proportion of SiH₃ is beneficial to the film growth with high qualities [29] leading to a smooth interface shown in Figure 4(b).

4. Conclusions

In this study, the effect of a-Si:H i-layer hydrogen content of 0–18% on performances of HJ solar cells is investigated. Both of the experimental and simulation results indicate that the i-layer with high-hydrogen content can lead to a higher degree of dangling bond passivation on c-Si surface. Compared to low-H i-layer, HJ solar cells with a high-H i-layer is found to have the i-layer/c-Si interface with reduced surface recombination and increased collection efficiency for blue light generated carriers. In addition to surface dangling bond passivation, the low-H solar cell exhibits a deteriorate i-layer/c-Si interface. The OES spectra clearly show the presence of Si* peak only found in the plasma of low-H i-layer deposition suggesting that the large SiH₂ portion may finally create voids and Si particles and thus decrease the i-layer/c-Si interface quality.

Acknowledgment

This work was supported by the National Science Council (102-2622-E-451-002-CC3, 102-2622-E-451-001-CC2, and 100-2628-E-451-002-MY2).

References

- [1] Y. Tsunomura, Y. Yoshimine, M. Taguchi et al., "Twenty-two percent efficiency HIT solar cell," *Solar Energy Materials and Solar Cells*, vol. 93, no. 6-7, pp. 670–673, 2009.

- [2] T. Mishima, M. Taguchi, H. Sakata, and E. Maruyama, "Development status of high-efficiency HIT solar cells," *Solar Energy Materials and Solar Cells*, vol. 95, no. 1, pp. 18–21, 2011.
- [3] T. Kinoshita, D. Fujishima, A. Yano et al., "The approaches for high efficiency HIT solar cell with very thin (<100 μm) silicon wafer over 23%," in *Proceedings of the 26th European Photovoltaic Solar Energy Conference and Exhibition*, pp. 871–874, Hamburg, Germany, 2011.
- [4] K. V. Maydell, H. Windgassen, W. A. Nositschka et al., "Basic electronic properties and technology of TCO/a-Si:H(n)/c-Si(p) heterostructure solar cells: a german network project," in *Proceedings of the 20th European Photovoltaic Solar Energy Conference and Exhibition*, p. 822, Barcelona, Spain, 2005.
- [5] H. Fujiwara and M. Kondo, "Effects of a-Si:H layer thicknesses on the performance of a-Si:H/c-Si heterojunction solar cells," *Journal of Applied Physics*, vol. 101, Article ID 054516, 2007.
- [6] T. H. Wang, E. Iwaniczko, M. R. Page et al., "Effective interfaces in silicon heterojunction solar cells," in *Proceedings of the 31st IEEE Photovoltaic Specialists Conference and Exhibition*, pp. 955–958, Orlando, Fla, USA, January 2005.
- [7] V. A. Dao, N. V. Duy, J. Heo et al., "Hydrogenated amorphous silicon layer formation by inductively coupled plasma chemical vapor deposition and its application for surface passivation of p-type crystalline silicon," *Japanese Journal of Applied Physics*, vol. 48, no. 6, Article ID 066509, 2009.
- [8] N. Dwivedi, S. Kumar, A. Bisht, K. Patel, and S. Sudhakar, "Simulation approach for optimization of device structure and thickness of HIT solar cells to achieve 27% efficiency," *Solar Energy*, vol. 88, pp. 31–41, 2013.
- [9] N. Hernández-Como, A. Morales-Acevedo, and Y. Matsumoto, "I-V characteristics of a-Si-c-Si hetero-junction diodes made by hot wire CVD," *Solar Energy Materials and Solar Cells*, vol. 95, no. 8, pp. 1996–2000, 2011.
- [10] A. Matsuda, M. Takai, T. Nishimoto, and M. Kondo, "Control of plasma chemistry for preparing highly stabilized amorphous silicon at high growth rate," *Solar Energy Materials and Solar Cells*, vol. 78, no. 1–4, pp. 3–26, 2003.
- [11] W. M. M. Kessels, R. J. Severens, A. H. M. Smets et al., "Hydrogenated amorphous silicon deposited at very high growth rates by an expanding Ar–H₂–SiH₄ plasma," *Journal of Applied Physics*, vol. 89, no. 4, pp. 2404–2413, 2001.
- [12] J. Gea, Z. P. Linga, J. Wonga, T. Muellera, and A. G. Aberlea, "Optimisation of intrinsic a-Si:H passivation layers in crystalline-amorphous silicon heterojunction solar cells," *Energy Procedia*, vol. 15, pp. 107–117, 2012.
- [13] L. Zhao, H. L. Li, C. L. Zhou, H. W. Diao, and W. J. Wang, "Optimized resistivity of p-type Si substrate for HIT solar cell with Al back surface field by computer simulation," *Solar Energy*, vol. 83, no. 6, pp. 812–816, 2009.
- [14] A. Datta, M. Rahmouni, M. Nath, R. Boubekri, P. R. Cabarrocas, and P. Chatterjee, "Insights gained from computer modeling of heterojunction with intrinsic thin layer "hIT" solar cells," *Solar Energy Materials and Solar Cells*, vol. 94, no. 9, pp. 1457–1462, 2010.
- [15] L. Zhao, C. L. Zhou, H. L. Li, H. W. Diao, and W. J. Wang, "Design optimization of bifacial HIT solar cells on p-type silicon substrates by simulation," *Solar Energy Materials and Solar Cells*, vol. 92, no. 6, pp. 673–681, 2008.
- [16] V. A. Dao, J. Heo, H. Choi et al., "Simulation and study of the influence of the buffer intrinsic layer, back-surface field, densities of interface defects, resistivity of p-type silicon substrate and transparent conductive oxide on heterojunction with intrinsic thin-layer (HIT) solar cell," *Solar Energy*, vol. 84, no. 5, pp. 777–783, 2010.
- [17] J. Gopea, S. Kumar, S. Sudhakar, K. Lodhi, C. M. S. Rauthana, and P. C. Srivastava, "Influence of argon dilution on the growth of amorphous to ultra nanocrystalline silicon films using VHF PECVD process," *Journal of Alloys and Compounds*, vol. 577, pp. 710–716, 2013.
- [18] A. A. Howling, B. Strahm, P. Colsters, L. Sansonnens, and C. Hollenstein, "Fast equilibration of silane/hydrogen plasmas in large area RF capacitive reactors monitored by optical emission spectroscopy," *Plasma Sources Science and Technology*, vol. 16, no. 4, pp. 679–696, 2007.
- [19] A. A. Howling, B. Strahm, and C. Hollenstein, "Non-intrusive plasma diagnostics for the deposition of large area thin film silicon," *Thin Solid Films*, vol. 517, no. 23, pp. 6218–6224, 2009.
- [20] N. Hernández-Como and A. Morales-Acevedo, "Simulation of hetero-junction silicon solar cells with AMPS-1D," *Solar Energy Materials and Solar Cells*, vol. 94, no. 1, pp. 62–67, 2010.
- [21] M. Schaper, J. Schmidt, H. Plagwitz, and R. Brendel, "20.1%-efficient crystalline silicon solar cell with amorphous silicon rear-surface passivation," *Progress in Photovoltaics: Research and Applications*, vol. 13, no. 5, pp. 381–386, 2005.
- [22] L. Zhao, H. L. Li, C. L. Zhou, H. W. Diao, and W. J. Wang, "Optimized resistivity of p-type Si substrate for HIT solar cell with Al back surface field by computer simulation," *Solar Energy*, vol. 83, no. 6, pp. 812–816, 2009.
- [23] D.-S. Wu, S.-Y. Lien, H.-Y. Mao et al., "Growth and characterization of polycrystalline Si films prepared by hot-wire chemical vapor deposition," *Thin Solid Films*, vol. 498, no. 1-2, pp. 9–13, 2006.
- [24] J. C. Knights, "Characterization of plasma-deposited amorphous Si: H thin films," *Japanese Journal of Applied Physics*, vol. 18, pp. 101–108, 1979.
- [25] F. J. Kampas, "Reactions of atomic hydrogen in the deposition of hydrogenated amorphous silicon by glow discharge and reactive sputtering," *Journal of Applied Physics*, vol. 53, no. 9, pp. 6408–6412, 1982.
- [26] H.-Y. Kim, K.-Y. Lee, and J.-Y. Lee, "The influence of hydrogen dilution ratio on the crystallization of hydrogenated amorphous silicon films prepared by plasma-enhanced chemical vapor deposition," *Thin Solid Films*, vol. 302, no. 1-2, pp. 17–24, 1997.
- [27] M. Jeon, S. Yoshida, and K. Kamisako, "Hydrogenated amorphous silicon film as intrinsic passivation layer deposited at various temperatures using RF remote-PECVD technique," *Current Applied Physics*, vol. 10, no. 2, pp. S237–S240, 2010.
- [28] A. Matsuda, "Control of plasma and surface conditions for low defect density a-Si:H at high growth rates," in *Proceedings of the 25th IEEE Photovoltaic Specialists Conference*, pp. 1029–1034, May 1996.
- [29] W. M. M. Kessels, J. P. M. Hoefnagels, P. J. van den Oever, Y. Barrell, and M. C. M. van de Sanden, "Temperature dependence of the surface reactivity of SiH₃ radicals and the surface silicon hydride composition during amorphous silicon growth," *Surface Science*, vol. 547, no. 3, pp. L865–L870, 2003.

Research Article

Numerical Simulation of Luminescent Downshifting in Top Cell of Monolithic Tandem Solar Cells

Mahfoud Abderrezek,^{1,2} Mohamed Fathi,¹ Farid Djahli,² and Mohammed Ayad¹

¹ UDES, Solar Equipment Development Unit/EPST CDER, RN11 Bou-Ismaïl BP. 386, 42415 Tipaza, Algeria

² L.I.S Laboratory, Department of Electronic, Faculty of Technology, Ferhat Abbas University, 19000 Setif, Algeria

Correspondence should be addressed to Mahfoud Abderrezek; mahfoud_cbi@yahoo.fr

Received 20 May 2013; Revised 8 July 2013; Accepted 10 July 2013

Academic Editor: Gaetano Di Marco

Copyright © 2013 Mahfoud Abderrezek et al. This is an open access article distributed under the Creative Commons Attribution License, which permits unrestricted use, distribution, and reproduction in any medium, provided the original work is properly cited.

The increase in the conversion efficiency of monolithic tandem solar cells is limited by the short-circuit current density matching between the top and the bottom cells. Generally, the top cell presents the lowest current in the two subcells. In this paper, in order to increase the short-circuit current density in the top cell, we present a theoretical survey of the luminescence downshifting (LDS) approach for the design of monolithic tandem solar cells. The photovoltaic (PV) glass encapsulation material is replaced with a polymer material of polymethyl methacrylate (PMMA) type which is doped with diverse kinds of organic dyes. The performance of the n-p-p+ GaInP structure has been simulated as a function of the organic dyes. Gains achieved for the short-circuit current density and conversion efficiency are, respectively, 13.13% and 13.38%, under AM1.5G illumination spectra.

1. Introduction

Multijunction solar cells can increase the efficiency of the cell by introducing another semiconductor able to reduce losses in high energy photons. There are three approaches, monolithic cells, mechanically stacked cells, and spatial-configuration approaches [1]. The monolithic solar cells present an elegant approach in reducing the number of processing steps by using a single substrate, but it requires two main conditions: first, the thin layers of epitaxial semiconductors must have closer lattice constant parameters, and second, we must have an adequate current matching between subcells. However, in this series connection, the subcell with the lowest photocurrent, limits the current generated by the full device structure [1, 2]. To fulfill the second criterion, we must adjust the top cell thickness because it presents lower short-circuit current density compared with the bottom cell of the tandem structure. Generally, we adjust short-circuit current density by adjusting the thickness of the top cell's base layer [2].

In 1990, under one-sun air mass 1.5 global radiation (AM1.5G) condition, efficiencies greater than 27% were achieved by changing the top-cell thickness to ensure current matching [3, 4]. However, increasing the thickness of the

base layer in the top cell leads to an increase in absorption losses, the radiances in tandem solar cells are attenuated exponentially with respect to the thickness of layer.

In the present study, we propose an alternative method to increase the short-circuit current density in the top cell, based on the manipulation of the incident spectrum before its absorption by the solar cell; the idea is to substitute PV glass encapsulation materials with a thin layer of polymer material PMMA doped with optically active components. It has been shown in previous works that this approach results in performance improvement on some single junctions (CdTe, mc-Si, c-Si, GaAs, and CIGS) [5–7]. Besides, it reduces the cost and weight of the final PV module.

2. Materials and Methods

2.1. Luminescence Downshifting Principle. Originally, luminescent Downshifting (LDS) was first proposed in the late seventies by Hovel et al. [8]. The LDS approach is based on shifting parts of high energy photons from the ultraviolet (UV) region where the quantum efficiency (QE) of the cell is poor to the visible and infrared regions where the QE is

TABLE 1: Optical properties of diver's kinds of dyes used.

| Dyes | Absorption range (nm) | Emission range (nm) | Max abs. (nm) | Max emis. (nm) | LQE (%) |
|------------|-----------------------|---------------------|---------------|----------------|---------|
| Violet 570 | 300–410 | 400–520 | 378 | 413 | 94 |
| Yellow 083 | 350–500 | 460–600 | 476 | 490 | 99 |
| Orange 240 | 440–550 | 520–650 | 524 | 539 | 100 |

higher. A thin layer of PMMA doped with organic dyes plays the role of a photon converter; it absorbs UV photons before they are absorbed by the encapsulated material and emits them in a longer wavelength. Figure 1 illustrates the concept of downshifting introduced by organic dyes on the AM1.5G solar spectrum [9]. Also, we see that the GaInP solar cell uses photon energies in the range between 300 nm and 660 nm; it has a significant visible spectrum and a poor sensitivity in the violet and blue regions [10].

For better matching between the LDS layer and the response of GaInP solar cell, organic dyes need to be selected to absorb photons at a short wavelength, where the GaInP cell exhibits low quantum efficiency, then reemits them at a longer wavelength where the solar cell exhibits a significantly better response.

2.2. Encapsulation Material and Luminescent Dyes. Poly-methyl methacrylate (PMMA) is an excellent photovoltaic encapsulation material which was introduced recently in the manufacturing process of photovoltaic modules. It has a set of appealing mechanical and optical properties [11], in addition to its high transmittance spectrum along the region where the solar cell's response is high. PMMA is robust against heat treatments that the solar cells undergo during their manufacturing process; besides, it has a photostability extending over long periods of 20–25 years [10]. It is also recyclable and has an excellent stability against ultraviolet (UV) radiations [12].

In the present study, we will investigate the three fluorescent organic dyes (BASF Lumogen Violet 570 (V570), Yellow 083 (Y083), and Orange 240 (O240)) [13]. They are all made of naphthalomide and perylene molecules, manufactured by BASF (Ludwigshafen, Germany). These organic dyes were studied in several papers of McIntosh et al. [12, 14]. They have many features; namely, they are cheap, photostable to UV, and easy to process in polymeric matrices, and they exhibit near-unity luminescence quantum efficiencies (LQE) [6]. The optical properties of dopants are listed in Table 1.

2.3. GaInP Devices. In this work, we have introduced an LDS layer on the top cell of the monolithic tandem solar cell studied by Takamoto et al. [21]. Figure 2 shows a schematic diagram of the tandem solar cell studied with LDS layer. The technological parameters for the different layers (thickness and doping level), used in this paper, are the same as those used by Takamoto et al. [21]. The top cell consists of a layer $p + \text{Ga}_{0.5}\text{In}_{0.5}\text{P}$ BSF, a base layer $p \text{Ga}_{0.5}\text{In}_{0.5}\text{P}$, an emitter $n + \text{Ga}_{0.5}\text{In}_{0.5}\text{P}$, and the window $n + \text{Al}_{0.52}\text{In}_{0.48}\text{P}$. The ZnS/MgF_2 antireflection coating (ARC) layer allows the reduction of the average reflectivity in the wavelength region between 400 and

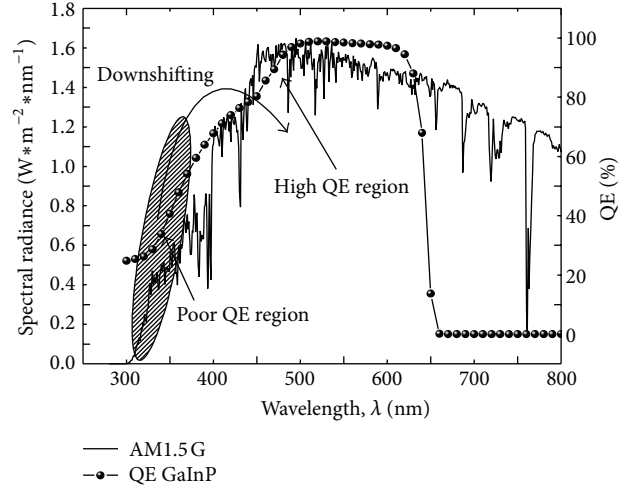


FIGURE 1: Solar spectrum AM1.5G, quantum efficiency of GaInP cell, and principle of downshifting.

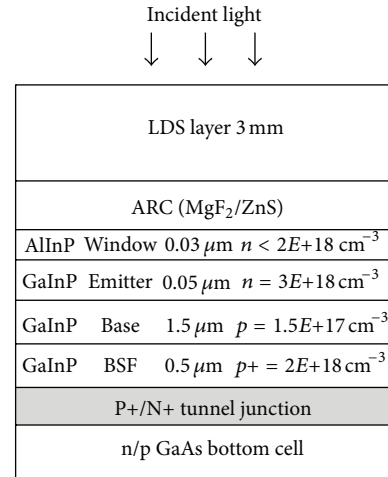


FIGURE 2: Schematic of a multijunction solar cell with LDS layer.

900 nm to less than 2% [21]. The main parameters used in the calculations are shown in Table 2.

Simulations of the heterostructure were performed using the solar cells simulator SCAPSI-D (solar cell capacitance simulator in one dimension), developed at ELIS laboratory (Electronics and Information Systems) in GENT University, Belgium [22].

2.4. Simulation Methods. To study the gain in the efficiency of GaInP solar cells as a function of the organic dyes, we made

TABLE 2: Main material parameters used in the simulation.

| Material | GaInP | AlInP |
|---|-----------------|-----------------|
| Band Gap (eV) | 1.9 [15] | 2.4 [1] |
| Electron affinity (eV) | 4.1 [15] | 4.2 [1] |
| CB effective density of states (cm ⁻³) | 1.3E + 20 [15] | 1.08E + 20 [16] |
| VB effective density of states (cm ⁻³) | 1.28E + 19 [15] | 1.28E + 19 [16] |
| Electron thermal velocity (cm/s) | 1.00E + 6 [15] | 1.00E + 7 [16] |
| Hole thermal velocity (cm/s) | 1.00E + 6 [15] | 1.00E + 7 [16] |
| Electron mobility (cm ² /Vs) | Varied [17, 18] | 100 [16] |
| Hole mobility (cm ² /Vs) | 40 [17, 18] | 10 [16] |
| Lattice constant <i>a</i> (Å) | 5.65 [15] | 5.65 [15] |
| Absorption coefficients α (m ⁻¹) | Data from [19] | Data from [20] |

a luminescent cascade (absorption and reemission) of photons so that a wide absorption can be reached. Several dyes can be mixed together within one layer in order to improve their absorption bandwidth, the Violet 570 absorption peak lies in the low QE region; however, it emits photons at wavelengths of Yellow 083 absorption range. This last emits photons at wavelengths of Orange 240 absorption range which in turn emits photon in the high QE region of the cell that ensures a better exploitation of the incident spectrum by the cell. Table 3 presents the three mixtures used in our study; the thickness of the PMMA used for the three samples is 3 mm; dyes' concentration was chosen to yield a peak absorption around 70%–90% in a 3 mm thick sample, typically the PMMA concentration is around 2-3 ppm (parts per million) [23].

The LDS layer is assumed to have complete absorption of all light incidents with wavelengths shorter than 400 nm. These dyes (Violet 570, Yellow 083, and Orange 240) were chosen because of their relatively high absorption coefficients and photoluminescent quantum yield (PLQY) [23].

When the structure (GaInP with LDS layer) is exposed to the incident solar spectrum $\varphi_s(\lambda)$, it is affected and modified by absorption and emission of photons in the PMMA mixed layer. The resulting spectrum $\varphi_{sae}(\lambda)$ is calculated from the amount of the absorbed and emitted photons. Furthermore, three quarters of the emitted photons are directed towards the solar cell, due to the internal reflection within the converter layer; the dye emission is isotropic [24].

The amount of photons absorbed depends on the thickness and the concentration of dyes in the LDS layer and is determined from the absorption spectrum of the dyes. The photon flux density decays exponentially after crossing a distance x in PMMA layer $\varphi(x, \lambda) = \varphi_0(\lambda) \exp(-\alpha(\lambda) \times x)$ where $\alpha(\lambda)$ is the absorption coefficient (cm⁻¹) of the LDS layer, and the exponential term is given by $\alpha(\lambda) \times x = \varepsilon_\lambda \times C \times D$, where ε_λ is the molar extinction coefficient (M⁻¹ cm⁻¹), C is the concentration (M), and D is the thickness of film

TABLE 3: The three mixed samples of PMMA doped with organic dyes used in the present study.

| Sample | Characteristic |
|--------|--------------------------------|
| S1 | PMMA doped with Violet 570 dye |
| S2 | S1 + Yellow 083 dye |
| S3 | S2 + Orange 240 dye |

(cm). In addition, the absorption is enhanced if the thickness of the PMMA and the concentration of the dyes are higher, besides, the amount of photons emitted in the infrared region $\varphi_e(\lambda)$ is calculated from the dyes emission spectrum, and the resulting spectrum $\varphi_{sae}(\lambda)$ serves as an input for the solar cell simulation models [24, 25]:

$$\varphi_{sae}(\lambda) = \varphi_s(\lambda) - \varphi_a(\lambda) + \varphi_e(\lambda), \quad (1)$$

where $\varphi_s(\lambda)$ is the incident solar spectrum, $\varphi_a(\lambda)$ the amount of photons absorbed by dyes introduced in PMMA layer, and $\varphi_e(\lambda)$ the amount of photons emitted by dyes introduced in PMMA layer.

The short-circuit current density (J_{sc}) of a solar cell is a function of the cell's quantum efficiency QE (λ) and the resulting spectrum $\varphi_{sae}(\lambda)$:

$$J_{sc} = q \int_{\lambda_1}^{\lambda_2} \text{QE}(\lambda) \times \varphi_{sae}(\lambda) d(\lambda), \quad (2)$$

where q is the elementary charge and λ_1 and λ_2 define the range of the spectrum for which the J_{sc} is to be calculated.

It follows that, in order to increase the short-circuit current density in the cell, more photons must be shifted from the poor QE region to the higher QE region.

3. Simulation Results and Discussions

The performance of the GaInP solar cell was simulated without an LDS layer, and the obtained results were in accordance with those in the literature [21]. When an LDS layer is introduced on the top of the solar cell, organic dyes produce a substantial modification on the incident AM1.5G spectrum; they oblige the photons in the ultraviolet region to shift towards the visible region. The simulation is carried out for different numbers of organic dyes (S1, S2, and S3); for each case the effect on AM1.5G spectrum is shown in Figure 3.

SCAPS-ID simulations were carried out using the three samples of mixed dyes (S1, S2, and S3), using the resulting modified spectrum as an input for our simulation model. The variation of fill factor and open-circuit voltage with respect to the number of dyes added is presented in Figure 4 where it is clear that the open circuit voltage (V_{oc}) and fill factor (FF) do not change significantly. This is due to the fact that there is no change in the electronic properties of the semiconductor material or in the resistance of the device.

On the other hand, we see from Figure 5 that the variations in the short circuit current density and conversion efficiency are substantial. The increase in conversion efficiency is a result of the increasing current generation because

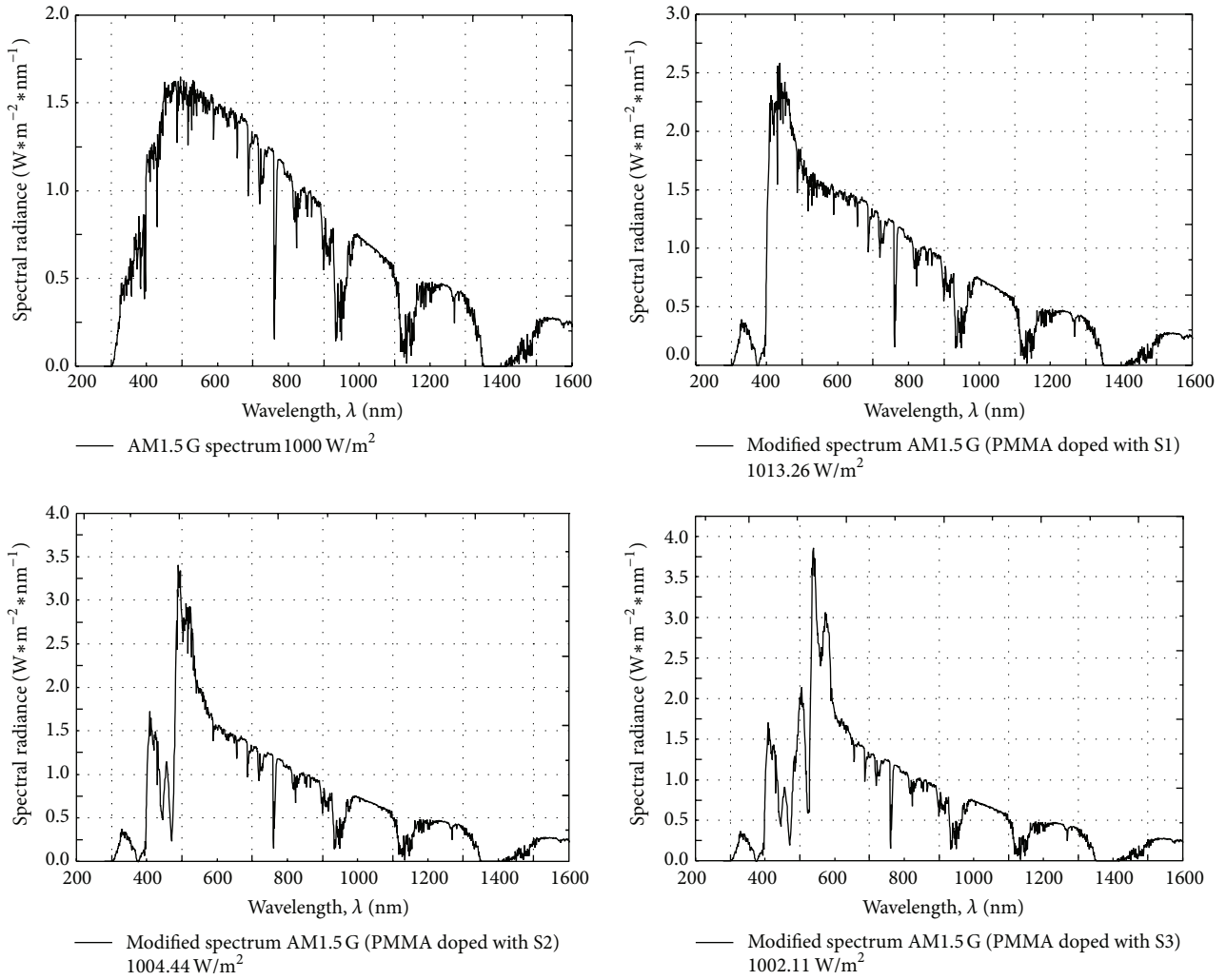


FIGURE 3: The luminescent downshift (LDS) effect on the AM1.5G solar spectrum.

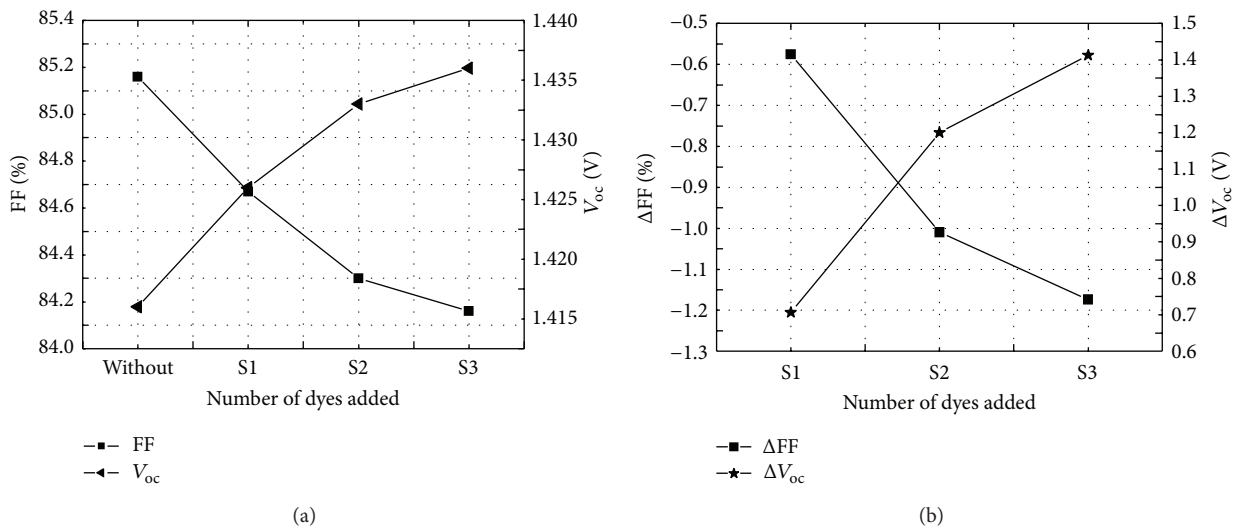


FIGURE 4: Simulation results of the variation of (a) fill factor and open-circuit voltage with the number of dyes added and (b) increase in fill factor and open-circuit voltage with the number of dyes added.

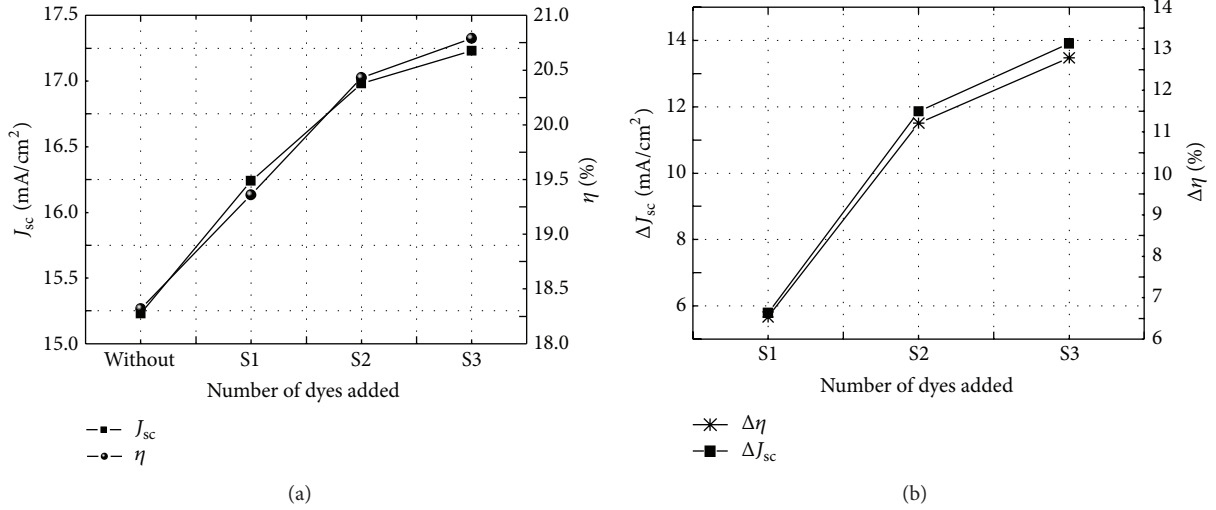


FIGURE 5: Simulation results of (a) the short-circuit current density and conversion efficiency variation with the number of dyes added and (b) the increase in the short-circuit current density and conversion efficiency variation with the number of dyes added.

TABLE 4: Short-circuit current density and efficiency of the GaInP solar cell with and without LDS.

| J_{sc} (mA/cm ²) GaInP cell without PMMA | J_{sc} (mA/cm ²) GaInP cell with PMMA doped (S3) | η (%) GaInP cell without PMMA | η (%) GaInP cell with PMMA doped (S3) | J_{sc} current improve (%) | Efficiency η improve (%) |
|--|---|--|---|---------------------------------|----------------------------------|
| 15.23 | 17.23 | 18.32 | 20.79 | 13.13 | 13.48 |

the short-circuit current density varies proportionally with the quantity of photons shifted by the LDS layer.

The study of the improvements brought by the LDS layer on the GaInP solar cell, as a function of the number of dyes added, has shown that better results are achieved for the samples S1 and S2 (violet, violet, and yellow) with gains in short-circuit current density of 6.63% and 4.86%, respectively, whereas the addition of the third dye contributes only with 1.64% in the total increase. This is due to the fact that the QE of GaInP is poor in the absorption and emission spectrum of the two samples S1 and S2; hence, there is more photon transfer from UV and blue regions, where the collection probability of these photons is lower to the visible region, where the probability of collection is higher. Furthermore, when we add the third dye (orange 240) to S2, it induces absorption and reemission of photons in the region where the QE of the cell is already high (QE above 80%). So, there is less contribution in the collected current of the GaInP solar cell.

The simulated J-V characteristics of the GaInP structure with and without our specific downshift (PMMA doped with S3) are shown in Figure 6 where we observe an important increase in the short circuit current density and the cell's conversion efficiency. The gains in short-circuit current density and the conversion efficiency are summarized in Table 4.

4. Conclusion

We proved, in this work, that the performances of the GaInP top monolithic solar cell are improved by introducing

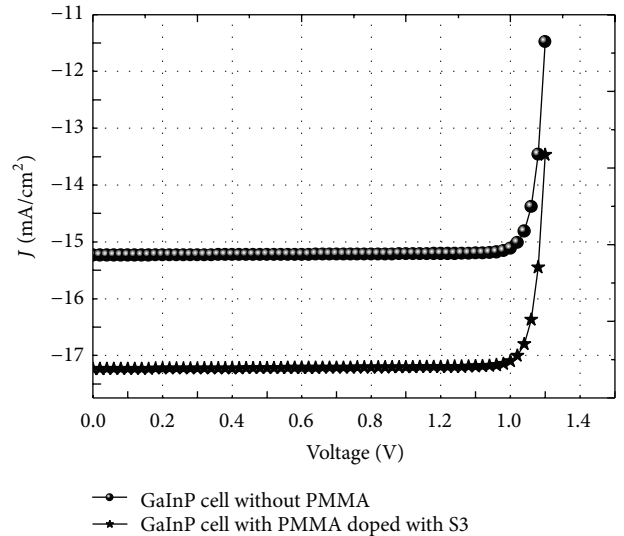


FIGURE 6: Simulation results of GaInP solar cell characteristics with and without LDS PMMA layer.

luminescence downshifting (LDS) layers. These performances have been simulated as a function of the mixture of the organic dyes (Violet 570, Yellow 083, and Orange 240). The simulation results have shown that, under the AM1.5G illumination spectrum, increases in the short-circuit current density and in the conversion efficiency of 13.13% and 13.48%

are, respectively, achieved by using an LDS layer doped by a mixture of the three dyes (Violet 570, Yellow 083, and Orange 240).

The two organic dyes Violet 570 and Yellow 083 have a great contribution in augmenting the efficiency of the solar cell compared to the Orange 240 dye; hence, they are more suited for GaInP solar cells with an LDS layer.

The use of an LDS layer allowed an increase in the efficiency of the GaInP top cell to values above 20%. Finally, in order to improve the solar cell performances, we plan in future works to study the behavior of the tandem solar cell with several dyes concentrations and obtain the optimum concentration corresponding to this structure.

Acknowledgment

The authors wish to thank Dr. M. Burgelman's group of Electronics and Information Systems (ELIS), University of Gent, for the SCAPS-ID program tool.

References

- [1] A. Luque and S. Hegedus, *Handbook of Photovoltaic Science and Engineering*, John Wiley & Sons, Hoboken, NJ, USA, 2003.
- [2] P. J. Faine, R. Sarah Kurtz, and J. M. Olson, "Modeling of two-junction, series-connected tandem solar cells using top-cell and coating thicknesses as adjustable parameters," in *Proceedings of the 21st IEEE Photovoltaics Specialists Conference (PVSC '90)*, Kissimmee, Fla, USA, 1990.
- [3] J. M. Olson, S. R. Kurtz, A. E. Kibbler, and P. Faine, "A 27.3% efficient Ga_{0.5}In_{0.5}P/GaAs tandem solar cell," *Applied Physics Letters*, vol. 56, no. 7, pp. 623–625, 1990.
- [4] S. R. Kurtz, P. Faine, and J. M. Olson, "Modeling of two-junction, series-connected tandem solar cells using top-cell thickness as an adjustable parameter," *Journal of Applied Physics*, vol. 68, no. 4, pp. 1890–1895, 1990.
- [5] D. Ross, E. Klampaftis, J. Fritsche, M. Bauer, and B. S. Richards, "Increased short-circuit current density of production line CdTe mini-module through luminescent down-shifting," *Solar Energy Materials and Solar Cells*, vol. 103, pp. 11–16, 2012.
- [6] E. Klampaftis, D. Ross, K. R. McIntosh, and B. S. Richards, "Enhancing the performance of solar cells via luminescent down-shifting of the incident spectrum: a review," *Solar Energy Materials and Solar Cells*, vol. 93, no. 8, pp. 1182–1194, 2009.
- [7] L. Danos, T. Parel, T. Markvart, V. Barrioz, W. S. M. Brooks, and S. J. C. Irvine, "Increased efficiencies on CdTe solar cells via luminescence down-shifting with excitation energy transfer between dyes," *Solar Energy Materials and Solar Cells*, vol. 98, pp. 486–490, 2012.
- [8] H. J. Hovel, R. T. Hodgson, and J. M. Woodall, "The effect of fluorescent wavelength shifting on solar cell spectral response," *Solar Energy Materials*, vol. 2, no. 1, pp. 19–29, 1979.
- [9] ASTM-Standard-G173-2003e1, "Standard TABLEs for Reference solar spectral irradiances: Direct normal and hemispherical on 37 degree tilted surface," Conshohocken, Pa, USA, 2003.
- [10] A. Vesselinka Petrova-Koch and R. Hezel Adolf Goetzberger, *High-Efficient Low-Cost Photovoltaics Recent Developments*, Springer, Berlin, Germany, 2009.
- [11] B. S. Richard and A. Shalav, "The role of polymers in the luminescence conversion of sunlight for enhanced solar cell performance," *Synthetic Metals*, vol. 154, no. 1–3, pp. 61–64, 2005.
- [12] K. R. McIntosh, G. Lau, J. N. Cotsell et al., "Increase in external quantum efficiency of encapsulated silicon solar cells from a luminescent down-shifting layer," *Progress in Photovoltaics*, vol. 17, no. 3, pp. 191–197, 2009.
- [13] "BASF Lumogen F datasheets," <http://www2.basf.us/additives/pdfs/lumvio570.pdf>, <http://www2.basf.us/additives/pdfs/lumyel083.pdf>.
- [14] B. S. Richards and K. R. McIntosh, "Increased mc-Si module efficiency using fluorescent organic dyes: a ray-tracing study," in *IEEE 4th World Conference on Photovoltaic Energy Conversion*, Waikoloa, Hawaii, USA, May 2006.
- [15] K. J. Singh and S. K. Sarkar, "Highly efficient ARC less InGaP/GaAs DJ solar cell numerical modeling using optimized InAlGaP BSF layers," *Optical and Quantum Electronics*, vol. 43, pp. 1–21, 2011.
- [16] A. S. Gudovskikh, N. A. Kaluzhniy, V. M. Lantratov, S. A. Mintairov, M. Z. Shvarts, and V. M. Andreev, "Numerical modelling of GaInP solar cells with AlInP and AlGaAs windows," *Thin Solid Films*, vol. 516, no. 20, pp. 6739–6743, 2008.
- [17] K. Ikeda and M. Kaneko, "Estimation of the composition parameter of electrochemically colored amorphous hydrogen tungsten oxide films," *Journal of Applied Physics*, vol. 66, Article ID 5285, 6 pages, 1989.
- [18] M. Y. Ghannam, A. S. Alomar, N. Posthuma, G. Flammad, and J. Poorthmans, "Optimization of the triple junction In_{0.5}Ga_{0.5}P/GaAs/Ge monolithic tandem cell aimed for terrestrial applications using an experimentally verified analytical model," *Kuwait Journal of Science and Engineering*, vol. 31, pp. 203–234, 2004.
- [19] L. Guijiang, W. Jyhchiang, and H. Meichun, "Theoretical modeling of the interface recombination effect on the performance of III-V tandem solar cells," *Journal of Semiconductors*, vol. 31, no. 8, Article ID 082004, 2010.
- [20] S. Adachi, *Optical Constants of Crystalline and Amorphous Semiconductors-Numerical Data And Graphical Information*, Springer, New York, NY, USA, 1999.
- [21] T. Takamoto, E. Ikeda, H. Kurita, and M. Ohmori, "High efficiency InGaP solar cells for InGaP/GaAs tandem cell application," in *Proceedings of the 1st World Conference on Photovoltaic Energy Conversion*, pp. 1729–1732, Waikoloa, Hawaii, USA, December 1994.
- [22] A. Niemegeers and M. Burgelman, "Effects of the Au/CdTe back contact on IV and CV characteristics of Au/CdTe/CdS/TCO solar cells," *Journal of Applied Physics*, vol. 81, Article ID 2881, 1997.
- [23] L. R. Wilson and B. S. Richards, "Measurement method for photoluminescent quantum yields of fluorescent organic dyes in polymethyl methacrylate for luminescent solar concentrators," *Applied Optics*, vol. 48, no. 2, pp. 212–220, 2009.
- [24] W. G. J. H. M. van Sark, "Simulating performance of solar cells with spectral downshifting layers," *Thin Solid Films*, vol. 516, no. 20, pp. 6808–6812, 2008.
- [25] W. G. J. H. M. Van Sark, A. Meijerink, R. E. I. Schropp, J. A. M. Van Roosmalen, and E. H. Lysen, "Enhancing solar cell efficiency by using spectral converters," *Solar Energy Materials and Solar Cells*, vol. 87, no. 1–4, pp. 395–409, 2005.

Research Article

Effects of Hole-Collecting Buffer Layers and Electrodes on the Performance of Flexible Plastic Organic Photovoltaics

Sungho Woo,¹ Hong-Kun Lyu,¹ Yoon Soo Han,² and Youngkyoo Kim³

¹ Green Energy Research Division, Daegu Gyeongbuk Institute of Science and Technology (DGIST), Daegu 711-873, Republic of Korea

² Department of Advanced Energy Material Science and Engineering, Catholic University of Daegu, Gyeongbuk 712-702, Republic of Korea

³ Organic Nanoelectronics Laboratory, Department of Chemical Engineering, Kyungpook National University, Daegu 702-701, Republic of Korea

Correspondence should be addressed to Sungho Woo; shwoo@dgist.ac.kr and Youngkyoo Kim; ykimm@knu.ac.kr

Received 11 June 2013; Accepted 8 July 2013

Academic Editor: Stefano Caramori

Copyright © 2013 Sungho Woo et al. This is an open access article distributed under the Creative Commons Attribution License, which permits unrestricted use, distribution, and reproduction in any medium, provided the original work is properly cited.

Here we report the influences of the sheet resistance (R_{sheet}) of a hole-collecting electrode (indium tin oxide, ITO) and the conductivity of a hole-collecting buffer layer (poly(3,4-ethylenedioxythiophene):poly(styrenesulfonate), PEDOT:PSS) on the device performance of flexible plastic organic photovoltaic (OPV) devices. The series resistance (R_s) of OPV devices steeply increases with increasing R_{sheet} of the ITO electrode, which leads to a significant decrease of short-circuit current density (J_{SC}) and fill factor (FF) and power conversion efficiency, while the open-circuit voltage (V_{OC}) was almost constant. By applying high-conductivity PEDOT:PSS, the efficiency of OPV devices with high R_{sheet} values of 160 Ω/\square and 510 Ω/\square is greatly improved, by a factor of 3.5 and 6.5, respectively. These results indicate that the conductivities of ITO and PEDOT:PSS will become more important to consider for manufacturing large-area flexible plastic OPV modules.

1. Introduction

Organic photovoltaic (OPV) devices have attracted considerable attention as a promising solution for next-generation solar energy conversion, due to their potential to realize low-cost, flexible, large-area, and simple solution processed photovoltaics [1, 2]. The power conversion efficiency (PCE) of OPVs has been greatly improved by introducing donor-acceptor bulk hetero junction (BHJ) structures, with a PCE of about 5% being achieved for a single junction cell based on blend systems of poly(3-hexylthiophene) (P3HT) and [6,6]-phenyl-C₆₁-butyric acid methyl ester (PCBM) [3–5]. There is still further potential to increase the PCE to above 10% by using low band gap materials and/or tandem cell structures [1, 6, 7]. To date, however, most studies have focused on performance improvement based on an indium-tin-oxide- (ITO-) coated rigid glass substrate so that the advantages of organic-based photovoltaic devices have not been fully exploited. A plastic substrate with an ITO electrode is considered the best candidate to achieve a fully flexible

OPV [8]. To increase the transparency and conductivity of an ITO thin film, it is necessary to heat the substrate at 200~300°C to enhance the ITO crystallization as well as to facilitate diffusion and substitution of tin ions during the ITO deposition process. With a plastic substrate, however, heating beyond that temperature is difficult due to its poor thermal stability, and thus the conductivity of ITO becomes lower than that of glass-based substrates. Probable limiting factor of the PCE for flexible plastic substrate-based OPVs relative to OPVs based on glass substrates are the low conductivity of the ITO electrode and the temperature limitation of the postthermal annealing process of the photoactive layer due to the weak thermal properties of plastic substrates.

Kang et al. reported that reducing R_{sheet} of the ITO electrode led to enhanced device performance by decreasing the R_s value of OPV devices [9]. Therefore, it is imperative to mitigate the high R_{sheet} (or bulk resistance) problem of ITO electrodes in flexible plastic substrate-based OPVs and/or large-area OPV module products. In case of using the same photoactive material and cathode electrode, the conductivity

of the hole-collecting buffer layer (HCBL) is another factor related to the R_s of OPV devices. The most commonly used HCBL material for OPVs is PEDOT:PSS, which plays an important role in organic electronics such as controlling the hole transport conditions, reducing surface roughness of the substrate, and converting nonohmic contacts into ohmic states. Representative commercially available PEDOT:PSS include *CLEVIOS P VP AI 4083* (AI4083) and *CLEVIOS PH 500* (PH500), with conductivity of $10^{-3} \text{ S cm}^{-1}$ and $10\sim 50 \text{ S cm}^{-1}$, respectively [10, 11]. It is well known that a highly conductive PEDOT:PSS would be helpful to enhance PCE by providing fast charge transfer with small resistance as well as improved surface or interface properties. Ko et al. [12] and Hu et al. reported that improved device performance could be attributed to the reduction of the resistance of PEDOT:PSS by doping organic solvents [13]. Xiao et al. [14] and Sun et al. suggested that enhanced performance can also be achieved through an increase of light absorption in the active layer by improving light scattering and by obtaining high surface area with solvent-treated PEDOT:PSS [15]. Lastly, improvement of interfacial properties and alignment of surface free energy between PEDOT:PSS and the active layer could be another factor to facilitate greater device performance [16–18]. However, the aforementioned experiments were mostly performed on glass-based low R_{sheet} ITO electrodes ($\sim 10 \Omega/\square$). Therefore, the influence of the PEDOT:PSS conductivity on the performance of OPVs with a high R_{sheet} ITO electrode warrants further study for understanding delicate changes in final solar module performances when flexible plastic OPV devices are commercialized.

In this work, we investigated the effect of R_{sheet} of ITO electrode on the performance of OPV devices and also assessed whether the high R_{sheet} of an ITO electrode on a flexible substrate could be compensated by using high-conductivity PEDOT:PSS in the normal configuration of flexible substrate/ITO/PEDOT:PSS/P3HT:PCBM/LiF/Al. Our results show that the conductivity of ITO and PEDOT:PSS strongly affects devices parameters including short-circuit current density (J_{SC}), fill factor (FF), and PCE through their influence on the device R_s .

2. Experimental

2.1. Materials and Device Fabrication. To investigate the influence of ITO and PEDOT:PSS conductivity on the device efficiency, we fabricated a total of 8 devices using four types of substrates, glass/ITO ($6 \Omega/\square$, from SUNIC System Ltd., Republic of Korea), poly(ethylene naphthalate) (PEN)/ITO ($21 \Omega/\square$, from Peccell Co., Japan), poly(ether sulfone) (PES)/ITO ($160 \Omega/\square$, from I-component Co., Republic of Korea), and poly(ethylene terephthalate) (PET)/ITO ($510 \Omega/\square$, from Toray Industries Inc., Japan), with two types of PEDOT:PSS buffer layers, AI4083 and PH500 (modified with 5% DMSO in our laboratory), from Heraeus Precious Metals GmbH & Co. KG.

The OPV devices were fabricated as follows: the patterned ITO substrates were sequentially cleaned by ultrasonic treatment in methanol, de-ionized water, and isopropyl alcohol

and dried in a vacuum oven. After being treated with UV- O_3 for 15 min, PEDOT:PSS was immediately spin-coated on the ITO substrate. The coated PEDOT:PSS films were baked on a hot plate for 15 min at 120°C to give a thickness of 30 nm and transferred to a glove box filled with N_2 gas for the remaining fabrication steps. P3HT and PCBM with weight ratios of 1:0.9 were dissolved in chlorobenzene, followed by stirring for 24 h at 50°C . An active layer consisting of P3HT:PCBM blends was spin-cast on top of the PEDOT:PSS layer and dried on a hot plate for 40 min at 50°C to give a thickness of 120 nm. A top electrode consisting of a LiF (1 nm) layer and a subsequent Al (100 nm) layer were deposited by thermal evaporation under a vacuum of $\sim 10^{-7}$ Torr. The deposited Al electrode defines an active area of the device as 0.09 cm^2 . The prepared devices were directly annealed on a hot plate for 15 min at 120°C . Although the device annealing process is generally performed at $140^\circ\text{C}\sim 150^\circ\text{C}$ for glass-based OPVs in order to develop well-ordered active layer morphology and enhance the device efficiency, we conducted the annealing process for all devices including a glass/ITO reference at 120°C because of device failure of our plastic/ITO-based OPV devices annealed at temperature over 130°C .

2.2. Measurements. The conductivity of the ITO electrode was measured in a unit of Ω/\square (R_{sheet}) by the 4-point probe method (CMT-series, Advanced Instrument Technology) [19], and the transmittance was measured with a UV-Vis spectrometer (Lambda 750, PerkinElmer). Photocurrent density-voltage (J - V) measurements were performed with a Keithley model 2400 Source Meter and a Newport 91192 solar simulator system (equipped with a 1KW xenon arc lamp, Oriel). Light intensity was adjusted to simulated AM1.5 radiation at 100 mW/cm^2 with a Radiant Power Energy Meter (model 70260, Oriel). The R_s value of OPV was calculated from the inverse slope of the J - V curve at high cell voltages ($J = 0$). All measurements were carried out under ambient conditions at room temperature.

3. Results and Discussion

To compare the performance of OPVs according to the conductivity of the ITO electrode and the PEDOT:PSS buffer layer, we fabricated several identically structured devices, but with different substrates of glass/ITO ($6 \Omega/\square$), PEN/ITO ($21 \Omega/\square$), PES/ITO ($160 \Omega/\square$), and PET/ITO ($510 \Omega/\square$) and also with different PEDOT:PSS of AI4083, PH500, as shown in Figure 1 (note the chemical structures of plastic substrates just below the device structures in Figure 1(b)). The conductivities of two different PEDOT:PSS samples are also given in this figure. As shown in Figure 1(c), the OPV devices fabricated with the plastic substrates were bendable and flexible even in small sizes compared to that fabricated with glass substrate.

The optical transmittance spectra of ITO-coated glass and three different ITO-coated plastic substrates are given in Figure 2. The transmittance at the wavelength between 450 nm and 550 nm was slightly lower for the plastic substrates than the glass substrate, whereas it was reversed

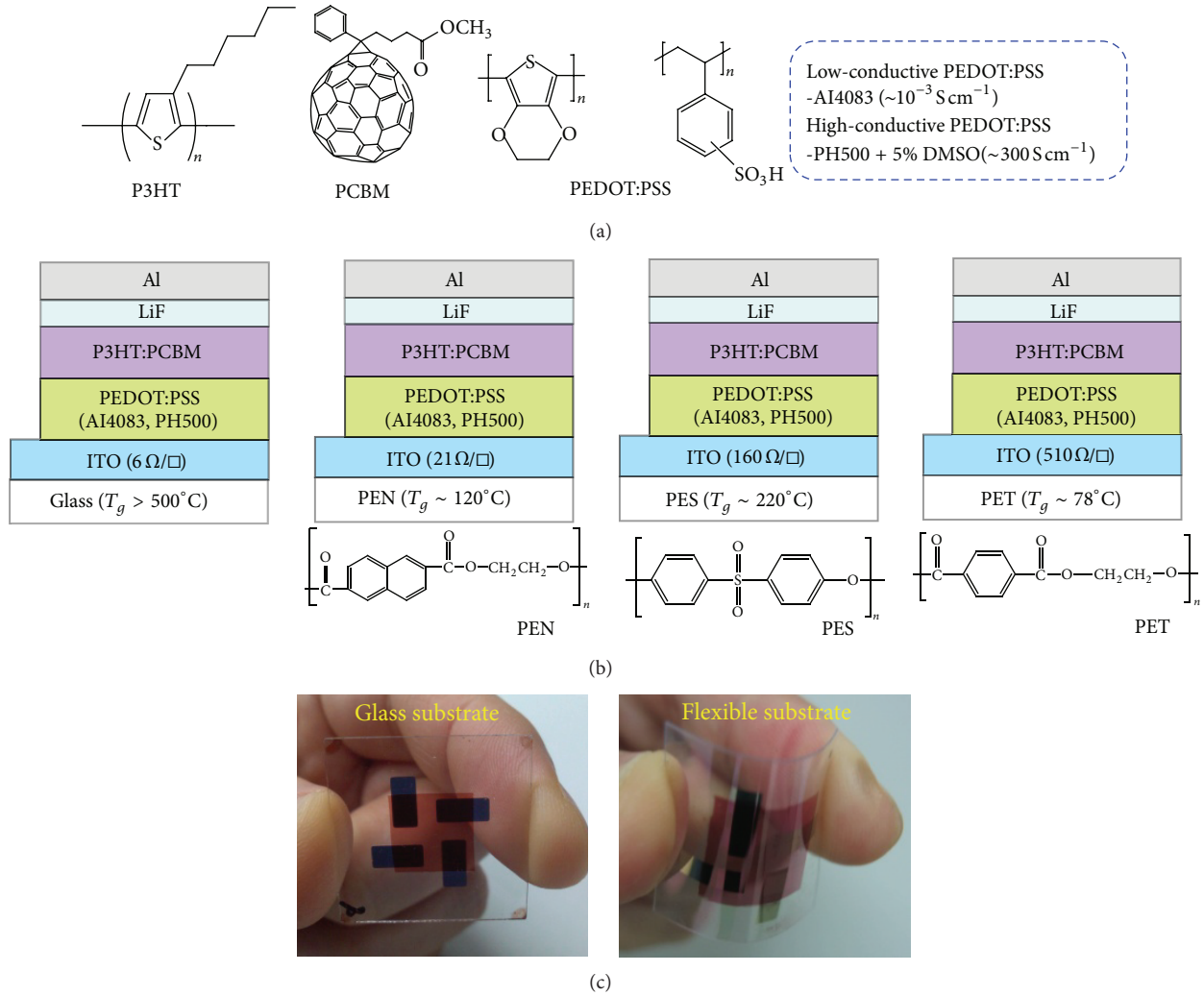


FIGURE 1: (a) Chemical structure of materials used in this work, (b) device structures with four different ITO substrates (glass and flexible plastics) and two different buffer layers (AI4083 and PH500) (note the chemical structures of plastic substrates), and (c) photographs of OPV devices fabricated using glass (left) and flexible plastic (right) substrates.

between 550 nm and 650 nm for the PEN and PET substrates (note that the P3HT absorption ends at around 650 nm). Interestingly, the PES substrate exhibited a sensitive transmittance response with the wavelength, which is different from other substrates.

The current density-voltage (J - V) characteristics of OPV devices under illumination of the simulated solar light (AM1.5, 100 mW/cm²) are shown in Figure 3. All devices show similar open-circuit voltage (V_{OC}) of about 0.6 V, suggesting good contact between the active layer and the buffer layers. For the devices using AI4083, their J_{SC} , FF, and PCE are, however, significantly decreased, from 6.2 mA/cm², 0.605, and 2.3% in the glass/ITO device to 0.5 mA/cm², 0.139, and 0.04% in the PET/ITO device, respectively. We note that the relatively low PCE of 2.3% in the glass/ITO device was due to the low postannealing temperature at 120°C after device fabrication, as mentioned in the Experimental section (our normal device has a PCE of over 3% after postannealing treatment at 140~150°C, as reported previously [20, 21]).

Based on the J - V characteristics, we tried to analyze the main factor to decrease the PCE with increasing substrate R_{sheet} . The efficiency of an OPV is typically influenced by the following relation [22]:

$$\eta = \eta_a \times \eta_g \times \eta_{diff} \times \eta_{dis} \times \eta_{tr} \times \eta_c, \quad (1)$$

where η_a is the photon absorption efficiency, η_g is the generation efficiency of excitons, η_{diff} is the exciton diffusion efficiency, η_{dis} is the efficiency of hole-electron separation (exciton dissociation), η_{tr} is the efficiency of carrier transport in the active layer towards the electrodes, and η_c is the charge collection efficiency at the respective electrodes. We can assume that each device has equal capacity of η_g , η_{diff} , η_{dis} , and η_{tr} , because their device structure including active (P3HT:PCBM) and buffer (AI4083) layers is exactly the same. η_a and η_c then remain as responsible factors. From Figure 1, the average optical transmittance of the ITO substrates at the wavelength of 400–700 nm is above 70%. The difference in transmittance among the ITO substrates, which is directly

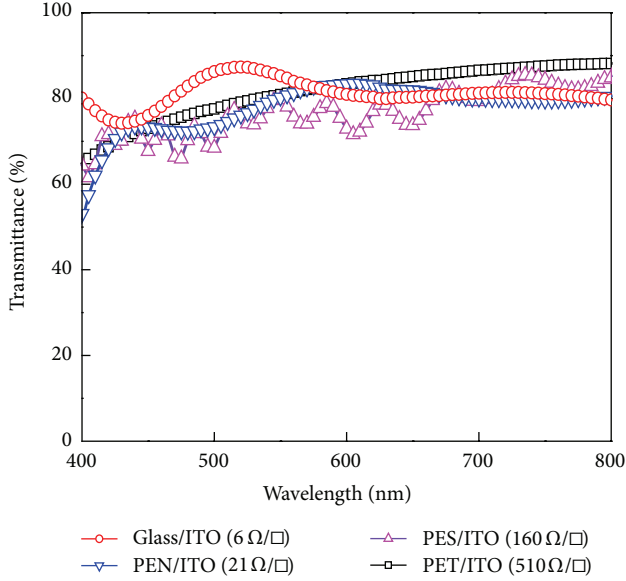
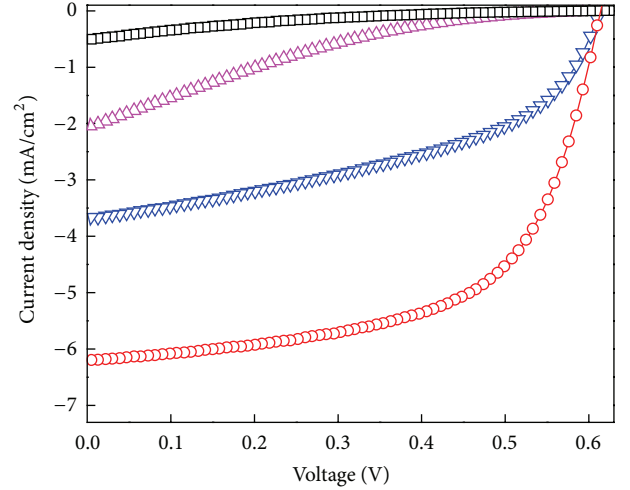


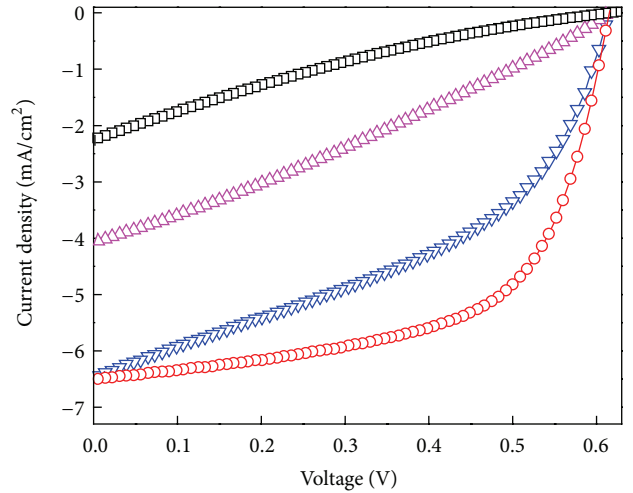
FIGURE 2: Optical transmittance of four different ITO substrates used in this work. The sheet resistance of each substrate is given in the legend.

related to η_a , is within 20%, while their R_{sheet} difference is almost two orders. Thus, the decreasing photovoltaic performance with increasing R_{sheet} of the substrate is not significantly related to the transmittance of the base substrate, but rather to the high R_{sheet} of the ITO electrode. This reflects that the main factor of limitation is the hole collection efficiency at the hole-collecting electrode (η_c), not the light absorption difference (η_a). Hence we tried to correlate the device performances with the conductivity of each substrate which can represent the hole collection efficiency in Figure 4.

Figure 4 presents the V_{OC} , J_{SC} , FF, PCE, and R_s changes as a function of R_{sheet} (ITO) of the substrates under illumination of AM1.5, which clearly shows the relations between these parameters. The V_{OC} is almost independent of R_{sheet} of ITO, as mentioned before. However, the J_{SC} and FF values gradually decreased with increasing R_{sheet} of the ITO, resulting in a decrease of the PCE. Moreover, the decreasing trend in J_{SC} , FF, and PCE is closely connected with the increase of R_s of the devices. The hole collection efficiency at the anode (η_c) is usually affected by R_s , which is also the dominant parameter determining the FF by altering the slope of the J - V curve near the V_{OC} and is a key factor for high-efficiency solar cells [22–25]. R_s represents the total resistance of the cell and depends on the resistivity of the organic material(s), the metal electrodes, and the metal/organic interface [24]. As all devices were fabricated with the same structure and active materials under an identical process, it is reasonable to assume that the resistances of PEDOT:PSS, P3HT:PCBM, and LiF/Al remained constant among devices. Therefore, R_s is mainly changed with R_{sheet} of the ITO anode in our case. Xue et al. reported that the contribution of R_{sheet} of the ITO electrode to the R_s of an OPV is more critical in the fabrication of the OPV for a large area of more than 0.01 cm^2



(a)



(b)

FIGURE 3: Current density-voltage (J - V) characteristics of OPV devices fabricated using four different ITO substrates and hole-collecting buffer layers (PEDOT:PSS): (a) AI4083 and (b) PH500. All measurements were performed under illumination of simulated solar light (AM1.5, 100 mW/cm^2).

[26]. Several other reports have described the effect of R_{sheet} on the R_s and the cell design rule to minimize the R_s in large area devices [27–31].

As additional indirect evidence for poor hole extraction (collection) due to the high-resistivity ITO, we can see a kink (or S-curve) characteristic in devices with high R_s such as PET/ITO/AI4083 and PES/ITO/AI4083. This kink causes a negative curvature that can substantially reduce the FF, and therefore the solar cell performance. The kink of the J - V curve under illumination was due to several reasons, such as large interfacial energy gaps at the electrode-active layer

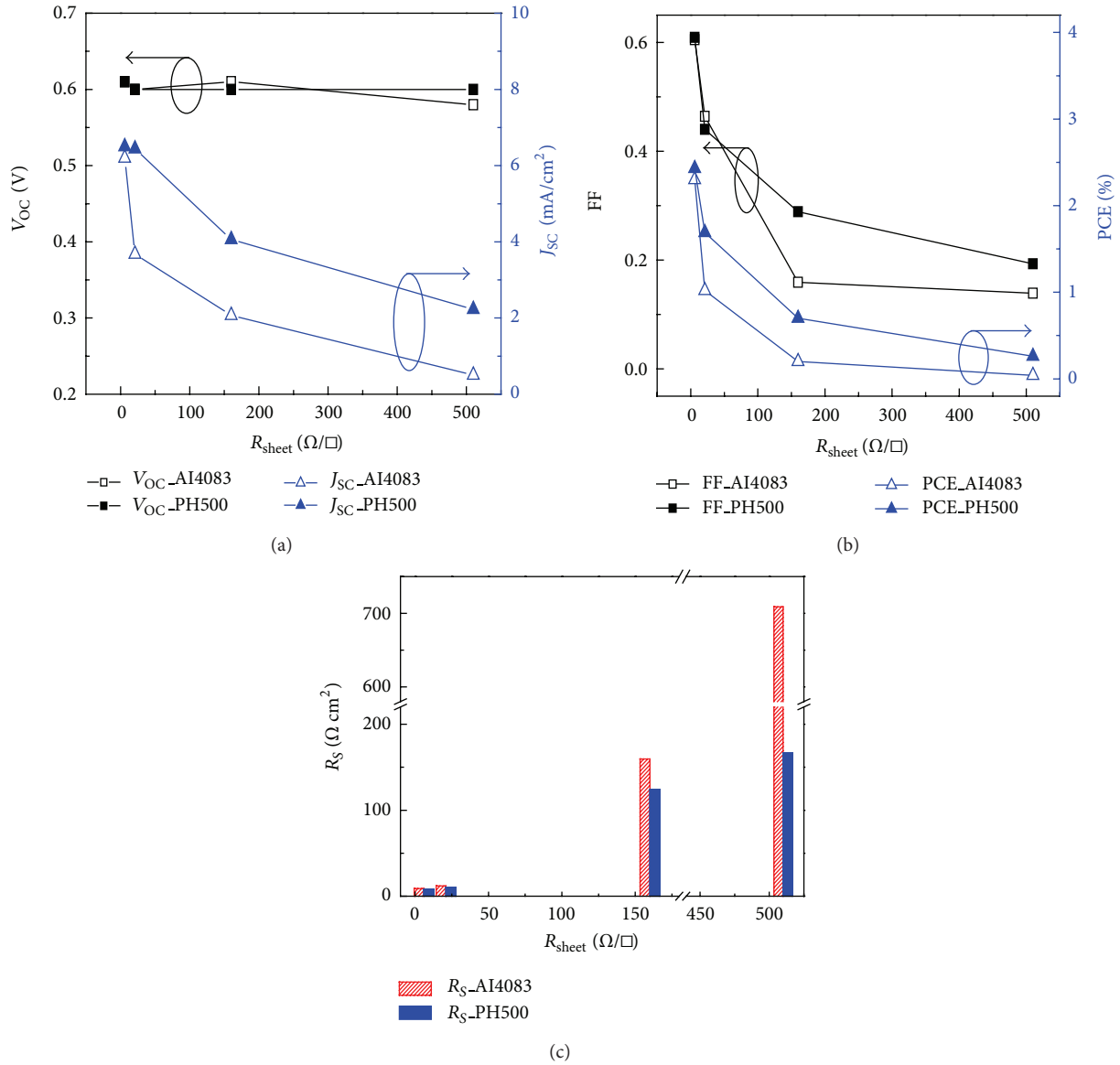


FIGURE 4: (a) Open-circuit voltage (V_{OC}) and short-circuit current density (J_{SC}), (b) FF and PCE, and (c) series resistance (R_S) as a function of the sheet resistance (R_{sheet}) of the ITO electrode on the substrates.

interface, unbalanced mobility between holes and electrons [32, 33], nonuniform contact or incomplete coverage of the metal over the active layer [34, 35], slow charge transfer at one of the electrical contacts of the active layer [36], strong interfacial dipoles, defects, and traps that can create barriers for charge extraction [37], and defect-induced nonefficient extraction of charge leading to buildup of a counter field [38, 39]. These can be summarized that the kink characteristic is caused by a counterfield created by accumulated space charges from unbalanced charge carrier extraction. In devices incorporating our high-resistivity ITO substrate, we may reasonably suppose that separated holes undergo restricted extraction at the anode and show a kink J - V curve.

Next, we checked whether these losses that originate from the high R_{sheet} ITO can be reduced by using a high-conductivity buffer layer. The conductivity of PEDOT:PSS

can be increased by up to two or three orders of magnitude by adding high-boiling point and/or polar compounds such as diethylene glycol (DEG), ethylene glycol (EG), dimethylsulfoxide (DMSO), sorbitol, and glycerol, due to the phase separation of each PEDOT-rich region and PSS-rich region, as reported in previous works [40–42]. We used PH500 doped with 5% DMSO (in this report, we call it PH500) to improve the conductivity up to 500 Ω/\square . From Figures 3 and 4, the J_{SC} , FF, and PCE were greatly improved by using a high-conductivity PH500 buffer layer. Typically, the effect of high-conductivity PH500 is more pronounced with the high R_{sheet} of the ITO electrode. As a result, PCE and R_S are, respectively, improved by a factor of 3.5 and 1.29 for PES/ITO and 6.5 and 4.25 for PET/ITO (see Table 1). This indicates that the poor conductivity of the ITO electrode can be partly compensated by a high-conductivity buffer layer via the reduction of R_S .

TABLE 1: Summary of device parameters for organic photovoltaic devices with four different ITO substrates (glass and flexible plastics) and two different buffer layers (AI4083 and PH500).

| Substrate | PEDOT : PSS | V_{OC} (V) | J_{SC} (mA/cm ²) | FF | PCE (%) | R_S (Ω cm ²) ^a |
|------------------------|-------------|---------------------|--------------------------------|---------------------|---------|---|
| Glass/ITO | AI4083 | 0.61 | 6.20 | 0.605 | 2.30 | 9.0 |
| | PH500 | (1.00) ^b | 6.50 | (1.05) ^b | 2.43 | (1.11) ^b |
| PEN/ITO | AI4083 | 0.60 | 3.68 | 0.464 | 1.02 | 12.0 |
| | PH500 | (1.00) ^b | 6.44 | (1.75) ^b | 1.69 | (1.66) ^b |
| PES/ITO | AI4083 | 0.61 | 2.07 | 0.159 | 0.20 | 159.7 |
| | PH500 | (0.98) ^b | 4.06 | (1.96) ^b | 0.70 | (3.50) ^b |
| PET/ITO | AI4083 | 0.58 | 0.50 | 0.139 | 0.04 | 708.8 |
| | PH500 | (1.03) ^b | 2.23 | (4.46) ^b | 0.26 | (4.25) ^b |
| Glass/PH500 (ITO-free) | | 0.61 | 3.98 | 0.364 | 0.88 | 90.5 |

^a R_S is calculated from the inverse slope of J - V curve at high cell voltages ($J = 0$). ^b The numbers in parentheses denote the ratio of PH500 to AI4083 (for V_{OC} , J_{SC} , FF, and PCE) or the ratio of AI4083 to PH500 (for R_S).

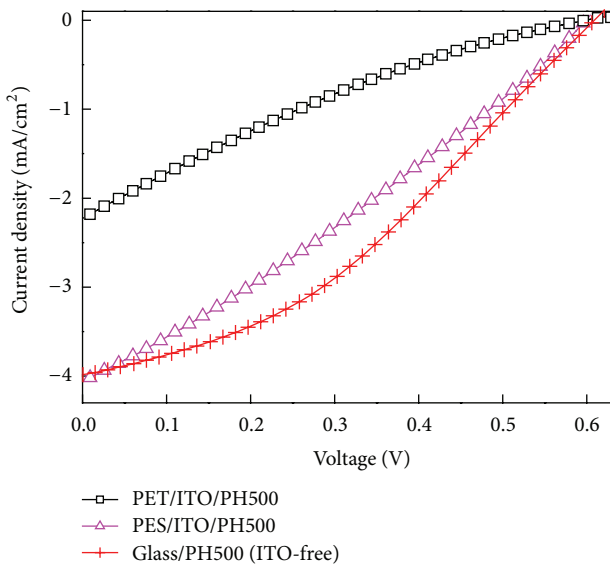


FIGURE 5: J - V characteristics of the ITO-free OPV device (glass/PEDOT:PSS(PH500)/P3HT:PCBM/LiF/Al), the PET/ITO-based flexible plastic device (PET/ITO/PEDOT:PSS(PH500)/P3HT:PCBM/ LiF/Al), and the PES/ITO-based flexible plastic device (PES/ITO/PEDOT:PSS(PH500)/P3HT:PCBM/LiF/Al).

Finally, we can suppose that an ITO electrode with similar or higher resistance than the buffer layer is not as helpful as an ITO-free case to extract hole carriers, because interfacial resistance at inorganic ITO/organic PEDOT:PSS inevitably arises. From this assumption, we fabricated an ITO-free device using PH500 (spin-coating at 2500 rpm, 30 nm, 500 Ω/\square) as an anode.

Figure 5 and Table 1 show that the ITO-free device has not only equivalent or higher J_{SC} but also a high FF with an improved kink curve compared with devices made on PET/ITO or PES/ITO. This indicates that the interface property between ITO and PEDOT:PSS is also another important consideration when developing high-efficiency large-area OPVs, as discussed in many reports [16, 17, 24].

4. Conclusions

Eight different OPV devices using four different types of ITO substrates have been fabricated to investigate the influence of the hole-collecting electrode (ITO) and buffer layers (PEDOT:PSS). The optical transmittance of flexible plastic substrates was slightly lower than that of the glass substrate. The J - V curve shape became worse as the ITO conductivity of substrates increased irrespective of the kind of PEDOT:PSS, indicating significant effect of the R_{sheet} of the ITO electrode in different substrates on the performance of OPV devices. However, the high-conductivity buffer layer (PH500) resulted in better device performances than the low-conductivity buffer layer (AI4083), which supports that the conductivity of hole-collecting buffer layer can compensate for the increase of R_S in OPV devices with a high R_{sheet} ITO electrode. The present result showed that the high conductivities of hole-collecting electrode (ITO) and buffer layer (PEDOT:PSS) are together beneficial to realize an efficient OPV devices by increasing the FF as well as the J_{SC} through reduction of the R_S of devices. Therefore, new transparent electrode and buffer layer materials with high conductivity should be key technological components for successful commercialization of OPV modules.

Acknowledgments

This work was supported by the DGIST R&D Program of the Ministry of Education, Science, and Technology of Republic of Korea (12-EN-02) and National Research Foundation Grant (2012-000523).

References

- [1] G. Dennler, M. C. Scharber, and C. J. Brabec, "Polymer-fullerene bulk-heterojunction solar cells," *Advanced Materials*, vol. 21, no. 13, pp. 1323–1338, 2009.
- [2] B. C. Thompson and J. M. J. Fréchet, "Polymer-fullerene composite solar cells," *Angewandte Chemie*, vol. 47, no. 1, pp. 58–77, 2008.

- [3] Y. Kim, S. Cook, S. M. Tuladhar et al., "A strong regioregularity effect in self-organizing conjugated polymer films and high-efficiency polythiophene:fullerene solar cells," *Nature Materials*, vol. 5, no. 3, pp. 197–203, 2006.
- [4] J. Y. Kim, S. H. Kim, H. Lee et al., "New architecture for high-efficiency polymer photovoltaic cells using solution-based titanium oxide as an optical spacer," *Advanced Materials*, vol. 18, no. 5, pp. 572–576, 2006.
- [5] M. D. Irwin, D. B. Buchholz, A. W. Hains, R. P. H. Chang, and T. J. Marks, "*p*-type semiconducting nickel oxide as an efficiency-enhancing anode interfacial layer in polymer bulk-heterojunction solar cells," *Proceedings of the National Academy of Sciences of the United States of America*, vol. 105, no. 8, pp. 2783–2787, 2008.
- [6] M. C. Scharber, D. Mühlbacher, M. Koppe et al., "Design rules for donors in bulk-heterojunction solar cells—towards 10% energy-conversion efficiency," *Advanced Materials*, vol. 18, no. 6, pp. 789–794, 2006.
- [7] G. Dennler, M. C. Scharber, T. Ameri et al., "Design rules for donors in bulk-heterojunction tandem solar cells—towards 15% energy-conversion efficiency," *Advanced Materials*, vol. 20, no. 3, pp. 579–583, 2008.
- [8] W. A. MacDonald, "Flexible substrates requirements for organic photovoltaics," in *Organic Photovoltaics: Materials, Device Physics, and Manufacturing Technologies*, C. Brabec, V. Dyakonov, and U. Scherf, Eds., chapter 17, pp. 471–489, Wiley-VCH, Weinheim, Germany, 2008.
- [9] J. Kang, S. Lee, D. Kim et al., "Reduction of series resistance in organic photovoltaic using low sheet resistance of ITO electrode," *Electrochemical and Solid-State Letters*, vol. 12, no. 3, pp. H64–H66, 2009.
- [10] A. Elschner and S. Kirchmeyer, "PEDOT-type materials in organic solar cells," in *Organic Photovoltaics: Materials, Device Physics, and Manufacturing Technologies*, C. Brabec, V. Dyakonov, and U. Scherf, Eds., chapter 7, pp. 213–242, Wiley-VCH, Weinheim, Germany, 2008.
- [11] <http://www.clevios.com/en/downloads/heraeus-conductive-polymers-downloads.aspx>.
- [12] C. Ko, Y. Lin, F. Chen, and C. Chu, "Modified buffer layers for polymer photovoltaic devices," *Applied Physics Letters*, vol. 90, no. 6, Article ID 063509, 2007.
- [13] Z. Hu, J. Zhang, Z. Hao, and Y. Zhao, "Influence of doped PEDOT:PSS on the performance of polymer solar cells," *Solar Energy Materials and Solar Cells*, vol. 95, no. 10, pp. 2763–2767, 2011.
- [14] T. Xiao, W. Cui, J. Andereg, J. Shinar, and R. Shinar, "Simple routes for improving polythiophene: fullerene-based organic solar cells," *Organic Electronics: Physics, Materials, Applications*, vol. 12, no. 2, pp. 257–262, 2011.
- [15] K. Sun, Y. Xia, and J. Ouyang, "Improvement in the photovoltaic efficiency of polymer solar cells by treating the poly(3,4-ethylenedioxythiophene): poly(styrenesulfonate) buffer layer with co-solvents of hydrophilic organic solvents and hydrophobic 1,2-dichlorobenzene," *Solar Energy Materials and Solar Cells*, vol. 97, pp. 89–96, 2012.
- [16] G. Kim, H. Song, and J. Y. Kim, "The effect of introducing a buffer layer to polymer solar cells on cell efficiency," *Solar Energy Materials and Solar Cells*, vol. 95, no. 4, pp. 1119–1122, 2011.
- [17] C. Gong, H. B. Yang, Q. L. Song, Z. S. Lu, and C. M. Li, "Mechanism for dimethylformamide-treatment of poly(3,4-ethylenedioxythiophene): poly(styrene sulfonate) layer to enhance short circuit current of polymer solar cells," *Solar Energy Materials and Solar Cells*, vol. 100, pp. 115–119, 2012.
- [18] P. G. Karagiannidis, N. Kalfagiannis, D. Georgiou et al., "Effects of buffer layer properties and annealing process on bulk heterojunction morphology and organic solar cell performance," *Journal of Materials Chemistry*, vol. 22, no. 29, pp. 14624–14632, 2012.
- [19] D. K. Schroder, *Semiconductor Material and Device Characterization*, pp. 1–60, chapter 1, John Wiley & Sons, Tempe, Ariz, USA, 2006.
- [20] S. Jeong, Y. Kwon, B. Choi, H. Ade, and Y. S. Han, "Improved efficiency of bulk heterojunction poly(3-hexylthiophene):[6,6]-phenyl-C₆₁-butyric acid methyl ester photovoltaic devices using discotic liquid crystal additives," *Applied Physics Letters*, vol. 96, no. 18, Article ID 183305, 3 pages, 2010.
- [21] S. Jeong, S. Woo, H. Lyu, and Y. S. Han, "Effects of a perfluorinated compound as an additive on the power conversion efficiencies of polymer solar cells," *Solar Energy Materials and Solar Cells*, vol. 95, no. 7, pp. 1908–1914, 2011.
- [22] A. Moliton and J. Nunzi, "How to model the behaviour of organic photovoltaic cells," *Polymer International*, vol. 55, no. 6, pp. 583–600, 2006.
- [23] Y. Huang, S. Dai, S. Chen et al., "Theoretical modeling of the series resistance effect on dye-sensitized solar cell performance," *Applied Physics Letters*, vol. 95, no. 24, Article ID 243503, 2009.
- [24] J. D. Servaites, M. A. Ratner, and T. J. Marks, "Organic solar cells: a new look at traditional models," *Energy and Environmental Science*, vol. 4, no. 11, pp. 4410–4422, 2011.
- [25] M. Kim, B. Kim, and J. Kim, "Effective variables to control the fill factor of organic photovoltaic cells," *ACS Applied Materials and Interfaces*, vol. 1, no. 6, pp. 1264–1269, 2009.
- [26] J. Xue, S. Uchida, B. P. Rand, and S. R. Forrest, "4.2% efficient organic photovoltaic cells with low series resistances," *Applied Physics Letters*, vol. 84, no. 16, pp. 3013–3015, 2004.
- [27] B. Muhsin, J. Renz, K. Drüe, G. Gobsch, and H. Hoppe, "Influence of polymer solar cell geometry on series resistance and device efficiency," *Physica Status Solidi A*, vol. 206, no. 12, pp. 2771–2774, 2009.
- [28] M. W. Denhoff and N. Drolet, "The effect of the front contact sheet resistance on solar cell performance," *Solar Energy Materials and Solar Cells*, vol. 93, no. 9, pp. 1499–1506, 2009.
- [29] S. Park, W. Jeong, D. Kim et al., "Large-area organic solar cells with metal subelectrode on indium tin oxide anode," *Applied Physics Letters*, vol. 96, no. 17, Article ID 173301, 2010.
- [30] G. T. Koishiyev and J. R. Sites, "Impact of sheet resistance on 2-D modeling of thin-film solar cells," *Solar Energy Materials and Solar Cells*, vol. 93, no. 3, pp. 350–354, 2009.
- [31] W. Jeong, J. Lee, S. Park, J. Kang, and J. Kim, "Reduction of collection efficiency of charge carriers with increasing cell size in polymer bulk heterojunction solar cells," *Advanced Functional Materials*, vol. 21, no. 2, pp. 343–347, 2011.
- [32] J. Nelson, J. Kirkpatrick, and P. Ravirajan, "Factors limiting the efficiency of molecular photovoltaic devices," *Physical Review B*, vol. 69, no. 3, Article ID 035337, 11 pages, 2004.
- [33] Y. Kim, A. M. Ballantyne, J. Nelson, and D. D. C. Bradley, "Effects of thickness and thermal annealing of the PEDOT:PSS layer on the performance of polymer solar cells," *Organic Electronics: Physics, Materials, Applications*, vol. 10, no. 1, pp. 205–209, 2009.
- [34] D. Gupta, M. Bag, and K. S. Narayan, "Correlating reduced fill factor in polymer solar cells to contact effects," *Applied Physics Letters*, vol. 92, no. 9, Article ID 093301, 2008.

- [35] D. Gupta, S. Mukhopadhyay, and K. S. Narayan, "Fill factor in organic solar cells," *Solar Energy Materials and Solar Cells*, vol. 94, no. 8, pp. 1309–1313, 2010.
- [36] M. Glatthaar, M. Riede, N. Keegan et al., "Efficiency limiting factors of organic bulk heterojunction solar cells identified by electrical impedance spectroscopy," *Solar Energy Materials and Solar Cells*, vol. 91, no. 5, pp. 390–393, 2007.
- [37] A. Kumar, S. Sista, and Y. Yang, "Dipole induced anomalous S-shape I-V curves in polymer solar cells," *Journal of Applied Physics*, vol. 105, no. 9, Article ID 094512, 2009.
- [38] J. Meiss, M. K. Riede, and K. Leo, "Optimizing the morphology of metal multilayer films for indium tin oxide (ITO)-free inverted organic solar cells," *Journal of Applied Physics*, vol. 105, no. 6, Article ID 063108, 2009.
- [39] J. Meiss, M. K. Riede, and K. Leo, "Towards efficient tin-doped indium oxide (ITO)-free inverted organic solar cells using metal cathodes," *Applied Physics Letters*, vol. 94, no. 1, Article ID 013303, 2009.
- [40] A. M. Nardes, R. A. J. Janssen, and M. Kemerink, "A morphological model for the solvent-enhanced conductivity of PEDOT:PSS thin films," *Advanced Functional Materials*, vol. 18, no. 6, pp. 865–871, 2008.
- [41] J. Hwang, F. Amy, and A. Kahn, "Spectroscopic study on sputtered PEDOT·PSS: role of surface PSS layer," *Organic Electronics: Physics, Materials, Applications*, vol. 7, no. 5, pp. 387–396, 2006.
- [42] S. Na, G. Wang, S. Kim et al., "Evolution of nanomorphology and anisotropic conductivity in solvent-modified PEDOT:PSS films for polymeric anodes of polymer solar cells," *Journal of Materials Chemistry*, vol. 19, no. 47, pp. 9045–9053, 2009.

Research Article

Enhanced Efficiency of GaAs Single-Junction Solar Cells with Inverted-Cone-Shaped Nanoholes Fabricated Using Anodic Aluminum Oxide Masks

Kangho Kim,¹ Hoang Duy Nguyen,² Sunil Mho,³ and Jaejin Lee¹

¹ Department of Electrical and Computer Engineering, Ajou University, Suwon 443-749, Republic of Korea

² Institute of Applied Materials Science, Vietnam Academy of Science and Technology, Ho Chi Minh 70999, Vietnam

³ Department of Energy Systems Research, Ajou University, Suwon 443-749, Republic of Korea

Correspondence should be addressed to Jaejin Lee; jaejin@ajou.ac.kr

Received 15 June 2013; Accepted 10 July 2013

Academic Editor: Leonardo Palmisano

Copyright © 2013 Kangho Kim et al. This is an open access article distributed under the Creative Commons Attribution License, which permits unrestricted use, distribution, and reproduction in any medium, provided the original work is properly cited.

The GaAs solar cells are grown by low-pressure metalorganic chemical vapor deposition (LP-MOCVD) and fabricated by photolithography, metal evaporation, annealing, and wet chemical etch processes. Anodized aluminum oxide (AAO) masks are prepared from an aluminum foil by a two-step anodization method. Inductively coupled plasma dry etching is used to etch and define the nanoarray structures on top of an InGaP window layer of the GaAs solar cells. The inverted-cone-shaped nanoholes with a surface diameter of about 50 nm are formed on the top surface of the solar cells after the AAO mask removal. Photovoltaic and optical characteristics of the GaAs solar cells with and without the nanohole arrays are investigated. The reflectance of the AAO nanopatterned samples is lower than that of the planar GaAs solar cell in the measured range. The short-circuit current density increased up to 11.63% and the conversion efficiency improved from 10.53 to 11.57% under 1-sun AM 1.5 G conditions by using the nanohole arrays. Dependence of the efficiency enhancement on the etching depth of the nanohole arrays is also investigated. These results show that the nanohole arrays fabricated with an AAO technique may be employed to improve the light absorption and, in turn, the conversion efficiency of the GaAs solar cell.

1. Introduction

GaAs is commonly used to fabricate the high conversion efficiency III-V solar cell based on multijunction tandem structure. An InGaP layer is utilized as a window layer on top of the GaAs emitter in a GaAs-based solar cell. Because of refractive index difference between InGaP and air, more than 30% of the incident light can be reflected from the surface of the solar cells [1]. It is therefore necessary to use an antireflection coating layer for improving the conversion efficiency. An antireflection coating using multilayers with different refractive index materials such as MgF₂, ZnS, ZnO, SiO₂, SiN_x, and TiO_x is usually used for the conventional solar cells [2–4]. However, this layer can invoke unexpected problems such as adhesion and thermal mismatch when the solar cell operates under the strong-irradiation condition. To overcome these drawbacks, surface texturing techniques

have been successfully introduced [1, 5–7]. By patterning the window surface layer, one can significantly reduce the reflection of the incident light through the enhanced absorption from the textured structures. Nanopatterning structures using metal nanoparticles or photonic crystal have attracted much attention because they can improve the light absorption due to the plasmonic and spontaneous effects [8, 9]. Several groups reported on using two-dimensional photonic crystals to improve conversion efficiency of Si or Ge solar cells [10, 11]. However, using expensive nanopatterning technique such as electron-beam lithography increases device cost significantly. Therefore, nonlithographic approach using nanoporous anodic aluminum oxide (AAO) template has attracted a lot of attention as a key nanofabrication method due to its simple and low-cost process [12]. Moreover, with the AAO mask, we can fabricate the nanohole arrays with a small diameter (below 100 nm) that is difficult to make by

the conventional lithography methods. It is worth noting that by using such a small opening mask, we can fabricate the nanoholes with an inverted cone shape that is close to the optimized form for the light-management architectures to achieve the high-efficiency solar cells [13].

In this study, we report on the improvement of the GaAs solar cells with the nanohole arrays on the InGaP window layer. The AAO masks with an opening size of about 50 nm are prepared using a two-step anodization process. The inverted-cone-shaped (ICS) nanoholes with different depths are formed on the surface of the solar cell after inductively coupled-plasma reactive-ion-etching (ICP-RIE) processes. The conversion efficiency improved from 10.53 to 11.57% under 1-sun AM 1.5 G conditions by using the nanohole arrays.

2. Experiment Details

The GaAs single-junction solar cell structures, as shown in Figure 1, are grown in a metalorganic chemical vapor deposition (MOCVD) system on n-type GaAs (100) substrates. Trimethylgallium (TMGa) and trimethylindium (TMIn) are used as group III precursors, while arsine (AsH_3) and phosphine (PH_3) are used as As and P sources, respectively. Silane (SiH_4) and diethylzinc (DEZn) are used as n- and p-doping sources, respectively. Ultra-high purity hydrogen gas (H_2) is used as a carrier gas. The reactor pressure and temperature are kept at 50 mbar and 680°C, respectively. Device structures from the substrate to the top consist of a 0.2 μm thick GaAs buffer layer for high crystal quality, a 0.05 μm thick highly doped $\text{In}_{0.5}\text{Ga}_{0.5}\text{P}$ back surface field (BSF) layer, a 3.5 μm thick GaAs base layer, a 0.5 μm thick GaAs emitter layer, a 0.2 μm thick highly doped $\text{In}_{0.5}\text{Ga}_{0.5}\text{P}$ window layer, and a 0.3 μm thick GaAs cap layer for ohmic contact.

The solar cell devices with the aperture area of 0.25 cm^2 are made using conventional fabrication processes. Metal contacts are defined by a UV photolithography technique. AuGe/Ni/Au and Ti/Pt/Au layers are deposited by an e-beam evaporator for the n- and p-type ohmic contacts, respectively. The samples then are annealed in an RTA station at 385°C for 30 s. The InGaP window layer is exposed by selectively etching p⁺-GaAs cap layer in an acid solution ($\text{CA}:\text{H}_2\text{O}_2:\text{H}_2\text{O} = 25:1:75$).

Nanohole arrays are patterned on the surface of the solar cell by an ICP-RIE etching using the AAO mask. The AAO masks are prepared by a typical two-step anodization process using a grain-free aluminum foil (99.99%, 100 μm in thickness, Tokai). The aluminum foil is electropolished in a 1:4 solution of perchloric acid and ethanol. After the first anodization in the 0.3 M oxalic acid at 40 V for 8 h, the anodized oxide layer on the Al foil is removed in a mixture of H_3PO_4 and CrO_3 . The sample is then exposed for the second anodization step resulting in a thin alumina film of 500–600 nm on top of the Al foil by controlling the anodization duration. A saturated HgCl_2 solution is used to remove the Al film at the bottom, leaving a thick anodized alumina layer. The removal of the barrier layer and hole widening are conducted in a 5 wt % H_3PO_4 solution. The AAO masks

| | | |
|---------------------------|---|-------------------|
| Front contact (Ti/Pt/Au) | | 500 nm |
| Ohmic | p-GaAs | 300 nm |
| Window | p- $\text{In}_{0.5}\text{Ga}_{0.5}\text{P}$ | 200 nm |
| Emitter | p-GaAs | 500 nm |
| Base | n-GaAs | 3500 nm |
| BSF | n- $\text{In}_{0.5}\text{Ga}_{0.5}\text{P}$ | 50 nm |
| Buffer | n-GaAs | 200 nm |
| Substrate | n-GaAs | 350 μm |
| Back contact (AuGe/Ni/Au) | | 500 nm |

FIGURE 1: Schematic structure of the fabricated GaAs single-junction solar cells.

are designed with a hole size of about 40 nm and a distance between holes of about 100 nm in a quasihexagonal geometry [14]. The AAO mask is placed on top of the GaAs solar cell structure. ICP-RIE etching is then applied to transfer the nanopattern from the AAO mask to the window layer of the solar cell. The etching process uses a mixture of BCl_3 and Cl_2 with the flows of 5 and 30 sccm, respectively, under an ICP source power of 200 W and an RF bias power of 50 W at a chamber pressure of 10 mTorr. The depths of the nanohole arrays are controlled by etching time that is varied from 10 to 60 s. The nanohole arrays are finally formed on top of the GaAs solar cell after removing the AAO masks. A GaAs solar cell without the nanohole pattern is used as a reference for the solar cell performance investigation. The morphologies of the GaAs solar cell with the nanohole arrays are studied by a field emission scanning electron microscopy (FE-SEM). To study the loss of the incident light, we carried out reflectance measurements at room temperature with a UV-Vis-NIR Cary 5000 Spectrometer from 300 to 900 nm. The photovoltaic current density-voltage (J - V) characteristics of the GaAs solar cells are evaluated by a solar simulator under 1-sun air mass (AM) 1.5 G-conditions at room temperature. The photocurrent response of the fabricated cells is also investigated with a quantum efficiency measurement system at room temperature.

3. Results and Discussions

Figure 2 shows the SEM images of the nanohole arrays on the solar cells. After a 40 s ICP/RIE etching and removal of the AAO mask, the nanohole arrays have the quasihexagonal symmetry with a mean diameter and depth of about 50 and 64 nm, respectively. The holes that formed on top of the solar cells are slightly larger than those of the AAO masks because the AAO masks may be etched out during the plasma etching process and/or the surfaces of solar cells in contact with the AAO masks are not completely smooth [12]. It is worth to note that the nanohole arrays retain an ICS form as can be observed clearly in the inset of Figure 2(b). The ICS nanoholes can be formed after a short-time dry etching process using masks with a small opening [15]. The depths of

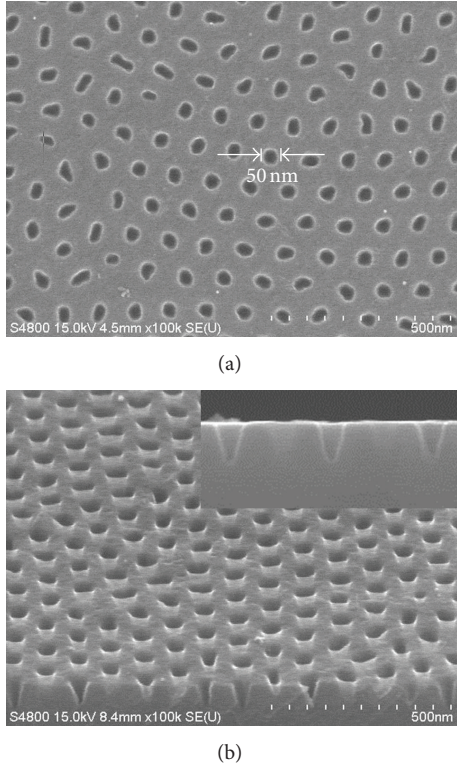


FIGURE 2: (a) Top- and (b) tilt-view FE-SEM images of the nanohole arrays formed on the InGaP window layer after ICP etching. The nanoholes have inverted-cone-shaped form with a top diameter of about 50 nm and a depth of about 64 nm after 40 s etching. The inset in (b) shows a magnification of the inverted-cone-shaped nanoholes.

the nanohole arrays are measured to be about 16, 48, 64, and 95 nm for 10, 30, 40, and 60 s etching times, respectively.

Figure 3(a) shows the reflectance spectra at the surface of the fabricated solar cell with and without the nanohole arrays. It can be seen that all nanopatterned surfaces have lower reflectances compared to the planar surface in the measured wavelength regions. In addition, the reflectance is reduced with the increase of the hole depth. The reduction of the reflectance at the nanopatterned surfaces may originate from the two possible mechanisms. The first one is based on the redistribution of the incident light. When the incident light comes to the solar cell surface with the nanohole arrays, it can be scattered by the subwavelength holes and will be redistributed. This redistribution results in a reduction of the reflectance at the textured surface [16, 17]. The second mechanism is based on the Fresnel reflection suppression [17], that is, a gradual change in the refractive index along the surface with the ICS nanoholes. The ICS nanohole structure may result in a Fresnel reflection suppression when the incident light comes to the solar cell surfaces. Figure 3(b) shows the calculated effective refractive indices near the surfaces of the solar cells with and without the ICS nanohole arrays at a wavelength of 600 nm [18]. In the non-patterned solar cell with a planar InGaP window layer, the refractive index changes sharply from air ($n_{\text{air}} = 1$) to InGaP ($n_{\text{InGaP}} = 3.62$) at 600 nm. When the ICS nanoholes are fabricated

on the InGaP window layer, the refractive index changes gradually because the hole diameter reduces continuously from the top to the bottom. Because the reflection from an interface between two materials with refractive indices of n_1 and n_2 is proportional to $(n_1 - n_2)^2$ [19], the refractive index gradient exhibited by the nanohole arrays leads to a lower reflection over a wavelength range of interest.

Figure 4 shows the external quantum efficiency (EQE) of the GaAs solar cells with and without the nanohole arrays at different wavelengths. It reveals that the EQE of the nanohole patterned solar cell is enhanced in the long wavelength region near the bandgap energy of GaAs (700–900 nm), while this value is slightly reduced in the short wavelength region compared to that of the planar surface solar cell. In the long wavelength region, the photocurrent can be further increased as the nanohole array depths increase. This may be attributed to a better light trapping with the deeper nanohole arrays. In the short wavelength region, the loss of high energy photons by thermalization and surface recombination due to the increased surface states of the InGaP window layer is more dominant than the efficiency gain by light trapping effect [13, 20]. However, this reduction is small compared to the enhancement of EQE at the long wavelength region in the solar cells with the nanohole arrays. As a result, the total conversion efficiency of the solar cell with the deeper nanohole arrays shows a higher value compared to that of the planar or shallow patterned solar cell, as shown in Figure 5.

Figure 5 shows the J - V characteristics of the GaAs single-junction solar cell with and without the nanohole arrays. The corresponding parameters are summarized in Table 1. It can be seen that the photovoltaic characteristics vary with the depth of the nanohole arrays. Especially, the short-circuit current density (J_{sc}) changes a lot compared to the other parameters due to the lower reflection. J_{sc} is increased up to 7.2, 10.4, 11.6, and 12.9% when the depths of the nanohole arrays on the surface of the GaAs solar cell are 16, 48, 64, and 95 nm, respectively. However, it is found that fill factor (FF) and open-circuit voltage (V_{oc}) are degraded when the nanohole depth increases. This may be attributed to the plasma-induced damage during the anisotropic etching process [21]. The damage is a complex function of many plasma characteristics such as the plasma energy, chemistry of plasma gas, pressure, and temperature. The plasma-induced surface states can cause a significant increase of carrier recombination at the etched surfaces and a decrease of the carrier life time, in turn, resulting in the reduction of the photocurrent. Taking into account the competition between the reduction of reflectance and the plasma damages by the deep nanohole arrays, we found that about 64 nm hole depth is the optimized value for the improvement of conversion efficiency in the studied system. The conversion efficiency improved from 10.53 to 11.57% under 1-sun AM 1.5 G conditions by using 64 nm deep hole arrays.

4. Conclusion

In summary, the ICS nanohole arrays with the depths of 16, 48, 64, and 95 nm have been fabricated on the InGaP

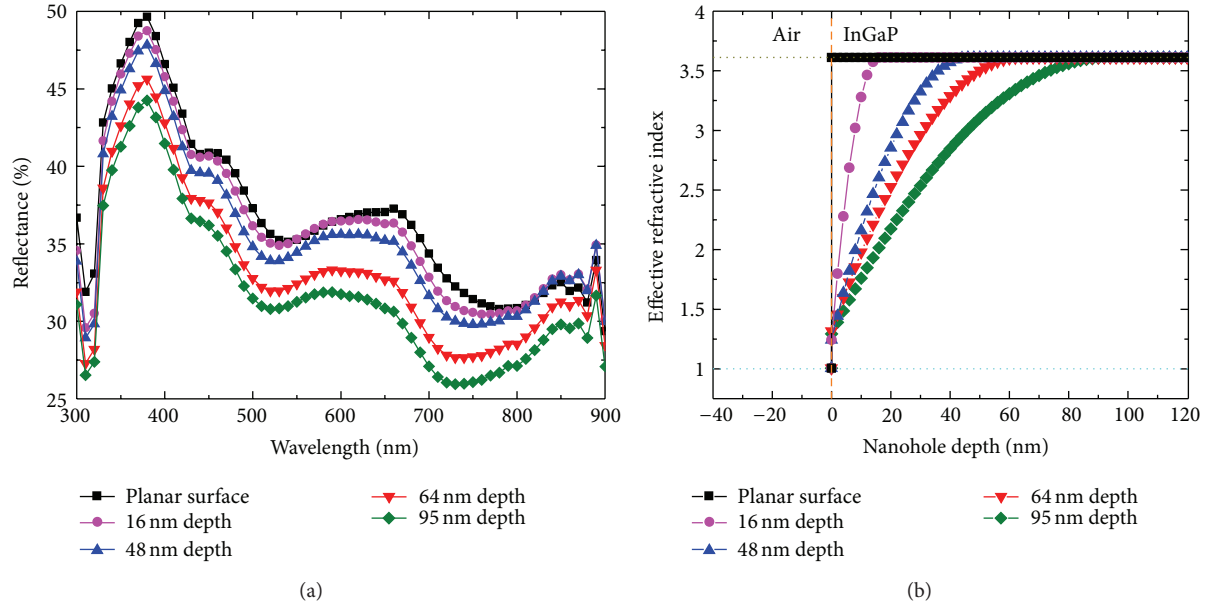


FIGURE 3: (a) Reflectance spectra at the surfaces of the solar cells with and without nanohole arrays and (b) calculated effective refractive index at $\lambda = 600$ nm near the surface of the solar cells with and without inverted-cone-shaped nanoholes.

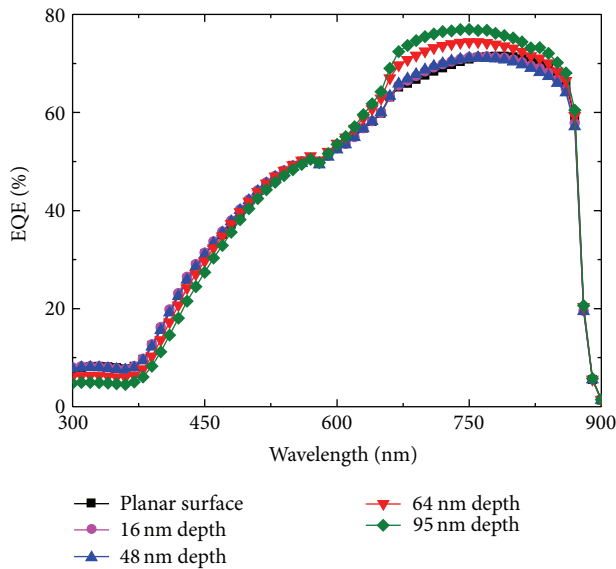


FIGURE 4: EQE of the solar cells with and without the nanohole arrays.

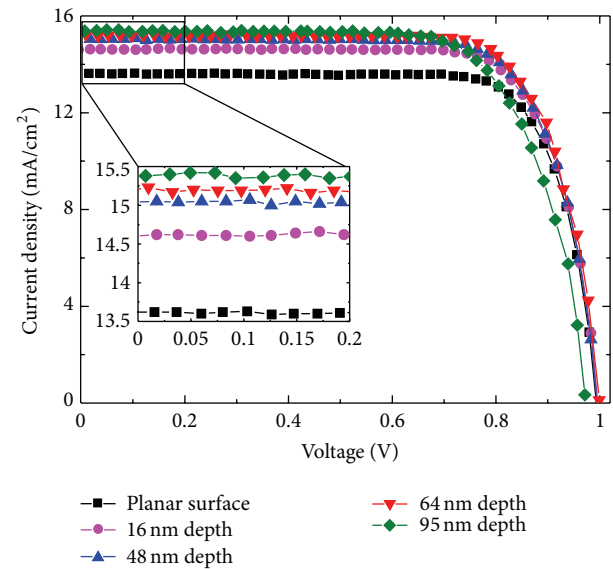


FIGURE 5: J - V curves of the GaAs solar cells with and without the nanohole arrays.

window layer of the GaAs single-junction solar cells using the AAO masks. Characteristics of the solar cells with and without the nanohole arrays have been investigated by the reflectance, external quantum efficiency, and current density-voltage curve measurements. The solar cells with the nanohole arrays show a lower surface reflectance compared to the unpatterned planar sample. The surface reflection is reduced with the increase of the nanohole depth. The external

quantum efficiency of the solar cell with the nanohole arrays is improved at the wavelength region near the GaAs bandgap energy due to the enhanced light absorption. The current density-voltage characteristics of the solar cells show that the conversion efficiency can be increased from 10.53 to 11.57% under the AM 1.5 G conditions by using the 64 nm deep ICS nanohole arrays.

TABLE 1: Current density-voltage characteristics of the GaAs single-junction solar cells with various depths of the nano-hole arrays.

| Sample | V_{oc} (V) | J_{sc} (mA/cm ²) | FF (%) | Eff. (%) |
|----------------|--------------|--------------------------------|--------|----------|
| Planar surface | 0.994 | 13.622 | 77.81 | 10.53 |
| 16 nm depth | 0.996 | 14.605 | 76.55 | 11.14 |
| 48 nm depth | 0.995 | 15.044 | 75.87 | 11.36 |
| 64 nm depth | 1.009 | 15.206 | 75.39 | 11.57 |
| 95 nm depth | 0.973 | 15.373 | 72.52 | 10.85 |

Acknowledgments

This work is supported by the Converging Research Center Program through the National Research Foundation (NRF) of the Korea funded by the Ministry of Education, Science and Technology (Grant no. 2011K000590). This work is also supported by the New & Renewable Energy of the Korea Institute of Energy Technology Evaluation and Planning (KETEP) grant funded by the Korea government Ministry of Knowledge Economy (Grant no. 20123010010110).

References

- [1] C.-H. Sun, B. J. Ho, B. Jiang, and P. Jiang, "Biomimetic subwavelength antireflective gratings on GaAs," *Optics Letters*, vol. 33, no. 19, pp. 2224–2226, 2008.
- [2] D. Li, F. Huang, and S. Ding, "Sol-gel preparation and characterization of nanoporous ZnO/SiO₂ coatings with broadband antireflection properties," *Applied Surface Science*, vol. 257, no. 23, pp. 9752–9756, 2011.
- [3] G. Zhang, J. Zhao, and M. A. Green, "Effect of substrate heating on the adhesion and humidity resistance of evaporated MgF₂/ZnS antireflection coatings and on the performance of high-efficiency silicon solar cells," *Solar Energy Materials and Solar Cells*, vol. 51, no. 3-4, pp. 393–400, 1998.
- [4] M. H. Kang, K. Ryu, A. Upadhyaya, and A. Rohatgi, "Optimization of SiN AR coating for Si solar cells and modules through quantitative assessment of optical and efficiency loss mechanism," *Progress in Photovoltaics*, vol. 19, no. 8, pp. 983–990, 2011.
- [5] J. Zhu, Z. Yu, S. Fan, and Y. Cui, "Nanostructured photon management for high performance solar cells," *Materials Science and Engineering R*, vol. 70, no. 3-6, pp. 330–340, 2010.
- [6] K.-S. Han, J.-H. Shin, W.-Y. Yoon, and H. Lee, "Enhanced performance of solar cells with anti-reflection layer fabricated by nano-imprint lithography," *Solar Energy Materials and Solar Cells*, vol. 95, no. 1, pp. 288–291, 2011.
- [7] Y.-F. Huang, S. Chattopadhyay, Y.-J. Jen et al., "Improved broadband and quasi-omnidirectional anti-reflection properties with biomimetic silicon nanostructures," *Nature Nanotechnology*, vol. 2, no. 12, pp. 770–774, 2007.
- [8] H. A. Atwater and A. Polman, "Plasmonics for improved photovoltaic devices," *Nature Materials*, vol. 9, no. 3, pp. 205–213, 2010.
- [9] E. Yablonovitch, "Inhibited spontaneous emission in solid-state physics and electronics," *Physical Review Letters*, vol. 58, no. 20, pp. 2059–2062, 1987.
- [10] C. Trompoukis, O. E. Daif, V. Depauw, I. Gordon, and J. Poortmans, "Photonic assisted light trapping integrated in ultrathin crystalline silicon solar cells by nanoimprint lithography," *Applied Physics Letters*, vol. 101, Article ID 103901, 4 pages, 2012.
- [11] I. Prieto, B. Galiana, P. A. Postigo, C. Algora, L. J. Martínez, and I. Rey-Stolle, "Enhanced quantum efficiency of Ge solar cells by a two-dimensional photonic crystal nanostructured surface," *Applied Physics Letters*, vol. 94, no. 19, Article ID 191102, 2009.
- [12] J. Liang, H. Chik, A. Yin, and J. Xu, "Two-dimensional lateral superlattices of nanostructures: nonlithographic formation by anodic membrane template," *Journal of Applied Physics*, vol. 91, no. 4, pp. 2544–2546, 2002.
- [13] A. Polman and H. A. Atwater, "Photonic design principles for ultrahigh-efficiency photovoltaics," *Nature Materials*, vol. 11, no. 3, pp. 174–177, 2012.
- [14] M. Jung, S.-I. Mho, and H. L. Park, "Long-range-ordered CdTeGaAs nanodot arrays grown as replicas of nanoporous alumina masks," *Applied Physics Letters*, vol. 88, no. 13, Article ID 133121, 2006.
- [15] S. Ohki, M. Oda, H. Akiya, and T. Shibata, "Cavernous undercuts appearing in reactive ion etched submicron-wide deep trenches," *Journal of Vacuum Science & Technology B*, vol. 5, pp. 1611–1616, 1987.
- [16] W. Stork, N. Streibl, H. Haidner, and P. Kipfer, "Artificial distributed-index media fabricated by zero-order gratings," *Optics Letters*, vol. 16, pp. 1921–1923, 1991.
- [17] D. H. Raguin and G. M. Morris, "Antireflection structured surfaces for the infrared spectral region," *Applied Optics*, vol. 32, no. 7, pp. 1154–1167, 1993.
- [18] D. G. Stavenga, S. Foletti, G. Palasantzas, and K. Arikawa, "Light on the moth-eye corneal nipple array of butterflies," *Proceedings of the Royal Society B*, vol. 273, no. 1587, pp. 661–667, 2006.
- [19] P. Nubile, "Analytical design of antireflection coatings for silicon photovoltaic devices," *Thin Solid Films*, vol. 342, no. 1, pp. 257–261, 1999.
- [20] K. Cho, D. J. Ruebusch, M. H. Lee et al., "Molecular monolayers for conformal, nanoscale doping of InP nanopillar photovoltaics," *Applied Physics Letters*, vol. 98, no. 20, Article ID 203101, 2011.
- [21] K. N. Lee, J. W. Lee, J. Hong, C. R. Abernathy, S. J. Pearton, and W. S. Hobson, "Effect of ion damage on the electrical and optical behavior of p-type GaAs and InGaP," *Journal of Electronic Materials*, vol. 26, no. 11, pp. 1279–1282, 1997.

Research Article

Characterization and Modeling of CdS/CdTe Heterojunction Thin-Film Solar Cell for High Efficiency Performance

Hamid Fardi and Fatima Buny

Department of Electrical Engineering, University of Colorado Denver, Campus Box 110, P.O. Box 173364, Denver, CO 80217-3364, USA

Correspondence should be addressed to Hamid Fardi; hamid.fardi@ucdenver.edu

Received 6 May 2013; Revised 20 June 2013; Accepted 25 June 2013

Academic Editor: Gaetano Di Marco

Copyright © 2013 H. Fardi and F. Buny. This is an open access article distributed under the Creative Commons Attribution License, which permits unrestricted use, distribution, and reproduction in any medium, provided the original work is properly cited.

Device simulation is used to investigate the current-voltage efficiency performance in CdTe/CdS photovoltaic solar cell. The role of several limiting factors such as back contact Schottky barrier and its relationship to the doping density and layer thickness is examined. The role of surface recombination velocity at back contact interface and extended CdTe layer is included. The base CdS/CdTe experimental device used in this study shows an efficiency of 16-17%. Simulation analysis is used to optimize the experimental base device under AM1.5 solar spectrum. Results obtained indicate that higher performance efficiency may be achieved by adding and optimizing an extended CdTe electron reflector layer at the back Schottky contact. In the optimization of the CdS/CdTe cell an extended electron reflector region with a barrier height of 0.1 eV and a doping density of $7 \times 10^{18} \text{ cm}^{-3}$ with an optimum thickness of 100 nm results in best cell efficiency performance of 19.83% compared with the experimental data.

1. Introduction

Among the thin-film solar cells, the commonly used are amorphous silicon, CuInGaSe₂, and CdTe. At the present, the amorphous silicon solar cells have the largest market share in the world with less a fraction of one percent to CuInGaSe₂ and about a few percent to CdTe cells. The benefit of using CdTe is for being a direct bandgap material with high absorption (in relationship with silicon) and the ease of device processing, can be deposited on glass in thin film typically a few micrometers and at low temperature [1-7].

Large-area CdTe photovoltaic panels can be economically fabricated, potentially making the CdTe thin-film solar cell a leading alternative energy source. However, the recorded experimental CdTe efficiency of 16.5% is much less than its theoretical maximum efficiency of 29%, where the open-circuit voltage of 0.845 V is well below what is expected for its bandgap of 1.42 eV [8-10]. The experimental measurement obtained by others is used as a benchmark for the optimization of the CdS/CdTe cell and for the development of the strategies to improve the efficiency referred to here as base device [11].

An important issue related to the limiting performance of the CdTe cells is the back contact. Experimental works show

that the CdTe cells at back contact form Schottky barrier thus degrading the cell efficiency and performance [12-18]. Other limiting factors in performance of CdTe cells are related to the unavailability of the physical material properties which is at incubator status when compared with the mature technology of the silicon and silicon electronics [19-26].

The modeling approach adopted in this paper allows us to examine device design and the role of material parameters in the performance and efficiency of the cell. Device simulation is used to predict the characteristics of CdS/CdTe heterojunction solar cells by identifying material parameters essential for improving the cell performance. Issues related to doping concentration, surface recombination, and extended region back contact Schottky barrier are investigated.

The modeling work on CdTe structures is based on simulation program, AFORS-HET [27-29]. The software program has been used in the development and design of several solar cells in the past. The device modeling solves relatively large number of nonlinear and tightly coupled partial differential diffusion equations and uses several position-dependent material and transport parameters that make it robust. The device equations are solved over a set of mesh geometry. In addition, for solar cell structures the model includes optical absorption and a broad spectrum of light input that can be

TABLE 1: Material parameters used in the simulation [10–12].

| Parameter | CdTe | CdS | ZnO (TCO) |
|--|--|---------------------------|---------------------------|
| E_g (eV) | 1.42 | 2.53 | 3.4 |
| Electron Affinity (eV) | 4.28 | 4.5 | 4.5 |
| μ_n ($\text{cm}^2/\text{v}\cdot\text{s}$) | 500 | 340 | 100 |
| μ_p ($\text{cm}^2/\text{v}\cdot\text{s}$) | 60 | 50 | 25 |
| Relative Dielectric Constant | 10.9 | 8.9 | 9 |
| Density of state for electron (cm^{-3}) | 7.8×10^{17} | 2.22×10^{18} | 2.22×10^{18} |
| Density of state for hole (cm^{-3}) | 1.8×10^{19} | 1.8×10^{19} | 1.9×10^{19} |
| Index of Refraction | 2.76 | 2.51 | 2.006 |
| Doping Density (cm^{-3}) | 7×10^{16} – 7×10^{18} p-type | 1×10^{18} n-type | 1×10^{18} n-type |
| ZnO/CdS ΔE_c (eV) | | 0.0 | |
| ZnO/CdS ΔE_v (eV) | | 0.87 | |
| CdS/CdTe ΔE_c (eV) | 0.22 | | |
| CdS/CdTe ΔE_v (eV) | 0.89 | | |

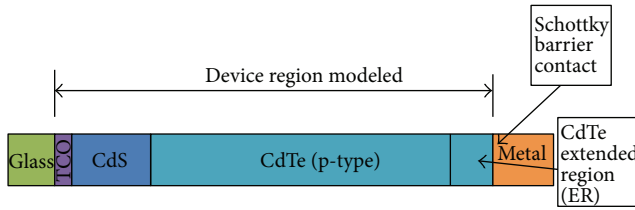


FIGURE 1: The configuration of a CdTe thin-film solar cell. A $2 \mu\text{m}$ CdTe layer, a 40 nm CdS layer, and $0.5 \mu\text{m}$ TCO(ZnO) are assumed for the simulation; layers are not scaled. Light is illuminated from left.

supplied to properly simulate the characteristics of a solar cell. In the next sections we will show in detail that the program works well for CdTe/CdS photovoltaic devices.

2. Device Design and Analysis

The schematic of a CdTe thin-film solar cell used in the simulation with TCO/CdS(n-type)/CdTe(p-type)/metal structure is shown in Figure 1.

In this design, the carrier density of CdTe p-type layer is $7 \times 10^{16} \text{ cm}^{-3}$ (similar to the experimental data) with heavy doped CdS n-layer of $1 \times 10^{18} \text{ cm}^{-3}$. The CdTe is a direct bandgap semiconductor with a large absorption coefficient. Because of this important optical property, very thin CdTe layers can be used for photovoltaic applications. For the simulation, we have used a film thickness of $2 \mu\text{m}$ as in the typical CdTe solar cell manufacturing [30–35]. Table 1 shows the characteristics of ZnO-TCO layer. A 500 nm thick TCO layer with an n-type doping density of $1 \times 10^{18} \text{ cm}^{-3}$ is assumed. For this structure, the depletion region is formed in CdTe absorption layer. That is, a $2 \mu\text{m}$ CdTe cell and a doping density of $7 \times 10^{16} \text{ cm}^{-3}$ become fully depleted. It is desirable to have photons absorbed in this region where light induced carriers can be collected with the assistance of the built-in electric field. Similarly, at a wavelength of 600 nm , a $2 \mu\text{m}$ of CdTe layer will absorb more than 99% of incident light,

making CdTe a suitable candidate for absorption material for photovoltaic applications.

Other device parameters are CdS layer with a thickness of a 40 nm and ZnO transparent conductive oxide (TCO) layer with a thickness of $0.5 \mu\text{m}$. The TCO layer with a bandgap energy of about 3.4 eV is used to minimize the optical loss where at this high sun energy TCO prevents less blue light from reaching CdTe for a thick CdS layer.

The layer of CdTe is assumed to have an electron affinity of 4.28 eV and a bandgap of 1.42 eV . In order to create an ohmic contact, a metal with a work function greater than or equal to 5.7 eV (the sum of electron affinity and bandgap) is required. As a result most metal contacts applied to p-type CdTe such as copper with work function of 4.6 eV , nickel with 5.1 eV , or titanium with 4.3 eV create nonohmic Schottky type barrier contact which limits the overall performance efficiency of the CdTe cell [36, 37]. As shown in Figure 4, the incorporation of an electron reflector (ER) at back contact is proposed by other investigators to improve the open-circuit voltage of solar cells, and to improve the efficiency of CdTe thin film [3, 8, 10–12].

In a heavily doped p-type metal back contact, the majority of hole carriers are transported by the tunneling in a thin junction of approximately a few nanometer. The optimization and development of the back contact is a limiting factor addressed in this paper and crucial for achieving a high efficiency cell.

3. Experimental Data

A device structure similar to one described in reference [11] is considered. As shown in Figure 3, the measured room temperature dark current-voltage characteristics of the ZnO/CdTe/CdS cell are compared with the simulation result. Data of Table 1 is used in the simulation analysis [10–12]. In addition, a carrier lifetime of $5 \times 10^{-10} \text{ s}$ is used. In this model it is assumed that the recombination center is located at the center of the bandgap energy resulting in modeling the recombination of carriers with a constant lifetime. The analysis shows that there is an extended portion of the

TABLE 2: Current-voltage characteristics of a CdTe cell with different Schottky barrier heights.

| Barrier height (eV) | V_{oc} (mV) | J_{sc} (mA/cm ²) | FF (%) | Efficiency (%) |
|---------------------|---------------|--------------------------------|--------|----------------|
| 0.1 | 916 | 28.36 | 75.91 | 19.72 |
| 0.2 | 916 | 28.35 | 75.76 | 19.67 |
| 0.4 | 830 | 28.23 | 69.8 | 16.36 |

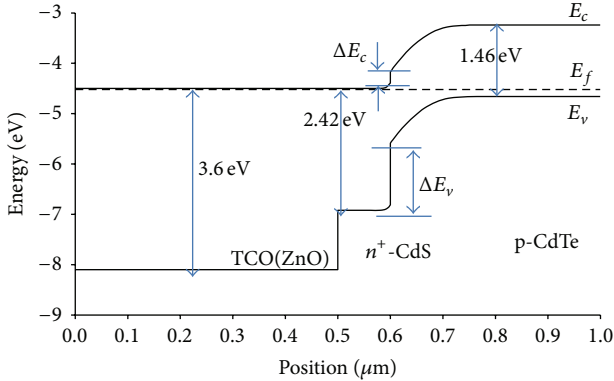


FIGURE 2: Band diagram of TCO/CdS/CdTe cell without electron reflector layer.

current-voltage curve (less than 0.8 V) that can be modeled with an ideality factor of about 2 where recombination in the space charge region is dominating. In this comparison the goal was not to obtain a best fit but rather to develop a realistic device structure to study the effect of back Schottky contact on the performance of the cell. Here, a structure with the p-type CdTe doping of $7 \times 10^{16} \text{ cm}^{-3}$ and a thickness of $2 \mu\text{m}$ becomes the base device for our optimization. This device shows a maximum short-circuit current density of about 28.4 mA/cm^2 which will be used throughout this study.

Simulation results for a base device show that by reducing the barrier height ϕ_e from 0.4 to 0.1 eV a higher open-circuit voltage may be obtained while the short-circuit current remains virtually constant. These results are summarized in Table 2. In addition a higher overall cell efficiency can be achieved with the reduced ϕ_e . An optimized device shows a ϕ_e of about 0.1 eV. The base device has an efficiency of about 16.38% similar to the experimental data. Moreover, the base device shows an efficiency of about 17.46% assuming an ohmic contact with an infinite surface recombination velocity of $1 \times 10^7 \text{ cm/s}$ (Figure 5). We chose the simulation data and analysis mostly around a device with a barrier height of 0.3–0.4 eV as this number is more closely related to a realistic CdTe device structure with back Schottky contact [12, 15–18, 31].

In the absence of an electron reflector or extended region, the band bending of the back surface results in surface recombination degrading the device performance (Figure 2). The surface recombination velocity is a function not only of the material quality and the device but also of the doping level. The exact value of surface recombination velocity is frequently not known but typically extracted from the

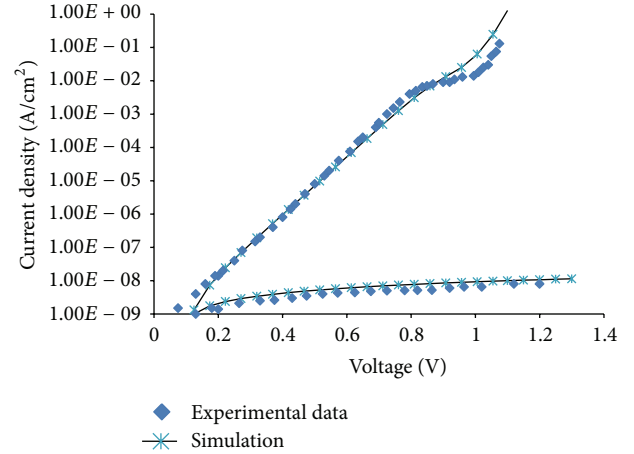


FIGURE 3: Current-voltage characteristics of thin-film CdS/CdTe cell. The measured experimental data is taken from [11].

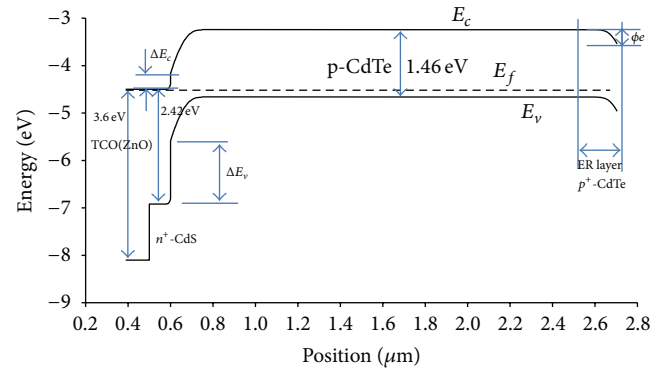
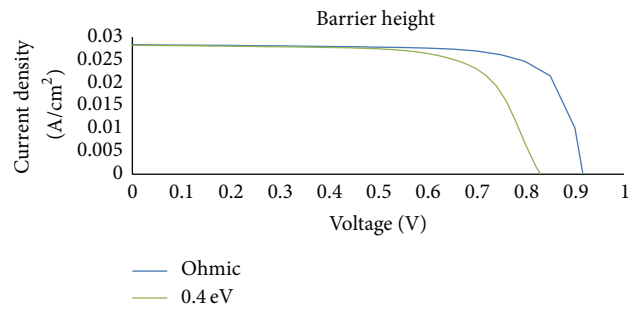


FIGURE 4: Band diagram of TCO/CdS/CdTe cell with added electron-reflector-extended region (ER layer).


 FIGURE 5: The simulated photocurrent voltage for both ohmic contact and Schottky contact with a barrier height (ϕ_e) of 0.4 eV. No extended region is used.

measured data of a given device. The back surface recombination is considered a major limitation factor on a cell's performance in thin devices. The built-in field at the back surface can drive the carriers away from the back surface, thereby affecting recombination rate. In addition, the electric field at back surface may also increase the probability for electron-hole generation near the back contact. A higher

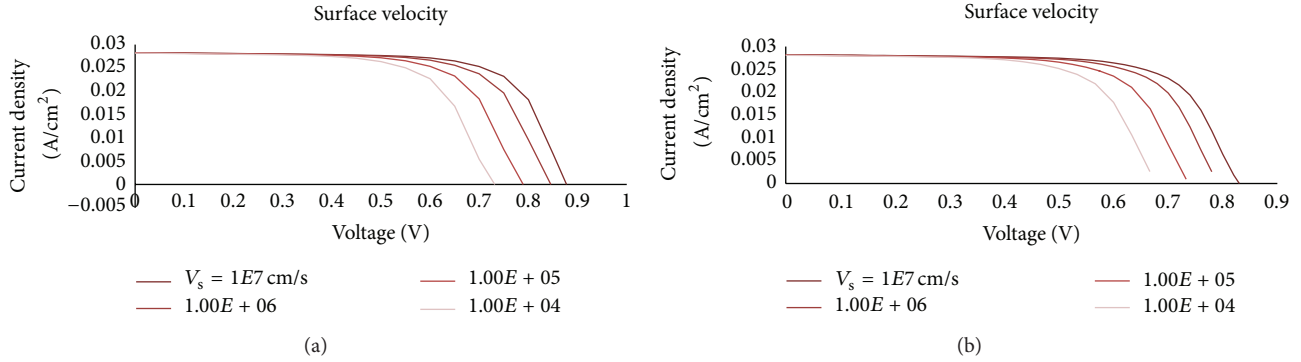


FIGURE 6: Effect of surface recombination velocity at back contact on cell performance. An ER thickness of 100 nm and a doping density of $7 \times 10^{18} \text{ cm}^{-3}$ are assumed; (a) barrier height of 0.1 eV; (b) barrier height of 0.4 eV.

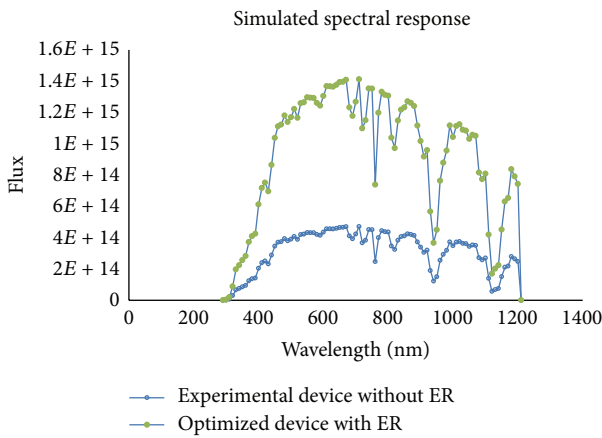


FIGURE 7: The simulated spectral response of an optimized CdTe cell with 100 nm extended region and a doping of $7 \times 10^{16} \text{ cm}^{-3}$.

velocity is desirable which improves the contact condition toward an ohmic status thus reducing the loss of carriers. As shown in Figure 6, simulation results show that surface recombination at the back contact significantly reduces the open-circuit voltage.

4. Electron Reflector Layer Thickness

For the optimization of the device an offset to the CdTe, absorption layer is considered by adding a CdTe layer as an electron-reflector-extended region (ER), (Figure 4). In addition to CdTe, other materials such as CdZnTe, CdMnTe, and CdMgTe may be employed in creating an ER layer [10, 14, 15, 17, 29, 36].

A thin-layer electron reflector causes the depletion region of the Schottky barrier contact to be narrow where majority of hole carriers can tunnel through minimizing the loss. The simulated spectral density of the CdTe cell with and without the introduction of the ER is shown in Figure 7. As shown in this figure an ER layer may also add an additional absorption layer to the structure thus increasing the spectral response by increasing photogenerated carriers. The thickness of ER layer

TABLE 3: Electron reflector layer thickness and cell performance. A barrier height of 0.3 eV and a doping of $7 \times 10^{16} \text{ cm}^{-3}$ are assumed.

| ER thickness (nm) | V_{oc} (mV) | J_{sc} (mA/cm ²) | FF (%) | Efficiency (%) |
|-------------------|---------------|--------------------------------|--------|----------------|
| 0 | 869.9 | 28.27 | 71.0 | 17.46 |
| 100 | 872.3 | 28.3 | 70.89 | 17.50 |
| 200 | 875.4 | 28.31 | 70.65 | 17.51 |
| 500 | 883.2 | 28.33 | 70.06 | 17.53 |

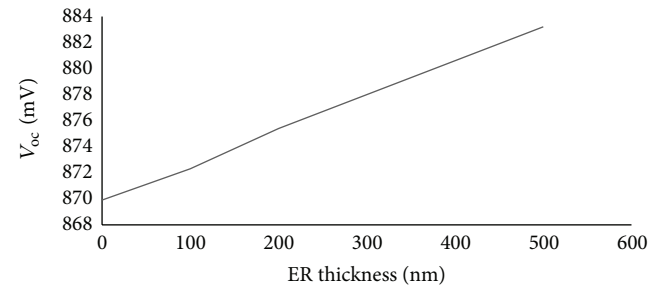


FIGURE 8: Effect of ER layer thickness on open-circuit voltage of the cell. A doping of $7 \times 10^{16} \text{ cm}^{-3}$ is assumed.

TABLE 4: ER layer with different values of doping density. Thickness of ER layer is 100 nm.

| ER with different doping (cm ⁻³) | V_{oc} (mV) | J_{sc} (mA/cm ²) | FF (%) | Efficiency (%) |
|--|---------------|--------------------------------|--------|----------------|
| 7×10^{16} | 872.3 | 28.3 | 70.89 | 17.50 |
| 7×10^{17} | 877.7 | 28.29 | 71.26 | 17.70 |
| 7×10^{18} | 891 | 28.32 | 71.21 | 17.97 |

used in the simulation of spectral response is 100 nm, and the ER doping density is assumed to be $7 \times 10^{16} \text{ cm}^{-3}$.

The tradeoff between the open-circuit voltage and short-circuit current when ER is included is shown in the simulated results of Table 3. As shown in Figure 8, the short-circuit current remain relatively constant with the ER layer thickness while the open-circuit voltage increases. In this example the thickness of extended region ranges from 50 nm to 500 nm

TABLE 5: Cell efficiency with ER layer thickness of 100 nm and doping density of $7 \times 10^{18} \text{ cm}^{-3}$. A barrier height of 0.1 eV is assumed.

| ER different thickness (nm) | V_{oc} (mV) | J_{sc} (mA/cm ²) | FF (%) | Efficiency (%) |
|-----------------------------|---------------|--------------------------------|--------|----------------|
| 100 | 917.6 | 28.45 | 75.99 | 19.83 |

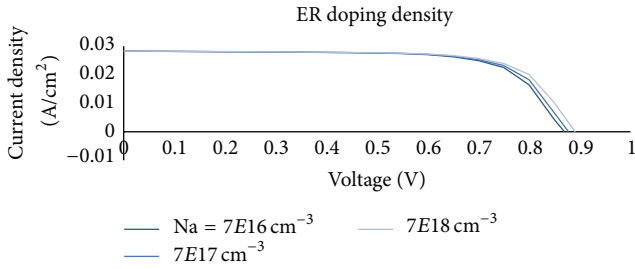


FIGURE 9: Photocurrent-voltage characteristics of CdTe cell at different doping densities of ER layer.

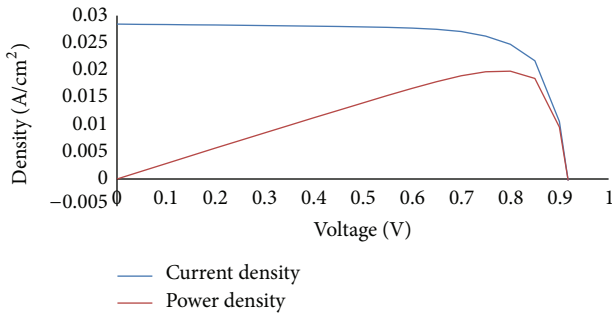


FIGURE 10: Optimized CdS/CdTe cell with V_{oc} of 917.6 mV, J_{sc} of 28.45 mA/cm², and an efficiency of 19.83%.

where the doping density and the barrier height are kept constant at $7 \times 10^{16} \text{ cm}^{-3}$ and 0.3 eV, respectively. As indicated earlier in the discussions, the simulation data and analysis are chosen mostly around a device structure with a barrier height of 0.3–0.4 eV as this number is closely related to a realistic CdTe device with Schottky barrier contact [12, 15–18, 31].

Normally the extended layer is heavily doped to minimize the negative effect of the Schottky barrier. Table 4 summarizes the simulated results for an example where the doping density of ER layer varied from $7 \times 10^{16} \text{ cm}^{-3}$ to $7 \times 10^{18} \text{ cm}^{-3}$. The thickness of ER layer and the barrier height are kept constant at 100 nm and 0.3 eV, respectively. Further simulation analysis and results show that the best performance efficiency of about 19.83% may be obtained with an ER layer doping of $7 \times 10^{18} \text{ cm}^{-3}$ and an ER thickness of 100 nm at a barrier height of 0.1 eV.

5. Conclusion

The analysis obtained shows that in the optimization of the cell combining the two mechanisms of heavy doping and extended region are the key parameters to achieve a better cell design. Our results show that in addition to a low surface

recombination velocity of 1000 cm/s at back contact and a barrier height of 0.1 eV, an ER layer of 100 nm with a doping density of $7 \times 10^{18} \text{ cm}^{-3}$ is also required to produce the best cell efficiency performance of 19.83% summarized in Table 5. The photocurrent characteristics of the optimized cell with V_{oc} of 917.6 mV, J_{sc} of 28.45 mA/cm², and an efficiency of 19.83% are shown in Figure 10. In the summary a number of different design parameters are used to optimize CdS/CdTe heterojunction thin-film cell (Figure 9). Simulation results show for an optimum efficiency performance a doping density of $7 \times 10^{18} \text{ cm}^{-3}$ and ER layer thickness of 100 nm are needed, as summarized in Table 5.

References

- [1] G. C. Morris and S. K. Das, “Some fabrication procedures for electrodeposited CdTe solar cells,” *International Journal of Solar Energy*, vol. 12, no. 1–4, pp. 95–108, 1992.
- [2] S. Ikegami, “CdS/CdTe solar cells by the screen-printing-sintering technique: Fabrication, photovoltaic properties and applications,” *Solar Cells*, vol. 23, no. 1–2, pp. 89–105, 1988.
- [3] T. L. Chu and S. S. Chu, “High efficiency thin film CdS/CdTe solar cells,” *International Journal of Solar Energy*, vol. 12, no. 1–4, pp. 121–132, 1992.
- [4] X. Wu, “High-efficiency polycrystalline CdTe thin-film solar cells,” *Solar Energy*, vol. 77, no. 6, pp. 803–814, 2004.
- [5] V. M. Nikale, S. S. Shinde, C. H. Bhosale, and K. Y. Rajpure, “Physical properties of spray deposited CdTe thin films: PEC performance,” *Journal of Semiconductors*, vol. 32, no. 3, Article ID 033001, 2011.
- [6] A. Luque and S. Hegedus, *Handbook of Photovoltaic Science and Engineering*, John Wiley & Sons, Chichester, UK, 2003.
- [7] V. M. Fthenakis, “Could CdTe PV Modules Pollute the Environment?” Working Paper, National Photovoltaic Environmental Health and Safety Assistance Center, Brookhaven National Laboratory, Upton, NY, USA, 2002.
- [8] J. Britt and C. Ferekides, “Thin-film CdS/CdTe solar cell with 15.8% efficiency,” *Applied Physics Letters*, vol. 62, no. 22, pp. 2851–2852, 1993.
- [9] M. Powalla and D. Bonnet, “Thin-film solar cells based on the polycrystalline compound semiconductors CIS and CdTe,” *Advances in OptoElectronics*, vol. 2007, Article ID 97545, 6 pages, 2007.
- [10] K. Hsiao, *Electron-reflector strategy for cdte thin-film solar cells [Ph.D. dissertation]*, Colorado State University, 2010.
- [11] L. Kosyachenko, “Efficiency of thin-film CdS/CdTe solar cells,” in *Solar Energy*, R. D. Rugescu, Ed., pp. 105–130, 2010.
- [12] J. Sites and J. Pan, “Strategies to increase CdTe solar-cell voltage,” *Thin Solid Films*, vol. 515, no. 15, pp. 6099–6102, 2007.
- [13] J. Han, C. Fan, C. Spanheimer et al., “Electrical properties of the CdTe back contact: a new chemically etching process based on nitric acid/acetic acid mixtures,” *Applied Surface Science*, vol. 256, no. 20, pp. 5803–5806, 2010.
- [14] I. M. Dharmadasa, “Latest developments in CdTe, CuInGaSe2 and GaAs/AlGaAs thin film PV solar cells,” *Current Applied Physics*, vol. 9, no. 2, pp. e2–e6, 2009.
- [15] S. H. Kim, J. H. Ahn, H. S. Kim, H. M. Lee, and D. H. Kim, “The formation of ZnTe:Cu and CuxTe double layer back contacts for CdTe solar cells,” *Current Applied Physics*, vol. 10, no. 3, pp. S484–S487, 2010.

- [16] M. A. Matin, M. Mannir Aliyu, A. H. Quadery, and N. Amin, "Prospects of novel front and back contacts for high efficiency cadmium telluride thin film solar cells from numerical analysis," *Solar Energy Materials and Solar Cells*, vol. 94, no. 9, pp. 1496–1500, 2010.
- [17] H. Lin, W. Xia, H. N. Wu, and C. W. Tang, "CdS/CdTe solar cells with MoO_x as back contact buffers," *Applied Physics Letters*, vol. 97, no. 12, Article ID 123504, 2010.
- [18] N. R. Paudel, A. D. Compaan, and Y. Yan, "Sputtered CdS/CdTe solar cells with MoO_{3-x}/Au back contacts," *Solar Energy Materials and Solar Cells*, vol. 113, pp. 26–30, 2013.
- [19] T. Surek, "Crystal growth and materials research in photovoltaics: progress and challenges," *Journal of Crystal Growth*, vol. 275, no. 1-2, pp. 292–304, 2005.
- [20] H. R. Moutinho, R. G. Dhere, C.-S. Jiang, Y. Yan, D. S. Albin, and M. M. Al-Jassim, "Investigation of potential and electric field profiles in cross sections of CdTe/CdS solar cells using scanning Kelvin probe microscopy," *Journal of Applied Physics*, vol. 108, no. 7, Article ID 074503, 2010.
- [21] Y. Ye, L. Dai, T. Sun et al., "High-quality CdTe nanowires: synthesis, characterization, and application in photoresponse devices," *Journal of Applied Physics*, vol. 108, no. 4, Article ID 044301, 2010.
- [22] K. W. Böer, "CdS enhances Voc and fill factor in CdS/CdTe and CdS/CuInSe₂ solar cells," *Journal of Applied Physics*, vol. 107, no. 2, Article ID 023701, 2010.
- [23] B. Yan, G. Yue, X. Xu, J. Yang, and S. Guha, "High efficiency amorphous and nanocrystalline silicon solar cells," *Physica Status Solidi A*, vol. 207, no. 3, pp. 671–677, 2010.
- [24] M. A. Green, "Thin-film solar cells: review of materials, technologies and commercial status," *Journal of Materials Science*, vol. 18, no. 10, supplement 1, pp. S15–S19, 2007.
- [25] Z. Fang, X. C. Wang, H. C. Wu, and C. Z. Zhao, "Achievements and challenges of CdS/CdTe solar cells," *International Journal of Photoenergy*, vol. 2011, Article ID 297350, 8 pages, 2011.
- [26] N. Romeo, A. Bosio, V. Canevari, and A. Podestà, "Recent progress on CdTe/CdS thin film solar cells," *Solar Energy*, vol. 77, no. 6, pp. 795–801, 2004.
- [27] A. Froitzheim, R. Stang, L. Elstner, M. Kriege, and W. Fuhs, *Afors-het: a computer-program for the simulation of heterojunction solar cells to be distributed for public use [M.S. thesis]*, Hahn-Meitner-Institut, Berlin, Germany, 2009.
- [28] R. Stangl, J. Haschke, and C. Leendertz, "Numerical simulation of solar cells and solar cell characterization methods: the open-source on demand program AFORS-HET, version 2.4," in *Solar Energy*, 2009.
- [29] N. Amin, K. Sopian, and M. Konagai, "Numerical modeling of CdS/CdTe and CdS/CdTe/ZnTe solar cells as a function of CdTe thickness," *Solar Energy Materials and Solar Cells*, vol. 91, no. 13, pp. 1202–1208, 2007.
- [30] L. Chen, *Random deposition model of CdS layer in CdSs/CdTe thin-film solar cells [M.S. thesis]*, Colorado State University, 2008.
- [31] X. H. Zhao, A. X. Wei, Y. Zhao, and J. Liu, "Structural and optical properties of CdS thin films prepared by chemical bath deposition at different ammonia concentration and S/Cd molar ratios," *Journal of Materials Science*, pp. 1–6, 2012.
- [32] T. M. Razykov, N. Amin, B. Ergashev et al., "Effect of CdCl₂ treatment on physical properties of CdTe films with different compositions fabricated by chemical molecular beam deposition," *Applied Solar Energy*, vol. 49, p. 35, 2013.
- [33] B. A. Korevaar, A. Halverson, J. Cao, J. Choi, C. Collazo-Davila, and W. Huber, "High efficiency CdTe cells using manufacturable window layers and CdTe thickness," *Thin Solid Films*, vol. 535, pp. 229–232, 2013.
- [34] B. L. Williams, D. P. Halliday, B. G. Mendis, and K. Durose, "Microstructure and point defects in CdTe nanowires for photovoltaic applications," *Nanotechnology*, vol. 24, no. 13, Article ID 135703, 2013.
- [35] T.-C. Hou, Y. Yanga, Z.-H. Lin et al., "Nanogenerator based on zinc blende CdTe micro/nanowires," *Nano Energy*, vol. 2, p. 387, 2013.
- [36] A. L. Fahrenbruch and R. H. Bube, *Fundamentals of Solar Cells. Photo Voltaic Solar Energy Conversion*, Academic Press, New York, NY, USA, 1983.
- [37] R. H. Bube, *Photoelectronic Properties of Semiconductors*, Cambridge University Press, Cambridge, UK, 1992.

Research Article

Nanostructured ZnO, TiO₂, and Composite ZnO/TiO₂ Films for Application in Dye-Sensitized Solar Cells

Myrsini Giannouli

Energy and Environment Laboratory, Physics Department, University of Patras, 26500 Patras, Greece

Correspondence should be addressed to Myrsini Giannouli; myrtwg@gmail.com

Received 24 May 2013; Revised 28 June 2013; Accepted 29 June 2013

Academic Editor: Gaetano Di Marco

Copyright © 2013 Myrsini Giannouli. This is an open access article distributed under the Creative Commons Attribution License, which permits unrestricted use, distribution, and reproduction in any medium, provided the original work is properly cited.

The effects of using composite semiconductor films on the efficiency and stability of dye-sensitized solar cells (DSSCs) were investigated. Four different types of composite ZnO/TiO₂ cells were developed and sensitized with the organic molecules Coumarin 343 (C343) and Rose Bengal (RB). A comparative assessment of the different composite cells was conducted, and the photovoltaic performance of single-semiconductor ZnO and TiO₂ solar cells was also compared to that of the composite ZnO/TiO₂ cells. It was observed that composite cells with ZnO/TiO₂ ratio equal to 90/10 have comparable efficiency to single-semiconductor cells and have the advantage of higher stability. The effects of using various multicomponent electrolytes on the efficiency and stability of the ZnO/TiO₂ cells were also investigated. It was observed that the combined properties of the materials used in these electrolytes enhance the efficiency of the composite ZnO/TiO₂ cells.

1. Introduction

Dye-sensitized solar cells (DSSCs), with highest efficiencies approximately 11%, are considered a promising alternative to conventional silicon solar cells [1] since they can be developed using low-cost production processes and non-toxic materials, are less sensitive to ambient temperature changes and have good performance in low-light conditions [2].

The basic structure of dye-sensitized solar cells consists of a nanostructured mesoporous semiconductor film deposited on a glass or a flexible substrate, a platinum or platinised counter electrode and a liquid, and gel or solid electrolyte containing a redox couple, which fills the space between the two electrodes [3]. A monolayer of dye is adsorbed on the surface of the semiconductor and acts as the sensitizer. In dye-sensitized solar cells the conversion of visible light to electricity is achieved through the spectral sensitization of wide bandgap semiconductors such as TiO₂ [4], ZnO [5], and SnO₂ [6].

The most efficient sensitizers for wide bandgap semiconductors are the well-known metalloorganic ruthenium complexes [2]. Several simple organic dyes though, and especially xanthene dyes (Eosin Y, Rose Bengal, etc.), yield efficiencies

comparable to those achieved with ruthenium complexes, especially when used to sensitize ZnO films [7–9]. Organic dyes such as these are inexpensive [10, 11], can be easily recycled [12], and do not rely on the availability of precious metals such as ruthenium. They also have high extinction coefficients, and their molecular structures contain adequate anchoring groups to be adsorbed onto the oxide surface. However, solar cells sensitized with such dyes tend to have low stability and efficiency compared to cells sensitized with ruthenium-based dyes [13, 14]. Xanthene dyes have also been used in solar cell applications in the form of hybrid core-shell nanoparticles where photoinduced electron transfer occurs for charge separation, and it has been observed that the rate of photoinduced electron transfer depends on the electron-accepting nature of the organic xanthene molecule on the shell layer [15, 16].

The development and optimization of solar cells is of great interest, both commercially and scientifically. However, dye-sensitized devices are still not commercially available in large volumes. Disadvantages such as their low efficiency and stability pose a hindrance to their commercialization.

The main parameters that affect dye-sensitized solar cell performance, with emphasis on their efficiency and stability,

are examined here, and an attempt is made to improve their overall performance. Nanostructured ZnO, TiO₂, and composite ZnO/TiO₂ thin films were considered for this purpose. The composite ZnO/TiO₂ films were developed with the aim to produce solar cells with improved photovoltaic properties compared to those displayed by either ZnO or TiO₂ cells. Composite films of four different ZnO/TiO₂ concentrations were developed in order to determine which ZnO/TiO₂ ratio leads to the production of the more efficient type of dye-sensitized solar cell. In addition, the performance of ZnO solar cells was studied using four different electrolytes: three multicomponent electrolytes and a standard-type electrolyte, which was used for comparison. The effect of using these multicomponent electrolytes compared to using a standard-type electrolyte on the efficiency and stability of the cells was examined. The performance of the ZnO cells was also compared to that of corresponding TiO₂ cells. All cells presented here were sensitized with the low-cost organic dyes Coumarin 343 (C343) and Rose Bengal (RB).

2. Methodology

Nanostructured ZnO, TiO₂, and composite ZnO/TiO₂ films were prepared as described in [17]. Commercial ZnO or TiO₂ nanopowder (Aldrich) with nanoparticle diameter less than 100 nm was used to create a colloidal paste. The powder was mixed with a small amount of distilled water containing acetyl acetone (10% v/v) [18, 19] in order to prevent the coagulation of nanoparticles and improve the porosity of the film [20]. A small amount of Triton X-100 was added to the mixture to reduce surface tension and enable even spreading of the paste [21, 22].

Composite ZnO/TiO₂ films were also developed. The use of composite electrodes facilitates charge carrier separation [23] and can enhance cell performance. Composite thin films containing both ZnO and TiO₂ were developed by mixing ZnO and TiO₂ paste in different quantities in order to obtain pastes with the following ZnO/TiO₂ ratios: 90/10, 75/25, 50/50, and 25/75.

The semiconductor oxide paste was spread on conductive glass substrates (K-glass-SnO₂:F with sheet resistance 16,7 Ω/sq, 80% transmittance in the visible, 0.38 cm glass thickness) via a doctor blade technique, and the electrodes were annealed for 30 min at 450°C in air to enhance the electrical contact between the nanoparticles as well as between the nanoparticles and the conductive substrate [24]. The thickness of the resulting films was measured by a stylus XP-1 Ambios Technology profilometer. As the thickness of the films can affect the performance of the DSSCs, the results presented in the paper were obtained for samples of approximately the same thickness (equal to 7.5 μm) [4].

The semiconductor films were sensitized with the low-cost dyes Coumarine 343 and Rose Bengal. Coating of the semiconductor surface with the dye was conducted by soaking the film in a solution of the dye in methanol (0.01 M) for 12 h.

Four different types of electrolytes were developed and used: a standard-type electrolyte containing potassium iodide

and iodine in propylene carbonate (PC) and three multicomponent electrolytes containing potassium iodide and iodine dissolved in varying mixtures of PC and EG (ethylene glycol). The standard-type electrolyte consists of 0.3 M potassium iodide and 0.03 M iodine in PC. The multicomponent electrolytes contain potassium iodide dissolved in a small amount of EG. Then, PC was added to the electrolyte in various quantities in order to obtain electrolyte solutions of different PC/EG concentrations. The following composite electrolytes were developed.

- (i) An electrolyte containing 0.5 M potassium iodide and 0.05 M iodine in an 80% PC and 20% EG solvent (named the 80/20 electrolyte).
- (ii) An electrolyte containing 0.5 M potassium iodide and 0.05 M iodine in a 90% PC and 10% EG solvent (named the 90/10 electrolyte).
- (iii) An electrolyte containing 0.5 M potassium iodide and 0.05 M iodine in a 95% PC and 5% EG solvent (named the 95/5 electrolyte).

It has been demonstrated that the presence of EG in the electrolyte solution increases the solubility of potassium iodide as well as the presence of iodide ions, enhancing the current density of TiO₂ cells [17]. The combined properties of the two solvents in the multicomponent electrolytes improve the efficiency and stability of the TiO₂ cells. The effectiveness of these electrolytes in ZnO cells sensitized with various dyes is investigated here.

Counter electrodes were prepared through thermal decomposition of a 5 mM hexachloroplatinic acid in isopropanol solution on conductive glass substrates. The sensitized semiconductor electrode and the counter electrode were assembled as a sandwich-type cell (area 1 cm²) sealed together with silicon, with the electrolyte filling the space between the two electrodes.

Scanning electron microscope (SEM) images were obtained with a JEOL JSM-6300 Scanning Electron Microscope in order to examine the morphology of the various semiconductor films. All SEM images were obtained with accelerating voltage equal to 20 kV. The elemental composition of the samples was determined through energy dispersive X-ray (EDX) analysis.

The properties of the solar cells were studied with emphasis on their efficiency and stability. Current-Voltage (*I-V*) curves of the cells were obtained using a computer-controlled AMEL Function Generator and a 50 W halogen lamp, which provides illumination intensity equal to 708 W/m². The main characteristics of the solar cells can be obtained from these *I-V* curves, namely, the open circuit voltage (*V_{oc}*), the short circuit current (*I_{sc}*), the fill factor (FF), and the efficiency (*η*) of the cell. The aforementioned properties were measured at regular intervals after the preparation of the cells in order to evaluate the stability of the devices over time.

Dark current measurements were also conducted for TiO₂, ZnO, and composite ZnO/TiO₂ solar cells. Dark current arises when triiodide ions from the electrolyte draw electrons from the semiconductor, reducing the triiodide to iodide. Since electrons are removed from the semiconductor,

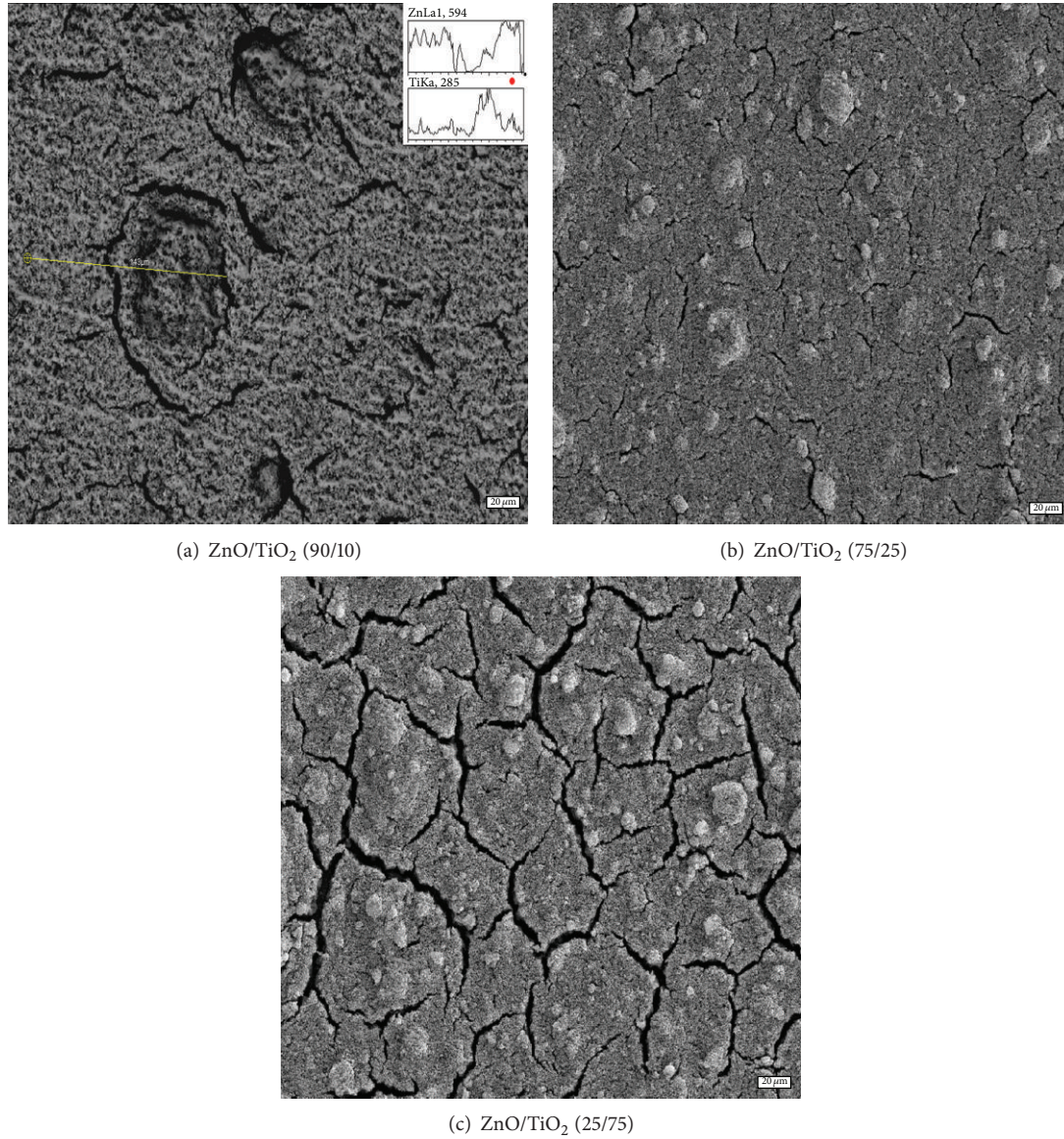


FIGURE 1: SEM images of semiconductor films. Images are magnified $\times 300$. The bar at the bottom right of the figures is $20 \mu\text{m}$.

the overall current produced in the photovoltaic cell is reduced by a small amount [25].

Incident photon to current efficiency (IPCE) spectra were obtained using a Newport setup with an AM1.5 Xe-lamp solar simulator and a Newport (Oriel Cornerstone) monochromator. IPCE corresponds to the number of electrons measured as photocurrent in the external circuit divided by the monochromatic photon flux that strikes the cell.

The IPCE factor is given by the following equation:

$$\text{IPCE (\%)} = \frac{1240 [\text{eV nm}] \times J_{\text{ph}} [\text{mA cm}^{-2}]}{\lambda [\text{nm}] \times \Phi [\text{mW cm}^{-2}]} \times 100, \quad (1)$$

where J_{ph} is the short-circuit photocurrent density for monochromatic irradiation and λ and Φ are the wavelength and the intensity, respectively, of the monochromatic light [26, 27].

3. Results and Discussion

SEM images of ZnO/TiO₂ films with ZnO/TiO₂ ratio equal to 90 : 10, 75 : 25, and 25 : 75 are shown in Figures 1(a), 1(b), and 1(c), respectively. In each of these figures dark patches can be observed throughout the surface of the film. Through SEM analysis, these patches were identified as areas with excess TiO₂, and the more bright spots that appear on the surface of the films were found to correspond to ZnO agglomerates. In addition, an analysis of the elemental composition of the films confirmed that the film shown in Figure 1(a) consists of approximately 90% ZnO and 10% TiO₂, the film shown in Figure 1(b) of approximately 75% ZnO and 25% TiO₂, and the film shown in Figure 1(c) of 25% ZnO and 75% TiO₂, as expected.

Figure 2 presents examples of the current density-voltage characteristics (I - V curves) of ZnO cells sensitized with Rose

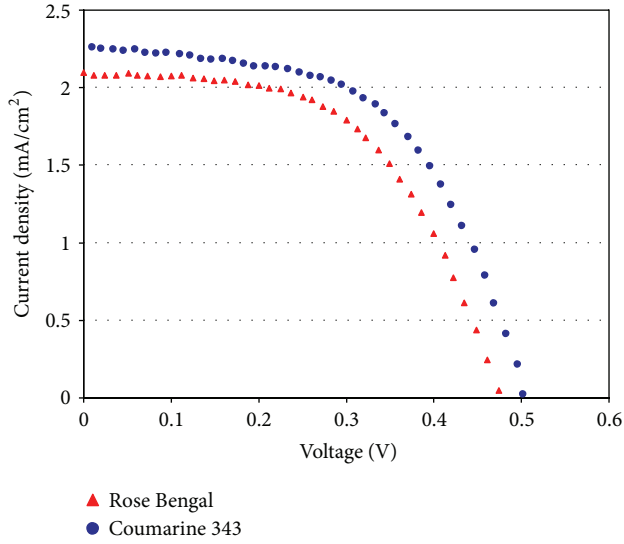


FIGURE 2: Current density (mA/cm^2) versus voltage (V) for ZnO cells sensitized with Rose Bengal and Coumarine 343.

Bengal and Coumarine 343. The standard-type electrolyte was used, and the results displayed in this figure are representative of the cells prepared during this study. From Figure 2, it can be observed that both the voltage and the current density of cells sensitized with C343 are higher than those of corresponding cells sensitized with RB. In general, the current density of cells sensitized with RB was 25–30% lower than that of cells sensitized with C343.

The main parameters that characterize the performance of the cells shown in Figure 2 are summarized in Table 1. The uncertainty in the results of Table 1 is mainly due to small differences in the morphology of the various cells prepared.

The effect of the multicomponent electrolytes on the efficiency of the cells is shown in Figures 3 and 4. Figure 3 shows the current I - V curves of ZnO cells sensitized with Rose Bengal, and Figure 4 shows the I - V curves of ZnO and TiO_2 cells sensitized with Coumarine 343. The cells presented in these figures were prepared using the four different electrolytes considered and are representative of the majority of the cells prepared and tested. From Figure 3, it can be observed that, for ZnO cells sensitized with RB, the cells with the 95/5 electrolyte have the highest current density and voltage and, hence, the highest efficiencies. Cells with the 90/10 electrolyte have also slightly higher efficiency than those with the standard-type electrolyte, while the cells with the 80/20 electrolyte have the lowest efficiency.

From Figure 4, it can be observed that, in general, ZnO cells sensitized with C343 have higher efficiencies than TiO_2 cells. The performance of ZnO and TiO_2 cells sensitized with C343 has been investigated in a previous work through femtosecond upconversion spectroscopy measurements, and it has been observed that ZnO films sensitized with C343 display faster electron injection rates than TiO_2 ones [28]. The higher efficiencies observed in ZnO cells sensitized with C343 compared to TiO_2 ones have partly been attributed to the faster electron injection of C343 on ZnO than on TiO_2 .

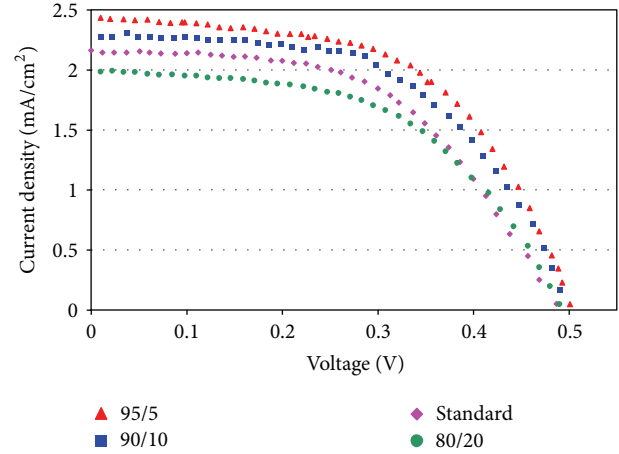


FIGURE 3: I - V characteristics of ZnO cells sensitized with Rose Bengal, each filled with one of the four different electrolytes.

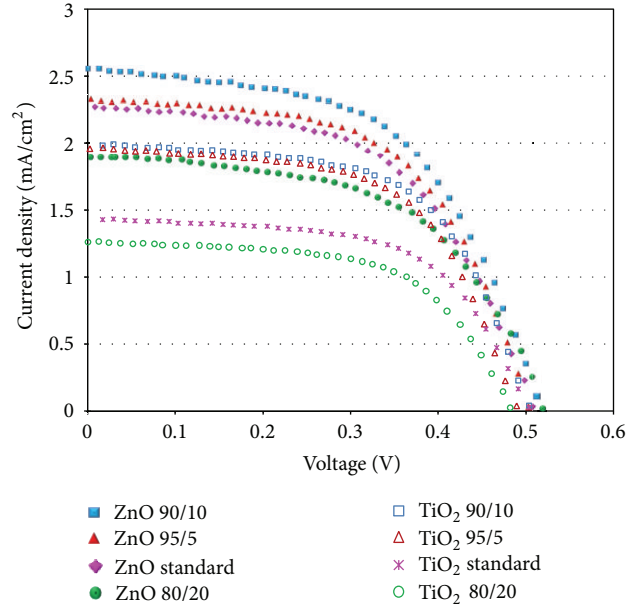


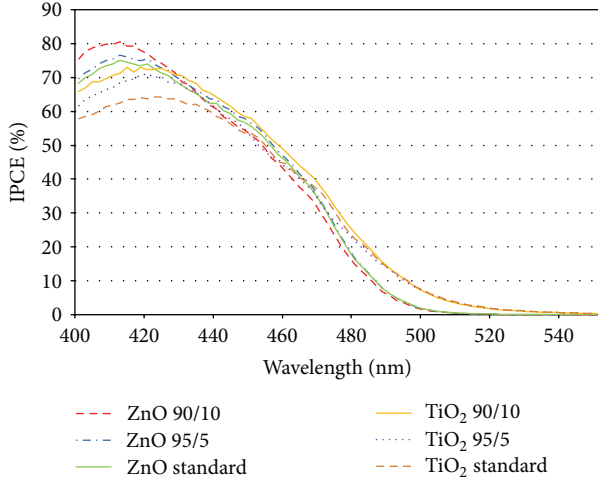
FIGURE 4: I - V characteristics of ZnO and TiO_2 cells sensitized with Coumarine 343, each filled with one of the four different electrolytes.

In addition, TiO_2 cells sensitized with C343 have been shown to have considerably higher dark current than corresponding ZnO cells, indicating faster electron recombination with accepting states in the electrolyte. The more efficient carrier recombination in TiO_2 cells sensitized with C343 is also partly responsible for their lower efficiency compared to ZnO cells [28].

From Figure 4, it can also be observed that, for both ZnO and TiO_2 cells, the multicomponent electrolytes have higher efficiencies than the standard electrolyte, with the exception of the 80/20 electrolyte. Cells that contain either the 95/5 or the 90/10 electrolyte exhibit considerably higher performance than those that contain the standard-type electrolyte, as shown in Figure 4. The cells with the 90/10 electrolyte yield

TABLE 1: Photovoltaic properties of ZnO cells sensitized with Rose Bengal and Coumarine 343.

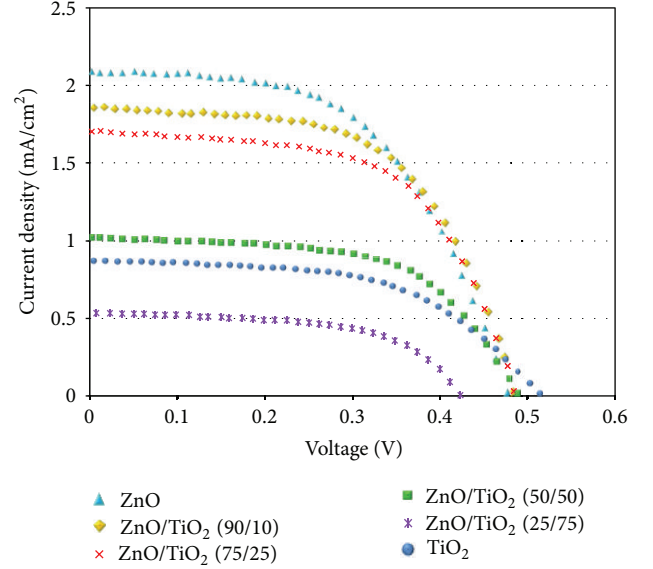
| | J_{sc} (mA/cm ²) | V_{oc} (V) | FF | η (%) |
|---------------|-----------------------------------|---------------------|---------------------|---------------------|
| Rose Bengal | 2.14 (± 0.05) | 0.49 (± 0.02) | 0.62 (± 0.02) | 0.88 (± 0.04) |
| Coumarine 343 | 2.34 (± 0.04) | 0.51 (± 0.03) | 0.60 (± 0.02) | 0.97 (± 0.03) |

FIGURE 5: IPCE spectra of TiO₂ and ZnO cells sensitized with C343.

the highest efficiencies, while cells filled with the 80/20 electrolyte have again the lowest efficiencies.

In a previous work we have discussed the performance of these multicomponent electrolytes in TiO₂ cells sensitized with Rhodamine B [17]. The increased efficiency of the cells with the multicomponent electrolytes was found to be mainly due to the aforementioned increase in the solubility of KI in the electrolyte. The increased solubility leads to increased ion concentrations in the mixture and, thus, to an increase in the conductivity of the electrolyte. The increase in the short-circuit current, which was observed for cells containing multicomponent electrolytes, is mainly due to this increase in the conductivity. Another factor that enhances the short-circuit current of cells containing the multicomponent electrolytes is the increased availability of anions, which reduce the oxidized dye from light absorption [17].

IPCE spectra of the various DSSCs were obtained in order to investigate the spectral response of the cells. Figure 5 shows the IPCE spectra of TiO₂ and ZnO cells sensitized with C343 and filled with different electrolytes. A small shift (less than 5 nm) of the spectral response to the blue was noticed in TiO₂ spectra with respect to ZnO ones. This shift was also confirmed through absorption measurements of TiO₂ and ZnO films sensitized with C343, obtained using a PerkinElmer Lambda 650 Spectrophotometer. From Figure 5, it is also apparent that the best photon-to-current conversion efficiency (resulting to the highest current) is given by cells filled with the 90/10 electrolyte, followed by those filled with the 95/5 electrolyte and then by those with the standard electrolyte. Those results are consistent with those presented in Figure 4 and show that the high efficiencies produced by

FIGURE 6: Current-Voltage characteristics of ZnO, TiO₂, and composite ZnO/TiO₂ cells sensitized with Rose Bengal.

both TiO₂ and ZnO cells filled with the 95/5 electrolyte are due to higher photon-to-current conversion. From Figure 5 we can also observe that ZnO cells have higher conversion efficiencies than TiO₂ ones, in line with the results presented in Figure 4. Moreover, the IPCE results presented in Figure 5 are in agreement with corresponding values for C343-based DSSCs presented in the literature [26].

The performance of the composite ZnO/TiO₂ cells was also investigated. Figure 6 shows the Current-Voltage characteristics of ZnO, TiO₂, and of composite ZnO/TiO₂ cells with the following ZnO/TiO₂ ratios: 90/10, 75/25, 50/50, and 25/75. All films were sensitized with the organic dye Rose Bengal. These results are representative of the majority of the results obtained during the study. As can be seen from this figure, ZnO cells sensitized with Rose Bengal have much higher efficiencies than corresponding TiO₂ cells. TiO₂ cells yield slightly higher voltage than ZnO ones, but ZnO cells have much higher current density than TiO₂ ones. In general, xanthene dyes such as Rose Bengal, Eosin Y, Mercurochrome, and Eosin B have a better performance when used to sensitize ZnO rather than TiO₂ cells [7]. The composite ZnO/TiO₂ cells with the 90/10 and 75/25 ratios follow closely the efficiency of the ZnO cells. The composite cells with the 50/50 and 25/75 ratios yielded considerably lower efficiencies, especially those with the 25/75 composition, which yielded very poor results.

TABLE 2: Photovoltaic properties of ZnO, TiO₂, and composite ZnO/TiO₂ cells sensitized with Rose Bengal.

| | J_{sc} (mA/cm ²) | V_{oc} (V) | FF | η (%) |
|------------------|-----------------------------------|---------------------|---------------------|---------------------|
| ZnO | 2.1 (± 0.06) | 0.48 (± 0.02) | 0.61 (± 0.02) | 0.87 (± 0.03) |
| TiO ₂ | 0.9 (± 0.08) | 0.51 (± 0.02) | 0.59 (± 0.03) | 0.39 (± 0.05) |
| 90/10 | 1.9 (± 0.06) | 0.48 (± 0.03) | 0.64 (± 0.02) | 0.81 (± 0.03) |
| 75/25 | 1.7 (± 0.08) | 0.49 (± 0.03) | 0.63 (± 0.02) | 0.76 (± 0.06) |
| 50/50 | 1.1 (± 0.11) | 0.49 (± 0.04) | 0.64 (± 0.03) | 0.49 (± 0.08) |
| 25/75 | 0.6 (± 0.14) | 0.43 (± 0.07) | 0.63 (± 0.04) | 0.23 (± 0.11) |

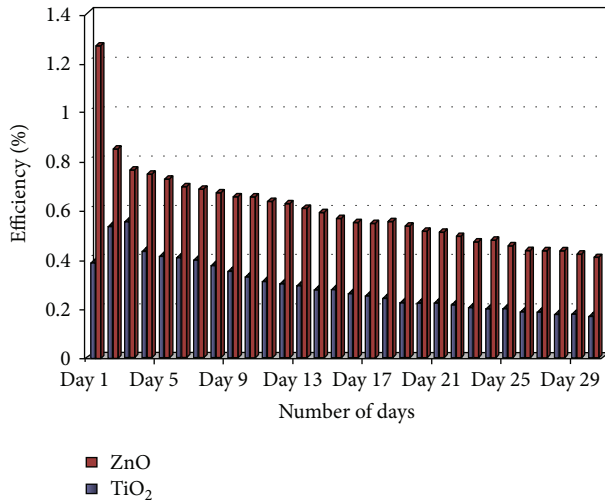


FIGURE 7: Evolution of cell efficiency with time over a 30-day period for a TiO₂ and a ZnO cell sensitized with Rose Bengal.

The main parameters that characterize the performance of the cells shown in Figure 6 are summarized in Table 2. Again, the uncertainty in the results originates from small differences in the morphology of the cells.

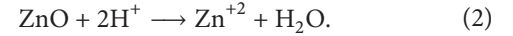
The stability of the solar cells plays a very important role in assessing their overall performance. The efficiency of DSSCs tends to decrease considerably with time mainly due to the degradation of the dye sensitizer [29, 30]. The stability of the cells was assessed by measuring their I - V characteristics daily for a 30-day period. Figure 7 shows the change in cell efficiency over a 30-day period for a TiO₂ and a ZnO cell, both sensitized with Rose Bengal. For TiO₂ cells it was observed that the efficiency reaches its maximum value on the 2nd or 3rd day after cell preparation and then gradually decreases. This decrease is mainly due to dye desorption and degradation. Only dye molecules which are adsorbed on the TiO₂ surface can sensitize spectrally the semiconductor and can, therefore, contribute to the photocurrent, so dye desorption causes a decrease in cell efficiency [31].

From Figure 7 it can also be observed that the most abrupt decrease in the current density of ZnO cells occurs between the first and the second day after cell preparation, mainly due to dye degradation. Dye degradation in ZnO films occurs more rapidly than in TiO₂ ones since protons originating

TABLE 3: Drop in efficiency over a 30-day period for ZnO, TiO₂, and composite ZnO/TiO₂ cells sensitized with Rose Bengal.

| | ZnO | TiO ₂ | 90/10 | 75/25 | 50/50 | 25/75 |
|------------------------|-----|------------------|-------|-------|-------|-------|
| Efficiency decline (%) | 68 | 52 | 51 | 58 | 69 | 76 |

from the dye may cause the dissolution of Zn surface atoms [32]. These Zn atoms then react with the protons from the dye, forming Zn²⁺/dye complexes:



The above reaction leads to the formation of inactive dye molecules which limits charge carrier injection and reduces the efficiency of the cells. The dissolution of Zn atoms depends on a number of factors, such as the dye concentration, the sensitization time, and the pH of the dye solution [33].

By comparing the TiO₂ and ZnO efficiency results presented in Figure 7, it is apparent that TiO₂ films have higher stability than ZnO films. The efficiency of ZnO solar cells is reduced more rapidly with time, while TiO₂ cells maintain relatively high efficiencies for some time after cells preparation. Specifically, it was observed that, 30-days after preparation, ZnO cells experience a drop of up to 70% in their efficiency, while TiO₂ cells lose approximately 50% of their original efficiency during the same time. On the other hand, the efficiencies achieved during the first days after cell preparation were considerably higher for ZnO than for TiO₂ cells so that, even after the passing of 30-days, ZnO cells still yield higher efficiencies than TiO₂ ones.

The composite ZnO/TiO₂ films were developed in order to improve the properties of dye-sensitized solar cells. The aim of this work was to develop cells with high efficiencies, such as those exhibited by ZnO cells, but with the increased stability of TiO₂ cells. As shown previously, the composite ZnO/TiO₂ cells with the 90/10 and 75/25 ratios yield efficiencies comparable to those of ZnO cells.

The stability of the composite cells was also examined. Table 3 summarizes the average drop in efficiency of ZnO, TiO₂, and composite ZnO/TiO₂ cells over a 30-day period. The results presented in this table show that TiO₂ cells and composite ones with the 90/10 and 75/25 ratios have the highest stability. ZnO and composite cells with the 50/50 and 25/75 ratios have considerably lower stability.

Figure 8 shows the efficiency of ZnO and composite ZnO/TiO₂ cells with the 90/10 and 75/25 ratios over a 30-day period. These two types of composite cells were considered in this comparison since they have exhibited both high efficiency and stability. The performance of the composite cells in this figure is compared against the performance of ZnO cells. All cells were sensitized with Rose Bengal. From Figure 8, it is apparent that the efficiency of the ZnO cells on the day they were assembled was considerably higher than that of the composite cells. However, the efficiency of the composite cells does not decrease as rapidly with time, so that, at the end of the 30-day period, composite cells with the 90/10 ZnO/TiO₂ ratio have higher efficiency than ZnO cells. The composite

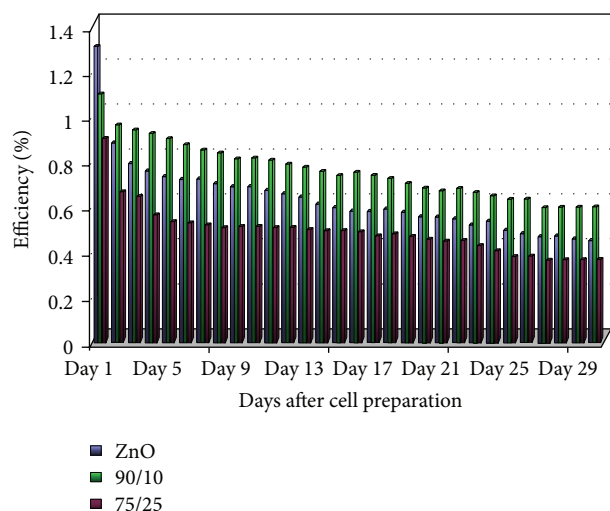


FIGURE 8: Cell efficiency over a 30-day period for a ZnO and two composite ZnO/TiO₂ cells sensitized with Rose Bengal.

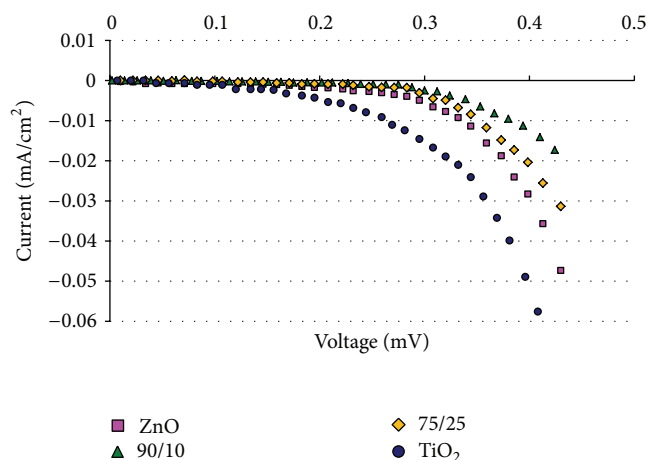


FIGURE 9: Dark current characteristics of ZnO, TiO₂, and ZnO/TiO₂ cells sensitized with Rose Bengal.

cells with the 75/25 ratio have only slightly lower efficiency than ZnO ones.

Dark current measurements were also conducted for ZnO, TiO₂, and composite ZnO/TiO₂ cells. Figure 9 shows dark current results for ZnO, TiO₂, and two types of composite ZnO/TiO₂ cells. All cells shown in this figure were sensitized with Rose Bengal. It was found that the composite cells have the lowest dark current, while the TiO₂ cells have the highest. The higher dark current in the TiO₂ cells is an indication of faster electron recombination than in ZnO and composite cells [34]. The relatively low current density produced by TiO₂ cells (Table 2) is partly due to higher recombination losses as evidenced by their higher dark current. As mentioned previously, similar measurements of ZnO and TiO₂ cells sensitized with C343 [28] have also shown that TiO₂ cells have higher dark current than ZnO ones when sensitized with C343. The higher recombination losses for TiO₂ cells sensitized with both C343 and Rose Bengal

are partly responsible for their lower efficiency compared to corresponding ZnO cells.

4. Conclusions

The aim of this study was to improve the performance of solar cells sensitized with simple organic dyes. ZnO, TiO₂, and composite ZnO/TiO₂ films sensitized with Rose Bengal were prepared and tested. It was observed that, in general, ZnO cells sensitized with simple organic dyes yield higher efficiencies than corresponding TiO₂ cells. However, TiO₂ cells exhibit higher stability than ZnO cells.

Four different types of composite cells were also considered, with ZnO/TiO₂ ratios equal to 90/10, 75/25, 50/50, and 25/75. It was observed that composite cells with ZnO/TiO₂ ratio equal to 90/10 have higher efficiencies than other composite cells and only marginally lower efficiencies than ZnO cells. Moreover, these cells have a higher stability than the other cells tested, so that, a month after cell preparation, they maintain higher efficiency values than ZnO cells.

Finally, multicomponent electrolytes were developed and used in ZnO cells sensitized with a simple organic dye. The performance of the cells with the multicomponent electrolytes was assessed by comparison with cells using a standard-type electrolyte. It was found that the combined properties of the materials used in these electrolytes improve cell efficiency.

References

- [1] F. Gao, Y. Wang, J. Zhang et al., "A new heteroleptic ruthenium sensitizer enhances the absorptivity of mesoporous titania film for a high efficiency dye-sensitized solar cell," *Chemical Communications*, no. 23, pp. 2635–2637, 2008.
- [2] M. Grätzel and B. O'Regan, "A low-cost, high-efficiency solar cell based on dye-sensitized colloidal TiO₂ films," *Nature*, vol. 353, no. 6346, pp. 737–740, 1991.
- [3] J. Navas, R. Alcántara, C. Fernández-Lorenzo, and J. Martín-Calleja, "Evaluation of decay photocurrent measurements in dye-sensitized solar cells: application to laser beam-induced current technique," *International Journal of Energy Research*, vol. 36, no. 2, pp. 193–203, 2012.
- [4] G. Syrokostas, M. Giannouli, and P. Yianoulis, "Effects of paste storage on the properties of nanostructured thin films for the development of dye-sensitized solar cells," *Renewable Energy*, vol. 34, no. 7, pp. 1759–1764, 2009.
- [5] M. Giannouli and F. Spiliopoulou, "Effects of the morphology of nanostructured ZnO films on the efficiency of dye-sensitized solar cells," *Renewable Energy*, vol. 41, pp. 115–122, 2012.
- [6] A. Birkel, Y. Lee, D. Koll et al., "Highly efficient and stable dye-sensitized solar cells based on SnO₂ nanocrystals prepared by microwave-assisted synthesis," *Energy and Environmental Science*, vol. 5, no. 1, pp. 5392–5400, 2012.
- [7] E. Guillén, F. Casanueva, J. Anta et al., "Photovoltaic performance of nanostructured zinc oxide sensitized with xanthene dyes," *Journal of Photochemistry and Photobiology A*, vol. 200, no. 2-3, pp. 364–370, 2008.
- [8] N. Plank, I. Howard, A. Rao et al., "Efficient ZnO nanowire solid-state dye-sensitized solar cells using organic dyes and

- core-shell nanostructures," *Journal of Physical Chemistry C*, vol. 113, no. 43, pp. 18515–18522, 2009.
- [9] B. Pradhan, S. K. Batabyal, and A. J. Pal, "Vertically aligned ZnO nanowire arrays in Rose Bengal-based dye-sensitized solar cells," *Solar Energy Materials and Solar Cells*, vol. 91, no. 9, pp. 769–773, 2007.
- [10] S. Hao, J. Wu, Y. Huang, and J. Lin, "Natural dyes as photosensitizers for dye-sensitized solar cell," *Solar Energy*, vol. 80, no. 2, pp. 209–216, 2006.
- [11] J. M. Kroon, N. J. Bakker, H. Smit et al., "Nanocrystalline dye-sensitized solar cells having maximum performance," *Progress in Photovoltaics*, vol. 15, no. 1, pp. 1–18, 2007.
- [12] W. Lee, H. Okada, A. Wakahara, and A. Yoshida, "Structural and photoelectrochemical characteristics of nanocrystalline ZnO electrode with Eosin-Y," *Ceramics International*, vol. 32, no. 5, pp. 495–498, 2006.
- [13] R. Harikisun and H. Desilvestro, "Long-term stability of dye solar cells," *Solar Energy*, vol. 85, no. 6, pp. 1179–1188, 2011.
- [14] M. Nazeeruddin, E. Baranoff, and M. Grätzel, "Dye-sensitized solar cells: a brief overview," *Solar Energy*, vol. 85, no. 6, pp. 1172–1178, 2011.
- [15] A. Guchhait, A. Rath, and A. Pal, "Hybrid core-shell nanoparticles: photoinduced electron-transfer for charge separation and solar cell applications," *Chemistry of Materials*, vol. 21, no. 21, pp. 5292–5299, 2009.
- [16] A. Guchhait and A. Pal, "Correlation between photoinduced electron transfer and photovoltaic characteristics in solar cells based on hybrid core-shell nanoparticles," *Journal of Physical Chemistry*, vol. 114, no. 45, pp. 19294–19298, 2010.
- [17] M. Giannouli, G. Syrokostas, and P. Yianoulis, "Effects of using multi-component electrolytes on the stability and properties of solar cells sensitized with simple organic dyes," *Progress in Photovoltaics*, vol. 18, no. 2, pp. 128–136, 2010.
- [18] M. K. Nazeeruddin, A. Kay, I. Rodicio et al., "Conversion of light to electricity by cis-X₂bis(2,2'-bipyridyl-4,4'-dicarboxylate)ruthenium(II) charge-transfer sensitizers (X = Cl⁻, Br⁻, I⁻, CN⁻, and SCN⁻) on nanocrystalline TiO₂ electrodes," *Journal of the American Chemical Society*, vol. 115, no. 14, pp. 6382–6390, 1993.
- [19] G. P. Smestad, "Education and solar conversion: demonstrating electron transfer," *Solar Energy Materials and Solar Cells*, vol. 55, no. 1-2, pp. 157–178, 1998.
- [20] F. Pichot, R. Pitts, and B. Gregg, "Low-temperature sintering of TiO₂ colloids: application to flexible dye-sensitized solar cells," *Langmuir*, vol. 16, no. 13, pp. 5626–5630, 2000.
- [21] Y. Liu, H. Wang, H. Shen, and W. Chen, "The 3-dimensional dye-sensitized solar cell and module based on all titanium substrates," *Applied Energy*, vol. 87, no. 2, pp. 436–441, 2010.
- [22] B. Van der Zanden and A. Goossens, "The nature of electron migration in dye-sensitized nanostructured TiO₂," *Journal of Physical Chemistry B*, vol. 104, no. 30, pp. 7171–7178, 2000.
- [23] K. Tennakone, P. K. Bandaranayake, P. V. Jayaweera, A. Konno, and G. Kumara, "Dye-sensitized composite semiconductor nanostructures," *Physica E*, vol. 14, no. 1-2, pp. 190–196, 2002.
- [24] V. Shklover, M. K. Nazeeruddin, S. M. Zakeeruddin et al., "Structure of nanocrystalline TiO₂ powders and precursor to their highly efficient photosensitizer," *Chemistry of Materials*, vol. 9, no. 2, pp. 430–439, 1997.
- [25] W. Xu, S. Dai, L. Hu et al., "Influence of different surface modifications on the photovoltaic performance and dark current of dye-sensitized solar cells," *Plasma Science and Technology*, vol. 9, no. 5, pp. 556–559, 2007.
- [26] K. Hara, Y. Tachibana, Y. Ohga et al., "Dye-sensitized nanocrystalline TiO₂ solar cells based on novel coumarin dyes," *Solar Energy Materials and Solar Cells*, vol. 77, no. 1, pp. 89–103, 2003.
- [27] Y. Chiba, A. Islam, Y. Watanabe, R. Komiya, N. Koide, and L. Han, "Dye-sensitized solar cells with conversion efficiency of 11.1%," *Japanese Journal of Applied Physics*, vol. 45, no. 24–28, pp. 638–640, 2006.
- [28] M. Giannouli and M. Fakis, "Interfacial electron transfer dynamics and photovoltaic performance of TiO₂ and ZnO solar cells sensitized with Coumarin 343," *Journal of Photochemistry and Photobiology A*, vol. 226, no. 1, pp. 42–50, 2011.
- [29] H. Tributsch, "Dye sensitization solar cells: a critical assessment of the learning curve," *Coordination Chemistry Reviews*, vol. 248, no. 13-14, pp. 1511–1530, 2004.
- [30] H. Liu, D. Zhou, X. Li, and P. Yue, "Photoelectrocatalytic degradation of Rose Bengal," *Journal of Environmental Sciences*, vol. 15, no. 5, pp. 595–599, 2003.
- [31] H. Tsubomura, M. Matsumura, K. Nakatani, K. Yamamoto, and K. Maeda, "Wet-type solar cells with semiconductor electrodes," *Solar Energy*, vol. 21, no. 2, pp. 93–98, 1978.
- [32] K. Keis, C. Bauer, G. Boschloo et al., "Nanostructured ZnO electrodes for dye-sensitized solar cell applications," *Journal of Photochemistry and Photobiology A*, vol. 148, no. 1–3, pp. 57–64, 2002.
- [33] D. W. Bahnemann, "Ultrasmall metal oxide particles: preparation, photophysical characterization and photocatalytic properties," *Israel Journal of Chemistry*, vol. 33, pp. 115–136, 1993.
- [34] M. Senevirathne, P. Pitigala, V. Sivakumar, P. Jayaweera, A. Perera, and K. Tennakone, "Sensitization of TiO₂ and ZnO nanocrystalline films with acriflavine," *Journal of Photochemistry and Photobiology A*, vol. 195, no. 2-3, pp. 364–367, 2008.

Research Article

Material Properties of Laser-Welded Thin Silicon Foils

**M. T. Hessmann,¹ T. Kunz,¹ M. Voigt,^{1,2} K. Cvecek,³ M. Schmidt,³ A. Bochmann,⁴
S. Christiansen,⁵ R. Auer,¹ and C. J. Brabec^{1,2}**

¹ Bavarian Center for Applied Energy Research (ZAE Bayern), Haberstraße 2a, 91058 Erlangen, Germany

² Institute Materials for Electronics and Energy Technology (i-MEET), University of Erlangen-Nuremberg, Martensstraße 7, 91058 Erlangen, Germany

³ BLZ-Bavarian Laser Center, Konrad-Zuse-Straße 2–6, 91052 Erlangen, Germany

⁴ University of Applied Sciences Jena, Carl-Zeiss-Promenade 2, 07745 Jena, Germany

⁵ Max-Planck-Institute for the Science of Light, Günther-Scharowsky-Straße 1, 91058 Erlangen, Germany

Correspondence should be addressed to M. T. Hessmann; hessmann@zae.uni-erlangen.de

Received 22 May 2013; Accepted 30 June 2013

Academic Editor: Leonardo Palmisano

Copyright © 2013 M. T. Hessmann et al. This is an open access article distributed under the Creative Commons Attribution License, which permits unrestricted use, distribution, and reproduction in any medium, provided the original work is properly cited.

An extended monocrystalline silicon base foil offers a great opportunity to combine low-cost production with high efficiency silicon solar cells on a large scale. By overcoming the area restriction of ingot-based monocrystalline silicon wafer production, costs could be decreased to thin film solar cell range. The extended monocrystalline silicon base foil consists of several individual thin silicon wafers which are welded together. A comparison of three different approaches to weld 50 μm thin silicon foils is investigated here: (1) laser spot welding with low constant feed speed, (2) laser line welding, and (3) keyhole welding. Cross-sections are prepared and analyzed by electron backscatter diffraction (EBSD) to reveal changes in the crystal structure at the welding side after laser irradiation. The treatment leads to the appearance of new grains and boundaries. The induced internal stress, using the three different laser welding processes, was investigated by micro-Raman analysis. We conclude that the keyhole welding process is the most favorable to produce thin silicon foils.

1. Introduction

Cost reduction is a major topic in the photovoltaic research and industry. One appropriate way to reduce costs within the production chain of silicon solar cells is to reduce kerf losses. The ZAE Bayern developed a method of producing an extended monocrystalline silicon base foil with a thickness of ca. 50 μm as depicted in Figure 1 [1, 2]. This base foil is manufactured by laser welding of several individual thin wafers. This will make it possible to produce an endless substrate which is feasible for a roll to roll process. By applying a layer transfer process as porous silicon (PSI) [3, 4], an appropriate layer can be detached from the base foil without sawing. In detail, on the surface of silicon two porous layers will be established; one layer will serve as a predetermined breaking layer, and the other as a seed layer for a large area epitaxial process which will be applied after an annealing step [5]. Following these steps, a solar cell

layer can be detached from the extended monocrystalline silicon base foil. It is only necessary to use silicon wafer-based substrates once to assemble the extended monocrystalline silicon base foil. Furthermore, layers for solar cell devices will be produced by a layer transfer technique and a large area epitaxy from the extended monocrystalline silicon base foil. Further information about the solar cell manufacturing process is published elsewhere [1].

In addition, the threshold of float-zone (FZ)-grown silicon crystals is not valid anymore for this kind of process. The size restrictions of ingot fabrication of FZ silicon lies at the moment by 8 inches in diameter and could be overcome by producing an extended monocrystalline silicon base foil. This would open a new field of large area substrates and processing. Moreover, a further reduction of material losses during the processing could be achieved.

The concept combines the low production costs of thin film solar cells with the high efficiencies of FZ-grown silicon

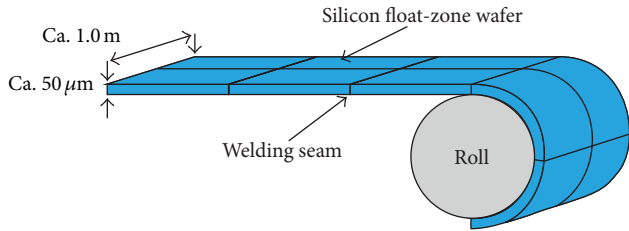


FIGURE 1: Illustration of the extended monocrystalline silicon base foil, which is welded together by individual silicon float-zone wafers, for further information for the solar cell manufacturing process please see [1].

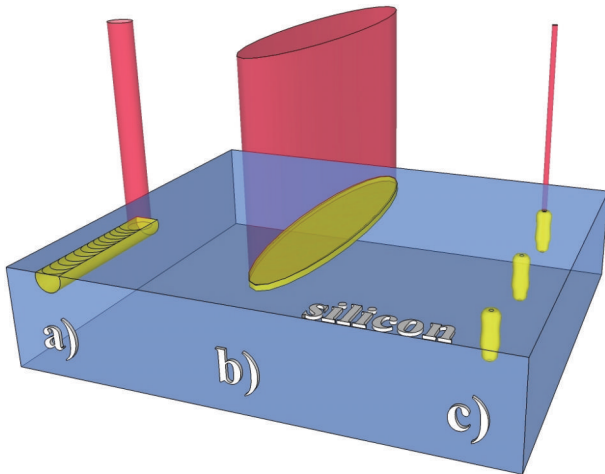


FIGURE 2: Application principle for laser welding: (a) Laser spot welding with low constant feed speed (b) Laser line welding (c) Keyhole welding. Laser beams are illustrated in red and areas which are influenced by the laser beam are colored in yellow.

solar cells. Recently, high cell efficiencies of 19.1% have been demonstrated by Petermann et al. [6] for the PSI approach on a Czochralski-grown substrate.

It is essential for the extended monocrystalline silicon base foil to create a lateral bonding of silicon wafers to achieve an endless belt-like substrate. In general, the study of lateral joining of silicon is still in the early stages. Concepts as the lateral epitaxy were introduced in the past, but no experimental data had been published as far as we know [7]. Preliminary laser spot welding tests of silicon were done by Kaufmann [8]. For a good quality of bonding, it is essential to have a well-defined surface structure, an absence of particles, and a very low surface roughness [9].

In our current work we show the recent progress of laser welding of thin silicon foils on a laboratory scale. The size of welded silicon will be scaled up in order to make a roll to roll process feasible [1]. We compared spot welding with a low constant feed speed, line welding (both at room temperature), and keyhole welding at preheated samples of 1000°C (see Figure 2). After the welding process the area which was irradiated by the laser was characterized by electron backscatter diffraction (EBSD) for revealing changes in

the grain structure and micro-Raman analysis for visualizing induced internal stress by the laser welding process.

2. Material and Methods

2.1. Sample Preparation. Samples of 5-inch-FZ silicon wafers had been prepared, with (100)-orientation, one side polished, p-type, with a thickness of $280 \pm 15 \mu\text{m}$ and a resistivity of $0.50 \pm 0.06 \Omega \text{ cm}$. All wafers were cut by laser into square pieces. To receive a thin and flexible base foil substrate, the sample thickness was decreased to ca. $50 \mu\text{m}$ by etching with potassium hydroxide (KOH). Additionally, this step removes laser damage from the edges which is very important to strengthen the mechanical stability. After the KOH etching, all samples were cleaned by an RCA process.

2.1.1. Laser Spot Welding with Low Constant Feed Speed.

For each welding process, two $19 \times 17 \text{ mm}^2$ samples were mounted in lap joint configuration onto a motorized 4-axis system, which consists of one rotary and three linear stages. The laser source was a single mode fiber laser model YLR-200-SM built by the company IPG Photonics with a wavelength of 1070 nm, operating at a power of 30 W, a duty cycle of 50% with a frequency of 2.5 kHz, and a laser spot diameter on the silicon surface of $300 \mu\text{m}$ [10, 11]. During the welding process the aligned samples on the sample holder were moved relative to the stationary laser beam with a feed speed of 1 mm/s (at room temperature).

2.1.2. Laser Line Welding.

Two $19 \times 17 \text{ mm}^2$ samples were placed in lap joint configuration within the focal area of the laser line at room temperature. The laser source for this welding process was the same as used for laser spot welding. By using a cylindrical lens and a microlens array in a homogenizer-like setup, the nearly Gaussian intensity distribution generated by the used laser was transformed into the laser line (for further details see [12]). The resulting laser line had a dimension of ca. 25 mm in length and ca. $700 \mu\text{m}$ in width at the focus level. Therefore, no movements of samples or laser beam were necessary. For the laser line welding process the power of the laser was increased linearly from 0 W to 141 W within 5 s. After reaching 141 W, the value was kept for 1 s and afterwards decreased linearly to 0 W within 1 s.

2.1.3. Keyhole Welding.

Two samples (each $25 \times 25 \text{ mm}^2$) were aligned in butt joint configuration, and a third one ($25 \times 25 \text{ mm}^2$) was placed centering on the back of the other two samples. This geometry was chosen because a normal butt joint configuration with two samples was not satisfactory. They were mounted on a sample holder consisting of quartz glass and then heated to 1015°C under nitrogen atmosphere. A laser beam irradiated the samples in the oven through a quartz glass window. The laser source was a single mode, continuous wave 1075 nm Yb-fiber laser, model YLR-1000-SM made by company IPG Photonics and operated at a power of 260 W (maximum power 1000 W). A galvanometer scanner system was used to focus and deflect the laser

beam onto the sample. The focal length of the objective was 370 mm, which resulted in an 80 μm spot diameter of the laser beam on the surface of the sample. The feed speed using the galvanometer scanner was 550 mm/s. Further details are described elsewhere [13].

2.2. Setup for Micro-Raman Measurements. An Alpha500 AR microscope from WITec GmbH, Ulm (Germany), was used for micro-Raman characterization. The microscope has a motorized sample stage of 150 mm \times 100 mm and a piezo-driven stage of 100 μm \times 100 μm \times 20 μm for fine measurements. The laser source is a Nd:YAG laser with an excitation wavelength of 532 nm. The measurements were carried out at an output power of 10 mW. The spectrometer is equipped with a Peltier-cooled CCD detector and an 1800 lines/mm grating. A magnification of 50 with a numerical aperture of 0.75 was used for the measurements. With this, we receive a spot size of less than 1 μm and a penetration depth in silicon of ca. 0.5 μm . All measurements of the cross-section of welded samples were carried out by using backscattering geometry at room temperature.

The software WITec Project was used for the evaluation of the recorded data. Peak parameters were determined by fitting Lorentz curves.

2.3. Setup for Electron Backscatter Diffraction (EBSD). A FIB-SEM LYRA_{XMU} system manufactured by the company TESCAN (Brno, Czech Republic) was used for EBSD analysis. The system is equipped with an EDAX/TSL "OIM XM4". For a good electrical contact between the measurement setup and the samples, all cross-sections were coated with a 10–20 nm carbon layer by sputtering. During the measurements, the samples were tilted by 70°. Properties of the electron beam were set to 30 keV electron beam energy and 5–12 nA beam currents, which results in a spot size of ca. 500–700 nm. The EBSD measurement was performed by an integration time of 25–80 ms, 4 \times 4 pixel binning, and 3 μm step size. Scanned areas are in the range of ca. 300 μm \times 500–1000 μm . As a software, EDAX/TSL Data Analysis 5.31 was used.

3. Results

For the purpose of revealing material changes within the silicon after laser beam irradiation, we analyzed cross-sections of welded samples by micro-Raman as well as EBSD. Plotting the micro-Raman data as a Lorentz peak area mapping reveals changes in the crystal structure of the irradiated silicon; the peak area is sensitive to the crystal orientation [14]. Furthermore, we applied an EBSD scan to determine the value of the crystal orientation of each grain in detail. To evaluate the stress caused by the laser processing, we derived the internal stress from mappings of the Raman frequency shift. For this purpose the following approximation is used, which is derived from silicon (100) under biaxial stress [15, 16]:

$$\sigma \text{ (MPa)} = -250 (\omega_s - \omega_r) \quad [1/\text{cm}], \quad (1)$$

where ω_s is the peak position with stress, respectively ω_r without stress. The depicted maximum values are with respect to the 5% and 95% thresholds of ω_s for tensile stress and compressive stress.

3.1. Laser Spot Welding with Low Constant Feed Speed. After applying laser spot welding to 50 μm thin silicon foils, structural changes within the silicon can be observed as shown in Figure 3. A crack can be seen in the left part of Figure 3(a). The welding region is mapped on the right side of the figure. The depicted shaded areas within the image next to the welding region are newly formed grains. Areas of silicon foil 1 which were underneath the silicon foil 2 during the laser irradiation and were not irradiated directly show no structural changes. For the same position of the sample, an EBSD scan was applied which is shown in Figure 3(b).

The EBSD mapping reveals a shift in crystal orientation and the presence of new grains in the material at the welding seam. An area of about 300 μm shows this appearance with different crystal orientations, which is correlated to the diameter of the irradiated laser beam. The whole affected area is not shown because of the high magnification of Figure 3. Newly formed grain boundaries are mostly $\Sigma 3$ and $\Sigma 9$ twin boundaries.

As can be seen previously, the laser beam impact into the silicon material causes material changes. The internal stress mapping shows a stress distribution within the welding region for laser spot welding as depicted in Figure 3(c). The inserted stress by laser irradiation appears only at locations where newly formed grains along the junction of the welding partners can be found in the EBSD mapping. The maximum tensile stress was 19.2 MPa and -90.5 MPa compressive stress, respectively.

Within this approach the welding partners undergo major structural changes around the welding seam. It is very likely that the laser-irradiated area was completely molten during the welding process and recrystallized afterwards during the cooling procedure. Only monocrystalline areas could be found in regions which were not laser irradiated directly and where the heat transition had to overcome the gap between the stacked silicon wafers.

3.2. Laser Line Welding. The result of lap joint welding using a laser line focus is depicted in Figure 4. No newly formed grains are observed in the EBSD mapping (Figure 4(a)) around the welding region so that the sample remains monocrystalline. However, the two welding partners don't have exactly the same crystal orientation. Although the laser irradiated area is bigger in width (ca. 700 μm) than by laser spot welding (ca. 300 μm), no evidence of crystal structural changes has been found. The correlation between the laser beam diameter and material changes is not as strong as for laser spot welding. Remarkable for the laser line welding is the growth in thickness of the welding partners around the welding seam.

Raman stress analysis in Figure 4(b) shows a very homogenous mapping. Within the laser-irradiated area, maximum values of tensile stress of 13.0 MPa and compressive

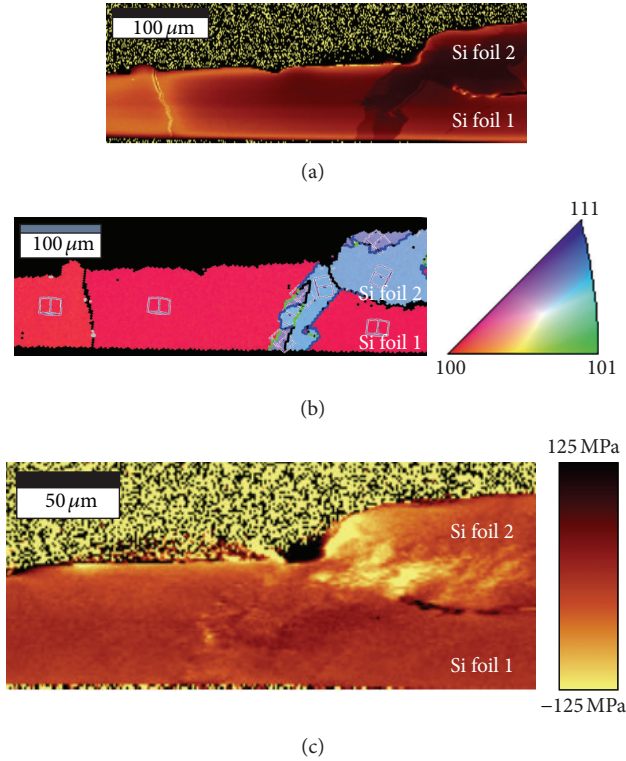


FIGURE 3: Cross-sections mappings of a spot welded sample, the laser beam was introduced from the top side. (a) Plot of the micro-Raman Lorentz peak area in arbitrary units. (b) EBSD mapping, color with respect to the wafer surface, grain boundaries are colored as followed: $\Sigma 3$ in blue, $\Sigma 9$ in green and angles between 15.0° to 62.8° in black. Definitions for the crystal orientation are plotted in the color coded map on the right side and as cubes within the mapping. (c) Micro-Raman internal stress mapping, maximum compressive stress of -90.5 MPa and tensile stress of 19.2 MPa are determined.

stress of -21.5 MPa are determined. Compared to the laser spot welding, the stress is lower.

We assume that the thickening of the welding partners at the welding region appears due to wetting and surface tension issues. It seems like the molten silicon flows towards the solid silicon, so that the thickening develops. The difference in crystal orientation is probably due to an unavoidable misalignment of the samples to each other by mounting the samples on a motorized sample holder system before welding. The absence of structural changes within the silicon material after the laser beam irradiation could be addressed to the broad irradiation and the reduced penetration depth by the laser line welding technique.

3.3. Keyhole Welding. Two samples are aligned on a quartz glass sample holder in a butt joint configuration, and a third one was placed centered on the back side of the other two. The sample holder was placed in an oven and heated up to 1015°C under nitrogen atmosphere. The laser beam for welding was introduced through a quartz window in the oven from the top side. Three bonding areas had been created and are shown in Figure 5; the areas between silicon foil 1 and 2

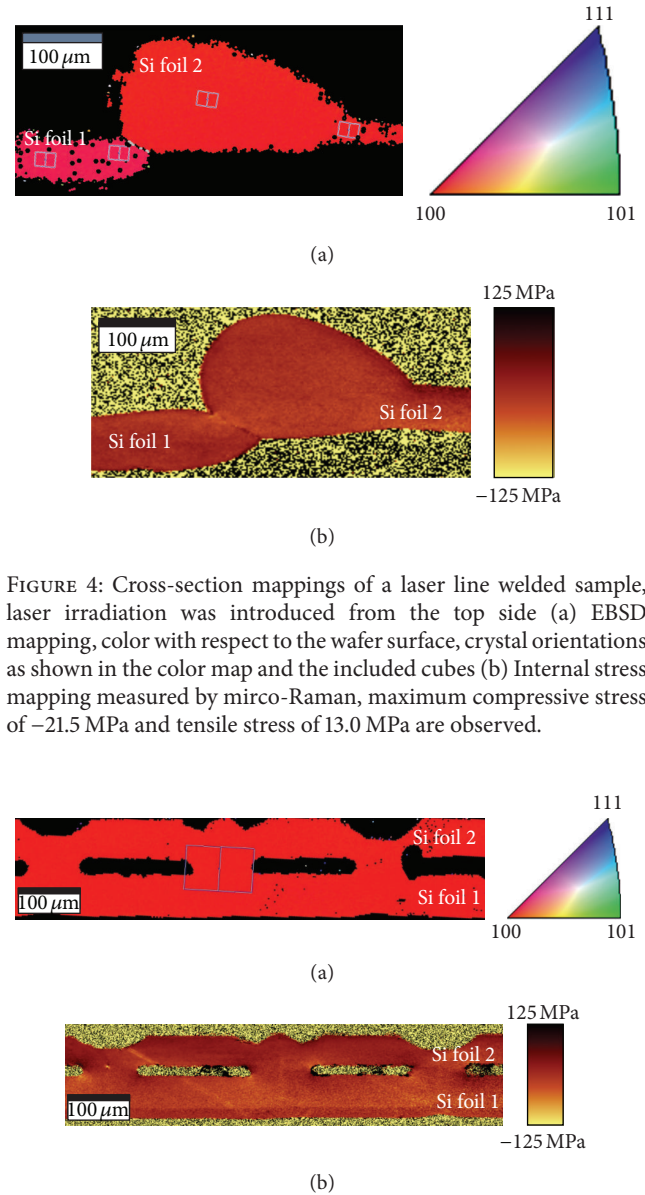


FIGURE 4: Cross-section mappings of a laser line welded sample, laser irradiation was introduced from the top side (a) EBSD mapping, color with respect to the wafer surface, crystal orientations as shown in the color map and the included cubes (b) Internal stress mapping measured by micro-Raman, maximum compressive stress of -21.5 MPa and tensile stress of 13.0 MPa are observed.

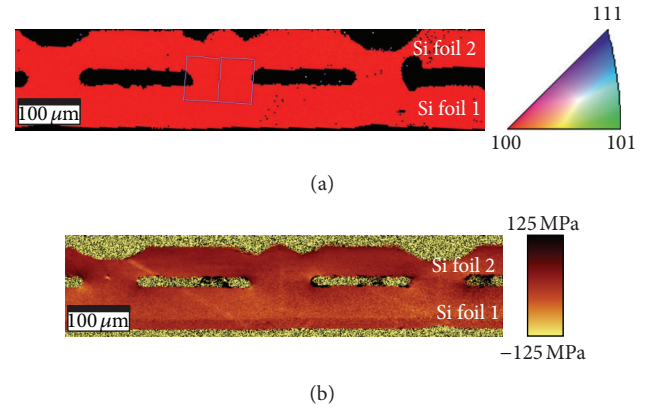


FIGURE 5: Cross-section mappings of a keyhole welded sample, three welding areas are illustrated and the laser beam was applied from the top side (a) EBSD mapping, color with respect to the wafer surface, crystal orientations as shown in the color map as well as the included cube (b) Internal stress mapping measured by micro-Raman, maximum compressive stress of -50.0 MPa and tensile stress of 27.5 MPa are measured.

next to the welding areas are gaps because keyhole welding is not a continuous laser process. The EBSD mapping (see Figure 5(a)) shows a very homogenous crystal structure after the welding process. No evidence of newly formed grains and grain boundaries can be observed. The crystal orientation remains the same. On the top, the two holes and one elevation of the top sample are caused by the high laser beam intensity within an area of about $80\ \mu\text{m}$. Furthermore, no thickening of the silicon material is observed after welding contrary to using a laser line.

The internal stress mapping, depicted in Figure 5(b), is very homogenous and shows only tiny areas of increased stress, and the bright angular lines are due to cross-section preparation. Maximum compressive stress of -50.0 MPa and tensile stress of 27.5 MPa had been determined. Those values are higher than stress values of laser line welding, but lower than values of laser spot welding.

The recent welding approach shows no multiple grain appearance. No material thickening at the welding seam can be observed. Only locally at the back side, formations of valleys and mountains can be observed which is due to the high laser irradiation on small an area to create keyholes. These connect the stacked silicon wafers without creating structural changes within the material. During the cooling procedure after irradiation all four neighboring points next to the keyholes with silicon in the solid state serve as seed layers for the recrystallization process, so that the laser-irradiated areas recrystallize into a monocrystalline structure.

4. Discussion

Although welding of silicon wafer material is very challenging, we could show three different approaches. Using a spot welding process with low constant feed speed at room temperature has been successfully demonstrated, but this welding process suffers from the formation of new grains within the welding seam. Two scenarios are feasible to explain this appearance of new grains. By mounting the samples onto the sample holder, an inevitable misalignment is expected; this should lead to at least one grain boundary between the two welding partners. Additionally, the cooling procedure after the welding process plays a dominant role for developing new grains. In this case an area of ca. $300\ \mu\text{m}$ is completely molten during the welding process; silicon phase boundaries on the left and right sides of the molten area are very small as compared to the area which is molten. Therefore, the monocrystalline silicon material on the left and right sides of the molten area cannot be the seed layer of the whole molten area because the cooling at the top and bottom sides as well as the transition back to the solid state will happen too fast. Thus, secondary seeding occurs, and grain boundaries appear. A $300\ \mu\text{m}$ wide area of different grains develops during the welding procedure. However, micro-Raman measurements determine high compressive stress values, which could be a problem for the mechanical stability of the silicon foil. Breaking tests of thin silicon foils with similar geometry determine an average breaking stress of 287.5 MPa as published elsewhere [1]. Breakage of an extended monocrystalline silicon base foil would cause major problems in a roll to roll process. Thus, this technique is not suitable for producing silicon foils.

Applying the welding process by using a laser line at room temperature is realized. Unfortunately, this way of welding suffers from thickening at the welding seam. Experiments with preheated welding samples show that the effect of thickening remains. Presumably, this is caused by wetting problems and differences in surface tension. This can be explained by the rule of Eötvös [17, 18], which states that the surface tension of a fluid decreases at increasing temperature.

Applying the laser line on the silicon causes a low heating rate due to the wide irradiated area, so that temperature gradients occur due to thermal conduction. At the outer irradiated area the surface tension is higher than that at the middle of the irradiated area. If the duration of the melting process for the silicon had been long enough, the molten silicon in the middle of the irradiated area flows towards the solid silicon and accumulates. Hence, the thickening occurs at the welding seam by welding using a laser line. However, one more effect appears in contrary to the laser spot welding with low constant feed speed. After the welding process, the two welding partners seem to not be joined together; instead, there is a small line between the two welding partners. We assume that this is caused by a native oxide on top of the welding partners before the welding process. On the other hand, the internal stress measurements show a very homogenous sample, and the stress values are low as compared to the other welding techniques. Unfortunately, the thickening of the silicon at the welding seam is a major problem. Therefore, this welding technique is not suitable to produce silicon foils for a roll to roll process.

Keyhole welding at room temperature is not performed due to the knowledge of the drastic changes within the silicon material and high inserted stress without preheating. However, the keyhole welding technique with preheated samples is successfully demonstrated. Furthermore, this welding process shows no newly formed grains after welding within the measurement accuracy. (Differences down to 1° in crystal orientation can be detected with the EBSD measurement setup.) In addition, no thickening of silicon can be observed around the welding seam. Sample mappings occur to be homogenous. The locally occurring roughness on the back side of the silicon foil due to the laser irradiation is negligible for the solar cell device. Stress measurements determine moderate stress values for tensile as well as compressive stress, so that the mechanical stability is reassured. In summary, this welding technique offers the possibility of the manufacturing of extended monocrystalline silicon base foil in a roll to roll process. With these remarkable properties keyhole welding is the most favorable and promising process to produce silicon foils.

5. Conclusions

We have presented a comparison of three welding processes for ca. $50\ \mu\text{m}$ thin silicon foils: laser spot welding with low constant feed speed at room temperature, laser line welding at room temperature, and keyhole welding at preheated samples of 1015°C . Welded thin silicon foils with the dimensions of up to $50 \times 25\ \text{mm}^2$ are successfully demonstrated. The material properties of the thin silicon foils after the impact of the laser beam were analyzed by micro-Raman spectroscopy and electron backscatter diffraction.

The characterization revealed newly formed grains and grain boundaries at the welding seam for laser spot welding. Additionally, this technique suffers from the high inserted stress values after welding. Silicon thickening is observed for laser line welding at the junction of both welding partners.

Thus, these two welding processes are not suitable for the production of thin silicon foils. Keyhole welding in comparison shows very homogenous material properties after laser irradiation. No evidence of newly formed grains or thickening at the welding seam could be found. Maximum tensile and compressive stress values are at a moderate level for keyhole welding higher than values for laser line welding, but lower for laser spot welding. Additionally, this technique can be performed in a configuration which leads to a flat silicon foil after welding. Therefore, keyhole welding is the most favorable process for welding several individual silicon thin wafers together to an extended monocrystalline silicon base foil. It should be interesting to investigate keyhole welding using double side polished wafer material. This could result in decreased internal stress values and higher mechanical stability of the silicon foils. The complex procedure of welding silicon needs further investigations as well as the support by a simulation model. Furthermore, solar cells on top of keyhole welded silicon foils are planned.

Acknowledgments

The authors thank the Deutsche Forschungsgemeinschaft (no.: KU 2601/1-2) for the financial support. Furthermore, the authors would like to acknowledge the technical assistance of Bernd Meidel and the sample preparation by Kerstin Schünemann and Georg Gries from Schott Solar AG in Alzenau (Germany).

References

- [1] M. T. Hessmann, T. Kunz, I. Burkert et al., "Laser process for extended silicon thin film solar cells," *Thin Solid Films*, vol. 520, no. 1, pp. 595–599, 2011.
- [2] T. Kunz, I. Burkert, R. Auer, and M. Zimmermann, "Towards extended free-standing crystalline silicon thin-films by laser joining," in *Proceedings of the 22nd European Photovoltaic Solar Energy Conference*, pp. 1946–1948, Milan, Italy, September 2007.
- [3] R. Brendel, "A novel process for ultrathin monocrystalline silicon solar cells on glass," in *Proceedings of the 14th European Photovoltaic Solar Energy Conference*, pp. 1354–1357, Barcelona, Spain, June 1997.
- [4] H. Tayanaka, K. Yamauchi, and T. Matsushita, "Thin-film crystalline silicon solar cells obtained by separation of a porous silicon sacrificial layer," in *Proceedings of the 2nd World Conference and Exhibition on Photovoltaic Solar Energy Conversion*, pp. 1272–1277, Vienna, Austria, 1998.
- [5] T. Kunz, I. Burkert, M. Grosch, M. Scheffler, and R. Auer, "Spatial uniformity of large-area silicon layers ($43 \times 43 \text{ cm}^{22}$) grown by convection-assisted chemical vapor deposition," in *Proceedings of the IEEE 4th World Conference on Photovoltaic Energy Conversion*, pp. 1620–1623, Waikoloa, Hawaii, USA, May 2006.
- [6] J. H. Petermann, D. Zielke, J. Schmidt, F. Haase, E. G. Rojas, and R. Brendel, "19%-efficient and $43 \mu\text{m}$ -thick crystalline Si solar cell from layer transfer using porous silicon," *Progress in Photovoltaics*, vol. 20, no. 1, pp. 1–5, 2012.
- [7] J. H. Werner, R. Dassow, T. J. Rinke, J. R. Köhler, and R. B. Bergmann, "From polycrystalline to single crystalline silicon on glass," *Thin Solid Films*, vol. 383, no. 1-2, pp. 95–100, 2001.
- [8] S. Kaufmann, *Grundlegende Untersuchungen zum Nd:YAG-Laserstrahlfügen von Silizium für Komponenten der Optoelektronik*, Meisenbach, Bamberg, Germany, 2002.
- [9] U. Gösele, Q. Y. Tong, A. Schumacher et al., "Wafer bonding for microsystems technologies," *Sensors and Actuators A*, vol. 74, no. 1-3, pp. 161–168, 1999.
- [10] L. Schaefer, H. Koch, K. Tangermann-Gerk et al., "Laser based joining of monocrystalline silicon foils," *Physics Procedia*, vol. 5, pp. 503–510, 2010.
- [11] L. Schaefer, S. Roth, and M. Heßmann, "Anforderungen an den Prozess und die Systemtechnik beim Laserstrahlschweißen von Silizium Zusammenfassung Einleitung Eigenschaften und Verarbeitbarkeit von Silizium," in *Proceedings of the 13th Laser in der Elektronikproduktion und Feinwerktechnik*, pp. 75–85, Fürth, Germany, 2010.
- [12] R. Völkel and M. Zimmermann, "Homogenisierung von Laserstrahlen," *Photonik*, pp. 76–79, 2006.
- [13] K. Cvecek, M. Zimmermann, U. Urmoneit, T. Frick, M. Heßmann, and T. Kunz, "Thermisches Prozessieren dünner Siliziumsubstrate für die solare Energieerzeugung," in *Proceedings of the 15th Laser in der Elektronikproduktion und Feinwerktechnik*, pp. 91–101, Fürth, Germany, 2012.
- [14] T. Kunz, M. T. Hessmann, B. Meidel, and C. J. Brabec, "Micro-Raman mapping on layers for crystalline silicon thin-film solar cells," *Journal of Crystal Growth*, vol. 314, no. 1, pp. 53–57, 2011.
- [15] I. De Wolf, "Micro-Raman spectroscopy to study local mechanical stress in silicon integrated circuits," *Semiconductor Science and Technology*, vol. 11, no. 2, pp. 139–154, 1996.
- [16] G. Sarau, M. Becker, G. Andrä, and S. Christiansen, "Residual stress measurements in multicrystalline silicon bulk and thin film solar cells using micro-Raman spectroscopy," in *Proceedings of the 23rd European Photovoltaic Solar Energy Conference*, pp. 2265–2270, Valencia, Spain, 2008.
- [17] L. Eötvös, "Über den Zusammenhang der Oberflächenspannung der Flüssigkeiten mit ihrem Molekularvolumen," *Annalen der Physik und Chemie*, vol. 27, pp. 448–459, 1886.
- [18] S. R. Palit, "Thermodynamic interpretation of the eötvös constant," *Nature*, vol. 177, no. 4521, p. 1180, 1956.

Research Article

The Effects of Malonic Acid Derivatives and Acetic Acid Derivatives as Coadsorbents on the Photovoltaic Performance of Dye-Sensitized Solar Cells

**Hiroaki Matsuyoshi, Haruo Tomita, Hitoshi Nishino,
Hiroki Sakamoto, and Kyohei Manabe**

Energy Technology Laboratories, Osaka Gas Co., Ltd., 6-19-9 Torishima, Konohana-ku, Osaka 554-0051, Japan

Correspondence should be addressed to Hiroaki Matsuyoshi; h-matsuyoshi@ogc.co.jp

Received 13 May 2013; Accepted 18 June 2013

Academic Editor: Stefano Caramori

Copyright © 2013 Hiroaki Matsuyoshi et al. This is an open access article distributed under the Creative Commons Attribution License, which permits unrestricted use, distribution, and reproduction in any medium, provided the original work is properly cited.

The effects of malonic acid derivatives and acetic acid derivatives as coadsorbents on the photovoltaic performance of D908 dye-sensitized nanocrystalline TiO₂ solar cells were investigated. Each of phenylmalonic acid (PMA) and cyclopentylacetic acid (CPEAA) coadsorptions was revealed to improve both the photocurrent and the photovoltage of the solar cells. The improved photocurrent was probably due to the suppression of self-quenching of the excited electrons in the dyes by coadsorption of PMA or CPEAA on the TiO₂ that increased in the electron-injection yields from the dye to the TiO₂. The improved photovoltage was probably due to suppression of recombination between the injected electrons and I₃⁻ ions on the TiO₂ surface. ATR-FTIR spectroscopy indicated that PMA or CPEAA coadsorption increased the content of bound dye on the TiO₂ surface. This result suggests that PMA or CPEAA coadsorption improved the photocurrent of the solar cells. Electrochemical impedance spectroscopy indicated that PMA or CPEAA coadsorption on the TiO₂ surface increased the charge recombination resistance (R₂) and decreased the diffusion resistance in the electrolyte (R₃). These results suggest that the coadsorption of PMA or CPEAA on the TiO₂ may improve its photovoltage and photocurrent.

1. Introduction

Dye-sensitized solar cells (DSCs) do not use high-purity silicon, and their manufacturing process is simple and of low cost. DSCs are expected to reduce the manufacturing cost significantly compared with conventional p-n junction solar cells.

A great deal of effort has been made to improve the photovoltaic performance of DSCs [1–4].

In our previous paper, we studied TiO₂ materials [5] and electrolytes [6].

The above study was found to be very important to control the interface between TiO₂ and dye electrolyte.

Dyes are required to be adsorbed on the TiO₂ in a monolayer without association or aggregation in order to suppress self-quenching of the excited electrons in the dyes.

To reduce association or aggregation of dyes, several carboxylic acid derivatives have been studied. For example, there are several reports using 3-phenylpropionic acid [7], deoxycholic acid [8], chenodeoxycholic acid [9], stearic acid [10], 4-guanidinobutyric acid [11], and hexadecylmalonic acid [12].

The coadsorption of dyes on the TiO₂ surface is expected to improve both the photocurrent and the photovoltage of DSC cells. The improved photocurrent can be attributed to a positive shift of the conduction band edge of TiO₂ [13] or to suppression of self-quenching of the excited electrons in the dyes [14]. The improved photovoltage can be caused by suppression of recombination between the injected electrons and I₃⁻ ions [12, 13].

In this paper, we report the effects of malonic acid derivatives and acetic acid derivatives as coadsorbents on the

photovoltaic performance of DSC cells sensitized by D-908 dye (Figure 1).

Especially, dicarboxylic acids such as malonic acid derivatives could be anchored to the surface of TiO_2 more effectively than monocarboxylic acids, and there are few previous papers about dicarboxylic acids as coadsorbents [12]. So, we choose malonic acids derivatives as coadsorbents.

2. Materials and Methods

2.1. D908 Dye. The molecular structure of D908 dye is shown in Figure 1.

D908 dye is one of the derivatives of Z907 dye. One of the protons bonded to the carboxylic groups is substituted by benzyltrimethylammonium cation.

D908 dye was purchased from Everlight Chemical Industrial Co., and used as supplied without further purification.

2.2. Malonic Acid Derivatives and Acetic Acid Derivatives. We chose six malonic acid derivatives including alkyl, cycloalkyl, and phenyl groups shown in Figure 2 and six acetic acid derivatives including alkyl, cycloalkyl, and naphthyl groups shown in Figure 3.

Isopropylmalonic acid (Tokyo Kasei Kogyo Co., Ltd.), n-butylmalonic acid (Wako Chemical Co., Ltd.), n-hexadecylmalonic acid (Oakwood Products, Inc.), cyclopentylmalonic acid (Tokyo Kasei Kogyo Co., Ltd.), phenylmalonic acid (Tokyo Kasei Kogyo Co., Ltd.), and benzylmalonic acid (Tokyo Kasei Kogyo Co., Ltd.) were used as supplied.

Cyclopropylacetic acid (Wako Chemical Co., Ltd.), cyclopentylacetic acid (Tokyo Kasei Kogyo Co., Ltd.), cyclohexylacetic acid (Tokyo Kasei Kogyo Co., Ltd.), cycloheptylacetic acid (Alfa Aesar), tert-butylacetic acid (Tokyo Kasei Kogyo Co., Ltd.), and 1-naphthylacetic acid (Tokyo Kasei Kogyo Co., Ltd.) were used as supplied.

2.3. Preparation of TiO_2 Electrodes Sensitized by D908 Dye. TiO_2 nanoparticle (ca. 20 nm) pastes were prepared by the method of the previous paper [15]. TiO_2 electrodes (apparent area 0.25 cm^2 ; thickness ca $14 \mu\text{m}$) were prepared on a glass substrate coated with F-doped SnO_2 by screen printing. The electrodes were heated at 550°C for 1 hour. The D908 dye (0.5 mM) and the coadsorbent (0.5 mM) were dissolved in a 50:50 (vol.%) solution of acetonitrile and tert-butyl alcohol. The solvents were purchased from Kanto Chemical Co., Inc. and used as supplied without further purification. The TiO_2 films were immersed in the dye solutions and kept at 25°C for 20 h.

2.4. Preparation of Electrolyte. The electrolyte consisted of 0.06 M iodine, 0.1 M LiI, 0.6 M 1-ethyl-3-methylimidazolium iodide, and 0.5 M 4-tert-butylpyridine in acetonitrile iodine (Wako Pure Chemical Industries, Ltd.), LiI (Kojundo Chemical Laboratory Co., Ltd.), 1-ethyl-3-methylimidazolium iodide (Kanto Chemical Co., Inc.), 4-tert-butylpyridine (Sigma-Aldrich), and acetonitrile (Kanto Chemical Co., Inc.) were used as supplied.

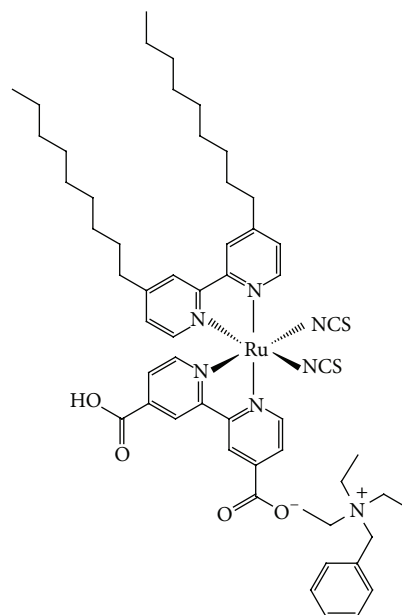
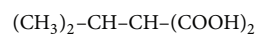
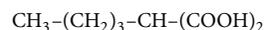


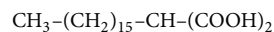
FIGURE 1: Structure of D908 dye.



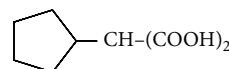
i-Propylmalonic acid



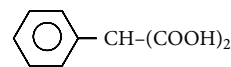
n-Butylmalonic acid



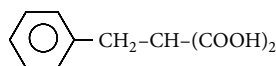
n-Hexadecylmalonic acid



Cyclopentylmalonic acid



Phenylmalonic acid



Benzylmalonic acid

FIGURE 2: Structures of malonic acid derivatives.

2.5. Fabrication of DSC Cells and Photovoltaic Measurement. The DSC cell consisted of the TiO_2 electrode, a counter electrode, a polyimide film spacer ($35 \mu\text{m}$ thick), and the electrolyte. The counter electrode was a Pt film sputtered on a TCO-coated glass plate.

Photovoltaic measurement employed an AM1.5 solar simulator equipped with a xenon lamp (San-ei Electric Co., Ltd.).

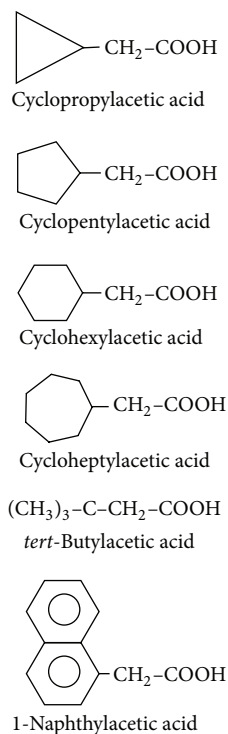


FIGURE 3: Structures of acetic acid derivatives.

2.6. Measurement of the Amount of Dye Adsorbed on TiO_2 . The areas around the TiO_2 films sensitized by D908 dye were wiped with ethanol. Then, the TiO_2 films were immersed in a 1.5 : 1.0 (vol.%) solution of ethanol and 0.1 M KOH for 10 minutes. After recognizing the dye desorption, 1.0 mL of the solution was used to measure its specific adsorption (maximum adsorption wavelength: 510 nm) by the spectrophotometer (Shimadzu UV-2550). The amounts of adsorbed dyes were calculated from the absorbance of 510 nm light for 1.0 mL desorbed sample solutions.

2.7. Measurement of Attenuated Total Reflection Fourier-Transformed IR (ATR-FTIR) Spectroscopy. The surfaces of TiO_2 films sensitized by D908 dye, D908 dye with phenylmalonic acid, and D908 dye with cyclopentylacetic acid were analyzed by ATR-FTIR (Nicolet, iN10MX) with 128 scans at a resolution of 8 cm^{-1} .

2.8. Measurement by Raman Spectroscopy. The surfaces of TiO_2 films sensitized by D908 dye, D908 dye with phenylmalonic acid, and D908 dye with cyclopentylacetic acid were analyzed with a Raman microscope (Renishaw, inVia) with an exciting light of 532 nm wavelength, an exciting light power of 0.5% (0.35 mW), an objective mirror of 50x magnification, an irradiation time of 3 seconds, 180-degree back scatter, and 5 times of scanning. The wave number was calibrated by silicone.

2.9. Measurement by Electrochemical Impedance Spectroscopy (EIS). The large DSC cells using the TiO_2 electrodes (apparent area 5.1 cm^2 , thickness ca $14 \mu\text{m}$) sensitized by D908 dye, D908 dye with phenylmalonic acid, and D908 dye with cyclopentylacetic acid were fabricated and measured with an electrochemical impedance spectroscopy (EIS) (Biologic, SP-300) under irradiation of 100 mW/cm^2 at 25°C .

3. Results and Discussion

3.1. Photovoltaic Performance. Table 1 shows the amount of D908 dyes adsorption and the photovoltaic parameters of DSC devices without coadsorbent (control) and with isopropylmalonic acid (IPMA), n-butylmalonic acid (BMA), n-hexadecylmalonic acid (HDMA), cyclopentylmalonic acid (CPMA), phenylmalonic acid (PMA), and benzylmalonic acid (BZMA).

As shown in Table 1, all the adsorbed amounts of the D908 dyes decreased when the six types of malonic acid derivatives were used as coadsorbents. These results indicate that malonic acid derivatives were adsorbed on the TiO_2 and suppressed D908 dye adsorption.

For the DSC device with HDMA, the amounts of the adsorbed D908 dyes dramatically decreased to $11.9 \times 10^{-8} \text{ mol/cm}^2$ relative to the control device ($19.4 \times 10^{-8} \text{ mol/cm}^2$). This result suggests that HDMA significantly suppressed D908 dye adsorption by its bulky steric effects. As a result of decreased dye adsorption, the value of J_{sc} decreased from 16.4 to 14.8 mA/cm^2 , and the value of conversion efficiency also decreased from 6.9% to 6.6%.

The other five DSC devices improved their conversion efficiencies. In particular, the DSC device with PMA showed the highest value of conversion efficiency (7.8%) among all the seven DSC devices. The amount of the adsorbed D908 dye decreased to $18.1 \times 10^{-8} \text{ mol/cm}^2$ relative to the control device ($19.4 \times 10^{-8} \text{ mol/cm}^2$), but the device showed a 6% improvement in the value of J_{sc} (17.4 mA/cm^2) relative to that of the control device (16.4 mA/cm^2). This result suggests that the coadsorption of PMA on the TiO_2 suppressed the aggregation of the dyes and the self-quenching of the excited electrons in the dyes by its steric effect. The effect is described in Section 3.2 ATR-FTIR spectroscopy and Section 3.4 electrochemical impedance spectroscopy. Therefore, the coadsorption of PMA increased in electron-injection yields from the dye to the TiO_2 .

The device also showed a 3% improvement in V_{oc} (0.66 V) relative to the control device (0.64 V). This result suggests that the coadsorption of PMA on the TiO_2 suppressed the recombination between the injected electrons and I_3^- ions. The effect is also described in Section 3.4 electrochemical impedance spectroscopy.

Table 2 shows the amounts of the adsorbed D908 dyes and the photovoltaic parameters of DSC devices with cyclopropylacetic acid (CPRAA), cyclopentylacetic acid (CPEAA), cyclohexylacetic acid (CHEAA), cycloheptylacetic acid (CHPAA), tert-butylacetic acid (TBAA) and naphthylacetic acid (NPAA). As shown in Table 2, all the amounts of the adsorbed D908 dyes decreased when the six types of

TABLE 1: Photovoltaic parameters of DSC devices with malonic acid derivatives.

| Coadsorbent | The amount of dye adsorption 10^{-8} mol/cm ² | J_{sc} (mA/cm ²) | V_{oc} (V) | FF | η (%) |
|-------------------------|---|-----------------------------------|-----------------|------|---------------|
| Control | 19.4 | 16.4 | 0.64 | 0.66 | 6.9 |
| Isopropylmalonic acid | 13.9 | 16.3 | 0.64 | 0.69 | 7.2 |
| n-Butylmalonic acid | 14.1 | 15.8 | 0.64 | 0.69 | 7.0 |
| n-Hexadecylmalonic acid | 11.9 | 14.8 | 0.64 | 0.70 | 6.6 |
| Cyclopentylmalonic acid | 14.8 | 16.7 | 0.64 | 0.68 | 7.3 |
| Phenylmalonic acid | 18.1 | 17.4 | 0.66 | 0.68 | 7.8 |
| Benzylmalonic acid | 12.6 | 16.4 | 0.63 | 0.68 | 7.0 |

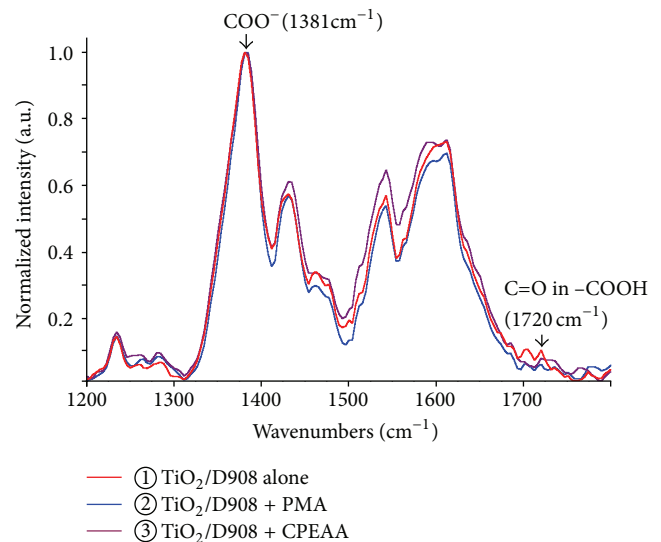
TABLE 2: Photovoltaic parameters of DSC devices with acetic acid derivatives.

| Coadsorbent | The amount of dye adsorption 10^{-8} mol/cm ² | J_{sc} (mA/cm ²) | V_{oc} (V) | FF | η (%) |
|------------------------|---|-----------------------------------|-----------------|------|---------------|
| Control | 19.4 | 16.4 | 0.64 | 0.66 | 6.9 |
| Cyclopropylacetic acid | 17.1 | 16.6 | 0.62 | 0.67 | 6.9 |
| Cyclopentylacetic acid | 17.2 | 17.0 | 0.66 | 0.68 | 7.6 |
| Cyclohexylacetic acid | 18.2 | 17.0 | 0.64 | 0.67 | 7.3 |
| Cycloheptylacetic acid | 17.3 | 16.5 | 0.62 | 0.67 | 6.9 |
| tert-Butylacetic acid | 18.7 | 16.6 | 0.63 | 0.68 | 7.1 |
| 1-Naphthylacetic acid | 18.0 | 16.3 | 0.61 | 0.68 | 6.8 |

acetic acid derivatives were used as coadsorbents. These results suggest that acetic acid derivatives were adsorbed on the TiO₂ and suppressed D908 dye adsorption. Three DSC devices with CPEAA, CHEAA, or TBAA improved their conversion efficiencies. In particular, the device with CPEAA showed the highest value of conversion efficiency (7.6%) among seven devices. The amount of adsorbed D908 dye decreased to 17.2×10^{-8} mol/cm² relative to the control device (19.4×10^{-8} mol/cm²), but the device showed a 4% improvement in J_{sc} (17.0 mA/cm²) relative to the control device (16.4 mA/cm²). The device also showed a 3% improvement in V_{oc} (0.66 V) relative to the control device (0.64 V). These results suggest that the coadsorption of CPEAA on the TiO₂ has an effect similar to that of PMA. The effect is also described in Section 3.2 ATR-FTIR spectroscopy and Section 3.4 Electrochemical impedance spectroscopy.

3.2. ATR-FTIR Spectroscopy. Figure 4 shows the attenuated total reflection Fourier-transformed IR (ATR-FTIR) spectra of TiO₂ films sensitized by D908 alone, D908 with PMA, and D908 with CPEAA in the range of 1200–1800 cm⁻¹. The assignments of the peaks were prepared by the previous papers [10, 16].

The peak at 1381 cm⁻¹ was assigned to the carboxylate groups (-COO⁻) anchored to the surface of the TiO₂, and the peak at 1720 cm⁻¹ was assigned to the free carboxylic acid (-COOH) of the D908 dye. The intensity at 1381 cm⁻¹ relative to that at 1720 cm⁻¹ (I_{1381}/I_{1720}) was calculated, and the values were 11.2 (D908 alone, control), 21.3 (D908 with PMA), and 17.2 (D908 with CPEAA), respectively.

FIGURE 4: ATR-FTIR spectra of TiO₂ films sensitized with D908 alone, D908 with PMA, and D908 with CPEAA.

Therefore, the amounts of D908 dyes anchored to the surface of TiO₂ were in the following order: D908 with PMA > D908 with CPEAA > control. This result provides an explanation for improved J_{sc} value for the DSC device with PMA or CPEAA, even though the amounts of dye were less.

3.3. Raman Spectroscopy. Figure 5 shows the Raman spectra of TiO₂ films sensitized by D908 alone, D908 with PMA, and D908 with CPEAA in the range of 400–1800 cm⁻¹. The

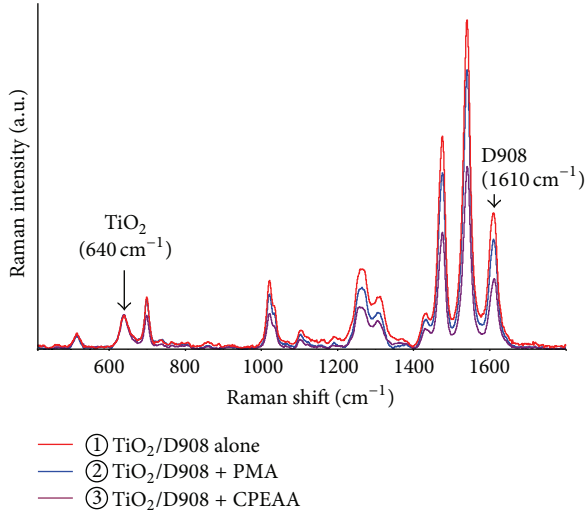


FIGURE 5: Raman spectra of the TiO_2 films sensitized with D908 alone, D908 with PMA, and D908 with CPEAA.

assignments of the peaks were prepared by the previous paper [17].

The peak at 640 cm^{-1} was assigned to the TiO_2 , and the peak at 1610 cm^{-1} was assigned to the D908 dye. The intensity at 1610 cm^{-1} relative to that at 640 cm^{-1} (I_{1610}/I_{640}) was calculated, and the values were 4.26 (D908 alone, control), 3.26 (D908 with PMA), and 2.03 (D908 with CPEAA), respectively.

Therefore, the amounts of D908 dye adsorbed on the surface of TiO_2 were in the following order: control > D908 with PMA > D908 with CPEAA. This result coincides with the order of the amounts of D908 dyes measured by the spectrophotometer as referred to in Section 2.7, and suggests that Raman spectra can be used for the evaluation of the amount of dye more conveniently.

3.4. Electrochemical Impedance Spectroscopy (EIS). Electrochemical impedance spectroscopy (EIS) was performed to investigate the interface in the DSC devices by the method of the previous papers [18, 19].

Figure 6 shows the Nyquist plots of DSC devices using the TiO_2 films sensitized by D908 alone, D908 with PMA, and D908 with CPEAA. The plots were fitted by the equivalent circuit of DSC shown in Figure 7, and R_s , R_1 , R_2 , and R_3 values were calculated.

R_s means the series resistance such as that of F-doped SnO_2 and interconnection.

R_1 (Pt) means the resistance of charge transfer between Pt and electrolyte. R_2 (TiO_2) means the charge recombination resistance from TiO_2 to I_3^- ions. R_3 (I) means the diffusion resistance in electrolyte. These parameters are shown in Table 3.

The values of R_2 in the DSC devices with PMA or CPEAA were larger than that of the control device. This result suggests that the coadsorption of PMA or CPEAA on the TiO_2 suppressed the recombination between the

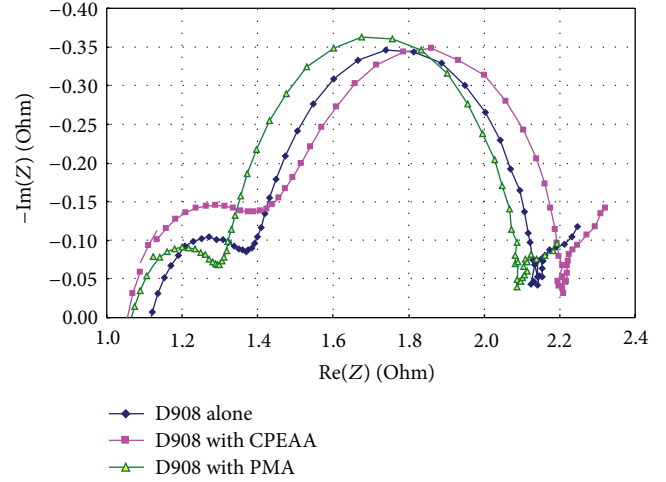


FIGURE 6: Nyquist plots for the DSC devices using TiO_2 films sensitized with D908 alone, D908 with PMA, and D908 with CPEAA.

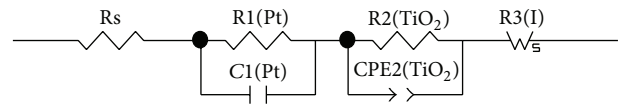


FIGURE 7: Equivalent circuit of DSC.

TABLE 3: Impedance parameters of DSC devices with PMA or CPEAA.

| Coadsorbent | R_s | R_1 (Pt) | R_2 (TiO_2) | R_3 (I) |
|------------------------|-------|------------|--------------------------|-----------|
| Control | 5.5 | 1.2 | 3.8 | 3.6 |
| Phenylmalonic acid | 5.5 | 1.2 | 4.0 | 3.4 |
| Cyclopentylacetic acid | 5.5 | 1.2 | 4.0 | 3.4 |

injected electrons and I_3^- ions; therefore, PMA or CPEAA coadsorption improved the V_{oc} of the DSC devices.

The values of R_3 in the DSC devices with PMA or CPEAA were smaller than that of the control device. This result suggests that the coadsorption of PMA or CPEAA on the TiO_2 suppressed the aggregation of the dyes and I^- ions were able to access the dyes more smoothly; thus PMA or CPEAA coadsorption improved the J_{sc} of the DSC devices.

4. Conclusions

Coadsorption of PMA or CPEAA improved both the J_{sc} and the V_{oc} values for DSC devices sensitized by D908 dye even though coadsorption decreased the amount of dye adsorbed on the TiO_2 electrode. The conversion efficiency increased from 6.9% to 7.8% for PMA and from 6.9% to 7.6% for CPEAA.

ATR-FTIR spectra suggested that coadsorption of PMA or CPEAA increased the amount of D908 dye anchored to the surface of TiO_2 . This result provides an explanation for the improved J_{sc} values.

Raman spectra suggested that coadsorption of PMA or CPEAA decreased the amount of D908 dye adsorbed on the surface of TiO₂. This result coincides with the amount of D908 dye measured by the spectrophotometer and suggests that Raman spectra can be used for the evaluation of the amount of dye more conveniently.

Electrochemical impedance spectroscopy suggested that the values of R2 in the DSC devices with PMA or CPEAA were larger than that of the control device. This result suggests that the coadsorption of PMA or CPEAA on the TiO₂ suppressed the recombination between the injected electrons and I₃⁻ ions, PMA or CPEAA coadsorption improving the V_{oc} of the DSC devices. The values of R3 in the DSC devices with PMA or CPEAA were smaller than that of the control device. This result suggests that the coadsorption of PMA or CPEAA on the TiO₂ suppressed the aggregation of the dyes and I⁻ ions were able to access the dyes more smoothly. Consequently, PMA or CPEAA coadsorption improved the J_{sc} of the DSC devices.

References

- [1] B. O'Regan and M. Grätzel, "A low-cost, high-efficiency solar cell based on dye-sensitized colloidal TiO₂ films," *Nature*, vol. 353, p. 737, 1991.
- [2] M. Grätzel, "Photoelectrochemical cells," *Nature*, vol. 414, p. 338, 2001.
- [3] M. Grätzel, "Solar energy conversion by dye-sensitized photo-voltaic cells," *Inorganic Chemistry*, vol. 44, p. 6841, 2005.
- [4] B. E. Hardin, H. J. Snaith, and M. D. McGehee, "The renaissance of dye-sensitized solar cells," *Nature Photonics*, vol. 6, no. 3, pp. 162–169, 2012.
- [5] H. Nishino, H. Matsuyoshi, H. Sakamoto et al., "TiO₂ nanotube utilizing a CNT template and its performance as the anode of a dye-sensitized solar cell," *Chemistry Letters*, vol. 41, no. 1, pp. 56–57, 2012.
- [6] H. Matsuyoshi, H. Tomita, H. Nishino, H. Sakamoto, K. Manabe, and H. Sasaki, "Effects of 1,3-alkylimidazolium iodide on electrolytes for dye-sensitized solar cell," *Electrochemistry*, vol. 79, no. 12, pp. 943–946, 2011.
- [7] P. Wang, S. M. Zakeeruddin, R. Humphry-Baker, and M. Grätzel, "A binary ionic liquid electrolyte to achieve ≥7% power conversion efficiencies in dye-sensitized solar cells," *Chemistry of Materials*, vol. 16, p. 2694, 2004.
- [8] K. Hara, Y. Dan-Oh, C. Kasada et al., "Effect of additives on the photovoltaic performance of coumarin-dye-sensitized nanocrystalline TiO₂ solar cells," *Langmuir*, vol. 20, no. 10, pp. 4205–4210, 2004.
- [9] A. Morandier, I. Lopez-Duarte, B. O'Regan et al., "Ru(II)-phthalocyanine sensitized solar cells: the influence of co-adsorbents upon interfacial electron transfer kinetics," *Journal of Materials Chemistry*, vol. 19, p. 5016, 2009.
- [10] J. Lim, Y. S. Kwon, and T. Park, "Effect of coadsorbent properties on the photovoltaic performance of dye-sensitized solar cells," *Chemical Communications*, vol. 47, p. 4147, 2011.
- [11] Z. Zhang, N. Evans, S. M. Zakeeruddin, R. Humphry-Baker, and M. Grätzel, "Effects of ω-guanidinoalkyl acids as coadsorbents in dye-sensitized solar cells," *Journal of Physical Chemistry C*, vol. 111, p. 398, 2007.
- [12] P. Wang, S. M. Zakeeruddin, P. Comte, R. Sharvet, R. H-Baker, and M. Grätzel, "Enhance the performance of dye-sensitized solar cells by co-grafting amphiphilic sensitizer and hexadecylmalonic acid on TiO₂ nanocrystals," *Journal of Physical Chemistry B*, vol. 107, p. 14336, 2003.
- [13] A. Kay and M. Grätzel, "Artificial photosynthesis. 1. Photosensitization of titania solar cells with chlorophyll derivatives and related natural porphyrins," *Journal of Physical Chemistry*, vol. 97, p. 6272, 1993.
- [14] J. He, G. Benkö, F. Korodi et al., "Modified phthalocyanines for efficient near-IR sensitization of nanostructured TiO₂ electrode," *Journal of the American Chemical Society*, vol. 124, p. 4922, 2002.
- [15] S. Ito, T. N. Murakami, P. Comte et al., "Fabrication of thin film dye sensitized solar cells with solar to electric power conversion efficiency over 10%," *Thin Solid Films*, vol. 516, no. 14, pp. 4613–4619, 2008.
- [16] M. K. Nazeeruddin, R. Humphry-Baker, P. Liska, and M. Grätzel, "Investigation of sensitizer adsorption and the influence of protons on current and voltage of a dye-sensitized nanocrystalline TiO₂ solar cell," *Journal of Physical Chemistry B*, vol. 107, p. 8981, 2003.
- [17] C. Ferez León, L. Kador, B. Peng, and M. Thelakkat, "Characterization of the adsorption of Ru-bpy dyes on mesoporous TiO₂ films with UV-Vis, Raman, and FTIR spectroscopies," *Journal of Physical Chemistry B*, vol. 110, no. 17, pp. 8723–8730, 2006.
- [18] Q. Wang, J.-E. Moser, and M. Grätzel, "Electrochemical impedance spectroscopic analysis of dye-sensitized solar cells," *Journal of Physical Chemistry B*, vol. 109, p. 14945, 2005.
- [19] F. Fabregate-Santiago, J. Bisquert, E. Palomares et al., "Correlation between photovoltaic performance and impedance spectroscopy of dye-sensitized solar cells based on ionic liquids," *Journal of Physical Chemistry C*, vol. 111, p. 6550, 2007.

Research Article

Advantages of N-Type Hydrogenated Microcrystalline Silicon Oxide Films for Micromorph Silicon Solar Cells

Amornrat Limmanee, Songkiate Kittisontirak, Sorapong Inthisang, Taweewat Krajangsang, Jaran Sritharathikhun, and Kobsak Sriprapha

Solar Energy Technology Laboratory, National Electronics and Computer Technology Center, National Science and Technology Development Agency, 112 Thailand Science Park, Phahonyothin Road, Klong 1, Klong Luang, Pathum Thani 12120, Thailand

Correspondence should be addressed to Amornrat Limmanee; amornrat.limmanee@nectec.or.th

Received 9 May 2013; Revised 30 May 2013; Accepted 30 May 2013

Academic Editor: Leonardo Palmisano

Copyright © 2013 Amornrat Limmanee et al. This is an open access article distributed under the Creative Commons Attribution License, which permits unrestricted use, distribution, and reproduction in any medium, provided the original work is properly cited.

We report on the development and application of n-type hydrogenated microcrystalline silicon oxide films ($n \mu\text{-SiO:H}$) in hydrogenated amorphous silicon oxide/hydrogenated microcrystalline silicon (a-SiO:H/ $\mu\text{-Si:H}$) micromorph solar cells. The $n \mu\text{-SiO:H}$ films with high optical bandgap and low refractive index could be obtained when a ratio of carbon dioxide (CO_2) to silane (SiH_4) flow rate was raised; however, a trade-off against electrical property was observed. We applied the $n \mu\text{-SiO:H}$ films in the top a-SiO:H cell and investigated the changes in cell performance with respect to the electrical and optical properties of the films. It was found that all photovoltaic parameters of the micromorph silicon solar cells using the n top $\mu\text{-SiO:H}$ layer enhanced with increasing the CO_2/SiH_4 ratio up to 0.23, where the highest initial cell efficiency of 10.7% was achieved. The enhancement of the open circuit voltage (V_{oc}) was likely to be due to a reduction of reverse bias at subcell connection— n top/ p bottom interface—and a better tunnel recombination junction contributed to the improvement in the fill factor (FF). Furthermore, the quantum efficiency (QE) results also have demonstrated intermediate-reflector function of the $n \mu\text{-SiO:H}$ films.

1. Introduction

Wide-bandgap silicon oxide based materials have been widely studied for thin film silicon solar cell applications because of their attractive optical and electrical properties [1–4]. Characterizations of boron doped hydrogenated amorphous and microcrystalline silicon oxide films (p a-SiO:H and $p \mu\text{-SiO:H}$) and their applications as window layer of solar cells have been reported by many research groups [5, 6]. N-type a-SiO:H and $\mu\text{-SiO:H}$ films also have been developed and applied in single junction and multijunction thin film silicon solar cells [7–11]. However, most works focused on an intermediate-reflector function of the $n \mu\text{-SiO:H}$ films in conventional a-Si:H/ $\mu\text{-Si:H}$ micromorph solar cells and paid little attention to their effects on junction connection and band diagram continuity [7–10]. Moreover, application of the $n \mu\text{-SiO:H}$ films to a-SiO:H based solar cells has not yet been reported; thus there is still much room for further research.

Our group has been investigating the wide bandgap SiO:H based materials and previously reported performance of the a-SiO:H based solar cells with single junction and multijunction structures—a-SiO:H, a-SiO:H/a-Si:H, and a-SiO:H/ $\mu\text{-Si:H}$ [12–15]. In this work, we focus on properties of the $n \mu\text{-SiO:H}$ films and their appropriateness to the use as the n top layer in the a-SiO:H/ $\mu\text{-Si:H}$ micromorph silicon solar cells. Properties of the $n \mu\text{-SiO:H}$ films are presented along with the performance of the micromorph silicon solar cells.

2. Experimental Details

2.1. Preparation of $n \mu\text{-SiO:H}$ Films. $n \mu\text{-SiO:H}$ films have been prepared by very high frequency plasma enhanced chemical vapor deposition (60 MHz VHF-PECVD) technique. The gas sources were silane (SiH_4), hydrogen (H_2), and carbon dioxide (CO_2), and phosphine (PH_3) was employed

as a doping source. For film characterizations, the n μc -SiO:H films were deposited on Corning glass substrates at the deposition temperature of 180°C , a plasma power of $70\text{ mW}/\text{cm}^2$, deposition pressure of 0.5 Torr , H_2/SiH_4 ratio of 35, PH_3/SiH_4 ratio of 0.38, and CO_2/SiH_4 ratio in the range of $0\sim 0.28$. The thickness of the films was kept at about 350 nm , which was measured by step profilometer. The crystalline volume fraction (X_c) of the n μc -SiO:H films was estimated by Raman scattering experiment. The Raman scattering spectra of the n μc -SiO:H films in the $400\text{--}600\text{ cm}^{-1}$ region can be deconvoluted into three spectra. A peak distribution around $470\text{--}475\text{ cm}^{-1}$ is assigned to the transverse optical (TO) mode of amorphous silicon, whose corresponding integrated area is identified as $I(a)$. A sharp peak arising at around $519\text{--}522\text{ cm}^{-1}$ corresponds to the transverse optical vibrational mode of crystalline silicon, and the associated integrated area is identified as $I(c)$. And the intermediate component corresponding to a peak at around $506\text{--}510\text{ cm}^{-1}$ is identified as $I(b)$. The crystalline volume fraction is calculated by using the simplified empirical relation as follows [16]:

$$X_c = \frac{[I(c) + I(b)]}{[I(a) + I(b) + I(c)]}. \quad (1)$$

We have measured the absorption data (α) of the films at visible range by UV/Visible spectrophotometer. Due to the varying structure of the films from microcrystalline to amorphous phase, we avoided Tauc's plots, and to give a numerical presentation of the shift in the absorption spectra we determined E_{04} , that is, the energy corresponding to $\alpha = 10^4\text{ cm}^{-1}$, as an indicator of relative optical bandgap (E_{op}). Refractive index (n) spectra of the films were estimated by Spectroscopic Ellipsometry (SE) using Tauc-Lorentz model [17]. The dark conductivity (σ_d) of the films was measured in a coplanar configuration with Al electrode at room temperature.

2.2. Fabrication of a -SiO:H/ μc -Si:H Micromorph Silicon Solar Cells. We have applied the n μc -SiO:H films as the n top layer of the micromorph silicon solar cells with the structure of TCO glass/ZnO/p- μc -SiO:H/i- a -SiO:H/n- μc -SiO:H/p- μc -SiO:H/i- μc -Si:H/n- μc -Si:H/ZnO/Ag (cell active area was 0.75 cm^2). Note that absorber layer of the top cell was wide-bandgap a -SiO:H film, and p μc -SiO:H films were used as p layer in both top and the bottom cells. There was no intermediate layer at the junction connection between the top and bottom cells. Thicknesses of the i top a -SiO:H and i bottom μc -Si:H layers were 400 and 1500 nm , respectively. The CO_2/SiH_4 ratio for the n top layer deposition was varied from 0 to 0.28 , while other conditions in cell fabrication were kept as the same. The thickness of the n top layer was approximately 30 nm . The current-voltage (I - V) characteristics of the solar cells have been investigated under the standard testing conditions—AM1.5, $100\text{ mW}/\text{cm}^2$, and 25°C —in a Wacom solar simulator. Quantum efficiency (QE) of the solar cells also has been evaluated by spectral response measurements.

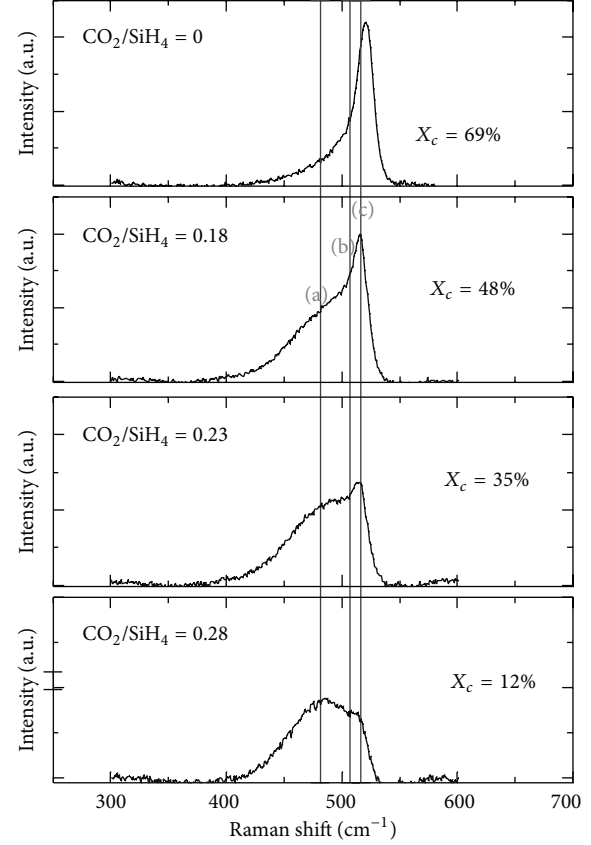


FIGURE 1: Raman spectra of n μc -SiO:H films deposited with different CO_2/SiH_4 ratios.

3. Results and Discussion

3.1. Properties of n μc -SiO:H Films. Figure 1 shows Raman spectra of the n μc -SiO:H films deposited with different CO_2/SiH_4 ratios. It is obviously shown that the peak corresponding to crystalline phase, peak (c), gradually decreased with increasing the CO_2/SiH_4 ratio, and the amorphous silicon (a) became a dominant phase at the ratio above 0.23. With no CO_2 addition the X_c of the film was 69%, decreasing to 12% at the CO_2/SiH_4 ratio of 0.28.

The optical bandgap of the films tended to increase while the refractive index measured at the wavelength of 550 nm showed an opposite change when the CO_2/SiH_4 ratio became higher, as shown in Figure 2. Incorporation of oxygen into the Si:H network has a direct consequence for optical gap widening. A component of the increase in optical bandgap is associated with the Si-O bonds because of the stronger bond energy of Si-O compared to those of Si-Si and Si-H [18]. Addition of oxygen atoms to Si:H films can widen optical bandgap; however, the more the participation of the oxygen atoms, the lower the conductivity of the films, as indicated in Figure 3.

3.2. Characteristics of a -SiO:H/ μc -Si:H Micromorph Silicon Solar Cells. As shown in Figure 4, open circuit voltage (V_{oc}), short circuit current density (J_{sc}), and fill factor (FF)

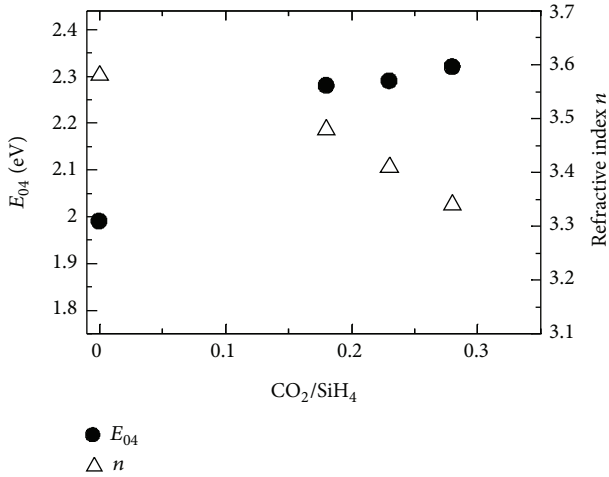


FIGURE 2: Optical bandgap (E_{04}) and refractive index (n) of $n \mu\text{c-SiO:H}$ films as a function of CO_2/SiH_2 ratio.

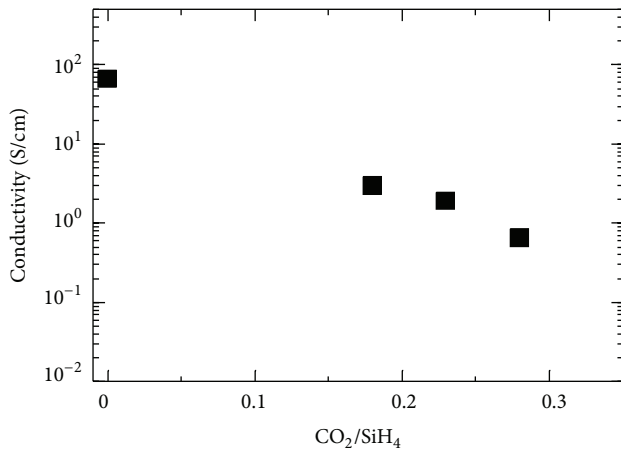


FIGURE 3: Dark conductivity of $n \mu\text{c-SiO:H}$ films as a function of CO_2/SiH_2 ratio.

of the solar cells obviously improved when the $n \mu\text{c-SiO:H}$ film was applied as the n top layer instead of the $n \mu\text{c-Si:H}$ film ($\text{CO}_2/\text{SiH}_4 = 0$). The best cell with initial conversion efficiency of 10.7% with $V_{oc} = 1.47 \text{ V}$, $J_{sc} = 10.6 \text{ mA/m}^2$, and $\text{FF} = 0.67$ has been achieved at the CO_2/SiH_4 ratio of 0.23, where the X_c of the film was approximately 35%. At the higher ratio, the J_{sc} of the cell began to drop, resulting in a decrease in the cell efficiency. Since the $n \mu\text{c-SiO:H}$ films possess wide optical bandgap of about 2.3 eV and higher defect density compared to the $n \mu\text{c-Si:H}$ film, these are supposed to allow a better continuity of band diagram and also a better tunnel recombination junction at the connection between the top and the bottom cells. As mentioned previously, the i top and p bottom layers in these solar cells were wide bandgap SiO:H based materials. The E_{04} of the p bottom $\mu\text{c-SiO:H}$ layer was estimated to be about 2.25 eV; thus the $n \mu\text{c-SiO:H}$ film with the E_{04} of 2.3 eV was probably better suited to the n top layer application for this cell structure. The enhancement in the V_{oc} was supposed to be due to a reduction of reverse bias

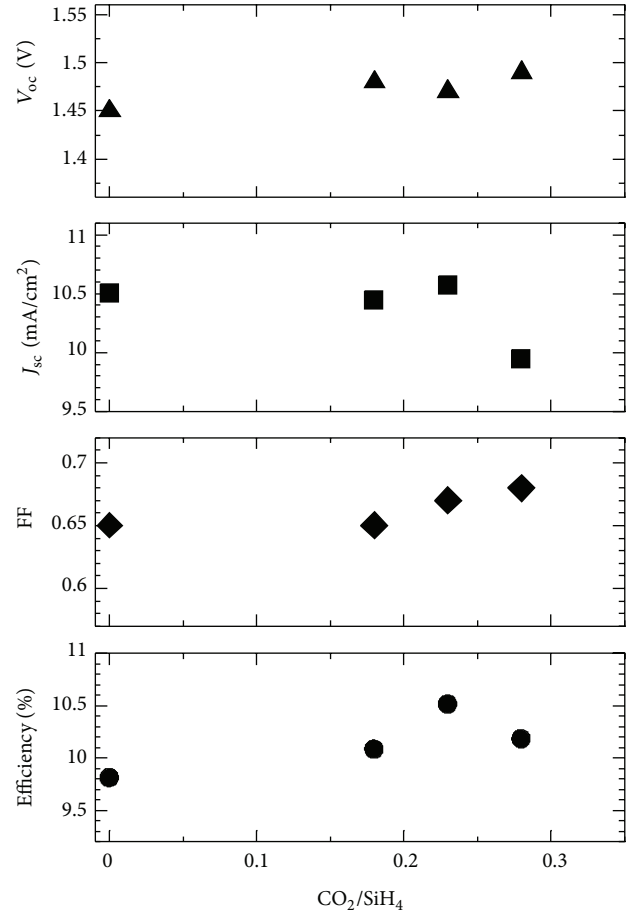


FIGURE 4: Photovoltaic parameters of $\text{a-SiO:H}/\mu\text{c-Si:H}$ micromorph silicon solar cells using n top $\mu\text{c-Si(O):H}$ layer deposited with various CO_2/SiH_2 ratios.

at subcell connection— n top/ p bottom interface. The series resistance (R_s) slightly increased while the shunt resistance (R_{sh}) significantly enhanced from 1500 to 3200 Ω when the CO_2/SiH_4 ratio increased from 0 to 0.28, as shown in Figure 5. The increase of the R_{sh} was supposed to be caused by the better tunnel recombination junction, contributing to the improvement in the FF.

According to the QE results shown in Figure 6, the spectrum response corresponding to the top a-SiO:H cell slightly enhanced while those of the bottom $\mu\text{c-Si:H}$ cell decreased with increasing the CO_2/SiH_2 ratio. This suggested that, besides allowing ohmic and low resistive electrical connection between the two adjacent cells in the $\text{a-SiO:H}/\mu\text{c-Si:H}$ micromorph silicon solar cell, the n top $\mu\text{c-SiO:H}$ film also worked as an intermediate reflector to enhance light scattering, as verified by the increase of the spectrum response corresponding to the top cell. The drop of the J_{sc} at the CO_2/SiH_2 ratio of 0.28 was thought to be due to current mismatch between the top and the bottom cells.

Experimental results have verified the excellent multi-function of the $n \mu\text{c-SiO:H}$ films when they are applied in the $\text{a-SiO:H}/\mu\text{c-Si:H}$ micromorph solar cells, in addition to the conventional $\text{a-Si:H}/\mu\text{c-Si:H}$ structure. Interestingly,

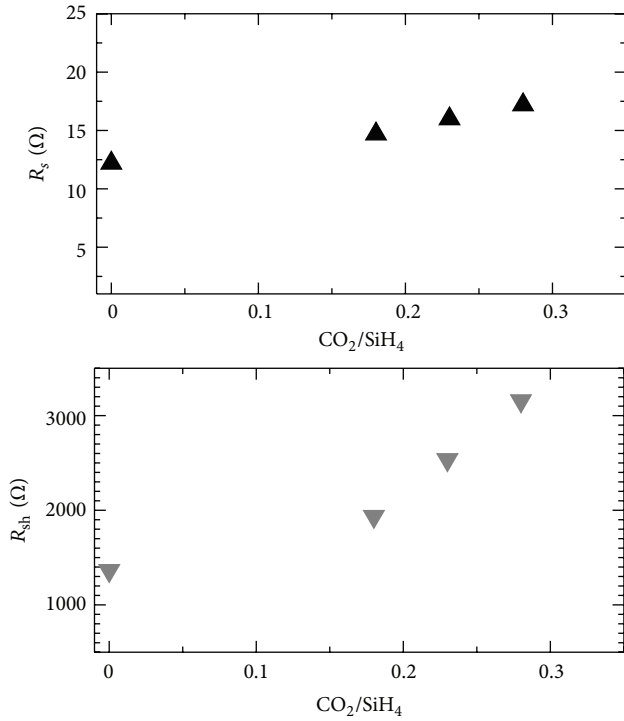


FIGURE 5: R_s and R_{sh} of a-SiO:H/ μ c-Si:H micromorph silicon solar cells using n top μ c-Si(O):H layer deposited with various CO_2/SiH_2 ratios.

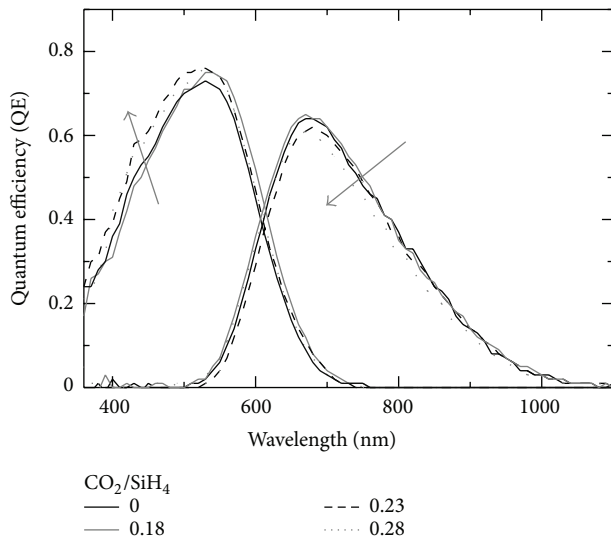


FIGURE 6: QE of a-SiO:H/ μ c-Si:H micromorph silicon solar cells using n top μ c-Si(O):H layer deposited with various CO_2/SiH_2 ratios.

the V_{oc} of our a-SiO:H/ μ c-Si:H micromorph solar cells was found to be high, compared to the conventional micromorph solar cells [7–10], and was further improved when the n top μ c-SiO:H layer was used. The V_{oc} of the conventional cells was about 1.38–1.42 V, while the a-SiO:H/ μ c-Si solar cells showed the V_{oc} as high as 1.47–1.49 V. The multijunction thin film silicon solar cells with high V_{oc} are considered to

have advantage of low temperature coefficients (TC) [15]. Although, at present, the efficiency of the a-SiO:H/ μ c-Si micromorph solar cells is lower than that of the micromorph solar cells using conventional structure, their advantages are expected to become more obvious when the cells are operating in high-temperature environment.

4. Conclusion

We have developed the n-type μ c-SiO:H films and applied them as the n top layer of the a-SiO:H/ μ c-Si:H micromorph silicon solar cells. The solar cells using the n top μ c-SiO:H layer showed higher V_{oc} , J_{sc} , and FF than the cell with the n top μ c-Si:H layer. Enhancements in the cell parameters were supposed to be due to the better tunnel recombination junction, the better continuity of band diagram at the subcell connection, and, equally importantly, the more efficient intermediate reflector, all of which were mainly owing to the n μ c-SiO:H films in the top cell.

Acknowledgment

This work was supported by Cluster and Program Management Office (CPM) of NSTDA, Thailand (P-00-10470).

References

- [1] K. Haga and H. Watanabe, "Optical properties of plasma-deposited silicon-oxygen alloy films," *Japanese Journal of Applied Physics*, vol. 29, no. 4, pp. 636–639, 1990.
- [2] Y. Matsumoto, F. Meléndez, and R. Asomoza, "Plasma CVD deposited p-type silicon oxide wide-bandgap material for solar cells," *Solar Energy Materials and Solar Cells*, vol. 52, no. 3-4, pp. 251–260, 1998.
- [3] P. Buehlmann, J. Bailat, D. Domínguez et al., "In situ silicon oxide based intermediate reflector for thin-film silicon micromorph solar cells," *Applied Physics Letters*, vol. 91, no. 14, Article ID 143505, 2007.
- [4] Y. Matsumoto, V. Sánchez R., and A. Avila G., "Wide optical bandgap p-type μ c-Si:O_x:H prepared by Cat-CVD and comparisons to p-type μ c-Si:H," *Thin Solid Films*, vol. 516, no. 5, pp. 593–596, 2008.
- [5] Y. Matsumoto, F. Meléndez, and R. Asomoza, "Performance of p-type silicon-oxide windows in amorphous silicon solar cell," *Solar Energy Materials and Solar Cells*, vol. 66, no. 1-4, pp. 163–170, 2001.
- [6] A. Sarker and A. K. Barua, "Development of high quality p-type hydrogenated amorphous silicon oxide film and its use in improving the performance of single junction amorphous silicon solar cells," *Japanese Journal of Applied Physics A*, vol. 41, no. 2, pp. 765–769, 2002.
- [7] P. Buehlmann, J. Bailat, D. Domínguez et al., "In situ silicon oxide based intermediate reflector for thin-film silicon micromorph solar cells," *Applied Physics Letters*, vol. 91, no. 14, Article ID 143505, 2007.
- [8] C. Das, A. Lambert, J. Huepkes, W. Reetz, and F. Finger, "A constructive combination of antireflection and intermediate-reflector layers for a-Si μ c-Si thin film solar cells," *Applied Physics Letters*, vol. 92, no. 5, Article ID 053509, 2008.

- [9] A. Lambertz, T. Grundler, and F. Finger, "Hydrogenated amorphous silicon oxide containing a microcrystalline silicon phase and usage as an intermediate reflector in thin-film silicon solar cells," *Journal of Applied Physics*, vol. 109, no. 11, Article ID 113109, 2011.
- [10] V. Smirnov, A. Lambertz, B. Grootoink, R. Carius, and F. Finger, "Microcrystalline silicon oxide ($\mu\text{c-SiO}_x\text{:H}$) alloys: a versatile material for application in thin film silicon single and tandem junction solar cells," *Journal of Non-Crystalline Solids*, vol. 358, no. 17, pp. 1954–1957, 2012.
- [11] S. Kim, H. Lee, J. W. Chung, S. W. Ahn, and H. M. Lee, "n-type microcrystalline silicon oxide layer and its application to high-performance back reflectors in thin-film silicon solar cells," *Current Applied Physics*, vol. 13, pp. 743–747, 2013.
- [12] K. Sriprapha, C. Piromjit, A. Limmanee, and J. Sritharathikhun, "Development of thin film amorphous silicon oxide/microcrystalline silicon double-junction solar cells and their temperature dependence," *Solar Energy Materials and Solar Cells*, vol. 95, no. 1, pp. 115–118, 2011.
- [13] K. Sriprapha, N. Sitthiphol, P. Sangkhawong, V. Sangsuwan, A. Limmanee, and J. Sritharathikhun, "P-Type hydrogenated silicon oxide thin film deposited near amorphous to microcrystalline phase transition and its application to solar cells," *Current Applied Physics*, vol. 11, no. 1, pp. S47–S49, 2011.
- [14] J. Sritharathikhun, A. Moollakorn, T. Trakul, T. Krajangsang, A. Limmanee, and K. Sriprapha, "Optimization of i-a-SiO_x:H absorber layer for thin film siliconsolar cells applications," *Thin Solid Films*. In press.
- [15] K. Sriprapha et al., "Development of thin film a-SiO:H/a-Si:H double-junction solar cells and their temperature dependence," *Thin Solid Films*. In press.
- [16] D. Das, M. Jana, and A. K. Barua, "Characterization of undoped $\mu\text{c-SiO:H}$ films prepared from ($\text{SiH}_4 + \text{CO}_2 + \text{H}_2$)-plasma in RF glow discharge," *Solar Energy Materials and Solar Cells*, vol. 63, no. 3, pp. 285–297, 2000.
- [17] H. Fujiwara, *Spectroscopic Ellipsometry*, Maruzen Publishing, Tokyo, Japan, 2003.
- [18] A. Singh and E. A. Davis, "The a-SiO_x:H_y thin film system I. Structural study by IR spectroscopy," *Journal of Non-Crystalline Solids*, vol. 122, no. 3, pp. 223–232, 1990.